

NASA Contractor Report 189193

Fuel Injector — Air Swirl Characterization Aerothermal Modeling Phase II Final Report — Volume I

M. Nikjooy and H.C. Mongia
*Allison Gas Turbine Division
Indianapolis, Indiana*

and

V.G. McDonell and G.S. Samuelson
*University of California
Irvine, California*

March 1993

Prepared for
Lewis Research Center
Under Contract NAS3-24350

NASA
National Aeronautics and
Space Administration

TABLE OF CONTENTS

<u>Section</u>	<u>Title</u>	<u>Page</u>
VOLUME I		
I	Introduction and Summary	1
1.1	Introduction	1
1.2	Summary	2
II	Selection of Experimental Configuration	5
2.1	Gas Turbine Combustor Flow Field Characteristics	5
2.2	Idealized Combustor Flow Model	7
2.2.1	Measurements of Solid-Particle-Laden Flows	7
2.2.2	Measurements in Sprays	8
2.3	Integrated Modeling/Experimental Approach	11
2.3.1	Air-Swirler Characterization	11
2.3.2	Fuel Injector and Injector Air Characterization	11
2.3.3	Combination Fuel-Injector Air-Swirler Characterization	12
III	Experimental Test Facility and Instrumentation	39
3.1	Test Facility	39
3.1.1	Unconfined Geometries	39
3.1.2	Confined Geometries	39
3.1.3	Positioning	40
3.1.4	Diagnostics Table	41
3.2	Materials for the Dispersed Phase	49
3.2.1	Glass Beads	49
3.3	Flow Systems	53
3.3.1	Air Delivery	53
3.3.2	Glass Bead Delivery	55
3.3.3	Methanol Delivery	56
3.4	Injector/Swirler Assemblies	63
3.4.1	Injector Flow Split Study	63
3.4.2	Nozzle Symmetry Evaluation	63
3.4.3	Aerodynamic Swirler	65
3.4.4	Evolution of Experimental Test Conditions	65
3.5	Diagnostics – Velocity Measurements	88
3.5.1	Laser Anemometry System	88
3.5.2	Seeding Systems	90
3.5.3	Sampling Bias	92
3.5.4	Validation of Velocity Measurement	92
3.6	Diagnostics – Particle Size Measurements	112
3.6.1	Phase Technique – Theory and Limitations	112
3.6.2	Probe Volume Correction	114
3.6.3	Validation of Technique	114
3.7	Discrimination Between Phases	126
3.7.1	Chromatic Discrimination	126
3.7.2	Amplitude Discrimination	126
3.7.3	Physical Discrimination	126
3.8	Vapor Concentration Measurements	133
3.9	Pressure Measurements in Confined Duct	135
3.10	Temperature Measurements	137
3.11	Flow Visualization	138
3.11.1	Photography	138
3.11.2	High Speed Cinematography	138

TABLE OF CONTENTS (cont)

<u>Section</u>	<u>Title</u>	<u>Page</u>
	3.11.3 Shadowgraph Photography	138
3.12	Data Format	140
IV	Data Presentation and Discussion	145
4.1	Data Case Descriptions	145
	4.1.1 Summary of Data Base	145
	4.1.2 Case Description and Geometries	146
	4.1.3 Data Collection and Reporting Protocol	146
	4.1.4 Nomenclature	147
4.2	Single Round Jet	149
	4.2.1 Unconfined Single-Phase Jet – CONF01#2	149
	4.2.2 Unconfined Jet in the Presence of 100-110 Micron Beads at Loading Ratio 0.2 and 1.0 – CONF07#6,#A	150
	4.2.3 Glass Beads in the Unconfined Jet at Loading Ratios of 0.2 and 1.0 – CONF07#5,#3	151
	4.2.4 Effect of Particle Mass Loading in the Unconfined Jet	152
	4.2.5 Unconfined Jet in the Presence of 25 and 105 Micron Beads – CONF13#2	153
	4.2.6 Mixture of 25 and 105 Micron Glass Beads in the Unconfined Jet – CONF13#4	153
	4.2.7 Confined Single Round Jet – CONF04#3	154
	4.2.8 Confined Jet in the Presence of 100-110 Micron Beads at Loading Ratios of 0.2 and 1.0 – CONF10#3,#5	154
	4.2.9 Glass Beads in the Confined Jet at Loading Ratios of 0.2 and 1.0 – CONF10#4,#6	155
	4.2.10 Effect of Particle Mass Loading Ratio in the Confined Jet	155
	4.2.11 Effect of Confinement on Jet	155
	4.2.12 Effect of Confinement on Glass Beads	155
4.3	Single Annular Jet – conf31#2	232
4.4	Single Swirling Annular Jet	239
	4.4.1 Unconfined Case – CONF32#1	239
	4.4.2 Confined Case – CONF34#1	239
	4.4.3 Effect of Swirl	239
	4.4.4 Effect of Confinement	239
4.5	Coaxial Jets	254
	4.5.1 Unconfined Coaxial Jets – CONF02#3	254
	4.5.2 Effect of Coflow on Single Jet	254
	4.5.3 Unconfined Jets in the Presence of 100-110 Micron Beads at Loading Ratio 0.2 – CONF08#1	254
	4.5.4 Glass Beads in the Unconfined Jets at Loading Ratios of 0.2 – CONF08#2	254
	4.5.5 Effect of Coflow on Glass Beads	255
	4.5.6 Confined Single-Phase Coaxial Jets – CONF05#2	255
	4.5.7 Confined Jets in the Presence of 100-110 Micron Beads at Loading Ratios of 0.2 and 1.0 – CONF11#1,#3	255
	4.5.8 Glass Beads in the Confined Jets at Loading Ratios of 0.2 and 1.0 – CONF11#2,#4	255
	4.5.9 Effect of Particle Mass Loading Ratio in the Confined Jet	256
	4.5.10 Effect of Confinement on Coaxial Jets	256
	4.5.11 Effect of Coflow on Confined Jet	256

TABLE OF CONTENTS (cont)

<u>Section</u>	<u>Title</u>	<u>Page</u>
	4.5.12 Effect of Confinement on Glass Beads in Coaxial Jets.....	256
4.6	Coaxial Jets With Swirling Annular Flow	310
	4.6.1 Unconfined Single-Phase Jets – CONF03#3.....	310
	4.6.2 Effect of Swirl on Coflowing Jets.....	310
	4.6.3 Unconfined Swirling Jets in the Presence of 100-110 Micron Beads – CONF09#4	310
	4.6.4 100-110 Micron Glass Beads in the Unconfined Swirling Jets – CONF09#3	310
	4.6.5 Effect of Swirl on 100-110 Micron Glass Beads in Unconfined Flow	310
	4.6.6 100-110 Micron Glass Beads in the Confined Swirling Jet – CONF12#4	310
	4.6.7 Effect of Swirl on Glass Beads in the Confined Flow	311
4.7	Airblast Injector	339
	4.7.1 Confined Single-Phase – CONF22#1	339
	4.7.2 Gas in the Presence of Confined Methanol Spray – CONF28#2.....	339
	4.7.3 Effect of Spray on Gas Phase Behavior in Confined Spray	339
	4.7.4 Confined Methanol Spray – CONF28#1.....	339
4.8	Airblast Injector With Annular Jet.....	356
	4.8.1 Gas in the Presence of Unconfined Methanol Spray – CONF26#2	356
	4.8.2 Unconfined Methanol Spray – CONF26#1	356
	4.8.3 Confined Single-Phase – CONF23#1	356
	4.8.4 Effect of Coflow on Gas Phase	356
	4.8.5 Confined Methanol Spray – CONF29#1.....	356
	4.8.6 Effect of Coflow on Spray	357
	4.8.7 Effect of Confinement on Spray.....	357

VOLUME II

V	Physical and Mathematical Models	391
5.1	Single-Phase Flow Models.....	391
5.2	Two-Phase Flow Models	395
	5.2.1 Dispersed Phase	395
	5.2.2 Continuous Phase	396
5.3	Mathematical Formulation	399
	5.3.1 Discretization	399
	5.3.2 Power-Law Differencing Scheme.....	399
	5.3.3 Flux-Spline Differencing Scheme	399
VI	Model Validation.....	405
6.1	Single Round Jet	405
	6.1.1 Unconfined Single Round Jet	405
	6.1.2 Confined Single Round Jet	421
6.2	Unconfined Single Annular Jet	461
6.3	Single Annular Swirling Jet	491
	6.3.1 Unconfined Annular Swirling Jet.....	491
	6.3.2 Confined Annular Swirling Jet	515
6.4	Coaxial Jets.....	548
	6.4.1 Unconfined Coaxial Jets.....	548
	6.4.1.1 The k- ϵ Turbulence Model	549
	6.4.1.2 The Algebraic Second-Moment Closure.....	553

TABLE OF CONTENTS (cont)

<u>Section</u>	<u>Title</u>	<u>Page</u>
	6.4.2 Confined Coaxial Jets	574
6.5	Unconfined Coaxial Jets with Swirling Annular Flow	608
6.6	Airblast Injector	639
VII	Concluding Remarks and Recommendations	655
7.1	Summary of the Present Work	655
7.2	Recommendation	655
Appendix A	Turbulent Flow Equations for the k- ϵ Model	659
Appendix B	Turbulent Flow Equations for DSM Closure	663
Appendix C	Publications Partially Supported by the List of this Study	669

LIST OF ILLUSTRATIONS

<u>Figure</u>	<u>Title</u>	<u>Page</u>
VOLUME I		
2.1-1	Model predictions of flow field around and within combustor	6
2.3.1-1	The flow and geometry test conditions for air-swirler characterization study	14
2.3.1-2	Numerical predictions of the case $m_p/m_s = 0.01$ for air-swirler characterization study; a) velocity vectors b) streamlines c) radial velocity d) kinetic energy	15
2.3.1-3	Numerical predictions of the case $m_p/m_s = 0.06$ for air-swirler characterization study; a) velocity vectors b) streamlines c) radial velocity d) kinetic energy	16
2.3.2-1	The flow and geometry test conditions for fuel-injector characterization study	17
2.3.2-2	Numerical predictions of single-phase flow for fuel-injector characterization study; a) velocity vectors b) streamlines c) radial velocity	18
2.3.2-3	Numerical predictions of two-phase flow without correction of gas turbulent diffusion due to particles of fuel-injector characterization study	19
2.3.2-4	Numerical predictions of two-phase flow with correction of gas turbulent diffusion due to particles of fuel-injector characterization study	21
2.3.2-5	Numerical predictions of two-phase flow without particle dispersion model for fuel-injector characterization study; a) velocity vectors b) streamlines c) kinetic energy	23
2.3.3-1	The flow and geometry test conditions for combination fuel-injector air-swirler characterization study	25
2.3.3-2	Numerical predictions of single-phase flow ($D_p = 0.394$ in.) for combination fuel injector air-swirler characterization study; a) velocity vectors b) streamlines c) radial velocity d) kinetic energy	26
2.3.3-3	Numerical predictions of two-phase flow ($D_p = 0.394$ in.) without correction of gas turbulent diffusion due to the particles for combination fuel-injector air-swirler characterization study	27
2.3.3-4	Numerical predictions of two-phase flow ($D_p = 0.394$ in.) with correction of gas turbulent diffusion due to the particles for combination fuel-injector air-swirler characterization study	29
2.3.3-5	Numerical predictions of single-phase flow ($D_p = 0.197$ in.) for combination fuel-injector air-swirler characterization study	31
2.3.3-6	Numerical predictions of two-phase flow ($D_p = 0.197$ in.) without correction of gas turbulent diffusion due to the particles for combination fuel-injector air-swirler characterization study	32
2.3.3-7	Numerical predictions of two-phase flow ($D_p = 0.197$ in.) with correction of gas turbulent diffusion due to the particles for combination fuel-injector air-swirler characterization study	34
3.1.1-1	Unconfined geometry	42
3.1.2-1	Confined geometry	43
3.1.2-2	Impact of confined duct on probe volume	44
3.1.2-3	Optical access in the confined duct	45
3.1.2-4	Effect of noise on measurement in the confined duct	46
3.1.3-1	Traverse system	47
3.1.3-2	Positioning interface	48
3.1.4-1	Optical table and diagnostic layout	48
3.2.1-1	Monosized glass beads	51
3.2.1-2	Size class discrimination	52
3.3-1	Flow system	57
3.3.1-1	Unconfined screen air manifold	58

LIST OF ILLUSTRATIONS (cont)

<u>Figure</u>	<u>Title</u>	<u>Page</u>
3.3.1-2	Confined screen air manifold	59
3.3.2-1	Particle-laden jet	60
3.3.2-2	Modified screw feeder	61
3.3.3-1	Hydraulic accumulator.....	62
3.4-1	Ex-Cell-O air-blast atomizer: detail of flow passages through atomizer with outer shroud removed	72
3.4-2	Ex-Cell-O air-blast atomizer: details of atomizer flow passages.....	73
3.4.1-1	Plenum used for flow split study	74
3.4.2-1	Symmetry of mean spray velocity profiles for three atomizers.....	75
3.4.2-2	Symmetry of spray SMD profiles for three atomizers	76
3.4.2-3	Measurement locations for detailed symmetry evaluation.....	77
3.4.2-4	Isopleths of mean axial velocity at an axial location of 50 mm.....	78
3.4.2-5	Profiles of mean azimuthal velocity at an axial location of 50 mm	79
3.4.2-6	Isopleths of volume flux at an axial location of 100 mm	80
3.4.3-1	Aerodynamic swirler	81
3.4.3-2	Symmetry of swirl vanes	82
3.4.4-1	Original geometries.....	83
3.4.4-2	Atomizer shroud evaluation: original cap	87
3.5.1-1	Two-component PDPA transmitter	95
3.5.1-2	Two-component PDPA receiver	95
3.5.1-3	Partitioning of the PDPA receiver lens	96
3.5.1-4	Evaluation of signal filtering.....	97
3.5.1-5	Detail of diffraction grating.....	98
3.5.2-1	Seeders used in the program: nebulizer based	99
3.5.2-2	Seeders used in the program: fluid bed-type	100
3.5.2-3	Fluid bed output rate	101
3.5.2-4	Seed morphology.....	102
3.5.2-5	Example of particle response study	103
3.5.3-1	Example of sampling bias in swirling flow	104
3.5.4-1	Setup of instrument comparison	105
3.5.4-2	Cube plots for sensitivity study results at centerline of free jet.....	106
3.5.4-3	Impact of PMT gain on TSI and PDPA velocity measurement at centerline of free jet	108
3.5.4-4	Impact of frequency shift on TSI and PDPA velocity measurement at centerline of free jet	110
3.6.1-1	Light scattering by a sphere	117
3.6.1-2	Spatial phase shift related to size	118
3.6.2-1	Dependency of probe size on particle size	119
3.6.3-1	Comparison of phase technique to visibility/IV	120
3.6.3-2	Comparison of phase technique to Malvern	121
3.6.3-3	Effect of frequency shift on PDPA and FFT processor measurement of air- assist spray	122
3.6.3-4	Detailed comparison of effect of PMT voltage on uncorrected size distribution measured by PDPA and FFT processor in air-assist spray	124
3.7.3-1	Measurement of seed particles and glass beads in recirculating flow	129
3.7.3-2	Size histograms for two types of seed particles	131
3.7.3-3	Sensitivity of velocity measurements to seed type and sizing enabled/disabled	132
3.8-1	Phase discrimination probe.....	134
3.9-1	Pressure measurement setup	136
3.11.3-1	Shadowgraph setup	139

LIST OF ILLUSTRATIONS (cont)

<u>Figure</u>	<u>Title</u>	<u>Page</u>
4.2.1-1	Geometry utilized for unconfined single round jet	157
4.2.1-2	Radial profiles of gas phase statistics in unconfined single-phase round jet	158
4.2.1-3	Repeatability and sensitivity of measurements in the unconfined single-phase round jet.....	165
4.2.2-1	Radial profiles of gas phase velocity measurements in unconfined round jet laden with 100-110 micron glass beads with a bead to-gas-mass loading ratio of 0.2	168
4.2.2-2	Radial profiles of gas phase velocity measurements in unconfined round jet laden with 100-110 micron glass beads with a bead-to-gas mass loading ratio of 1.0.....	173
4.2.3-1	Radial profiles of particle measurements in unconfined round jet laden with 100-110 micron glass beads with a bead-to-gas mass loading ratio of 0.2 ...	178
4.2.3-2	Radial profiles of particle measurements in unconfined round jet laden with 100-110 micron glass beads with a bead-to-gas mass loading ratio of 1.0 ...	183
4.2.4-1	Comparison of gas phase velocities and shear stress in (1) unconfined single- phase round jet, (2) unconfined round jet laden with 100-110 micron particles at mass loading of 0.2, and (3) unconfined round jet laden with 100-110 micron particles at mass loading ratio of 1.0	188
4.2.4-2	Comparison of particle velocities and data rate in unconfined round jet laden with particles at a mass loading ratio of 0.2 and 1.0	190
4.2.5-1	Radial profiles of gas phase velocity measurements in unconfined round jet laden with equal number of 20-30 micron and 100-110 micron glass beads with a bead-to-gas mass loading ratio of 0.2	192
4.2.6-1	Radial profiles of particle measurements in unconfined round jet laden with equal numbers of 20-30 micron and 100-110 micron glass beads with a bead-to-gas mass loading ratio of 0.2	197
4.2.7-1	Geometry utilized for confined single round jet	202
4.2.7-2	Radial profiles of gas phase statistics in confined single-phase round jet	203
4.2.7-3	Repeatability of measurements of mean and fluctuating axial velocity in the confined single-phase round jet	208
4.2.8-1	Radial profiles of gas phase velocity measurements in confined round jet laden with 100-110 micron glass beads with a bead-to-gas mass loading ratio of 0.2	209
4.2.8-2	Radial profiles of gas phase velocity measurements in confined round jet laden with 100-110 micron glass beads with a bead-to-gas mass loading ratio of 1.0	212
4.2.9-1	Radial profiles of particle measurements in confined round jet laden with 100-110 micron glass beads with a bead-to-gas mass loading ratio of 0.2 ...	217
4.2.9-2	Radial profiles of particle measurements in unconfined round jet laden with 100-110 micron glass beads with a bead-to-gas mass loading ratio of 1.0 ...	220
4.2.10-1	Comparison of gas phase velocities and shear stress in (1) confined single- phase round jet, (2) confined round jet laden with 100-110 micron particles at mass loading of 0.2, and (3) confined round jet laden with 100-110 micron particles at mass loading ratio of 1.0	225
4.2.10-2	Comparison of particle velocities and data rate in confined round jet laden with particles at a mass loading ratio of 0.2 and 1.0	227
4.2.11-1	Comparison of mean and fluctuating axial velocities in the confined and unconfined single-phase round jet	229

LIST OF ILLUSTRATIONS (cont)

<u>Figure</u>	<u>Title</u>	<u>Page</u>
4.2.12-1	Comparison of mean and fluctuating axial velocities and data rates for 100-110 micron beads in the round jet with and without confinement for a bead-to-gas mass flow rate ratio of 1.0	230
4.3-1	Geometry utilized for unconfined single-phase annular jet	233
4.3-2	Radial profiles of gas phase statistics in unconfined single-phase annular jet	234
4.4.1-1	Geometry utilized for unconfined single-phase swirling annular jet	240
4.4.1-2	Radial profiles of gas phase statistics in unconfined single-phase swirling annular jet	241
4.4.2-1	Geometry utilized for confined single-phase swirling annular jet	246
4.4.2-2	Radial profiles of gas phase statistics in confined single-phase swirling annular jet	247
4.4.3-1	Comparison of mean and fluctuating axial velocities in the single-phase unconfined annular jets with and without swirl	252
4.4.4-1	Comparison of mean and fluctuating axial velocities in the single-phase swirling annular jet with and without confinement	253
4.5.1-1	Geometry utilized for unconfined coaxial jets	257
4.5.1-2	Radial profiles of gas phase statistics in the unconfined single-phase coaxial jets	258
4.5.1-3	Assessment of repeatability in the unconfined single-phase coaxial jets	263
4.5.2-1	Comparison of mean and fluctuating axial velocities in unconfined single-phase round and coaxial jets	266
4.5.3-1	Radial profiles of gas phase velocity measurements in unconfined coaxial jets with central jet laden with 100-110 micron glass beads at a bead-to-gas mass loading ratio of 0.2	267
4.5.4-1	Radial profiles of particle measurements in unconfined coaxial jets with central jet laden with 100-110 micron glass beads at a bead-to-gas mass loading ratio of 0.2	272
4.5.5-1	Comparison of mean and fluctuating axial velocities and data rates for 100-110 micron beads in the round jet with and without coflow for a bead-to-gas mass flow rate ratio of 0.2	277
4.5.6-1	Geometry utilized for confined coaxial jets	279
4.5.6-2	Radial profiles of gas phase statistics in the confined single-phase coaxial jets	280
4.5.6-3	Assessment of repeatability of mean and fluctuating axial velocities in confined single-phase coaxial jets	285
4.5.7-1	Radial profiles of gas phase velocity measurements in confined coaxial jets with central jet laden with 100-110 micron glass beads at a bead-to-gas mass loading ratio of 0.2	286
4.5.7-2	Radial profiles of gas phase velocity measurements in confined coaxial jets with central jet laden with 100-110 micron glass beads at a bead-to-gas mass loading ratio of 0.2	289
4.5.8-1	Radial profiles of particle measurements in confined coaxial jets with central jet laden with 100-110 micron glass beads with a bead-to-gas mass loading ratio of 0.2	294
4.5.8-2	Radial profiles of particle measurements in confined coaxial jets with central jet laden with 100-110 micron glass beads with a bead-to-gas mass loading ratio of 1.0	297
4.5.9-1	Comparison of gas phase velocity and shear stress in confined coaxial jets with central jet laden with 100-110 micron particles at two particle-to-gas mass loading ratios	302

LIST OF ILLUSTRATIONS (cont)

<u>Figure</u>	<u>Title</u>	<u>Page</u>
4.5.9-2	Comparison of particle velocity and data rate in confined coaxial jets with central jet laden with 100-110 micron particles at two particle-to-gas mass loading ratios	304
4.5.10-1	Comparison of gas phase mean and fluctuating axial velocities in confined and unconfined single-phase coaxial jets	306
4.5.11-1	Comparison of gas phase mean and fluctuating axial velocities in confined single-phase jets with and without coaxial flow	307
4.5.12-1	Comparison of particle axial velocities and data rate in confined and unconfined coaxial jets with the central jet laden with 100-110 micron particles at a particle-to-gas mass loading ratio of 0.2.....	308
4.6-1	Geometry utilized for unconfined round jet with swirling annular flow	312
4.6.1-1	Radial profiles of gas phase statistics in the unconfined single-phase coaxial jets with swirling annular air	313
4.6.2-1	Comparison of mean and fluctuating axial velocities in unconfined coflowing jets with and without swirling annular air	318
4.6.3-1	Radial profiles of gas phase velocities in the unconfined jet with swirling annular air flow with the central jet laden with 100-110 micron particles in a particle-to-gas mass loading ratio of 0.2	319
4.6.4-1	Radial profiles of particle velocities in the unconfined jet with swirling annular air flow with the central jet laden with 100-110 micron particles in a particle-to-gas mass loading ratio of 0.2	324
4.6.5-1	Comparison of particle velocities and data rate in unconfined flows with the central jet laden with 100-110 micron particles at a particle-to-gas mass loading ratio of 0.2: free jet versus swirling annular coflow	329
4.6.6-1	Geometry utilized for confined round jet with swirling annular air	331
4.6.6-2	Radial profiles of particle measurements in confined coaxial jets with swirling annular air with central jet laden with 100-110 micron particles at a particle-to-gas mass loading ratio of 1.0	332
4.6.7-1	Comparison of particle axial velocity and data rate in confined round jet laden with 100-110 micron particles in a particle-to-gas mass loading of 1.0 with and without swirling annular air	337
4.7.1-1	Geometry utilized for the confined methanol spray	340
4.7.1-2	Radial profiles of gas phase statistics in confined single-phase flow from air-blast injector	341
4.7.2-1	Radial profiles of the gas phase measurements in the confined methanol spray	344
4.7.3-1	Comparison of gas phase measurements in the confined air-blast atomizer flow with and without methanol	349
4.7.4-1	Radial profiles of the droplet measurements in the confined methanol spray	352
4.8.1-1	Geometry utilized for unconfined methanol spray with annular coflow	358
4.8.1-2	Radial profiles of the gas phase measurements in the unconfined methanol spray with annular coflow	359
4.8.2-1	Radial profiles of the droplet measurements in the unconfined methanol spray with annular air	364
4.8.2-2	Comparison of the gas phase and droplet velocities in the unconfined methanol spray with annular coflow	368
4.8.3-1	Geometry utilized for the confined methanol spray with annular coflow	370
4.8.3-2	Radial profiles of the gas phase measurements in the confined methanol spray with annular coflow	371
4.8.4-1	Comparison of gas phase velocities in the confined single-phase flow from the air-blast atomizer with and without coflow	376

LIST OF ILLUSTRATIONS (cont)

<u>Figure</u>	<u>Title</u>	<u>Page</u>
4.8.5-1	Radial profiles of the droplet measurements in the confined methanol spray with annular coflow	379
4.8.6-1	Comparison of droplet measurements in the confined methanol spray with and without coflow	383
4.8.7-1	Comparison of the droplet measurements in the methanol spray with and without confinement	386
VOLUME II		
5.3.1-1	Control volume around the grid point P	402
5.3.3-1	One-dimensional condition	402
6.1.1-1	Test facility: unconfined injector only	409
6.1.1-2	Radial profiles of normalized mean axial velocity, turbulence kinetic energy, and shear stress for the single-phase jet	410
6.1.1-3	Radial profiles of normalized rms velocity components and turbulence kinetic energy for the single-phase jet	411
6.1.1-4	Radial profiles of normalized mean axial velocity, turbulence kinetic energy, and shear stress for the single-phase jet; influence of initial ϵ	412
6.1.1-5	Axial distribution of normalized centerline values of gas mean velocity, and particle mean velocity and number density	413
6.1.1-6	Radial profiles of normalized gas axial velocity and particle axial and radial velocity components, LR = 0.2	414
6.1.1-7	Radial profiles of normalized gas turbulence kinetic energy, shear stress, and axial turbulence intensity, and particle axial turbulence intensity at loading ratio, LR = 0.2	415
6.1.1-8	Radial profiles of rms radial and azimuthal velocity components of gas and particles at loading ratio, LR = 0.2	416
6.1.1-9	Radial profiles of normalized gas axial velocity and particle axial and radial velocity components, LR = 1.0	417
6.1.1-10	Radial profiles of normalized gas turbulence kinetic energy, shear stress, and axial turbulence intensity, and particle axial turbulence intensity at loading ratio, LR = 1.0	418
6.1.1-11	Radial profiles of rms radial and azimuthal velocity components of gas and particles at loading ratio, LR = 1.0	419
6.1.1-12	Effect of single-phase and two-phase turbulence models on gas phase turbulence kinetic energy and shear stress for the two loading ratios, LR = 0.2 and LR = 1.0	420
6.1.2-1	Confined round jet geometrical details	428
6.1.2-2	Confined round jet grid layout	429
6.1.2-3	Confined single round jet inlet condition, single phase	430
6.1.2-4	Comparison of predicted mean axial velocity by k- ϵ model with data	431
6.1.2-5	Comparison of predicted turbulent shear stress by k- ϵ model with data	432
6.1.2-6	Comparison of predicted turbulent kinetic energy by k- ϵ model with data	433
6.1.2-7	Comparison of predicted mean axial velocity by k- ϵ and DSM with data	434
6.1.2-8	Comparison of predicted U velocity by ASM with data	435
6.1.2-9	Comparison of calculated streamwise turbulence intensity by ASM with data	436
6.1.2-10	Comparison of calculated radial turbulence intensity by ASM with data	437
6.1.2-11	Comparison of calculated tangential turbulence intensity by ASM with data	438
6.1.2-12	Comparison of calculated U velocity profiles by DSM and ASM with data	439
6.1.2-13	Comparison of calculated streamwise turbulence intensity by DSM and ASM with data	440

LIST OF ILLUSTRATIONS (cont)

<u>Figure</u>	<u>Title</u>	<u>Page</u>
6.1.2-14	Comparison of calculated radial turbulence intensity by DSM and ASM with data	441
6.1.2-15	Comparison of calculated tangential turbulence intensity by DSM and ASM with data	442
6.1.2-16	Comparison of calculated turbulent shear stress profiles by DSM and ASM with data	443
6.1.2-17	Comparison of calculated k by k- ϵ , ASM, and DSM with data	444
6.1.2-18	Comparison of calculated turbulent shear stress profiles by k- ϵ , ASM, and DSM with data	445
6.1.2-19	Measured profiles for continuous phase at the inlet plane ($x = 4$ mm), particle-laden jet	446
6.1.2-20	Measured profiles for dispersed phase at the inlet plane ($x = 4$ mm), particle-laden jet	447
6.1.2-21	Comparison of predicted gas phase U velocity profiles by DSM and k- ϵ with data, particle-laden jet	448
6.1.2-22	Comparison of predicted gas phase shear stress profiles by DSM and k- ϵ with data, particle-laden jet	449
6.1.2-23	Comparison of predicted gas phase k profiles by DSM and k- ϵ with data, particle-laden jet	450
6.1.2-24	Comparison of predicted gas phase U velocity profiles by ASM and DSM with data, particle-laden jet	451
6.1.2-25	Comparison of calculated gas phase streamwise turbulence intensity profiles by ASM and DSM with data, particle-laden jet	452
6.1.2-26	Comparison of calculated gas phase radial turbulence intensity profiles by ASM and DSM with data, particle-laden jet	453
6.1.2-27	Comparison of calculated gas phase tangential turbulence intensity profiles by ASM and DSM with data, particle-laden jet	454
6.1.2-28	Comparison of calculated gas phase shear stress profiles by ASM and DSM with data, particle-laden jet	455
6.1.2-29	Comparison of calculated dispersed phase axial velocity (U_p) profiles by k- ϵ with data	456
6.1.2-30	Comparison of calculated dispersed phase axial velocity (U_p) profiles by DSM with data	457
6.1.2-31	Comparison of calculated dispersed phase streamwise turbulence intensity by DSM with data	458
6.1.2-32	Comparison of calculated dispersed phase radial turbulence intensity by DSM with data	459
6.1.2-33	Comparison of calculated dispersed phase tangential turbulence intensity by DSM with data	460
6.2-1	Unconfined annular flow configuration	466
6.2-2	Unconfined single annular jet - grid layout.....	467
6.2-3	Unconfined single annular jet inlet conditions	468
6.2-4	Comparison of predicted mean axial velocity by DSM with data	469
6.2-5	Comparison of calculated rms axial velocity profiles by DSM with data	471
6.2-6	Comparison of calculated rms radial velocity profiles by DSM with data	473
6.2-7	Comparison of calculated rms tangential velocity profiles by DSM with data	475
6.2-8	Comparison of calculated turbulent shear stress profiles by DSM with data	477
6.2-9	Comparison of predicted mean axial velocity by k- ϵ model with data.....	479
6.2-10	Comparison of predicted turbulent kinetic energy by k- ϵ model with data	481
6.2-11	Comparison of calculated U velocity by k- ϵ and DSM with data	483

LIST OF ILLUSTRATIONS (cont)

<u>Figure</u>	<u>Title</u>	<u>Page</u>
6.2-12	Comparison of calculated uv profiles by k- ϵ and DSM with data	485
6.2-13	Comparison of calculated U velocity by k- ϵ and DSM with data	487
6.2-14	Comparison of calculated uv profiles by k- ϵ and DSM with data	489
6.3.1-1	Unconfined annular swirling jet geometrical details	496
6.3.1-2	Unconfined annular swirling jet grid layout.....	497
6.1.3-3	Measured profiles at the inlet ($x = 3$ mm)	498
6.3.1-4	Comparison of calculated mean axial velocity by DSM and k- ϵ with data	500
6.3.1-5	Comparison of calculated mean tangential velocity by DSM and k- ϵ with data	501
6.3.1-6	Comparison of calculated axial rms velocity by DSM with data	503
6.3.1-7	Comparison of calculated radial rms velocity by DSM with data	504
6.3.1-8	Comparison of calculated tangential rms velocity by DSM with data	506
6.3.1-9	Comparison of calculated turbulent shear stress profiles by k- ϵ and DSM with data	507
6.3.1-10	Comparison of predicted mean axial velocity by k- ϵ with data	509
6.3.1-11	Comparison of predicted mean tangential velocity by k- ϵ with data	510
6.3.1-12	Comparison of predicted turbulent shear stress with data	512
6.3.1-13	Comparison of predicted turbulent kinetic energy with data	513
6.3.2-1	Confined annular swirling jet - geometrical details	521
6.3.2-2	Confined annular swirling jet grid layout	522
6.3.2-3	Measured profiles at the inlet plane ($x = 4$ mm)	523
6.3.2-4	Staggered arrangement of Reynolds stress components	524
6.3.2-5	Inlet dissipation profiles	524
6.3.2-6	Comparison of calculated mean axial velocity by k- ϵ model using various ϵ_{in}	525
6.3.2-7	Comparison of calculated mean tangential velocity by k- ϵ model using various ϵ_{in}	527
6.3.2-8	Comparison of calculated turbulent kinetic energy by k- ϵ model using various ϵ_{in}	529
6.3.2-9	Comparison of calculated turbulent shear stress by k- ϵ model using various ϵ_{in} ...	531
6.3.2-10	Comparison of calculated mean axial velocity by DSM using various ϵ_{in}	533
6.3.2-11	Comparison of calculated mean tangential velocity by DSM using various ϵ_{in}	534
6.3.2-12	Comparison of calculated streamwise turbulence intensity by DSM using various ϵ_{in}	535
6.3.2-13	Comparison of calculated turbulent shear stress by DSM using various ϵ_{in}	536
6.3.2-14	Comparison of calculated mean axial velocity using various ϕ , models with data	537
6.3.2-15	Comparison of calculated mean tangential velocity using various ϕ , models with data	538
6.3.2-16	Comparison of calculated U velocity with IP and QI models for confined annular swirling jet	539
6.3.2-17	Comparison of calculated uv profiles with data	540
6.3.2-18	Comparison of calculated streamwise turbulence intensity with measurements	541
6.3.2-19	Comparison of calculated radial turbulence intensity with measurements	542
6.3.2-20	Comparison of the predicted mean and turbulence quantities by ASM and DSM with data	543
6.3.2-21	Comparison of the predicted mean and turbulence quantities by ASM and DSM with data	544
6.3.2-22	Comparison of the predicted mean and turbulence quantities by ASM and DSM with data	545
6.3.2-23	Comparison of the predicted mean and turbulence quantities by ASM and DSM with data	546

LIST OF ILLUSTRATIONS (cont)

<u>Figure</u>	<u>Title</u>	<u>Page</u>
6.3.2-24	Comparison of the predicted mean and turbulence quantities by ASM and DSM with data	547
6.4.1-1	Unconfined coaxial jets geometry	556
6.4.1-2	Measured profiles at the inlet plane ($x = 2$ mm)	557
6.4.1-3	Unconfined coaxial jets grid layout	558
6.4.1-4	Comparison of measurements with mean axial velocity calculations for unconfined coaxial jets	559
6.4.1-5	Comparison of measurements with turbulent kinetic energy calculations	560
6.4.1-6	Inlet dissipation rate profiles	561
6.4.1-7	Profiles of mean axial velocity and turbulent kinetic energy using different inlet turbulent dissipation rate	562
6.4.1-8	Comparison of the k - ϵ and the ASM predictions of axial velocity using flux-spline with measurements	563
6.4.1-9	Comparison of the ASM prediction of turbulent shear stress with data	564
6.4.1-10	Comparison of the ASM prediction of axial normal stress with data	565
6.4.1-11	Comparison of the ASM prediction of radial normal stress with data	566
6.4.1-12	Comparison of the ASM prediction of tangential normal stress with data	567
6.4.1-13	Radial profiles of normalized mean axial velocity, turbulent kinetic energy, and shear stress for the single-phase coaxial jets	568
6.4.1-14	Radial profile of normalized rms velocity components for the single-phase coaxial jets	569
6.4.1-15	Radial profiles of normalized mean axial velocity, turbulent kinetic energy, and shear stress for the particle-laden coaxial jets	570
6.4.1-16	Measurements of rms gas velocity component for the particle-laden coaxial jets ...	571
6.4.1-17	Radial profiles of normalized particle axial velocity	572
6.4.1-18	Radial profiles of rms of particle velocity components	573
6.4.2-1	Confined coaxial jets – geometrical details	578
6.4.2-2	Confined coaxial jets – grid layout	579
6.4.2-3	Measured profiles at the inlet plane ($x = 4$ mm)	580
6.4.2-4	Comparison of predicted mean axial velocity by k - ϵ model with data	581
6.4.2-5	Comparison of predicted turbulent shear stress by k - ϵ model with data	582
6.4.2-6	Comparison of predicted turbulent kinetic energy by k - ϵ model with data	583
6.4.2-7	Comparison of predicted mean axial velocity by DSM with data	584
6.4.2-8	Comparison of predicted axial rms velocity by DSM with data	585
6.4.2-9	Comparison of predicted radial rms velocity by DSM with data	586
6.4.2-10	Comparison of predicted tangential rms velocity by DSM with data	587
6.4.2-11	Comparison of predicted turbulent shear stress by DSM with data	588
6.4.2-12	Comparison of predicted mean axial velocity by DSM and ASM with data	589
6.4.2-13	Comparison of predicted axial rms velocity by DSM and ASM with data	590
6.4.2-14	Comparison of predicted radial rms velocity by DSM and ASM with data	591
6.4.2-15	Comparison of predicted tangential rms velocity by DSM and ASM with data	592
6.4.2-16	Comparison of predicted turbulent shear stress profiles by DSM and ASM with data	593
6.4.2-17	Comparison of predicted turbulent kinetic energy by k - ϵ , DSM, and ASM with data	594
6.4.2-18	Measured profiles at the inlet plane ($x = 4$ mm)	595
6.4.2-19	Comparison of calculated normalized mean axial velocity of the continuous phase by DSM with data	597
6.4.2-20	Comparison of calculated normalized streamwise turbulence intensity of continuous phase by DSM with data	598

LIST OF ILLUSTRATIONS (cont)

<u>Figure</u>	<u>Title</u>	<u>Page</u>
6.4.2-21	Comparison of calculated normalized radial turbulence intensity of continuous phase by DSM with data	599
6.4.2-22	Comparison of calculated normalized tangential turbulence intensity of continuous phase by DSM with data	600
6.4.2-23	Comparison of calculated normalized shear stress of continuous phase by DSM with data	601
6.4.2-24	Comparison of calculated normalized mean axial velocity of dispersed phase (U_p) by DSM with data	602
6.4.2-25	Comparison of calculated normalized mean radial velocity of dispersed phase (V_p) by DSM with data	603
6.4.2-26	Comparison of calculated normalized streamwise turbulence intensity of dispersed phase by DSM with data	604
6.4.2-27	Comparison of calculated normalized radial turbulence intensity of dispersed phase by DSM with data	605
6.4.2-28	Comparison of calculated normalized tangential turbulence intensity of dispersed phase by DSM with data	606
6.4.2-29	Number density distribution	607
6.5-1	Unconfined axisymmetric swirling coaxial jets geometry	613
6.5-2	Unconfined swirling coaxial jets grid layout	614
6.5-3	Measured profiles at the inlet plane ($x = 4$ mm)	615
6.5-4	Comparison of calculated mean axial velocity by k- ϵ model with data	617
6.5-5	Comparison of calculated mean tangential velocity by k- ϵ model with data	619
6.5-6	Comparison of predicted turbulent kinetic energy by k- ϵ model with measurement	621
6.5-7	Comparison of predicted turbulent shear stress by k- ϵ model with data	623
6.5-8	Comparison of calculated mean axial velocity by k- ϵ and DSM with data	625
6.5-9	Comparison of calculated mean tangential velocity by k- ϵ and DSM with data	627
6.5-10	Comparison of calculated axial rms velocity component by DSM with data	629
6.5-11	Comparison of calculated radial rms velocity component by DSM with data	631
6.5-12	Comparison of calculated tangential rms velocity component by DSM with data	633
6.5-13	Comparison of calculated uv profiles by k- ϵ and DSM with data	635
6.5-14	Comparison of calculated uw profiles by DSM with data	637
6.6-1	Airblast injector flow configuration	643
6.6-2	Airblast injector flow inlet conditions	644
6.6-3	Airblast injector flow grid layout	645
6.6-4	Comparison of calculated mean axial velocity profiles by DSM with data	646
6.6-5	Comparison of calculated rms axial velocity profiles by DSM with data	647
6.6-6	Comparison of calculated rms radial velocity profiles by DSM with data	648
6.6-7	Comparison of calculated rms tangential velocity profiles by DSM with data	649
6.6-8	Comparison of calculated shear stress profiles by DSM with data	650
6.6-9	Comparison of calculated mean axial velocity profiles by k- ϵ with data	651
6.6-10	Comparison of calculated turbulent kinetic energy profiles by k- ϵ with data	652
6.6-11	Comparison of calculated turbulent shear stress profiles by k- ϵ with data	653

LIST OF TABLES

<u>Table</u>	<u>Title</u>	<u>Page</u>
VOLUME I		
3.3-I	Flow system circuit specification	54
3.4-I	Results of flow split test	64
3.4-II	Initial test conditions	66
3.4-III	Impingement testing results	68
3.4-IV	Initial test conditions and changes made	70
3.4-V	Test conditions based on screening tests	71
3.5-I	Milestones in development of UCICL PDPA system	91
3.7-I	Verification of discrimination in the free jet	128
4.1-I	Case numbers used in the tabulated results	145
4.1-II	Quantities measured and diagnostics employed	146
VOLUME II		
5.1-I	Values of constants in the k-e model	392
5.1-II	Values of constants in the ASM and DSM closures	393
6.1-I	Experimental flow conditions at 0.04D downstream of pipe exit	406
6.1-II	Confined single jet experimental flow conditions	421
6.1-III	Confined single jet experimental flow conditions	423
6.2-I	Unconfined single annular jet experimental flow conditions	461
6.2-II	Single annular jet grid definition	462
6.3-I	Unconfined annular swirling jet test configuration	491
6.3-II	Unconfined annular swirling jet grid definition	492
6.3-III	Confined annular swirling jet test configurations	515
6.3-IV	Confined annular swirling jet grid definition	516
6.4-I	Unconfined coaxial jets experimental conditions at 2 mm downstream of pipe exit	548
6.4-II	Confined coaxial jets grid definition	550
6.4-III	Confined coaxial jets experimental conditions at 4 mm downstream of nozzle exit	574
6.5-I	Unconfined swirling coaxial jets experimental conditions	608
6.5-II	Unconfined swirling coaxial jets grid definition	609
6.6-I	Airblast injector flow grid definition	640

TABLE OF CONTENTS

<u>Section</u>	<u>Title</u>	<u>Page</u>
I	Introduction and Summary	1
1.1	Introduction	1
1.2	Summary	2

I. INTRODUCTION AND SUMMARY

1.1 INTRODUCTION

Combustor liner durability is one of the major challenges in high pressure ratio turbopropulsion engines. To resolve conflicting combustor performance requirements along with enhanced structural durability in a cost-effective manner, conventional (empirical) combustor design techniques need to be complemented by multidimensional aerothermal analysis.

To improve predictive capabilities of aerothermal models, NASA Lewis Research Center sponsored Phase I aerothermal modeling activities (Sturgess, 1983; Kenworthy et al, 1983; Srinivasam et al, 1983*) to assess current state-of-the-art numerical schemes and physical models. The main objectives of aerothermal modeling Phase II are

1. Develop advanced numerical schemes.
2. Collect benchmark quality experimental data to quantify interaction between dome swirlers and primary jets.
3. Collect benchmark quality data for fuel nozzles and their interaction with dome swirlers.
4. Use advanced numerics and benchmark quality data to validate advanced aerothermal models.

Two advanced numerical schemes were developed by Karki et al (1988) under NASA HOST (Hot-Section Technology) sponsorship. The experimental activities and model validation efforts for swirler-jet interaction were conducted jointly at Purdue University and Allison Gas Turbine Division of General Motors Corporation (Nikjooy et al, 1992). This report summarizes a joint Allison/University of California at Irvine (UCI) effort on benchmark quality data and model validation for nozzle-swirler interaction for an idealized nonreacting primary zone. The report consists of seven sections, including Section I, and three appendices.

In Section II an overview of gas turbine combustor flowfield characteristics is presented. This is followed by a description of idealized combustor flow model and an explanation of integrated modeling/experimental approach.

Section III presents the details of the experimental rig and instrumentation. This chapter describes the test facility, flow systems, and various measurement techniques for single- and two-phase flows. Finally, flow visualization, instrumentation, and data reduction results are presented.

In Section IV the experimental data are presented and discussed. This includes dome annular jets, primary jets, and dome annular jets and primary jets.

In Section V the problem of calculating turbulent flows is posed more precisely by introducing and discussing the averaged equations governing the mean flow quantities. The appearance of turbulent transport terms in these equations makes apparent the necessity of introducing turbulence models. The models are discussed in order of increasing complexity. The details of the solution procedure adopted for the highly coupled and nonlinear governing equations are explained next.

In Section VI the computational results are compared with experimental data. The results are presented for the standard k- ϵ model, algebraic second-moment (ASM) closure, and differential second-moment (DSM) closure.

Finally, Section VII summarizes the main conclusions that emerged from this study and puts forward some recommendations for future work.

* References for Section I are listed at the end of the section.

1.2 SUMMARY

A joint analytical/experimental investigation was conducted to provide benchmark quality data and assess state-of-the-art turbulence and spray dynamics models that can be used to quantify the interaction between fuel nozzle and dome swirlers. After taking into consideration a number of often conflicting requirements, an axisymmetric test configuration was defined jointly by Allison Gas Turbine and the Combustion Laboratory of UCI.

Benchmark quality data were taken to quantify effects of confinement and the pressure of glass beads on the following configurations

- single round jet
- single annular jet
- single swirling annular jet
- coaxial jets
- coaxial jets with swirling annular flow

Benchmark quality data were also obtained for a practical prefilming airblast nozzle and its interaction with an annular jet.

Flow field predictions were also obtained using the three levels of turbulence models, namely $k-\epsilon$, ASM, and DSM closure. The modeled conservation equations were based on an Eulerian approach for the gas (continuous) phase and a stochastic-Lagrangian approach for the dispersed (discrete) phase. In order to reduce the effects of numerical (false) diffusion on the predicted results, a higher order numerical scheme, namely the flux-spline differencing scheme, was employed.

REFERENCES

- Karki, K. C., Patankar, S. V., Runchal, A. K., and Mongia, H. C., 1988, "Improved Numerical Methods for Turbulent Viscous Recirculating Flows," Aerothermal Modeling Phase II Final Report, NASA CR-182169.
- Kenworthy, M. J., Correa, S. M., and Burrus, D. L., 1983, "Aerothermal Modeling: Phase I Final Report - Volume 1 Model Assessment," NASA CR-168296.
- Nikjooy, M., Mongia, H. C., Sullivan, J. P., and Murthy, S.N.B., 1992, "Flow Interaction Experiment Aerothermal Modeling Phase II Final Report," NASA CR-189192.
- Srinivasan, R., Reynolds, R., Ball, I., Berry, R., Johnson, K., and Mongia, H. C., 1983, "Aerothermal Modeling Program: Phase I Final Report," NASA CR-168243.
- Sturgess, G. J., 1983, "Aerothermal Modeling: Phase I Final Report," NASA CR-168202.

TABLE OF CONTENTS

<u>Section</u>	<u>Title</u>	<u>Page</u>
II	Selection of Experimental Configuration.....	5
2.1	Gas Turbine Combustor Flow Field Characteristics	5
2.2	Idealized Combustor Flow Model	7
2.2.1	Measurements of Solid-Particle-Laden Flows	7
2.2.2	Measurements in Sprays.....	8
2.3	Integrated Modeling/Experimental Approach	11
2.3.1	Air-Swirler Characterization.....	11
2.3.2	Fuel Injector and Injector Air Characterization	11
2.3.3	Combination Fuel-Injector Air-Swirler Characterization	12

II. SELECTION OF EXPERIMENTAL CONFIGURATION

2.1 GAS TURBINE COMBUSTOR FLOW FIELD CHARACTERISTICS

Gas turbine combustion systems need to be designed and developed to meet many mutually conflicting design requirements, including high combustion efficiency over a wide operating envelope and low NO_x emissions, low smoke and low lean flame stability limits and good starting characteristics, low combustion system pressure loss, low pattern factor, and sufficient cooling air to maintain low wall temperature levels and gradients commensurate with structural durability. The flow field around and within the combustor liner (Figure 2.1-1^{*}) is quite complex in that it includes swirl, regions of recirculation, field injection, atomization, fuel evaporation, mixing, turbulent combustion, soot formation/oxidation, and convective and radiative heat transfer processes. The phenomenological understanding of these processes is not well established, and the relevant nonlinear coupled transport equations are difficult to solve.

The combustor design and development process has been empirically based with limited help from multidimensional calculations. A number of correlations have been used by combustor designers to help during the design and development activities. Many researchers (Lefebvre, 1984 and 1985; Plee and Mellor, 1978 and 1979[†]) have proposed semiempirical correlations for gaseous emissions, smoke, lean blowout, ignition, pattern factor, and combustion efficiency. Professors Lefebvre and Mellor have developed very useful correlations that can be used for scaleup, for data correlations, and for providing some insight. These correlations or their variants are being used by the gas turbine industry (Steele et al, 1987; Rizk and Mongia, 1989).

The empirical/analytical combustor design methodology introduced by Mongia and Smith (1978) has been used for designing a number of gas turbine combustors (Mongia, 1982; Mongia et al, 1986). The multidimensional calculations provide a good understanding of combustor internal flow field and therefore can be used for guiding a combustor design process. However, because of incomplete understanding of the various combustion processes and numerical diffusion, the three-dimensional calculations for practical gas turbine combustors cannot be considered quantitatively accurate (Srinivasan et al, 1983; Kenworthy et al, 1983; Sturgess, 1983). Some progress is being made in further improving the numerical methods (Karki and Mongia, 1989), however more effort is needed to achieve the capability required for accurately predicting combustor performance parameters including radial profile, combustion efficiency, smoke and gaseous emissions, and wall temperature levels and gradients.

Although encouraging qualitative comparisons between data and calculations were achieved for the practical combustors (Rizk and Mongia, 1991), it became quite clear that a significantly increased level of effort is required to achieve the model accuracy required for providing definitive guidance during design process. Moreover, each important process of combustion (e.g., turbulence, kinetics, turbulence/kinetic interaction, spray, etc) should be investigated separately and in combination so as to improve fundamental understanding. Model calculations were, therefore, performed for existing data from simple to complex flow under HOST sponsorship (Srinivasan et al, 1983) and the following main conclusions were made

1. Improve phenomenological understanding of nonreacting flows relevant to those encountered in gas turbine combustors.
2. Make benchmark quality measurements in critical areas of interest.
3. Undertake a systematic model validation effort to identify areas of further improvement.

^{*} Figures for Section II appear at the end of each subsection. The figure number identifies the subsection in which the figure is discussed.

[†] References for Section II are listed at the end of the section.

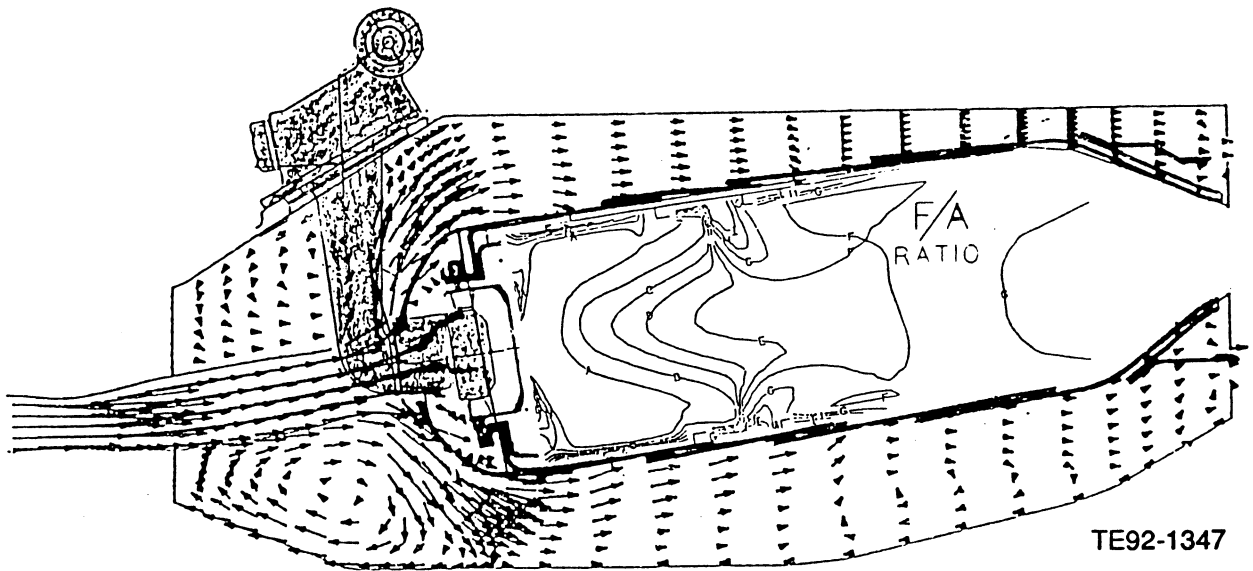


Figure 2.1-1. Model predictions of flow field around and within combustor.

2.2 IDEALIZED COMBUSTOR FLOW MODEL

Measurements in sprays present formidable experimental difficulties. Aside from the dense spray region near the injector, which is almost intractable, the dilute portions of the spray consist of drops of various sizes traveling at various velocities and angles of flight. These drops interact with the turbulent structure of the gas phase and this interaction controls the turbulent mixing evaporation and combustion processes in the spray. At any given point in the spray, both gas-phase properties (mean and fluctuating velocities, concentrations and temperatures, etc) and liquid-phase properties (drop size, velocities, liquid flux, etc) need to be measured to validate spray models. Moreover, initial conditions of these properties, which involve measurements in the dense spray regions, are needed as input for the separated flow category of spray models.

In the following, measurements in solid-particle-laden jets (nonevaporating) are first considered. Such flows have experimental advantages because they are amenable to detailed measurements of flow structure. These data are also useful to evaluate the hydrodynamic aspects of spray models. Recent measurements of sprays are then discussed, highlighting the data which have the potential for evaluating separated flow models.

2.2.1 Measurements of Solid-Particle-Laden Flows

Yuu et al (1978) report measurements in an air jet containing monodispersed particles (20 micron) injected into still air. Measurements were made of mean gas velocities and particle concentrations. Particle quantities were measured using an isokinetic sampling tube. McComb and Salih (1977 and 1978) reported measurements for a gas jet with small particles of 2.3 and 5.7 micron diameter. The particle concentration was studied using laser Doppler anemometer (LDA) techniques. The smaller particles act nearly like tracer particles while the flow in this case approaches the locally homogeneous model limit.

The measurements of both Yuu et al and McComb and Salih were limited to very low particle loadings. This implies that while gas flow influences particle dispersion, the effect of the particles on the structure of the gas flow was small. Measurements at relatively high particle loading have been reported by Loats and Frishman (1970) and Levy and Lockwood (1981). Significant effects of particles on the structure of the gas phase were observed in these experiments.

Elghobashi and his coworkers (Modarress et al, 1982 and 1983) also present measurements in particle-laden jets, with particle size of 50 and 200 microns. In contrast to the other measurements discussed above, they provided information of initial conditions of both phases, although not in great detail. Profiles of mean and fluctuating velocities of both phases and Reynolds stress of gas phase were reported at an axial location of 20 injector diameters downstream. Their study shows that the expansion rate of a two-phase jet is smaller than that of a single-phase jet and that velocity fluctuations decrease as particle loading increases.

Shuen et al (1985) have reported measurements in particle-laden jets. Properties were carefully characterized so that the measurements could be employed to evaluate separated flow models at the injector exit. The structure measurements included mean and fluctuating velocities of both phases, gas-phase Reynolds stress, and particle mass fluxes. Their study shows that effects of particle dispersion are important under their test conditions.

Bulzan (1988) conducted both experimental and computational studies to investigate weakly swirling, particle-laden turbulent flow. In order to establish baseline data for the particle-laden jets, single-phase flow measurements with swirl numbers ranging from 0 to 0.33 were performed. Experiments were also conducted for turbulent jet flow of air with glass beads. The beads' diameters were 39 microns and were injected with a mass loading ratio of 0.2 (the ratio being the mass flow rate of particles per unit mass flow rate of air). Predictions were obtained using the standard k- ϵ model with curvature correction for continuous phase and three different methods, namely, locally homogenous flow (LHF), deterministic sepa-

rated flow (DSF), and stochastic separated flow (SSF) using the Lagrangian technique for dispersed phase.

Hardalupas et al (1989) conducted an experimental study to quantify the velocity and flux characteristics of the spherical glass beads and of the gas phase in the presence of the beads as a function of bead diameter and of the mass loading ratio. The measurements were taken for the velocity and flux of particles with nominal diameters of 200, 80, and 40 microns in a round, unconfined air jet. The presence of the particle phase in a free jet of air causes reduction of the rate of the axial gas velocity and of the jet radial spread because of momentum transfer from the discrete to the gaseous phase. The axial turbulence intensity of the glass beads and the gas phase were comparable and both decreased with increasing loading ratio and the rate of spread of the jet increased with an increasing loading ratio.

2.2.2 Measurements in Sprays

There have been several studies conducted on the structure of combustng sprays (Faeth, 1979 and 1983; Chigier, 1977; Gosman and Johns, 1980; El Banhawy and Whitelaw, 1980 and 1982; Mao et al, 1980 and 1986; Onuma and Ogassaare, 1975 and 1977; Chigier and Roett, 1972; McCreath and Chigier, 1973; Hutchinson et al, 1977; Fonti et al, 1979). It was often concluded that the liquid-fuel spray feeds a diffusion-type flame surrounding a region of reverse flow and that drop evaporation is the controlling mechanism in the combustion process. Most of the studies also revealed that an increase in mean drop diameter was associated with a reduction in combustion intensity at the region immediately downstream of the fuel injector and, in particular, at large radii. The extent of this effect was found to increase when inlet swirl number decreases.

The measurements of gas-phase properties and overall flame structures abound in combustng spray studies. However, the droplet properties at the nozzle exit, i.e., velocity, size, and concentration, were absent from nearly all existing measurement, until recently. With this vital information provided by recent experiments, no real progress can be achieved in the development and evaluation of combustng spray models.

Popper et al (1974) present measurements in a nonevaporating turbulent jet. The motion of oil droplets (diameter less than 50 micron) in a round turbulent air jet injected from a 25 mm diameter nozzle was studied by means of an laser Doppler velocimeter (LDV). Droplet sizes were not accurately determined, the loading of the dispersed phase was extremely low, and only mean velocities of the two phases were recorded. Therefore, this study does not permit complete evaluation of spray models.

Onuma and Ogassaare (1975 and 1977) used flow perturbing probes (e.g., thermocouple, pitot tube, emissions sampling probe, etc) to conduct a phenomological investigation on the combustion of kerosene and heavy fuel from an air atomizing injector. They concluded that most of the droplets did not burn individually. The vapor cloud from the droplets burned as turbulent diffusion flame.

Yule et al (1982) present measurements in nonevaporating and evaporating fuel sprays at different conditions. A twin-fluid atomized kerosene spray was injected into a coflowing secondary stream of air which could be preheated. Information on drop sizes and mean drop and gas velocities were provided. However, all the spray conditions studied involved very small drops, e.g., the mass mean droplet diameters were 10-30 microns in the major portion of the spray. Hence, it could be assumed that the droplets closely follow the local gas-flow field after their initial acceleration. This condition does not adequately represent a practical spray where appreciable slip between the large drops and the gas phase can exist even far downstream.

Shearer et al (1979) present measurements of the structure of an evaporating Freon-11 spray having approximately 30 micron Sauter mean diameter (SMD). However, the spray model that was examined involved application of the locally homogeneous flow (LHF) approximation which only precisely represents a spray consisting of infinitely small drops. Predictions of the LHF model overestimated the rate of

development of the spray, indicating the need for a separated flow treatment of practical spray processes. Since an LHF model was evaluated in the study, no attempt was made to measure individual drop velocities or investigate the evaluation of drop sizes, which are important factors during evaluation of separated flow models.

Tishkoff et al (1982) have reported measurements for evaporating sprays. The system studied was an n-heptane spray from a solid cone atomizer which was injected into a low velocity, coaxial flow of air. The spray plume shape was studied using photographic, shadowgraph, and light-scattering techniques. In addition, droplet size distributions, liquid-phase volume fractions, and vapor concentration measurements were also made at two axial locations.

As an extension of the same study, Tishkoff (1982) measured correlations of drop size and velocity using an imaging technique. However, initial drop velocities and sizes for the injected liquid were not measured. In both studies, gas-phase mean and turbulent velocities were not measured; therefore, neither the overall rate of development of the spray nor the turbulent dispersion and evaporation of drops can be definitely assessed.

Spray characteristics including droplet size and velocity distributions can have profound effects on flame structure (Styles and Chigier, 1977) and so does the surrounding air jet velocity (Miutani et al, 1977). Although most of these measurements (Faeth, 1979 and 1983; Chigier, 1977; Gosman and Johns, 1980; El Banhawy and Whitelaw, 1980 and 1982; Mao et al, 1980; Onuma and Ogassaare, 1975 and 1977; Tishkoff, 1982; Chigier and Roett, 1972; McCreath and Chigier, 1973; Hutchinson et al, 1977; Fonti et al, 1979; Popper et al, 1974; Yule et al, 1982; Shearer et al, 1979; Tishkoff et al, 1982; Styles and Chigier, 1977; Miutani et al, 1977) improved the fundamental understanding of spray flow interaction, the available data did not provide the detailed information needed for validation of spray models.

Foster et al (1991) studied the dispersion and evaporation of liquid droplets in nonisothermal, turbulent flow fields. In their investigations, an ambient temperature airstream was seeded dilutely with water droplets and brought into contact with a heated stream of air at a higher velocity in a two-dimensional mixing layer configuration. Foster et al applied measurement techniques based on light attenuation and scattering to unveil some of the qualitative features of dispersion and evaporation.

Brena de la Rosa et al (1992) investigated the behavior and structure of a liquid spray immersed in a strong swirling field. They measured the properties of the dispersed phase, such as velocity and size distribution, as well as the mean velocity and turbulence properties for the gas phase.

Chehroudi and Ghaffarpour (1991 and 1992) studied a hollow-cone spray generated by a pressure-swirl fuel nozzle. A phase Doppler particle analyzer was used to measure drop size, drop velocity, and size distribution. Hassa et al (1992) also utilized a research airblast atomizer/combustion chamber configuration to measure gas and drop velocities in the confined swirling isothermal flow for the validation of a mathematical model of two phase flows in a gas turbine combustor.

Zurlo et al (1991) measured the spatial distribution of droplet mean size and number density from a hollow-cone kerosene spray. They carried out the measurement using three different droplet sizing techniques, ensemble scattering/polarization ratio, phase/Doppler interferometry, and light intensity deconvolution. Fairfield et al (1992) also examined the effect of swirl on droplet transport processes in a pressure-atomized, hollow-cone kerosene spray injecting into coflowing nonswirling and swirling air flow fields. An ensemble light scattering/polarization ratio technique was applied to measure the local values of droplet mean size and number density in dense regions of the spray. Measurement of droplet size and velocity distribution was carried out using a phase Doppler interferometer.

Wang et al (1991) examined droplet dynamics of a model combustor swirl cup in the absence of reaction. Droplet axial, radial, and tangential velocities, as well as size, were measured using phase Doppler interferometry. Wang et al (1992) investigated the effect of scale on the behavior of the continuous phase and

droplets by comparing the continuous phase velocity and droplet size and velocity at geometrically analogous positions.

The dispersed-phase structure of the dense spray was studied by Tseng et al (1992) for atomization break up conditions. They investigated the break up of water jets in still air at various ambient pressures. Drop sizes and velocities and liquid volume fractions and fluxes were measured using holography.

Solomon et al (1984a and 1984b) present some comprehensive measurements of the detail structure of nonevaporating and evaporating sprays. Both fine and coarse sprays were studied, with diameters of 30 and 87 microns for nonevaporating sprays and 31 and 58 microns for evaporating sprays. Experiments considered axisymmetric sprays produced by an air-atomizing injector directed vertically downward in still air. The spray structure measurements included mean and fluctuating gas velocities and Reynolds stresses, drop sizes, and velocities, mean liquid fluxes, and mean gas-phase temperatures. Initial conditions were carefully characterized to provide an appropriate data base for the evaluation of spray models. These data have been employed for the evaluation of typical spray models and the results indicate that the effects of turbulence on drop dispersion and evaporation are important.

The brief review above indicates that a few measurements useful for evaluation of noncombusting spray models are available. The majority of these data involved oversimplified flow configuration, i.e., axisymmetric jet flows with no zones of recirculation. This arrangement has certain advantages in terms of experimental effort to map the flow field and in obtaining accurate numerical solutions with mathematical models. In a gas turbine combustor, however, spray structure is significantly influenced by swirl, recirculation, streamline curvature, and secondary jets. A decisive evaluation of practical spray models would have to address the aerodynamic effects of these complications. Unfortunately, measurements which provide detail structure information of both phases as well as injector properties are not available in the literature.

Spray model evaluation has generally lagged behind model development due to the lack of systematic measurements in sprays. There has been no comprehensive study of the structure of evaporating sprays in practical gas turbine combustor geometries. New measurements of this kind are most urgently needed in current spray research work. Until this need is fulfilled, the goal of developing a spray model as a reliable design tool cannot be achieved.

2.3 INTEGRATED MODELING/EXPERIMENTAL APPROACH

A 2-D elliptic code that incorporates spray dispersion model is used to determine the significant experimental variables. These variables include both geometric and flow parameters. The calculations are performed to establish significant variables for the experimental programs, and to determine areas of strong velocity gradients where measurements would want to be taken. Since the purpose of this program is to obtain benchmark quality data with which to verify 2-D turbulence/spray models, it is necessary to involve the 2-D models in the selection of the experimental configurations. Before the proposed experimental configuration was selected, a number of preliminary cases were computed. The calculations are made for the two-equation $k-\epsilon$ model. There are several reasons for not using advanced turbulence models. First, these are only illustrations used to help select the experimental configuration. Secondly, the results are obtained with a relatively coarse grid. Since these calculations are not grid independent there is an excessive amount of numerical diffusion, thus obscuring the advantages offered by advanced models.

2.3.1 Air-Swirler Characterization

The flow and geometry test conditions for this study are shown in Figure 2.3.1-1. The primary tube has a diameter of 1 in. and negligible wall thickness. The primary tube is surrounded by a swirler with a hub diameter of 1 in. and a tip diameter of 1.5 in. The flow undergoes a sudden expansion to the outer tube with a diameter of 3 in. and length of 15 in.

The parameter selected for sensitivity analysis in this study is the mass flow rate (or the inlet velocity) in the primary coaxial tube. Two cases with m_p/m_s of 0.01 and 0.06 were run to study the characteristics of the air-swirler and its interaction with the primary particle-laden jets.

The first case has a small amount of air flowing through the primary tube and basically represents a pure-swirling flow. The calculated results, as shown in Figure 2.3.1-2, indicate a recirculation zone formed near the exit of the swirler. A stagnation point with axial distance of 9 in. is found along the centerline of the tube. The results show considerable radial gradients in the profiles at the tube outlet. This did not cause any convergence problem.

The second case has a larger m_p ($= 0.06$ ms) and was run to illustrate the effect of the nozzle airflow on the main swirler induced flow field. The calculated results are shown in Figure 2.3.1-3. The flow structure of this case is similar to that of the first case. The size of the recirculation zone is slightly smaller. The distance between the two axial stagnation points is also shorter, 8.0 in. versus 9.0 in. These interesting observations indicate significant influence of the injector air on the combustor recirculation patterns.

2.3.2 Fuel Injector and Injector Air Characterization

The flow and geometry test conditions for this study are shown in Figure 2.3.2-1. The primary tube has an inside diameter of 0.394 in. and wall thickness of 0.106 in. The primary tube is surrounded by non-swirling secondary tube with a diameter of 3 in. Four cases were run to study the characteristics of the fuel injector. The initial spray particle size distribution is arbitrarily assumed and tabulated as follows

<u>Particle group number</u>	<u>Size (microns)</u>	<u>Mass fraction (%)</u>
1	15	0.62
2	25	20.00
3	40	30.00
4	55	30.00
5	80	19.38

For the first test case the primary stream (injector) airflow rate is 6% of the secondary (main) stream airflow rate, i.e., $m_{pg} = 0.06 m_s$. No particles are injected in this baseline configuration. The main stream and injector air have no swirl. Injector air and main stream flow interaction is shown in Figure 2.3.2-2, wherein velocity vectors, streamlines, isopleths of radial velocity, axial velocity and turbulence kinetic energy levels are plotted. Other than a small wake caused by the simulated nozzle shroud, there is no reverse-flow region in this case. The high-velocity injector jet is decayed slowly as shown in Figure 2.3.2-2. The corresponding increase in turbulence kinetic energy is indicated in Figure 2.3.2-2.

The second case includes nonevaporating spray particles in the injector with fuel-to-air ratio equal to 1.0. The particle inlet velocity is assumed to be twice the primary tube (injector) gas inlet velocity; spray particle diffusion due to turbulence is ignored. The calculated results are shown in Figure 2.3.2-3.

The width and the penetration depth of the injector gas are larger in the second case than in the baseline case. This finding indicates that the particle inlet velocity also has an effect on the turbulent flow field (see streamlines on Figures 2.3.2-2 and 2.3.2-3). The results also show that the rate of particle spreading is dependent on particle size.

The effect of turbulence on particle diffusion is illustrated in the third case. This case includes correction of gas turbulent diffusion rates due to the presence of particles. The calculated results shown in Figure 2.3.2-4 indicate that injector-air jet width and penetration depth (compare Figures 2.3.2-3 and 2.3.2-4) are increased noticeably by including correction of the gas turbulent diffusion due to the presence of particles.

The last case of this study is also designed to explore the effect of turbulent gas dynamics on spray particle motion. This case, however, assumes the particle motion is mainly due to bulk aerodynamic particle drag. The gas turbulent diffusion flux has no contribution to the particle motion, but the presence of particles has an influence on gas turbulent diffusion. The calculated results, as shown in Figure 2.3.2-5, are comparable with those in the third case (Figure 2.3.2-2). This comparison demonstrates that the rate of particle spreading is lower in this case than previously calculated.

2.3.3 Combination Fuel-Injector Air-Swirler Characterization

The flow and geometry test conditions for this study are shown in Figure 2.3.3-1. The analytical calculations were performed with the primary tube (injector) internal diameter as a parameter. The shroud diameter of 1 in. was kept constant. The injector is surrounded by a swirler with a hub diameter of 1 in. and a tip diameter of 1.5 in. The flow undergoes a sudden expansion to the downstream tube with a diameter of 3 in. and length of 15 in. The parameters selected for sensitivity analysis in this study are the spray particle phase, correction of gas turbulent diffusion due to particles, and the primary tube diameter. For each primary tube diameter, three cases were run to study the characteristics of the combination fuel-injector/air-swirler.

Figure 2.3.3-2 shows the calculated results of the baseline case for the primary tube diameter of 0.394 in. (1 cm). This baseline case does not include spray particles in the primary tube. The flow test conditions are similar to the second case in the Air-Swirler Characterization Study. The flow structure is characterized by a recirculation zone formed near the exit of the swirler. The axial distance between two stagnation point is 7 in. The turbulent flow is not fully developed at the outlet of the tube. This is due to the fact that the tube length selected is not long enough to have fully developed turbulent flow. These findings again indicate that the effect of the initial velocity of the primary jets on the turbulent flow field is significant.

Figure 2.3.3-3 shows the calculated results of the case including spray particle phase in the primary jets ($m_{pg}/m_s = 0.06$ and $m_{pp}/m_s = 0.06$). In this case, particle diffusion due to turbulence is not considered. The presence of particles with the specified inlet conditions, as mentioned in the Fuel-Injector Characterization Study, is found to decrease the size of the recirculation zone. It also shortens the axial distance

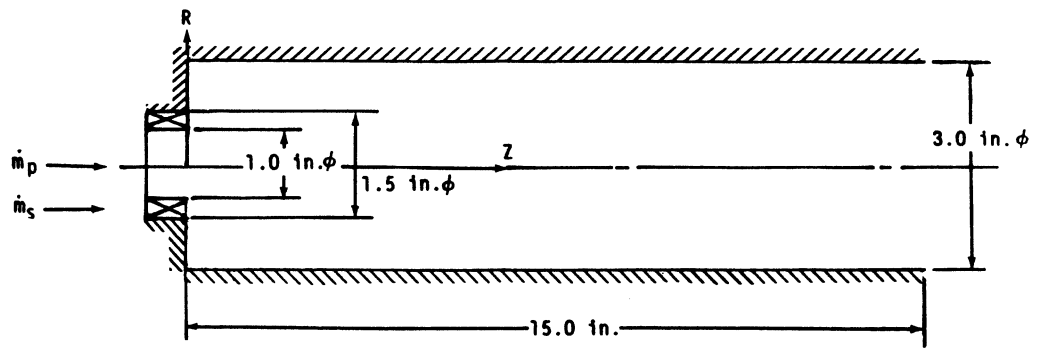
between two stagnation points, 4.2 in. versus 7.0 in. The turbulent flow is not fully developed at the outlet of the tube. The results of particle number density contours show that the state of spray particle spreading is dependent of particle size. Bigger particles have a lower rate of spreading. The particle number density contours, as shown in Figure 2.3.3-3, are compared with those in Figure 2.3.2-3. This comparison demonstrates the effect of swirling flow on particle spreading. The swirling flow can carry the spray particles into the recirculation zone and increase the rate of particle spreading.

The last case for the primary tube diameter of 0.394 in. is designed to study the effect of turbulence on particle diffusion. The flow and geometry test conditions for this case are similar to those of the previous case. The calculated results, as shown in Figure 2.3.3-4, are compared with those in Figure 2.3.3-3. The comparison indicates that primary jet width and penetration depth are increased significantly by including turbulent diffusion.

To do further investigation on the flow interaction between an injector and swirling flow, the injector internal diameter is reduced to 0.197 in. (0.5 cm) in this case. The flow test conditions in this case are similar to the baseline case in this study. The calculated results, as shown in Figure 2.3.3-5, are compared with those in Figure 2.3.3-2. This comparison indicates that the size of the recirculation zone is smaller in this case. The axial distance between front and rear stagnation points is also shorter, 5.8 in. versus 7.0 in. The turbulent flow is not fully developed at the outlet of the tube.

Figure 2.3.3-6 shows the calculated results for spray particles in the injector with fuel-to-air ratio of 1.0. In this case, the particle dispersion due to turbulence is not included. The flow test conditions in this case are similar to the second case in this study. The calculated results, as shown in Figure 2.3.3-6, are compared with those in Figure 2.3.3-3. This comparison again indicates that the effect of the initial velocity of the primary jets on the turbulent flow field is significant. In this case, the stagnation points cannot be located along the centerline of the tube; this is because both gas and particle inlet velocities in the primary tube are much bigger. The comparison also shows that the swirling flow cannot effectively carry the spray particles with very big inlet velocity into the recirculation zone and the rate of particle spreading is lower in this case.

The last case of the Combination Fuel-Injector/ Air-Swirler Characterization Study is designed to investigate the effect of particle dispersion due to the diffusion for the above case. The calculated results, as shown in Figure 2.3.3-7, should be compared with Figure 2.3.3-6. Calculations demonstrate that primary jets width and penetration depth are increased significantly by including turbulent diffusion.



\dot{m}_p = Mass flow rate in the primary tube
 \dot{m}_s = Mass flow rate in the swirler

Swirler--Air

Swirl No. = 1.46
 Swirler angle = 60 deg
 \dot{m}_s = 0.062 lbm/sec

Primary tube--Air

\dot{m}_p/\dot{m}_s = 0.01 and 0.06

TE84-1730

Figure 2.3.1-1. The flow and geometry test conditions for air-swirler characterization study.

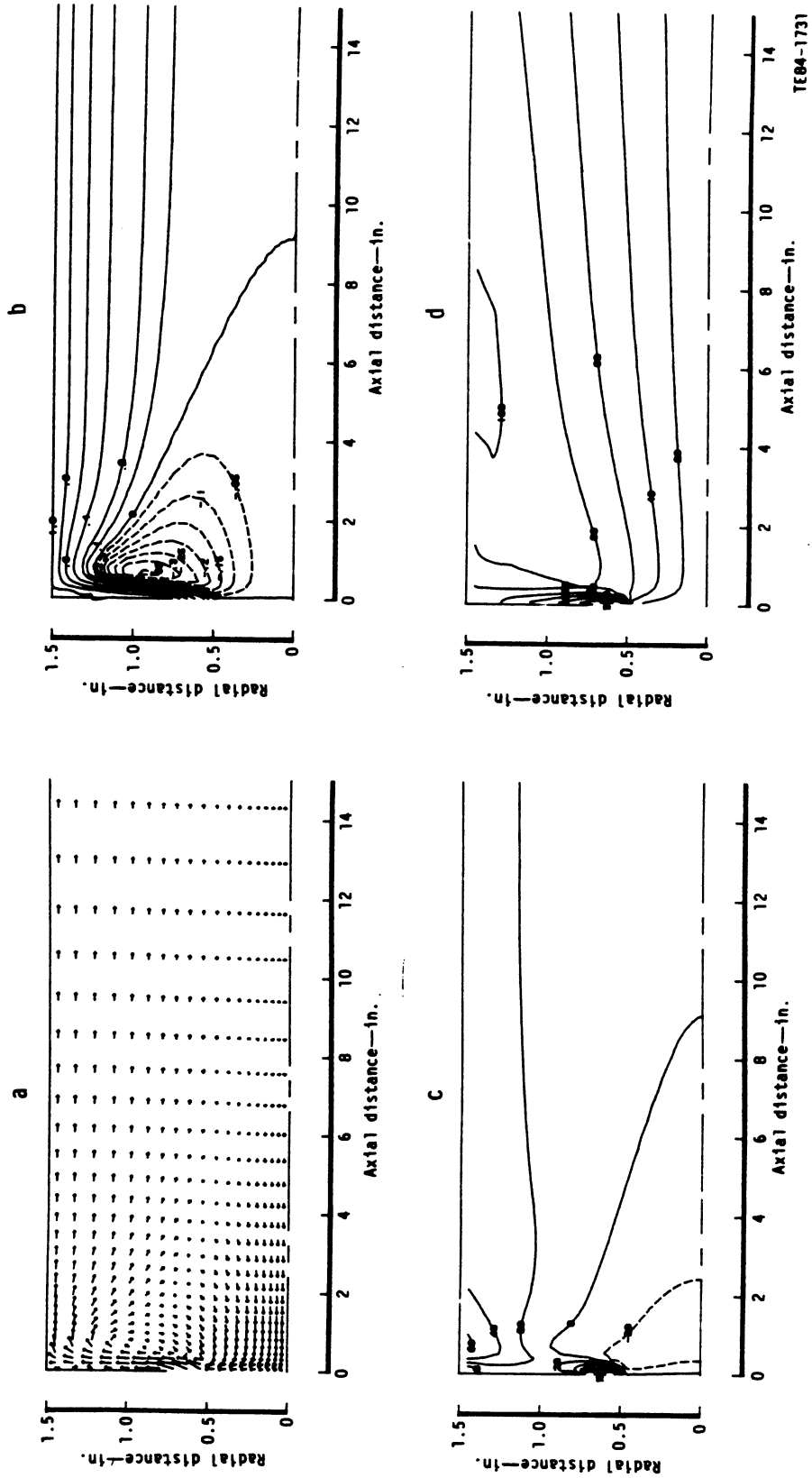


Figure 2.3.1-2. Numerical predictions of the case $m_p/m_s = 0.01$ for air-swirler characterization study;
a) velocity vectors b) streamlines c) radial velocity d) kinetic energy.

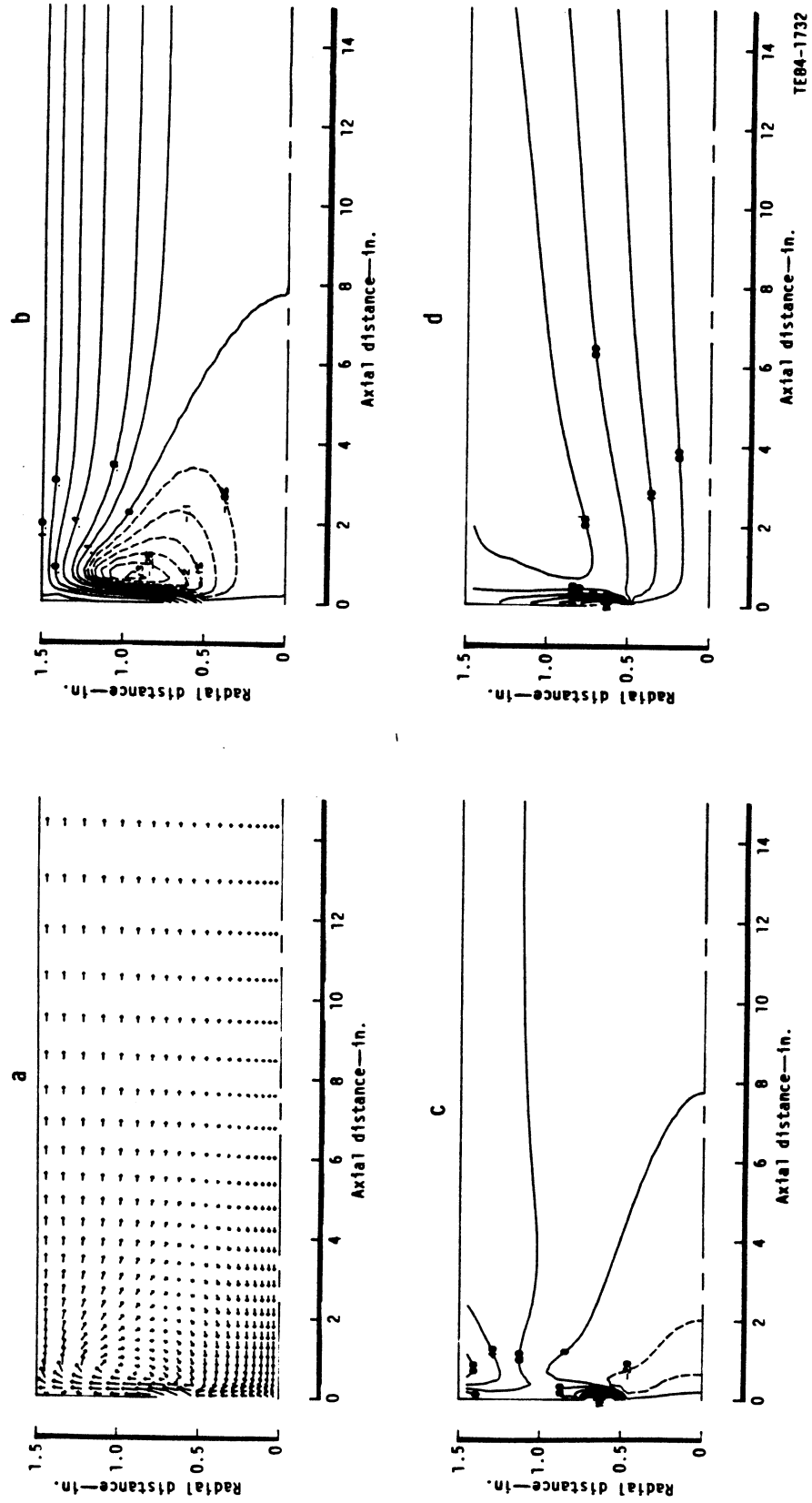
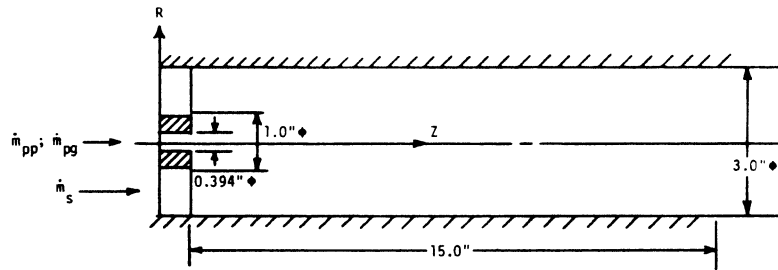


Figure 2.3.1-3. Numerical predictions of the case $m_p/m_s = 0.06$ for air-swirler characterization study;
a) velocity vectors b) streamlines c) radial velocity d) kinetic energy.



\dot{m}_{pg} : Air mass flow rate in the primary tube

\dot{m}_{pp} : Spray particle mass flow rate in the primary tube

\dot{m}_s : Air mass flow rate in the secondary tube

Secondary tube--Air

$$\dot{m}_s = 0.062 \text{ lbm/s}$$

Primary tube--Air with or without spray particles

$$\frac{\dot{m}_{pp}}{\dot{m}_s} = 0.06$$

$$\frac{\dot{m}_{pg}}{\dot{m}_s} = 0.06$$

$$\frac{\text{Inlet particle velocity}}{\text{Inlet gas velocity}} = 2.0$$

TE84-1733A

Figure 2.3.2-1. The flow and geometry test conditions for fuel-injector characterization study.

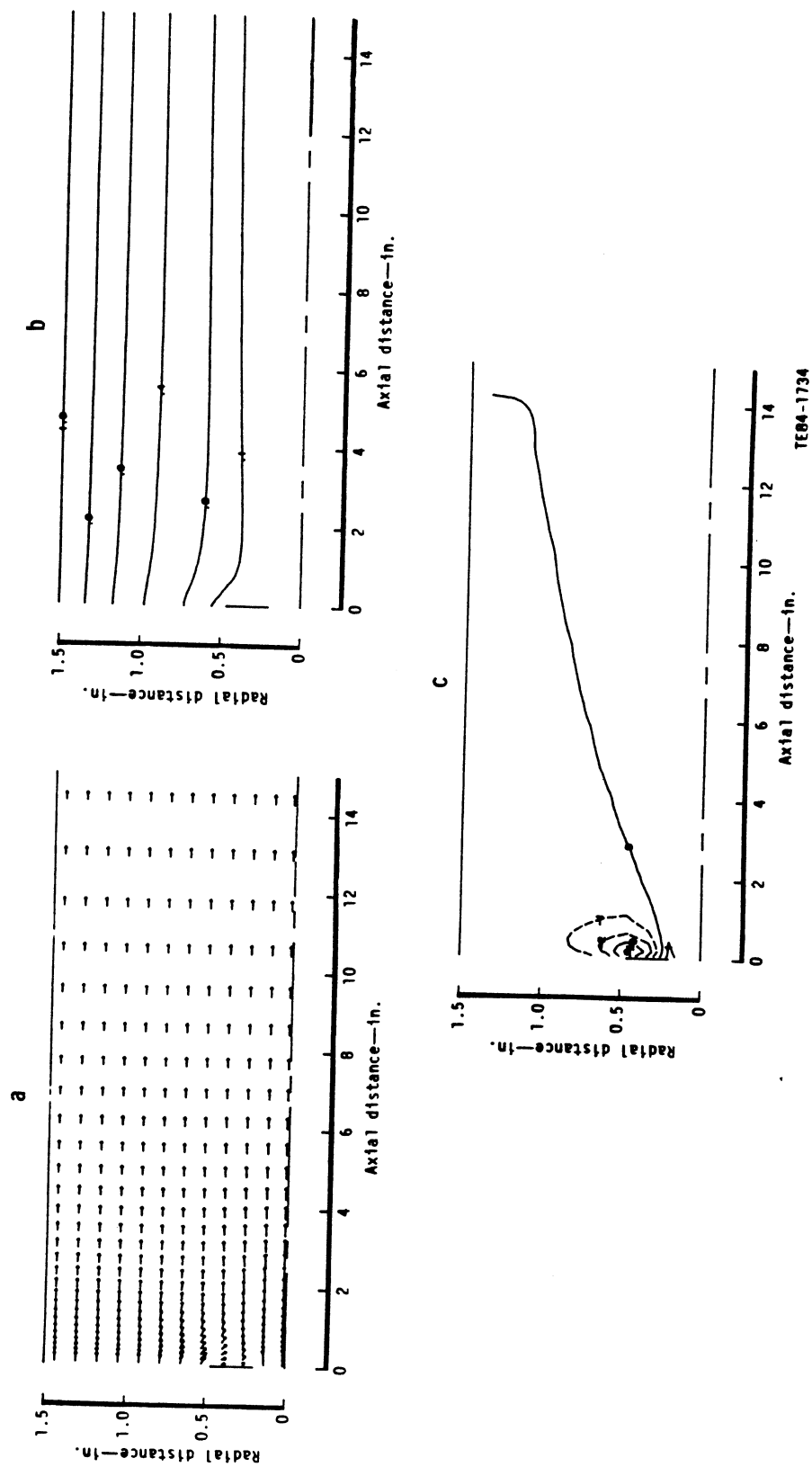


Figure 2.3.2-2. Numerical predictions of single-phase flow for fuel-injector characterization study;
a) velocity vectors b) streamlines c) radial velocity.

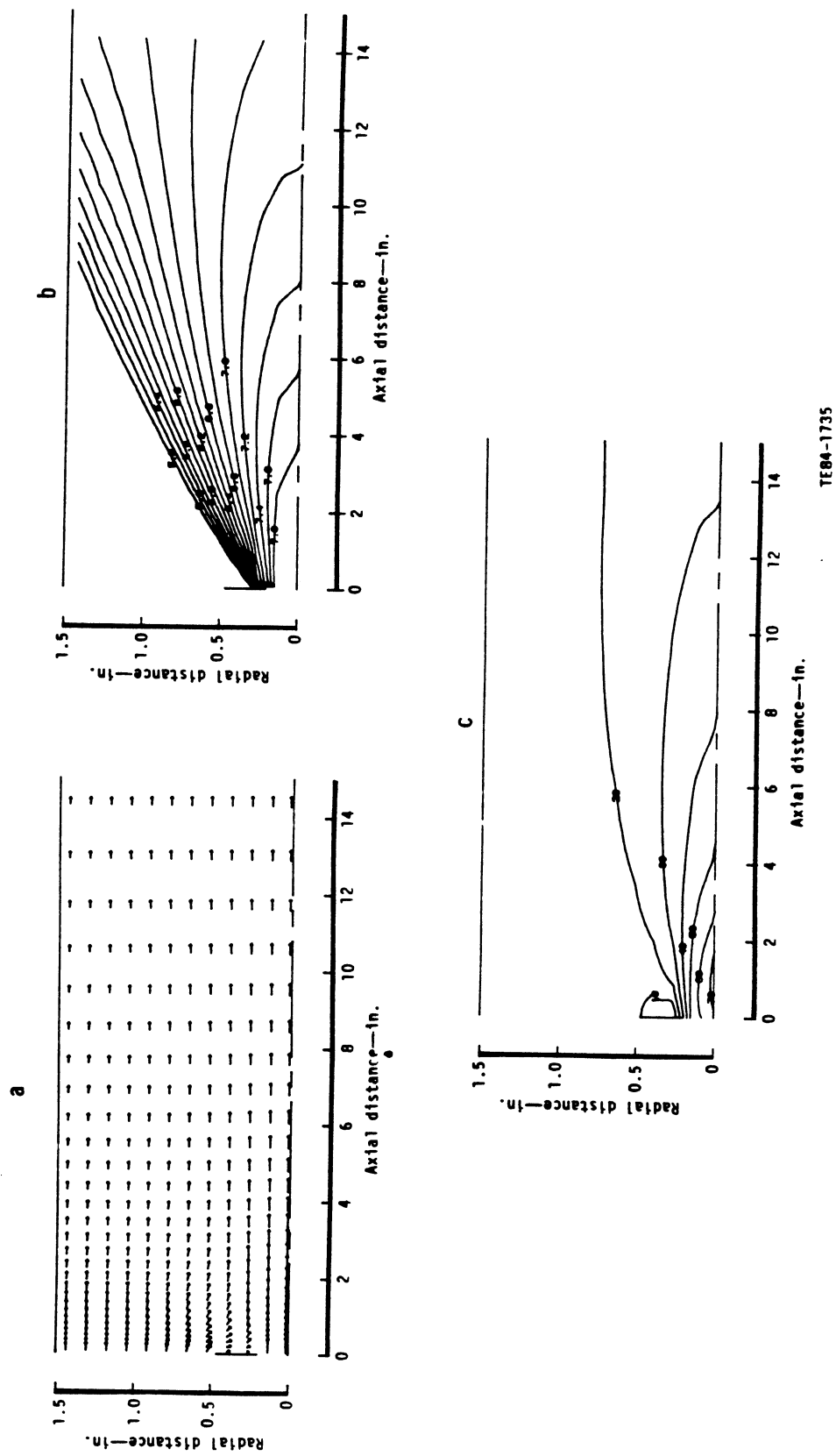


Figure 2.3.2-3. Numerical predictions of two-phase flow without correction of gas turbulent diffusion due to particles of fuel-injector characterization study (1 of 2).

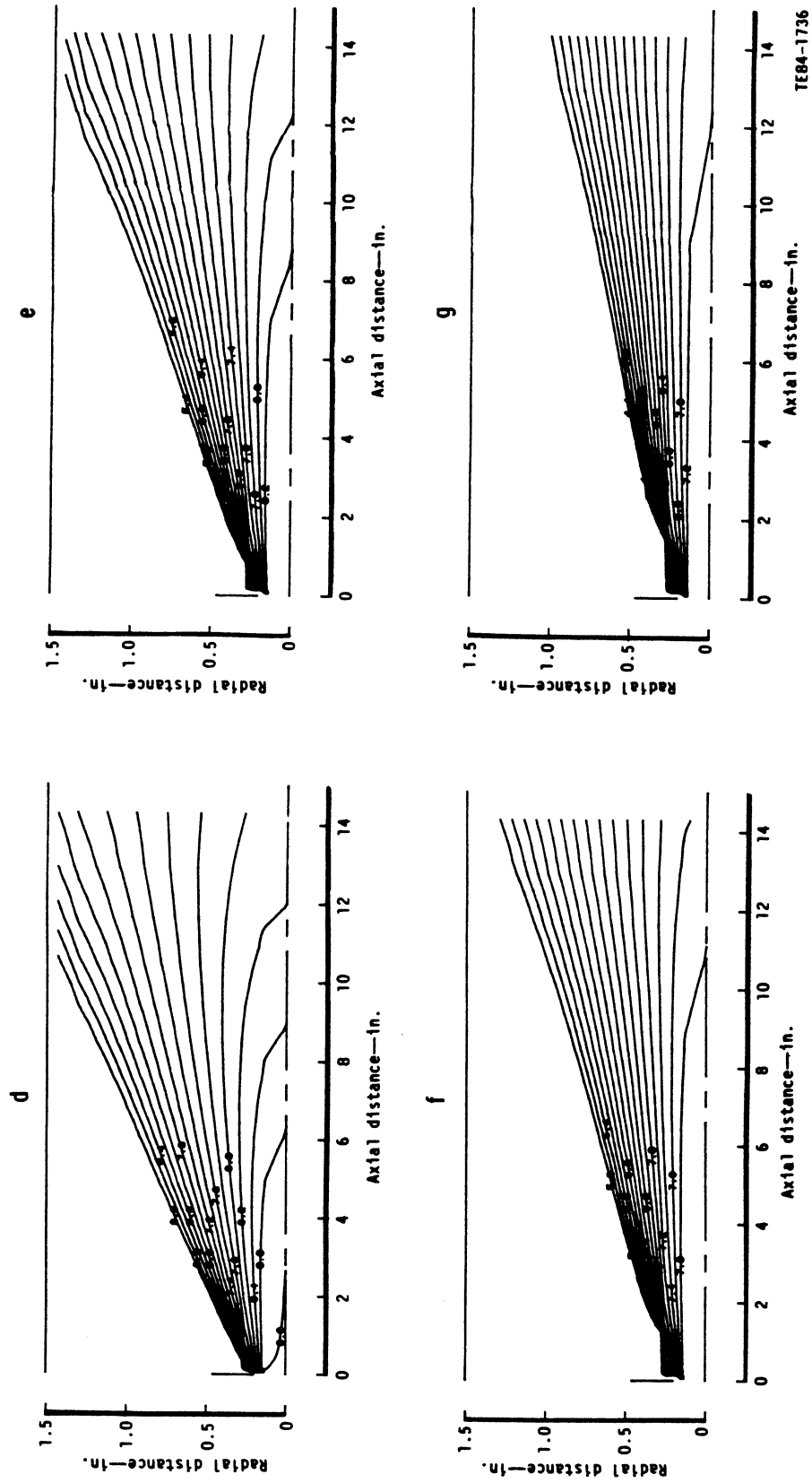


Figure 2.3.2-3. Numerical predictions of two-phase flow without correction of gas turbulent diffusion due to particles of fuel-injector characterization study (2 of 2).

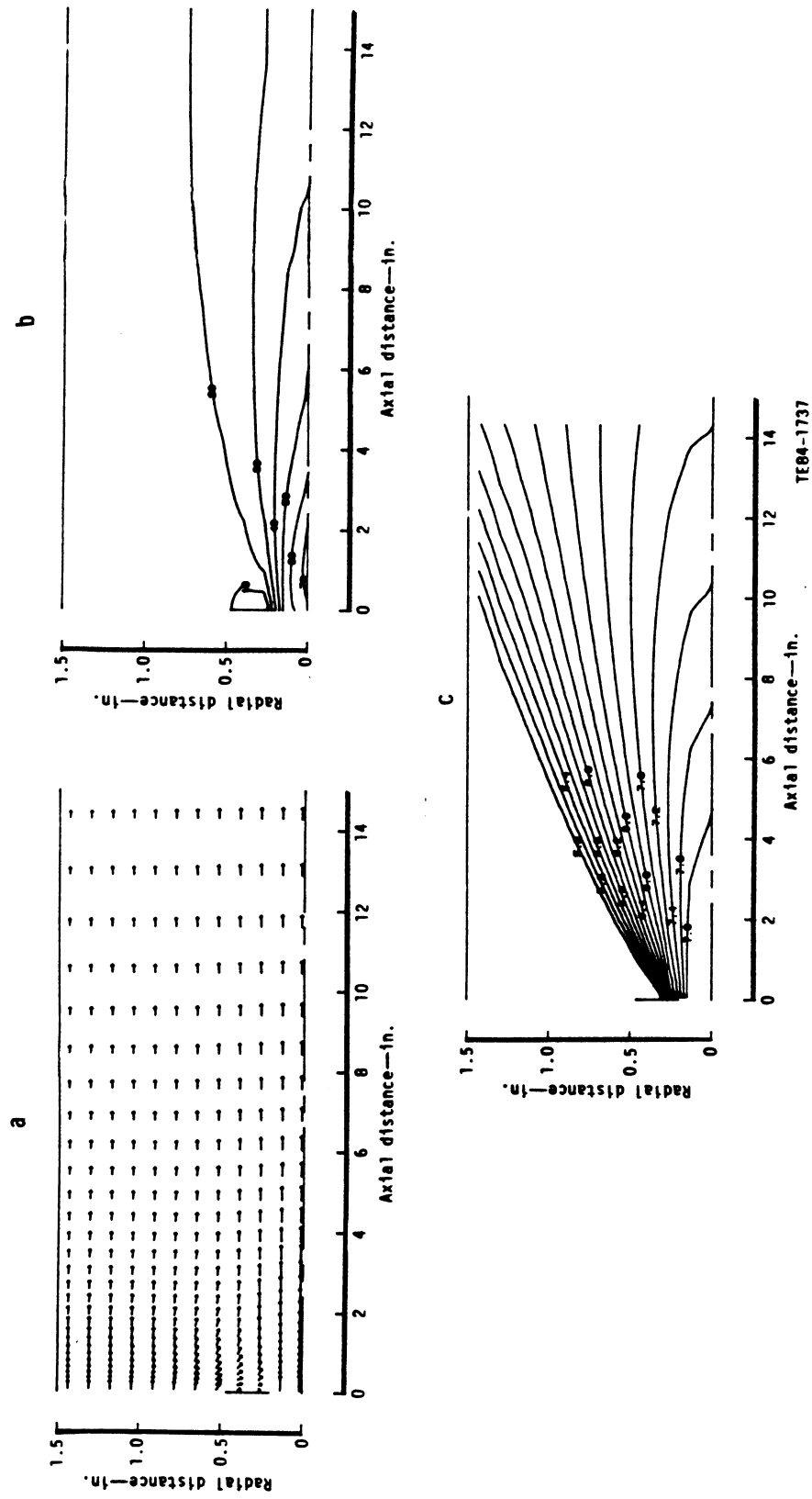
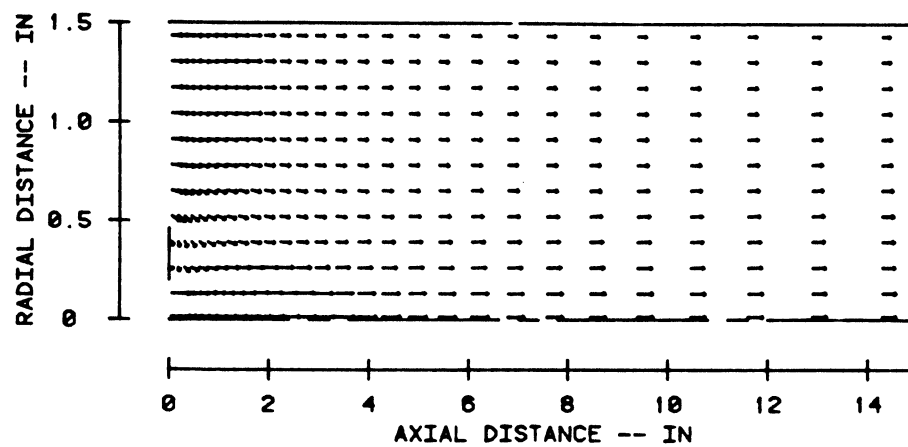
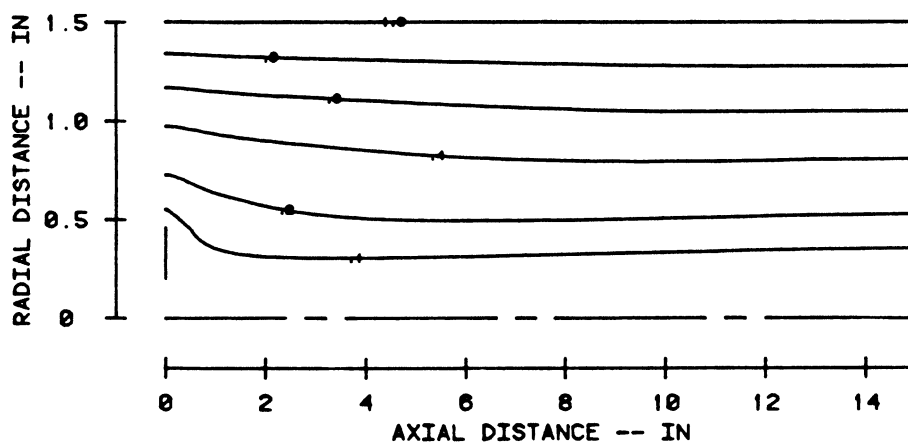


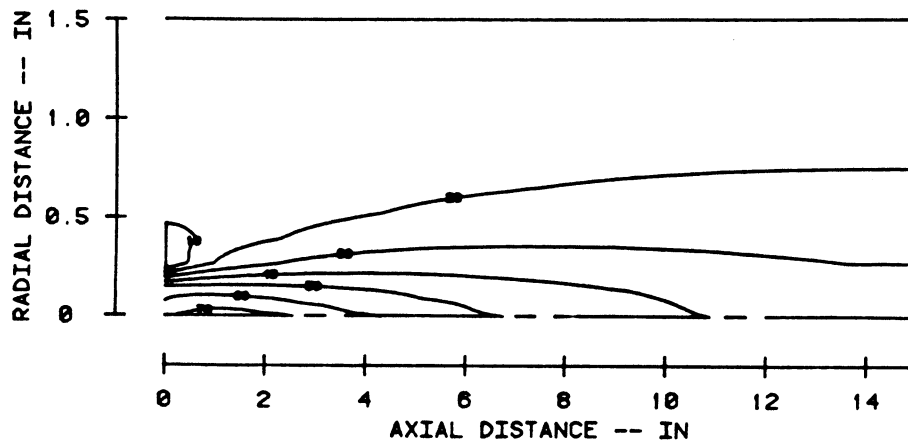
Figure 2.3.2-4. Numerical predictions of two-phase flow with correction of gas turbulent diffusion due to particles of fuel-injector characterization study (1 of 2).



a



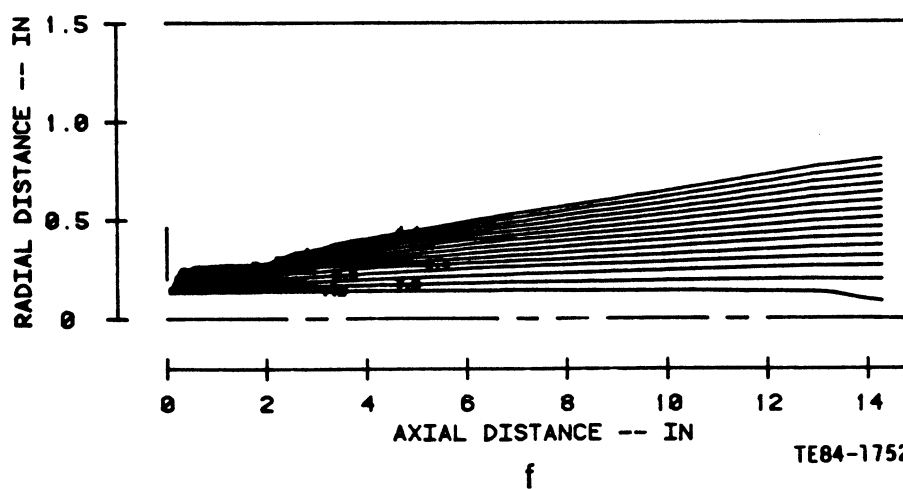
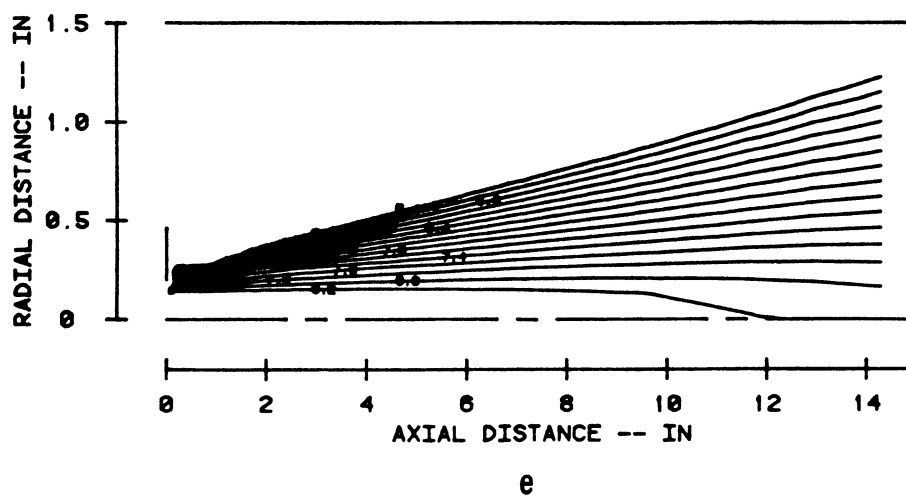
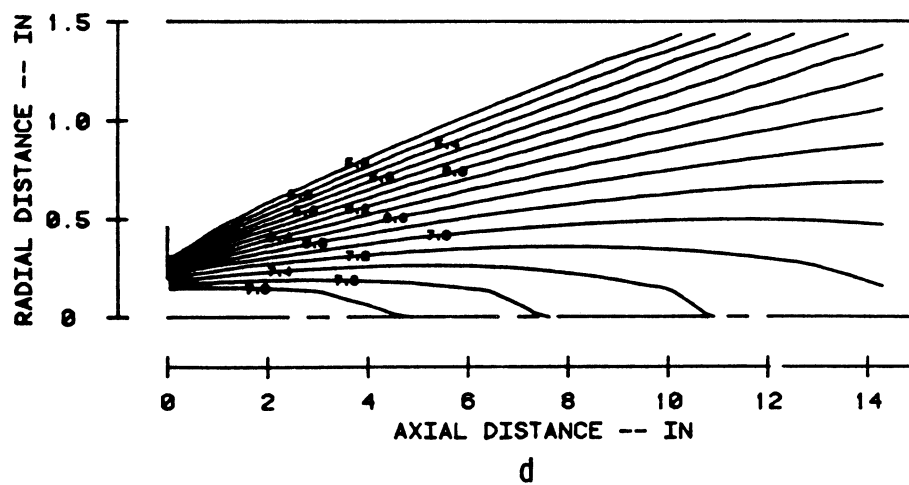
b



c

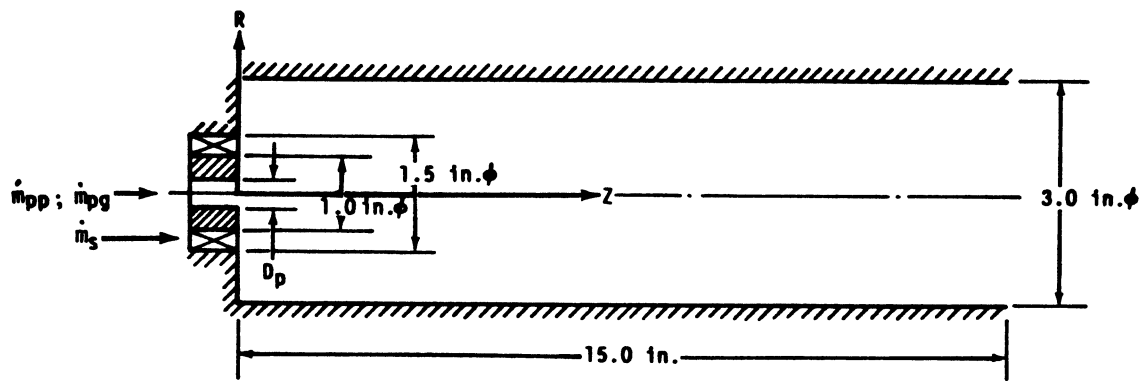
TE84-1751

Figure 2.3.2-5. Numerical predictions of two-phase flow without particle dispersion model for fuel-injector characterization study; a) velocity vectors b) streamlines c) kinetic energy (1 of 2).



TE84-1752

Figure 2.3.2-5. Numerical predictions of two-phase flow without particle dispersion model for fuel-injector characterization study; a) velocity vectors b) streamlines c) kinetic energy (2 of 2).



\dot{m}_{pg} = Air mass flow rate in the primary tube

\dot{m}_{pp} = Spray particle mass flow rate in the primary tube

\dot{m}_s = Air mass flow rate in the swirler

D_p = Primary tube diameter

Swirler—Air

Swirl No. = 1.46

Swirler angle = 60 deg

\dot{m}_s = 0.062 lbm/sec

Primary tube—Air with or without spray particles

\dot{m}_{pp}/\dot{m}_s = 0.06

\dot{m}_{pg}/\dot{m}_s = 0.06

D_p = 0.394 in. and 0.197 in.

TE84-1740

Figure 2.3.3-1. The flow and geometry test conditions for combination fuel-injector air-swirler characterization study.

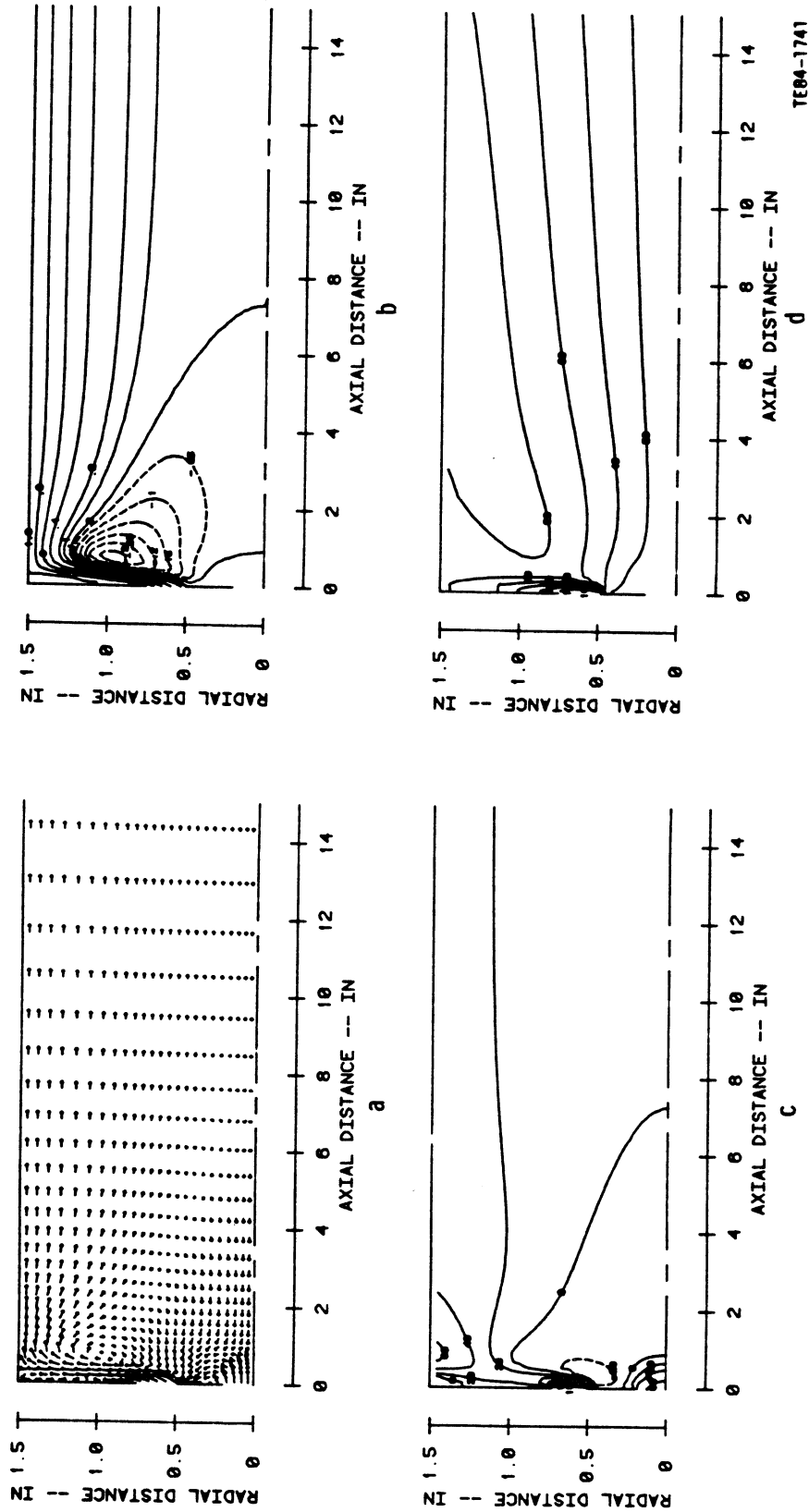
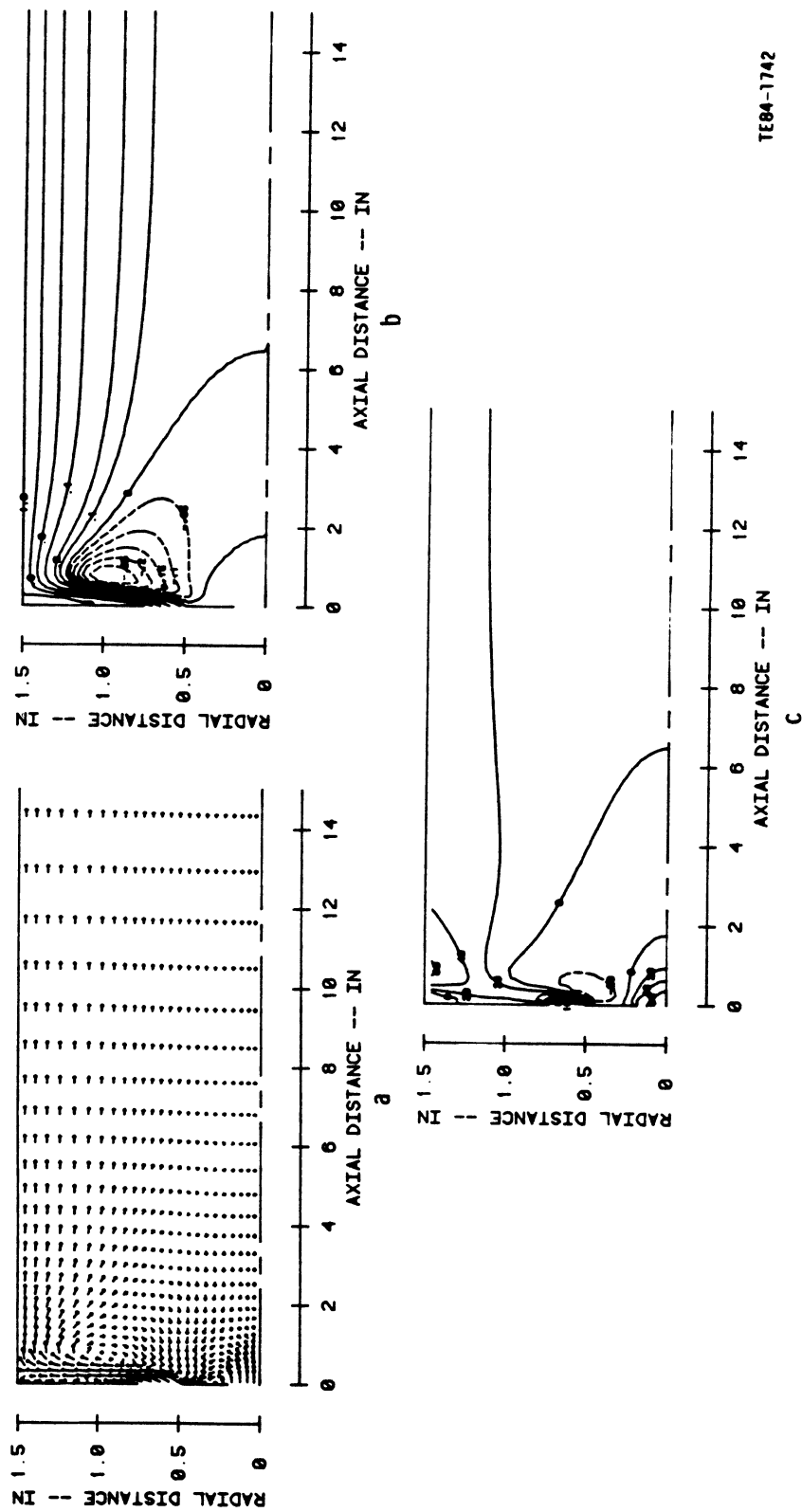


Figure 2.3.3-2. Numerical predictions of single-phase flow ($D_p = 0.394$ in.) for combination fuel injector air-swirler characterization study; a) velocity vectors b) streamlines c) radial velocity d) kinetic energy.



TE84-1742

Figure 2.3.3-3. Numerical predictions of two-phase flow ($D_p = 0.394$ in.) without correction of gas turbulent diffusion due to the particles for combination fuel-injector air-swirler characterization study (1 of 2).

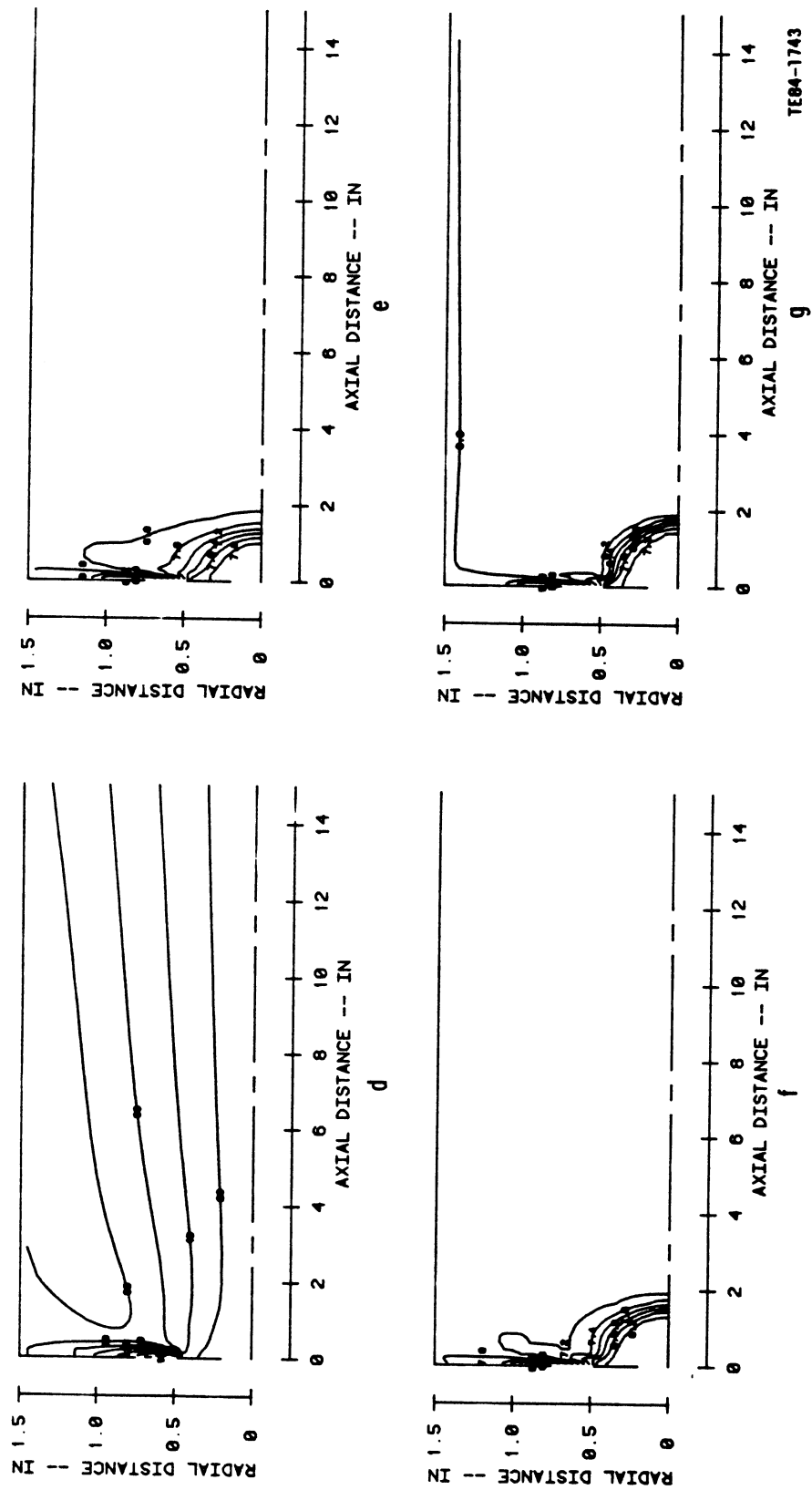
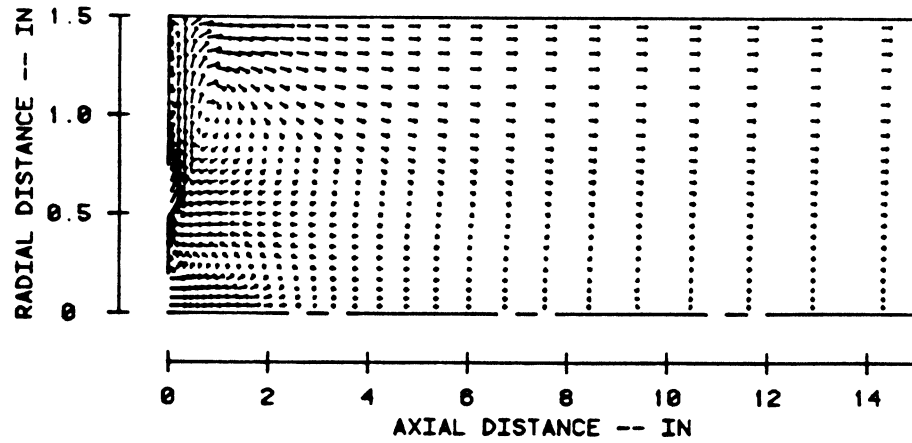
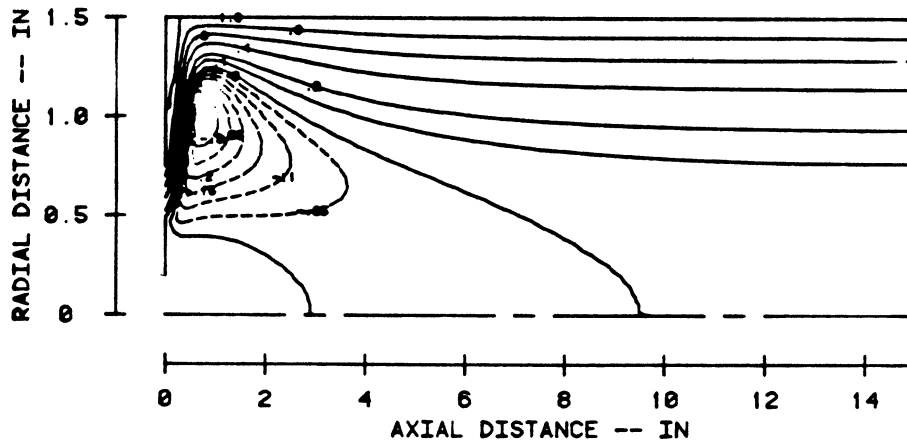


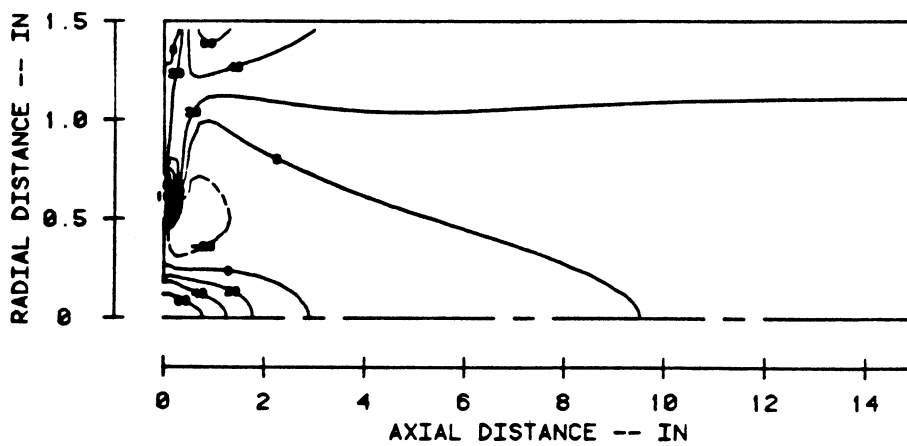
Figure 2.3.3-3. Numerical predictions of two-phase flow ($D_p = 0.394$ in.) without correction of gas turbulent diffusion due to the particles for combination fuel-injector air-swirler characterization study (2 of 2).



a



b



c

TE84-1744

Figure 2.3.3-4. Numerical predictions of two-phase flow ($D_p = 0.394$ in.) with correction of gas turbulent diffusion due to the particles for combination fuel-injector air-swirler characterization study (1 of 2).

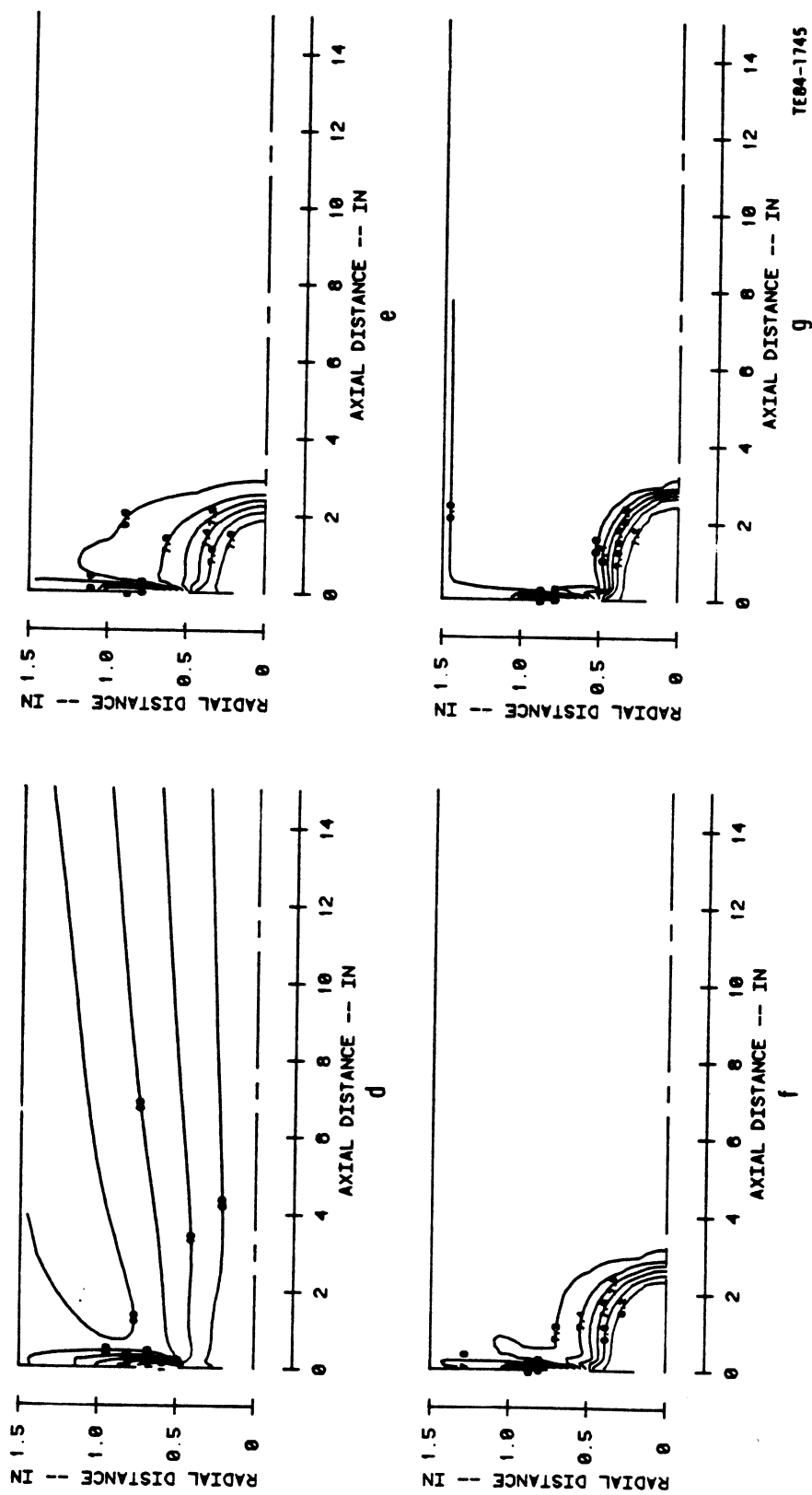


Figure 2.3.3-4. Numerical predictions of two-phase flow ($D_p = 0.394$ in.) with correction of gas turbulent diffusion due to the particles for combination fuel-injector air-swirler characterization study (2 of 2).

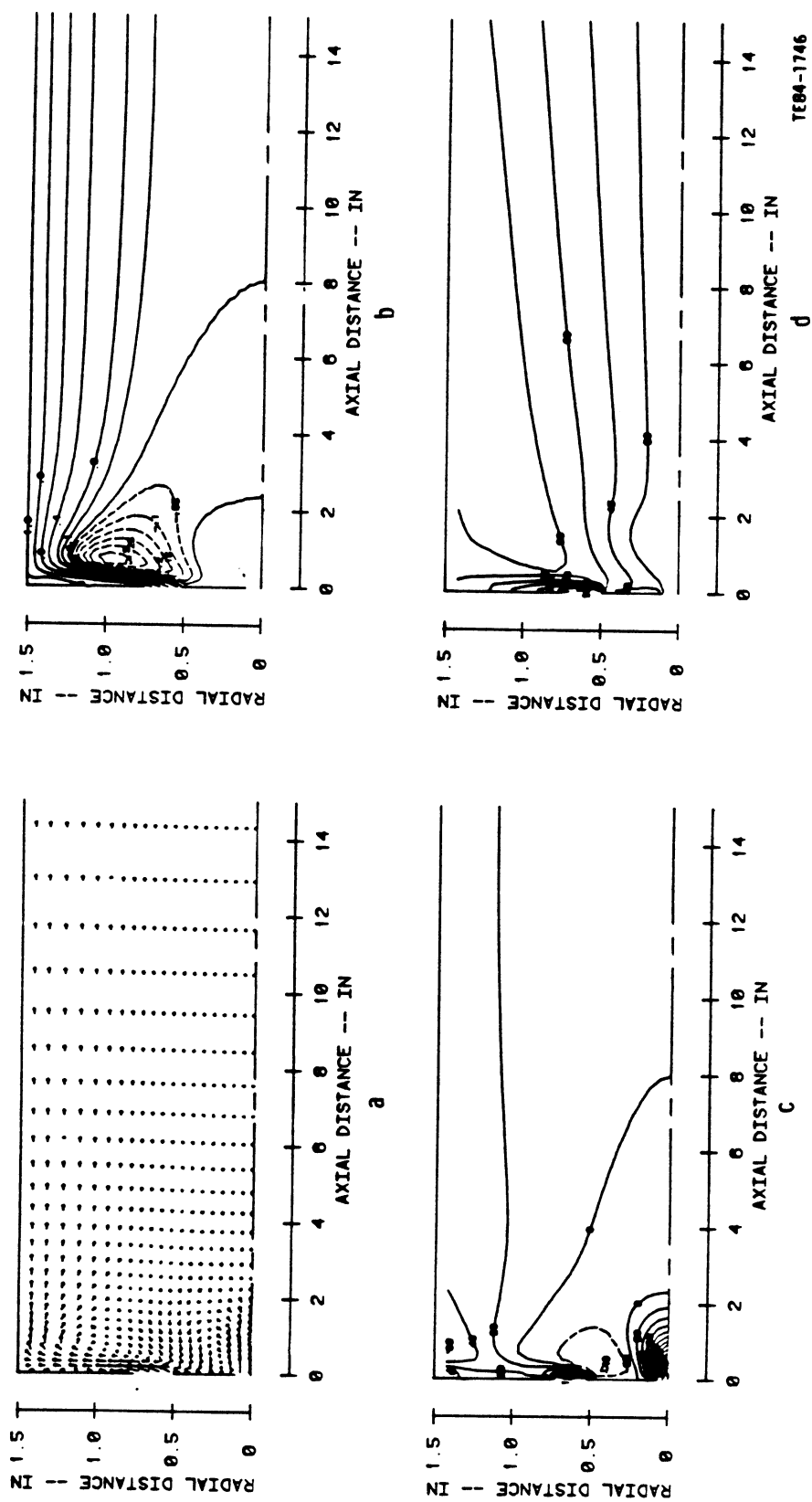
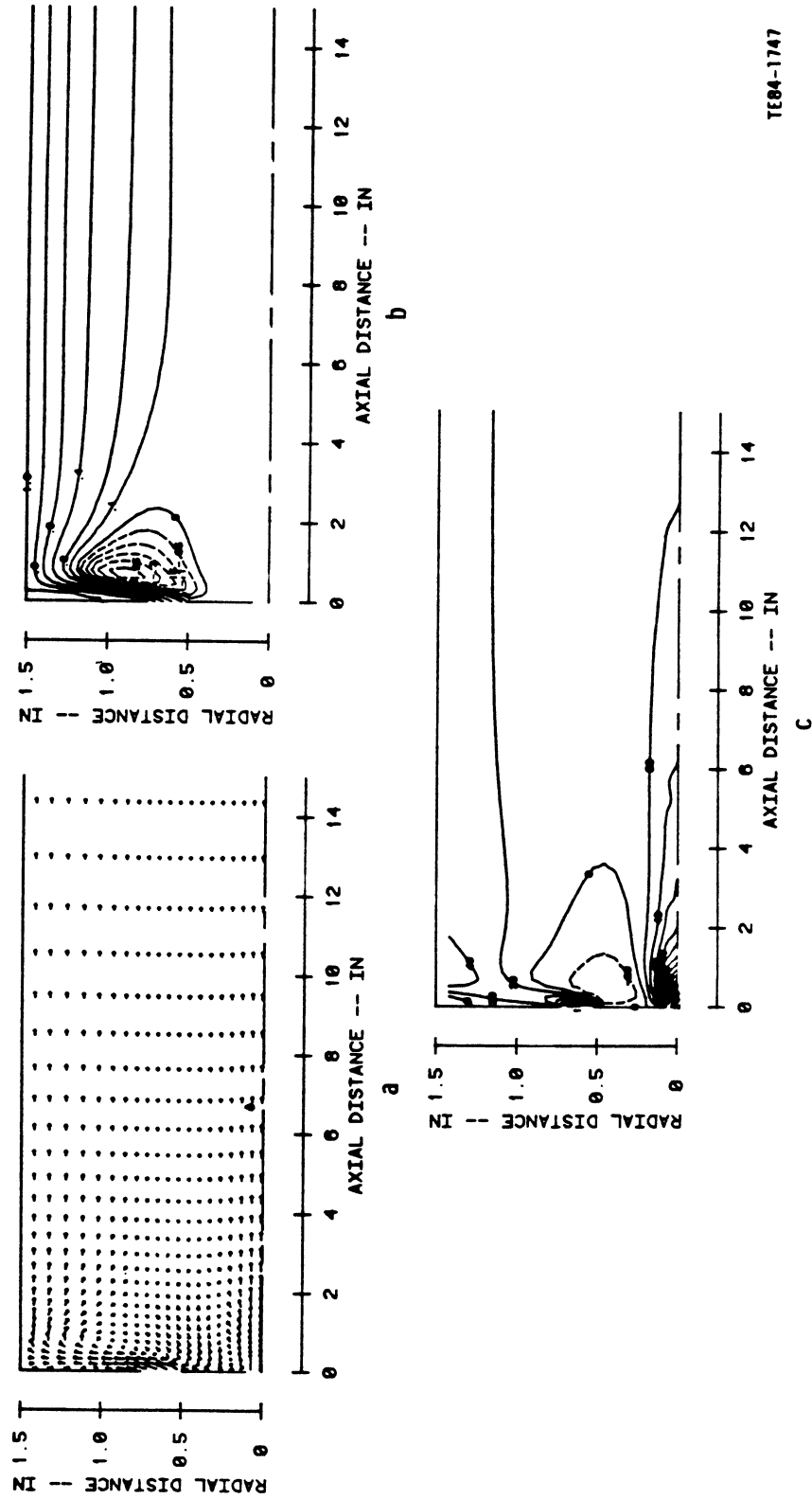


Figure 2.3.3-5. Numerical predictions of single-phase flow ($D_p = 0.197$ in.) for combination fuel-injector air-swirler characterization study.



TE84-1747

Figure 2.3.3-6. Numerical predictions of two-phase flow ($D_p = 0.197$ in.) without correction of gas turbulent diffusion due to the particles for combination fuel-injector air-swirler characterization study (1 of 2).

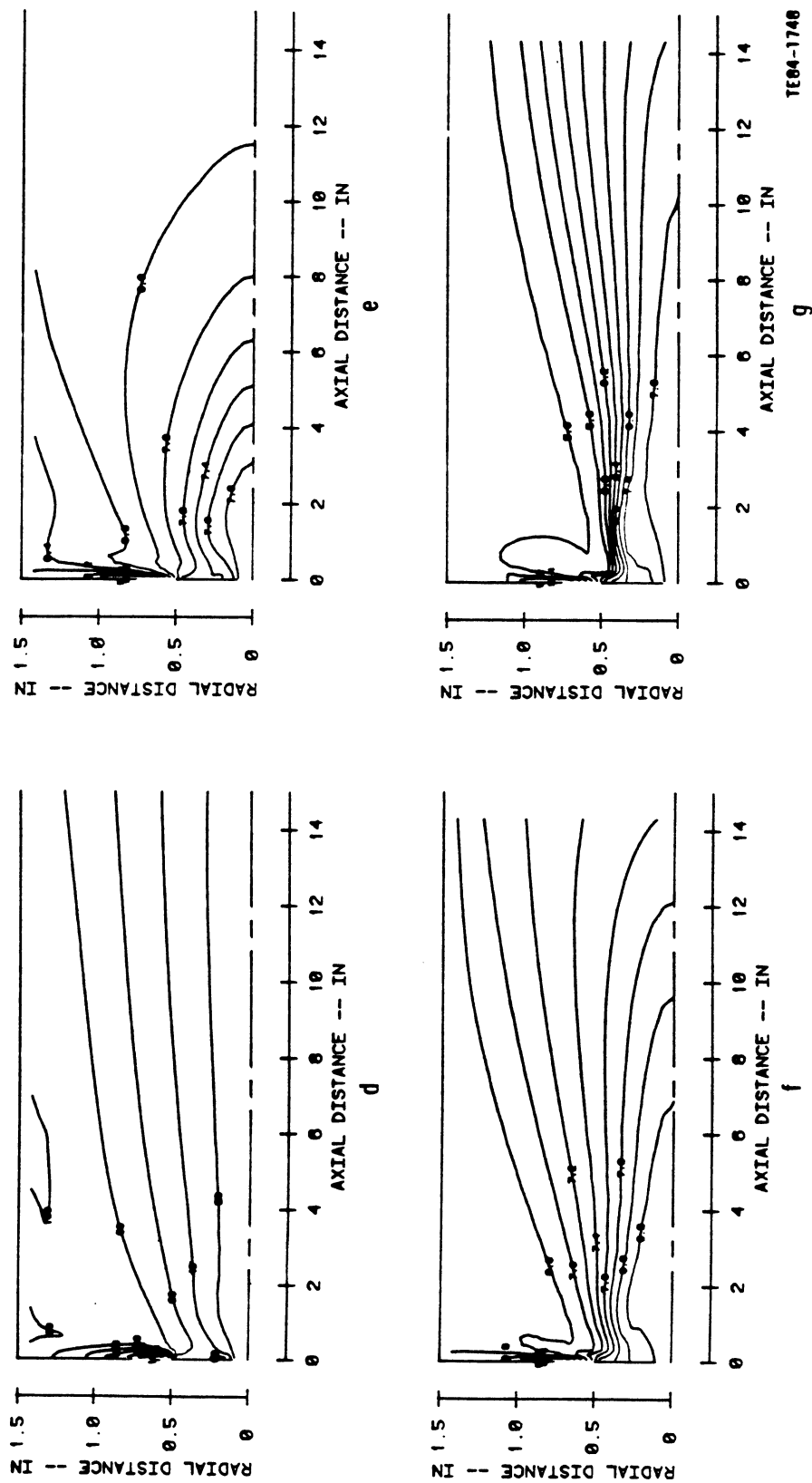
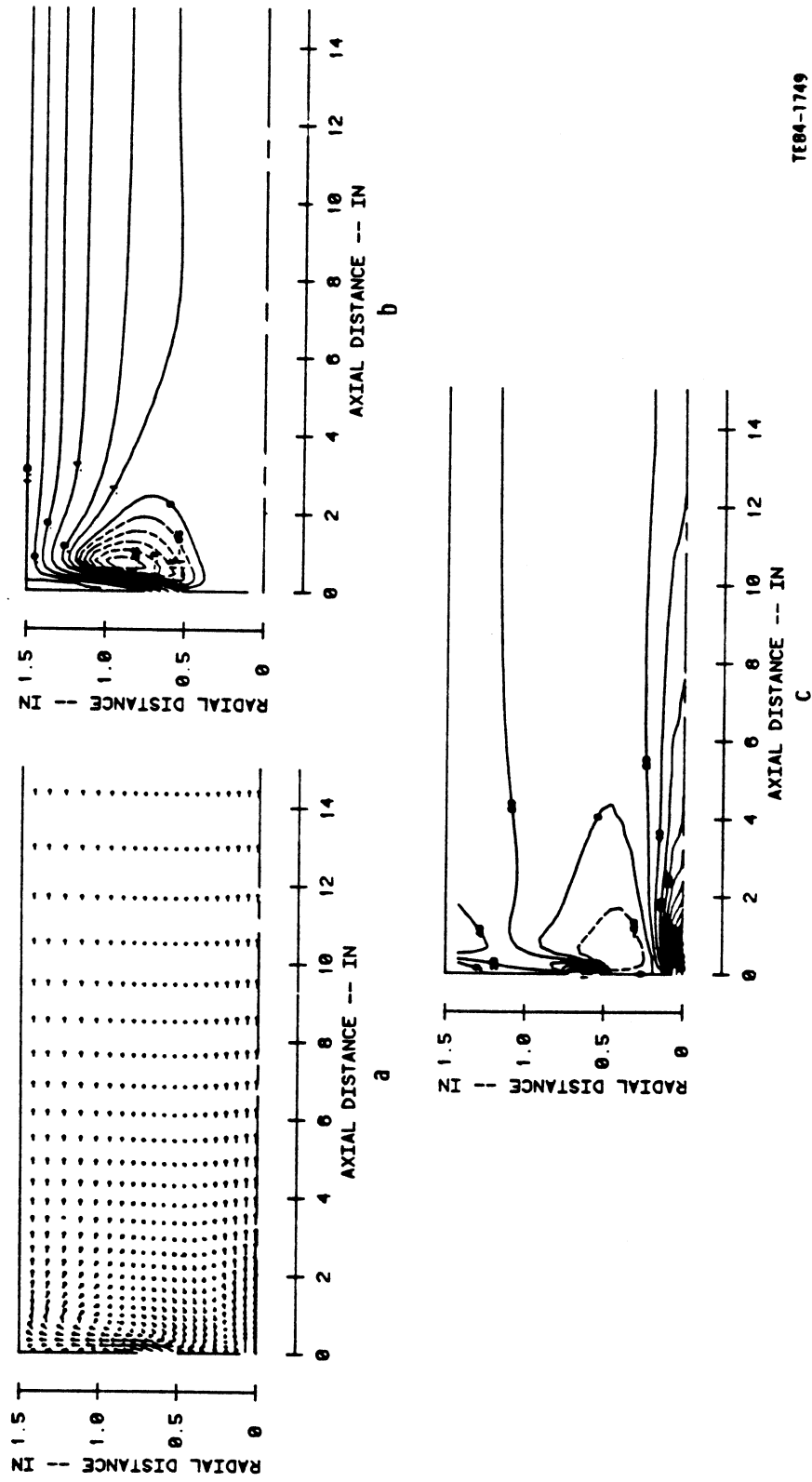


Figure 2.3.3-6. Numerical predictions of two-phase flow ($D_p = 0.197$ in.) without correction of gas turbulent diffusion due to the particles for combination fuel-injector air-swirler characterization study (2 of 2).



TE84-1749

Figure 2.3.3-7. Numerical predictions of two-phase flow ($D_p = 0.197$ in.) with correction of gas turbulent diffusion due to the particles for combination fuel-injector air-swirler characterization study (1 of 2).

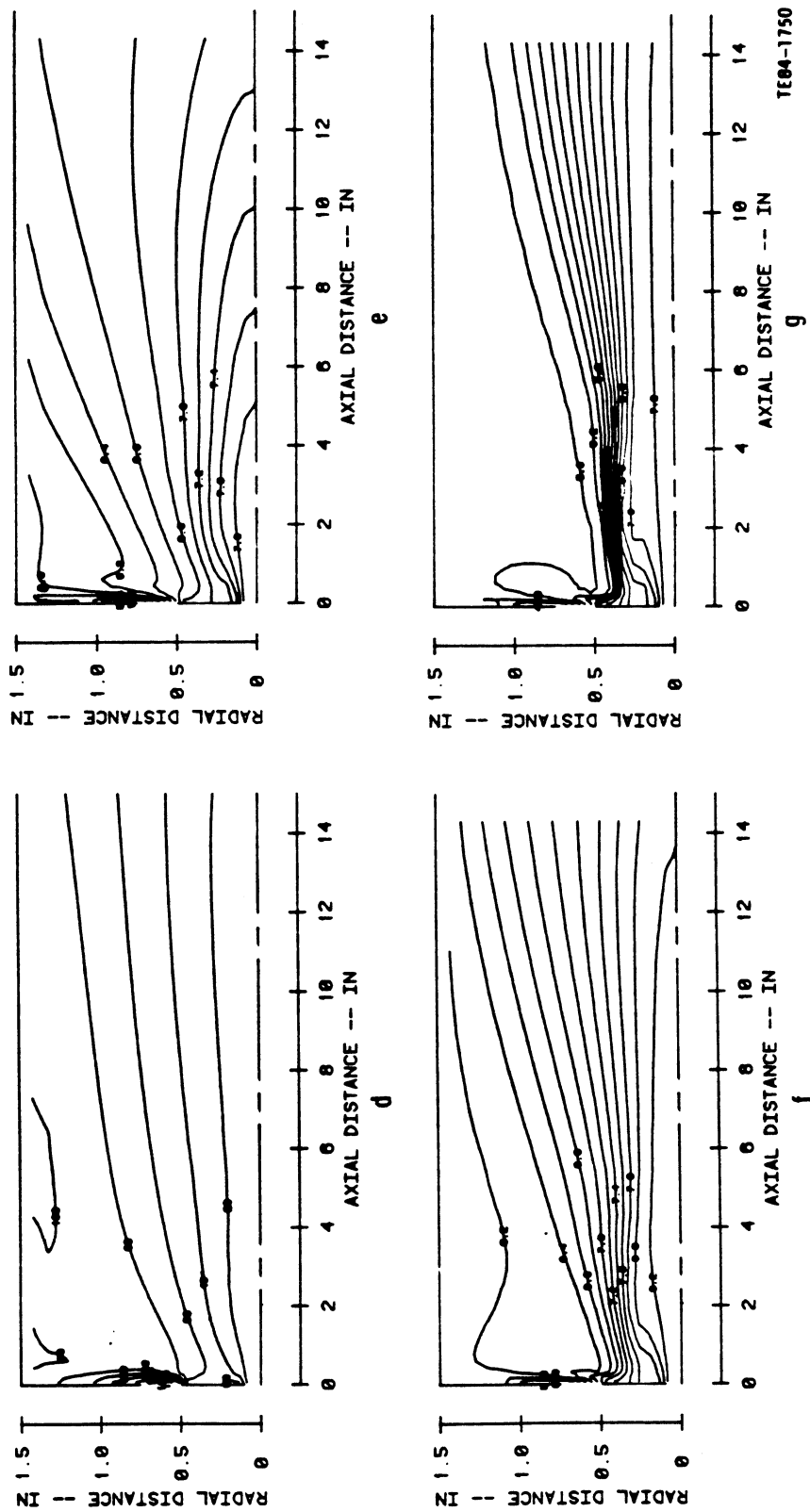


Figure 2.3.3-7. Numerical predictions of two-phase flow ($D_p = 0.197$ in.) with correction of gas turbulent diffusion due to the particles for combination fuel-injector air-swirler characterization study (2 of 2).

REFERENCES

- Brena de la Rosa, A., Sankar, S. V., Wang, G., and Bachalo, W. D., 1992, "Particle Diagnostics and Turbulence Measurements in a Confined Isothermal Liquid Spray, ASME 92-GT-113.
- Bulzan, D. L., 1988, "Particle-Laden Weakly Swirling Free Jets: Measurements and Predictions," NASA Technical Memorandum 100881.
- Chehroudi, B. and Ghaffarpour, M., 1991, "Spray Drop Size and Velocity Measurements in a Swirl Stabilized Combustor," ASME 91-GT-43.
- Chehroudi, B. and Ghaffarpour, M., 1992, "Structure of a Hollow-Cone Spray with and without Combustion," ASME, 92-GT-124.
- Chigier, N. A., 1977, "The Atomization and Burning of Liquid Fuel Sprays," *Prog Energy Combust Sci*, Vol 2, pp 97-114.
- Chigier, N. A. and Roett, M. F., 1972, "Twin-Fluid Atomizer Spray Combustion," ASME Winter Annual Meeting, New York, Paper NO. 72-WA/HT-25.
- El Banhawy, Y. and Whitelaw, J. H., 1980, "Calculation of the Flow Properties of a Confined Kerosene-Spray Flame," *AIAA J*, Vol 18, pp 1503-1510.
- El Banhawy, Y. and Whitelaw, J. H., 1982, "Experimental Study of the Interaction Between a Fuel Spray Surrounding Combustion Air," *Comb and Flame*, Vol 42, pp 253-275.
- Faeth, G. M., 1979, "Spray Combustion Models—A Review," AIAA paper 79-0293.
- Faeth, G. M., 1983, "Evaporation and Combustion of Sprays," *Prog Energy Combust Sci*, Vol 9, pp 1-76.
- Fairfield, M. S., Butler, T. D., Presser, C., Gupta, A. K., and Semerjean, H. G., 1992, "Aerodynamic Effects on Fuel Spray Structure – Experiment and Theory," AIAA-92-0227.
- Fonti, M., Hutchinson, P., and Whitelaw, J. H., 1979, "Measurements and Calculations of a Kerosene Fueled Flow in a Model Furnace," Report FS/79/19, Mechanical Engineering Department, Imperial College, London.
- Foster, S. G., Tageldin, M., and Cetegen, M., 1991, "Dispersion and Evaporation of Liquid Droplets in a Turbulent, Planar Mixing Layer," AIAA/ASME/SAE/ASEE 27th Joint Propulsion Conference, AIAA-91-2312.
- Gosman, A. D. and Johns, R. J. R., 1980, "Computer Analysis of Fuel-Air Mixing in Direct-Injection Engines," SAE paper No. 800091.
- Hardalupas, Y., Taylor, A.M.K.P., Whitelaw, J. H., 1989, "Velocity and Particle-Flux Characteristics of Turbulent Particle-Laden Jets," *Proc. R. Soc. Lon.* Vol. 426, pp. 31-78.
- Hassa, C., Blumcke, E., Brandt, M., and Elckhoff, H., 1992, "Experimental and Theoretical Investigation of a Research Atomizer/Combustor Chamber Configuration," ASME 92-GT-137.
- Hutchinson, P., Khalil, E. E., and Whitelaw, J. H., 1977, "Measurement and Calculation of Furnace Flow Properties," *J Energy*, Vol 1, pp 212-219.
- Karki, K. and Mongia, H. C., 1989, "Recent Developments in Computational Combustion Dynamics," AIAA Paper 89-2808, July.
- Kenworthy, M. J., Correa, S. M., and Burrus, D. L., 1983, "Aerothermal Modeling: Phase I Final Report – Volume I Model Assessment," NASA CR-168296.
- Lefebvre, A. H., 1984, "Fuel Effects on Gas Turbine Combustion-Liner Temperature, Pattern Factor, and Pollutant Emissions," *Journal of Aircraft*, Vol 21, No. 11, pp 887-898.
- Lefebvre, A. H., 1985, "Fuel Effects on Gas Turbine Combustion-Ignition, Stability, and Combustion Efficiency," *Transactions of the ASME, Journal of Engineering for Gas Turbines and Power*, Vol 107, No. 1, pp 24-37.
- Levy, Y. and Lockwood, F. C., 1981, "Velocity Measurements in a Particle Laden Turbulent Free jet," *Combustion and Flame*, Vol 40, pp 33-339.
- Loats, M. K. and Frishman, F. A., 1970, "Scattering of an Inert Admixture of Different Grain Size in a Two-Phase Axisymmetric Jet," *Heat Transfer-Soviet Res*, Vol 2, pp 7-12.
- Mao, C. P., Szekely, Jr., G. A., and Faeth, G. M., 1980, "Evaluation of a Locally Homogeneous Flow Model of Spray Combustion," NASA CR-3203.
- Mao, C. P., Wang, G., and Chigier, N., 1986, "An Experimental Study of Air-Assist Atomizer Spray Flames," 21st (Int) Symp. Combustion, The Combustion Institute, pp. 665-673.

- McComb, W. D. and Salih, S. M., 1977, "Measurement of Normalized Radial Concentration Profiles in a Turbulent Aerosol Jet Using a Laser-Doppler Anemometer," *J. Aerosol Sci*, Vol 8, pp 171-181.
- McComb, W. D. and Salih, S. M., 1978, "Comparison of Some Theoretical Concentration Profiles for Solid Particles in a Turbulent Jet with Results of Measurements Using a Laser-Doppler Anemometer," *J. Aerosol Sci*, Vol 9, pp 299-313.
- McCreath, C. G. and Chigier, N. A., 1973, "Liquid Spray Burning in the Wake of a Stabilizer Disc," *Fourteenth Symposium (International) on Combustion*, The Combustion Institute, Pittsburgh, pp 1355-1363.
- Miutani, Y., Yasuma, G., and Katsuki, M., 1977, "Stabilization of Spray Flames in a High-Temperature Stream," *Sixteenth (International) Symposium on Combustion*, pp 631-638, The Combustion Institute, Pittsburgh, Pennsylvania.
- Modarress, D., Wuerer, J., and Elghobashi, S., 1982, "An Experiment Study of a Turbulent Round Two-Phase Jet," AIAA paper No. 82-0964.
- Modarress, D., Tan, H., and Elghobashi, S., 1983, "Two-Component LDA Measurement in a Two-Phase Turbulent Jet," AIAA paper No. 83-0052.
- Mongia, H. C., 1982, "Application of Multidimensional Modeling Techniques to the Design and Development of Gas Turbine Combustors," 1982 Air Force Office of Scientific Research, Annual Contractors Meeting.
- Mongia, H. C., Reynolds, R. S., and Srinivasan, R., 1986, "Multidimensional Gas Turbine Combustion Modeling: Applications and Limitations," *AIAA Journal*, Vol 24, No. 6, June, pp 890-904.
- Onuma, Y. and Ogassaare, M., 1975, "Studies on the Structure of a Spray Combustion Flame," *Fifteenth Symposium (International) on Combustion*, The Combustion Institute, Pittsburgh, pp 453-465.
- Onuma, Y. and Ogassaare, M., 1977, "Further Experiments on a Spray Combustion Flame," *Sixteenth Symposium (International) on Combustion*, The Combustion Institute, Pittsburgh, pp 561-567.
- Plee, S. L. and Mellor, A. M., 1978, "Flame Stabilization in Simplified Pre-vaporizing Partially Vaporizing and Conventional Gas Turbine Combustors," *Journal of Energy*, Vol 2, No. 6, pp 346-353.
- Plee, S. L. and Mellor, A. M., 1979, "Characteristic Time Correlation for Lean Blowoff of Bluff-Body-Stabilized Flames," *Combustion and Flame*, Vol 35, pp 61-80.
- Popper, J., Abuaf, N., and Hetsroni, G., 1974, "Velocity Measurements in a Two-Phase Turbulent Jet," *Int J. Multiphase Flow*, Vol 1, pp 715-726.
- Rizk, N. K. and Mongia, H. C., 1989, "Correlations of High Density Fuel Effects," AIAA Paper 89-0216, January.
- Rizk, N. K. and Mongia, H. C., 1991, "Gas Turbine Combustor Performance Evaluation," AIAA Paper 91-0640, January.
- Shearer, A. J., Tamura, H., and Faeth, G. M., 1979, *Journal of Energy*, 3, 271.
- Shuen, J. S., Solomon, A. S. P., Zhang, Q. F., and Faeth, G. M., 1985, "Structure of Particle-Laden Jets: Measurements and Predictions," *AIAA J*, Vol. 23, No. 3, pp. 396-404.
- Solomon, A. S. P., Shuen, J. S., Zhang, Q. F., and Faeth, G. M., 1984a, "Measurements and Predictions of the Structure of Evaporating Sprays," submitted for presentation at 22nd ASME/AIChE National Heat Transfer Conference, Niagara Falls, New York, August.
- Solomon, A. S. P., Shuen, J. S., Zhang, Q. F., and Faeth, G. M., 1984b, "Structure of Nonevaporating Sprays: Measurements and Predictions," AIAA paper No. 84-0125.
- Srinivasan, R., Reynolds, R., Ball, I., Berry, R., Johnson, K., and Mongia, H. C., 1983, "Aerothermal Modeling Program: Phase I Final Report," NASA CR-168243.
- Steele, L. L., Grant, J. R., Harrold, D. P., and Erhart, J. J., 1987, "Application of System Identification Techniques to Combustor Post-Stall Dynamics," Air Force Wright Aeronautical Lab, Wright-Patterson AFB, Ohio, AFWAL-TR86-2105, February.
- Sturgess, G. J., 1983, "Aerothermal Modeling: Phase I Final Report," NASA CR-168202.
- Styles, A. C. and Chigier, N. A., 1977, "Combustion of Airblast Atomized Spray Flames," *Sixteenth (International) Symposium on Combustion*, pp 619-630, The Combustion Institute, Pittsburgh, Pennsylvania.
- Tishkoff, J. M., 1982, "Measurements of Particle Size and Velocity in a Fuel Spray," paper presented at the Second International Conference on Liquid Atomization and Spray Systems, Madison, Wisconsin, 20-24 June.

- Tishkoff, J. M., Hammond, Jr., D. C., Chraplyvy, A. R., 1982, "Diagnostic Measurements of Fuel Spray Dispersion," *J Fluids Engr*, Vol 104, pp 313-317.
- Tseng, L. K., Wu, P. K., and Faeth, G. M., 1992, "Dispersed Phase Structure of Pressure-Atomized Sprays at Various Gas Densities," AIAA-92-0230.
- Wang, H., Sowa, W., McDonell, V., and Samuelsen, G., 1991, "Dynamics of Discrete Phase in a Gas Turbine Co-axial, Counter-Swirling, Combustor Dome Swirl Cup," AIAA/SAE/ASME/ASEE 27th Joint Propulsion Conference, AIAA-91-2353.
- Wang, H. Y., McDonell, V. G., Sowa, W. A., and Samuelsen, G. S., 1992, "Scaling of the Two-Phase Flow Downstream of a Gas Turbine Combustor Swirl Cup; Mean Quantities," ASME 92-GT-207.
- Yule, A. J., Ah Seng, C., Felton, P. G., Ungut, A., and Chigier, N. A., 1982, "A Study of Vaporizing Fuel Sprays by Laser Techniques," *Combustion and Flame*, 44, pp 71-84.
- Yuu, S., Yasukouchi, N., Hirose, Y., and Jotaki, T., 1978, "Particle Turbulent Diffusion in a Dust Laden Round Jet," *AIChE J*, Vol 24, pp 509-519.
- Zurlo, J. R., Presser, C., Gupta, A. K., Semerjan, 1991, "Determination of Droplet Characteristics in Spray Flames Using Three Different Sizing Techniques," AIAA-91-2200.

TABLE OF CONTENTS

<u>Section</u>	<u>Title</u>	<u>Page</u>
III	Experimental Test Facility and Instrumentation	39
3.1	Test Facility	39
3.1.1	Unconfined Geometries	39
3.1.2	Confined Geometries.....	39
3.1.3	Positioning	40
3.1.4	Diagnostics Table	41
3.2	Materials for the Dispersed Phase	49
3.2.1	Glass Beads	49
3.3	Flow Systems	53
3.3.1	Air Delivery	53
3.3.2	Glass Bead Delivery.....	55
3.3.3	Methanol Delivery	56
3.4	Injector/Swirlers Assemblies	63
3.4.1	Injector Flow Split Study	63
3.4.2	Nozzle Symmetry Evaluation	63
3.4.3	Aerodynamic Swirler	65
3.4.4	Evolution of Experimental Test Conditions.....	65
3.5	Diagnostics – Velocity Measurements	88
3.5.1	Laser Anemometry System	88
3.5.2	Seeding Systems	90
3.5.3	Sampling Bias	92
3.5.4	Validation of Velocity Measurement	92
3.6	Diagnostics – Particle Size Measurements	112
3.6.1	Phase Technique – Theory and Limitations.....	112
3.6.2	Probe Volume Correction	114
3.6.3	Validation of Technique	114
3.7	Discrimination Between Phases	126
3.7.1	Chromatic Discrimination	126
3.7.2	Amplitude Discrimination	126
3.7.3	Physical Discrimination	126
3.8	Vapor Concentration Measurements	133
3.9	Pressure Measurements in Confined Duct	135
3.10	Temperature Measurements.....	137
3.11	Flow Visualization	138
3.11.1	Photography	138
3.11.2	High Speed Cinematography	138
3.11.3	Shadowgraph Photography	138
3.12	Data Format	140

III. EXPERIMENTAL TEST FACILITY AND INSTRUMENTATION

This section describes the experimental hardware developed in support of the program. Section 3.1 describes the test chamber, the hardware and supporting facility associated with it, as well as positioning. Section 3.2 discusses materials used for the dispersed phase. Section 3.3 discusses the flow systems associated with the facility. Instrumentation and the supporting computational hardware are described in sections 3.6 through 3.12.

It is noteworthy that the entire facility was disassembled and moved from one location to another during the testing in June 1988. The majority of the nonevaporating tests were conducted prior to the move and the majority of the evaporating tests were conducted after the move. Tests of repeatability indicated that the move had no impact on the performance of the diagnostics or the facility. Examples of such tests are found in Section IV.

3.1 TEST FACILITY

In order to meet the program objective, several requirements were established for the test facility. First, the inlet and boundary conditions must be controlled to a high degree. Second, versatility is required to provide a variety of configurations against which to check predictions. To this end, two confinement configurations, three degrees of swirl, and two modes of discrete phase injection were included. The following sections describe the final design and discuss the development of that design.

3.1.1 Unconfined Geometries

A schematic of the unconfined environment used for the testing is shown in Figure 3.1.1-1*. The injector is centrally located within a 457 mm² (18 in.²) assembly constructed from 19 mm (0.75 in.) aluminum bars. The sides of the assembly are open to the surrounding environment down to an exhaust plenum formed by panels mounted on the assembly. In turn, the assembly is isolated from the room by a Plexiglass wall and plastic tarp assembly. The Plexiglass walls form a 990 x 990 x 1220 mm (39 x 39 x 48 in.) chamber. The plastic tarp seals from the tops of these walls to the upper part of the injector assembly and from the lower edge of the walls to the chamber exhaust plenum, effectively creating a room within a room. A flexible seal was required to permit traversing of the test assembly. Injected air is removed from the exhaust plenum via two outlets located symmetrically on opposing sides near the bottom of the plenum. A pressure tap between the legs is used to ensure equal draw through each.

The exhaust is adjusted so that the total pressure within the Plexiglass/tarp assembly is nominally atmospheric. The reason for this seemingly complex establishment of an unconfined environment is two fold. First, simpler, more typical unconfined environments established by the use of a large tube (Modarress et al, 1984[†]) (if ambient flow rate is desired) or a screened enclosure (Solomon et al, 1985) were dismissed through a collaborative effort with Allison, which determined that recirculation would be present near the wall at the point of injector impingement. Second, the later approach did not permit the monitoring of entrained air, nor could the effect of this air be studied via velocity measurements.

3.1.2 Confined Geometries

To provide data in an environment representative of a can combustor configuration, a confined duct 152.4 mm (6 in.) in diameter is utilized. This configuration is shown in Figure 3.1.2-1. The injector assembly resides centrally within the 152.4 mm duct. Entrainment flow is injected at the top of the duct to help reduce back flow of air and spray within the duct. The amount of air used was determined via a series of

* Figures for Section III appear at the end of each subsection. The figure number identifies the subsection in which the figure is discussed.

† References for Section III are listed at the end of the section.

tests as described in section 3.4.4. Flow straighteners are utilized to provide an even plug flow through the duct. In addition, the exhaust plenum is modified to seal near the bottom of the duct. In this way, the pressure inside the duct can be monitored and used to determine the amount of exhaust necessary to clear the flows input to the duct.

Measurements within curved ducts using optical techniques are challenging due to the impact of curvature on the laser beams. For the Plexiglass tube used in the present study, the distortion is significant over a wide part of the measurement domain as shown by Figure 3.1.2-2. This is especially true of the beams used to measure the radial velocity.

What is difficult to see in Figure 3.1.2-2 is that a displacement of more than 50 microns between each probe volume (for the beam waists used in this study) results in an invalid coincident measurement. This invalidates two-component measurements in all but the innermost 10 mm of the duct radius without realignment at each point. In addition, along the x traverse (needed for measurement of the azimuthal velocities) the fringe spacing, and thus the velocity measurement, varies by 3%. Thinner material could have been utilized, but this would still not eliminate the problem. Also, the need to make size measurements further limits the ability of the instrument to perform in a cylindrical duct.

Hence, in the present case, optical access is provided by two flats in the side of the duct located at the optical height (Figure 3.1.2-3). These flats are required to ensure coincidence of both beam crossings used for velocity measurements. The receiving optics also utilize an optical flat. This option was selected over an open port approach because of the difficulty of balancing the exhaust to prevent an influx or outflux of mass through the ports. Such a phenomena would be intractable for the modeler to represent simply. It was more straight forward to seal the duct completely and to adjust the optical flats in order to provide minimum disturbance to the flow inside the duct. Figure 3.1.2-3 shows the cross section of the optical port section of the confined duct. To reduce the impact on the flow, the flat size was minimized, resulting in the measurement domain shown in Figure 3.1.2-3.

Use of the duct increased the amount of randomly scattered laser light and, as a result, the signal-to-noise ratio for the phase/Doppler system was considerably lower than in the unconfined case. Figure 3.1.2-4 shows the effect of the increased noise on the measurement of velocity. When measuring the gas phase velocity in the presence of particles (described in section 3.7), the voltages required to provide sensitivity for the seed particles enables light randomly scattered by the particles and reflected by the Plexiglass surfaces to be detected as well, causing errors due to noise. The measured velocity of the particles is not affected by the noise since the signal is very strong. The measured single-phase velocity is not affected because the seed particles do not cause a strong random scatter and, as a result, the noise levels are significantly lower. The voltage range needed to give the proper velocities (less than 500 volts) for the gas phase in the presence of beads led to sampling times which are too long for the data needed (5 Hz at 500 volts).

Subsequent blackening of the interior surfaces and higher quality antireflectance coated optical ports increased the signal-to-noise ratio by a factor of 20 and provided a much wider range over which the voltage could be set to measure velocities of both phases at reasonable data rates.

3.1.3 Positioning

There are two means by which to map out spatially-resolved measurements. Either the experimental hardware or the optical diagnostics can be moved. It is advantageous to move the experimental hardware and leave the optics fixed because this provides better maintenance of optical alignment. Also, the need for three degrees of freedom would require sophisticated mechanisms for provision of motion from the optics. Thus, the optics remain fixed, and the hardware itself is moved in the present case.

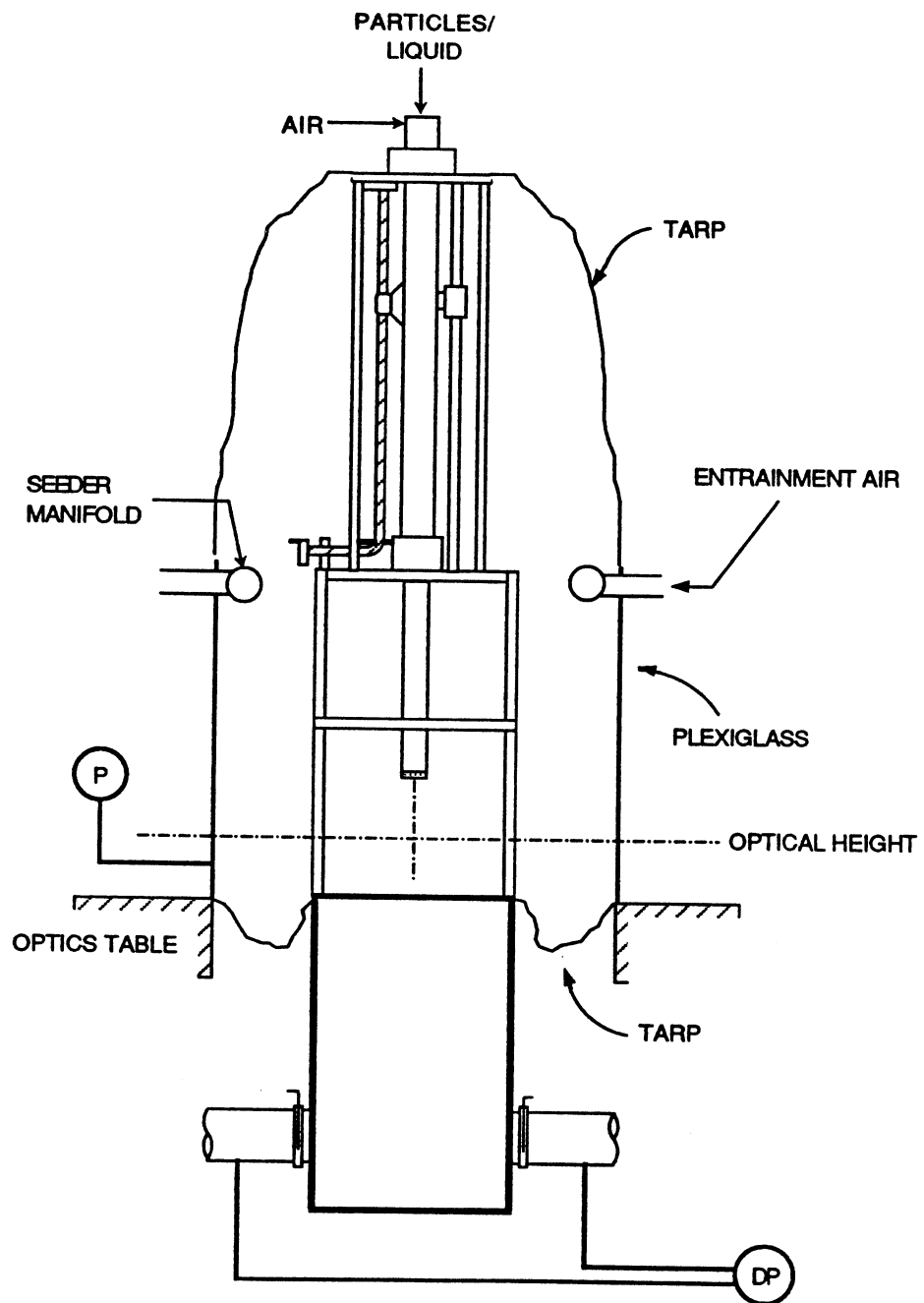
A schematic of the traversing system is shown in Figure 3.1.3-1. The horizontal motions are provided by perpendicular lead screw (12.5 mm [0.5 in.]) mechanisms. The vertical positioning is provided by a lead

screw attached to the nozzle fuel/air delivery tube. The two horizontal lead screws are designed to provide 550 mm of travel (the full extent of the cutout), and the vertical traverse provides 500 mm of travel.

Often, mechanical counters are utilized to provide feedback about position (e.g., Jackson, 1985). For the purposes of this study, inaccuracies associated with mechanical counter backlash and hysteresis could not be tolerated. As such, each direction of travel is complemented by an optical linear encoder. Thus computer control is afforded to the facility. Values of position are read out digitally (Mitutoyo Model No. GML-3705T) to the nearest 5 microns. This spatial resolution is very critical in situations where high gradients in the parameters of interest exist. The Mitutoyo readout is interfaced to the IBM AT used for data acquisition so that the location of each data point is recorded with the data acquired. A schematic of the interface is shown in Figure 3.1.3-2. A further extension of the system calls for installation of motor controllers which will enable the system to be traversed remotely by the user all by computer. This aspect of the traverse was not implemented during the program.

3.1.4 Diagnostics Table

The table from which all hardware and optical diagnostics are supported is shown in Figure 3.1.4-1. The diagnostics are discussed in sections 3.5 through 3.11. The 5 ft x 10 ft Newport Research Corporation table (custom design) provides stable operation with a maximum of vibration isolation to reduce errors due to beam wandering. In addition, vibration can lead to uncertainties in the position of the test article with respect to the optical probe. The table utilized in the experiment provides for minimum error due to this phenomena.



TE92-1631

Figure 3.1.1-1. Unconfined geometry.

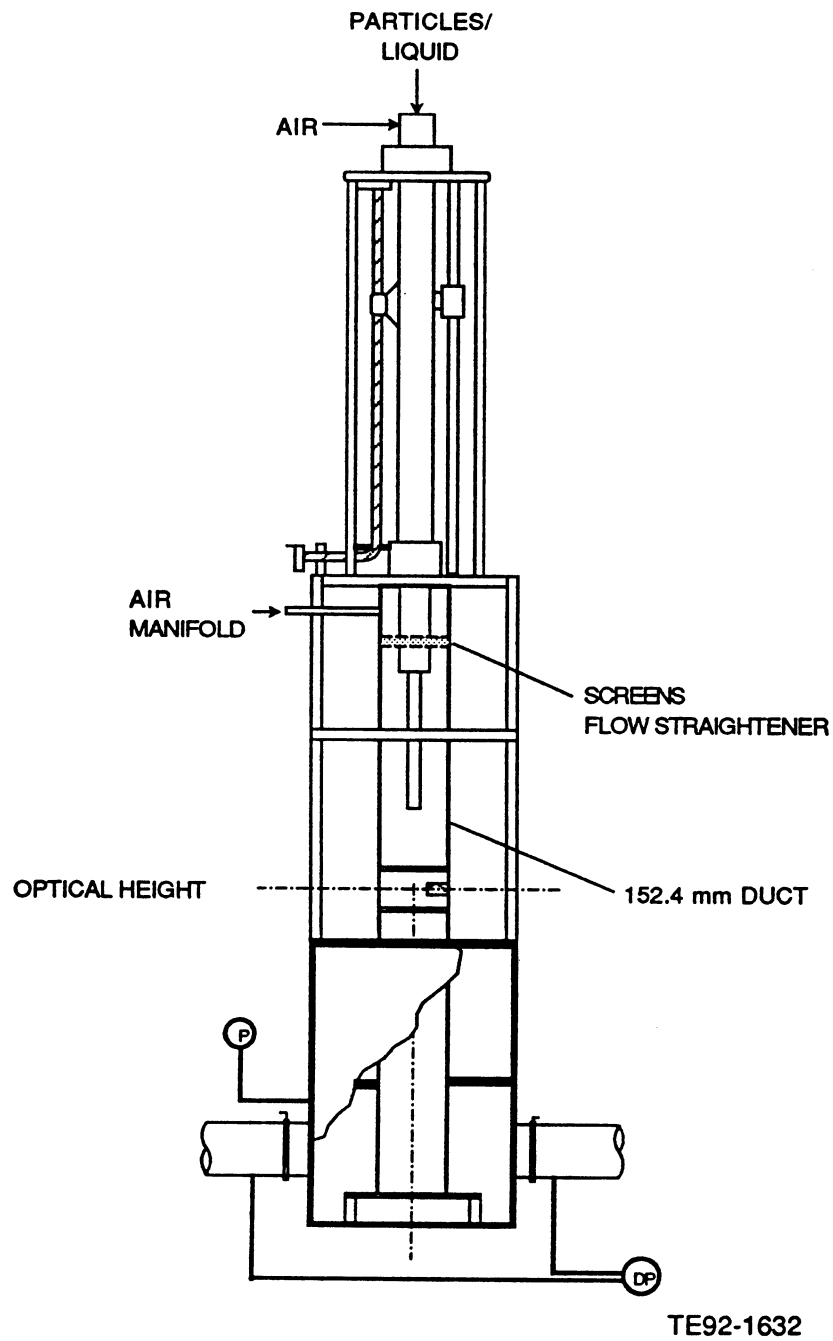


Figure 3.1.2-1. Confined geometry.

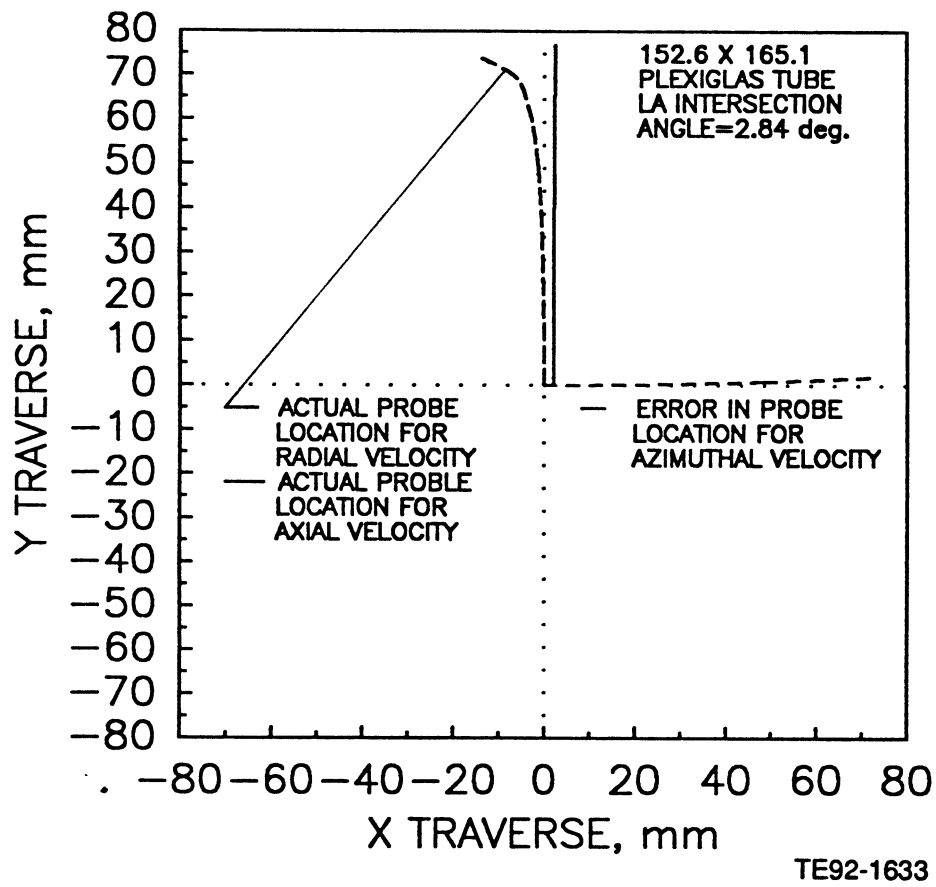
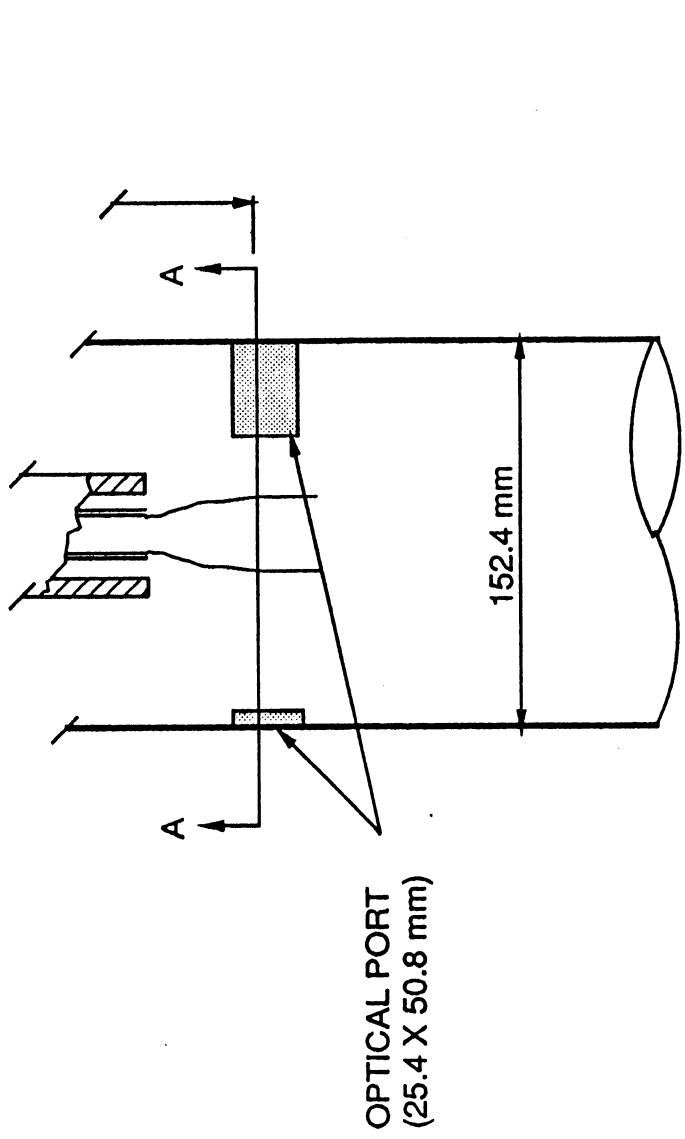
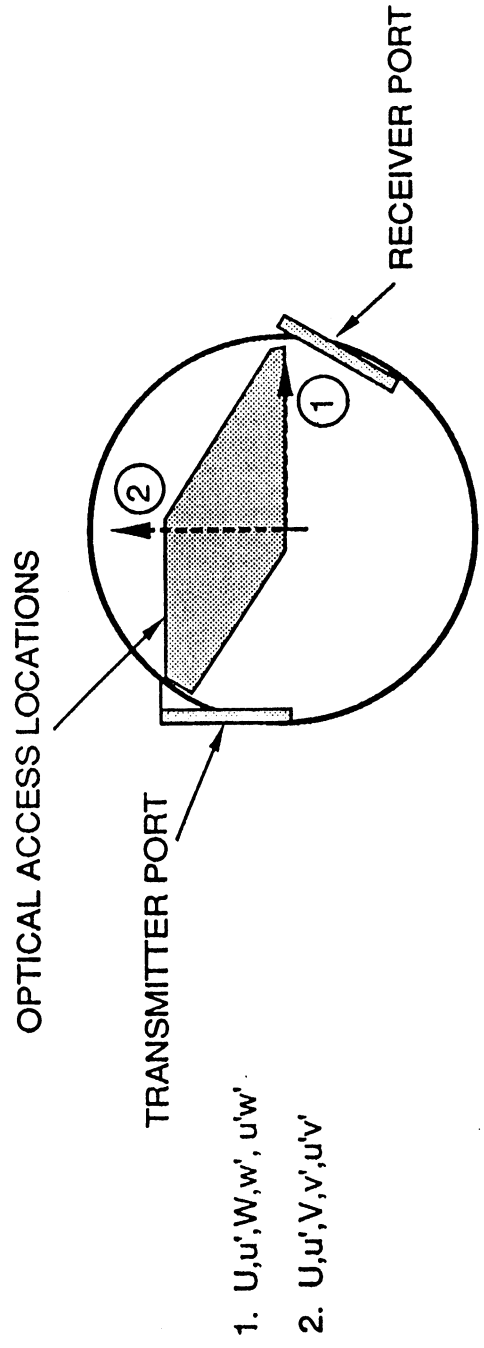


Figure 3.1.2-2. Impact of confined duct on probe volume.



SECTION A-A



TE92-1634

Figure 3.1.2-3. Optical access in the confined duct.

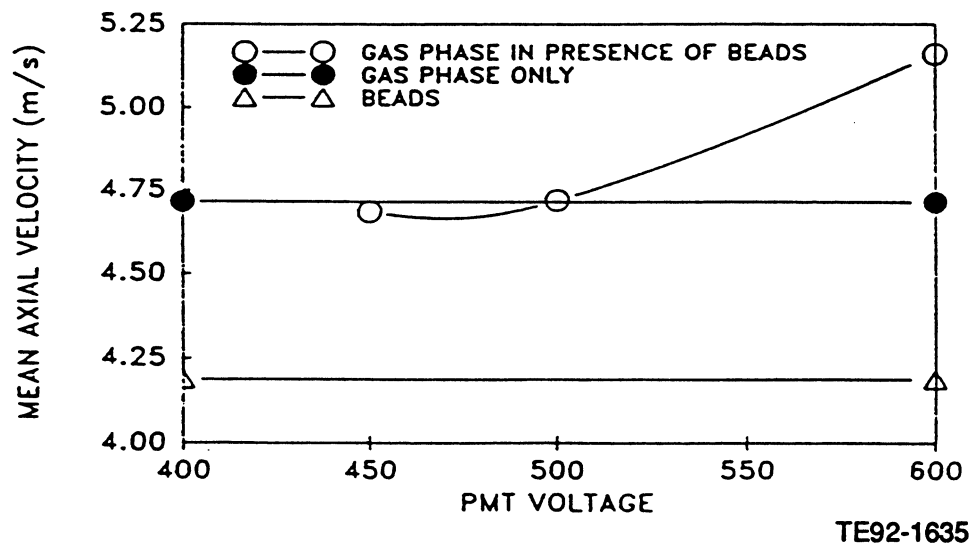


Figure 3.1.2-4. Effect of noise on measurement in the confined duct.

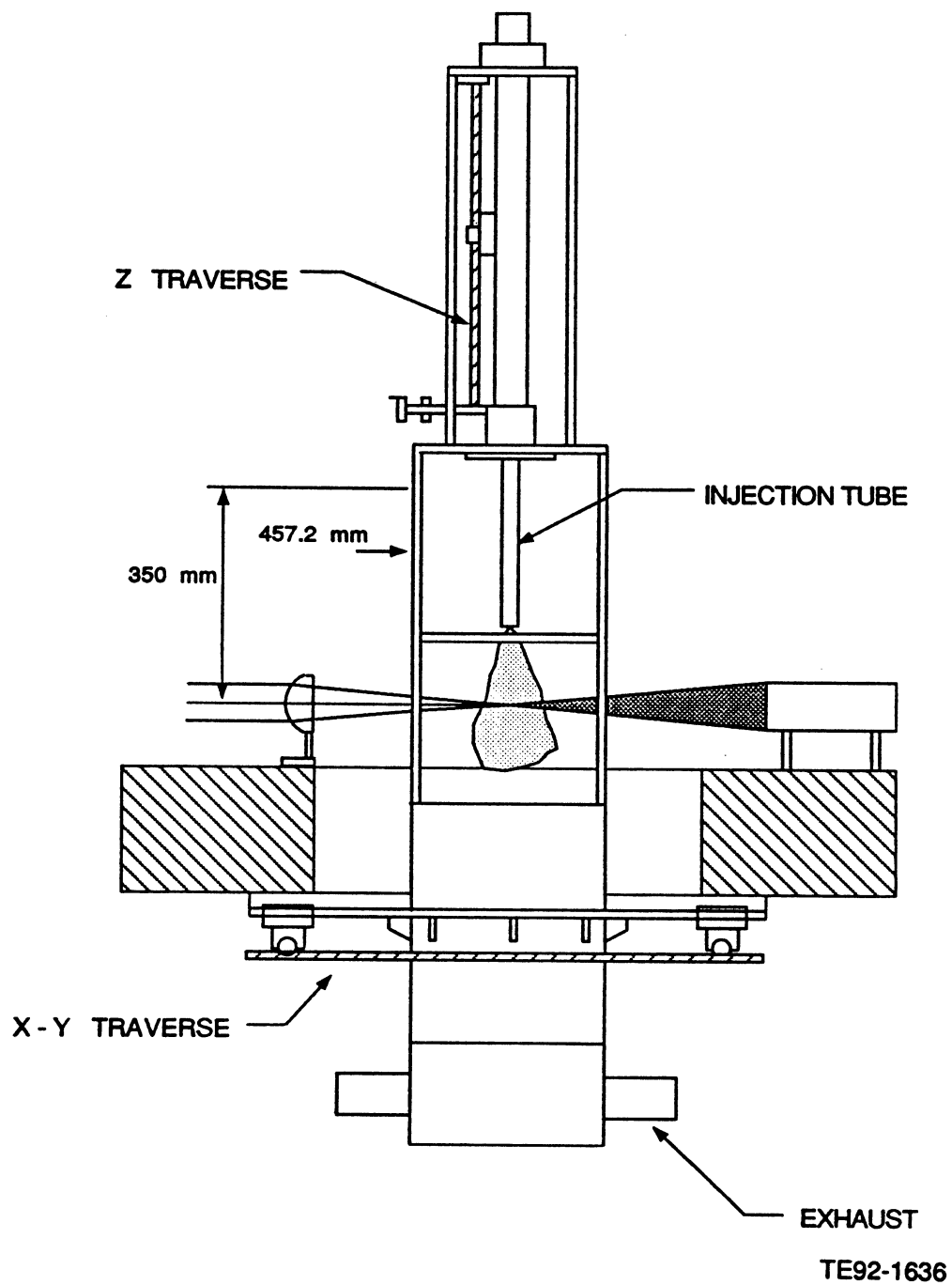
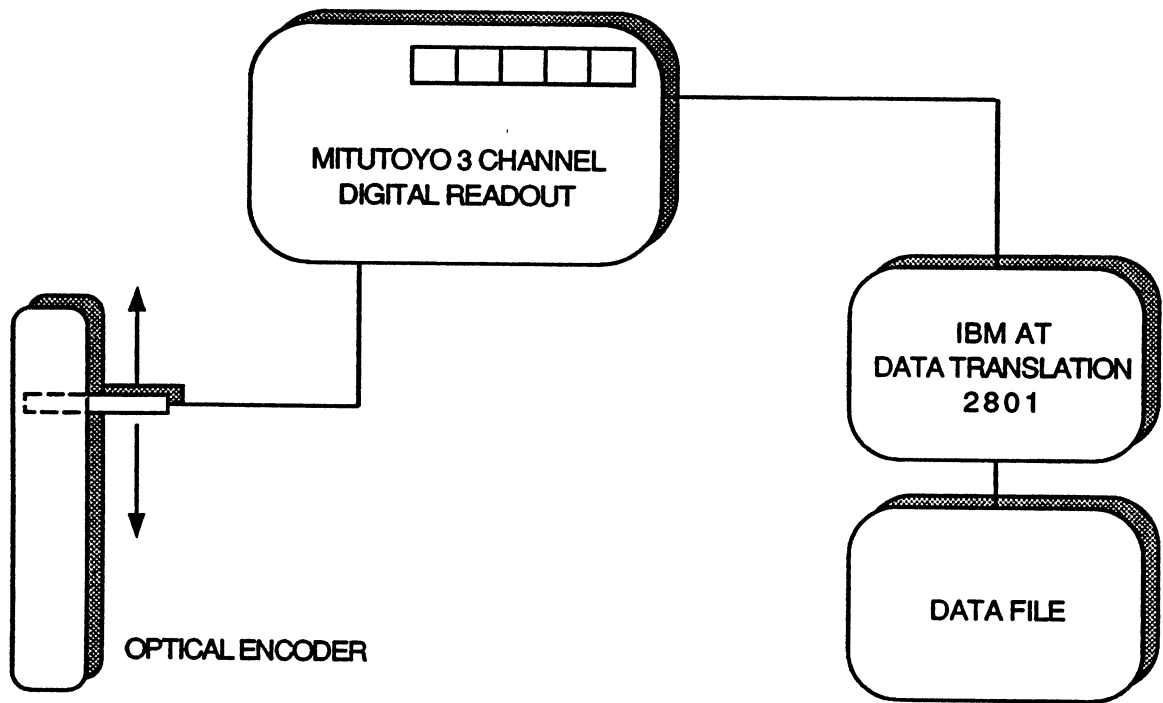
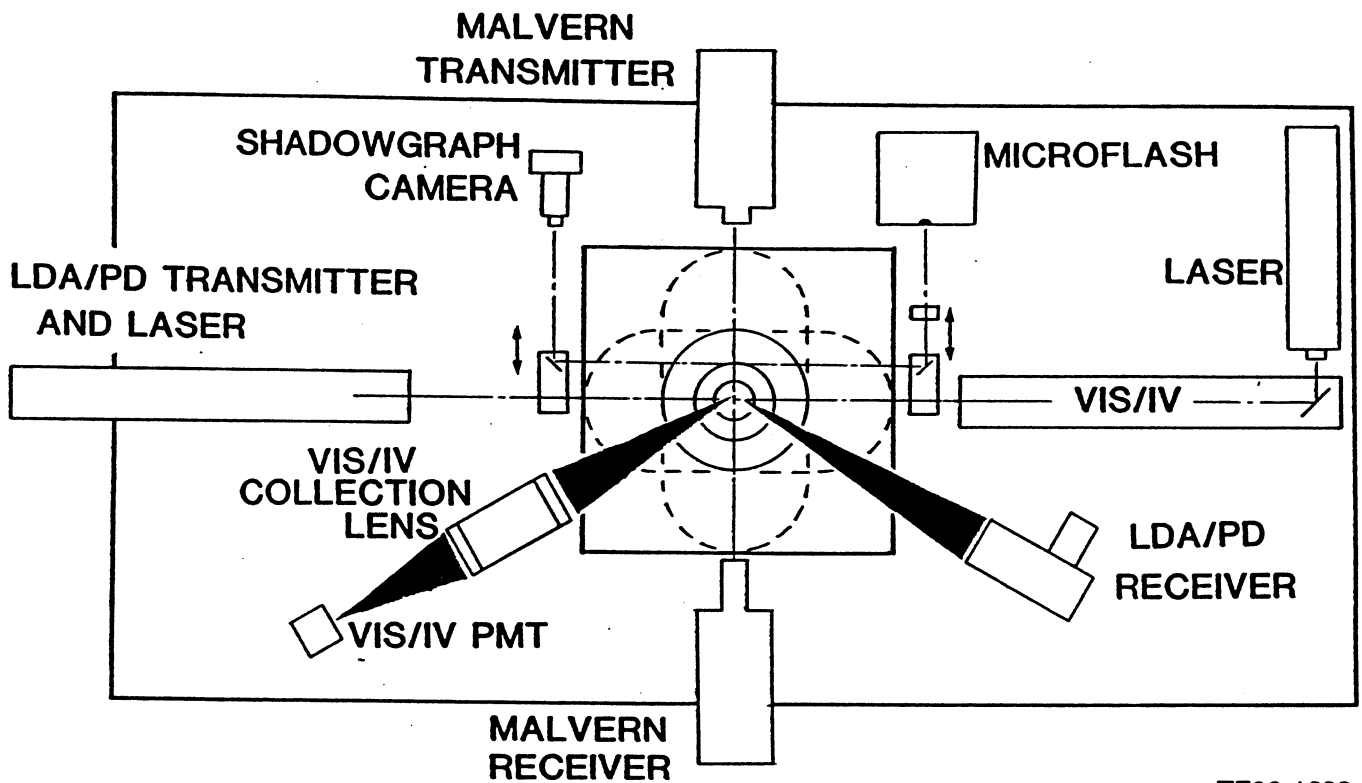


Figure 3.1.3-1. Traverse system.



TE92-1637

Figure 3.1.3-2. Positioning interface.



TE92-1638

Figure 3.1.4-1. Optical table and diagnostic layout.

3.2 MATERIALS FOR THE DISPERSED PHASE

This section discusses the materials selected for the dispersed phase, in this case, glass beads and methanol. Reasons for the selection of the materials are outlined, as are the procedures utilized to optimize quality and eliminate ambiguity due to problems associated with the materials themselves.

3.2.1 Glass Beads

The reason for inclusion of configurations utilizing glass beads is to provide cases representing either monosized or bisized, nonevaporating "spray" fields. As such, beads of uniform shape and properties with a narrow size range were required.

To acquire beads with an acceptably narrow size range, two options were available: purchasing high quality beads or narrowing the size range of an inferior quality bead by an inexpensive means of classification. The cost of the high quality beads was too great in comparison to classification. Hence, medium quality beads were obtained from the Cataphote Division of Ferro Corporation (Class IV, nominal ± 15 microns). An example of these beads "as received" is shown in Figure 3.2.1-1 (a).

The classification procedure is based upon weight and drag, and separates sizes of uniform material to a ± 5 micron size range. Figure 3.2.1-1 (b) also shows the effectiveness of classification. Classification is also a convenient method for reoptimizing beads that have been contaminated or for some other reason fall below the desired level of quality.

The size ranges selected for the beads were based upon two criterion. It was desired that discrimination between the two sizes selected and the seed particles could be maintained and the sizes used were representative of typical drop sizes produced by an air-blast atomizer. Using these criteria, size ranges of 20-30 microns and 100-110 microns were selected.

Owing to the theory behind the phase technique, the discrimination between the two different sized beads is not perfect. This is due to the requirement that the scatterer be spherical and of homogeneous properties. Figure 3.2.1-1 (a) shows particles which are ellipsoidal, cracked, or which have bubbles despite the air classification. These types of particles lead to broadening of the measured size distribution. It is noteworthy that the instrument is not expected to size the glass beads properly. It is required to distinguish between the size classes on the histogram produced. Figure 3.2.1-2 (a) shows a typical distribution obtained for the two sizes when mixed together. Clear separation is evident between the data obtained for each size. Note in Figure 3.2.1-2 (b) that there is little deviation in mean velocity within a given size group, indicating that the classification process has given good results. Post-processing is then used for the calculation of statistics for each size group.

Careful consideration was made in the selection of the liquid used in the studies of spray fields. Methanol (CH_3OH) was selected for several reasons.

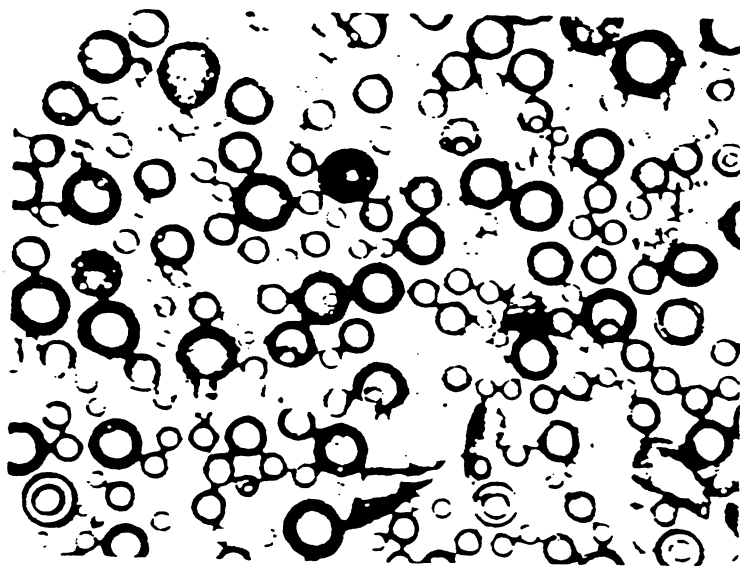
In order to incorporate the modeling of evaporation, a primary challenge for modelers, a fluid having a high vapor pressure was required. This can be achieved by several methods, such as using a heated environment. However, in order to run long tests, this becomes expensive. As a result, it was desired to utilize a fluid which has a high vapor pressure at normal room temperatures and pressures. Methanol meets these needs in addition to providing several other positive features.

Methanol possesses a simple chemical structure which affords its availability in high purity and at a reasonable cost. In addition, methanol vapor has nearly the same density as air (1.32 versus 1.2 kg/m^3) which enables the effects of buoyancy to be eliminated and the effects of vapor diffusion and convection to be simulated as a homogeneous, continuous phase without regard for density gradients. Further, individual droplet temperature effects are reduced by introducing the methanol at -10°C , which is the equi-

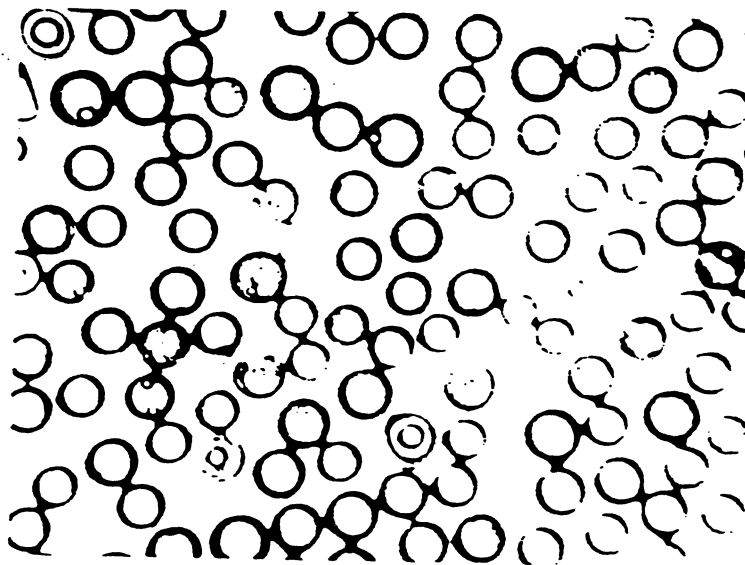
librium or saturation temperature of methanol in air at STP. This value was determined through analysis by Allison and verified through wet bulb/dry bulb experiments. By injecting the methanol at -10°C , the liquid temperature remains constant throughout evaporation. Also to be considered is the temperature of the air, which will drop owing to evaporation of the methanol. This problem is exacerbated by the injection of chilled methanol, since even more heat will be drawn from the air. The worst case can be considered where the air is cooled to -10°C . In this case, the density of the surrounding air will be less than the injected air by 12 percent. In reality, however, the mixing of the different air streams will be rapid and the effects of buoyancy due to thermal gradients will be less than this.

Methanol was obtained from Fischer Scientific (Certified ACS: Catalog No. A412).

a) Unclassified



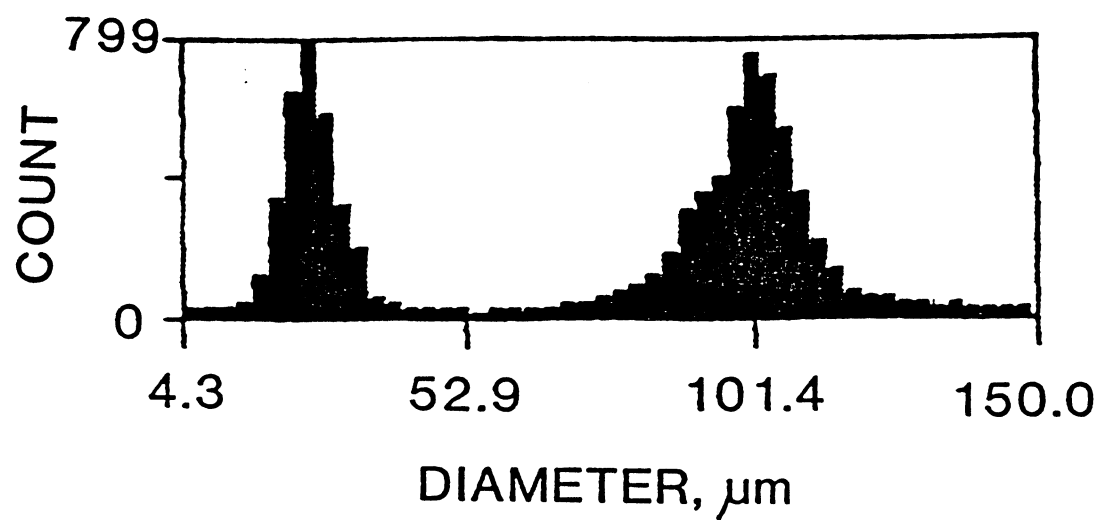
b) Classified



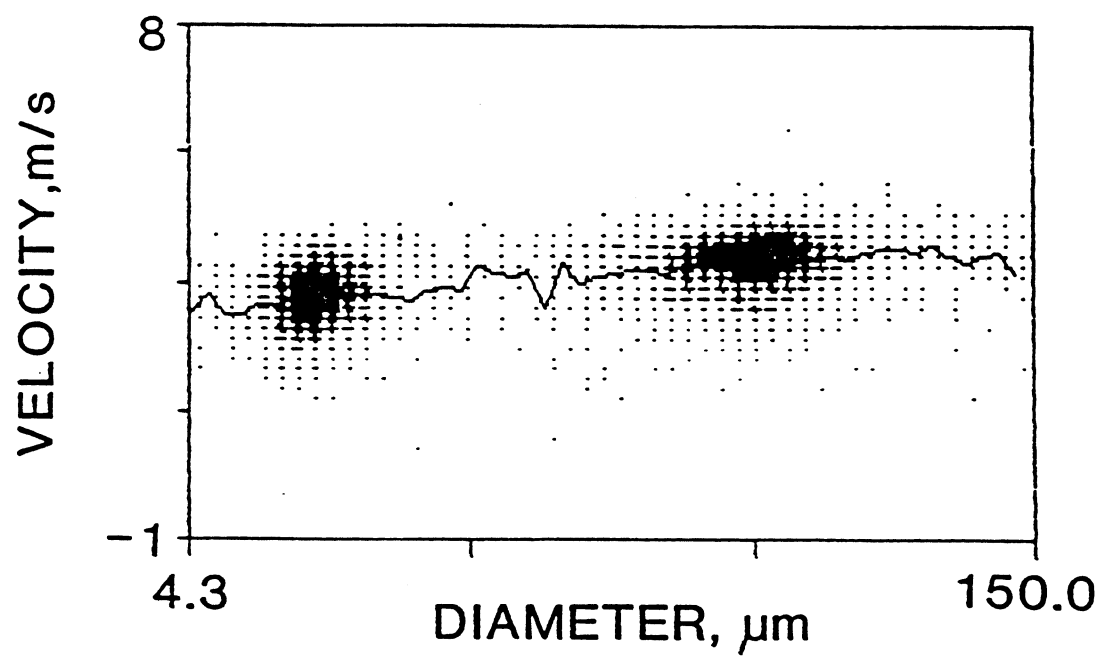
TE92-1639

Figure 3.2.1-1. Monosized glass beads.

a) Histogram



b) Size-Velocity Correlation



TE92-1640

Figure 3.2.1-2. Size class discrimination.

3.3 FLOW SYSTEMS

Figure 3.3-1 illustrates the flow system for the spray facility. Each component of the flow system plays an important part in the generation of a carefully defined and controlled flow field. The need to select and add flows in various manners prescribed by the test protocol requires a high degree of sophistication in the design of the flow system. The flow system can be broken down into four primary components: air delivery, methanol delivery, glass bead delivery, and the exhaust system.

3.3.1 Air Delivery

In the original facility location, dry air (8% relative humidity) is provided to the facility at the house pressure of 585 kPa (85 psig). It is first passed through a Hankinson Centriflex separator/filter (Model No. 3405-1) and a Hankinson Aerolesce Coalescing oil removal filter (Model No. 1306-1) to ensure the removal of all particulate and oil. The air is then passed through a two-stage pressure regulator (Norgren Model No. 11-042-045). This is required to minimize pressure fluctuations in the house air which can lead to slight changes in the delivered air flow rate (+/- 1%). At the second experiment location, the air was not as dry (relative humidity about 20%) and was maintained at 1035 kPa (150 psig). An additional pressure regulator was added to bring this supply down to 585 kPa. The air was then run through the same filter bank as described above.

Clean, dry air is required for two reasons. The first is to prevent condensation of moisture inside the various metering devices. The second reason is to ensure that the cold methanol does not create fog due to the condensation of water vapor in the air. This was expected to be a problem in the confined duct when the windows cooled below the dew point, and is discussed in section 3.3.3.

From here, the air is split into the various required circuits. There are 10 circuits which are supplied with filtered regulated air. These are split off in the order of greatest demand. The highest flowing circuits are split first and the least flowing last. In this way, line losses become less of a factor in the amount of air delivered. Each of these circuits will be discussed in order. Table 3.3-I shows the specifications for the various circuits.

Screen Air Circuit

This circuit provides air to the Plexiglass enclosure. The air passes through a pressure regulator and a 19.05 mm (0.75 in.) critical flow orifice. The flow is regulated by a throttling valve (Lunkenheimer Model No. 2140-1). Pressure taps are placed in the line on either side of the orifice and the deflection of red oil is used to determine flow. After the valve, the air enters a 63.5 mm (2.5 in.) hose which carries the air to the Plexiglass structure. The hose splits and each half carries part of the air to either side of the Plexiglass structure.

Figure 3.3.1-1 shows the manifold into which the air is then dumped. The manifold is designed to distribute the air evenly within the structure. This is achieved by utilizing different sized holes in the manifold and directing them upwards away from the flow field being studied. The two hole sizes were picked to generate different amounts of penetration into the structure. This combination of upward directing and varying penetration provides good mixing of the air and creates the necessary quiescent environment for accurate boundary conditions. Coupled with the exhaust system, the air provided to the Plexiglass structure defines the environment into which all the flows are injected.

Table 3.3-I.
Flow system circuit specification.

<u>Circuit</u>	<u>Pressure regulator</u>	<u>Calibrated pressure kPa (psi)</u>	<u>Valve</u>	<u>Rotometer^a</u>	<u>Maximum flow rate at calibrated pressure (kg/sec)^b</u>	<u>Operating flow (kg/sec)^b</u>
Methanol liquid ^c	—	—	part of rotometer	Sho-rate 1355-8506 Tube # R-2-15B	3.3×10^{-3} (carboly ball)	2.1×10^{-3}
Seeder air						
Nebulizer	Norgren #R07-200- RNKA	207 (30)	part of rotometer	Sho-rate 1355-8506 Tube # R-2-15B	1.1×10^{-4} (sapphire ball)	1.0×10^{-4}
Dilution	Norgren #R07-200- RNKA	207 (30)	part of rotometer	Sho-rate 1355-8506 Tube # R-6-15B	1.04×10^{-3} (sapphire ball)	2.08×10^{-4}
Atomizing air	Norgren #R12-400-RNLA	207 (30)	Whitey SS-21RS4	1110 Tube # R-8-2M5-4	2.83×10^{-3} (float # 8RV3)	2.1×10^{-3}
Swirl air	Norgren #R12-400-RNLA	207 (30)	Whitey B-18VF8	1110 Tube # R-8-2M5-4	1.87×10^{-2} (float # 8LJ-48)	3.3×10^{-3}
Screen air	Watts R119-126	69 (10)	Lunkenheimer	Dwyer Well Manometer #310	6.23×10^{-2} (red gage oil)	1.7×10^{-2}

^a Brooks, unless otherwise specified

^b airflows: multiply kg/sec by 1767 to get standard cubic feet per minute

^c operating flow: 16.6 lb/hr

Confined Screen Air

The air circuit for confined screen air is the same as the air circuit described above. The difference is that the air is introduced into the confined duct using a manifold arrangement as shown in Figure 3.3.1-2. The flow is split into four flows which are recombined as opposed jets in the manifold. A flow straightener is used to dampen out any local velocity peaks in the resulting flow as it travels down the duct towards the measurement region. Measurement in the duct shows that the flow is well developed at the measurement plane and that the optical ports do not perturb the central portion of the flow field.

Swirl Air Circuit

This circuit is similar in nature to the two described above. A rotometer arrangement is used to provide good sensitivity and flow rate monitoring. A 12.7 mm (0.5 in.) line is used to transport the air from the

valve to the swirl air passage. The air travels 1325 effective duct diameters (based on hydraulic diameter of the swirl passage) before it reaches the swirler location.

Atomizing Air Circuit

A rotometer arrangement is utilized again. The selection of tube size and float type were made to give the maximum sensitivity for the flow rates called for in the testing protocol.

Seeding Air Circuits

The seeding circuits require little air flow. However, in the present experiment, the exact matching of flow rates is required. As a result, the seeding system (described later) utilizes monitored air circuits. Rotometers are utilized owing to their ability to monitor very low flow rates.

All the air circuits were calibrated using a Laminar Flow Element (Meriam Model No. 50MW20-1) or a GCA/Precision Scientific wet test meter (Model No. 63111) depending on the amount of flow being calibrated. All flows were calibrated at 30 psig. Necessary correction for flow temperature and pressure were made. All flow circuits were then checked for critical flow in all configurations. A gauge is placed immediately downstream of the regulating valve for the nozzle air to continuously monitor the back pressure and ensure maintenance of critical flow at the calibrated pressure.

3.3.2 Glass Bead Delivery

The beads are added directly to the nozzle air which is run into the bead injector. Primary concerns with the injection of the beads include the mixing of the beads in the flow field to ensure a uniform concentration of the beads throughout the flow field at the exit of the bead injector and uniformity of delivery. To facilitate mixing of the beads in the air stream, an upstream location of $z/D = 150$ for injection of beads was selected. The manner in which the beads are injected ensures that the beads remain suspended in the nozzle air, with the drag force due to the nozzle air being three orders of magnitude greater than the force due to gravity.

The dryness of the air into which the beads are injected, in combination with the aluminum and nylon hoses which carry the two phase flow, promotes a buildup of static charge and, thus, local peaks in concentration in the flow field. Figure 3.3.2-1 (a) demonstrates the effect of static charge on the flow field. To eliminate this problem, several approaches were considered.

To eliminate the problem, a controlled amount of moisture was added to the air stream. Variations in the amount of moisture were controlled by humidifier nebulizers fully contained within the flow circuits. It was found that the addition of 1.5% by volume of water vapor sufficiently increased the humidity to offset the buildup of charge on the beads. Fortunately, these nebulizers were available as part of the seeding system described in more detail in section 3.5. Figure 3.3.2-1 (b) shows the resulting flow field after adding moisture. The amount of water vapor added is not enough to introduce new errors due to density gradients as discussed. To further enhance the elimination of charge, a strongly dissociating substance such as salt can be added to the water which is nebulized to provide better charge transfer.

The second area of concern involved the steady injection of beads into the flow field. To minimize cost, a screw feeder was selected to feed the beads into the nozzle air. Several modifications were made to the discharging end of the feeder as shown in Figure 3.3.2-2. A mixer tube was sealed over the discharge tube as shown. The discharge tube is oriented so that the opening points slightly upwards. The mixer tube tends to fill up, damping out the pulsations that would otherwise occur from the motion of the screw. Prior to the inductor, the nozzle air is split into two portions. The smaller portion is directed to a tube above the opening of the discharge tube which directs a jet of air onto the beads sitting in the tube, mixing them in the discharge tube and mixer further damping out pulsations. The remainder of the air is directed through the Venturi inductor creating a suction on the body of the inductor, entraining the beads

into the nozzle air. The split air circuit permits careful balancing of pressure or vacuum in the inductor body. By monitoring the pressure/vacuum gauge, stable operating conditions are then identified for the system. The configuration can then be changed and brought back to the same conditions. High speed cinematography demonstrated careful use of the above system establishes a flow field with no pulsations.

3.3.3 Methanol Delivery

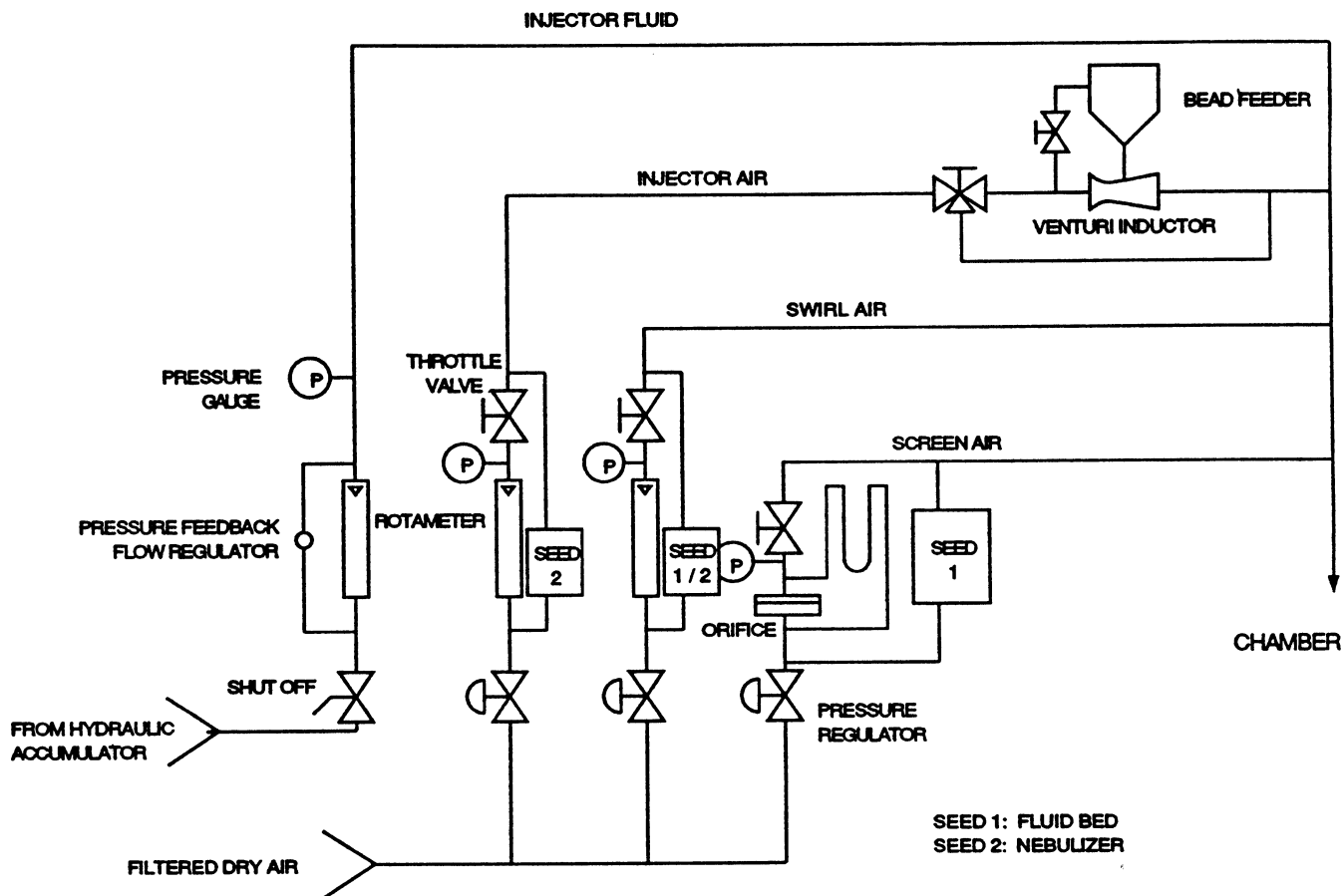
Steps taken to eliminate variables associated with the delivery of methanol included the use of a hydraulic accumulator and refrigeration.

A schematic of the accumulator is shown in Figure 3.3.3-1. The accumulator provides the advantages of a constant pressure reservoir delivery system as well as those of a gear pump arrangement, while eliminating the disadvantages of both. The methanol delivery pressure originally required for the flow rates selected for this study was nominally 105 psig. Tests demonstrated that, at this head pressure, the pressurizing gas is absorbed into the methanol. These tests involve the pressurizing of a gaseous volume above a standing reservoir of methanol for a given period of time. Such a setup is typically used for fuel delivery in atomization experiments. It is noteworthy that the data sets obtained by Solomon et al (1985) and Shearer et al (1979) used this technique for delivery of the fluid without concern for gas absorption. Subsequent removal of the pressure as the methanol is atomized allows the gas to escape rapidly. This escape of gas causes secondary atomization or "flashing" as the spray field evolves. The effects of this phenomenon have been utilized to enhance atomization and have been documented by Solomon et al (1985). The hydraulic accumulator permits the methanol to be isolated from the pressurizing gas and, as a result, eliminates the phenomena described above. The elimination of secondary atomization reduces ambiguity in the development of the spray field, permitting only aerodynamic and mass transfer effects to be studied, hence minimizing complications for the modeler. Ironically, modifications to the atomizer to create a more flexible system revealed that 90% of the pressure drop was due to a filter in the fuel passage. In the configurations used for testing, in fact, no filter was used, and the pressure drop reduced to about 12 psig. Because of this, the use of the accumulator was not as critical.

Calculations and experiments were used to determine a saturation temperature of methanol of -10°C . By injecting the liquid at this temperature, the need to account for changes in temperature of the liquid as it evaporates is eliminated. The elimination of this effect is important for modeling (Mostafa and Mongia, 1987). An inline refrigerator (Weber Engineering and Manufacturing custom design) was designed for application to this problem.

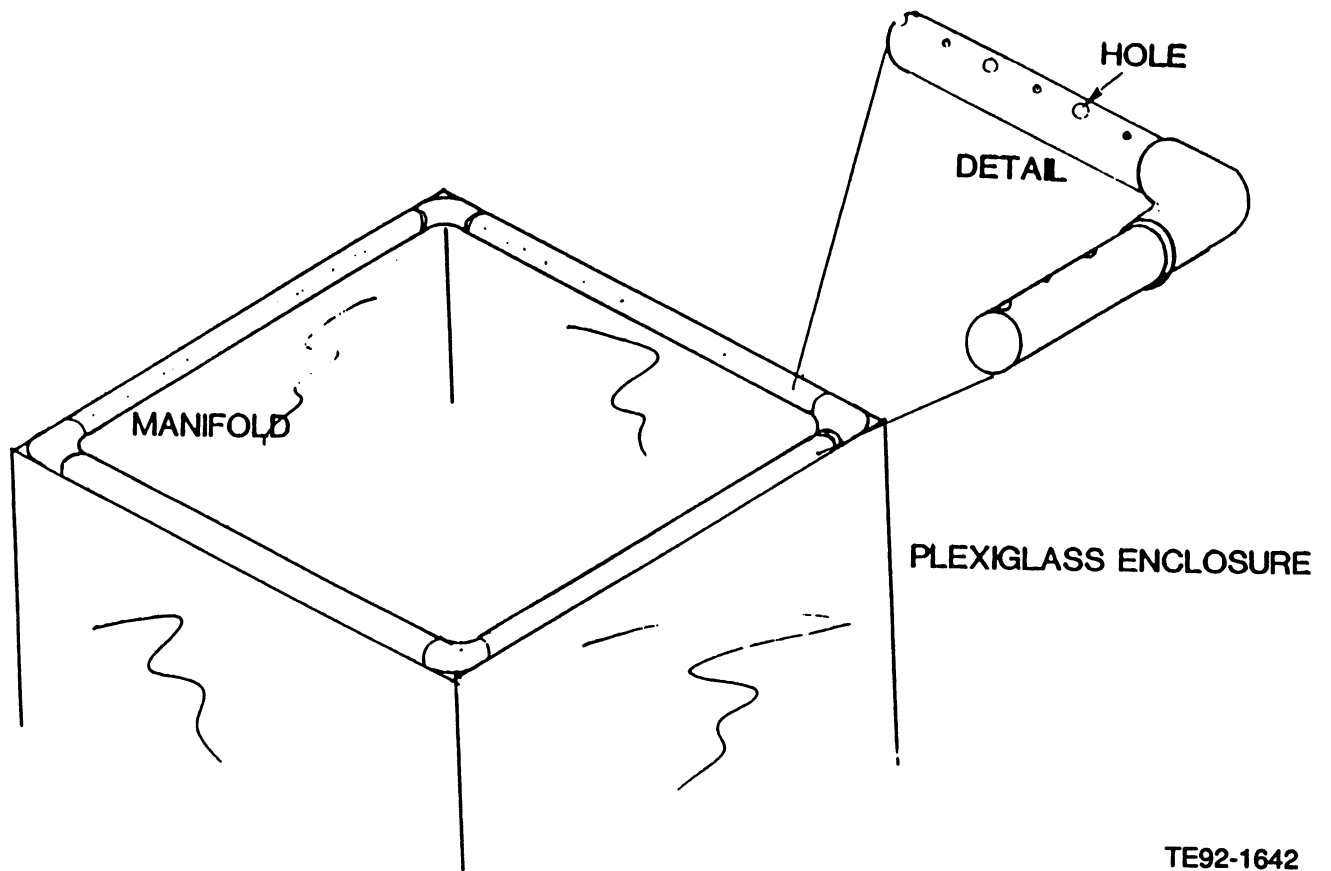
A potential problem with injection at -10°C was fogging. The cold temperatures in the air could cause water vapor to condense out, creating fog within the chamber. This was especially a concern in the confined duct. During the testing, the room conditions were maintained at 30% relative humidity. The relative humidity of the air supplied to the experiment was consistently below this due to the driers and filters used. At 30% relative humidity, the dew point is 13.8°C . Measurements within the spray using a thermocouple shielded from direct impact of the spray showed that the air temperature was 14 to 16°C . Based on these findings, fog was not expected to occur when using the dry experiment air. Subsequent testing in the confined duct revealed that some fogging did occur on the outside of the duct on the optical windows. No fogging was observed on the inside of the duct. The fog on the outside was cleared by blowing a stream of air from the compressor system across the windows.

Additional concern was raised when using the seeders which placed water into the experiment air. Calculations showed that, in the worst case, the seeder water raised the relative humidity within the chamber by no more than 3%. Examination of the confined duct while running the seeders revealed no fogging inside. As an extra precaution, methanol was used in the seeders when running the methanol experiments requiring seed.



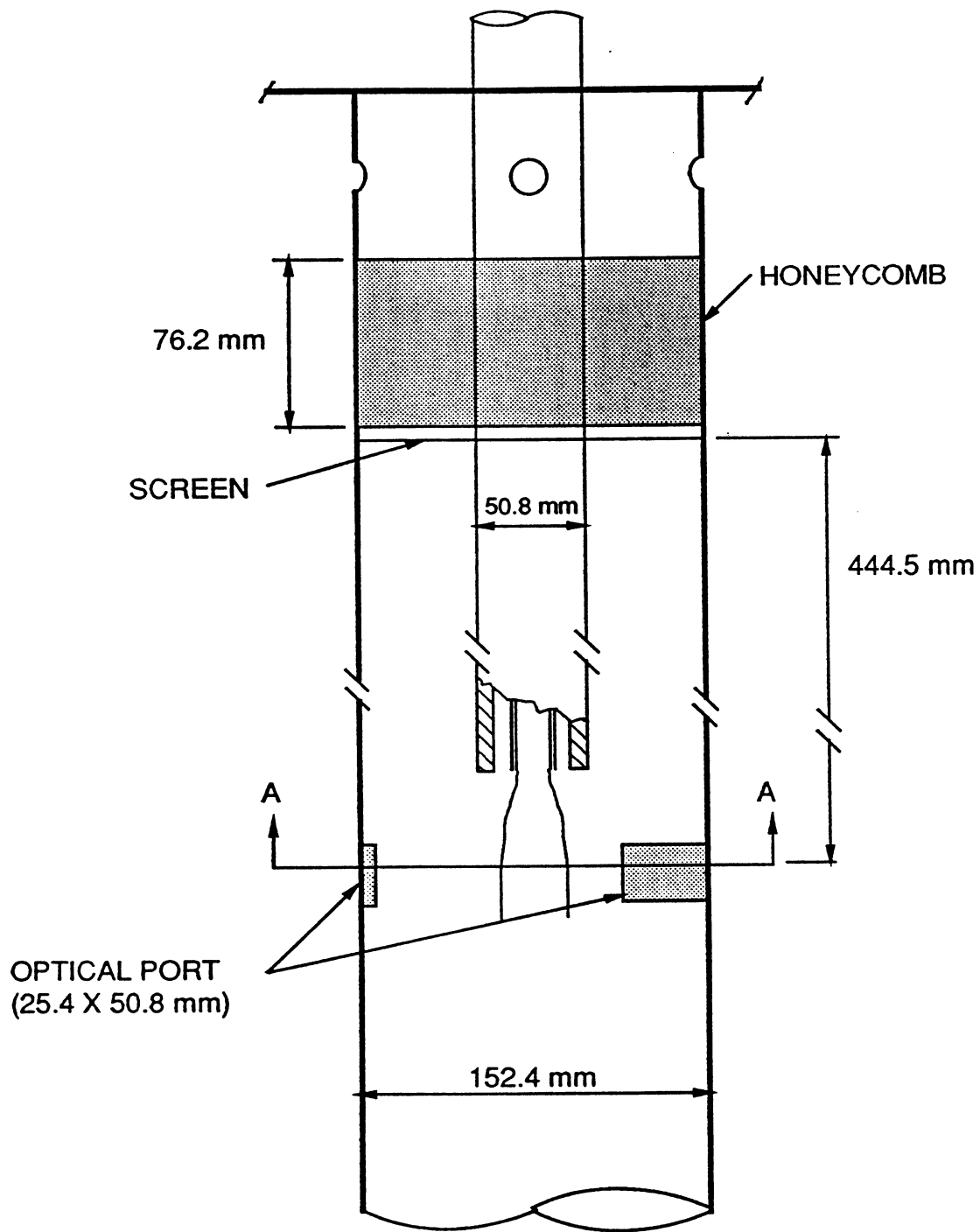
TE92-1641

Figure 3.3-1. Flow system.



TE92-1642

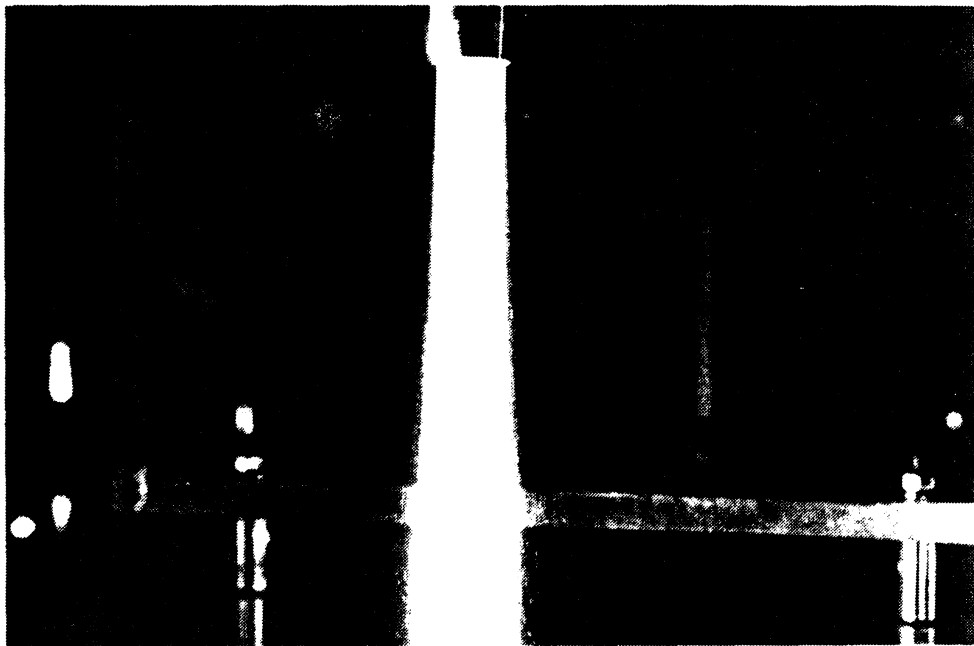
Figure 3.3.1-1. Unconfined screen air manifold.



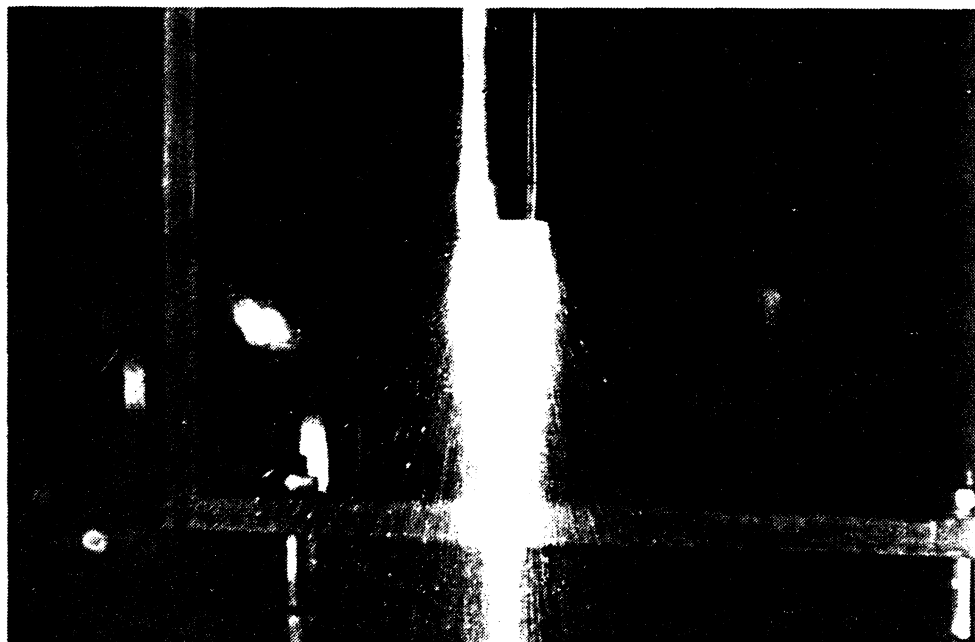
TE92-1643

Figure 3.3.1-2. Confined screen air manifold.

a) With Water Vapor

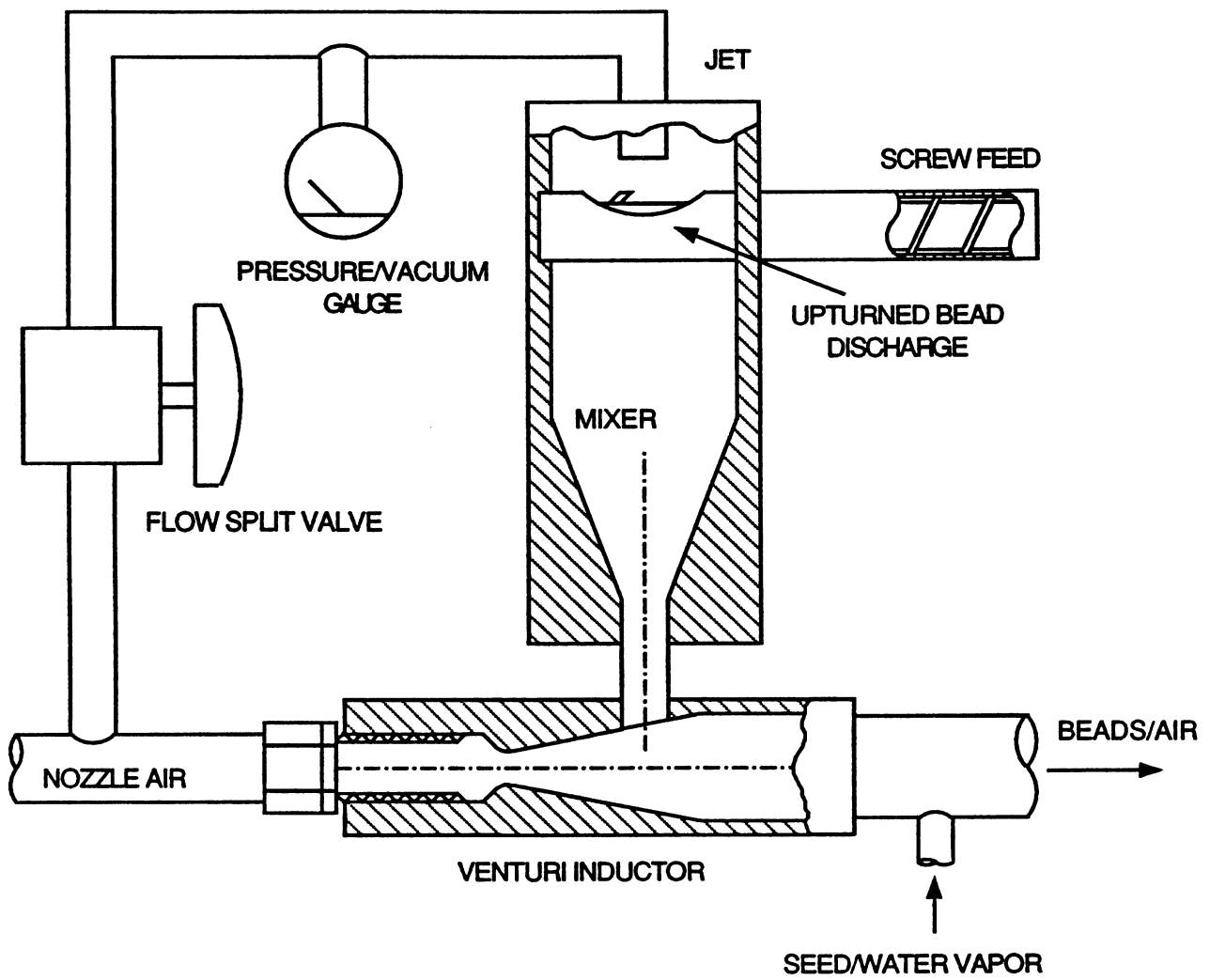


b) Without Water Vapor



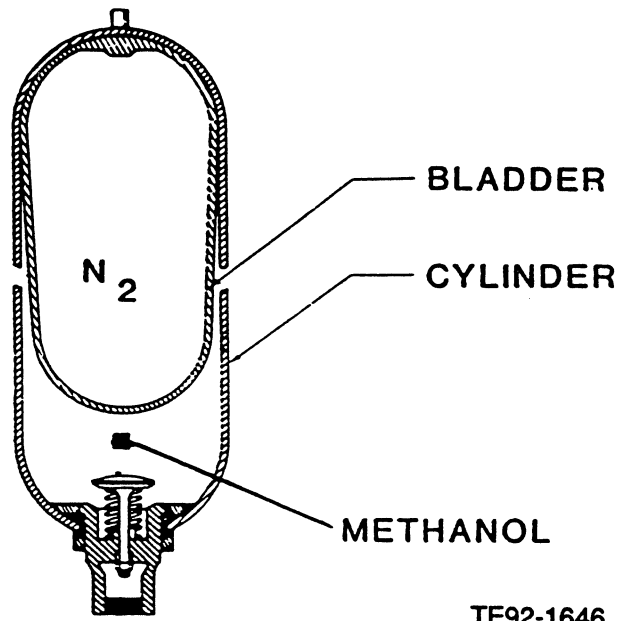
TE92-1644

Figure 3.3.2-1. Particle-laden jet.



TE92-1645

Figure 3.3.2-2. Modified screw feeder.



TE92-1646

Figure 3.3.3-1. Hydraulic accumulator.

3.4 INJECTOR/SWIRLER ASSEMBLIES

In the interest of providing data relevant to practical combustor systems, the hardware studied for methanol injection was selected from an actual combustor system. The atomizer used is a production helicopter gas turbine fuel injector (Ex-Cell-O P/N 506P020) typical of the air-blast variety found in current gas turbine combustor designs. A schematic of the atomizer is shown in Figures 3.4-1 and 3.4-2. Figure 3.4-1 shows a detailed schematic of the atomizer without the nozzle air cap. The dotted outline of the 0.25-inch fuel tube is shown at the top of the injector. The dotted line which appears at the bottom of the contraction on the shaft of the nozzle corresponds to the end of an adaptor piece constructed to interface the fuel tube to the atomizer. The adaptor replaces the standard AN fitting and a threaded mounting piece which holds the atomizer in place in the actual engine. To facilitate easy installation, and to provide long lengths of pipe upstream of the swirler, the adaptor concept was employed.

With the adaptor, the nozzle is fitted into the fuel tube as shown in Figure 3.4-2. A recess on the O.D. near the end of the 27.50 mm tube corresponds to the location of the swirl vanes when the outer air tube is in place. Note that the vanes, when in place, are recessed 6.35 mm behind the nozzle exit. This will later be discussed in more detail.

3.4.1 Injector Flow Split Study

Because the atomizer features two air circuits, one on either side of the liquid filming surface, it is important to quantify the air flow through each. In order to do this, a series of tests were conducted in which one passage was blocked and air was flowed through the other circuit at a known rate.

A plenum was used for the tests as shown in Figure 3.4.1-1. A square box 150 x 150 x 250 mm was used. The pressure drop was recorded for a variety of flow rates with each circuit blocked and with neither circuit blocked. In addition, tests were run with and without methanol flowing at the design rate. This information was used to calculate the effective area of the atomizer as a whole and of the individual air circuits using Equation 1 (Chang, 1985).

$$A_{cd} = m T_1^{0.5} / (2.0547 * P_1 * F(r_2)) \quad (1)$$

where

m = mass flow of air

T_1 = inlet temperature ($^{\circ}R$)

P_1 = inlet pressure (psia)

$F(r_2) = [(r_2)^{1.4286} - (r_2)^{1.7143}]^{0.5}$

where

$r_2 = P_2/P_1$, where P_2 is the outlet pressure

The results of the tests are summarized in Table 3.4-I. Note that the sum of the individual areas is not equal to the area of the overall area. This is consistent with tests run at Textron Turbo Components, where typically it was found that areas do not sum properly due to stream interaction not present in the cases where a single passage is blocked. In summary, the flow split between each passage is about the same, and the total area is reduced when methanol is present.

3.4.2 Nozzle Symmetry Evaluation

The goal of the symmetry testing was to identify a nozzle which provided an axisymmetric flow. Because of the practical hardware utilized, symmetry was a concern. To this end, nearly two dozen nozzles were screened for symmetry. Because most of these were "burnt" (i.e., run in engine tests), many had obvious defects such as bent bodies, or dented air shrouds. These were eliminated without significant evaluation. The remaining half-dozen atomizers were screened more carefully. In an effort to obtain a highly sym-

Table 3.4-I.
Results of flow split test.

<u>Case</u>	<u>A_{cd}</u>
No Blockage	
No methanol	0.0359 in ²
Methanol	0.0309 in ²
Center Blocked	
No methanol	0.0184 in ²
Methanol	0.0181 in ²
Outer Blocked	
No methanol	0.0206 in ²
Methanol	0.0185 in ²

metric atomizer, a handmade version with tight machining tolerances was included in the nozzles obtained.

An example of the comparison among three of the atomizers is presented in Figures 3.4.2-1 and 3.4.2-2, where the effect of nozzle orientation on the mean spray velocity and SMD are presented, respectively. Note that, for example, nozzle C is significantly less symmetric than either A or B. Based on this study, nozzles A and B were judged to be the best, and nozzle B was selected for testing. Interestingly, the handmade nozzle (A) was expected to perform better than the others, and, in fact, was subjected to detailed preliminary testing before considering nozzles B or C.

The preliminary tests on nozzle A were detailed in nature and considered both the symmetry of the gas phase as well as the drops. Interestingly, symmetry of the spray did not necessarily guarantee symmetric gas flows. The results from nozzle A are shown in Figures 3.4.2-3 through 3.4.2-6. Figure 3.4.2-3 presents the locations at which data were collected. Note that all data were collected along a single radial traverse, and that, for plotting, the results from each profile were rotated about the centerline to reflect the rotation of the nozzle.

Figure 3.4.2-4 presents isopleths of the mean axial velocity at 50 mm downstream of the injector for the case without and with the spray. The case without the spray (Figure 3.4.2-4 [a]) exhibits a kidney shaped result, rather than a circular pattern. When the spray is turned on, the pattern becomes much more symmetric (Figure 3.4.2-4 [b]). The lobed nature of the patterns with the spray could be attributed to the distinct passages through the atomizer.

The azimuthal velocity results (shown in Figure 3.4.2-5) exhibit trends which are correlated directly to the observations in Figure 3.4.2-4. In Figure 3.4.2-5 (a), the locations where the azimuthal velocity profiles show the highest values correspond to the location of the major axis of the ellipsoid formed by the axial velocity isopleths.

Based on this, the more circular pattern of the axial velocity isopleths with the spray on should result in uniform azimuthal velocity profiles. And this is the case, as observed in Figure 3.4.2-5 (b).

In summary, for nozzle A, it was observed that the gas phase velocity fields were quite symmetric for the case with the spray. However, the single-phase cases were not as symmetric. Similar results for the liquid flux distribution were also observed, as shown in Figure 3.4.2-6. Although nozzle A was made quite carefully, it did not perform ideally.

Based on the detailed studies of nozzle A, it was decided to use nozzle B in the actual data runs for the program. Subsequent testing of nozzle B revealed that, in fact, it was more symmetric, in the single-phase case, but that it still revealed some asymmetry. This will be shown in Section IV.

3.4.3. Aerodynamic Swirler

The swirler used in the conditions calling for swirl is manufactured by Allison for use in conjunction with the above atomizer in the same production gas turbine combustor. A schematic of the swirler is shown in Figure 3.4.3-1. Based on the design of the swirler, a swirl number of 1.53 was determined using Equation 2 (Beer and Chigier, 1976)

$$S = \frac{2}{3} \left| \frac{1 - (R_h/R)^3}{1 - (R_h/R)^2} \right| \tan \alpha \quad (2)$$

where

R_h = radius of hub (27.55/2)

R = radius of outer wall (36.68/2)

α = angle of vane from flowstream (60 degrees)

As with the atomizer, the use of industry hardware for the swirler, while making the data obtained more relevant to practical systems, also introduces problems associated with relatively low manufacturing tolerances. As such, the testing protocol requires testing the swirlers for symmetry. In this case, two swirlers were evaluated. For this study, air was run through the central 24.9 mm pipe and through the swirler surrounding it. Two tests were run, both of which required measurements of velocity at a radial location of 18 mm from the centerline at two axial locations. The first test involved rotating the central tube (nozzle) while leaving the swirl vanes fixed. The second test involved rotating the swirl vane assembly while leaving the central tube fixed. The results are presented in Figure 3.4.3-2.

Swirler 1 (Figure 3.4.3-2 [a]) shows little variation in axial velocity when the nozzle is rotated independent of the swirler. However, when the swirler is rotated independent of the nozzle, a modest local maximum in the velocity is observed at the 120 and 150 deg orientation at the 75 and 150 mm axial locations.

In comparison, swirler 2 (Figure 3.4.3-2 [b]) shows similar results for the case where the nozzle is rotated independent of the swirler, but shows a more random behavior for the case where the swirler is rotated independent of the nozzle. Further, the amount of variation for a given orientation is less for the second swirler. Based on this study, swirler 2 was selected for use in the testing.

3.4.4 Evolution of Experimental Test Conditions

The original flow conditions were set based upon typical operating conditions for the Ex-Cell-O nozzle/swirler configuration. The swirl flow condition was set by Allison based on a gas velocity of 300 ft/sec through the 60 deg swirler. From this velocity, and knowledge of the effective area of the 60 deg swirler, the representative mass flow of 0.0133 kg/s was established. To determine the nozzle operation condition, flow rates for the air and fuel that represented the average flow conditions for the Ex-Cell-O nozzle were selected. Thus the mass flow of methanol was set at 0.0021 kg/s and the desired air-to-fuel ratio of 1.0 set the corresponding atomizing air flow at the same value.

Both confined and unconfined configurations were desired. The former condition was established by the use of a 6-inch diameter Plexiglass duct concentrically located around the nozzle/swirler assembly. The original unconfined condition called for an 18-inch duct located in the same manner.

The confined condition called for modest screen air (air injected into the annulus between the nozzle/ swirler assembly and the wall of the surrounding 6-inch duct) for the nozzle-only condition. Both the 60 deg and 0 deg swirl conditions called for blockage of the screen air passage to better represent actual combustor geometry. The above conditions are tabulated in Table 3.4-II and depicted graphically in Figure 3.4.4-1, where the figure letter corresponding to the condition is indicated in the second column.

Table 3.4-II.
Initial test conditions.

Case No.	Figure No.	Injected material	m_a kg/s	m_p kg/s monosized particles	m_p kg/s multisized particles	Confinement		m_s kg/s 0 deg	Swirler ms kg/s 60 deg
						m_c kg/s 457.2 mm duct	m_c kg/s 152.4 mm duct		
1	3.4.4-1 a	Air only	0.0021			0.097			
2	3.4.4-1 b	as base	0.0021			0.0		0.0133	
3	3.4.4-1 b	for effect	0.0021			0.0			0.0133
4	3.4.4-1 e	of	0.0021				0.01		
5	3.4.4-1 f	particles	0.0021				0.0	0.0133	
6	3.4.4-1 f		0.0021				0.0		0.0133
7	3.4.4-1 a	Unconfined	0.0021	0.0021		0.097			
8	3.4.4-1 b	mono-	0.0021	0.0021		0.0		0.0133	
9	3.4.4-1 b	dispersed	0.0021	0.0021		0.0			0.0133
10	3.4.4-1 e	Confined	0.0021	0.0021			0.0025		
11	3.4.4-1 f	mono-	0.0021	0.0021			0.0	0.0133	
12	3.4.4-1 f	dispersed	0.0021	0.0021			0.0		0.0133
13	3.4.4-1 b	Multisized	0.0021		0.0021	0.0		0.0133	
14	3.4.4-1 b	particles	0.0021		0.0021	0.0			0.0133
15	3.4.4-1 f		0.0021		0.0021		0.0	0.0133	
16	3.4.4-1 f		0.0021		0.0021		0.0		0.0133
17	3.4.4-1 c	Air only	0.0021			0.097			
18	3.4.4-1 d	for air-	0.0021			0.0		0.0133	
19	3.4.4-1 d	blast	0.0021			0.0			0.0133
20	3.4.4-1 g	atomizer	0.0021				0.01		
21	3.4.4-1 h		0.0021				0.0	0.0133	
22	3.4.4-1 h		0.0021				0.0		0.0133
23	3.4.4-1 c	Unconfined	0.0021		0.0021*	0.097			
24	3.4.4-1 d	spray	0.0021		0.0021*	0.0		0.0133	
25	3.4.4-1 d		0.0021		0.0021*	0.0			0.0133
26	3.4.4-1 g	Confined	0.0021		0.0021*		0.01		
27	3.4.4-1 h	spray	0.0021		0.0021*		0.0	0.0133	
28	3.4.4-1 h		0.0021		0.0021*		0.0		0.0133

* Polydispersed methanol spray

Modification 1 – Hardware

Discussions of the original conditions led to some modest changes in the hardware. The ability of the 18-inch duct to properly reflect an unconfined environment was questioned. It was decided to replace the Plexiglass duct with one made of screen mesh. The reasoning was that the permeable wall would permit efflux of downstream air that before would have interacted with the physical wall as influx of entrained air. The drawback to this approach was the difficulty of properly seeding the entrainment air. This problem was handled by surrounding the entire delivery tube/plenum assembly with another confined structure. The resulting Plexiglass/tarp confinement structure provided the ability to monitor entrainment air flow and thus ensuring proper seeding.

In summary, the unconfined case is represented by a screen structure 18 in. in diameter which is in turn surrounded by a Plexiglass/tarp assembly which seals the entire test structure from the room. At this point, no flow rate changes were made with the exception that the entrainment air which before was screen air in the 18-inch duct now had no set flow rate. To determine the proper flow, it was decided to balance the pressure inside the Plexiglass/tarp assembly with the room air. The resulting configuration is shown in Figure 3.1.1-1.

Modification 2 – Hardware Changes to Reduce Impingement in the Six-Inch Duct

Impingement in the 6-inch duct was expected to be a problem. Initial testing with the proposed flow rates demonstrated the realization of these expectations. Impingement occurred nearest the nozzle exit (0 in. below) when the 60 deg swirl conditions were used. Because the 60 deg condition most closely represented the operating conditions and geometry of an actual combustor, there was great desire to retain that condition in the test matrix. Two solutions were considered. One was hardware changes to reduce impingement, the other was to modify the flow rates. Because the general goal of the program was to study effect of hardware changes rather than flow condition changes, the first option was exercised initially.

It was decided that a reduction in the spray-cone angle would move the impingement point away from the nozzle exit. Thus, the shroud concept was incorporated. The shroud was to take the place of the original cap at the end of the nozzle assembly. The shroud channeled a portion of the atomizing air around the outside of the nozzle as shown in Figure 3.4.4-2.

Although conceptually sound, the shroud introduced complexities both experimentally and analytically. Experimentally, there was no practical way to monitor the flow rate through the new passage, nor was the concentricity of the nozzle/shroud cap ensured. Analytically, the boundary and inlet conditions were further complicated.

Despite the above drawbacks, one shroud design was evaluated. The design is depicted in Figure 3.4.4-2 (c). The design selected created tractable inlet conditions but the experimental flaws remained. Initial testing of the design proved to be encouraging enough to consider its use.

Modification 3 – Flow Rates

Comparison of the shroud and the no-shroud cases in the 6-inch duct demonstrated that more than physical modifications would need to be considered. Allison and UCICL decided the approach to take would be as follows (for the methanol, confined, 60 deg swirl configuration)

1. vary nozzle flow rates
2. cut swirl air by a factor of 2
3. use the screen air instead of blocking the passage
4. 3-inch dome region adequate for this study

Initial testing demonstrated that the nozzle flow rates did not strongly affect the cone angle; that the swirl air flow rate dramatically affected the cone angle; the screen air was needed to prevent recirculation back above the nozzle, but did not strongly affect the cone angle; and that the 3-inch region would be the limit for testing. Formal testing then followed.

Evaluation of all nozzle/swirler configurations was conducted in the 6-inch duct. It was decided to vary to swirl air, the screen air, and the use of the shroud. The results are summarized in Table 3.4-III.

Overall conclusions drawn from the flow rate studies were

- Screen air is required to eliminate recirculation eddies at the wall.
- Swirl air has the strongest influence on the location of impingement.
- All of the above flows possessed medium to high dynamics which result in the "periodic impingement" above.

From the above it appeared that the condition using the shroud, 0.031 kg/s of screen air, and 50% swirl air would be satisfactory because the majority of the impingement occurred at 3 in. below the nozzle exit. However, the dynamics leading to periodic impingement were unacceptable.

Table 3.4-III.
Impingement testing results.*

<u>Shroud</u>	<u>Configuration</u>	<u>Swirl</u>	<u>Screen (kg/s)</u>	<u>Periodic impinge</u>	<u>Continuous impinge</u>
no	60 deg	100%	0.031	0	+50
		100%	0	-50**	0
		50%	0.031	+25†	+50
		50%	0	-87	+25
yes	60 deg	100%	0.031	+30	+70
		100%	0	-12	+12
		50%	0.031	+28	+75
		50%	0	-38	+25
no	0 deg	100%	0.031	+100	~
		100%	0	-75	~
		50%	0.031	+95	~
		50%	0	-75	~
yes	0 deg	100%	0.031	+88	~
		100%	0	-50	~
		50%	0.031	+88	~
		50%	0	-87	~
no	nozzle-only		0.031	+100	~
			0	-125	~
yes	nozzle-only		0.031	+112	~
			0	-125	~

* Impingement values in mm

** + indicates downstream of injector

† - indicates upstream

Steps to reduce the dynamics were then initiated. The screen air circuit was replumbed to provide higher flow rates. It was found that increasing the screen air created a better behaved flow field, but dynamics still persisted.

Next, the swirl air flow was reduced to 25% of its original value. This reduction indicated that the swirl air was largely responsible for the dynamics. The dynamics with 25% swirl air, 0.040 kg/s screen air, and shroud in place were acceptable. Further, even at 25% of the original flow, the swirl air had a significant effect on the flow field. At this point, the flow conditions were set as follows

nozzle	
fuel	0.0021 kg/s
air	0.0042 kg/s (half to go to shroud circuit)
swirler	0.0033 kg/s
screen air	@ 0.04 kg/s
entrainment air (unconfined)	to be determined

The above conditions were evaluated for the other nozzle/swirler configurations and found to be acceptable.

With the glass beads, it was found that less screen air was required to minimize impingement. As a result, the screen air for the cases with beads was set at 0.027 kg/s. The screen air flow rate of 0.040 kg/s was retained for the cases with spray.

As a last step, it was decided to evaluate the new conditions in the unconfined regime. The conditions were acceptable for glass beads. However, when methanol was evaluated, substantial asymmetries were noted. Subsequent testing of the nozzle-only condition with and without the shroud identified the shroud as the cause of the asymmetries. When the shroud was not used, all configurations operated acceptably.

The asymmetry problem required a new evaluation of the use of the shroud. Testing in the confined duct resumed. It was found that the increased screen air flow (previously unavailable) provided acceptable conditions for the no-shroud case. Before, the use of the shroud moved the impingement point by 25 mm. With the increased screen air, the use of the shroud moved the impingement point 6.5 mm, thus the use of the shroud was dropped in favor of symmetry.

A follow-up evaluation of the no-shroud case in the unconfined regime demonstrated symmetry and well behaved flow. Thus the following flow rates were decided upon

nozzle/bead injector	
air	0.0021 kg/s
methanol or beads	0.0021 kg/s
swirler	0.0033 kg/s
screen air (in all confined testing)	
spray tests	0.040 kg/s
bead tests	0.027 kg/s
entrainment air (all unconfined testing)	to be determined

Because the reduction in swirl air made that flow unrealistic, it was decided to do a limited additional study in both the confined and unconfined cases.

In the confined case, for the conditions above, a test will be run using only air, both 0 and 60 deg swirlers, and a disk blocking the nozzle air passage. This will provide additional data to bridge between element B and C.

In summary, the test matrix shown in Table 3.4-IV represents, in a similar format as the original, the changes made in the testing conditions. The final testing matrix is shown in Table 3.4-IV, including additional configurations added as described above. Note that the case numbers are not continuous. This is because tests were run out of order and the matrix was modified based on modeling needs after this convention for the cases was adopted. The results reported within Sections IV and V reflect the measurements made using the matrix presented in Table 3.4-V. The final geometries have been discussed in section 3.1, and can now be reviewed with the perspective behind their selection.

Table 3.4-IV.
Initial test conditions and changes made.

Case No.	Figure No.	Injected material	m_a kg/s	m_p kg/s monosized particles	m_p kg/s multisized particles	Confinement		m_s kg/s 0 deg	Swirler ms kg/s 60 deg
						m_c kg/s 457.2 mm* duct	m_c kg/s 152.4 mm duct		
1	3.4.4-1 a	Air only	0.0021			0.097*			
2	3.4.4-1 b	as base	0.0021			0.0*		0.0133**	
3	3.4.4-1 b	for effect	0.0021			0.0*		0.0133**	
4	3.4.4-1 e	of	0.0021				0.01 [†]		
5	3.4.4-1 f	particles	0.0021				0.0 [†]	0.0133**	
6	3.4.4-1 f		0.0021				0.0 [†]	0.0133**	
7	3.4.4-1 a	Unconfined		0.0021	0.0021		0.097*		
8	3.4.4-1 b	mono-	0.0021	0.0021		0.0*		0.0133**	
9	3.4.4-1 b	dispersed	0.0021	0.0021		0.0*		0.0133**	
10	3.4.4-1 e	Confined	0.0021	0.0021			0.0025 [†]		
11	3.4.4-1 f	mono-	0.0021	0.0021			0.0 [†]	0.0133**	
12	3.4.4-1 f	dispersed	0.0021	0.0021			0.0 [†]	0.0133**	
13	3.4.4-1 b	Multisized	0.0021		0.0021	0.0*		0.0133**	
14	3.4.4-1 b	particles	0.0021		0.0021	0.0*		0.0133**	
15	3.4.4-1 f		0.0021		0.0021		0.0 [†]	0.0133**	
16	3.4.4-1 f		0.0021		0.0021		0.0 [†]	0.0133**	
17	3.4.4-1 c	Air only	0.0021			0.097*			
18	3.4.4-1 d	for air-	0.0021			0.0*		0.0133**	
19	3.4.4-1 d	blast	0.0021			0.0*		0.0133**	
20	3.4.4-1 g	atomizer	0.0021				0.01 [†]		
21	3.4.4-1 h		0.0021				0.0 [†]	0.0133**	
22	3.4.4-1 h		0.0021				0.0 [†]	0.0133**	
23	3.4.4-1 c	Unconfined		0.0021		0.0021 ^{††}	0.097*		
24	3.4.4-1 d	spray	0.0021		0.0021 ^{††}	0.0*		0.0133**	
25	3.4.4-1 d		0.0021		0.0021 ^{††}	0.0*		0.0133**	
26	3.4.4-1 g	Confined	0.0021		0.0021 ^{††}		0.01 [†]		
27	3.4.4-1 h	spray	0.0021		0.0021 ^{††}		0.0 [†]	0.0133**	
28	3.4.4-1 h		0.0021		0.0021 ^{††}		0.0 [†]	0.0133**	

* Duct replaced by screen. Entrained air taken as needed by flow.

** Swirl flow reduced to 0.0033 kg/s (0.25 times original flow).

† Confinement screen air set at 0.045 kg/s for all confined cases.

†† Polydispersed methanol spray

Table 3.4-V.
Test conditions based on screening tests.

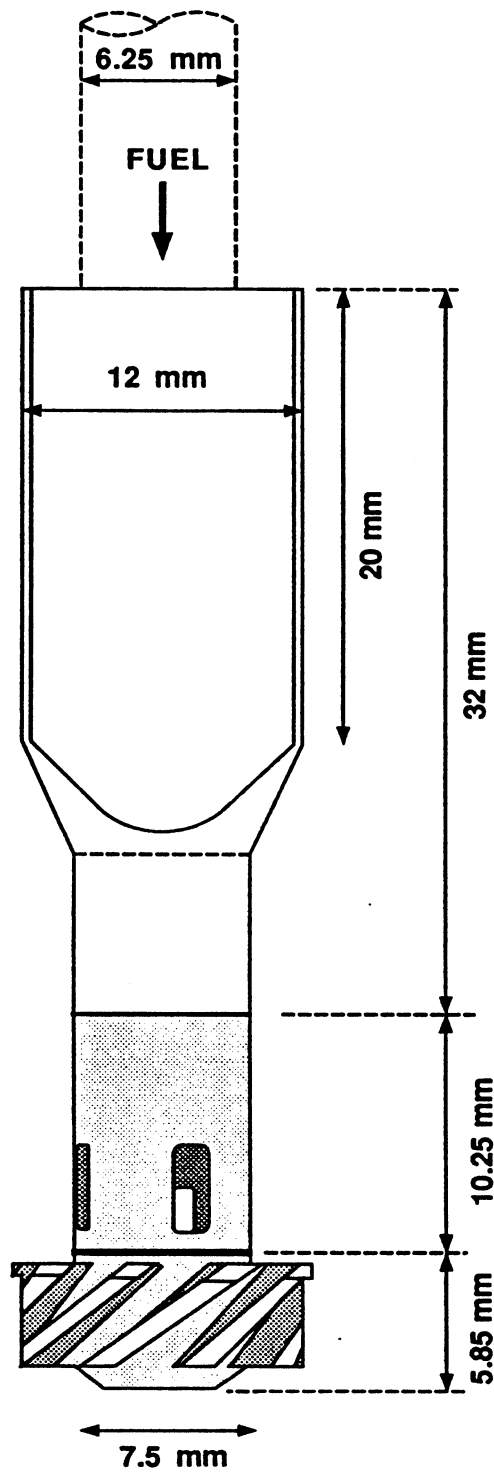
Case No.	Figure No.	Injected material	m_a kg/s	m_p kg/s monosized particles	m_p kg/s multisized particles	Confinement		m_s kg/s 0 deg	Swirler ms kg/s 60 deg
						m_c kg/s 457.2 mm duct	m_c kg/s 152.4 mm duct		
1	3.1.1-1	Air only	0.0021			**		0.0033	
2	3.1.1-1	as base	0.0021			**			0.0033
3	3.1.1-1	for effect	0.0021			**			
4	3.1.2-1	of	0.0021				0.045		
5	3.1.2-1	particles	0.0021				0.045	0.0033	
6	3.1.2-1		0.0021				0.045		0.0033
7	3.1.1-1	Unconfined	0.0021	0.0021 [†]		**			
8	3.1.1-1	mono-	0.0021	0.0021 [†]		**		0.0133	
9	3.1.1-1	dispersed	0.0021	0.0021 [†]		**			0.0133
10	3.1.2-1	Confined	0.0021	0.0021 [†]			0.045		
11	3.1.2-1	mono-	0.0021	0.0021 [†]			0.045	0.0133	
12	3.1.2-1	dispersed	0.0021	0.0021 [†]			0.045		0.0133
13	3.1.1-1	Multisized	0.0021		0.0021	**			
14 ^{††}	3.1.1-1	particles	0.0021		0.0021	**		0.0033	
15 ^{††}	3.1.1-1		0.0021		0.0021	**			0.0033
16 ^{††}	3.1.2-1		0.0021		0.0021		0.045		
17 ^{††}	3.1.2-1		0.0021		0.0021		0.045	0.0133	
17 ^{††}	3.1.2-1		0.0021		0.0021		0.045		0.0133
19	3.1.1-1	Air only	0.0021			**			
20	3.1.1-1	for air-	0.0021			**		0.0133	
21	3.1.1-1	blast	0.0021			**			0.0133
22	3.1.2-1	atomizer	0.0021				0.045		
23	3.1.2-1		0.0021				0.045	0.0133	
24	3.1.2-1		0.0021				0.045		0.0133
25	3.1.1-1	Unconfined	0.0021		0.0021*	**			
26	3.1.1-1	spray	0.0021		0.0021*	**		0.0133	
27	3.1.1-1		0.0021		0.0021*	**			0.0133
28	3.1.2-1	Confined	0.0021		0.0021*		0.045		
29	3.1.2-1	spray	0.0021		0.0021*		0.045	0.0133	
30	3.1.2-1		0.0021		0.0021*		0.045		0.0133
31	3.1.1-1	Swirl only						0.0033	
32	3.1.1-1								0.0033
33	3.1.2-1						0.045	0.0033	
34	3.1.2-1						0.045		0.0033

* Polydispersed methanol spray

** Entrained air provided as needed by flow. Amount of air not measured directly.

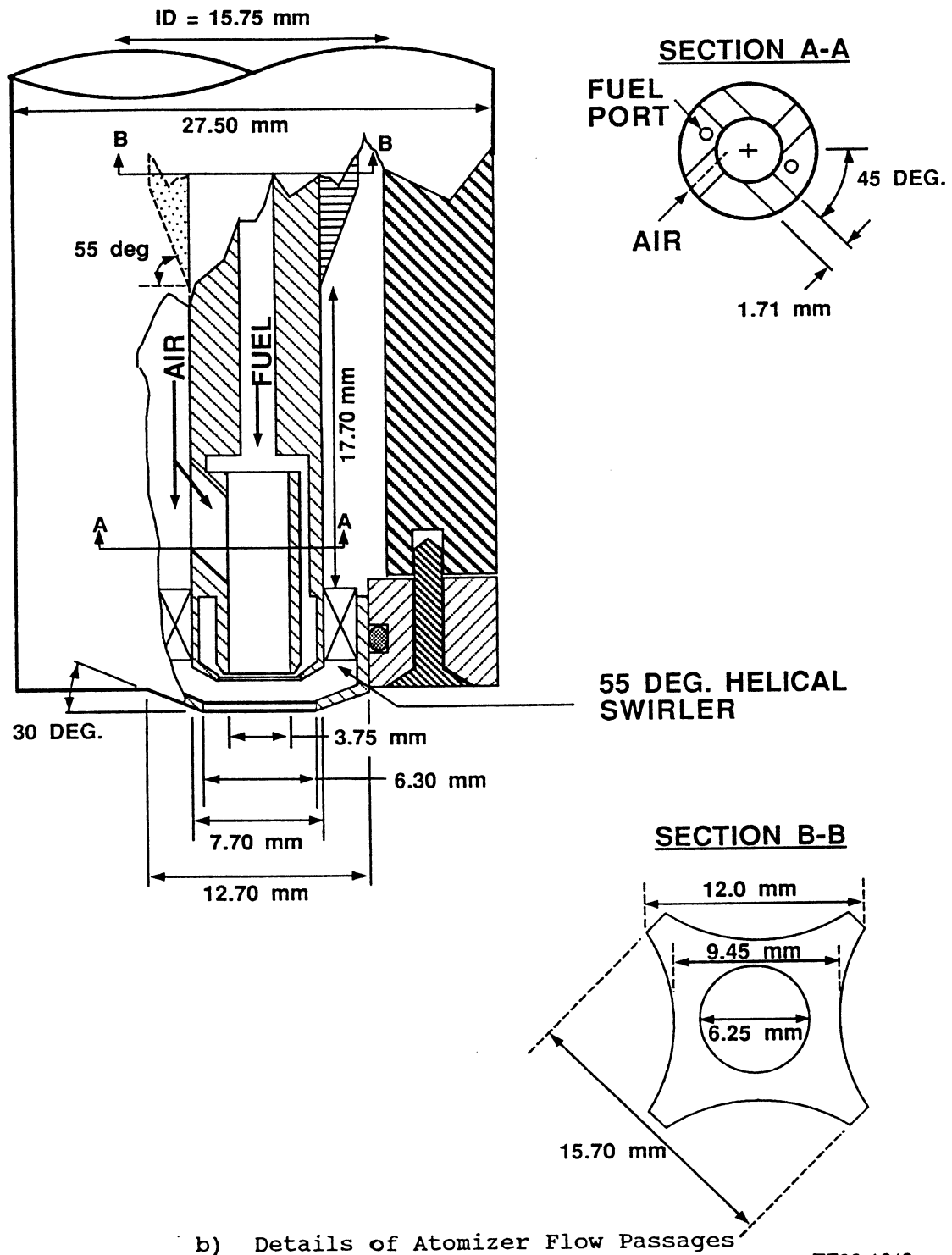
a Both 0.00042 and 0.0021 kg/s considered instead of items denoted with b.

b Lack of impact of 25 micron beads made these cases redundant. Difficulty with feeding two sizes with one feeder also required additional funds for second feeder.



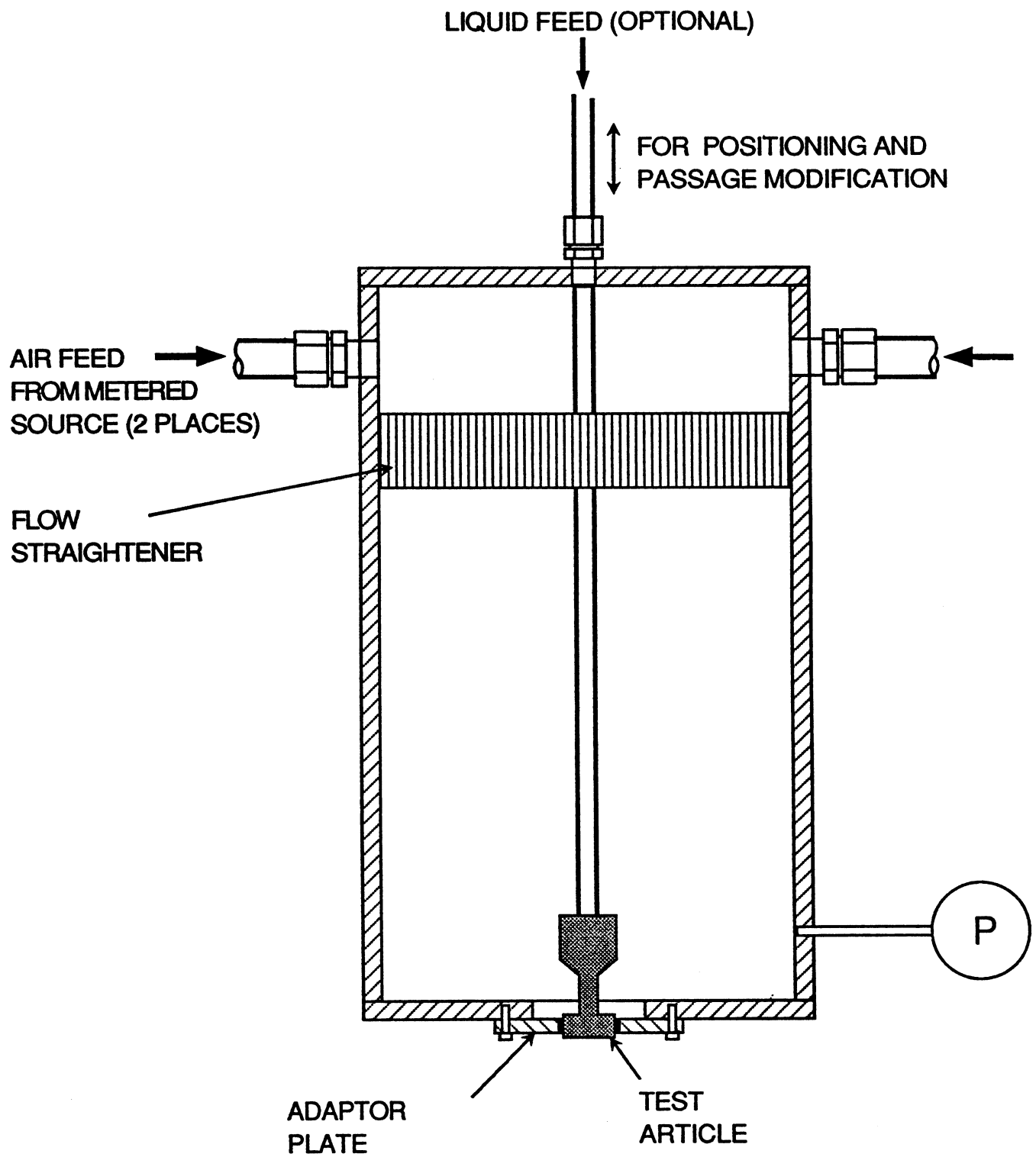
TE92-1647

Figure 3.4-1. Ex-Cell-O air-blast atomizer: detail of flow passages through atomizer with outer shroud removed.



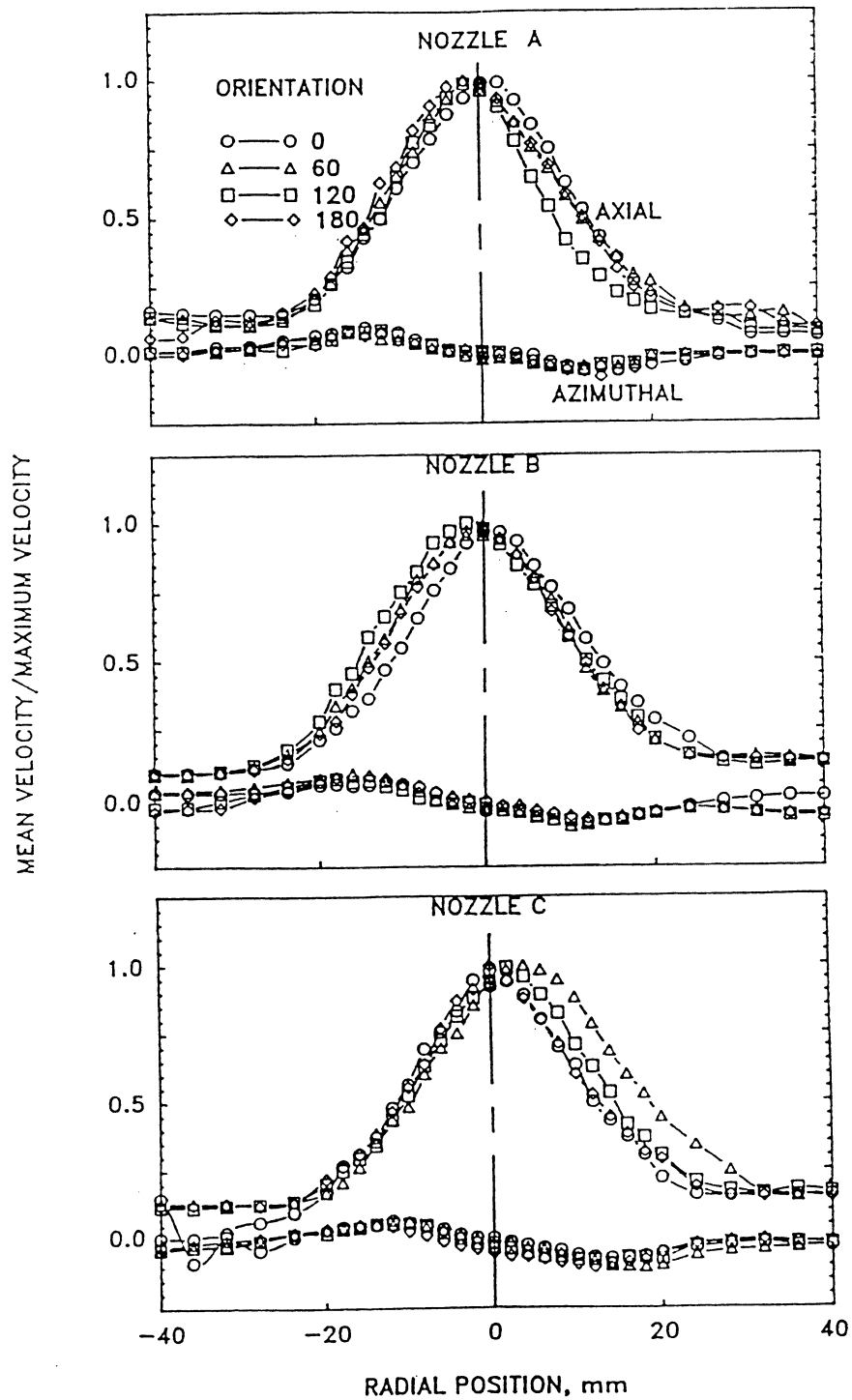
TE92-1648

Figure 3.4-2. Ex-Cell-O air-blast atomizer: details of atomizer flow passages.



TE92-1649

Figure 3.4.1-1. Plenum used for flow split study.



TE92-1650

Figure 3.4.2-1. Symmetry of mean spray velocity profiles for three atomizers (McDonnell, Cameron, and Samuelsen, 1990).

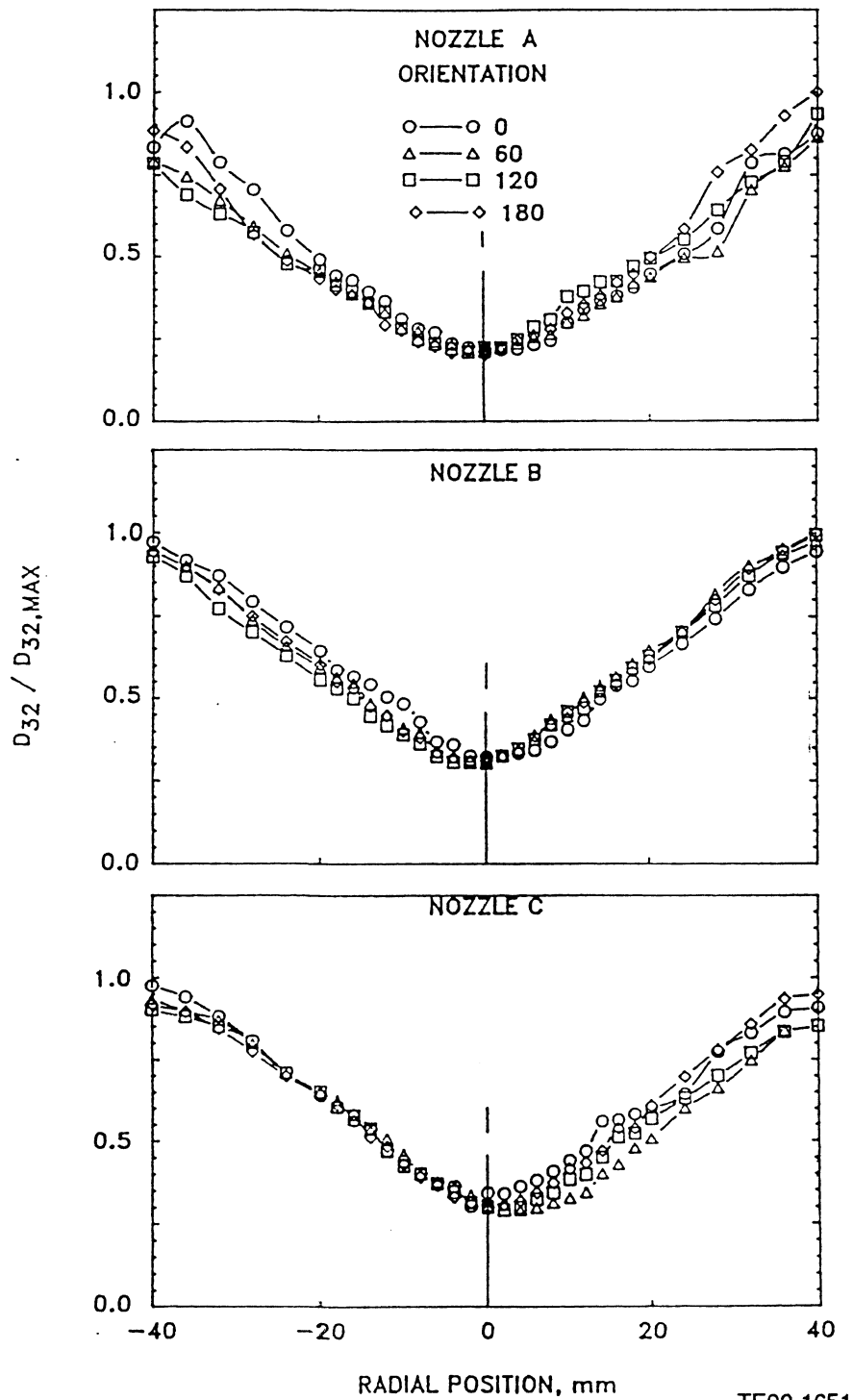
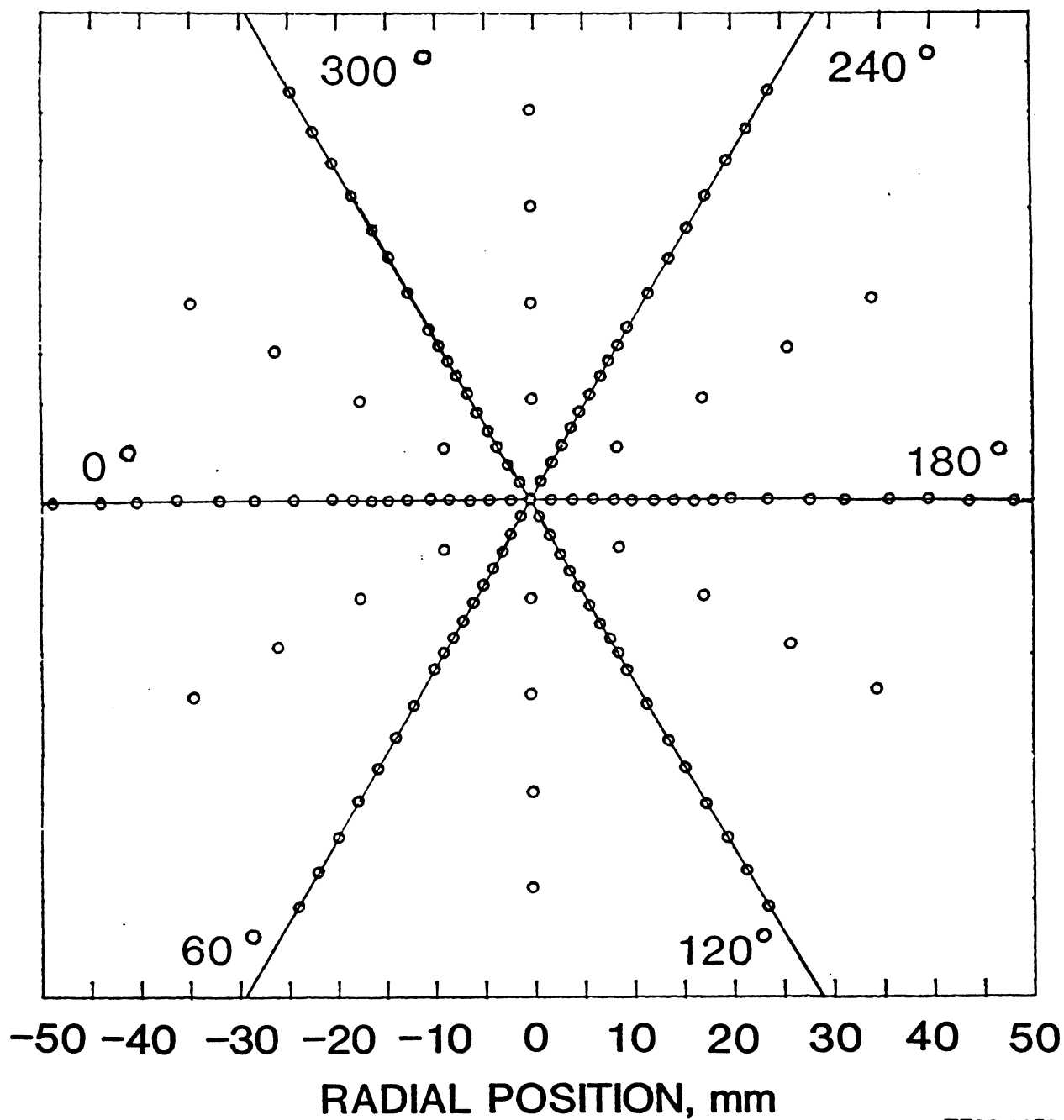


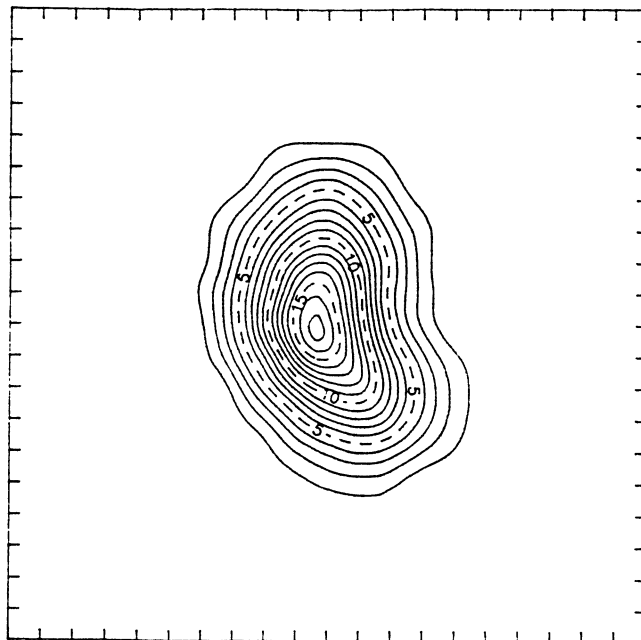
Figure 3.4.2-2. Symmetry of spray SMD profiles for three atomizers (McDonnell, Cameron, and Samuelsen, 1990).



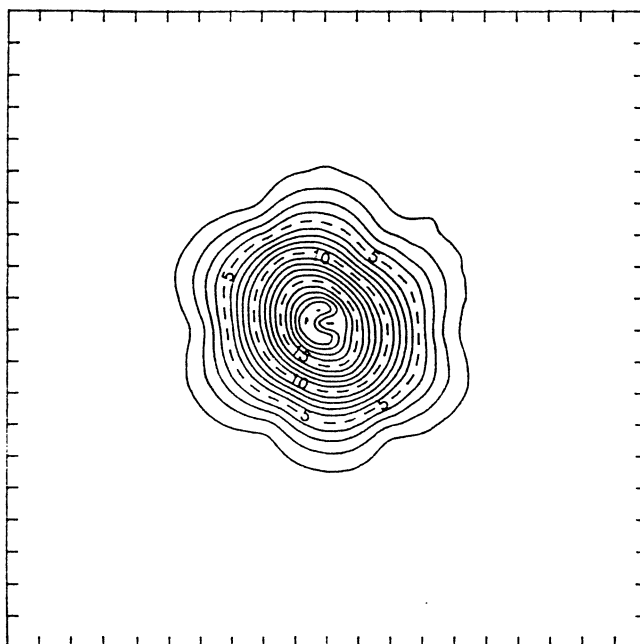
TE92-1652

Figure 3.4.2-3. Measurement locations for detailed symmetry evaluation
(McDonnell and Samuelsen, 1990b).

a) In the Absence of Spray



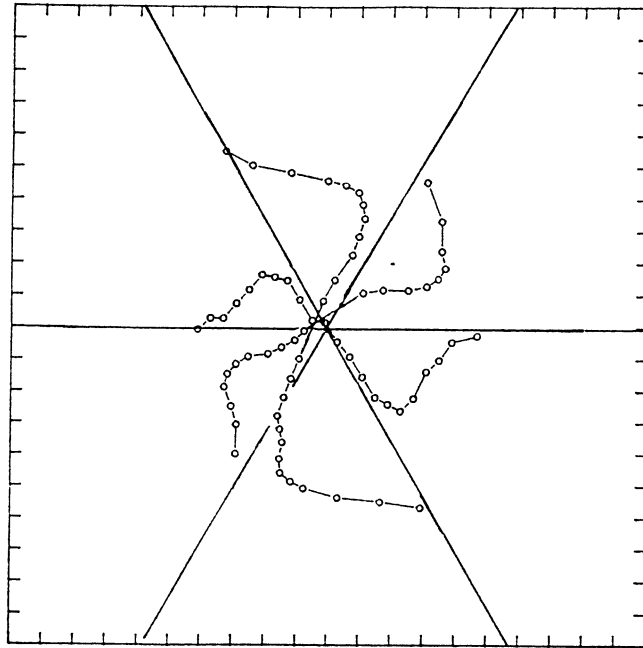
b) In the Presence of Spray



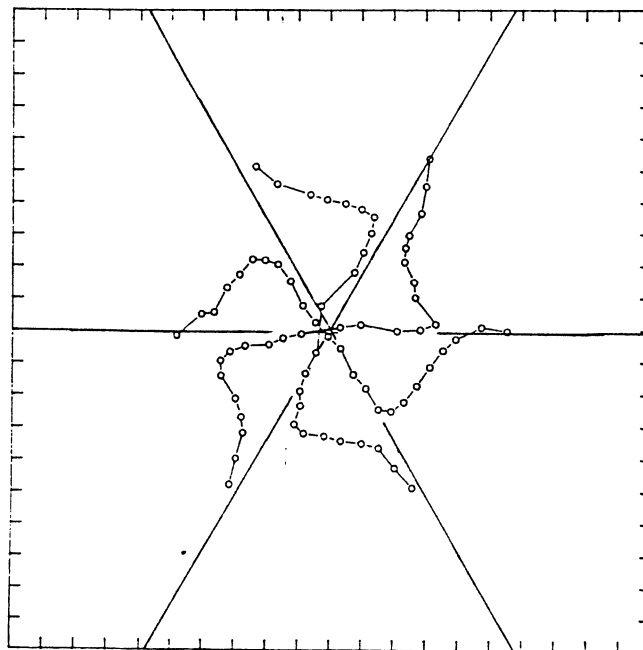
TE92-1653

Figure 3.4.2-4. Isopleths of mean axial velocity at an axial location of 50 mm (McDonell and Samuelsen, 1990b).

a) In the Absence of Spray



b) In the Presence of Spray



TE92-1654

Figure 3.4.2-5. Profiles of mean azimuthal velocity at an axial location of 50 mm (McDonell and Samuelsen, 1990b).

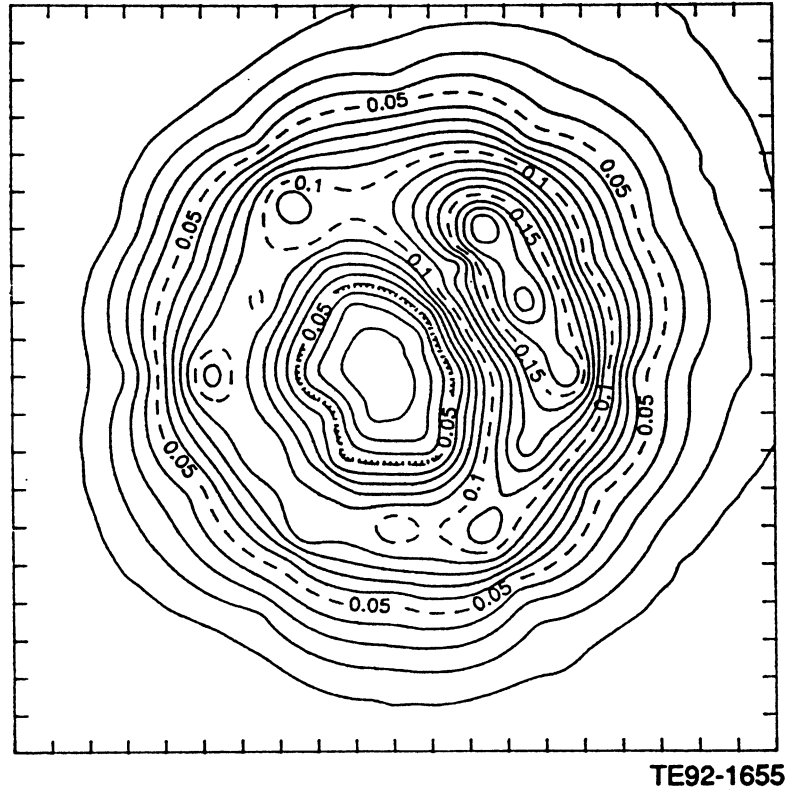


Figure 3.4.2-6. Isopleths of volume flux at an axial location of 100 mm (McDonell and Samuelsen, 1990b).

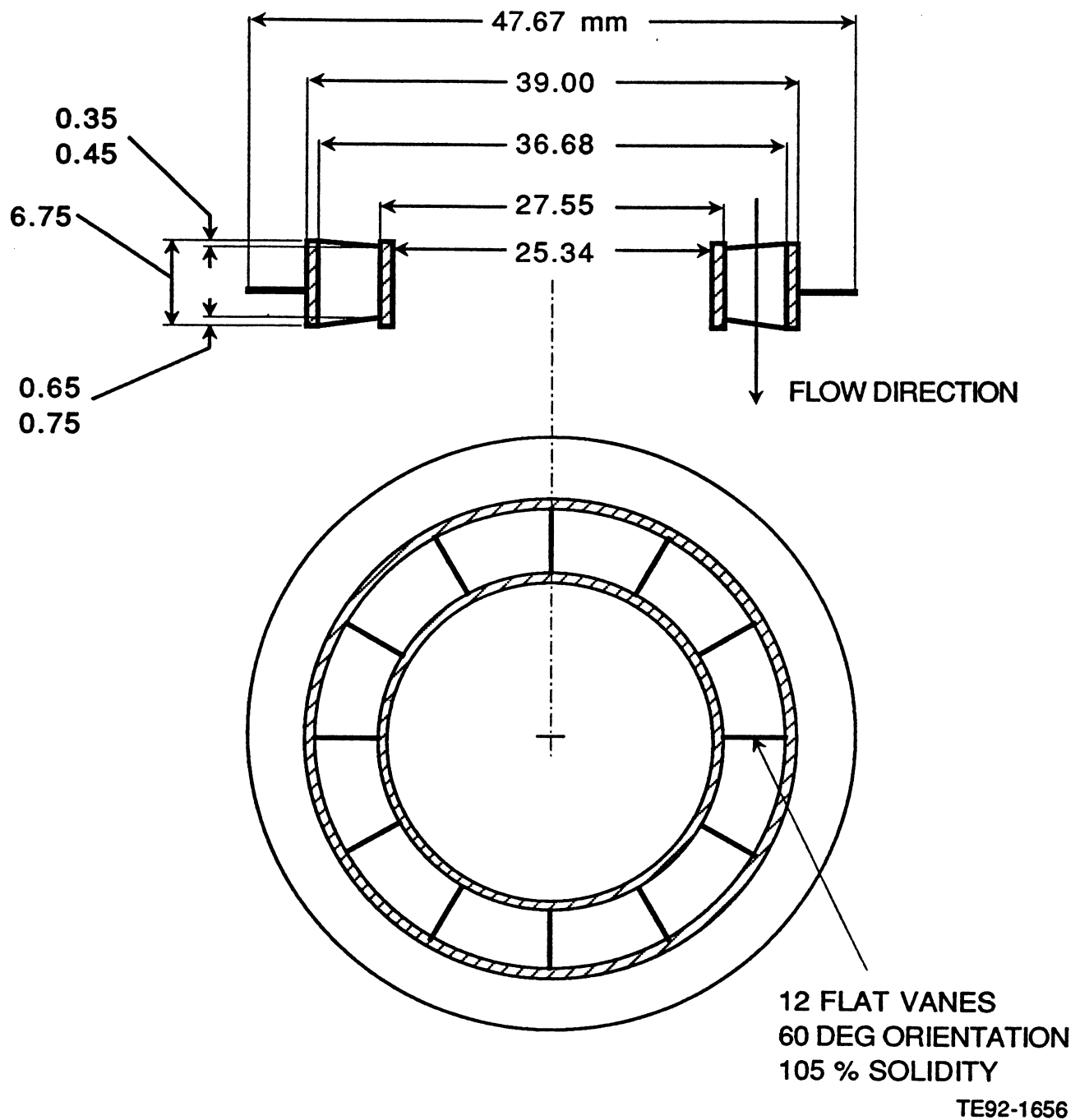


Figure 3.4.3-1. Aerodynamic swirler.

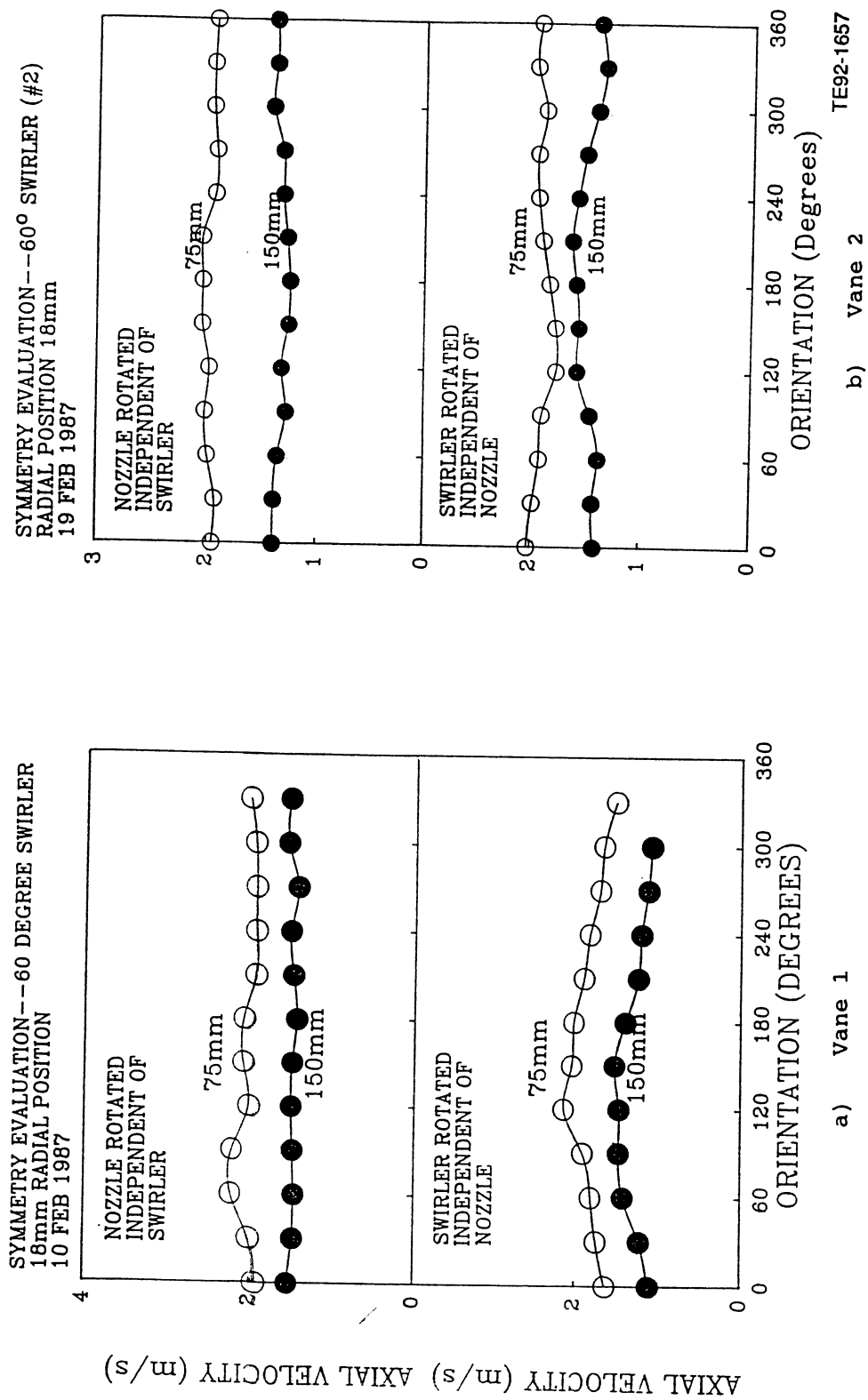


Figure 3.4.3-2. Symmetry of swirl vanes.

a) Non-Evaporating, Unconfined
No Coflow

b) Non-Evaporating, Unconfined
0 or 60 deg. Coflow

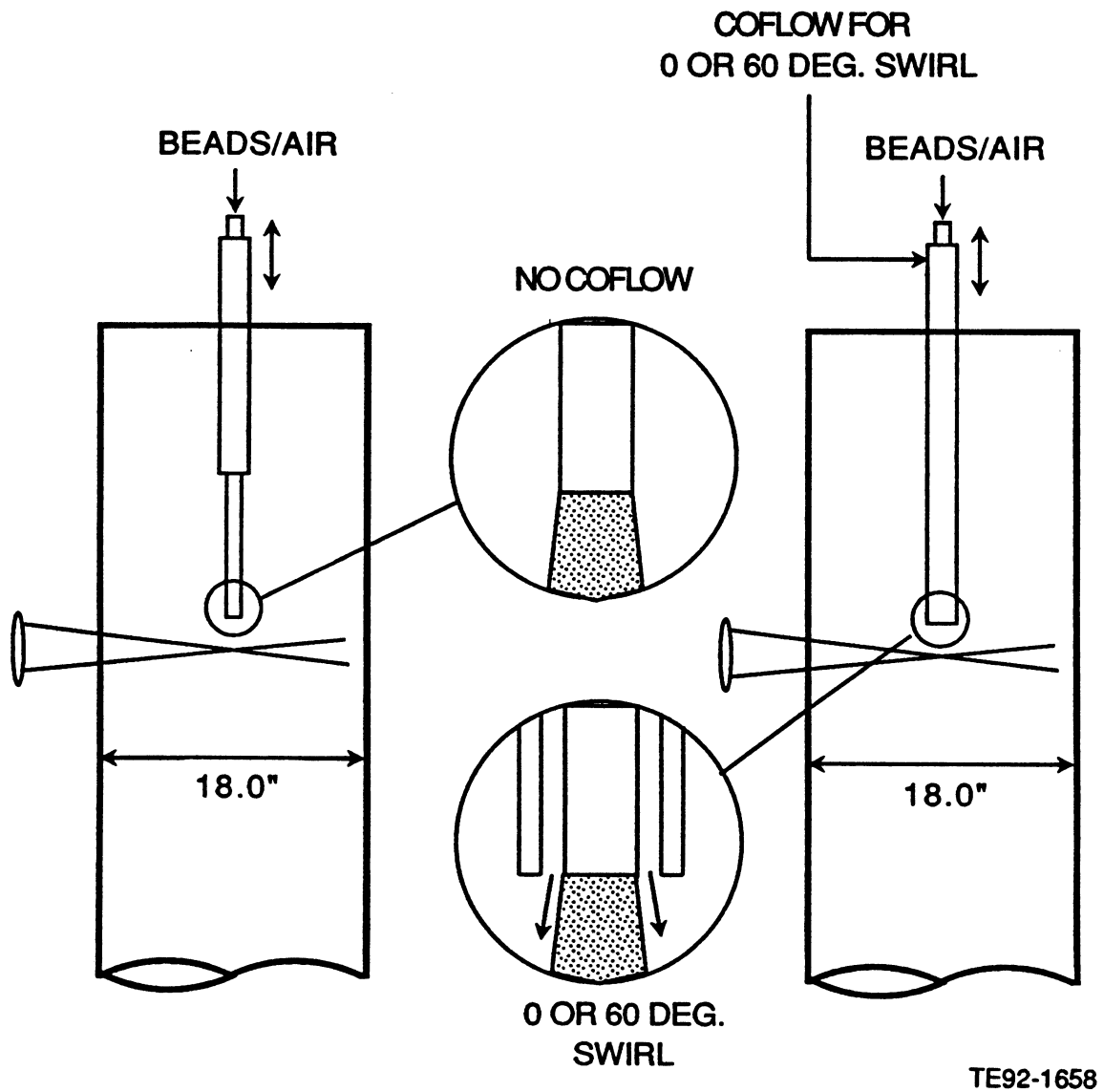


Figure 3.4.4-1. Original geometries (1 of 4).

c) Evaporating, Unconfined
No coflow

d) Evaporating, Unconfined
0 or 60 deg. Coflow

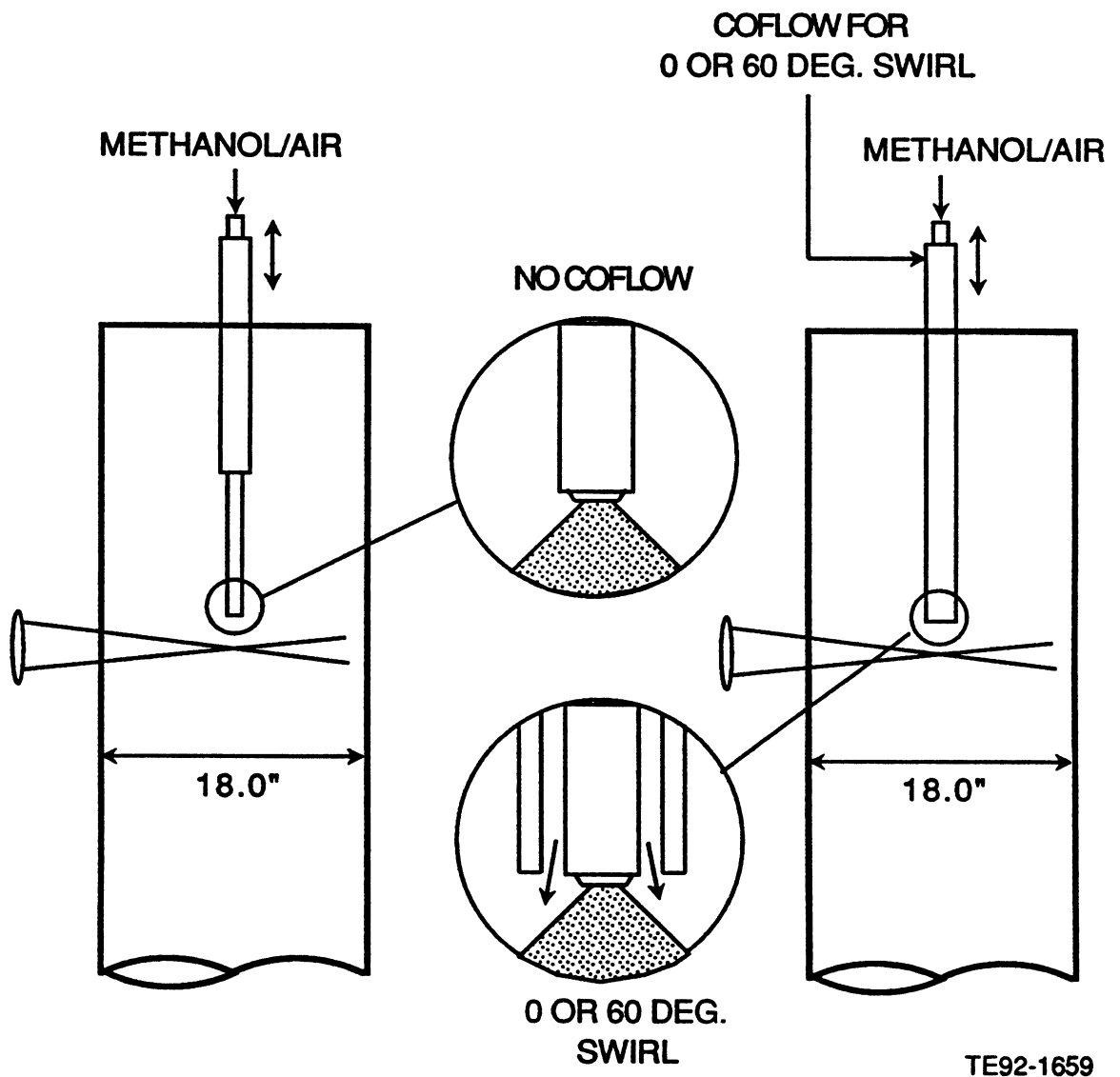


Figure 3.4.4-1. Original geometries (2 of 4).

e) Non-Evaporating, Confined
No coflow

f) Non-Evaporating, Unconfined
0 or 60 deg. Coflow

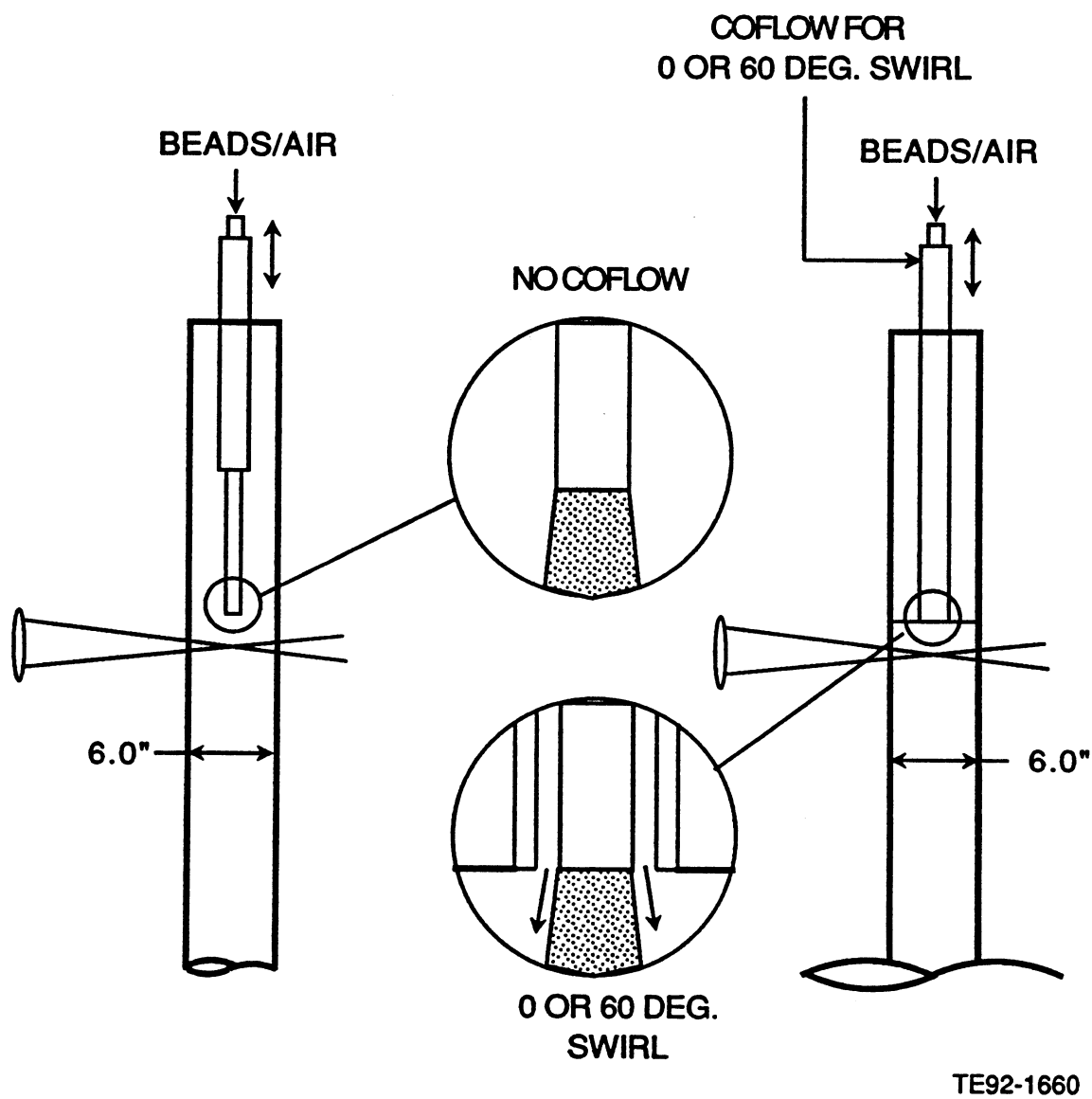


Figure 3.4.4-1. Original geometries (3 of 4).

g) Evaporating, Confined
No coflow

h) Evaporating, Confined
0 or 60 deg. Coflow

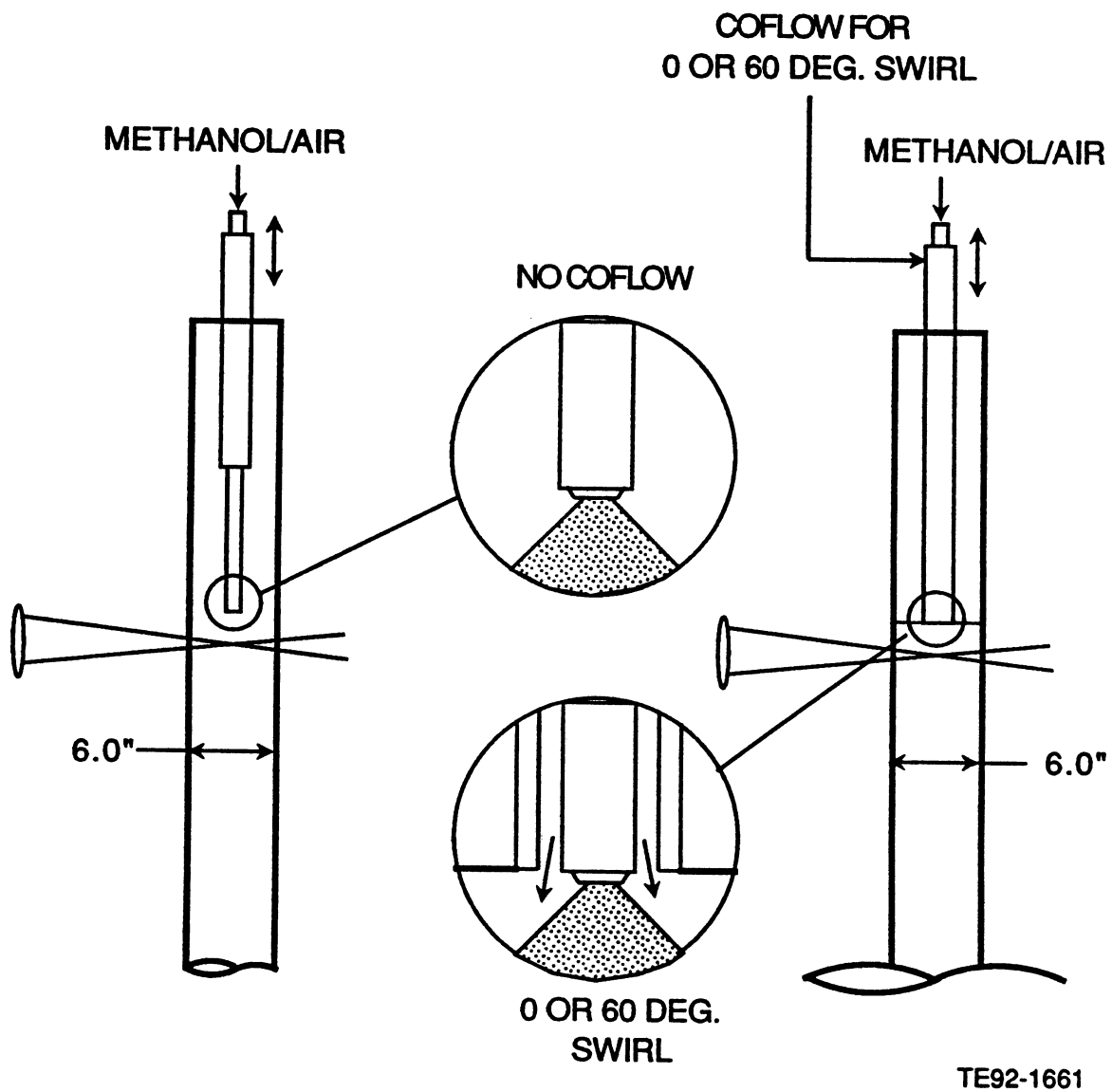
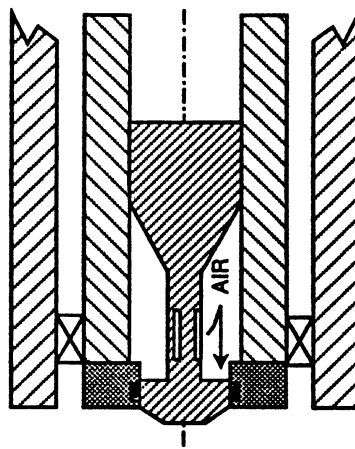
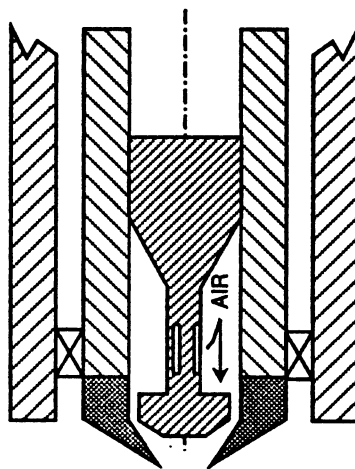


Figure 3.4.4-1. Original geometries (4 of 4).

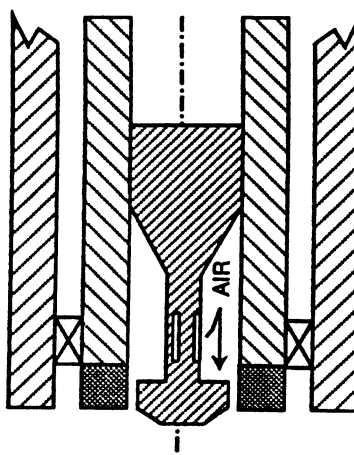
a) Original Cap



b) Shroud Concept



c) Evaluated Shroud



TE92-1662

Figure 3.4.4-2. Atomizer shroud evaluation: original cap.

3.5 DIAGNOSTICS – VELOCITY MEASUREMENTS

This section describes the laser anemometry setup used in the acquisition of velocity measurements. In reality, several versions of the system were used throughout the testing done in support of this program. Hence, historical perspective is included in this section which provides the reader with an appreciation of the evolution of the diagnostics which occurred through close interaction with the manufacturer.

3.5.1 Laser Anemometry System

Selection of the laser anemometry (LA) system was made considering the test plan as a whole. An LA system could have been used for the measurement of the single-phase flows, and then the phase Doppler interferometer (PDI) could have been used for measurement of the dispersed phases. However, the need to measure gas phase velocities in the presence of the dispersed phase required more consideration, as described in section 3.7. Finally, it was decided that use of two independent instruments was unreasonable, and that a phase Doppler instrument, operated without sizing should be used for characterization of the single-phase flows. However, the phase Doppler instrument was designed with sizing as the first priority and with velocity as a secondary consideration which led to some challenges in applying the instrument as an LA system. These challenges will be discussed within this section.

In general, the applications of interferometry for making velocity measurements have been well established (e.g., Durst et al, 1976). As such, the choice of LA for making velocity measurements in two-phase flows is clear.

A two-component instrument (Aerometrics, Inc.) is used in a nonsizing mode to obtain simultaneous measurements of two orthogonal components of velocity. A schematic of the transmitter is shown in Figure 3.5.1-1. The system is driven with a 1 W Lexel Argon-Ion laser. The beam is horizontally polarized and is split into blue (488.0 nm) and green (514.5 nm) beams via a dichroic mirror. The mirror is optimized to reflect 78% of the blue and 0.6% of the green, and to transmit 84% of the green and 1.4% of the blue. Each color beam is then directed through a line filter which eliminates any broad-band wavelengths present. The output from each line filter is focused onto a rotating diffraction grating which serves to split the single beam into several ordered pairs of beams. Once split, the two first order beams of each wavelength are recombined on the original axis using another dichroic mirror and subsequently collimated with either a 160 mm or 300 mm achromat lens. The two pairs of mutually collimated beams are then focused with a 495 mm f/6.4 lens to form overlapping probe volumes for two components of velocity. The nominal size of the probe volume waist was varied depending upon the application. For the measurement of the glass beads, the 300 mm lens was utilized, resulting in a beam waist of about 115 microns. For the sprays, the 160 mm collimation lens was used which provided a beam waist of about 220 microns.

The scattered light from both color probe volumes is collected by the same receiver lens. A schematic of the receiver is shown in Figure 3.5.1-2. The light is collected by a 629 mm f/5.7 lens and focused by an air-spaced triplet lens onto a 100 micron x 1 mm slit which acts as a spatial filter. The lens design was optimized to provide a 5 micron blur spot and to eliminate chromatic aberration, providing an accurate definition of the imaged slit on the probe volume and improving signal-to-noise ratios. The light passing through the slit is then collimated and is chromatically split by another dichroic mirror. The blue light is sent directly to a photomultiplier tube (Hamamatsu model R928HA) and the resulting signal is sent to the processor. The green light is split into three portions, each of which is directed at a separate photomultiplier tube. The splitting of the light is required for sizing purposes as described below. As a result of the splitting, the intensity of the green light hitting a given photomultiplier tube is less than that for the blue light. The portion of light hitting the top area of the receiver lens is used for determining the velocity of the scatterer in the axial direction. Figure 3.5.1-3 indicates the approximate area division of the receiver lens and the corresponding distances between the effective collection areas for the three detectors employed in the measurement of size, which is described in the next section.

To determine the velocity of the event, the processor utilizes the entire portion of the burst (total burst mode) which exceeds the threshold value. The use of this technique rather than a fixed-cycle approach (e.g., comparing average frequencies from the first five and first eight fringe crossings) can lead to errors if the signal is not carefully filtered. The reason for using this approach is described in the section under sizing. Figure 3.5.1-4 shows examples of properly and improperly filtered signals. The system provides feedback to the user during the collection of data by indicating how many events were rejected and for what reason.

Prior to acceptance into the processor, the event must satisfy three criteria. First, the event must include a minimum of four fringe crossings for both components of velocity. Also, a degree of simultaneity must be ensured. The amount of overlap of the signal is used as this criterion. For the present work, if any portion of the signal is overlapping, the signal is considered coincident.

Reasons for rejection during processing are summarized as follows (in order of checking by the processor)

- divide by zero This error will occur if the processor encounters an attempted divide by zero. Reasons for this occurrence involve situations where the electronics are saturated by extremely high data rates.
- overflow This error occurs if the clock is allowed to run for a period of time at a given resolution such that the allotted 47 bits become filled. Reasons for such occurrences include very slow events and filtering at too high a frequency. The net error incurred by not attempting to reduce the amount of these errors is an indicated velocity which is greater in magnitude than the actual.
- out of range This error occurs if the velocity measured is greater or less than the values selected by the user to define the velocity pdf limits set up within the window established by the filters. This error indicates that modification in the velocity pdf range parameters selection be made by the user. This error sometimes results when the velocity sensitive range selected seems correct. This occurs due to low frequency noise which is not filtered properly. Thus, this error is not always an indication that portions of good data are being rejected.
- excess fringe crossings This error is designed to reject signals due to multiple particles in the probe volume. The value assigned for the limit varies from a minimum number dictated by velocity range, frequency shift, and probe volume waist, to a maximum of 256. Again, very slow events can be rejected erroneously due to this check.

In general, data are of better quality due to the real time indication of these errors because minor adjustments can be easily made to optimize the quality of the data.

To discriminate between flow direction, frequency shifting is utilized. Classically, frequency shifting is accomplished via opto-acoustic cells, which typically operate around 40 MHz. Because of the sophisticated timing and signal conditioning required for sizing measurement, the effective bandwidth of the instrument originally used in the program was 10 MHz. Since no satisfactory commercially available gratings were available, the original system was used with no shift. This proved to be very limiting in applying the instrument to gaseous flows, and render two-component operation impossible, since many of the flow studies featured little or no radial or azimuthal velocity components.

During the beginning of the program, an alternative to the opto-acoustic cells was identified (Jackson, 1985) which would be appropriate for use with the relatively low frequency range of the PDI system,

namely, rotating diffraction gratings. Each component of velocity is shifted independently using rotating diffraction gratings. It is noteworthy that the gratings and the motors evolved throughout the duration of the program. At the time the program started, only one vendor could be identified for the circular gratings required, Technisch Physische Dienst. The typical grating used features three "tracks" which have different numbers of line pairs. Each track is located concentric to the others and to the center of the disk.

The first version of the gratings were software controlled and provided continuous shift between 0 and 8000 rpm. Using the relation for the frequency shift and rpm

$$f_s = 2 N f_r \quad (3)$$

where

f_s = the frequency shift (MHz)

N = the number of lines on the track

f_r = the rotational speed (rps)

and given the number of lines on the different tracks. For the optical setup used for measurement of the glass beads, this permits reverse velocities of up to 21 m/s. The 2.2 MHz limit is imposed by the stability of the motors which are controlled by a separate controller box interfaced to the IBM AT by an RS232 connector. Because of the four fringe minimum required, reverse velocities approaching 20 m/s may be missed depending on trajectory through the probe due to insufficient fringe crossings and, as such, 15 m/s is a more realistic limit. Although not a serious problem for the modest velocity flows involving the glass beads, this was a serious limitation for the measurements in the sprays.

Because the diffraction angle is a function of the line pair spacing, the different tracks give flexibility to the user. However, the geometry of the grating causes fundamental problems to be raised.

Figure 3.5.1-5 shows the details regarding the grating geometry. If the grating is mounted slightly off-center, the line pair spacing will vary, and as a result so will the fringe spacing. The early version of the gratings suffered from this problem, which led to an increase in the measured velocity rms, especially when high frequency shift was used in low turbulence environments. Such concerns over the stability of the motors and the manner in which the gratings are mounted to the motor shaft resulted in optimization of the motor assembly (e.g., McDonell and Samuelson, 1990a; Jackson, 1990).

To address these issues and to extend the frequency bandwidth, Aerometrics developed better versions of the grating motor (using preloaded bearings) and a better grating mounting methodology to reduce grating wobble. Besides the increased stability offered by the new motors, their maximum rpm was increased to 16,000.

In summary, Table 3.5-I presents the evolution of the instrument, and how it ended up in its present state. Because of time constraints, the upgrade to DIG4 did not impact the present program.

3.5.2 Seeding Systems

To provide scattering of the laser light from the probe volume, particles are needed to seed the flow. It is desired to have steady, consistent production of seed to avoid biases due to concentration fluctuations (see below). One of two systems is used depending upon the flow to be seeded. For flows requiring low amounts of seed, a system developed by Ikioka et al (1983) is used. This seeder is shown schematically in Figure 3.5.2-1. In flows requiring high volumes of seed, a fluid bed-type seeder is used, as shown in Figure 3.5.2-2. Vibrator motors reduce pulsations from the fluid bed as shown in Figure 3.5.2-3. Figure 3.5.2-3 shows the results without the motors. A reduction in seed output is quite evident with time. With the motor, the seed output remains relatively stable as shown in Figure 3.5.2-3 (b). The fluid bed is inherently less stable than the nebulizer system but is able to provide higher volume of seed.

Table 3.5-I.
Milestones in development of UCICL PDPA system.

<u>Date</u>	<u>Development</u>
7/85	Prototype 1-D system delivered to UCI. No frequency shift. Software v. 2.2.
8/85	Verified system calibration.
10/85	Aerometrics provides "velocity only" software which permits system to be used as LDV system without sizing.
1/86	Frequency shift added to software. Enables UCI transmitter to be used.
7/86	Two-component system arrives. Debugging of software begins beginning with v.2.1.
9/86	Version 3.0 installed. Chromatic-aberration free receiver lens installed. Production data collection started.
10/86	Version 3.10 installed. Data series implemented to provide reduced data file.
12/86	Summary of hardware issues remaining: PMT power drift occurring, analog filters switching, insufficient frequency shift on CH2 velocities.
4/87	Version 3.49 installed. Incorporates new probe volume correction scheme.
12/87	Version 3.50 installed. Time series implemented. Too many bugs to be useful.
6/88	Transmitter sent to Aerometrics for upgrade. Software v. 3.62 installed incorporating a new probe volume correction scheme.
7/88	Received upgraded transmitter. Increase in frequency shift amount and stability. Alignment much easier. Software v. 3.67 installed fixing last of bugs. Time series data available, but no offline support available.
8/88	Ch 1 analog box fails. Repaired.
8/89	Higher speed processor Dig 4 received from Aerometrics. Includes offline support for time series data. Eliminates problems observed with previous processor.

Both systems permit monitoring of flow rates and, as such, the flow for the seeding system can be accounted for in establishing each required flow rate. In addition, because each seeder has a steady output rate directly proportional to the flow rate through it, the concentration of seed in the individual air streams can be well regulated, reducing the effects of concentration bias (see below).

In all cases, aluminum oxide is used as seed (GB-1200, nominally 2.0 microns; Microgrit Corporation). Figure 3.5.2-4 shows an example of the morphology of the seed output by the two systems. No particles greater than 10 microns are observed, and the majority are less than 5 microns. Other types of alumina seed particles were considered. Discussions with Microgrit Corporation led to the selection of the GB powder, which is blockier than most other types of powders. Because of the desire to have particles as spherical as possible, the GB powder was judged to be the best choice for this application.

In the flows outlined by the test matrix, there are no situations for which a 5 micron particle will not track the flow. Thus, the velocity measured is that of the gas phase, since slipping between the seed and the flow it is tracking is negligible. Durst et al (1976) described relations to determine the maximum size particle that will track a turbulent flow. Recent work by Bachalo et al (1987) also supports the use of particles which are less than 5 microns for the flows studied here. Figure 3.5.2-5 shows the methodology in

establishing the maximum particle size which will track the flow. This study is done for each configuration to ensure proper measurement of gas velocities and associated statistics.

3.5.3 Sampling Bias

There are two primary sources of sampling bias to be addressed in the measurement of gas phase velocities using individual realization laser anemometry. The first is velocity bias which has been described in detail by McLaughlin and Tiederman (1973). Velocity bias can occur when measuring evenly seeded air streams which are of different velocities. Faster moving packets are more likely to have realizations recorded than the slower moving packets. The approach taken by McLaughlin and Tiederman, for the removal of this bias, uses of the mean velocity measured together with the velocity of the realization. If the velocity of each event is weighted by the ratio of the mean overall velocity to that of the event, the bias can be removed, according to McLaughlin and Tiederman. They also acknowledge that overcorrection can occur in situations where the flow is not highly turbulent, and making this approach questionable for use in general. In swirling flows, trajectory effects must also be considered, and the full magnitude of the velocity should be used in making the correction suggested by McLaughlin and Tiederman.

Another bias can be realized in mixing layers where one layer is seeded in a different concentration than another. Clearly, the more heavily seeded circuit will have more realizations recorded, and the resulting measured mean will be biased towards that layer. This bias is minimized in the flows studied in this work, by carefully controlling the seeding rates. Figure 3.5.3-1 shows an example of the error that can be induced by concentration bias in the swirling cases where the variation is up to 0.5 m/s. Note that the actual velocity lies between the two curves shown.

Techniques for removing the bias due to both concentration and velocity involve the transformation of a Poisson distribution (i.e., random arrival rate) into a constant time interval arrival rate. Hoesel and Rodi (1977), Simpson and Chew (1979), and others have proposed techniques by which bias can be eliminated. Studies done by Gould et al (1986) and Craig et al (1986) independently identified constant time interval sampling as the only effective technique by which to remove bias due to both concentration and bias. This was also found to be the case for two-component measurements by Nejad (1986). This technique was to be utilized in the current work based on the above findings.

The constant time interval sampling technique can be implemented in two ways, during data acquisition or after. The online approach involves inhibiting the processor in some manner for a fixed time period and then allowing it to grab a single sample. The key to success in this approach is the seeding concentration. It must be high enough to ensure a scatterer will be in the probe volume every time the processor is allowed to grab for a sample. A safer approach is to remove the bias offline. This approach requires the time at which each scattering event occurred to be recorded. Subsequent to their acquisition, the data are stepped through using different fixed time intervals until one is found which always contains data, yet is long enough to minimize bias. There will be a range of time intervals that can be used to provide proper elimination of bias.

It is expected that the flow fields with swirl may require correction, especially in the unconfined cases. However, as shown in Table 3.5-I, the time tagging necessary to do this bias removal was not incorporated until late in the development of the instrument and could not really be utilized in the data collection for this program.

3.5.4 Validation of Velocity Measurement

In order to validate the measurement of velocity, three approaches were taken: sensitivity studies, instrument comparisons, and mass balances. For the sensitivity tests, exit profiles were taken from the free jet studied in this program and integrated. Instrument comparisons were conducted in order to verify operation of the new instrument and correlate irregular behavior with the measurements obtained via an independent source.

The sensitivity studies were conducted to help quantify errors in the velocity measurements. In general, the measurements were found to be reliable in terms of known mass balances. The fluctuating velocities measured were found to be artificially high, primarily in regions of low turbulence (e.g., McDonell and Samuelsen, 1990a; Jackson, 1990). This work led to improvements in the transmitter as described in section 3.5.1.

As an example of both comparison and sensitivity studies, the setup shown in Figure 3.5.4-1 was used, and measurements were conducted at the centerline of the free jet at an axial location of 2.0 mm. In this case, the PDPA instrument was compared to TSI counters. In the setup, care was taken to ensure similar setups of the two instruments (e.g., same processing criteria, same minimum fringe count).

An example of the results obtained in the sensitivity tests is shown in Figure 3.5.4-2 (a) which presents a "cube plot" of the PDPA measurements as a function of four variables: PMT gain, filter selection, frequency shift, and threshold. In this case, a two-level study was carried out as indicated on the extremes of the cube axes, and the mean axial velocity, fluctuating axial velocity, and validation rate are examined for dependency upon the four variables. The extremes were selected based upon experience, and would be considered a good range of settings which should in theory provide accurate results. Figure 3.5.4-2 (a) shows several important results. In general, little dependency of the mean velocity is observed, as expected. However, the fluctuating velocity shows significant dependency upon all four variables. From Laufer (1954) and knowing the measured axial velocities, it is expected that the fluctuating velocity should be 0.310 - 0.320 m/s. It is observed that minimization of PMT and frequency shift and increased thresholds are necessary to reach these levels. PMT and threshold settings are expected to impact the results, but the extent to which this impact occurs is shown in Figure 3.5.4-2 (a). Further, the dependency upon frequency shift stands out as inappropriate, as this quantity should be independent of the results. This is an example of the problems with the gratings discussed in section 3.5.1. Fortunately, in higher turbulence flows, this problem was not significant. These sensitivity tests help guide the instrument settings and enhanced confidence in the results.

In addition, experiments were conducted which compared the measurements obtained by both PDPA and other signal processors. A schematic of the setup used for this test is shown in Figure 3.5.4-1. In this case, the PDPA system was compared directly to TSI counters. The PMT gain and filtering of signals was done with the PDPA system. The TSI system was set up to mimic closely the PDPA system (i.e., using total burst mode, eight fringe minimum).

To complement the results shown in Figure 3.5.4-2 (a), Figure 3.5.4-2 (b) presents the cube plot for the TSI system. The results show trends similar to those of the PDPA system. Noteworthy is that the validation is lower than that of the PDPA. This is partially attributed to the inability of the TSI system used in this study to utilize DMA. Also, the PDPA threshold had no influence on the TSI system. To emulate this function, the TSI "gain" selector was used. A higher gain was used to reflect a lower threshold. An independent study of the impact of the gain on the TSI measurement was carried out and showed no impact over the range used in this study.

The fluctuating velocities show trends similar to those of the PDPA. Recalling that the value should be 0.310 to 0.320 m/s, the increase in shift has a strong impact on the measured fluctuating velocity. It is observed that the PMT setting has less impact on TSI than on PDPA.

The results from the sensitivity study indicate that PMT gain and frequency shift have the strongest impact on the results measured by both the PDPA and TSI counters. As a result, these two parameters were examined in more detail in a separate study. Examples of these results are shown in Figures 3.5.4-3 and 3.5.4-4.

Figure 3.5.4-3 presents, at the centerline of the jet, the dependency of the measured quantities upon PMT gain setting. Figure 3.5.4-3 (a) presents the results for the axial velocity. At the lowest voltages, the TSI

instrument measures a relatively high value. Increasing the voltage results in systematically increasing PDPA values but fairly stable TSI values.

The fluctuating velocities are presented in Figure 3.5.4-4 (b). Both instruments exhibit little dependency upon voltage until 550 volts is reached. At this level, both instruments measure slightly higher fluctuating velocities which increase with continued voltage increases.

The turbulence intensity is presented in Figure 3.5.4-4 (c), and it is observed that similar trends occur for the fluctuating velocity. Departure from the expected values increases with higher voltages, but less so for the TSI measurement. This result helps to dictate the maximum voltages that may be used and still measure accurate fluctuating velocities.

The validation rate shown in Figure 3.5.4-4 (d) shows the expected increase with increased voltages. It is tempting to increase the voltage in order to achieve higher data rates, but this leads to erroneous scores and results in artificially high levels of turbulence, as indicated by Figure 3.5.4-3 (c).

An example of the impact of the PMT voltage is shown in Figure 3.5.4-4. Figure 3.5.4-4 (a) shows that the TSI mean axial velocity increases systematically with shift. An exception is the value measured with no shift, which like the PDPA result is locally high. The TSI dependency is attributed to shift/fringe spacing mismatch in the TSI setup.

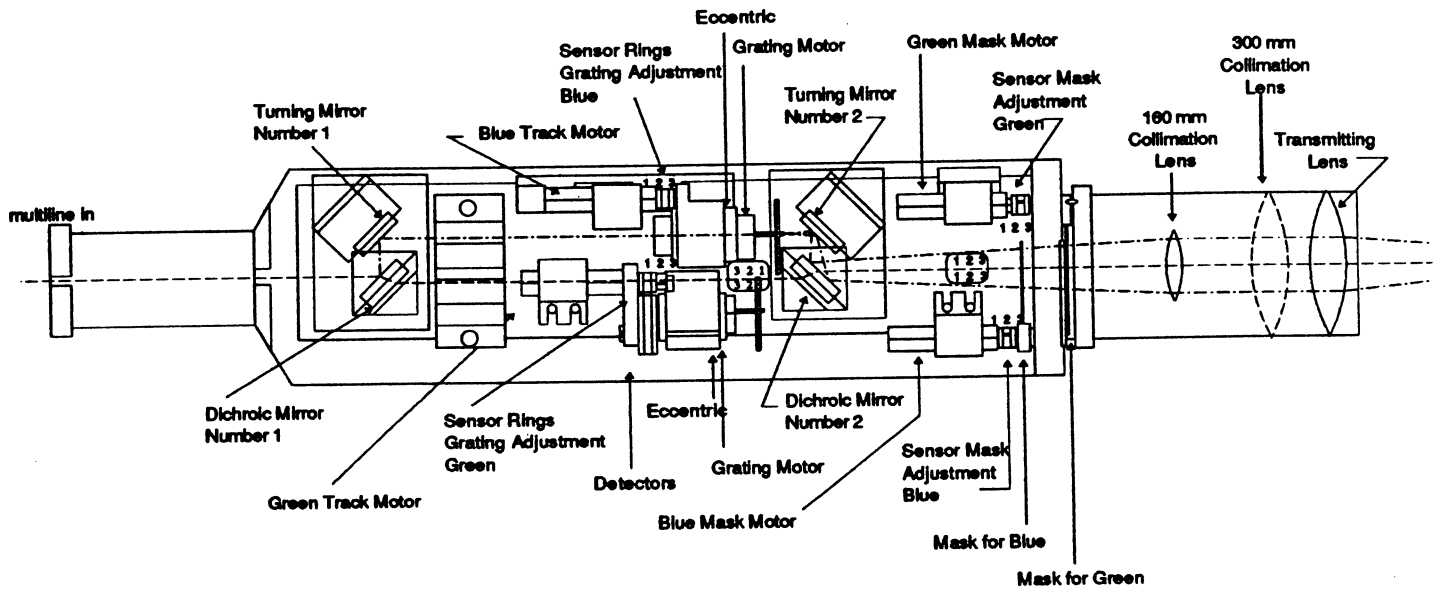
The fluctuating velocity (Figure 3.5.4-4 [b]) increases modestly with frequency shift for the TSI case, but rather dramatically for the PDPA at shift values above 3.0 MHz.

The dependency of the turbulence intensity upon the frequency shift is shown in Figure 3.5.4-4 (c). Again, the TSI equipment appears less sensitive to shift values than does the PDPA. However, at shift values less than 3.0 MHz either processor gives reasonably accurate results.

The validation (Figure 3.5.4-4 [d]) reveals a systematic decrease for both instruments. Note that the TSI dependency is nearly linear, whereas the PDPA result drops off quickly with increased shift.

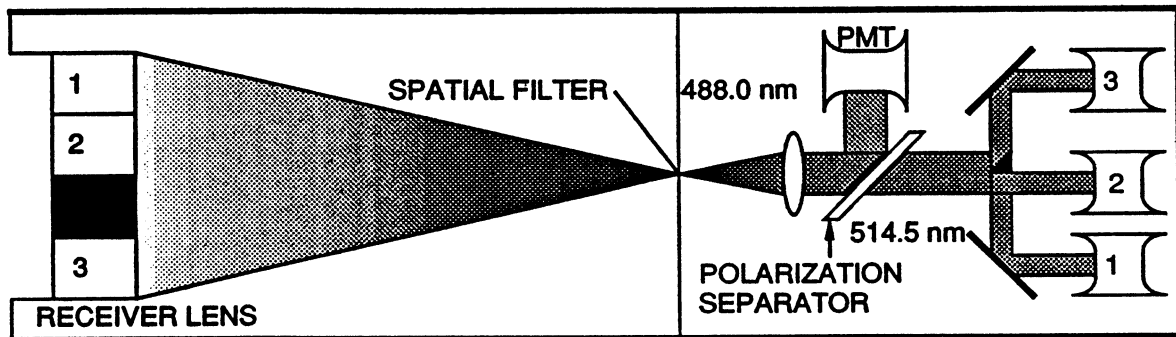
The results show that the PDPA instrument is more sensitive to shift and PMT settings than is the TSI instrument. However, if constraints are placed upon the settings, the PDPA instrument also obtains accurate results. Although the TSI instrument is less sensitive in a velocity measurement mode, it cannot measure size. More details regarding the checkout of the instrument are given in section 3.6.3 and in a separate report which documents additional tests run (McDonell and Samuelsen, 1991).

In order to check measurements in other flows, the axial velocity profiles are integrated to provide a measure of the mass flow. Comparisons of measured profile based mass flows and injected mass flows were regularly within 1% of each other. Examples of this are given in section 3.5.



TE92-1663

Figure 3.5.1-1. Two-component PDPA transmitter.



TE92-1664

Figure 3.5.1-2. Two-component PDPA receiver.

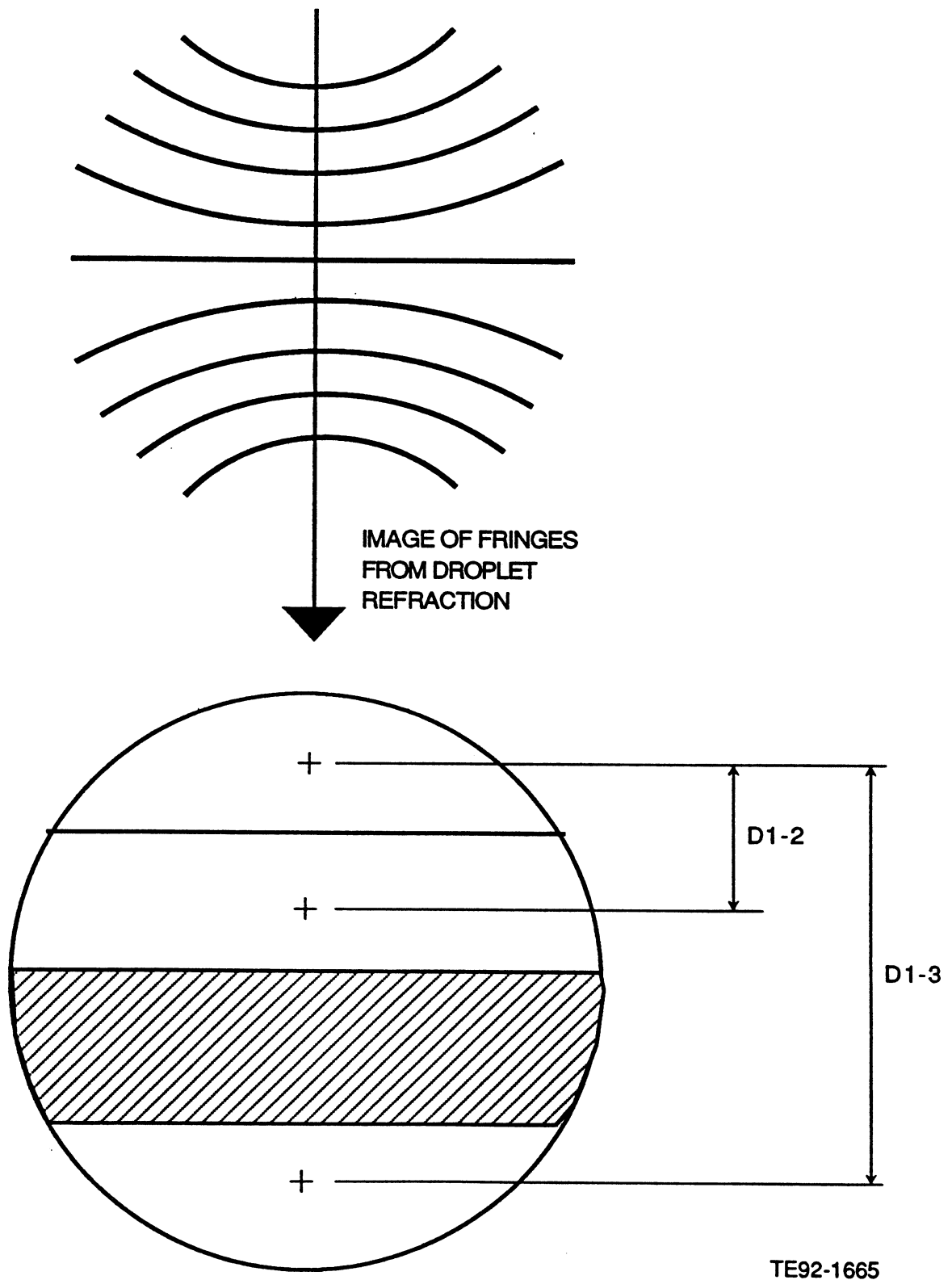
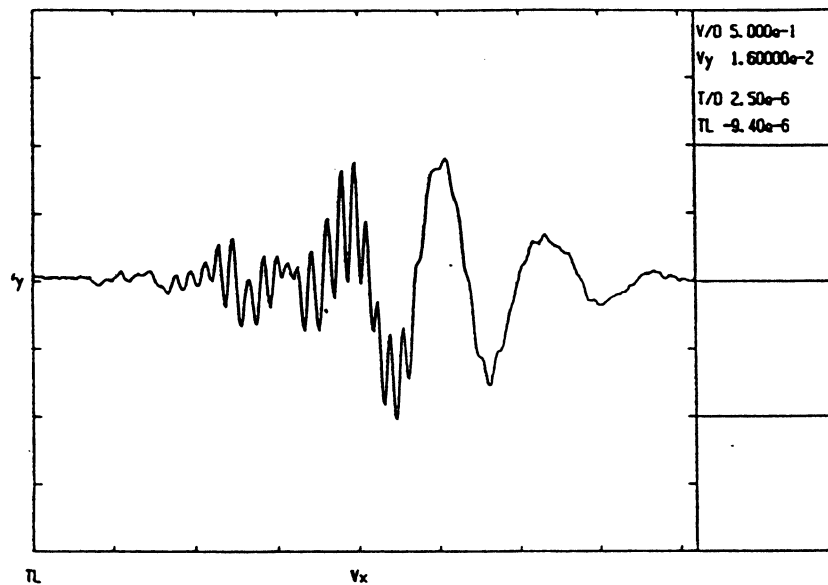
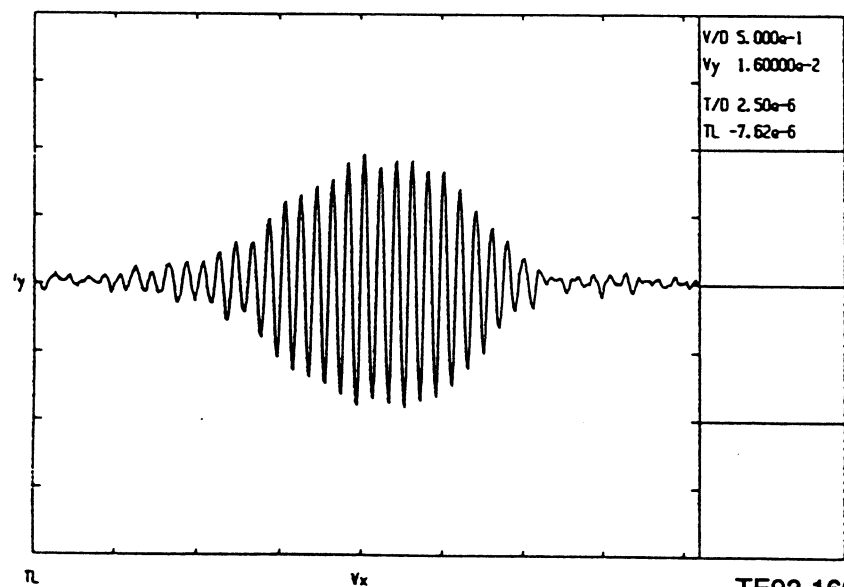


Figure 3.5.1-3. Partitioning of the PDPA receiver lens.

a) Improperly Filtered (Filter Feedthrough)



b) Properly Filtered



TE92-1666

Figure 3.5.1-4. Evaluation of signal filtering.

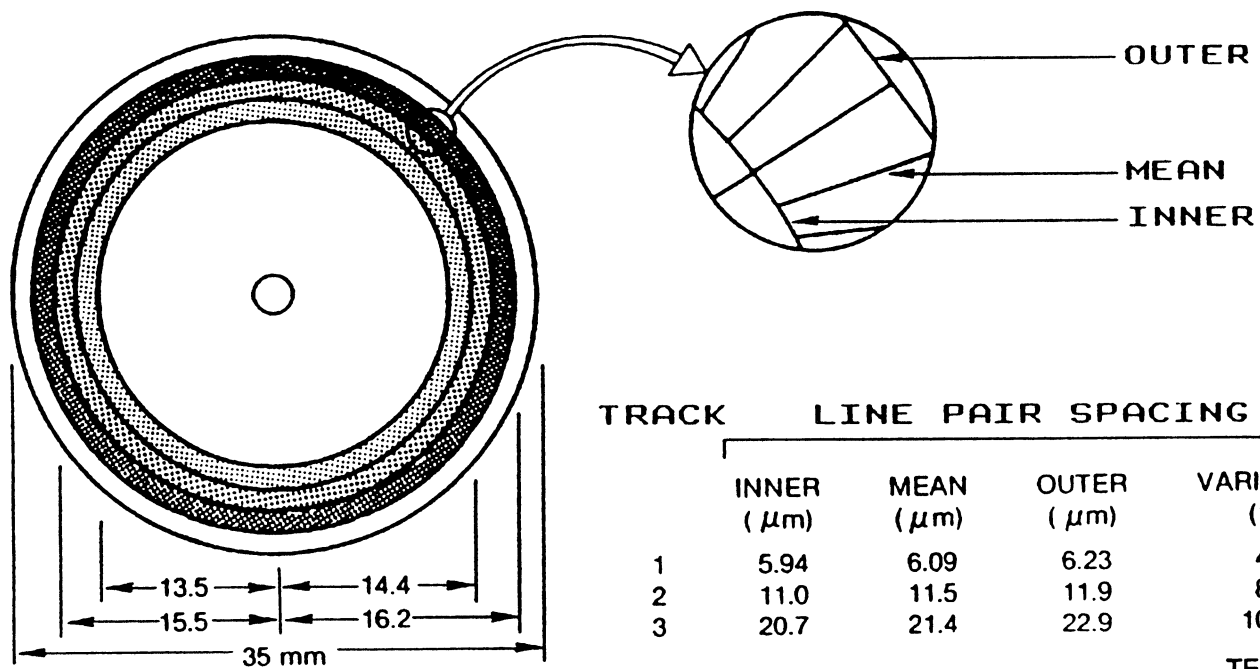


Figure 3.5.1-5. Detail of diffraction grating (Jackson, 1990).

a) Nebulizer Based (Ikioka, et al., 1983)

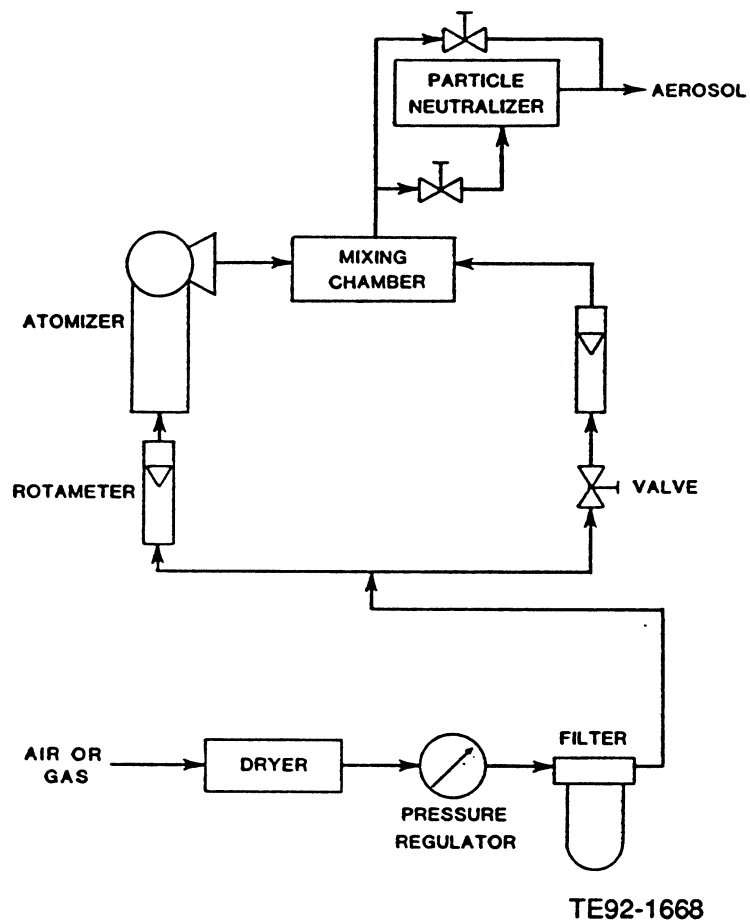
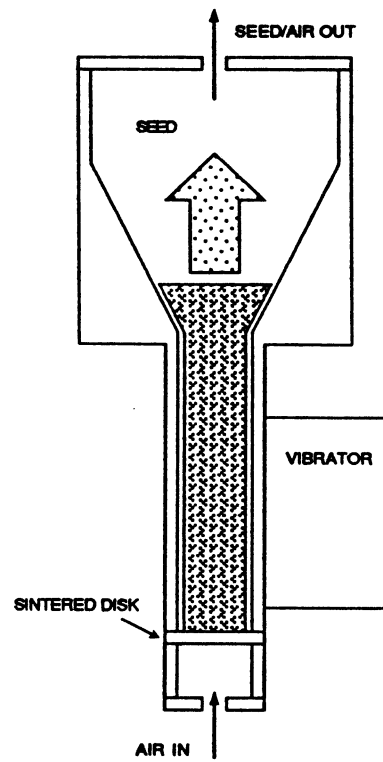


Figure 3.5.2-1. Seeders used in the program: nebulizer based (Ikioka, Brum, and Samuelsen, 1983).

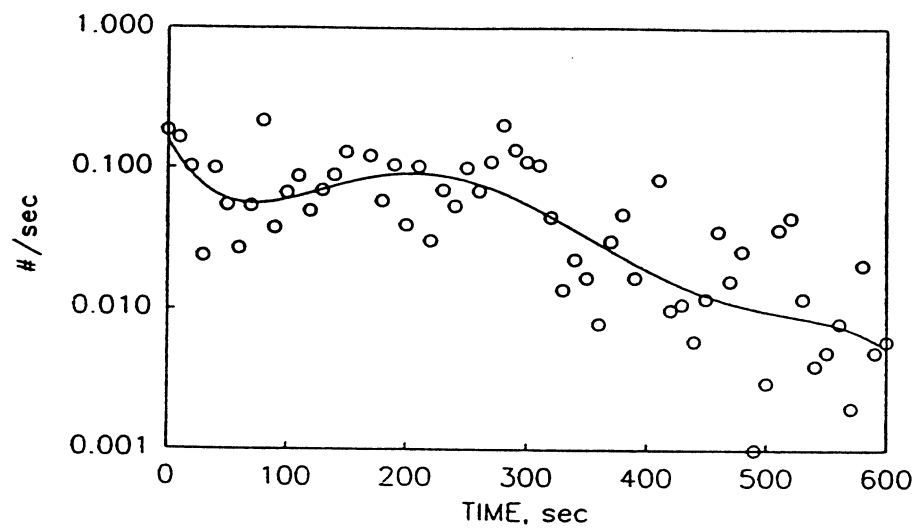
b) Fluid Bed Type



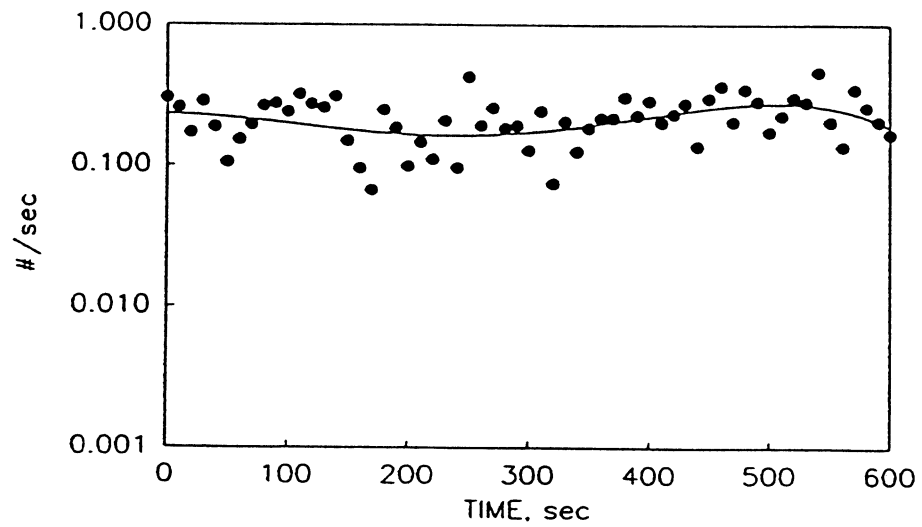
TE92-1669

Figure 3.5.2-2. Seeders used in the program: fluid bed-type.

a) Without Vibrator Motor



b) With Vibrator Motor



TE92-1670

Figure 3.5.2-3. Fluid bed output rate.

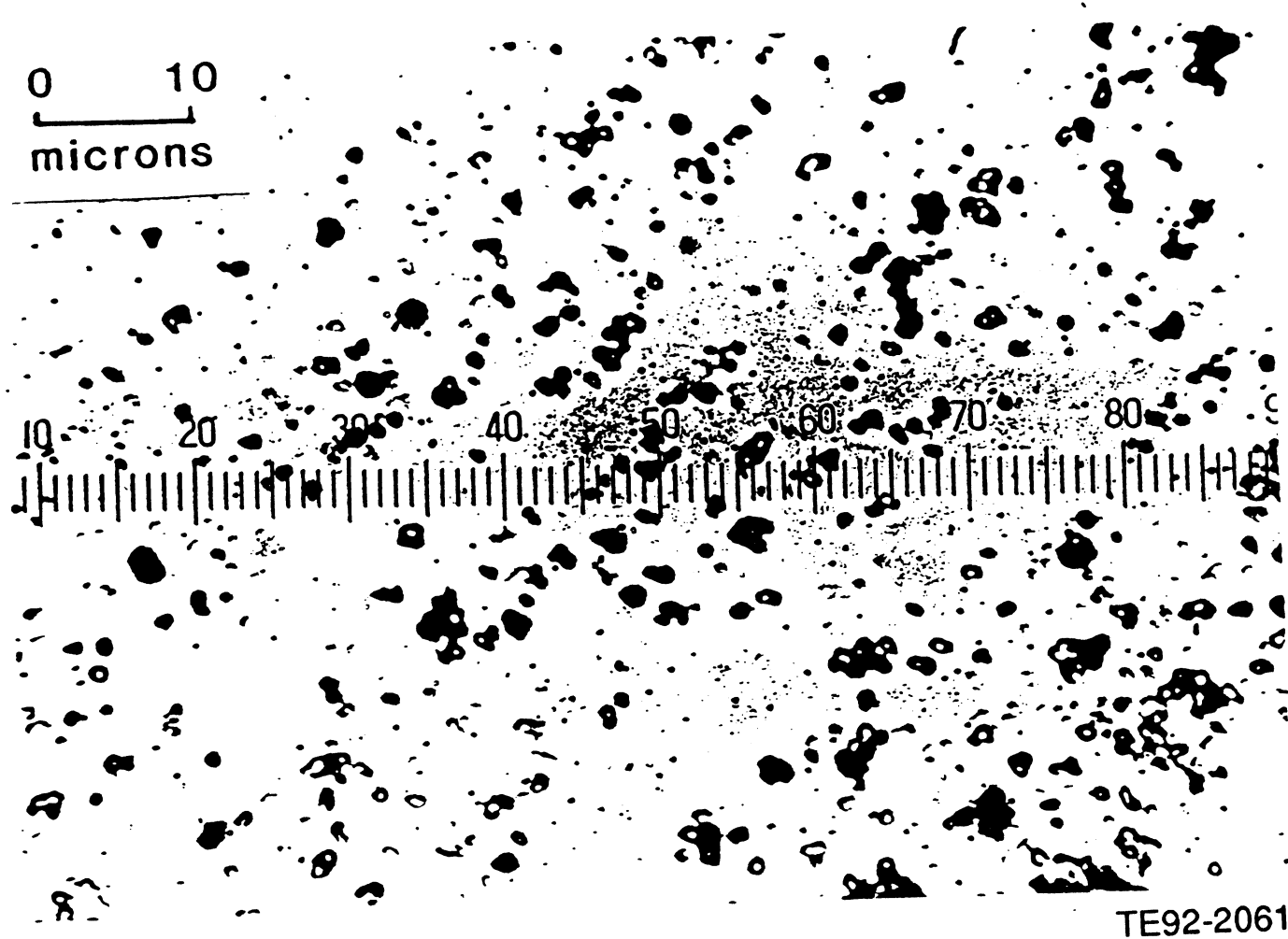
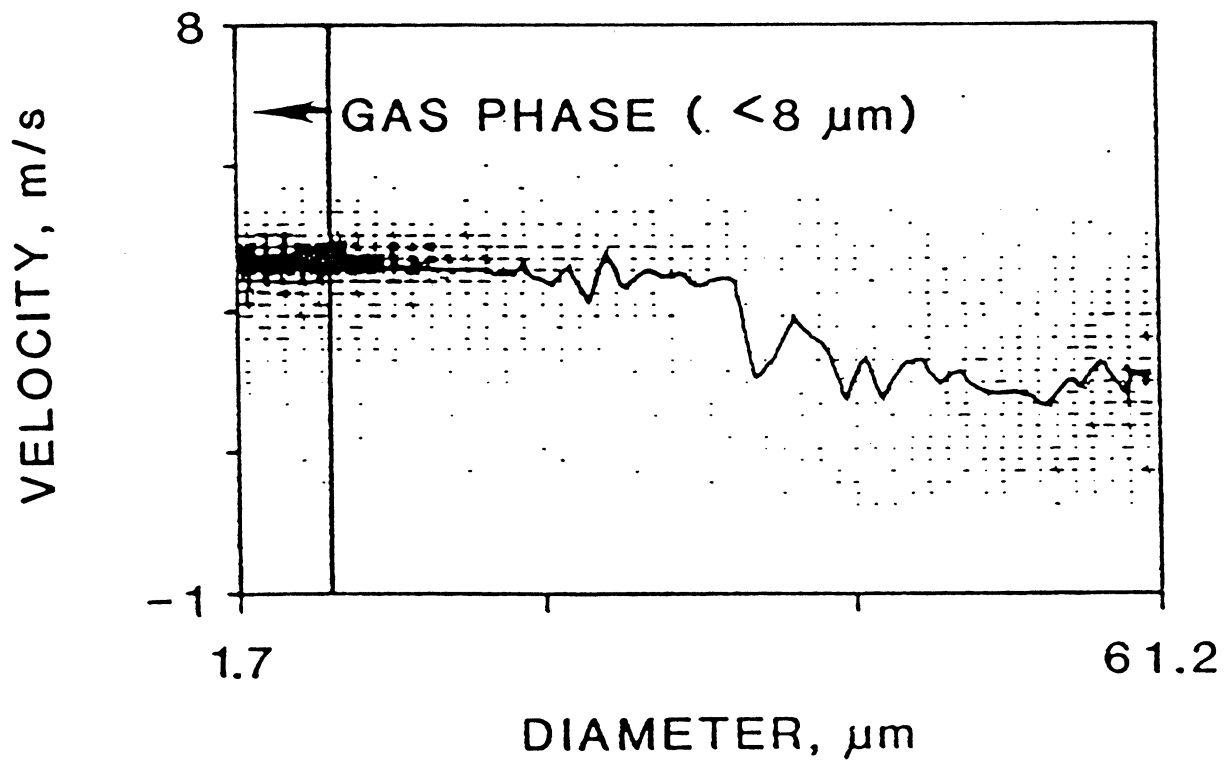
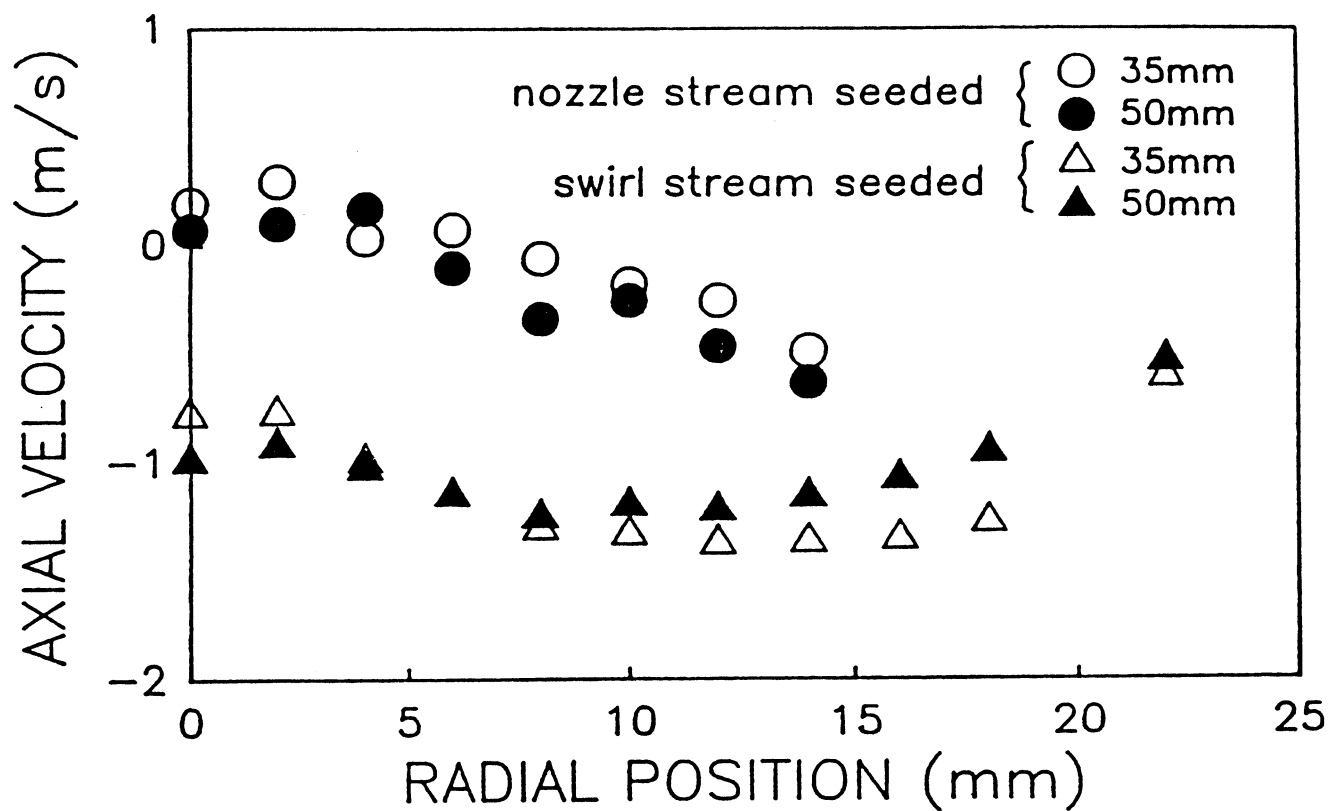


Figure 3.5.2-4. Seed morphology.



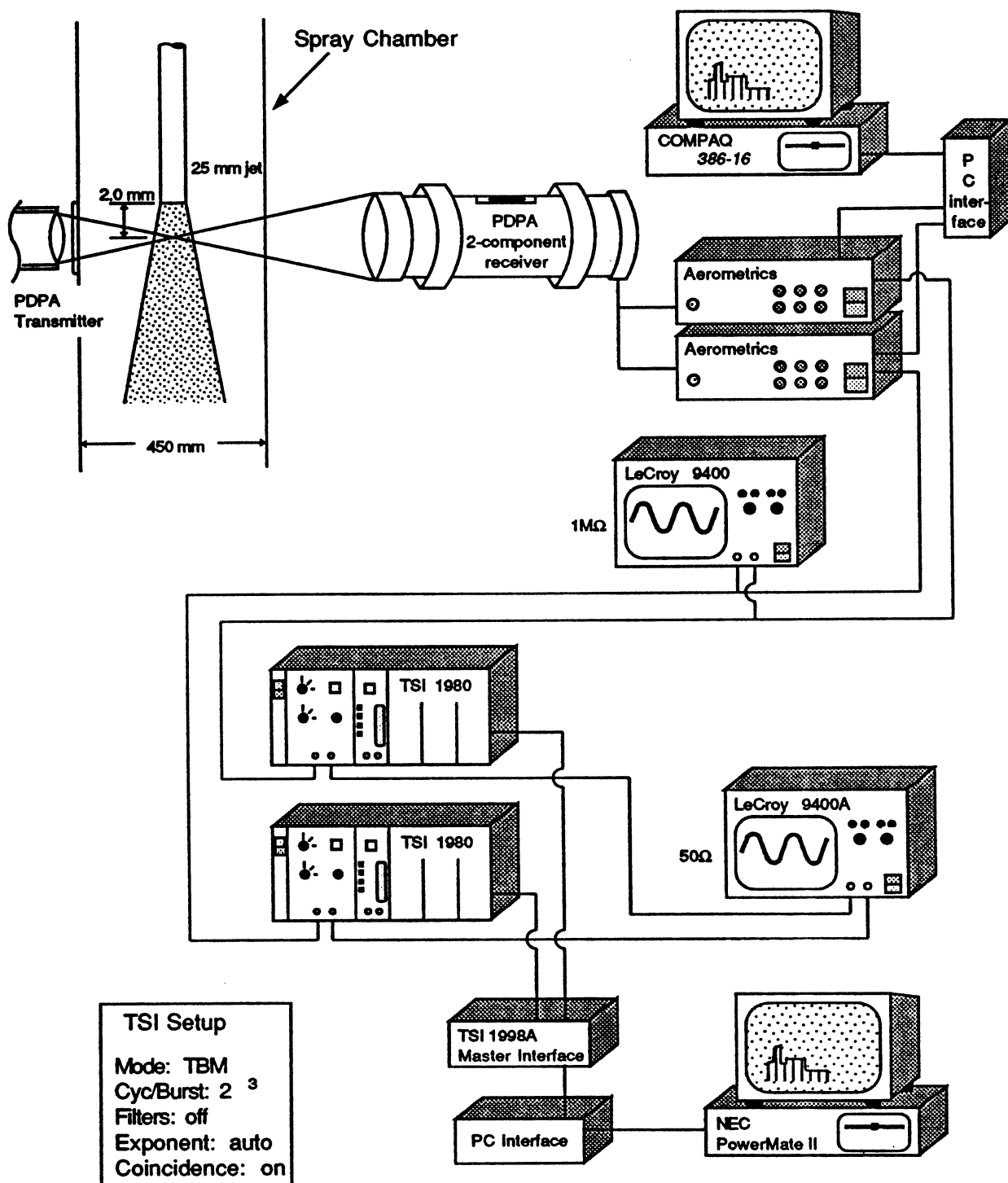
TE92-1671

Figure 3.5.2-5. Example of particle response study.



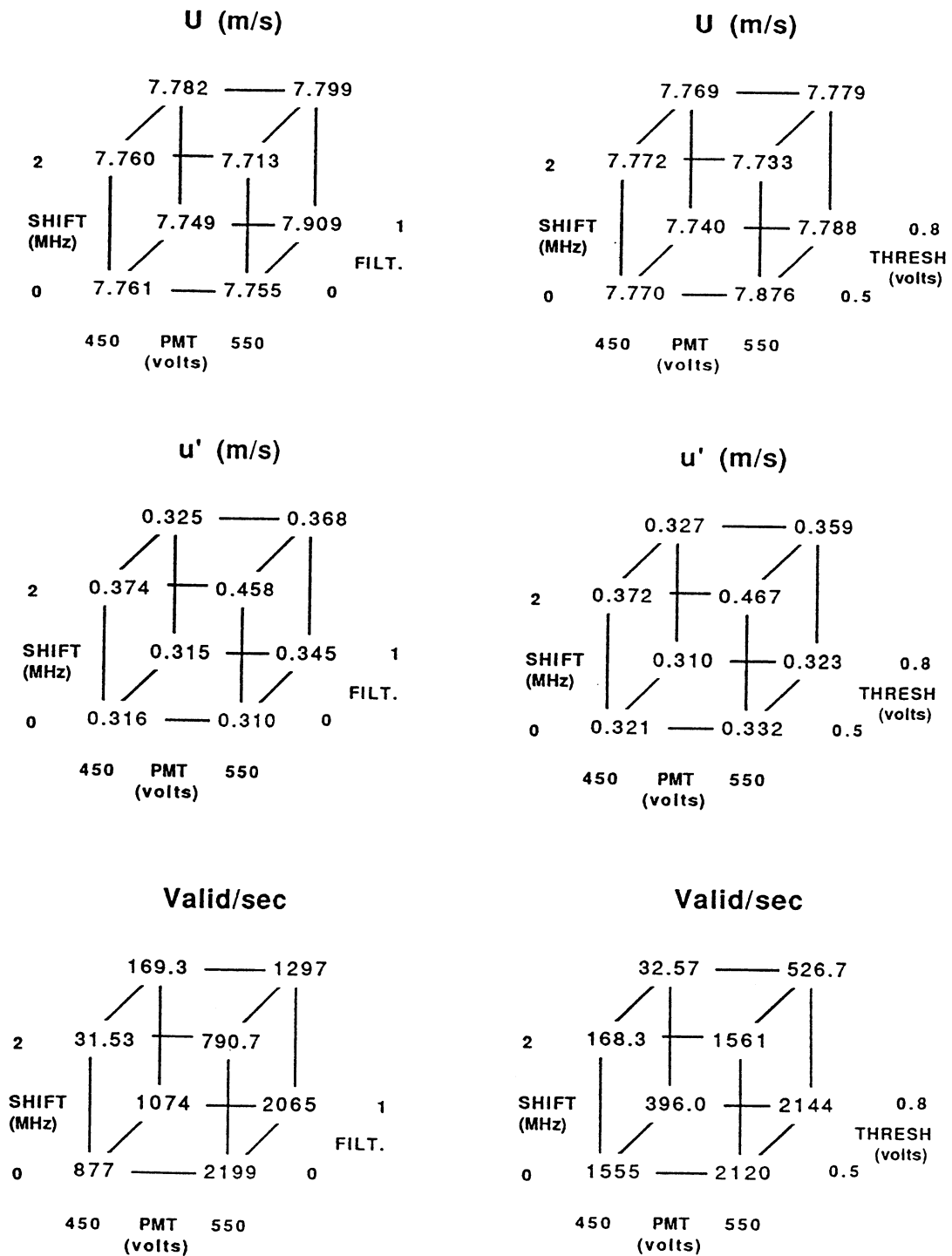
TE92-1672

Figure 3.5.3-1. Example of sampling bias in swirling flow.



TE92-1673

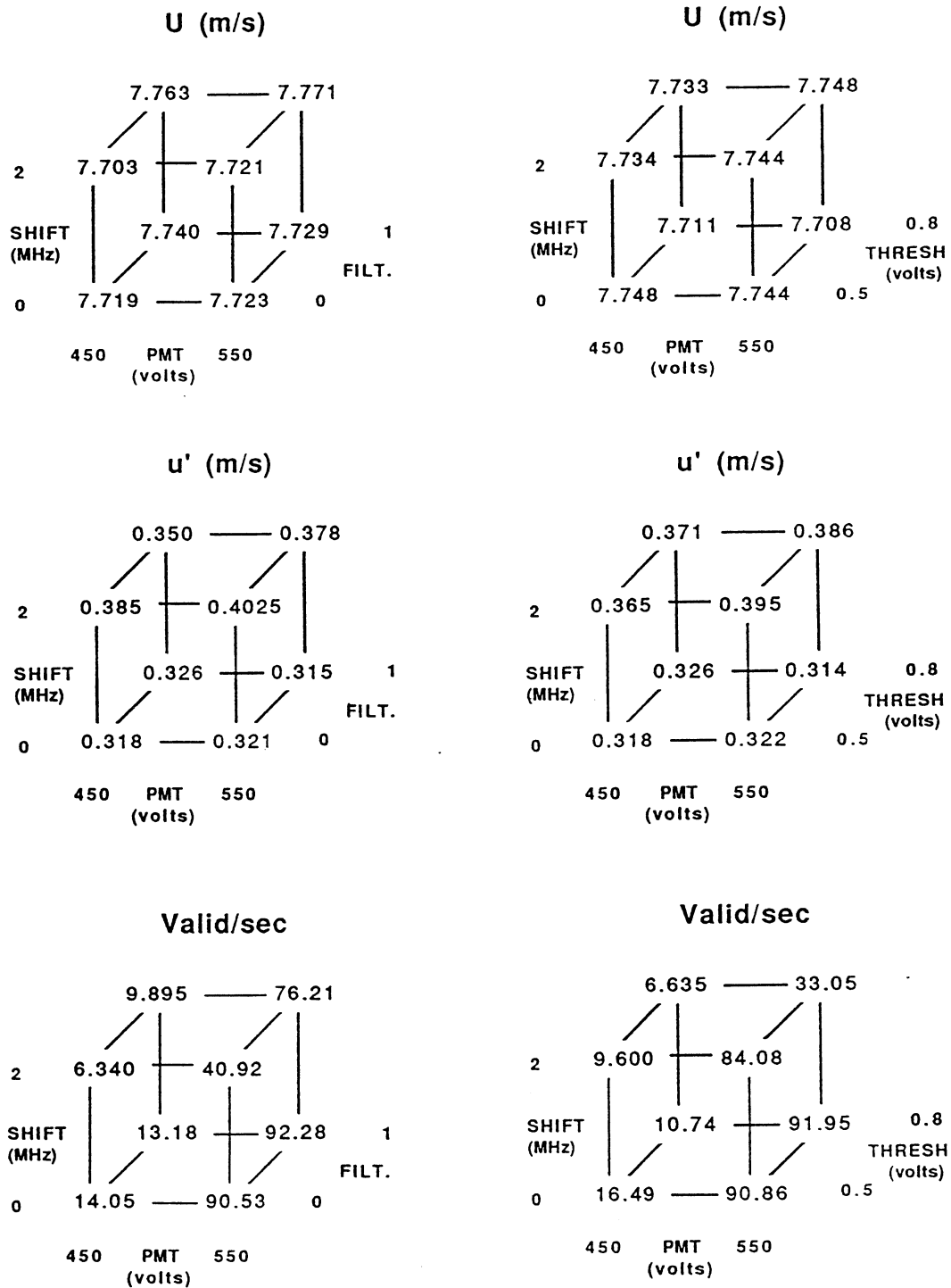
Figure 3.5.4-1. Setup of instrument comparison.



a) PDPA

TE92-1674

Figure 3.5.4-2. Cube plots for sensitivity study results at centerline of free jet (1 of 2).

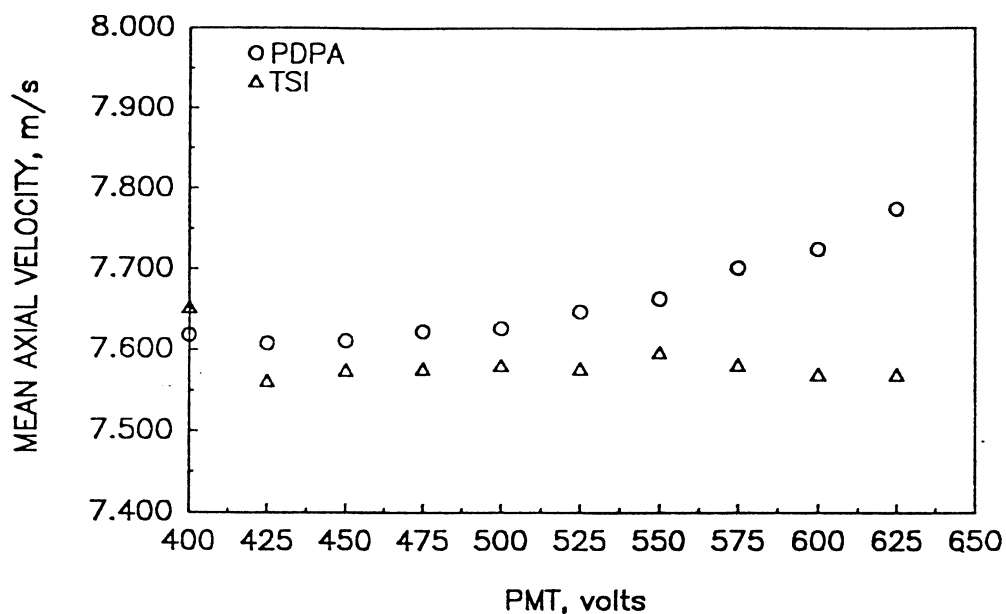


b) TSI

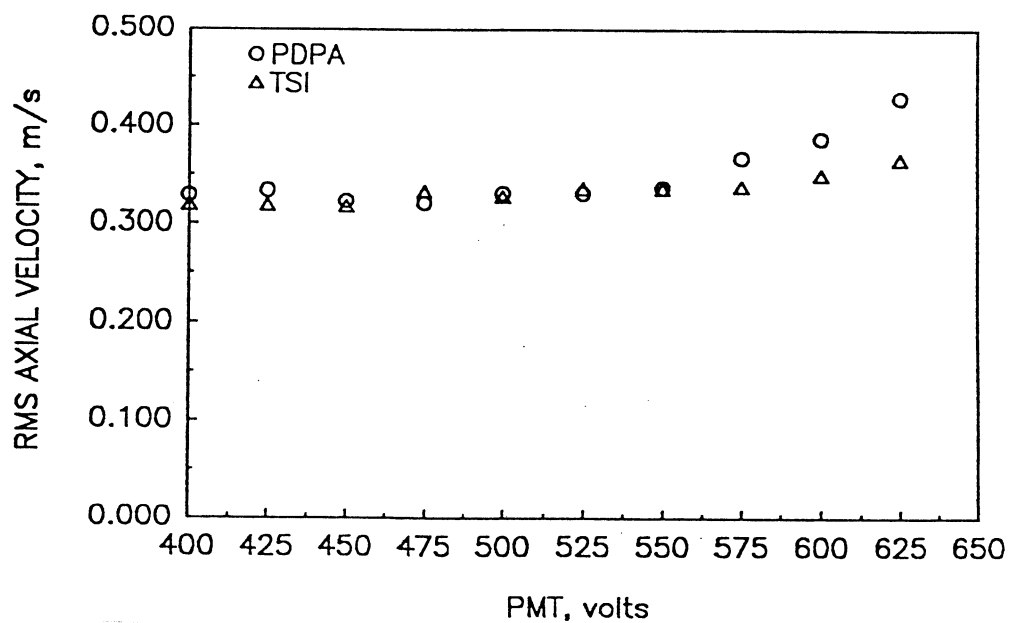
TE92-1675

Figure 3.5.4-2. Cube plots for sensitivity study results at centerline of free jet (2 of 2).

a) Mean Axial Velocity



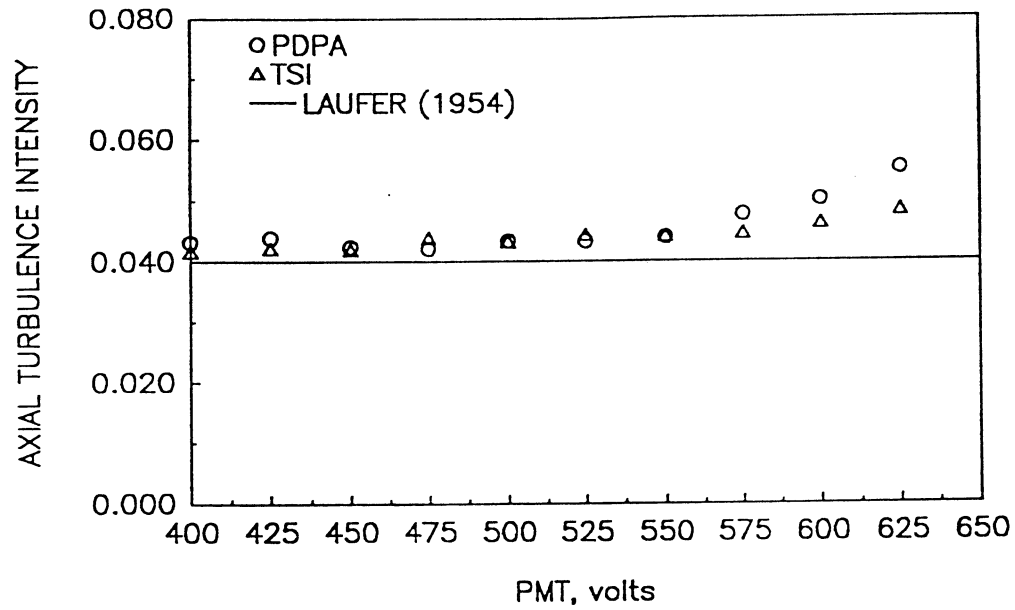
b) RMS Axial Velocity



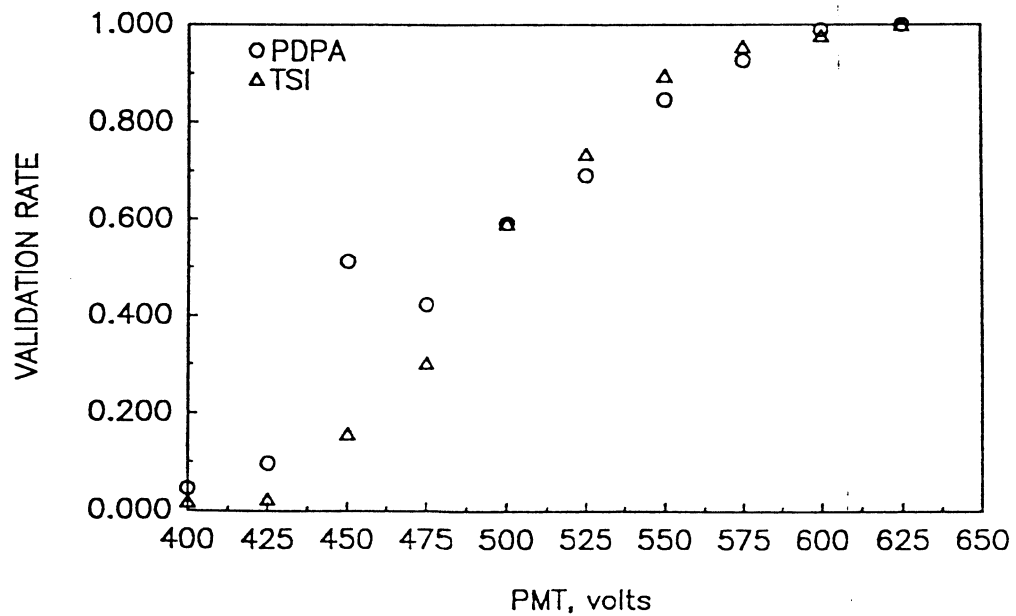
TE92-1676

Figure 3.5.4-3. Impact of PMT gain on TSI and PDPA velocity measurement at centerline of free jet (1 of 2).

c) Axial Turbulence Intensity



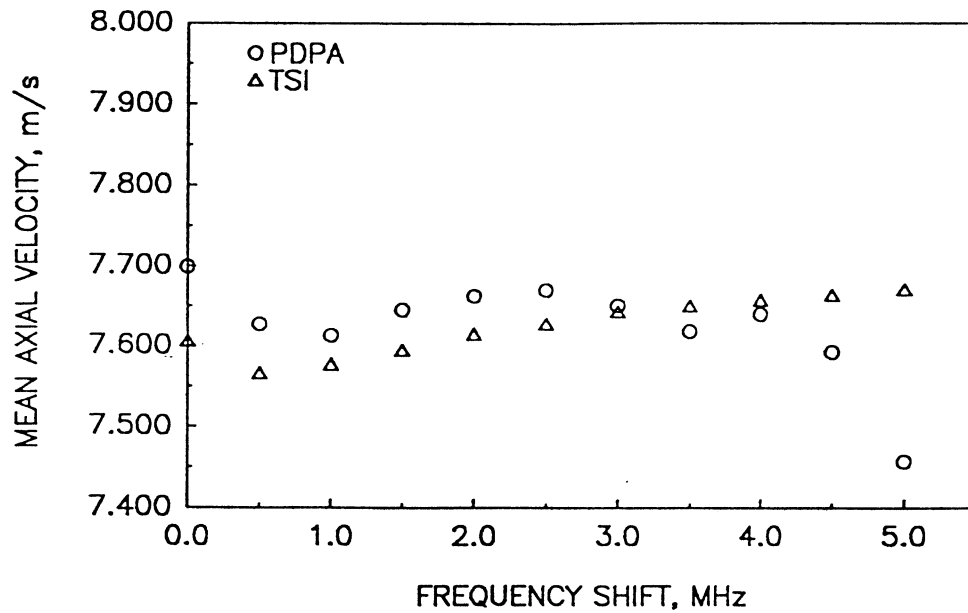
d) Validation



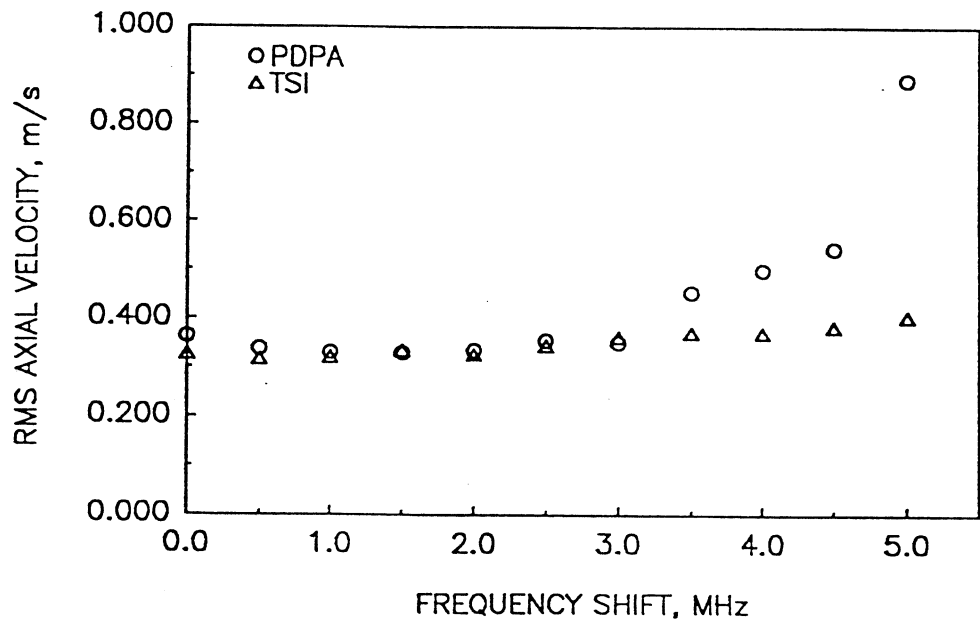
TE92-1677

Figure 3.5.4-3. Impact of PMT gain on TSI and PDPA velocity measurement at centerline of free jet (2 of 2).

a) Mean Axial Velocity



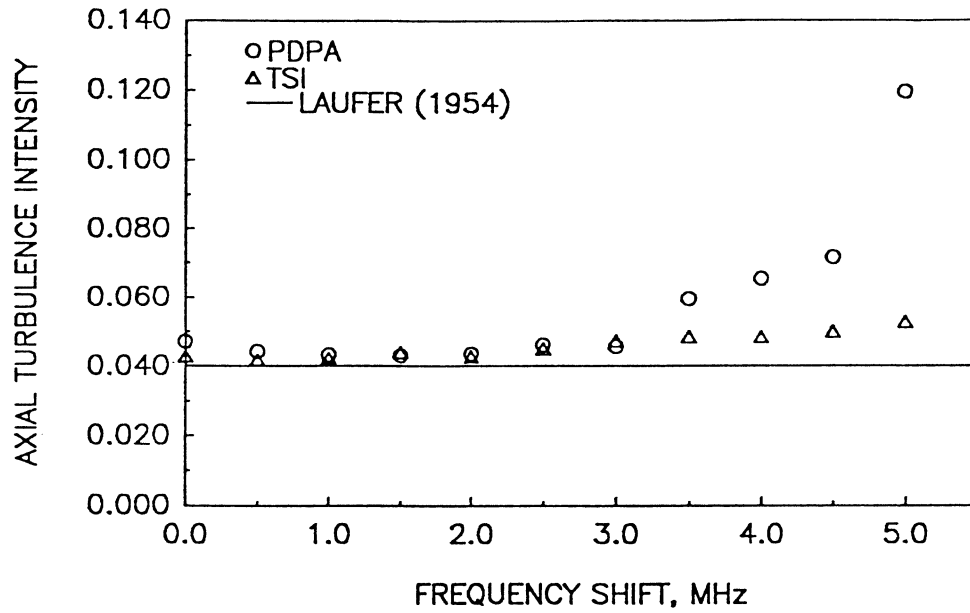
b) RMS Axial Velocity



TE92-1678

Figure 3.5.4-4. Impact of frequency shift on TSI and PDPA velocity measurement at centerline of free jet (1 of 2).

c) Axial Turbulence Intensity



d) Validation

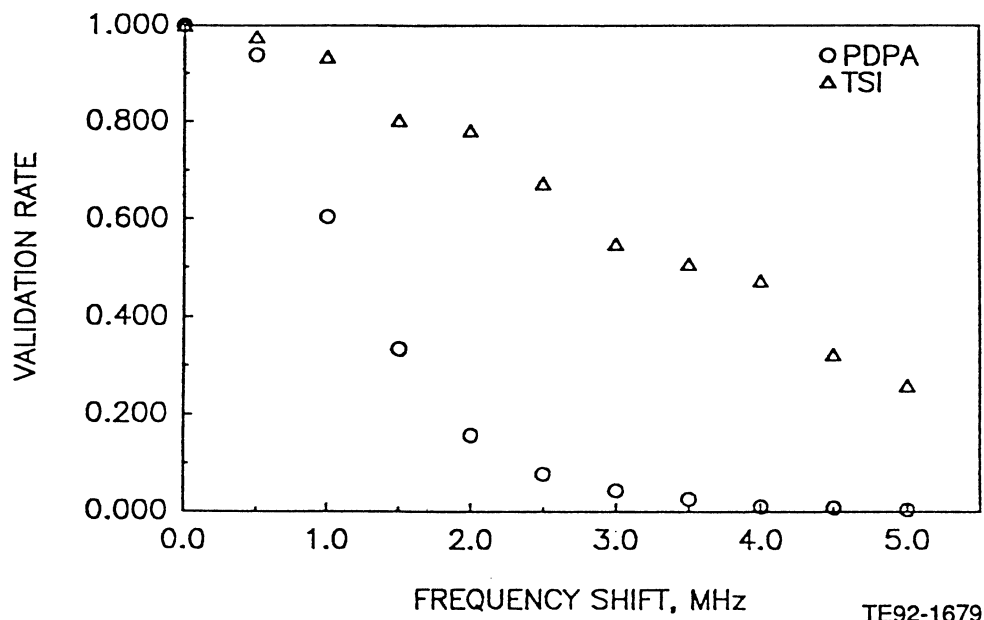


Figure 3.5.4-4. Impact of frequency shift on TSI and PDPA velocity measurement at centerline of free jet (2 of 2).

3.6 DIAGNOSTICS – PARTICLE SIZE MEASUREMENTS

This section describes the use of the phase technique in making size measurements. In addition, comparison to other techniques is presented. Finally, the extension of the technique for making measurements of volume flux and concentration is discussed.

3.6.1 Phase Technique – Theory and Limitations

The use of the phase technique to measure the size of spheres is described by Bachalo (1980). The theory makes use of the sphere acting as a lens, either refracting or reflecting incident light. The theory demonstrates that the size of the sphere is linearly proportional to the phase shift of the light which is refracted or reflected. The use of refracted light is the most common application of the theory and is the mode of operation used in the present case.

Figure 3.6.1-1 shows the means by which light is refracted and reflected through a sphere. At 30 deg off-axis, the refracted portion of light is maximized relative to the portions scattered by either reflection or diffraction. As such, scattering due to refraction can be isolated. Figure 3.6.1-2 (a) shows the relation of the spatial phase shift to the sizing parameter. This linear relation arises in the following manner. If a spherical drop is suspended in space and images the probe volume onto a distant surface, a fringe pattern will be projected. Knowing the optical properties of the drop/probe volume system (i.e., refractive index, probe volume fringe spacing) and distance to the surface, the spacing of the imaged fringes can be theoretically related to the size of the drop. It is apparent that a smaller sphere will result in an imaged fringe pattern with wider separation than that of a larger sphere. The relationship between the imaged fringe pattern separation and the size of the sphere is linear, and is the physical basis for the measurement of size.

However, because in general the spheres are moving, the imaged fringe pattern is swept through space. As a result, the spatial phase shift is measured by fixing two detectors in space and measuring the relative time shift between the signals received by the detectors. Figure 3.6.1-2 (b) demonstrates the spatial phase shift measured by using multiple detectors. These signals are obtained from the detectors as indicated in Figure 3.5.1-3. Similarly, time lag measurements can be made by the other detectors at known spacings as a means of checking the results. Since the signal is also processed for velocity, the period of a single fringe crossing is known. The ratio between the time difference measured by detectors at a known separation and the total period required for one fringe crossing gives the separation of the imaged fringe pattern. This can be related to phase by assuming that the period of the time between fringes is equivalent to 360 deg of phase shift.

$$\sigma_{1-3} = 360 \frac{\phi_{1-3}}{\phi_d} \quad (4)$$

ϕ_{1-3} = temporal phase shift between detector 1 to detector 3

ϕ_d = the Doppler period

σ_{1-3} = the spatial phase shift associated with the imaged fringe pattern

Note that if ϕ_{1-3} exceeds ϕ_d then there will be ambiguity in the resulting spatial phase shift (i.e., shifts greater than 360 deg cannot be distinguished from those less than 360 deg). This limiting case establishes the ultimate particle size range that can be covered and is a function of the optical setup. Using Mie Theory or geometrical optics, the relation obtained in Equation 4 can be related to the size of the sphere. All that is required is the optical properties of the setup, including the refractive index of the sphere (for refractive light), the fringe spacing, the focal length of the receiver lens, and the detector spacing. Noteworthy is that the detector spacing cannot be determined physically. This is due to the complex image integration which occurs over the face of the lens. As a result, the distances must be determined via calibration. Typically, a monodispersed drop stream is used to fix the separation.

The technique is limited to quasispherical particles. As a result, the technique cannot be relied upon to measure the size of nonspherical or nonhomogeneous particles. This limitation was confirmed experimentally by Alexander et al (1985). Thus, application of the instrument in regions of sprays where ligaments still persist is not possible and other means are required to characterize these regions in the spray field.

The primary advantage of the technique is that it utilizes a standard laser anemometry probe volume. Hence, the addition of size measuring capability to an existing laser anemometry setup is straightforward. This is accomplished by adding two more detectors to the receiver to measure phase shift.

Although total burst mode operation may require care when measuring velocity, it improves the accuracy of the size measurement. If the velocity of particles with a wide variety of sizes is measured, a variation in cycles will occur depending on the size of the scatterer (discussed in detail in section 3.6.2). A fixed-cycle processor will use the beginning, and hence noisy, portion of the signal from large particles. Thus, the full signal is used to ensure that the best parts of the signal are used regardless of the size of the scatterer. This approach is also employed for velocity measurements, so that the same processing electronics may be utilized. As shown in section 3.5.4, the use of the total burst may require additional care to be taken when measuring velocity only.

Another inherent limit imposed largely by electronics is the size range that can be detected. In a typical spray, the amplitude of the scattered light can be assumed to be proportional to the diameter squared. For example, a 100 micron drop will scatter 10,000 times more light than will a 1 micron drop. This means that the electronics must be able to pick out 1 part in 10,000 in terms of amplitude, which is unrealistic. More realistic is 1 part in 1,000, so a limit in size range of 35 to 1 was set as the limit. Therefore, if the instrument is set to detect a maximum size of 70 microns, the minimum size it can be expected to detect is 2 microns.

In addition to the validation checks made for velocity as mentioned in section 3.5.1, checks are also made for size validity. These checks are as follows

- phase error A band of phases are assigned to each size class. This band is set by the user and is typically 10-15%. The phase shift is measured by two sets of detectors, each having a unique phase/size relationship. If the measured phase by each set of detectors does not correspond to the same size within this band, the event is rejected.
- out of range If the measured size falls outside of the size range selected by the user, the event is rejected. This implies that the 35:1 size range is exceeded.
- saturation If the signal detected exceeds the limit of the preamp output (10V), the PMT is assumed to be saturated and the event is rejected.

As a result of the many checks that the signals undergo, it is possible to have many events rejected, depending upon the particles being measured. As previously mentioned, nonspherical particles will give rise to phase errors, as will multiple particles in the probe volume.

In general, it can be stated that the primary limitation of the instrument is imposed by high concentration sprays. As a result, measurements close to the nozzle in typical gas turbine atomizer sprays generally cause problems. However, it has been suggested recently that in a typical twin-fluid atomized spray the rejections due to multiple particles in the probe volume do not strongly impact values such as D_{32} (Edwards and Marx, 1991).

3.6.2 Probe Volume Correction

Like all single particle counters, the phase/Doppler instrument must account for the Gaussian intensity profile of the laser beam. Figure 3.6.2-1 (a) illustrates how particle size influences the effective probe volume size. Several approaches are available to correct for the Gaussian profile. There are approaches which compensate for the Gaussian nature of the beam by making assumptions regarding the size distribution in the flow (e.g., Yule et al, 1982) and those which eliminate the Gaussian intensity profile by using masking to enable only the most intense part of the beam to be used (e.g., Hess, 1984). Those which make assumptions about the size distribution are questionable since it is the same distribution that is being measured. Those which attempt to eliminate the Gaussian nature offer a more realistic approach to providing accurate information. However, these techniques suffer in that disturbances to the probe volume, such as those occurring in dense sprays, may not be accounted for.

In principle, the best way to correct for variation in probe volume size due to particle size is to measure the variation during the measurement. The result is that a pdf of particle size versus number of fringes crossed can be generated. An example of the cross correlation of particle size with fringes crossed is shown in Figure 3.6.2-1 (b). By normalizing the counts to a given value of fringe crossings, the effect of the Gaussian beam is eliminated. The primary, and perhaps only, drawback to this approach is the ambiguity associated with the number of fringes which to normalize. If the number selected is too large, too many particles will be counted across the total distribution, and the mass flux measured will be too high. The opposite will occur if the number is too low.

During the development of the PDPA system, as used in the current program, several approaches to the probe volume correction scheme were used. All were based upon measured fringe crossing information. Each approach was retained as proprietary, and as a result, independent approaches were evaluated. For the majority of the work done with glass beads, a value was selected which was equal to the mean number crossed for all the samples added with the rms of the fringes crossed for all samples.

Later versions of the software (v. 3.62 and higher) use a more sophisticated approach involving least squares fitting of the measured data. However, this approach requires extrapolation of measured data, which can lead to serious error. Additional information regarding probe volume related phenomena can be found elsewhere (McDonell and Samuelsen, 1991; McDonell and Sowa, 1990).

Essentially, the probe volume correction scheme is important for values such as volume flux, concentration, and distribution linear mean. The results for size distribution D_{32} (D_{32} is the diameter of a droplet whose ratio of volume to surface area is equal to that of the entire sample) are less sensitive because the correction techniques, in general, impact the population of small drops the most. Since D_{32} is derived largely from the population of big drops, it is not strongly affected by the correction scheme used.

3.6.3 Validation of Technique

In order to verify the performance of the instrument, several approaches were taken. Fundamental tests such as checking the detector calibration by measuring a monodispersed drop stream were run every few months. Other tests involved comparing the results obtained via phase Doppler to those obtained via other techniques. Finally, tests were run later in the program comparing the results measured by the phase technique but using different types of processors. The last two types of tests are discussed in the following paragraphs.

Several workers have made comparisons between the phase technique and diffraction or visibility techniques: these include Jackson and Samuelsen (1987), Dodge et al (1987), McDonell et al (1986), and Young and Bachalo (1987), among others. Typical results are shown for the comparison of the phase technique to visibility/IV (Jackson and Samuelsen, 1987) and to Malvern (McDonell et al, 1986) in Figures 3.6.3-1 and 3.6.3-2.

Figure 3.6.3-1 shows the comparison of Malvern, visibility/IV, and PDPA size distributions measured at the centerline of a twin-fluid atomizer spray. The results suggest that the general distribution shape is matched by all three techniques. However, closer inspection reveals that the PDPA distribution is weighted towards the larger drops, especially compared to Malvern Rosin-Rammeler.

Jackson developed a technique to compare Malvern data to phase/Doppler data acquired along a radial profile. This is not a straightforward task, as the Malvern measures a line of sight ensemble SMD in a spatial or volume sensitive manner and the phase/Doppler measures a spatially resolved temporal or flux sensitive SMD. The details of the algorithm used to compare the two techniques are given by Jackson (1985). The primary difference between the flux sensitive and volume sensitive SMD is that the volume sensitive SMD cannot account for size velocity correlations and detects more slower moving droplets. In the algorithm to compare the two data types, any dependency of droplet velocity on size must be removed.

Figure 3.6.3-2 presents a comparison of PDPA line averaged, or composite, SMD (PDC) and Malvern derived SMDs based on both model independent (MI) and Rosin-Rammeler (RR) algorithms obtained in a spray similar to that used for the results in Figure 3.6.3-1. Close to the nozzle, the phase Doppler results are higher than either Malvern-based result. Farther downstream the model independent treatment and PDPA results become similar. However, even at the farther axial location, the RR treatment gives an SMD which is much lower than that measured using PDPA.

The results shown in both Figure 3.6.3-1 and 3.6.3-2 are based on the use of a single velocity component to make the correction for size/velocity correlation. In theory, since a dependency may exist for all three components of velocity, these must be considered as well. As part of the current program, the work of Jackson was extended to account for two velocity components, which will make the comparison more accurate. Details of the algorithm used are given by Jackson (1985).

Other tests run involved comparing the results obtained using the Aerometrics instrument to those obtained using an independent signal processor. This approach is similar to that described in section 3.5.4. For sizing, an independent signal processor (Quality Signal Processors [QSP] [Tan, 1990]) was utilized. This is the same signal processor used in the INVENT phase Doppler instrument (INVENT, 1991), and based not on counter technology, but on frequency domain processing. In this study, the Aerometrics transmitter and receiver and signal preparation (i.e., amplification, filtering) were used, and the signals from detectors 1 and 2 were fed into the QSP. In this manner, the signals were identical, but being processed by two independent processors.

As an example of the types of results obtained in this type of study, Figures 3.6.3-3 and 3.6.3-4 present a comparison of the sizes measured by each instrument. Figure 3.6.3-3 presents the effect of frequency shift on the distribution number and Sauter mean diameters at one location in an air-assist spray. In addition, the effect of shift on the validation is presented.

Figure 3.6.3-3 (a) presents the effect of frequency shift on the uncorrected distribution means. Uncorrected means that the probe volume compensation required for single particle counters was not employed. The results show that, for both instruments, a modest reduction in the distribution means are observed with increased shift. This is true for both number and Sauter mean diameters. At modest shift levels (less than 25 m/s), little variation is observed for either processor, as expected. The reason for the decrease at higher shifts is not known. Note that in each case the QSP distribution means are systematically smaller than those for PDPA. This is attributed to the increased sensitivity to small drops that the QSP has.

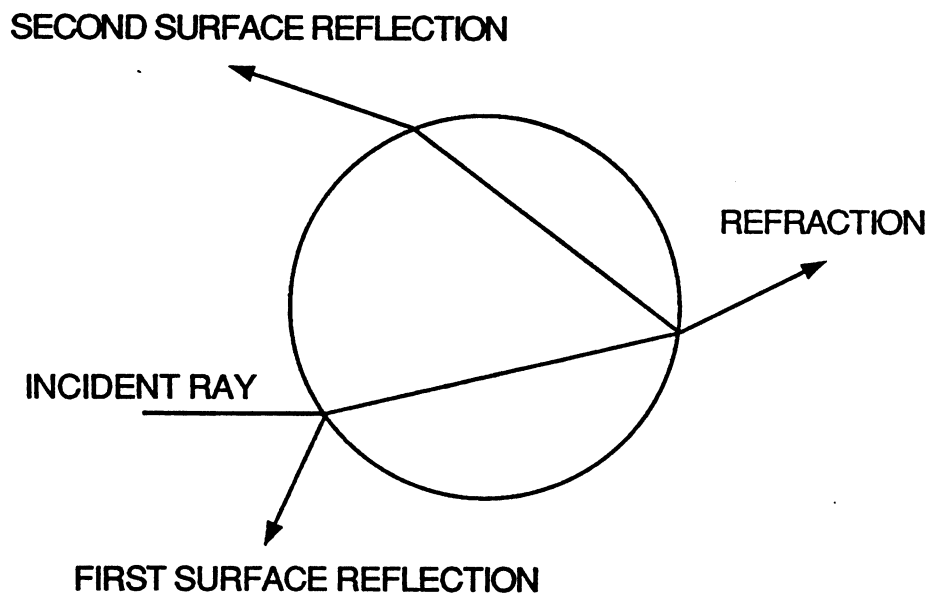
When the distribution is corrected for probe volume/drop size dependency, the results shown in Figure 3.6.3-3 (b) are obtained. In this case, even more dependency is observed. The corrected distribution means for each instrument show less difference than do the uncorrected results. This helps to show that

the correction scheme used by PDPA in this case provides reasonable correction. The systematic reduction in distribution means is still apparent in the corrected results.

Finally, Figure 3.6.3-3 (c) presents the results for the validation. In this case, both instruments validate the majority of the signals. The QSP tends to reject fewer drops at the higher shifts, again owing to the inherent ability of the frequency domain processor to operate in lower S/N ratios than the counter.

Another type of result is presented in Figure 3.6.3-4, where the uncorrected distributions are examined in more detail, this time as a function of PMT setting. Figure 3.6.3-4 (a) presents the dependency of the distribution means on the PMT setting. In this case, the QSP results are essentially independent of the PMT setting, whereas the PDPA results exhibit a strong correlation of decreasing means with increased voltage. To examine the reason why, the distributions obtained for three PMT settings are presented in Figure 3.6.3-4 (b, c, and d). At the lower voltage (Figure 3.6.3-4 [b]), it is observed that the QSP detects considerably more small drops than does the PDPA. Increasing the voltage to 320 volts (Figure 3.6.3-4 [c]) results in similar distributions, but with still more small drops detected by QSP. Finally, at the higher voltages (Figure 3.6.3-4 [d]), the distribution means are very similar (Figure 3.6.3-4 [a]), but the distributions themselves still reveal differences. In this case, the QSP detects not only more smaller drops but also more intermediate drops than the PDPA (McDonell and Samuelsen, 1991). Some of these results are not surprising, since it is expected that the QSP can detect smaller drops even at low voltages. Essentially, however, the results show that the two processors give similar results for the distributions and for the distribution means.

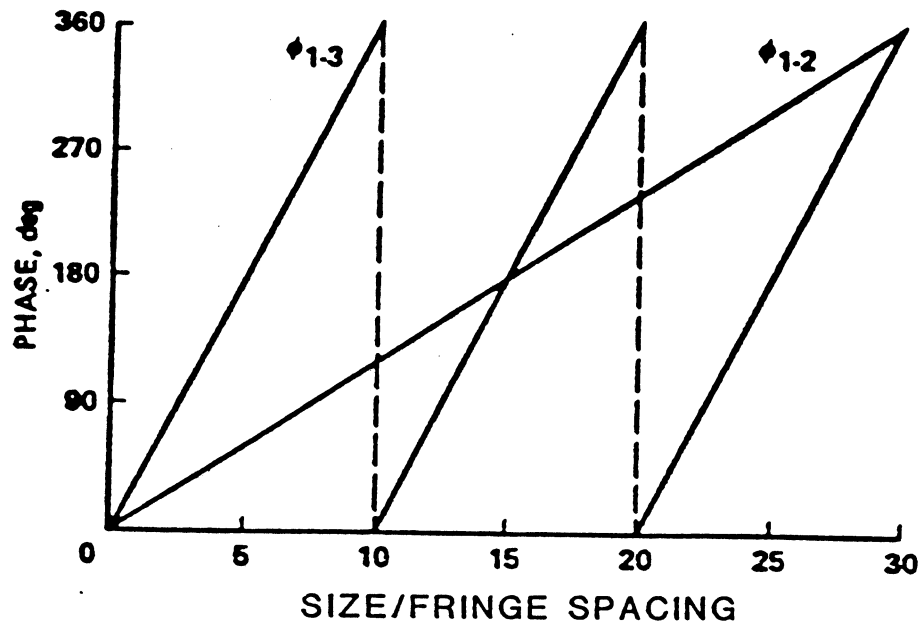
It is difficult to interpret comparisons of the corrected results because the two systems use different probe volume correction schemes. Essentially, the corrected results from the PDPA agree reasonably well with the QSP results. Additional information regarding these types of tests is available elsewhere (McDonell and Samuelsen, 1991).



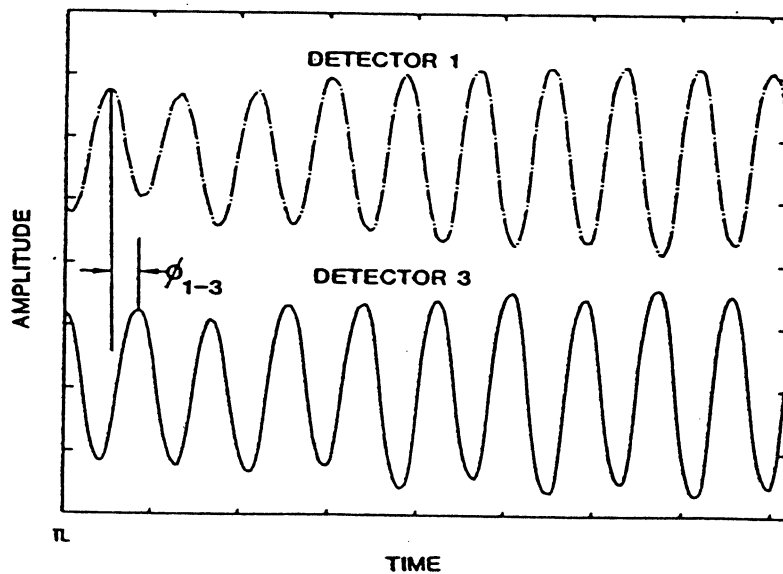
TE92-1680

Figure 3.6.1-1. Light scattering by a sphere (Bachalo, 1980).

a) Relation of Spatial Phase Shift to Size Parameter



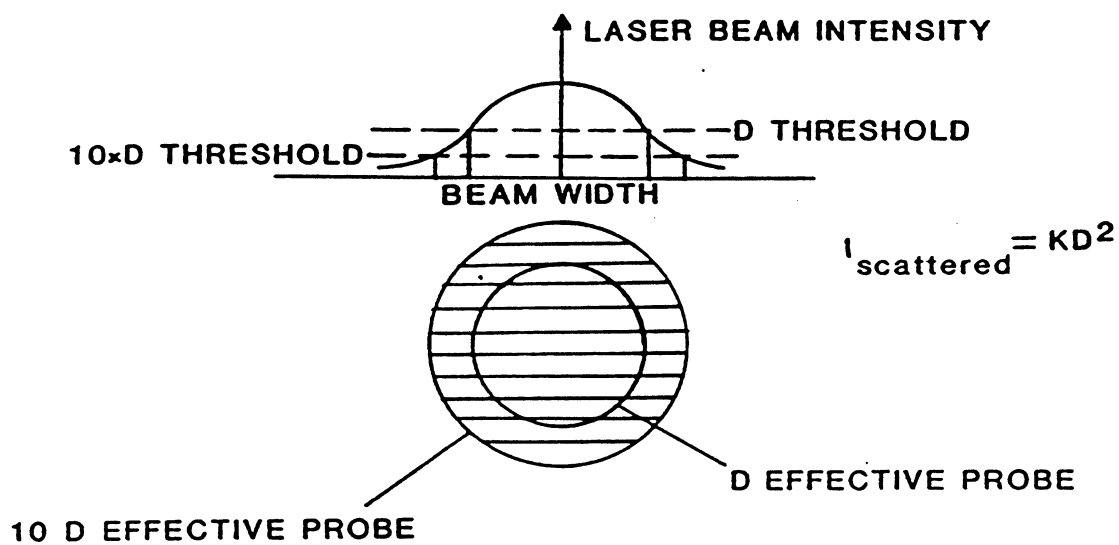
b) Spatially Shifted Signals



TE92-1681

Figure 3.6.1-2. Spatial phase shift related to size.

a) Effective Probe Sizes



b) Measured Probe Width

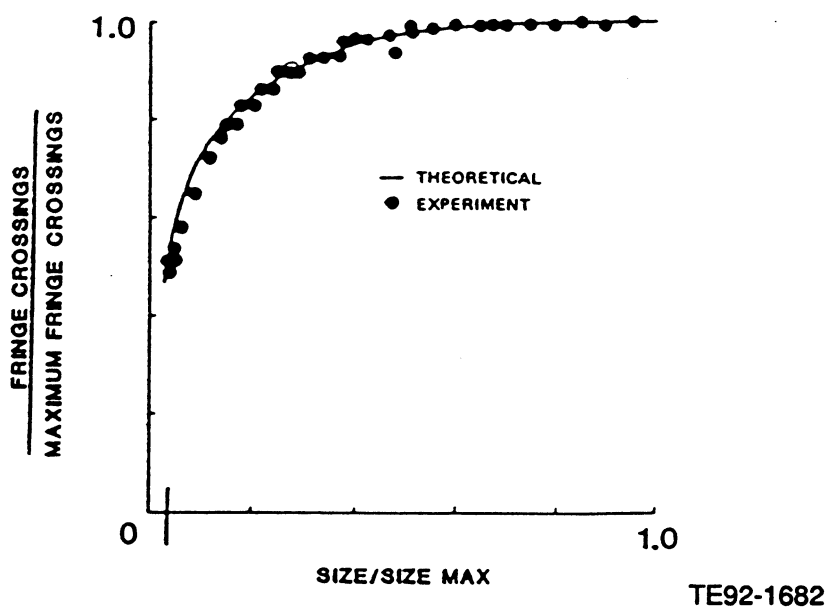


Figure 3.6.2-1. Dependency of probe size on particle size.

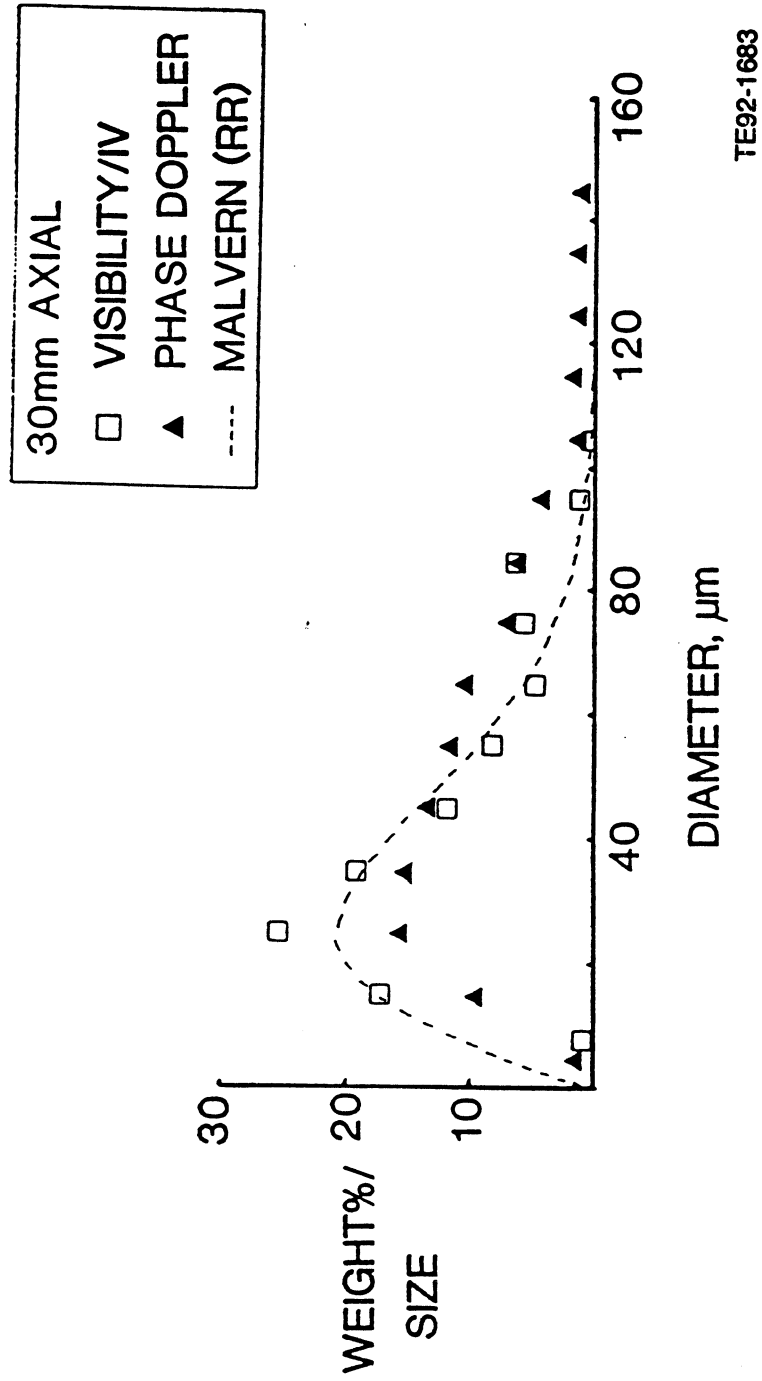
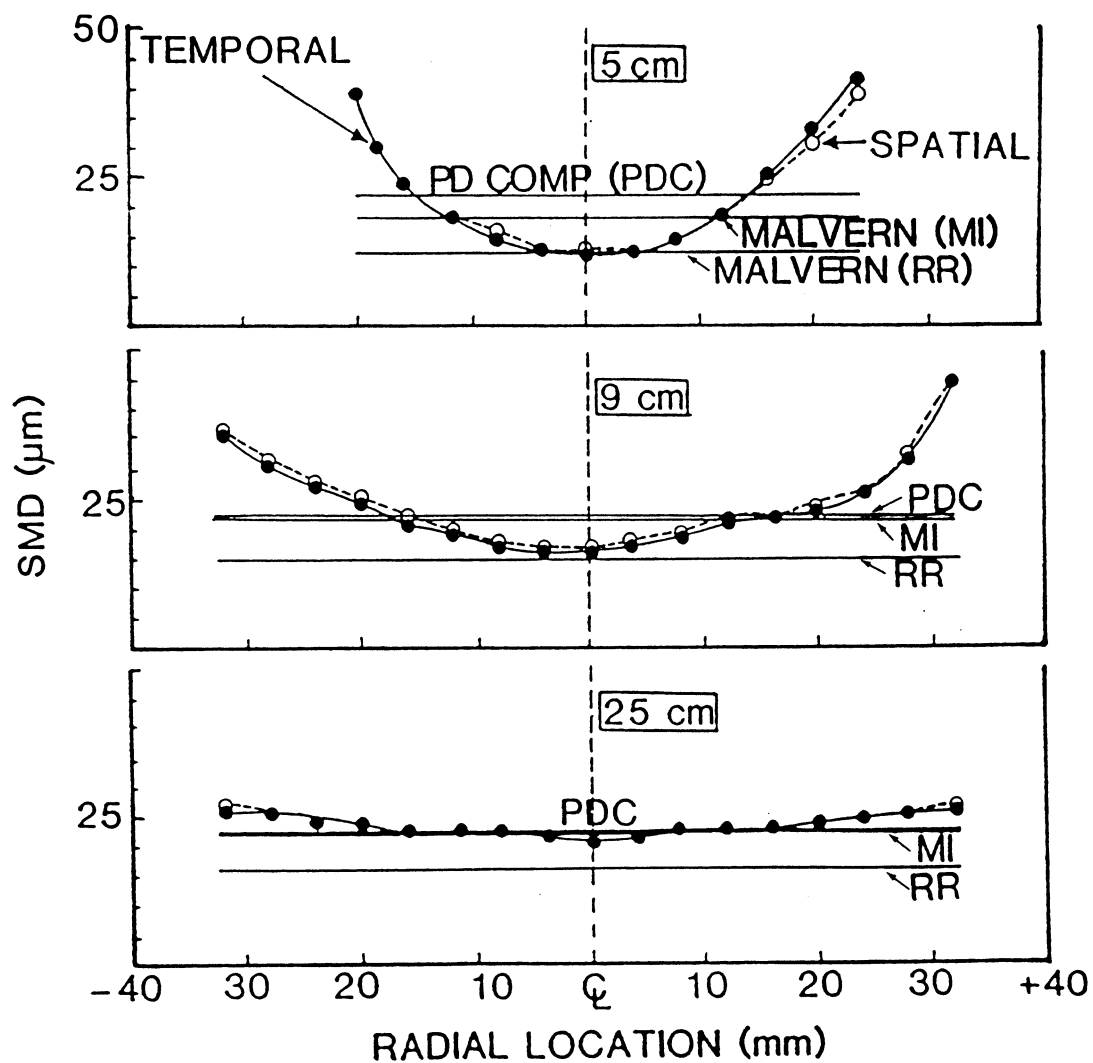


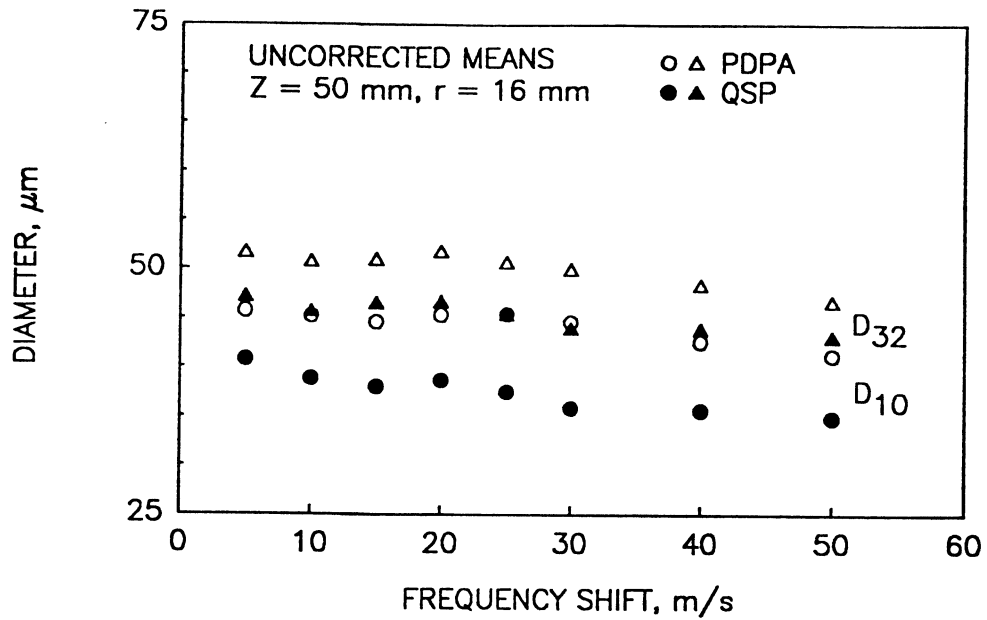
Figure 3.6.3-1. Comparison of phase technique to visibility/IV (Jackson and Samuelsen, 1987).



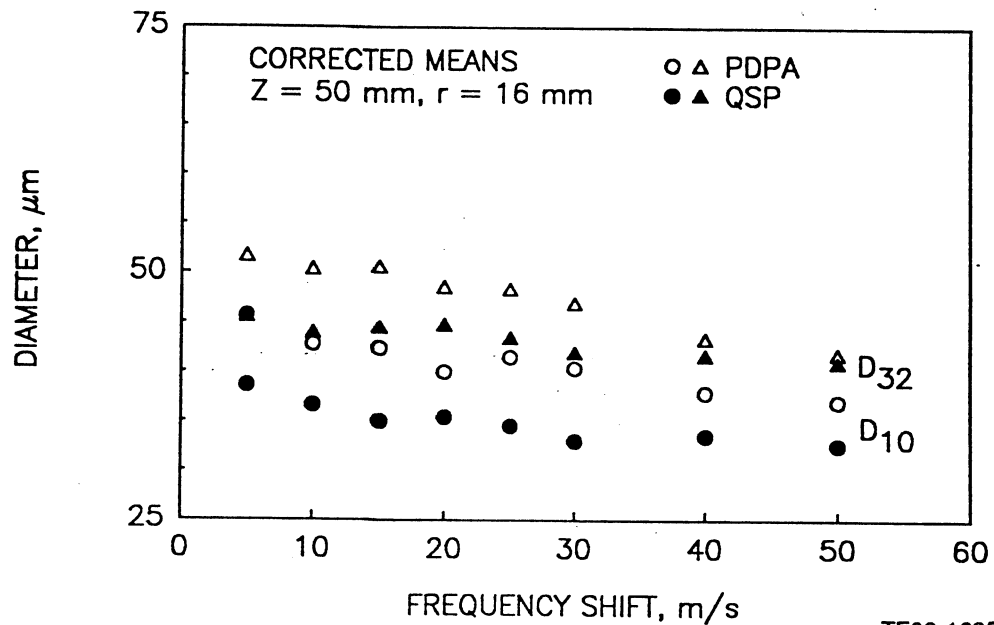
TE92-1684

Figure 3.6.3-2. Comparison of phase technique to Malvern (McDonell, Wood, and Samuelsen, 1986).

a) Uncorrected Sizes



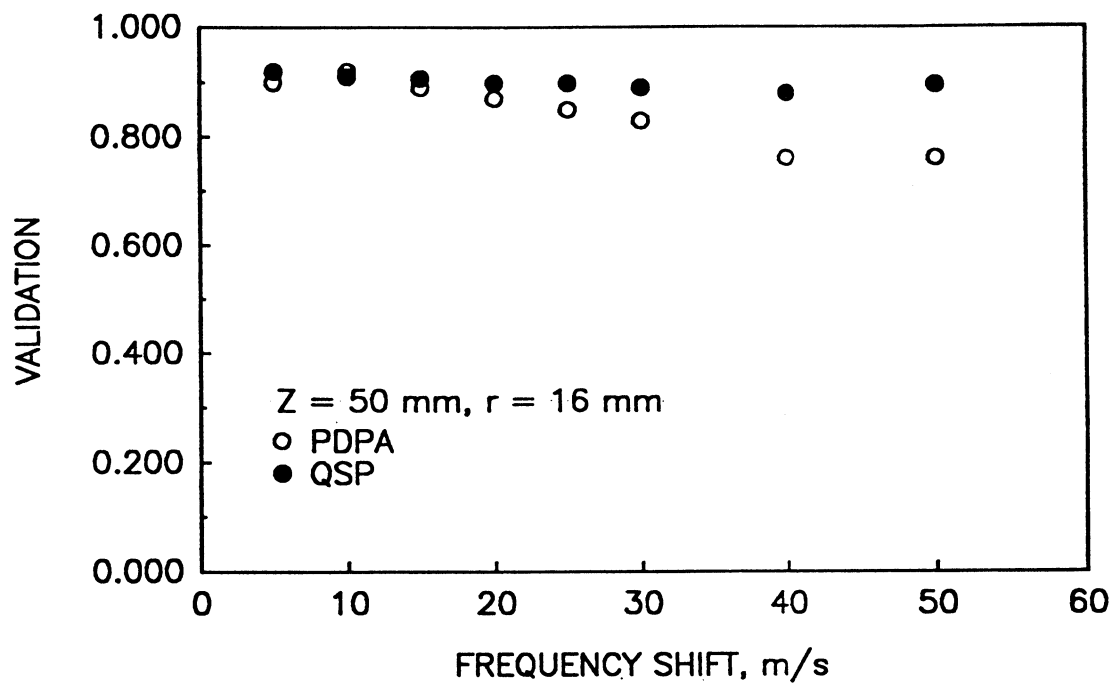
b) Corrected Sizes



TE92-1685

Figure 3.6.3-3. Effect of frequency shift on PDPA and FFT processor measurement of air-assist spray (McDonnell and Samuelsen, 1991) (1 of 2).

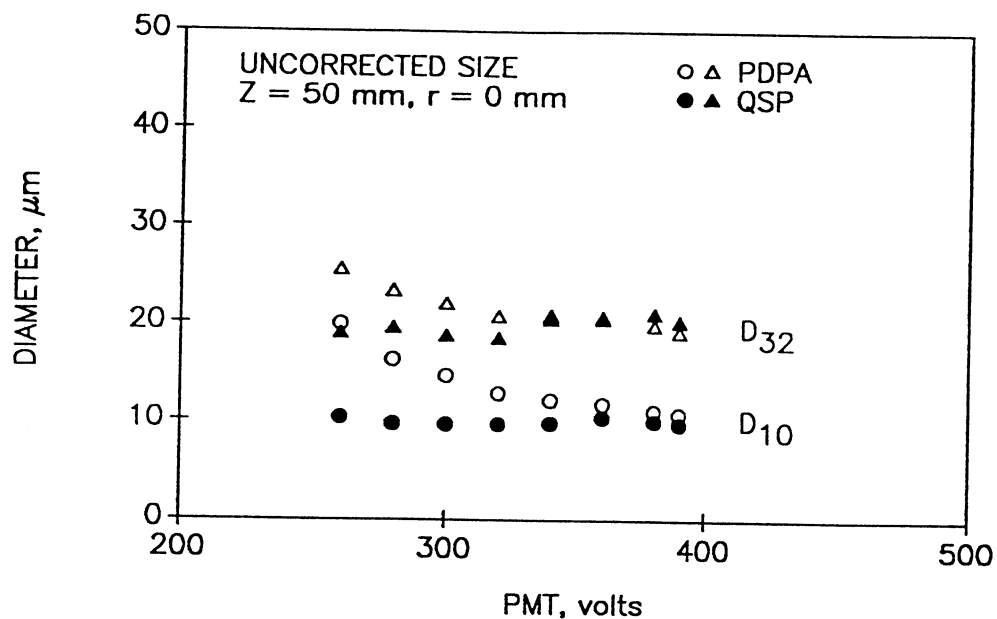
c) Validation



TE92-1686

Figure 3.6.3-3. Effect of frequency shift on PDPA and FFT processor measurement of air-assist spray (McDonell and Samuelsen, 1991) (2 of 2).

a) Mean Comparison



b) PMT = 280 volts

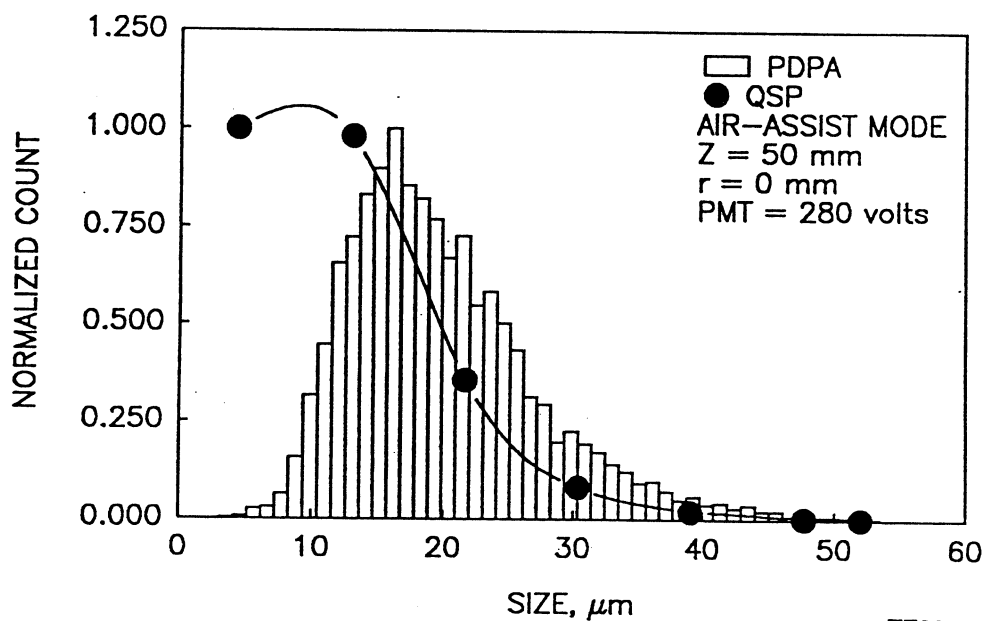
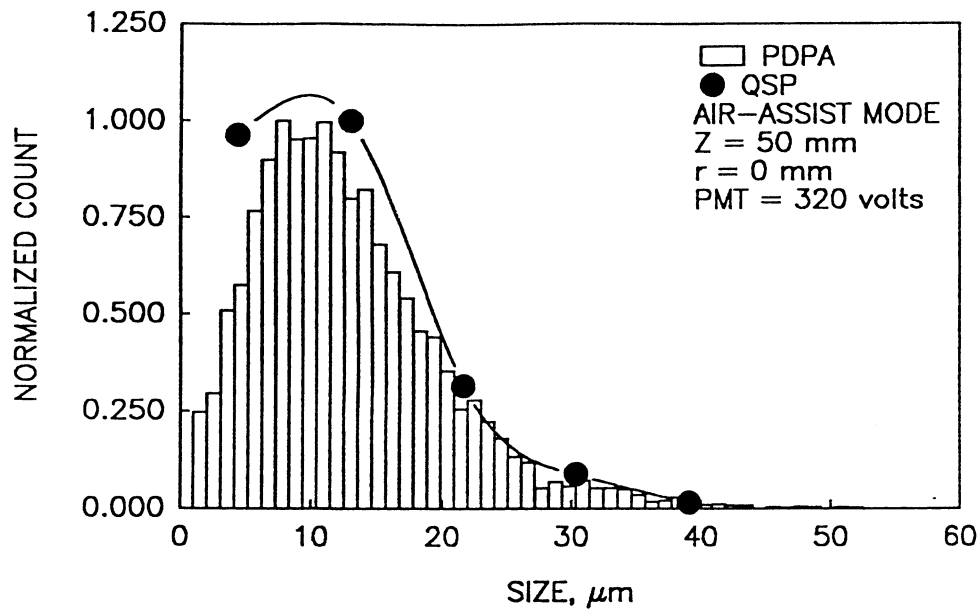
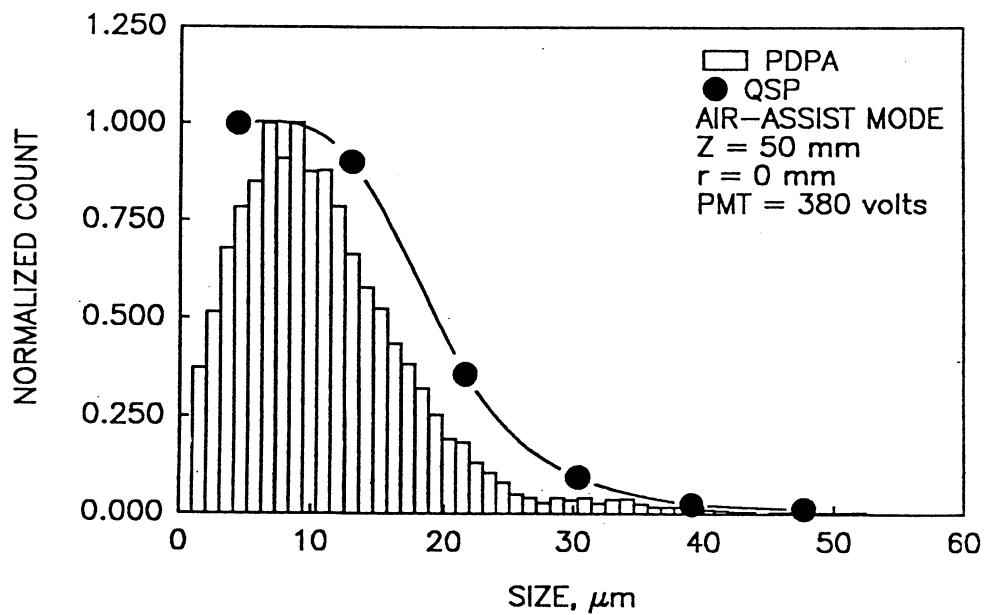


Figure 3.6.3-4. Detailed comparison of effect of PMT voltage on uncorrected size distribution measured by PDPA and FFT processor in air-assist spray (McDonnell and Samuelsen, 1991) (1 of 2).

c) PMT = 320 volts



d) PMT = 380 volts



TE92-1688

Figure 3.6.3-4. Detailed comparison of effect of PMT voltage on uncorrected size distribution measured by PDPA and FFT processor in air-assist spray (McDonell and Samuels, 1991) (2 of 2).

3.7 DISCRIMINATION BETWEEN PHASES

There have been many approaches taken in attempting to discriminate between the continuous and discrete phases. In laser anemometry measurements, owing to the inherent light scatter, amplitude can be utilized to discriminate between phases since the amplitude of the scattered light is roughly proportional to the diameter of the scatterer squared (Van de Hulst, 1981).

3.7.1 Chromatic Discrimination

Originally it was planned to incorporate fluorescences as the discrimination. This was to be done by adding a dye to either the methanol or the seed particles and then using a fifth detector to detect the fluorescences' wavelength. The measurement would be tagged with a bit to indicate the presence of fluorescences and then post-processed to extract the distributions of fluorescing and nonfluorescing particles. Although promising, this technique created significant hardware and software challenges for the manufacturer of the instrument. Further, given the duration of the program, the cost of the dyes, and the challenges with signal amplitude on the dye channel, an alternative approach was sought.

3.7.2 Amplitude Discrimination

Levy and Lockwood (1981) used a threshold discriminator, realizing that the signal from a 200 micron sand particle would be markedly different than that from a seed particle. This approach was also applied by Tsuji et al (1984). The approach only suffers from intensity variations due to the Gaussian intensity profile of the probe volume and extinction effects due to other particles in the path of the beam, which effect intensity-based measurements in general. The Gaussian intensity profile causes cross talk between phases since a large particle in the wing of the Gaussian can scatter as much light as a seed particle in the center of the probe volume as illustrated in Figure 3.6.2-1.

This approach has also been used by Lee and Durst (1982) in a study of a two-phase turbulent pipe flow. They also incorporated a wide array of filters in addition to amplitude to help discriminate between the signal from each phase.

The amplitude technique was extended further by Modarress and Tan (1983), who not only incorporated an amplitude discriminator, but also reduced the Gaussian intensity problem as well by using one probe volume which was smaller than the other. If signals are accepted from the large probe volume only when they occur simultaneously with those from the smaller probe volume, then it is ensured that the scatterer passed through the central or most intense part of the large probe. This clever approach is one of the reasons that this data set has been strongly accepted by the modeling community.

Amplitude and relative concentration of the particles compared to the seed were used by Shuen et al (1985) and Solomon et al (1985). The weakness of this approach is that no attempt is made to eliminate scores from the other phase when one is being measured. The seeding concentration is stated to be two orders of magnitude greater for the seed when measuring gas phase in the presence of particles at a given location. Some particles will be recorded and different locations in the flow may give rise to different concentrations.

3.7.3 Physical Discrimination

The approach incorporated in the present work has also been used by Bulzan (1988), Brena de la Rosa et al (1990), and others. The approach is to use the phase/Doppler instrument to size all scatterers and then use the size measured to discriminate between phases when calculating velocity statistics. Figure 3.7.3-1 (a) shows a typical size distribution obtained while measuring the seed particles in the presence of glass beads in a recirculating flow. Note that the size range recorded for the gas phase is broader than the morphology indicates; this is due to the asphericity of the seed particles and noise due to the presence of beads. The corresponding velocity distribution is shown in Figure 3.7.3-1 (b). The bimodal distribution is

due to the slip velocity between the gas and the beads. This is shown in Figure 3.7.3-1 (c), where the corresponding size-velocity correlation is presented.

To ensure that only seed scores are used, only the first few bins are used for gas phase statistics following the approach delineated in Figure 3.5.2.5. A data reduction program was developed to perform the extraction of the gas phase size ranges and calculate the gas phase velocity statistics. When measuring the gas phase velocity in the presence of the spray, very small drops will also contribute to the gas velocity. However, in the present case, drops smaller than 2 or 3 microns can track the flow quite accurately.

In the present case, dry alumina was used as seed. Other researchers have used mists (e.g., Brena de la Rosa et al, 1990) to avoid the ambiguity of using nonspherical particles. Some researchers have shown, theoretically, that even spheres in the size range of 1 to 8 microns cannot be accurately sized using the phase method (e.g., Hardalupas and Taylor, 1988; Martin et al, 1990). Sankar et al (1990) pointed out that generalization of this statement is strongly dependent upon the optical configuration used, and demonstrated, both experimentally and theoretically, that optimum collection angles, fringe spacings, and focal lengths can be utilized to precisely size fine particles. The theoretical studies indicate that errors in the measurement of particles less than 3 microns are ± 2 microns using the optical setup used in this study. Fortunately, this is probably adequate for most flows since 5 micron particles will track nearly as well as 3 micron particles.

The question regarding the use of phase Doppler accurate sizing of fine particles is insufficiently answered. In the present case, however, phase Doppler is not being used for accurate sizing of the seed particles, only for measurement of the size which falls into bins which are less than 4 microns. As a result, as long as the seed particles are known to be small enough to track the flow and only scores which are less than 4 microns are used, the ensuing statistics should be independent of whether a 2 micron particle is scored as an 8 micron particle. Another problem is that the acceptance rate may decrease.

To further investigate the issue of measuring seed particles, a test was carried out which compared measurements of alumina powder and a mist produced from a 50/50 mixture by volume of glycerin and water. Based on the specification of the nebulizer unit, the average size of the mist should be 2.0 microns and no particles greater than 5 microns should be produced. The powder and mist were dispersed using the seeder shown in Figure 3.5.2-1. Figure 3.7.3-2 presents an example of the measured distributions for each seed type. The mist provides a significantly tighter distribution (Figure 3.7.3-2 [a]) which is attributed to the spherical particles. In that no scores are recorded which are greater than 3.2 microns, the capability of the instrument to accurately size the small particles is demonstrated. However, the acceptance rate is only about 10%, with the majority of the errors arising from phase errors.

Although the size distribution for the alumina (Figure 3.7.3-2 [b]) is wider than that for the mist, it is similar to that stated by the manufacturer (mean size of 2.0 microns, with 99% of the material < 15 microns). In addition, of the cases examined, no appreciable dependency of velocity on measured size was observed, indicating that the material, even if improperly sized, is still tracking the flow. This result suggests that, perhaps, the fine particles are being sized as larger particles, so that they still track the flow. In the case of the alumina, the acceptance rate ranged from 10 to 15%.

The low acceptance rates could be due to ambiguities arising from the measurement of fine particles. Comparison of the velocities measured using either particle reveals the same results for both mean and fluctuating velocities, as shown in Figure 3.7.3-3. In this case, the measurements were conducted in a low velocity region of the flow. In addition, Figure 3.7.3-3 presents results obtained with and without sizing enabled to see the effect of the increased constraints and reduced acceptance rates imposed by sizing. In all cases, the measurements were repeated three times, and the error bars shown reflect the standard deviation about the means of the three results.

The conclusion is that this approach to the discrimination of phases works well in the present case for either type of particle.

An additional check was conducted by examining the exit plane profiles measured in the single- and two-phase free jet. Integration of these profiles in the radial and azimuthal direction gives the mass flow of air. In this case, the presence of the particle had an appreciable effect on the gas phase velocity profiles (see Sections IV and VI). As such, integration of the profiles is a good check on whether the discrimination technique is working. Table 3.7-I summarizes the results obtained.

Table 3.7-I shows that in all cases reasonable mass conservation is obtained, supporting the use of this approach for phase discrimination.

Table 3.7-I.
Verification of discrimination in the free jet.

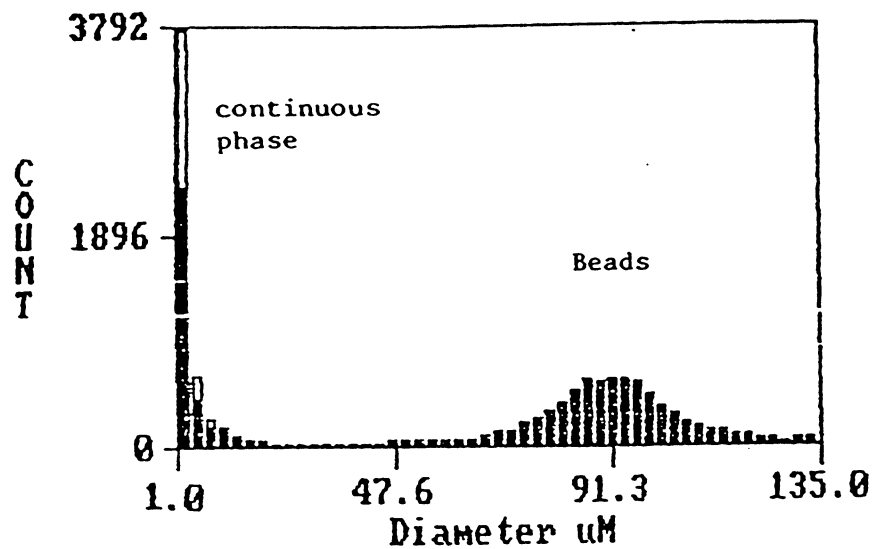
<u>Loading ratio*</u>	<u>Profile integrated**</u>	<u>Mass flow[†] (g/s)</u>
Free Jet	Azimuthal	2.17
	Radial	2.02
1.0	Radial	2.12
0.2	Azimuthal	2.06
0.2	Radial	2.19

* mass of beads to air injected

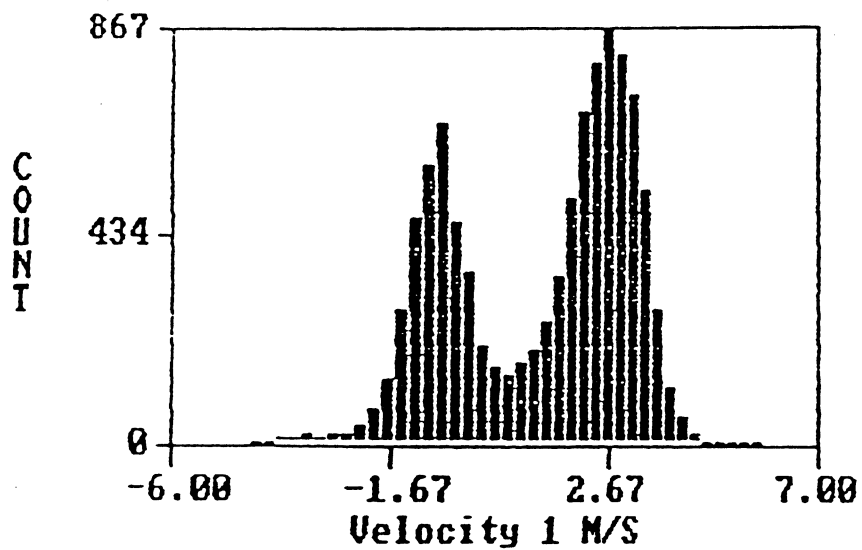
** refers to the velocity associated with second component

† injected flow 2.10 g/s

a) Size Distribution



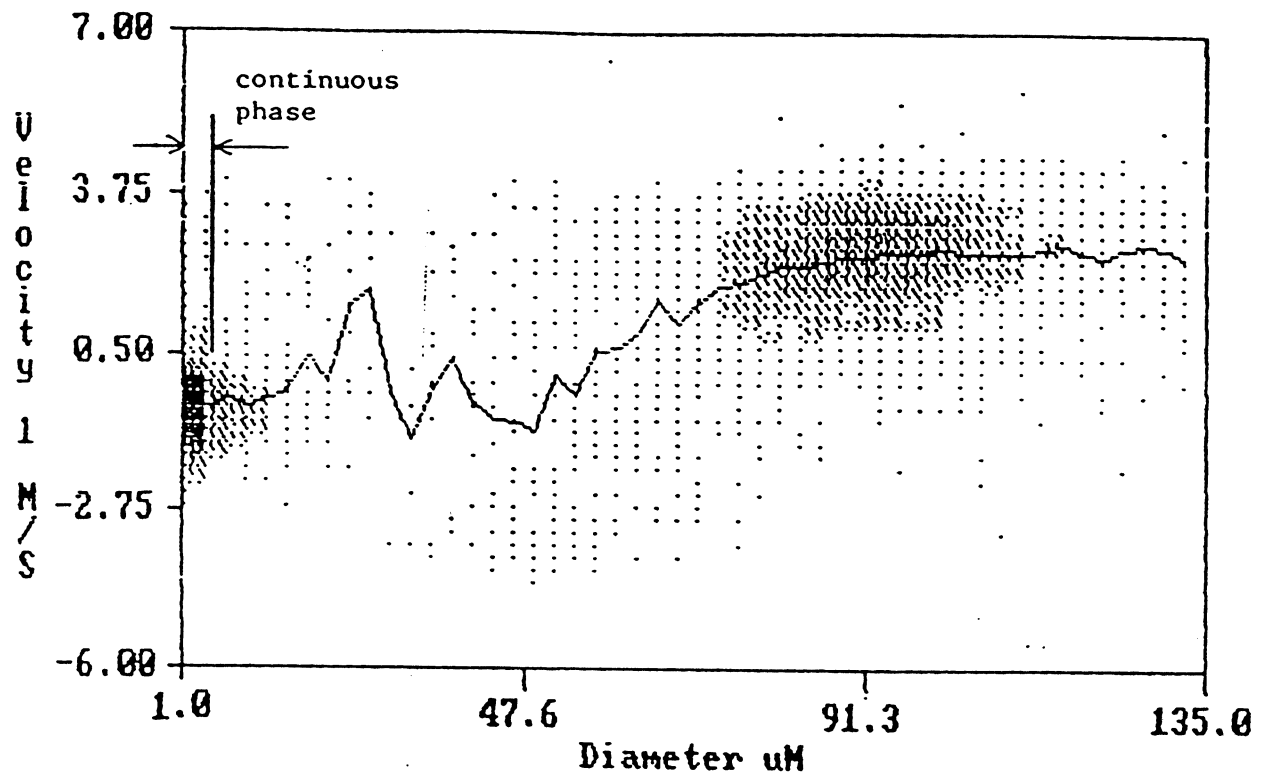
b) Velocity Distribution



TE92-1689

Figure 3.7.3-1. Measurement of seed particles and glass beads in recirculating flow (1 of 2).

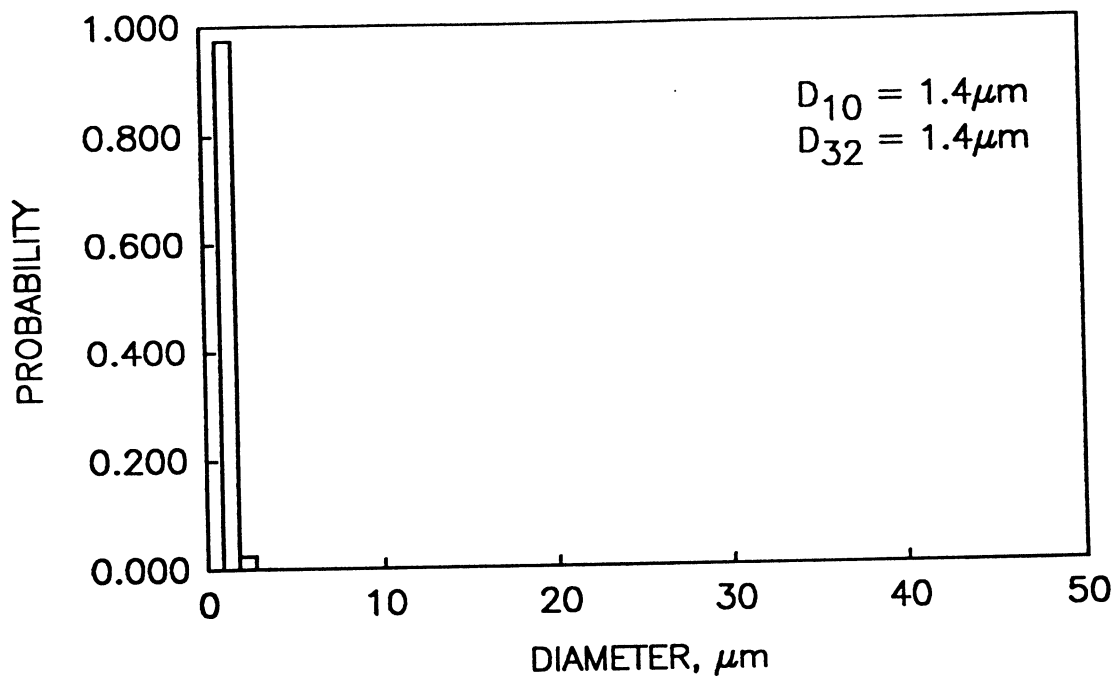
c) Size/Velocity Correlation



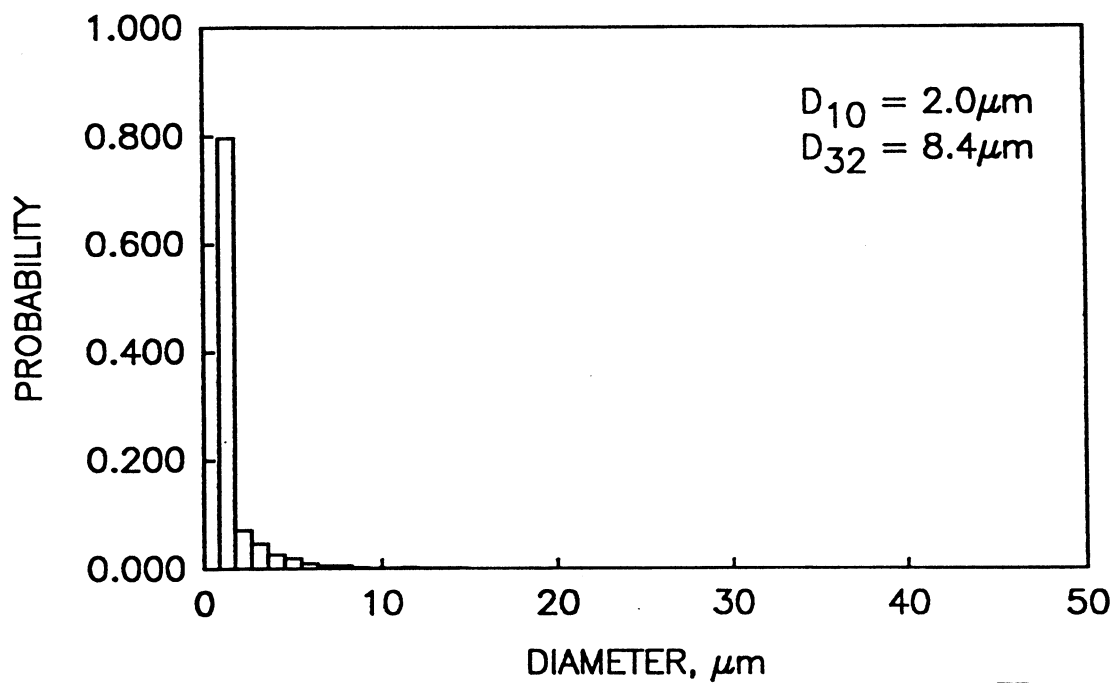
TE92-1690

Figure 3.7.3-1. Measurement of seed particles and glass beads in recirculating flow (2 of 2).

a) Nebulized Glycerin/Water Mixture



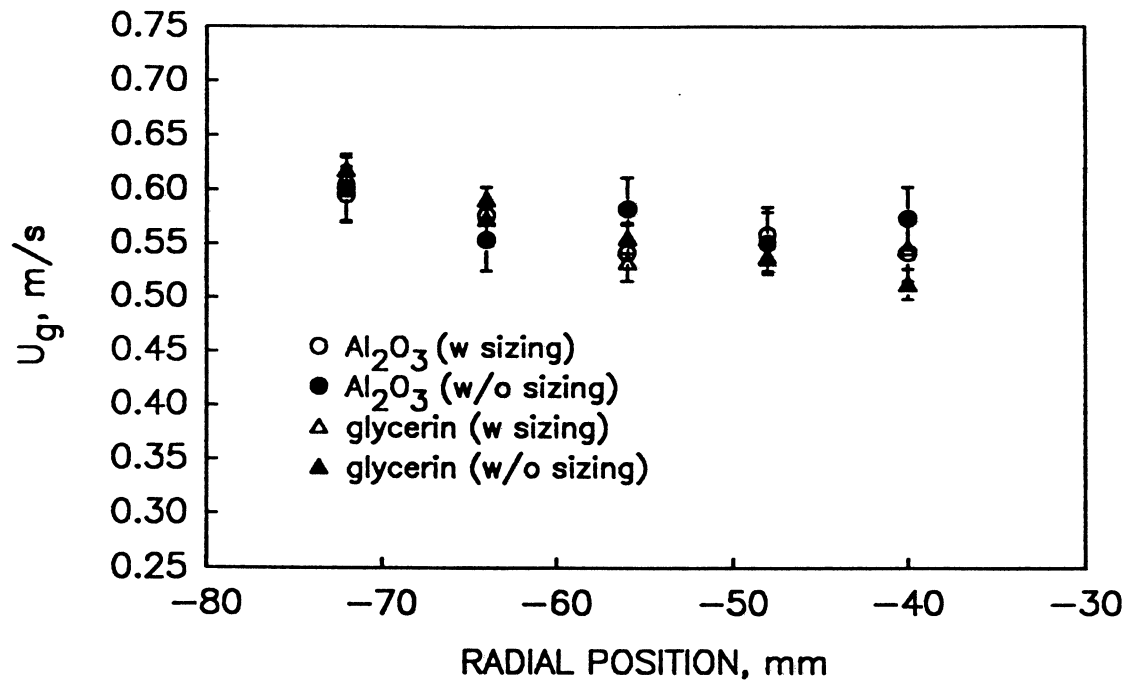
b) Al_2O_3 Dispersed With a Fluidized Bed



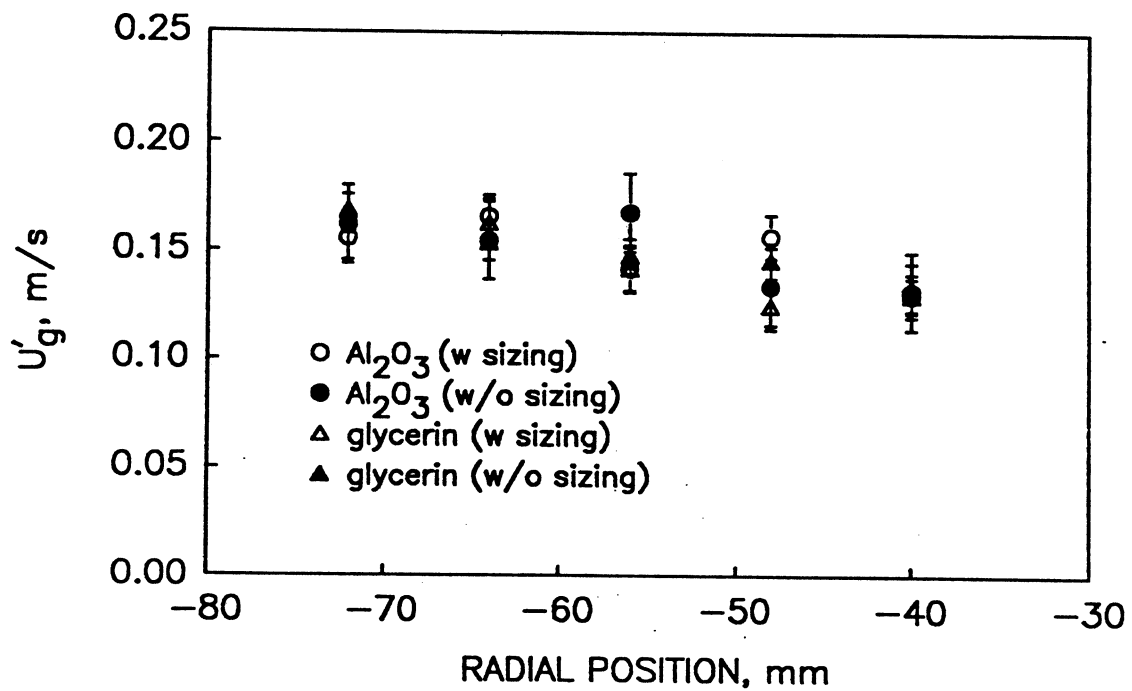
TE92-1691

Figure 3.7.3-2. Size histograms for two types of seed particles.

a) Mean Axial Velocity



b) Fluctuating Axial Velocity



TE92-1692

Figure 3.7.3-3. Sensitivity of velocity measurements to seed type and sizing enabled/disabled.

3.8 VAPOR CONCENTRATION MEASUREMENTS

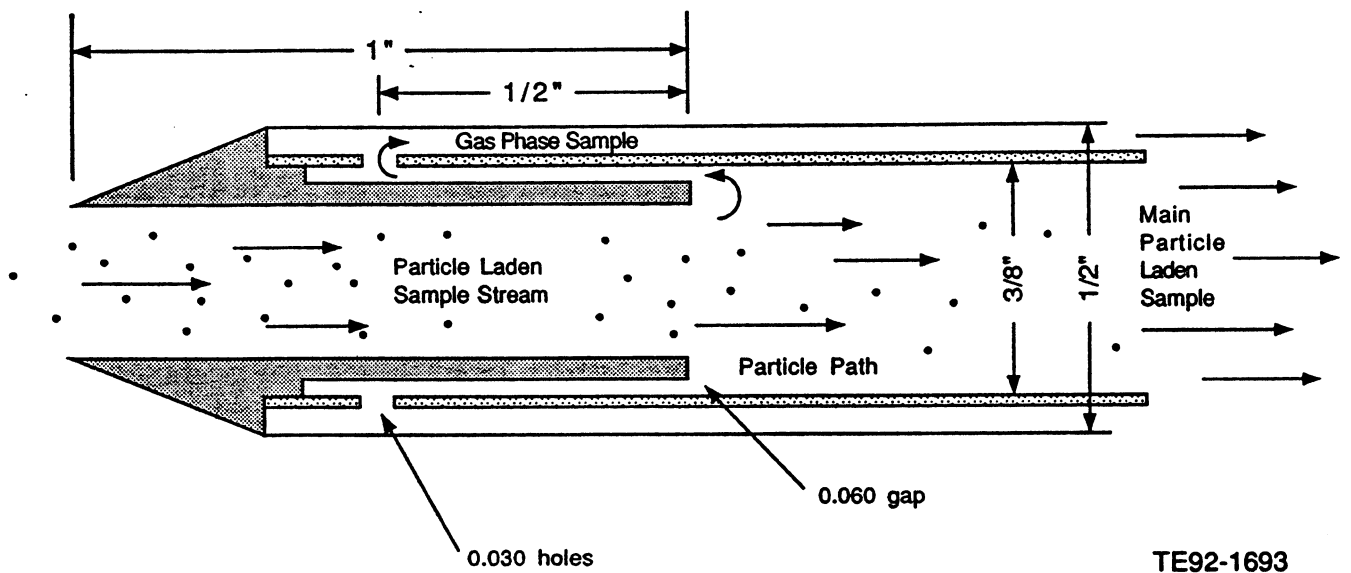
For the cases where the methanol spray is being studied, measurements of the vapor evaporated are required. These measurements can also be used to compare to phase/Doppler measurements.

Originally, these measurements were to be obtained using a phase discrimination probe. A schematic of the probe is shown in Figure 3.8-1. The figure shows how the discrimination takes place. Droplets, even the smallest, cannot make the extreme turns that the gas phase is required to make. In addition, a very low velocity at the inlet of the gas phase ports is maintained to further eliminate flow tracking by the smallest drops. A hydrocarbon analyzer (Beckman 402 hot FID) is used to determine the amount of methanol vapor present in the gas phase.

By fixing the probe to the NRC table, the test article can be traversed about and point measurements of the methanol concentration in the gas phase can be made. The probe is intrusive, but its effects are minimized by sampling isokinetically, using the velocities measured by the phase/Doppler to match the sampling velocities. The measurement has a spatial resolution of 1.5 mm.

Initial measurements with the probe proved difficult because of the continually varying probe temperature. Because the methanol is continuously accumulating on the tip, drops run down the inside of the probe and provide local sources of vapor to the gas sample. The probe temperature varies as a function of position in the spray, and as a result, the local vapor source from the drops accumulated on the probe varies. Because of this, measurements obtained were quite unreliable and unreasonable amounts of time were required for equilibrium to be reached at each point. Initial results suggested that, at the centerline of the spray without swirl, the concentration was between 2 and 5% by volume. This corresponds reasonably well with the saturation condition implied by the -10°C temperature of the methanol. Chilling the probe tip would have helped this problem, but was considered beyond the scope of the program.

Optical techniques (e.g., Chraplyvy, 1981; Tishkoff et al, 1982) have been used to observe the vapor field on a whole and were pursued late into the program. The results obtained were promising and development of an instrument was undertaken (Adachi et al, 1991) but not completed in time to use in support of the current program. As such, no quantitative vapor concentration results were obtained in support of this program.



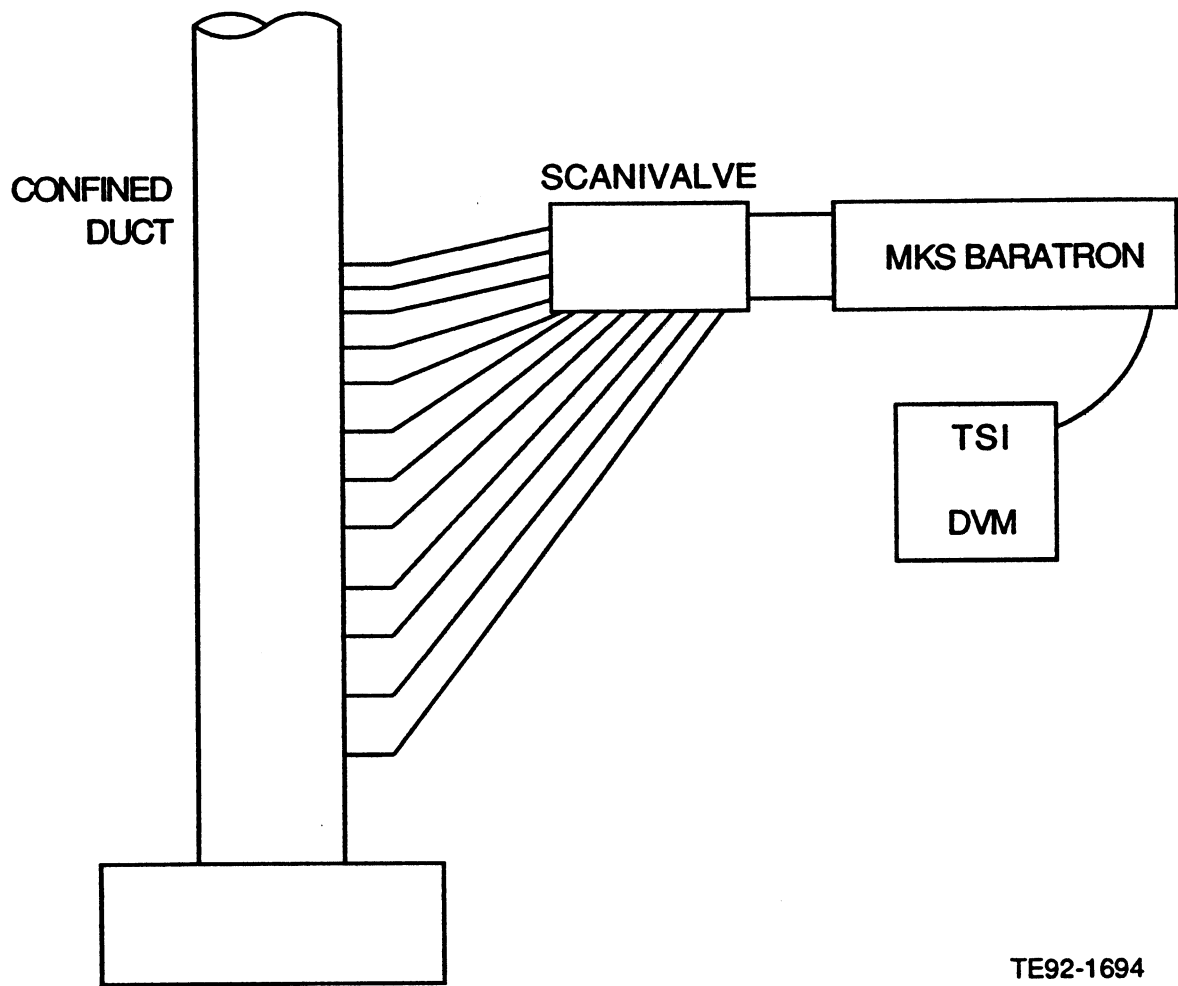
TE92-1693

Figure 3.8-1. Phase discrimination probe.

3.9 PRESSURE MEASUREMENTS IN CONFINED DUCT

In the case of the confined measurements, the accurate measurements of axial pressure gradients are required. The measurement of this gradient is critical to successful modeling as pointed out by Zhang et al (1985). In their predictions of the data of Modarress et al (1984), a slight negative axial pressure gradient ($dP/dz = -5 \text{ Pa/m}$) was required to match the data. This is thought by Zhang et al to be due to the presence of the 600 mm duct surrounding the jet studied. Unfortunately, Modarress et al did not report measurements of the axial pressure gradient.

For the above reasons, it is critical that these measurements be made to quantify the gradient, if any. To make the measurements required, taps are placed in the confined duct at 18 axial locations. Used in the duct is 1 mm (0.0625 in.) stainless steel tubing, and tygon tubing is used to interface the taps to a Scanivalve static pressure manifold (Model W0602/1P-24T). The ports to be measured are then connected to an MKS Baratron membrane pressure transducer which is sensitive to 0.0001 torr. Measurements are made either relative to the inlet plane port or to atmospheric pressure. The pressure is read directly from a TSI integrating DVM using a time constant of 10 and 100 seconds. Readings are made after a two minute time period. A schematic of the setup is shown in Figure 3.9-1. Measurements in the confined duct under the final test conditions did show the presence of a very slight negative pressure gradient which maintained nearly linear behavior typical of pipe flow. The result indicated that no special pressure measurements were necessary for the confined flow.



TE92-1694

Figure 3.9-1. Pressure measurement setup.

3.10 TEMPERATURE MEASUREMENTS

Temperature measurements are required in all air circuits and in the methanol circuit to ensure that density variations do not occur and, as a result, throw off the calibrations of each. All measurements are made using shielded type J thermocouples (Iron-Constantan) directly in the flow circuit of interest. A 12-channel single-digital readout is used to monitor the temperatures. The only crucial circuit is that for methanol owing to the nonroom temperature (-10°C) usage. A thermocouple is maintained 50 mm (2 in.) from the entrance to the airblast atomizer so that the exit temperature is measured.

3.11 FLOW VISUALIZATION

Flow visualization is utilized for all the flow fields studied. It is used to provide insight into the dynamics of the flow fields as well as to provide a quantitative estimate of the length scales involved.

3.11.1 Photography

Still photography is used in combination with laser sheet lighting to isolate sections of the flow field in order to generate streaklines and study global features such as symmetry. In addition, this technique can provide quantitative evidence of perturbation to the flow due to patternation or probes. Tri-X (ASA 400) is used and developed in-house to provide quick turnaround on the results. The film is developed using Microdol-X which further accentuates the green wavelengths selectively recorded by the Tri-X emulsion. A Spectra Physics 5-Watt Argon-Ion laser is used to generate the sheet of light. The beam is collimated at 3 mm and sent through a cylindrical lens which generates the sheet of light. The sheet can be used either horizontally or vertically, depending upon the type of information needed.

3.11.2 High Speed Cinematography

To study dynamics and to evaluate scales in the flow fields, high speed cinematography is used. A Hy-cam II is used with Kodak 7277 (ASA 400, 100 ft) 16 mm black and white reversal film, which is again most sensitive in the green wavelengths. For cinematography, either sheetlighting or white light backlighting is used. Sheetlighting does not provide light energy as intense as the backlighting and as such the frame rate is limited to 80 frames/sec. The sheetlighting setup is the same as above. For backlighting, two 250-watt photofloods are placed behind the flow at 30 deg to either side of the axis of the normal to the film plane. With this setup, the framing rate can be increased to 200 frames/sec. These rates give the necessary stopping to determine scales in the flow fields.

3.11.3 Shadowgraph Photography

This technique is used to document regions of the flow field where the phase/Doppler is limited by non-spherical particles. In addition, the technique can be used to verify the phase/Doppler measurements. In a high magnification mode, the shadowgraph setup shown in Figure 3.11.3-1 can provide size distributions to which the phase/Doppler measurements can be compared. The system utilizes an EG&G spark gap flash unit which provides a 1 μ s flash which is suitable to freeze the particles being studied. The magnification factor can be adjusted to provide the necessary field of view and to resolve small particles.

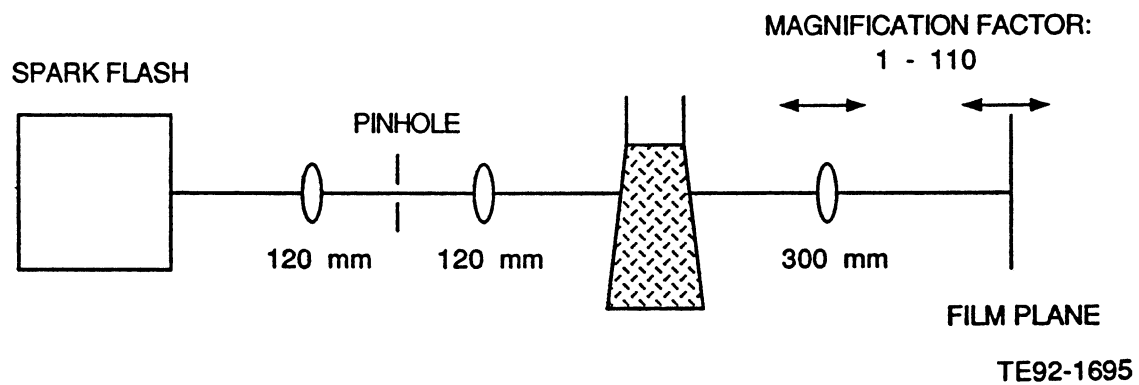


Figure 3.11.3-1. Shadowgraph setup.

3.12 DATA FORMAT

In each case, the data are available in a tabulated fashion (McDonell, 1987a and 1987b). The name of each file is based on the number of the configurations listed in Table 3.4-V. In each case, each radial profile is stored as a separate file. Since two orthogonal profiles are required, and up to 8 axial stations are measured, up to 16 files make up a data set.

The data file names are based on DOS-based operating systems. The first four characters are CONF, the next two reflect the configuration number as shown in Table 3.4-V, the following two characters reflect the repetition of the data set, and the extension of the file reflects the axial location and which profile is included. If more than nine repetitions are made, letters are used (for example, the tenth repetition of CONF07 is #A). The extension follows the format of .ABC, where a refers to the axial station. A value of A = 0 refers to the inlet station. Unless noted in the documentation file (discussed below), A = 1 refers to 15 mm, A = 2 refers to 25 mm, A = 3 refers to 35 mm, A = 4 refers to 50 mm, A = 5 refers to 75 mm, A = 6 refers to 150 mm, and A = 7 refers to 300 mm. The B value is either t or r, where t indicates that the tangential and axial velocity components were measured and r indicates that the radial and axial velocity components were measured. C refers to the repetition of the profile within a given repetition of the data set. The first repetition is a, the second b, and so forth. Finally, a file with extension .doc refers to a documentation file which contains details regarding the flow rates and other special points of interest regarding the data set.

As an example, consider a file with the name CONF01#2.3ta. Referring to Table 3.4-V, the first 6 characters indicate that this file is from the free jet without coflow in an unconfined environment. "#2" indicates that this is second time the data set was collected. ".3ta" indicates that the radial profile contained within the file was taken at the 35 mm axial station, and that the axial and tangential velocity components were measured.

REFERENCES

- Adachi, M., McDonell, V. G., and Samuelsen, G. S., 1991, "Non-Intrusive Measurement of Gas Species in Reacting and Non-Reacting Sprays," *Combustion Science and Technology* 75, 179.
- Alexander, D. R., Wiles, R. J., Schaub, S. A., and Seeman, M. P., 1985, "Effects of Non-Spherical Drops on a Phase Doppler Spray Analyzer, SPIE Volume 573.
- Bachalo, W. D., 1980, "Method for Measuring the Size and Velocity of Spheres by Dual-Beam Light Scatter Interferometry," *Applied Optics* 19, 363.
- Bachalo, W. D., Rudoff, R. C., and Houser, M. J., 1987, "Laser Velocimetry in Turbulent Flowfields: Particle Response," AIAA Paper 87-0118.
- Beer, J. M. and Chigier, N. A., 1976, *Combustion Aerodynamics*.
- Brena de la Rosa, A., Bachalo, W. D., and Rudoff, R. C., 1990, "Spray Characterization and Turbulence Properties in an Isothermal Spray with Swirl," *American Society of Mechanical Engineers Journal of Engineering for Gas Turbines and Power* 112, 60.
- Bulzan, D. L., 1988, "Particle-Laden Swirling Free Jets: Measurements and Predictions," NASA TM-10881.
- Chang, J., 1985, *Interoffice Memo*, Excello Corporation, File #85JC3814. July 19.
- Chraplyvy, A. R., 1981, "Nonintrusive Measurements of Vapor Concentrations Inside Sprays," *Applied Optics* 20, 2620.
- Craig, R. R., Nejad, A. S., and Hahn, E. Y., 1986, "A General Approach for Obtaining Unbiased LDV Data in Highly Turbulent Non-Reacting and Reacting Flows," AIAA Paper No. 86-0366.
- Dodge, L. G., Rhodes, D. J., and Reitz, R. D., 1987, "Comparison of Drop-Size Measurement Techniques in Fuel Sprays: Malvern Laser Diffraction and Aerometrics Phase Doppler," *Applied Optics* 26, 2144.
- Durst, F. K., Melling, and Whitelaw, J. H., 1976, "Principles and Practices in Laser Doppler Anemometry."
- Edwards, C. F. and Marx, K. D., 1991, "Application of Poisson Statistics to the Problem of Size and Volume Flux Measurement by Phase Doppler Anemometry," Fifth meeting of ICLASS.
- Gould, R. D., Stevenson, W. D., and Thompson, H. D., 1986, "A Parametric Study of Statistical Velocity Bias, *Proceedings*, Laser Institute of America 58, ICALEO.
- Hardalupas, Y. and Taylor, A. M. K. P., 1988, "The Identification of LDA Seeding Particles by the Phase Doppler Technique," *Experiments in Fluids* 6, 137.
- Hess, C. F., 1984, "A Technique Combining the Visibility of a Doppler Signal with Peak Intensity of the Pedestal to Measure the Size and Velocity of Droplets in a Spray," AIAA Paper No. 84-0203.
- Hoesel, W. and Rodi, W., 1977, "New Biasing Elimination Method for Laser Doppler Velocimeter Counter Processing," *Review of Scientific Instruments* 48, 910.
- Ikioka, L. M., Brum, R. D., and Samuelsen, G. S., 1983, "A Laser Anemometer Seeding Technique for Combustion Flows with Multiple Stream Injection," *Combustion and Flame* 49, 155.
- INVENT, 1991, "Phase Doppler Expansion Unit Description," INVENT, GmbH, Erlangen.
- Jackson, T. A., 1985, *Ph.D. Dissertation*, University of California, Irvine.
- Jackson, T. A., 1990, "Droplet Sizing Interferometry," in Hirleman, E. D., Bachalo, W. D., and Felton, P. G. (Eds.), *Liquid Particle Size Measurement Techniques: 2nd Volume, ASTM STP 1083*, American Society for Testing and Materials, Philadelphia, PA, pp. 151-169.
- Jackson, T. A. and Samuelsen, G. S., 1987, "Droplet Sizing Interferometry: A Comparison of the Visibility and Phase/Doppler Techniques," *Applied Optics* 26, 2137.
- Laufer, J., 1954, "The Structure of Turbulence in Fully Developed Pipe Flow," NASA TN 2954.
- Lee and Durst, 1982, "On the Motion of Particles in Turbulent Duct Flows," *International Journal of Multiphase Flows* 8, 193.
- Levy, Y. and Lockwood, F. C., 1981, "Velocity Measurements in a Particle-Laden Turbulent Free Jet," *Combustion and Flame* 40, 333.
- Martin, S. R., Drain, L. E., Livesley, D. M., and Yeoman, M. L., 1990, "Resolution Limits of the Phase Doppler Technique and its Extension to Monitor Non-Ideal Fine Particles in Two-Phase Flows," *Applications of Laser Anemometry to Fluid Mechanics*, Springer-Verlag
- McDonell, V. G., 1987a, "Detailed Data Set: Two-Component Gas and Particle Velocity Statistics in a Particle-Laden Axisymmetric Jet," UCI Combustion Laboratory, University of California, Irvine, ARTR-87-15.

- McDonell, V. G., 1987b, "Detailed Data Set: Two-Component Gas and Particle Velocity Statistics in Axisymmetric Methanol Sprays," UCI Combustion Laboratory, University of California, Irvine, ARTR-87-16.
- McDonell, V. G., Wood, C. P., and Samuelsen, G. S., 1986, "A Comparison of Spatially-Resolved Drop Size and Drop Velocity Measurements in an Isothermal Chamber and a Swirl-Stabilized Combustor," *Twenty-First Symposium (International) on Combustion*. The Combustion Institute, Pittsburgh, PA, pp. 685-694.
- McDonell, V. G., Cameron, C. D., and Samuelsen, G. S., 1990, "Symmetry Assessment of an Air-Blast Atomizer Spray," *AIAA Journal of Propulsion and Power* 6, 375.
- McDonell, V. G. and Samuelsen, G. S., 1990a, "Sensitivity Assessment of a Phase Doppler Interferometer to User Controlled Settings," in Hirleman, E.D., Bachalo, W.D., and Felton, P.G. (Eds.), *Liquid Particle Size Measurement Techniques: 2nd Volume*, ASTM STP 1083, American Society for Testing and Materials, Philadelphia, PA, pp. 170-189.
- McDonell, V. G. and Samuelsen, G. S., 1990b, "Influence on the Continuous and Dispersed Phases on the Symmetry of a Gas Turbine Air-Blast Atomizer," *ASME Journal of Engineering for Gas Turbines and Power* 112, 44.
- McDonell, V. G. and Sowa, W. A., 1990, "Evaluation of Sample Volume Characteristics in Interferometric Drop Measurements," *Fifth Symposium on Applications of Laser Techniques to Fluid Mechanics*, Lisbon, Portugal.
- McDonell, V. G. and Samuelsen, G. S., 1991, "Data Quality Control Evaluation of the Aerometrics Two-Component Phase Doppler Interferometer," *Technical Report UCI-ARTR-91-1*.
- McLaughlin, D. K. and Tiederman, W. G., 1973, "Biasing Correction for Individual Realization of Laser Anemometer Measurements in Turbulent Flows," *Physics of Fluids* 1, 129.
- Modarress, D. and Tan, H., 1983, "LDA Signal Discrimination in Two-Phase Flows," *Experiments in Fluids* 1, 129.
- Modarress, D., Tan, H., and Elghobashi, S. E., 1984, "Two-Component LDA Measurements in a Two-Phase Turbulent Jet," *AIAA Journal* 22, 624.
- Mostafa, A. A. and Mongia, H. C., 1987, "On the Modeling of Turbulent Evaporating Sprays: Eulerian Versus Lagrangian Approach," *International Journal of Heat and Mass Transfer*.
- Nejad, A. S., 1986, "Sampling Bias in Two-Component LDV Measurements," *Proceedings*, Laser Institute of America, Vol. 58., ICALEO.
- Sankar, S. V., Weber, B. J., Kamemoto, D. Y., and Bachalo, W. D., 1990, "Sizing Fine Particles with the Phase Doppler Interferometric Technique," *Proceedings of the Second International Congress on Optical Particle Sizing*, pp. 277-287.
- Shearer, A.J., Tanmura, H., and Faeth, G.M., 1979, "Evaluation of a Locally Homogeneous Flow Model of Spray Evaporation," *Journal of Energy* 3, 271.
- Shuen, J. S., Solomon, A. S. P., Zhang, Q. F., and Faeth, G. M., 1985, "Structure of Particle-Laden Jets: Measurements and Predictions," *AIAA J*, Vol. 23, No. 3, pp 369-404.
- Simpson, R. L. and Chew, Y. T., 1979, "Measurements in Steady and Unsteady Separated Turbulent Boundary Layers," *Laser Velocimetry and Particle Sizing*, Hemisphere Publishing.
- Solomon, A.S.P., Shuen, J. S., Zhang, Q. F., and Faeth, G. M., 1985, "Structure of Non-Evaporating Sprays, Part I: Initial Conditions and Mean Properties," *AIAA Journal* 23, 1548.
- Tan, J., 1990, "Phase/Doppler Signal Processor QPDA40 User Guide," Quality Signal Processors, Irvine, CA.
- Tishkoff, J. M., Hammond, Jr., D. C., Chraplyvy, A. R., 1982, "Diagnostic Measurements of Fuel Spray Dispersion," *J Fluids Engr*, Vol 104, pp 313-317.
- Tsuji, Y., Morikawa, Y., and Shiomi, H., 1984, "LDV Measurements of an Air-Solid Two-Phase Flow in a Vertical Pipe," *Journal of Fluid Mechanics* 139, 417.
- Van de Hulst, H.C., 1981, *Light Scattering by Small Particles*, Dover Publications, Newark.
- Young, B. W. and Bachalo, W. D., 1987, "The Direct Comparison of Three 'In-Flight' Droplet Sizing Techniques for Pesticide Spray Research," *Proceedings*, International Symposium on Optical Particle Sizing: Theory and Practice, Rouen, France.
- Yule, A. J., Ah Seng, C., Felton, P. G., Ungut, A., and Chigier, N. A., 1982, "A Study of Vaporizing Fuel Sprays by Laser Techniques," *Combustion and Flame*, 44, pp 71-84.

Zhang, Q. F., Shuen, J. S., Solomon, A. S. P., and Faeth, G. M., 1985 "Structure of Ducted Particle Laden Turbulent Flows," *AIAA Journal* 23, 1123.

TABLE OF CONTENTS

<u>Section</u>	<u>Title</u>	<u>Page</u>
IV	Data Presentation and Discussion	145
4.1	Data Case Descriptions	145
4.1.1	Summary of Data Base	145
4.1.2	Case Description and Geometries	146
4.1.3	Data Collection and Reporting Protocol.....	146
4.1.4	Nomenclature	147
4.2	Single Round Jet	149
4.2.1	Unconfined Single-Phase Jet – CONF01#2	149
4.2.2	Unconfined Jet in the Presence of 100-110 Micron Beads at Loading Ratio 0.2 and 1.0 – CONF07#6,#A	150
4.2.3	Glass Beads in the Unconfined Jet at Loading Ratios of 0.2 and 1.0 – CONF07#5,#3	151
4.2.4	Effect of Particle Mass Loading in the Unconfined Jet	152
4.2.5	Unconfined Jet in the Presence of 25 and 105 Micron Beads – CONF13#2	153
4.2.6	Mixture of 25 and 105 Micron Glass Beads in the Unconfined Jet – CONF13#4	153
4.2.7	Confined Single Round Jet – CONF04#3	154
4.2.8	Confined Jet in the Presence of 100-110 Micron Beads at Loading Ratios of 0.2 and 1.0 – CONF10#3,#5	154
4.2.9	Glass Beads in the Confined Jet at Loading Ratios of 0.2 and 1.0 – CONF10#4,#6	155
4.2.10	Effect of Particle Mass Loading Ratio in the Confined Jet	155
4.2.11	Effect of Confinement on Jet	155
4.2.12	Effect of Confinement on Glass Beads.....	155
4.3	Single Annular Jet – conf31#2	232
4.4	Single Swirling Annular Jet	239
4.4.1	Unconfined Case – CONF32#1	239
4.4.2	Confined Case – CONF34#1	239
4.4.3	Effect of Swirl	239
4.4.4	Effect of Confinement	239
4.5	Coaxial Jets	254
4.5.1	Unconfined Coaxial Jets – CONF02#3.....	254
4.5.2	Effect of Coflow on Single Jet.....	254
4.5.3	Unconfined Jets in the Presence of 100-110 Micron Beads at Loading Ratio 0.2 – CONF08#1	254
4.5.4	Glass Beads in the Unconfined Jets at Loading Ratios of 0.2 – CONF08#2	254
4.5.5	Effect of Coflow on Glass Beads	255
4.5.6	Confined Single-Phase Coaxial Jets – CONF05#2.....	255
4.5.7	Confined Jets in the Presence of 100-110 Micron Beads at Loading Ratios of 0.2 and 1.0 – CONF11#1,#3.....	255
4.5.8	Glass Beads in the Confined Jets at Loading Ratios of 0.2 and 1.0 – CONF11#2,#4	255

TABLE OF CONTENTS (cont)

<u>Section</u>	<u>Title</u>	<u>Page</u>
	4.5.9 Effect of Particle Mass Loading Ratio in the Confined Jet	256
	4.5.10 Effect of Confinement on Coaxial Jets	256
	4.5.11 Effect of Coflow on Confined Jet	256
	4.5.12 Effect of Confinement on Glass Beads in Coaxial Jets	256
4.6	Coaxial Jets With Swirling Annular Flow	310
	4.6.1 Unconfined Single-Phase Jets – CONF03#3	310
	4.6.2 Effect of Swirl on Coflowing Jets	310
	4.6.3 Unconfined Swirling Jets in the Presence of 100-110 Micron Beads – CONF09#4	310
	4.6.4 100-110 Micron Glass Beads in the Unconfined Swirling Jets – CONF09#3	310
	4.6.5 Effect of Swirl on 100-110 Micron Glass Beads in Unconfined Flow	310
	4.6.6 100-110 Micron Glass Beads in the Confined Swirling Jet – CONF12#4	310
	4.6.7 Effect of Swirl on Glass Beads in the Confined Flow	311
4.7	Airblast Injector	339
	4.7.1 Confined Single-Phase – CONF22#1	339
	4.7.2 Gas in the Presence of Confined Methanol Spray – CONF28#2	339
	4.7.3 Effect of Spray on Gas Phase Behavior in Confined Spray	339
	4.7.4 Confined Methanol Spray – CONF28#1	339
4.8	Airblast Injector With Annular Jet	356
	4.8.1 Gas in the Presence of Unconfined Methanol Spray – CONF26#2	356
	4.8.2 Unconfined Methanol Spray – CONF26#1	356
	4.8.3 Confined Single-Phase – CONF23#1	356
	4.8.4 Effect of Coflow on Gas Phase	356
	4.8.5 Confined Methanol Spray – CONF29#1	356
	4.8.6 Effect of Coflow on Spray	357
	4.8.7 Effect of Confinement on Spray	357

IV. DATA PRESENTATION AND DISCUSSION

This section presents the data acquired which are considered useful for model challenges. Some of the cases were not completed with the quality desired, and as a result, are not included as part of the "benchmark" data sets. The next section describes all of the data cases and delineates which of those are included in the discussion and which are not included and for what reasons. In the presentation of the data, only a representative sample of the data is presented. This includes the "inlet station" and two downstream axial locations. The rest of the data are available in tabulated form in both hardcopy and on magnetic media. In addition, plots of all the data obtained are included in the model comparison results presented in the Section VI.

4.1 DATA CASE DESCRIPTIONS

4.1.1 Summary of Data Base

Table 4.1-I summarizes the flow configurations presented in this section. Table 4.1-II summarizes the diagnostics utilized for each configuration. Each data set can be obtained (McDonell, 1987a and 1987b*) in a standardized format (Faeth and Samuelsen, 1986) which makes it readily accessible to modelers. In the present case, the statistics are not normalized because this can lead to confusion in the comparison of different conditions. Instead, complete documentation is provided so that the modeler can use the normalization desired for any condition.

Table 4.1-I.
Case numbers used in the tabulated results.

<u>Number</u>	<u>Description</u>
1	Unconfined single-phase round jet
2	Unconfined single-phase round jet with annular coflow
3	Unconfined single-phase round jet with swirling annular coflow
4	Confined single-phase round jet
5	Confined single-phase round jet with annular coflow
7	Unconfined two-phase round jet: monodispersed
8	Unconfined two-phase round jet with annular coflow: monodispersed
9	Unconfined two-phase round jet with swirling annular coflow: monodispersed
10	Confined two-phase round jet: monodispersed
11	Confined two-phase round jet with annular coflow: monodispersed
12	Confined two-phase round jet with swirling annular coflow: monodispersed
13	Unconfined two-phase round jet: two sizes
22	Confined single-phase atomizer
23	Confined single-phase atomizer with annular coflow
26	Unconfined spray with annular coflow
28	Confined spray
29	Confined spray with annular coflow
31	Unconfined single-phase annular jet
32	Unconfined single-phase swirling annular jet
34	Confined single-phase swirling annular jet

* References for Section IV are listed at the end of the section.

Table 4.1-II.
Quantities measured and diagnostics employed.

<u>Configuration</u>	<u>Quantities measured^{*,**}</u>	<u>Diagnostic</u>
1-5, 22, 23, 31, 32, 34	$U^{\dagger}, V, W, u'^{\dagger\dagger}, v', w', u'v', u'w'$	Laser Anemometry
7-13, 26-29	$U, V, W, u', v', w', u'v', u'w'$ $U_i^{\ddagger}, V_i, W_i, u'_i, v'_i, w'_i, u'v'_i, u'w'_i$ mass flux _i	Phase Doppler
7, 9, 26	still photos of discrete phase	Olympus OM-1
26	high speed cinematography of discrete phase	Hycam
04	same as configurations 1-5 + $P^{\ddagger\dagger}$	Baratron

* U, V, and W correspond to axial, radial, and azimuthal velocities, respectively
** for all laser anemometry, phase Doppler, data are obtained at 15, 25, 35, 50, 75, 150, and 300 mm axially. In addition, measurements are made as near to the inlet plane as possible (between 1 and 5 mm axially). At each axial station, data are obtained at enough radial locations to resolve gradients. In the confined spray cases, measurements could not be obtained at all axial locations due to impingement
[†] the overbar indicates time averaged
^{††} ' designates fluctuating quantities
[‡] i corresponds to particle size i
^{‡†} P corresponds to pressure

4.1.2 Case Description and Geometries

In each case, the geometry of the condition is presented first and the pertinent file name is indicated in the section title so that the reader can be cognizant of the setup used and can select the appropriate files when modeling the given setup. The description and contents of each data file are explained in the next section. Where no case number is presented in the section title, the discussion within that section is a comparison of results or does not deal specifically with a given case.

4.1.3 Data Collection and Reporting Protocol

The focus of the study was on the developing region of the flows. However, to retain a bridge between the developing region and the far field, at least one profile was obtained in the far field. Nevertheless, the near field is of greatest interest, because, in gas turbine flows, all important phenomena associated with the fuel injector occur here.

Because a two component system is utilized in measuring three velocity components, two orthogonal traverses are required. As such, the axial velocity component is measured twice. This results in an inherent check of flow symmetry and repeatability.

Data for each case were obtained over as short a period as possible in order to eliminate the chance of day to day variables from impacting the results. In general, data were obtained at 8 axial locations, and at 10

to 20 radial locations at each of the 8 axial locations. Since the radial profiles were repeated twice, an average of $8 \times 15 \times 2$, or 240, points make up one data set. In addition, many of the data sets were repeated up to three times. The results contained within this program represent over 15,000 data points, each requiring approximately 10 minutes to obtain, reduce, tabulate, and plot. This reflects over one year of time at 40 hours per week dedicated entirely to data collection without allowing for any facility modifications or issues related to diagnostics.

An important criterion in the testing protocol includes the establishment and definition of the flowfield edge. In the present case, data collection for the continuous phase stopped at the radial point where the axial velocity was less than 5% of the maximum velocity for any of the three components for the given axial station. In the case of the discrete phase, collection stopped when the number density had been reduced by 95% of the maximum value for a given axial station.

Following this protocol, with great attention given to the monitoring of flowrates, spatial positioning, repeatability, optical alignment, and other details, data of the highest quality (benchmark) is ensured. To support the quality of the data, a quality control plan (McDonell and Samuelsen, 1991) is available which identifies limitations and sensitivity of the instrument.

In each case, the data are available in a tabulated fashion. The name of each file is based on the number of the configurations listed in Table 3.4-V. In each case, each radial profile is stored as a separate file. Since two orthogonal profiles are required, and up to 8 axial stations are measured, up to 16 files make up a data set.

The data file names are based on DOS-based operating systems. The first four characters are CONF, the next two reflect the configuration number as shown in Table 3.4-V, the following two characters reflect the repetition of the data set, and the extension of the file reflects the axial location and which profile is included. If more than nine repetitions are made, letters are used (for example, the tenth repetition of CONF07 is #A). The extension follows the format of .ABC, where A refers to the axial station. A value of $A = 0$ refers to the inlet station. Unless noted in the documentation file (discussed below), $A = 1$ refers to 15 mm, $A = 2$ refers to 25 mm, $A = 3$ refers to 35 mm, $A = 4$ refers to 50 mm, $A = 5$ refers to 75 mm, $A = 6$ refers to 150 mm, and $A = 7$ refers to 300 mm. The B value is either t or r, where t indicates that the tangential and axial velocity components were measured and r indicates that the radial and axial velocity components were measured. C refers to the repetition of the profile within a given repetition of the data set. The first repetition is a, the second b, and so forth. Finally, a file with extension .doc refers to a documentation file which contains details regarding the flow rates and other special points of interest regarding the data set.

As an example, consider a file with the name CONF01#2.3ta. Referring to Table 3.4-V, the first six characters indicate that this file is from the free jet without coflow in an unconfined environment. #2 indicates that this is second time the data set was collected. .3ta indicates that the radial profile contained within the file was taken at the 35 mm axial station, and that the axial and tangential velocity components were measured.

4.1.4 Nomenclature

U	mean axial velocity
V	mean radial velocity
W	mean azimuthal velocity
u'	rms of the axial velocity
v'	rms of the radial velocity
w'	rms of the azimuthal velocity
$u'v'$	axial - radial shear stress
$u'w'$	axial - tangential shear stress

R correlation coefficient
N data rate

subscripts

uv based on axial and radial components
uw based on axial and azimuthal components
p discrete phase

4.2 SINGLE ROUND JET

4.2.1 Unconfined Single-Phase Jet – CONF01#2

Figure 4.2.1-1* presents the geometry utilized for the unconfined single-phase jet. Briefly, the flow is injected downwards from a centrally located injector. The injector is attached to a traverse which provides motion in the vertical direction along the centerline. The vertical traverse is mounted on top of a $457 \times 457 \text{ mm}^2$ frame which is constructed from 19 mm^2 bars. The sides of the frame are open up to the point where the exhaust plenum begins. The frame is suspended from an optical table via a two-dimensional traverse. Hence three degrees of freedom are afforded to the test article. The entire frame assembly is isolated from the surrounding room by a Plexiglass/tarp system. Air for entrainment is provided through a manifold. Additional details are provided in Section III.

The details of the geometry are provided in the blowup view of the injector. For the single round jet, the simple geometry shown is utilized. Air and seed are introduced far upstream of the pipe at a mass flow rate of 0.0021 kg/s . Enough air is injected through the screen air manifold to maintain a pressure balance between the room and the inside of the enclosure. This air is seeded so that entrained air can also be measured.

The results for the single-phase single round jet are presented in Figures 4.2.1-2 and 4.2.1-3. Figure 4.2.1-2 presents the complete set of results for axial locations of 1.0, 25, and 75 mm. Figure 4.2.1-2 provides radial profiles of the mean axial velocity. Note that two sets of results are shown. This is a result of the inherent need to repeat the axial velocity measurement. As a result, the mean and fluctuating axial velocities are shown twice in Figure 4.2.1-2 (a) and in all other figures showing redundant results obtained from the two orthogonal traverses.

The mean axial velocity shows a peak at the centerline as expected, which decays very little by 75 mm. The velocity decays in the radial direction due to mixing with the surrounding still air and the no-slip condition at the wall of the tube. The shear layer formed at the tube wall rises to increased mixing in this region, resulting in a local peak in the fluctuating velocity. As the flow develops downstream, it spreads radially as momentum is exchanged with the still surrounding air. The shear layer again results in a local peak in the fluctuating velocity component. By 75 mm, the mixing has nearly penetrated the centerline, as indicated by the movement of the peak in the fluctuating velocity towards the centerline. In each case, the flow exhibits excellent symmetry as indicated by the agreement in the results obtained along the two traverses.

The mean and fluctuating radial velocities are shown in Figure 4.2.1-2. Note that the values are slightly nonzero at the centerline. This is attributed to a modest variation in the measured and actual fringe spacing and slight rotation of the fringes from the vertical plane. The results are very slight (magnitude $< 0.1 \text{ m/s}$) and reflect the resolution to which the laser anemometry system can be expected to perform. At 1.0 mm, the radial velocity is nominally zero at all locations except at the very edge, where the negative values indicate the presence of entrained air. By 25 mm, the evidence for entrainment is even stronger. By 75 mm, the jet shows some modest spreading along with entrainment at the edge. In general, the radial velocities are quite small. The fluctuating velocity shows a local peak at the shear layer, as expected.

The azimuthal velocity component is shown in Figure 4.2.1-2 (c). In this flow, the mean azimuthal velocity should be zero everywhere. This is true for the most part, with the exception of near the edge of the flow at 25 and 75 mm. However, the magnitude of these velocities are again quite small. The fluctuating azimuthal velocity component exhibits trends quite similar to the fluctuating radial velocity component, namely a local peak appears at the shear layer.

* Figures for Section IV appear at the end of each subsection. The figure number identifies the subsection in which the figure is discussed.

The cross correlations are shown in Figure 4.2.1-2 (d, e, f, and g). The correlation between the axial and radial velocities is shown in Figure 4.2.1-2 (d). The results are as expected and are equal to zero at the centerline. Again, a local peak is observed which corresponds to the location of the maximum in dU/dr . For completeness, Figure 4.2.1-2 (e) provides radial profiles of the correlation coefficient based on u' and v' .

Figure 4.2.1-2 (f) presents the radial profile of the correlation between u' and w' . This quantity, like W , should be zero everywhere. In this case, it is true. Again for completeness, Figure 4.2.1-2 (g) provides the correlation coefficient based on these same quantities, and again, the values are nearly zero at all points.

To assess the repeatability and sensitivity of the results to the selection of the inlet plane location, Figure 4.2.1-3 presents radial profiles taken at 1.0, 3.0, and 5.0 mm downstream of the pipe exit. Figure 4.2.1-3 (a) presents the radial profiles of the mean and fluctuating axial velocity measured on the traverse required for the radial velocity. Note that the three profiles were obtained on different days, spanning a six month period of time. As shown, the results show very little dependency upon the axial location.

Figure 4.2.1-3 (b) shows the corresponding results from the traverse required to measure the azimuthal velocity. Again, little or no difference is observed for either the mean or fluctuating velocities.

Figure 4.2.1-3 (c) provides the mean and fluctuating radial velocities. The mean values show some dependency but the difference is on the order of 0.01 m/s, which is roughly the accuracy of the system. The alignment of the optics was enhanced slightly from the time the 1.0 mm and the other profiles were obtained, so the variation between 3.0 and 5.0 could reflect a trend. The fluctuating values show little variation.

Figure 4.2.1-3 (d) presents the mean and fluctuating azimuthal component. Again, the enhanced alignment is evident in that the mean values are closer to 0 for the 3.0 and 5.0 mm profiles. However, the overall values are less than 0.1 m/s, so this velocity component is not very important. Once again, the fluctuating values are identical.

Figure 4.2.1-3 (e) presents the correlation between u' and v' . A modest peak is evident at all three axial locations, with a maximum at 5.0 mm. This is attributed to the start of the shear layer at this radial location.

Figure 4.2.1-3 (f) provides the correlation between u' and w' , and reveals zero correlation for all three axial locations, as expected.

4.2.2 Unconfined Jet in the Presence of 100-110 Micron Beads at Loading Ratio 0.2 and 1.0 – CONF07#6.#A

For this case, the geometry and flow rates described in section 4.2.1 are used. In addition, glass beads (100-110 microns) are introduced at a mass flow rate of 0.00042 or 0.0021 kg/s, corresponding to an injected dispersed phase to continuous phase mass loading ratio of 0.2 and 1.0, respectively. This section presents the profiles measured for the gas phase in the presence of the glass beads. Sections 4.2.3 and 4.2.4 present the profiles for the beads and comparative results, respectively.

Figure 4.2.2-1 presents the results for the 0.2 mass loading case. Figure 4.2.2-1 (a) provides the results for the mean and fluctuating axial velocity of the gas. In general, the structure of the axial velocity appears quite similar to that of the single-phase jet as shown in Figure 4.2.1-2. A noteworthy difference is a modest mismatch in the results from the two orthogonal traverses which is evident at the 1.5 mm station. The results still show the development of the jet manifested by the increased radial spread and decay of the peak axial velocities. The fluctuating velocity profiles are quite symmetric and reflect the development of shear layer.

The radial velocities are presented in Figure 4.2.2-1 (b). At the 1.5 mm station, 2 points appear to be outliers, those at the centerline and 10 mm. Besides these two points, the profiles are well behaved. As in the single-phase jet, imperfections in the alignment lead to nonzero values at the centerline, but again, the magnitude of the velocities is quite small. As the flow develops, radial velocities away from the centerline are evident, as is the peak in the fluctuating velocities corresponding to the location of the shear layer.

The azimuthal velocities are shown in Figure 4.2.2-1 (c) and, like the radial velocities, reflect some minor problems associated with alignment. In general, the mean azimuthal velocities are quite small. The fluctuating velocities again appear similar to the single-phase case, with local maximums occurring in the regions of most intense mixing.

The shear stress values are presented in Figure 4.2.2-1 (d and e). Both quantities behave as expected. The change in sign of $u'v'$ from the single-phase jet is due to a change in the optical setup (i.e., change in the radial velocity sign).

The results for the higher loading ratio case are presented in Figure 4.2.2-2. These results were obtained approximately six months after the results presented in Figure 4.2.2-1. Improvements in the optical alignment and in data collection protocol resulted in improved measurements which are borne out in these results. Figure 4.2.2-2 (a) provides the mean and fluctuating axial velocities. In this case a modest asymmetry is apparent in the mean velocities. The fluctuating velocities show good symmetry. The mean velocity profile at $Z = 1.0$ and 25.0 mm appears flatter than it does for the single-phase case, due to the presence of the glass beads. This will be examined in more detail in section 4.2.4.

Figure 4.2.2-2 (b) presents radial profiles of the mean and fluctuating radial velocities. The improved alignment is evident in these profiles where zero values are now measured at the centerline. Note that the radial velocities deviate only slightly from zero. The fluctuating velocities still exhibit a local maximum as observed previously in both the single-phase jet and the 0.2 mass loading jet.

Figure 4.2.2-2 (c) provides profiles of the mean and fluctuating azimuthal velocities. The mean values tend towards zero, in general. Near the edge of the jet, some nonzero values are observed but, again, the magnitude is small. The fluctuating values appear flat at both the 1.0 and 25 mm axial planes. At 75 mm, a local peak is observed.

Figure 4.2.2-2 (d and e) present radial profiles of $u'v'$ and $u'w'$, respectively. The profiles of $u'v'$ appear flatter than they did for the single-phase case, and show only modest shearing at $Z = 75$ mm. Again, the sign change relative to the single-phase case is due to a change in traversing and optical setups. The values for $u'w'$ are everywhere zero as expected.

4.2.3 Glass Beads in the Unconfined Jet at Loading Ratios of 0.2 and 1.0 – CONF07#5,#3

The radial profiles for the 100-110 micron glass beads are presented in Figures 4.2.3-1 and 4.2.3-2 for the 0.2 and 1.0 mass loading ratio cases, respectively. Note that a subscript p is used on the legend to represent a quantity measured for the dispersed phase.

The mean and rms for axial velocities are presented in Figure 4.2.3-1 (a) for the 0.2 mass loading case. The maximum velocity is observed at the centerline, and the velocity decay in the radial direction starts away from the centerline. The mean velocity does not go to zero at the edge of the flow due to gravity. The profiles for each traverse are virtually identical, indicating good symmetry in the dispersed phase flow field.

The rms values show a local peak right at the edge of the jet at the inlet plane, which is due to the interaction of the particles with the wall of the pipe in this region. However, by an axial location of 25 mm, this interaction has decreased and the rms profile becomes flatter. By $Z = 75$ mm, the rms profile is flat.

The mean and fluctuating radial velocity components are shown in Figure 4.2.3-1 (b). At $Z = 1.0$ mm, a consistent radial component is measured. However, this is due to modest misalignment of the optics and is indicative of the error associated with this measurement for this case. With increased distance from the injector, the mean radial velocities increase away from the centerline, indicating that the beads are being transported outwards. The rms values are flat at the inlet and exhibit a local maximum at the centerline at the downstream locations.

Radial profiles of the mean and fluctuating azimuthal profiles are shown in Figure 4.2.3-1 (c). The mean values are expected to be zero everywhere. The nonzero measurement (note that $|W| < 0.1$ m/s) is again indicative of the systematic measurement error associated with this case. The fluctuating velocities, like those for the radial component, feature a local maximum at the centerline.

The cross correlation between the particle fluctuating velocities in the axial and radial direction are presented in Figure 4.2.3-1 (d). A slight positive correlation is observed, which is consistent with the physics of the flow. A slow moving particle traveling in the axial direction is less likely to be transported radially outwards, whereas faster moving particles are likely to penetrate outwards.

Finally, the particle data rate is presented in Figure 4.2.3-1 (e). The results show that the concentration is at a maximum at the centerline and it falls off rapidly at the edge of the jet. Comparison of the profiles obtained along the two orthogonal directions reveals reasonable symmetry.

Figure 4.2.3-2 presents the same results for the 1.0 mass loading case. The results appear similar in structure to those for the 0.2 mass loading case. The nonzero V and W values at the centerline again correspond to modest misalignment and can be taken as the error associated with the measurement. A comparison of the two cases is discussed in section 4.2.4.

4.2.4 Effect of Particle Mass Loading in the Unconfined Jet

Figure 4.2.4-1 presents a comparison of the gas phase results measured in the free jet and in the particle-laden jet at mass loading ratios of 0.2 and 1.0. The results for the mean and fluctuating axial velocity are presented in Figure 4.2.4-1 (a). At the inlet location, the differences are small. However, the increased loading ratio results in a modification of the velocity profile shape and a reduction in the fluctuating velocity. The lower loading ratio has no effect on the shape of the velocity profile. The modestly higher axial velocities are attributed to variation in day-to-day operation of the facility. These differences, however, are not significant in terms of mass flow, as demonstrated by the similarity in the mass flow rate obtained by integrating the profiles.

At an axial location of 25 mm, the same trends are observed. The low loading case appears more similar to the single-phase case, as does the higher loading case. The reduction in the fluctuating velocity is apparent. Farther downstream the same trends are observed, but the fluctuating velocity shows modestly higher values for the high loading case. Note that the higher loading case results in a narrowing of the jet relative to the single-phase case. The lower loading case has less impact on the gas phase, but appears to widen the jet. This appearance is attributed to the difference in overall flow, as shown by the inlet profile as well, and may not be a fair comparison.

The shear stress, shown in Figure 4.2.4-1 (b), reveals trends which are similar to those for the axial velocity. The apparent sign change is due to differences in the alignment of the optics and should not be taken as being physically correct. At the inlet, little or no difference is observed for the three cases. At $Z = 25$ mm, the magnitude of the shear is reduced for the higher loading case. By $Z = 75$ mm, the three cases ap-

pear similar. Note, however, that the peak in the shear occurs closer to the centerline for the single-phase case, showing quicker development of the jet for that case.

The effect of the particle loading ratio on behavior of the particles is shown in Figure 4.2.4-2, where a comparison of the two cases is made. The comparison of the mean and fluctuating axial velocities is presented in Figure 4.2.4-2 (a). The fluctuating velocity shows little change with variation in the particle mass flow. The mean velocity, however, shows a significant variation. The higher loading ratio results in a much flatter velocity profile at the inlet. The values along the centerline are suppressed compared to the lower loading ratio. This is due to the ability of the wall effect to be transferred to the centerline by the higher concentration of beads in the high loading case. As the flow develops, the centerline values remain significantly lower for the high loading case. Interestingly, at the edge of the flow, the velocities in both cases are similar, suggesting that the interaction between particles is much less at the edge.

Figure 4.2.4-2 (b) provides the data rate profiles for the two cases. As expected, the lower loading ratio case has approximately an order of magnitude lower data rate. The shapes of the profiles are similar.

4.2.5 Unconfined Jet in the Presence of 25 and 105 Micron Beads – CONF13#2

Figure 4.2.5-1 provides gas phase results obtained in the free jet laden with an equal number of 20-30 and 100-110 micron glass beads. The overall loading ratio of beads to air is 0.2.

The results are similar to those obtained for the previous gas phase jet cases. Essentially, the flow structure appears identical to that of a free jet, showing again that the 0.2 mass loading has only a small effect on the overall structure of the gas phase.

4.2.6 Mixture of 25 and 105 Micron Glass Beads in the Unconfined Jet – CONF13#4

Figure 4.2.6-1 presents the results for the glass bead behavior. In this case, equal numbers of 25 and 105 micron beads were injected at a mass loading ratio of 0.2 relative to the gas phase. Figure 4.2.6-1 (a) provides the radial profiles of the mean axial velocity at axial locations of 1, 25, and 150 mm. In this figure, the circles and triangles represent the value from the 25 micron beads, whereas the squares and upside down triangles represent the 105 micron beads. It can be seen that the mean axial velocity profile for the large beads is much flatter compared to that of the small beads. The same is true for the fluctuating velocity profiles. The symmetry of the axial velocity profiles for the two different sizes is quite reasonable for each axial location. By 150 mm downstream, note that the larger beads possess a greater velocity than do the smaller beads at all radial locations. This is due to the greater momentum and larger mass of the large beads.

Figure 4.2.6-1 (b) provides the mean and fluctuating radial velocities for the bead mixture. In this figure, and those that follow, the open symbols reflect the behavior of the small beads and the filled symbols reflect the behavior of the large beads. The radial velocity shows little variation between the two sizes and is, in general, quite small. The largest radial velocities are observed at the edge of the jet, and both sizes exhibit similar values. The fluctuating velocity shows that near the edge the smaller beads have larger values, and at 150 mm downstream the values are consistently twice the value for the larger beads. This is attributed to the larger inertia of the larger beads.

The mean and fluctuating azimuthal velocities are shown in Figure 4.2.6-1 (c) and exhibit trends which are identical to those for the radial velocities.

The axial and radial velocity cross correlation is shown in Figure 4.2.6-1 (d). In this case, the circles represent the smaller beads. The cross correlation shows that the smaller particles have a stronger correlation. This is attributed to their small inertia compared to the larger beads.

The data rate is presented in Figure 4.2.6-1 (e). At the inlet plane the results for the smaller beads are a little noisy, but it is apparent that the profiles show less small beads. By 150 mm downstream the smaller beads show an increased spread relative to the larger beads, as expected.

4.2.7 Confined Single Round Jet – CONF04#3

Figure 4.2.7-1 presents the geometry associated with the confined single round jet. The setup is similar to that used for the unconfined testing with several important exceptions. First, a 152.4 mm i.d. Plexiglas tube concentrically surrounds the jet. Air is introduced at the top of the duct via a manifold. This air is distributed as uniformly as possible by a series of flow straighteners. The 152.4 mm duct enters the exhaust plenum via a sealed entrance. The plenum is evacuated by the exhaust blower and the flow rate is adjusted by slide valves until the pressure inside is less than atmospheric.

Figure 4.2.7-2 provides the results measured within the duct. Figure 4.2.7-2 (a) provides the measured mean and fluctuating axial velocities. Overall, the results at the inlet appear quite similar to those obtained in the absence of confinement (Figure 4.2.1-2). The primary differences occur at the edge of the jet, where the presence of the coflowing air is evident. Note that the axial velocities obtained while measuring the radial component extend to only 38 mm. This is due to the optical access provided. The symmetry of the jet flow in terms of both mean and fluctuating values is quite good. However, the mean axial velocity in the outer flow exhibits some asymmetry, where the results from one profile differ by up to 0.4 m/s compared to the other. This is attributed to the relative position of the duct air flow manifold to the measurement plane and to challenges associated with providing a uniform velocity profile.

Figure 4.2.7-2 (b) presents the mean and fluctuating radial velocities. In this case, positive mean radial velocities correspond to flow towards the centerline. Hence, at the mixing layer between the two streams it is apparent that the jet expands slightly into the slower moving surrounding stream and that the outer stream is entrained towards the jet, as expected. The fluctuating radial velocity peaks in the vicinity of the shear layer at the 25 and 75 mm axial locations.

Figure 4.2.7-2 (c) provides the mean and fluctuating azimuthal velocities. In this case, it is expected that the mean value be everywhere equal to zero. This is essentially true with the exception of slight nonzero values in the outer flow. Again, this is attributed to challenges of introducing the coflowing air such that it appears uniform at the measurement plane. The fluctuating value behaves as expected and again peaks in the vicinity of the shear layer. At the inlet plane the fluctuating velocity appears as twin peaked which is due to the shear along the inside and outside of the pipe.

The cross correlations are presented in Figure 4.2.7-2 (d and e). The correlation between axial and radial values (Figure 4.2.7-2 [d]) is strong at the shear layer. With increasing downstream distance the shearing begins to weaken. The correlation between the axial and azimuthal components is expected to be zero and the measurements reflect this quite well (Figure 4.2.7-2 [e]).

To provide an estimation of the repeatability of the measurements, Figure 4.2.7-3 provides a sample of the comparison between data sets obtained nine months apart. The repeatability in the jet dominated region is quite good, but the outer flow region exhibits some differences. In general, these differences are within the variation produced by nonuniformities in the screen air flow.

4.2.8 Confined Jet in the Presence of 100-110 Micron Beads at Loading Ratios of 0.2 and 1.0 – CONF10#3,#5

Figure 4.2.8-1 presents results for the gas phase velocities in the presence of glass beads with a bead-to-gas phase mass loading ratio of 0.2. The results appear similar to those presented in section 4.2.7, with little exception. It is apparent that the low loading ratio has little impact on the gas phase behavior. The azimuthal velocity (Figure 4.2.8-1 [b]) exhibits some unexpected behavior near the edge of the jet, but the

overall values are small. The correlation of the fluctuating axial and azimuthal velocities is small everywhere, as expected.

Figure 4.2.8-2 provides the results for the jet with beads in a mass loading ratio of 1.0. The results again appear similar to those presented in section 4.2.7. The symmetry of the axial velocity profiles (Figure 4.2.8-2 [a]) is quite good. In general, the results appear as expected.

4.2.9 Glass Beads in the Confined Jet at Loading Ratios of 0.2 and 1.0 – CONF10#4,#6

Figures 4.2.9-1 and 4.2.9-2 present the velocity and number density results for the glass beads in the confined particle-laden jet for bead-to-gas phase mass loading ratio of 0.2 and 1.0, respectively.

The behavior of the beads in the low loading case appears similar to that in the absence of confinement (section 4.2.3). The bead velocity is at a maximum at the centerline, with magnitudes slightly lower than that of the gas phase (Figure 4.2.8-1). The fluctuating velocity is constant. The azimuthal velocity (Figure 4.2.9-1 [b]) shows similar behavior as the case in the absence of confinement (section 4.2.3), as does the number density (Figure 4.2.9-1 [c]). With confinement, the data rate maximum is lower, which is attributed more to a decrease in detectability through the glass of the confined duct than it is to physics.

Figure 4.2.9-2 presents the same results for the case with a bead-to-gas mass loading ratio of 1.0. Figure 4.2.9-2 (a and e) shows that the flow field exhibits good symmetry. The radial velocities (Figure 4.2.9-2 [b]) show transport of the beads away from the jet. A slight nonzero value of the azimuthal velocity indicates slight mismatch of the fringe spacing and orientation of the transmitter.

4.2.10 Effect of Particle Mass Loading Ratio in the Confined Jet

To directly see the effect of the particle mass loading ratio on the gas phase behavior, Figure 4.2.10-1 provides results from the single-phase confined jet along with the results for the gas phase in the presence of glass beads at the two mass loading ratios.

The axial velocities reveal trends similar to those in the unconfined case. The presence of the beads reduces the axial velocities of the gas phase. In addition, the beads tend to reduce the spread of the jet. The high mass loading reduces the fluctuating gas phase velocity compared to the single-phase case.

Figure 4.2.10-2 (a) provides a comparison of the glass bead velocities for the two cases. In this case, the higher loading ratio has higher mean velocities but lower fluctuating velocities. The comparison of the data rates is shown in Figure 4.2.10-2 (b). As expected the data rates are roughly five times higher for the 1.0 loading ratio.

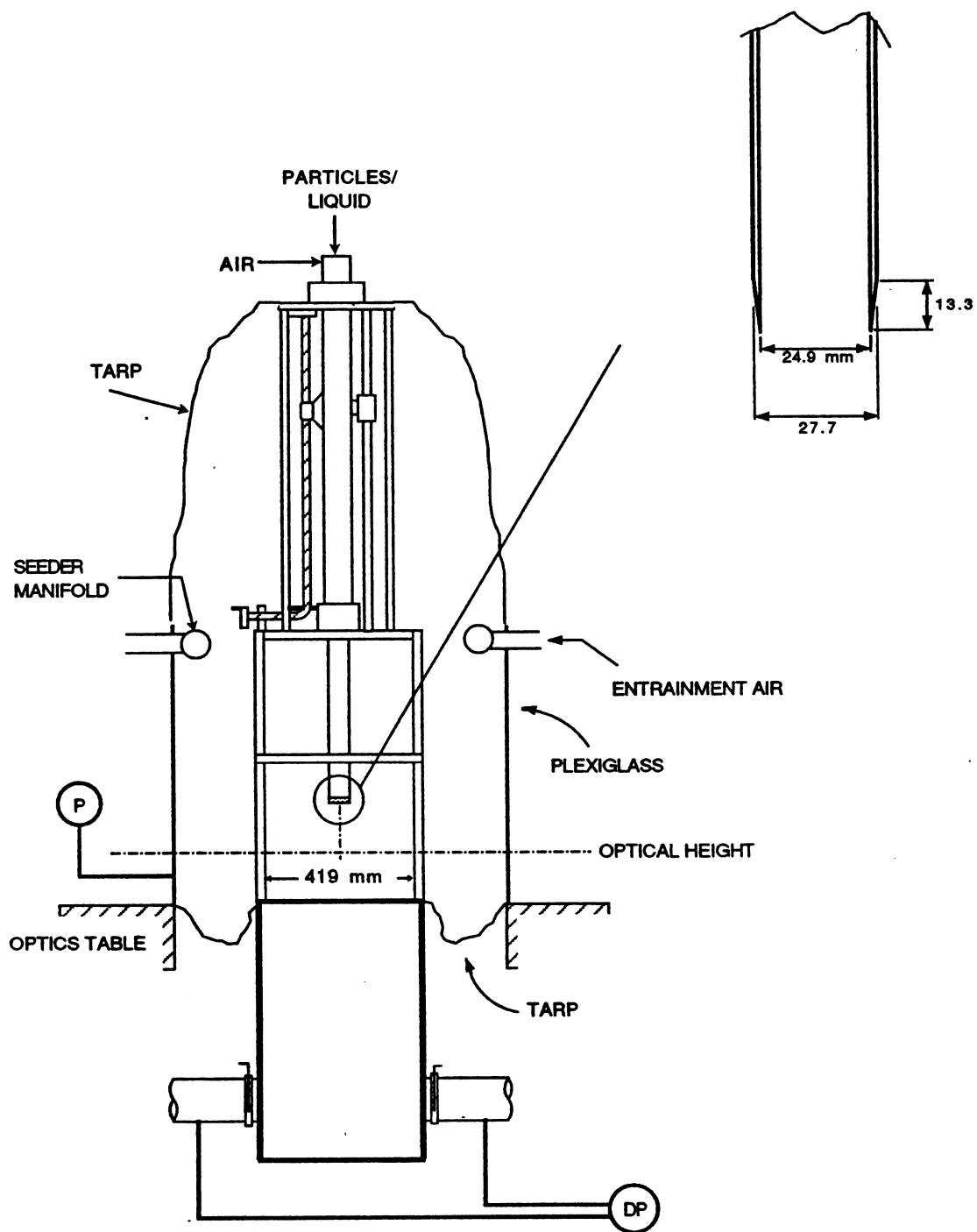
4.2.11 Effect of Confinement on Jet

To show the effect of confinement on the free jet, Figure 4.2.11-1 presents the axial velocity results from the two cases. The main structure of the jet is retained in both cases. However, the effect of the coflowing air in the 152.4 mm duct is evident in the confined case. Also, a slight reduction in the fluctuating velocity at the 75 mm axial station is evident.

4.2.12 Effect of Confinement on Glass Beads

Figure 4.2.12-1 shows the influence of the confinement on the behavior of the glass beads. In this case, the loading ratio is 1.0. Figure 4.2.12-1 (a) presents the mean and fluctuating axial velocity component. The only significant difference is observed at the centerline. The fluctuating velocity reveals little or no impact.

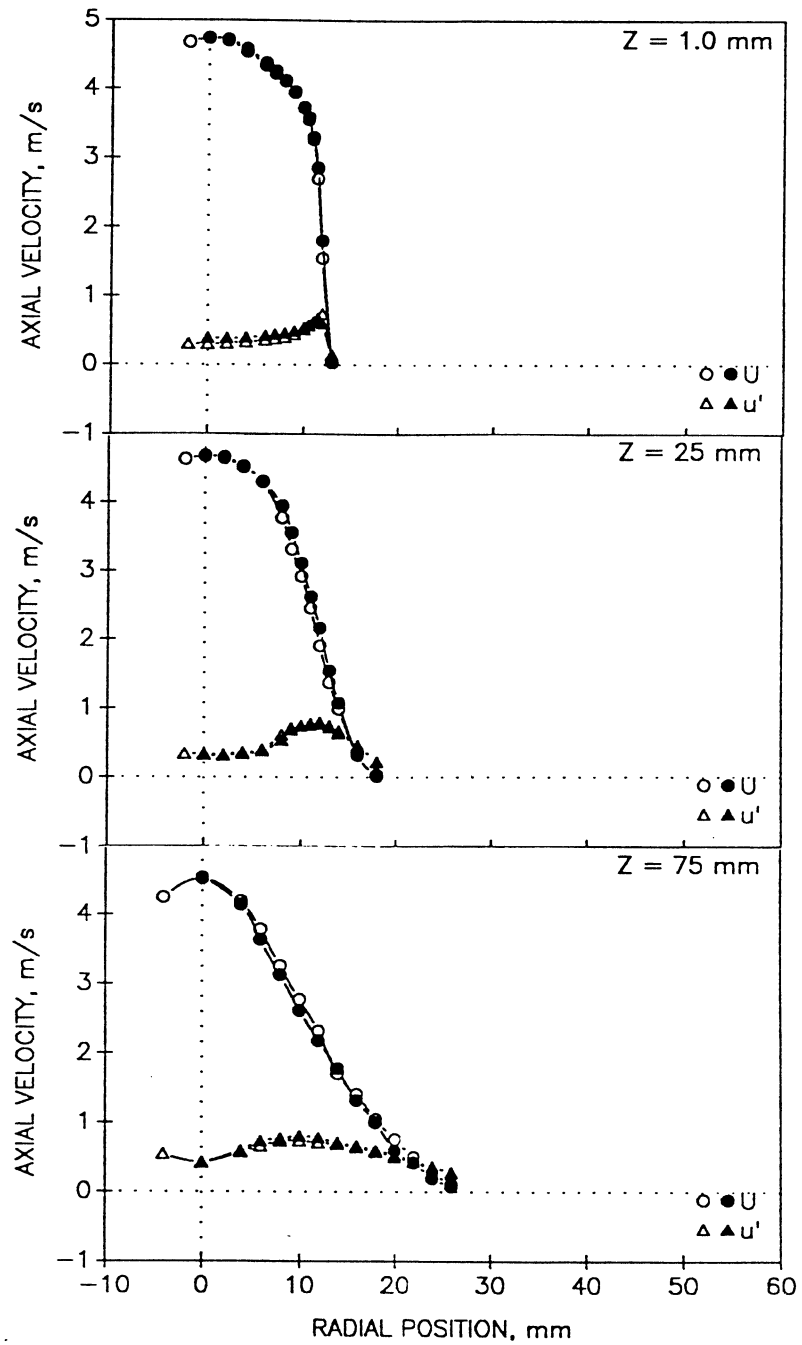
Figure 4.2.12-1 (b) shows the impact on the data rate. In this case, it is not likely that the flowfield is giving rise to the difference. In fact, it is likely that the beads are slightly less detectable in the confined duct due to the presence of windows.



TE92-1696

Figure 4.2.1-1. Geometry utilized for unconfined single round jet.

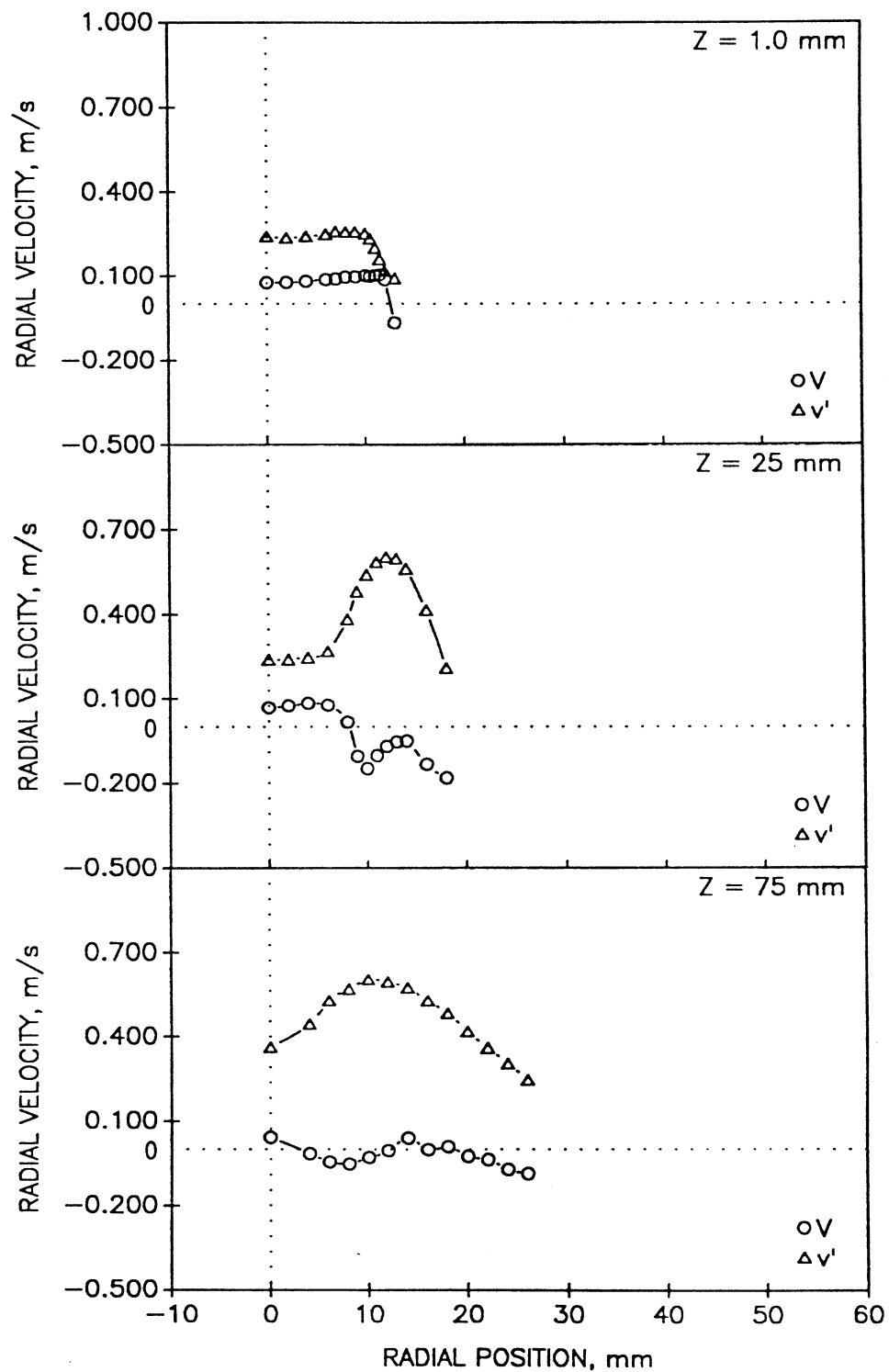
a) Mean and Fluctuating Axial Velocities



TE92-1697

Figure 4.2.1-2. Radial profiles of gas phase statistics in unconfined single-phase round jet (1 of 7).

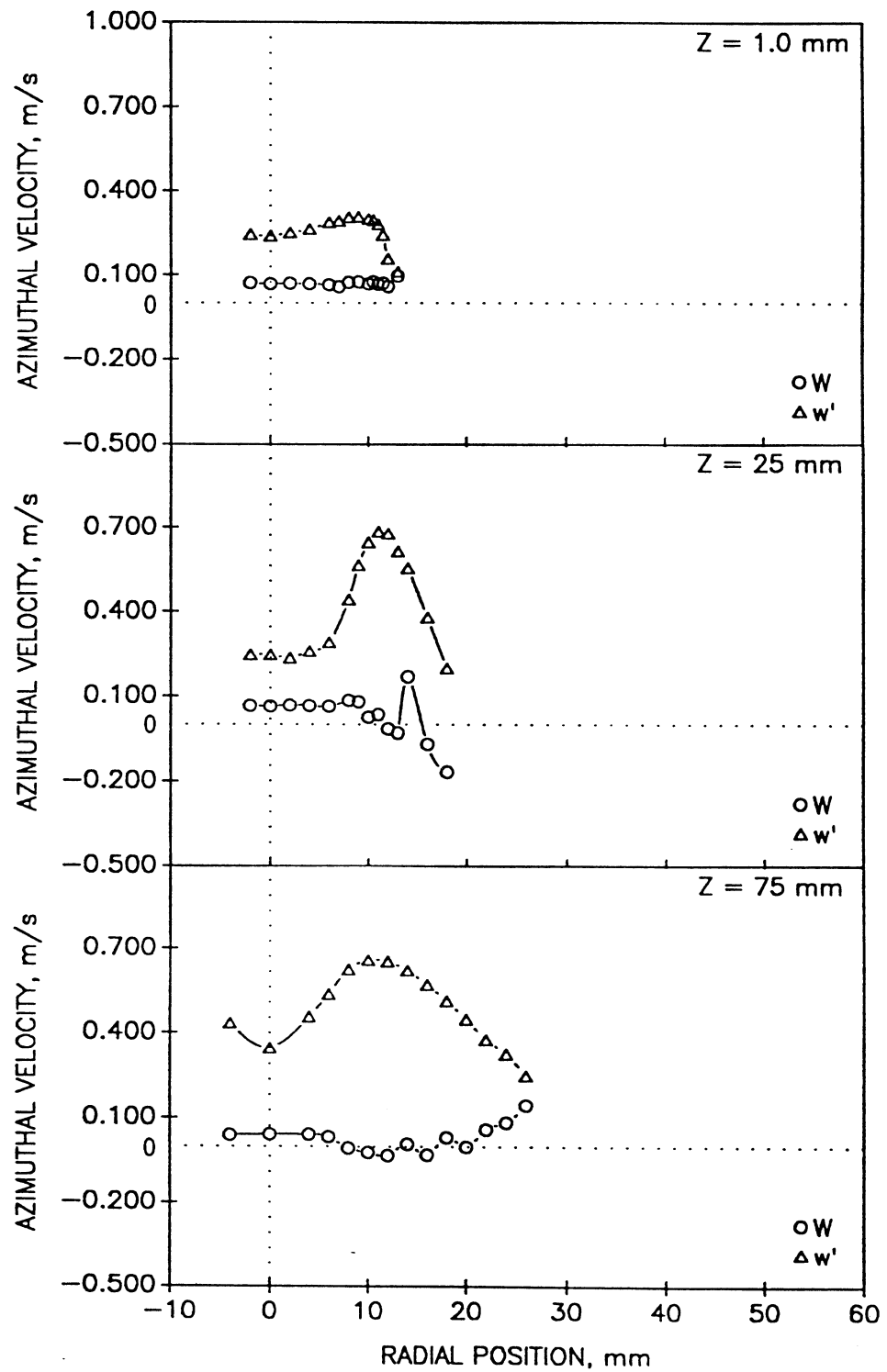
b) Mean and Fluctuating Radial Velocities



TE92-1698

Figure 4.2.1-2. Radial profiles of gas phase statistics in unconfined single-phase round jet (2 of 7).

c) Mean and Fluctuating Azimuthal Velocities



TE92-1699

Figure 4.2.1-2. Radial profiles of gas phase statistics in unconfined single-phase round jet (3 of 7).

d) Shear Stress Based on Axial and Radial Velocities

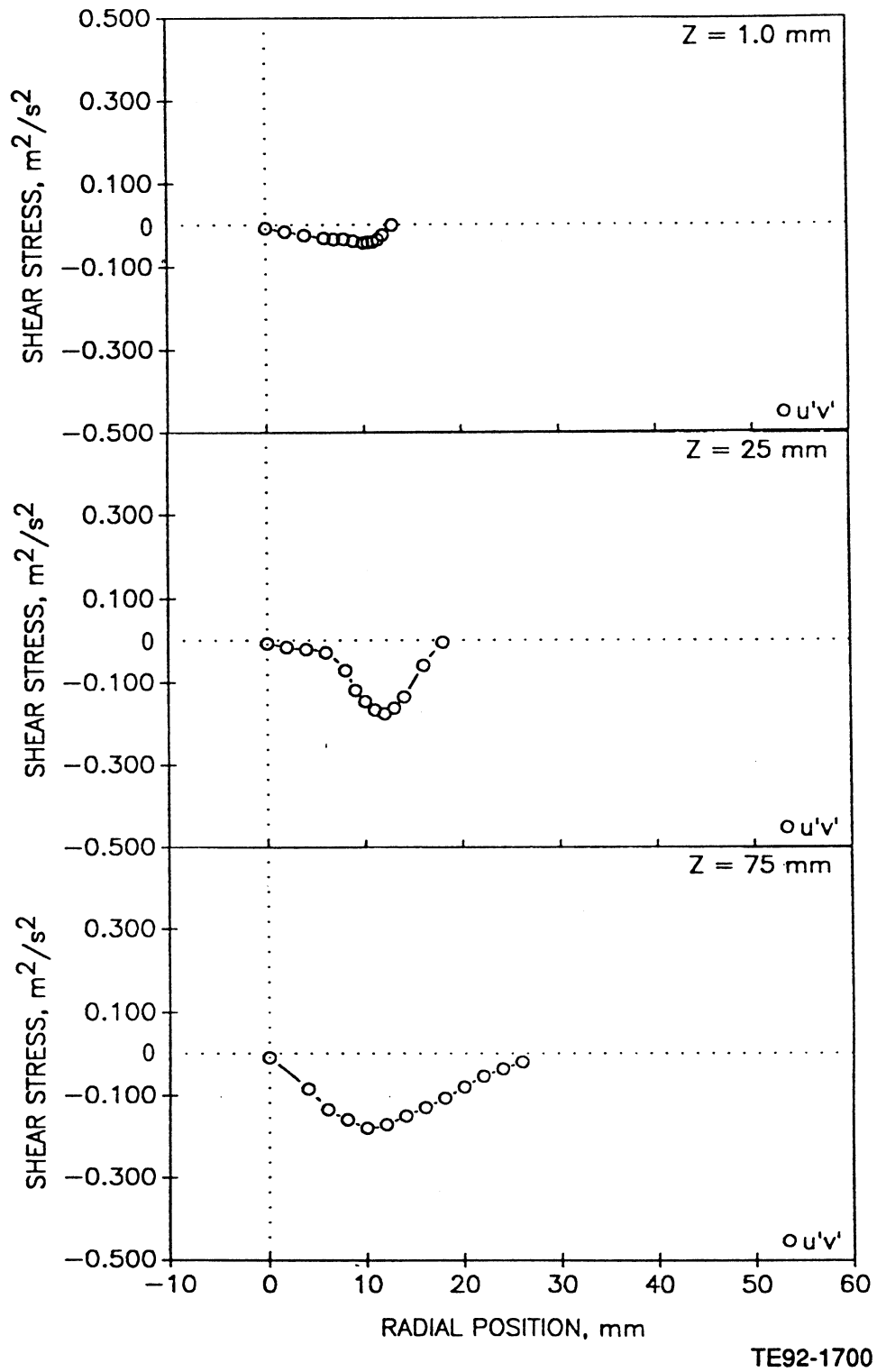


Figure 4.2.1-2. Radial profiles of gas phase statistics in unconfined single-phase round jet (4 of 7).

e) Correlation Coefficient Between the
Fluctuating Axial and Radial Components

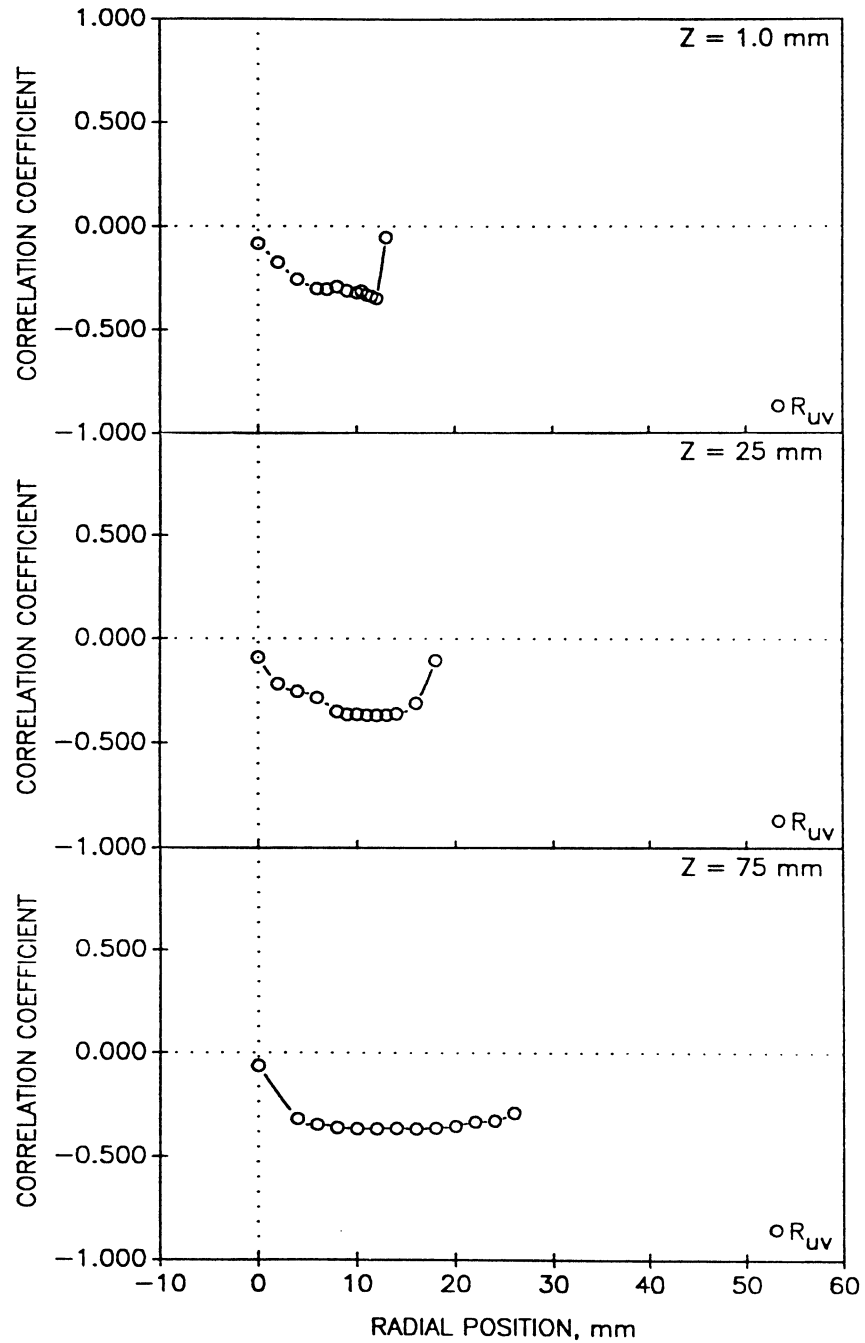
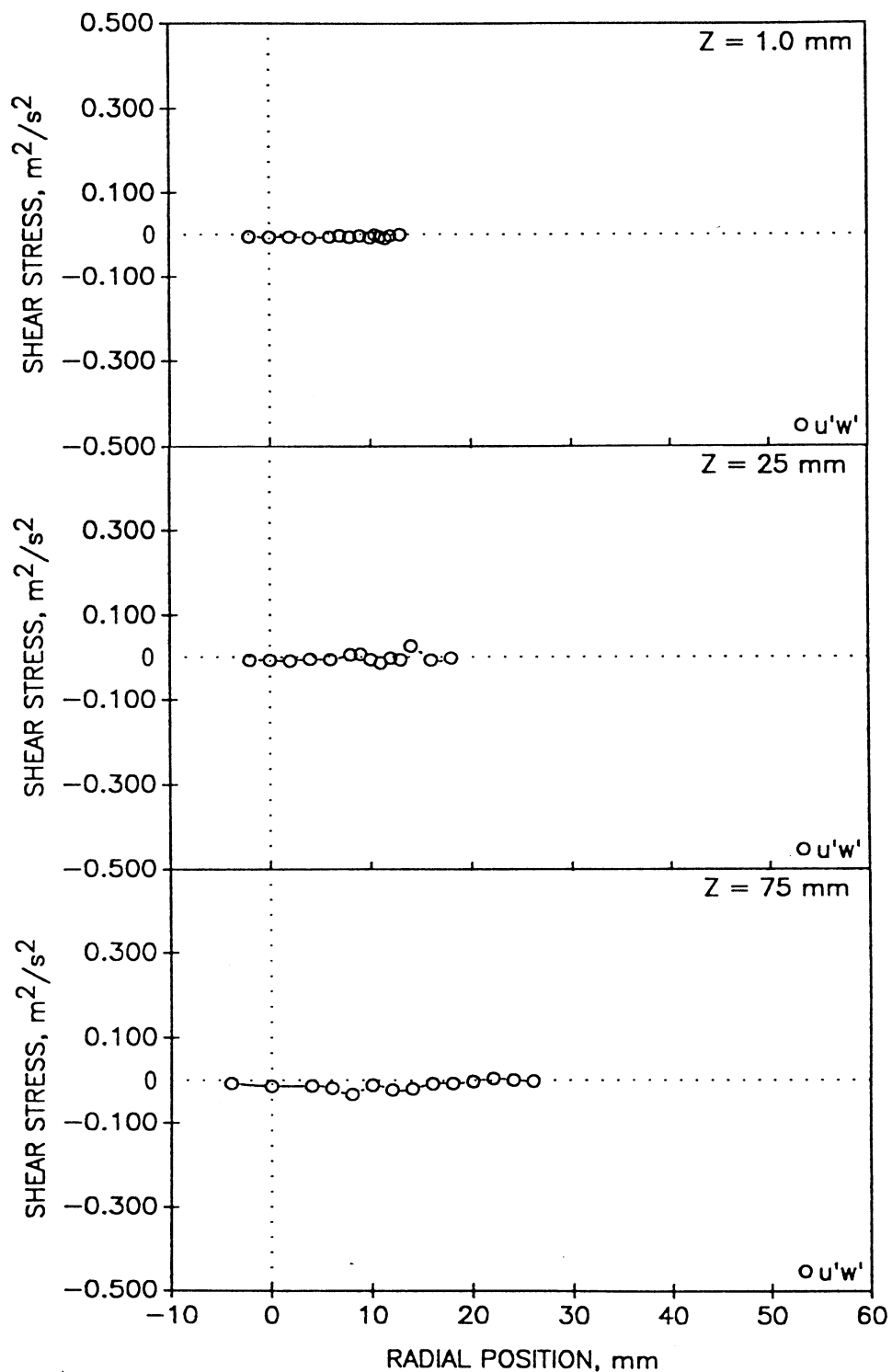


Figure 4.2.1-2. Radial profiles of gas phase statistics in unconfined single-phase round jet (5 of 7).

f) Shear Stress Based on Axial and Azimuthal Velocities



TE92-1702

Figure 4.2.1-2. Radial profiles of gas phase statistics in unconfined single-phase round jet (6 of 7).

g) Correlation Coefficient Between the
Fluctuating Axial and Azimuthal
Components

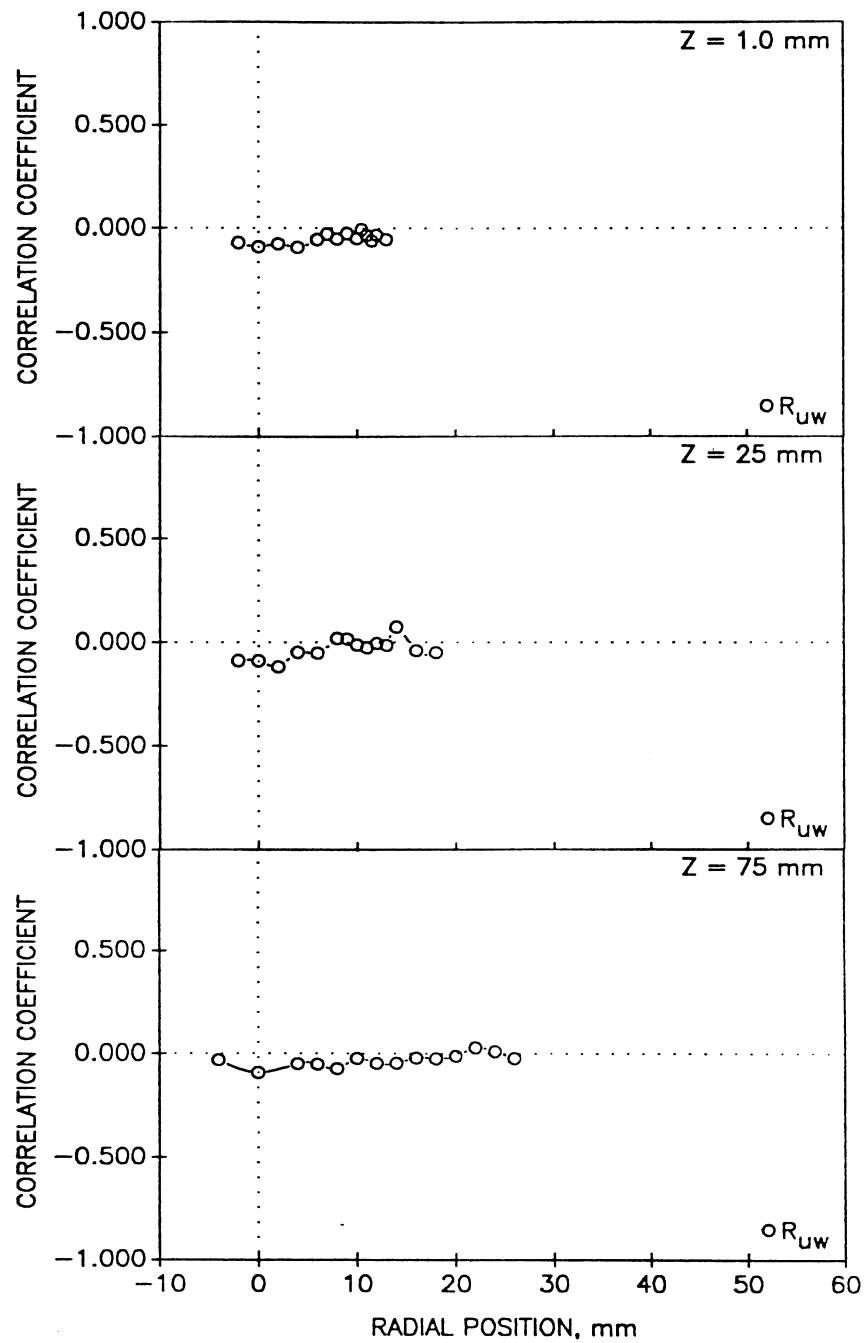
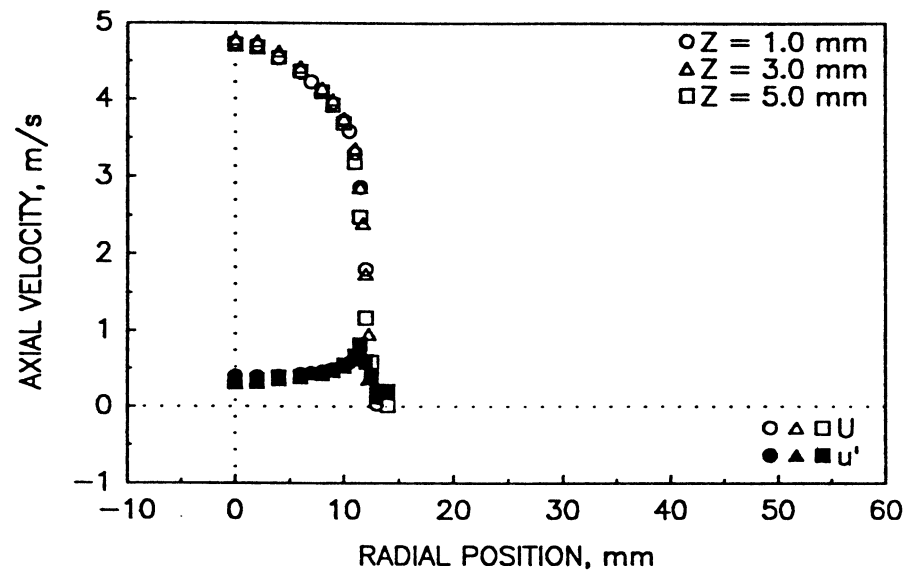
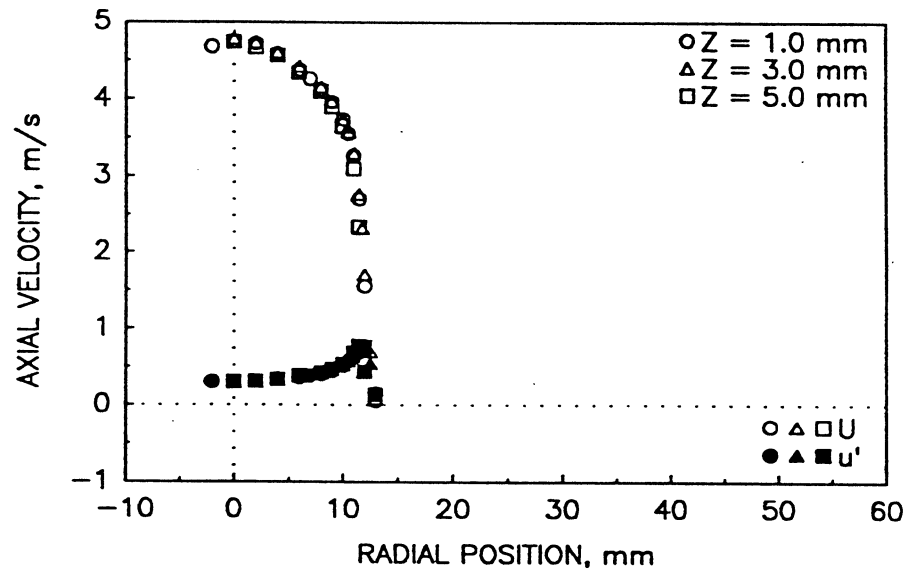


Figure 4.2.1-2. Radial profiles of gas phase statistics in unconfined single-phase round jet (7 of 7).

a) Mean and Fluctuating Axial Velocity
Measured Along Traverse for the Radial
Velocity



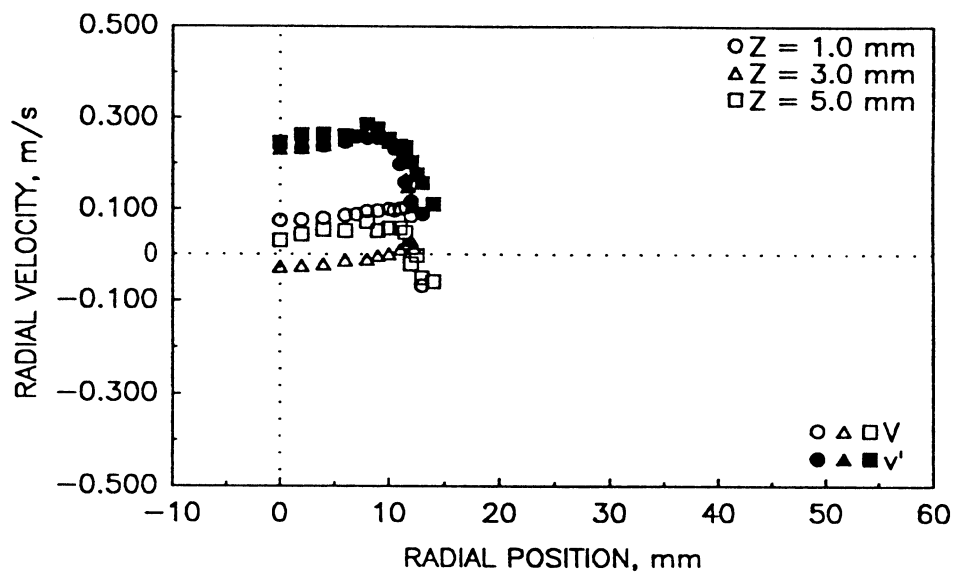
b) Mean and Fluctuating Axial Velocity
Measured Along Traverse for the
Azimuthal Velocity



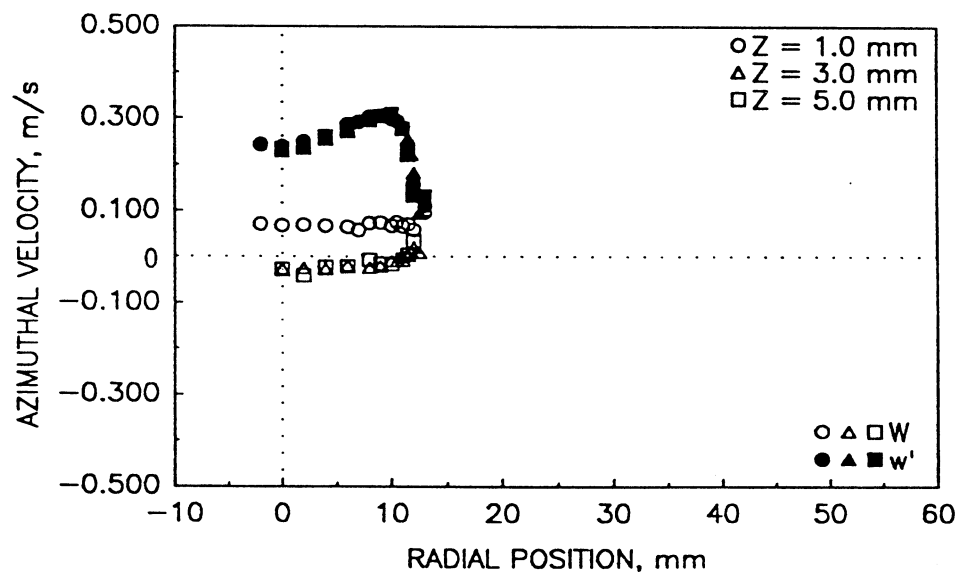
TE92-1704

Figure 4.2.1-3. Repeatability and sensitivity of measurements in the unconfined single-phase round jet (1 of 3).

c) Mean and Fluctuating Radial Velocity



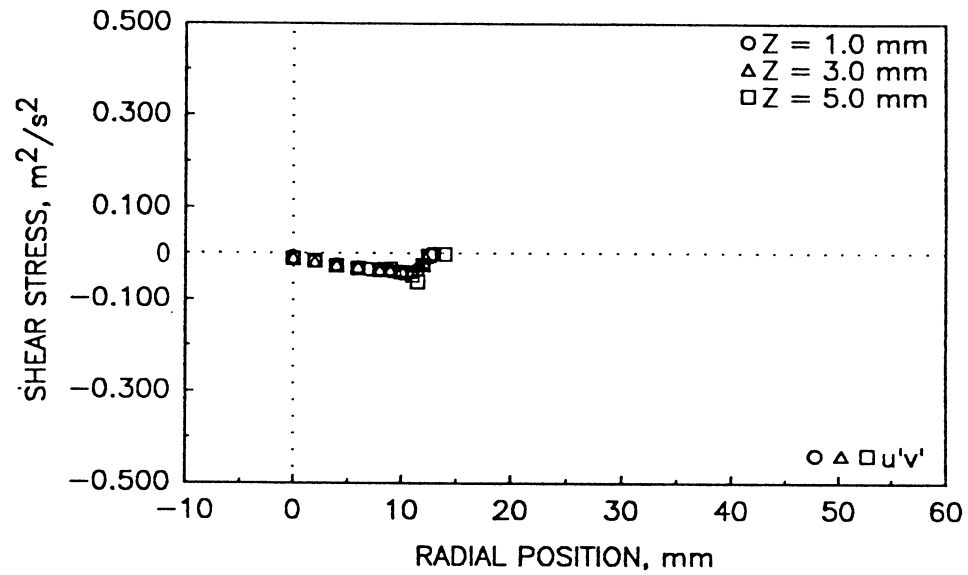
d) Mean and Fluctuating Azimuthal Velocity



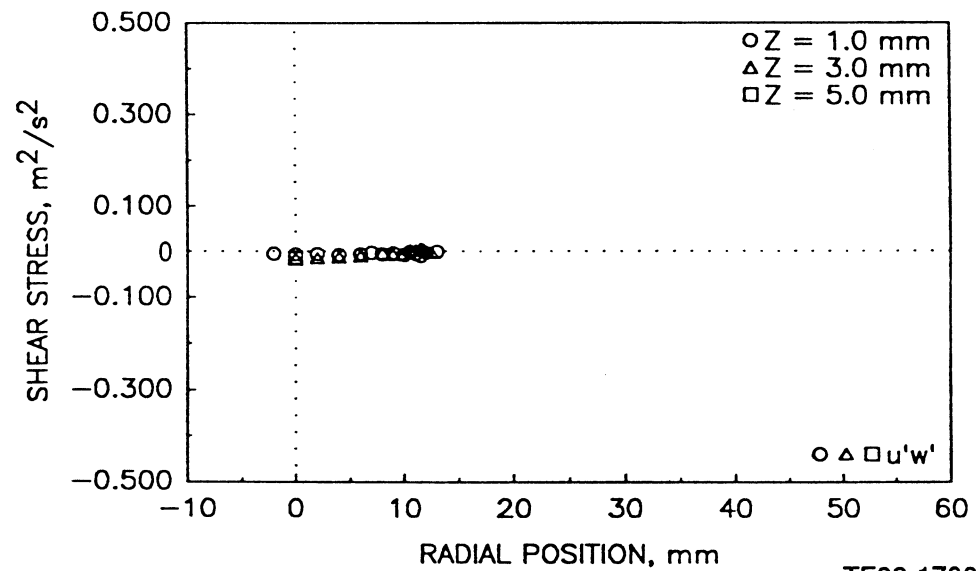
TE92-1705

Figure 4.2.1-3. Repeatability and sensitivity of measurements in the unconfined single-phase round jet (2 of 3).

e) Shear Stress Based on Axial and Radial Velocities



f) Shear Stress Based on Axial and Azimuthal Velocities



TE92-1706

Figure 4.2.1-3. Repeatability and sensitivity of measurements in the unconfined single-phase round jet (3 of 3).

a) Mean and Fluctuating Axial Velocities

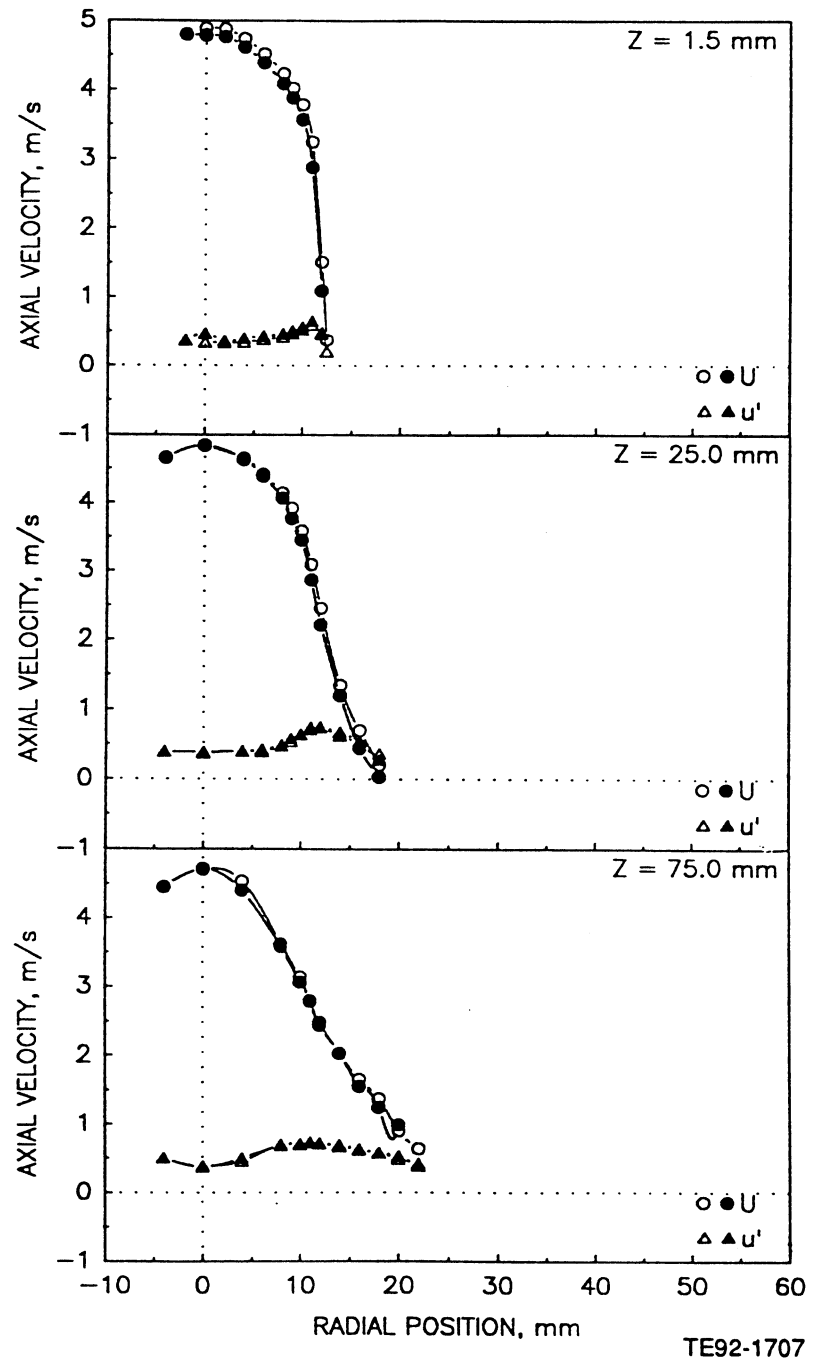


Figure 4.2.2-1. Radial profiles of gas phase velocity measurements in unconfined round jet laden with 100-110 micron glass beads with a bead to-gas-mass loading ratio of 0.2 (1 of 5).

b) Mean and Fluctuating Radial Velocities

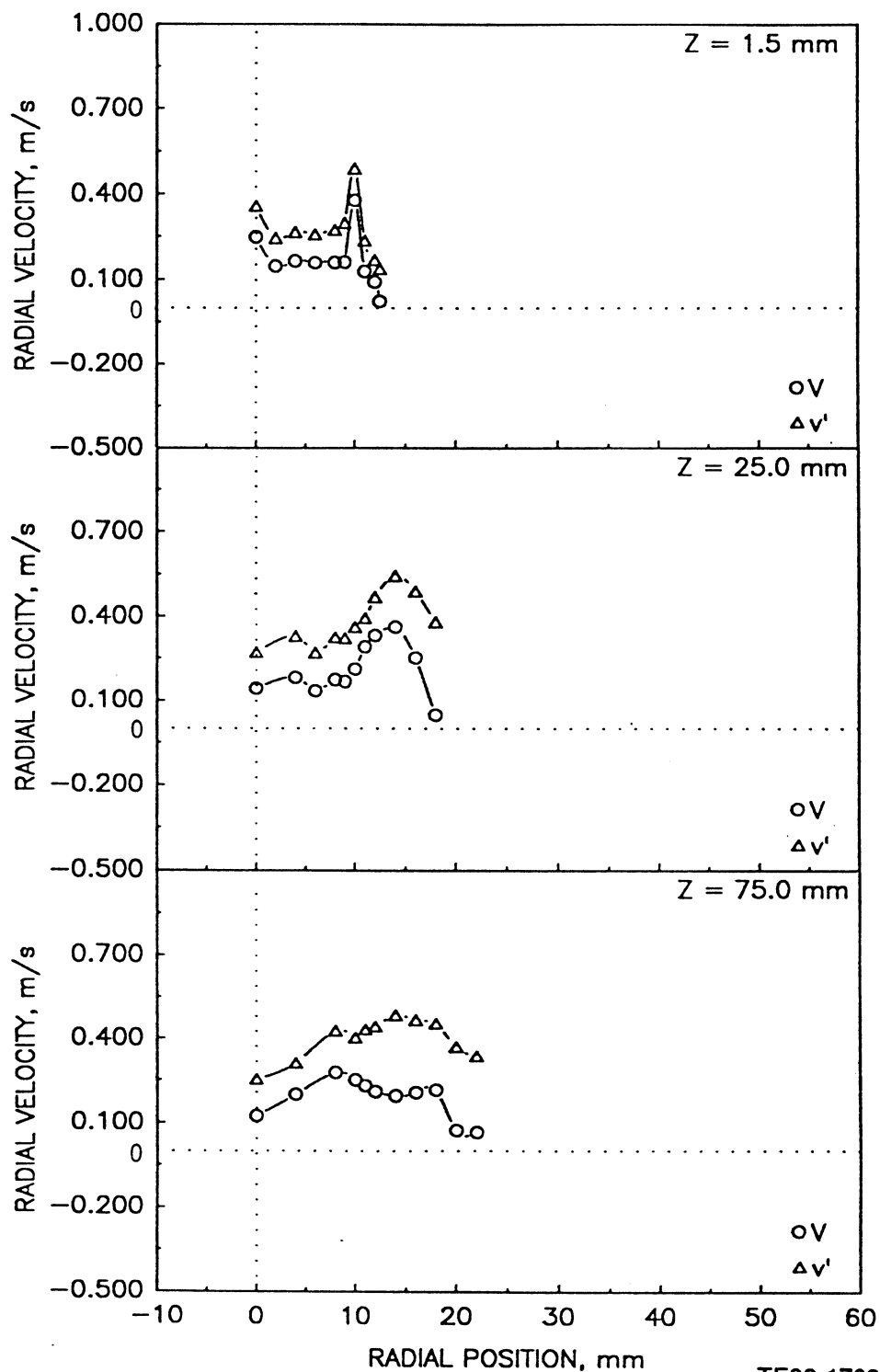


Figure 4.2.2-1. Radial profiles of gas phase velocity measurements in unconfined round jet laden with 100-110 micron glass beads with a bead-to-gas mass loading ratio of 0.2 (2 of 5).

c) Mean and Fluctuating Azimuthal Velocities

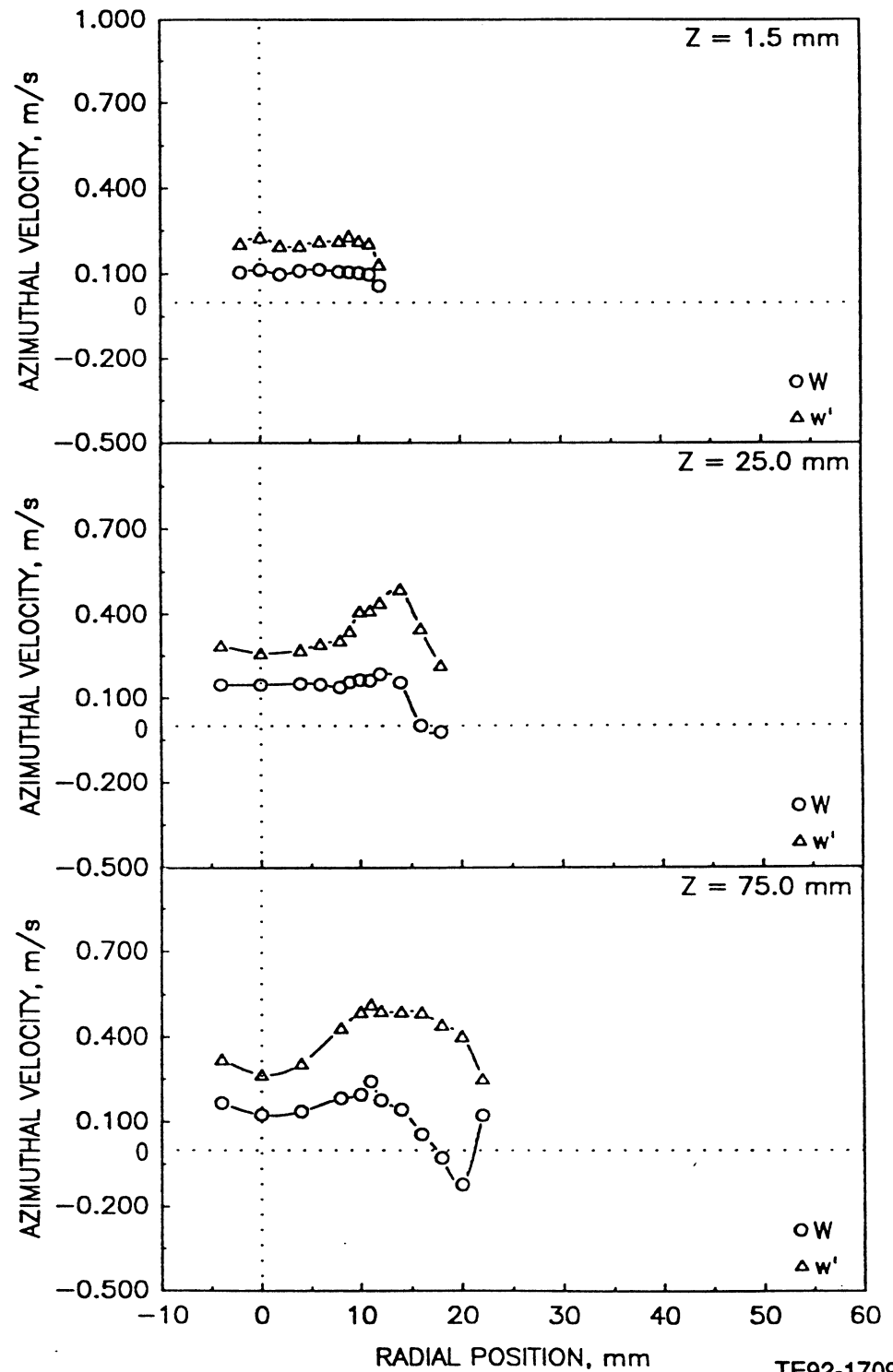


Figure 4.2.2-1. Radial profiles of gas phase velocity measurements in unconfined round jet laden with 100-110 micron glass beads with a bead-to-gas mass loading ratio of 0.2 (3 of 5).

d) Shear Stress Based on Axial and Radial Velocities

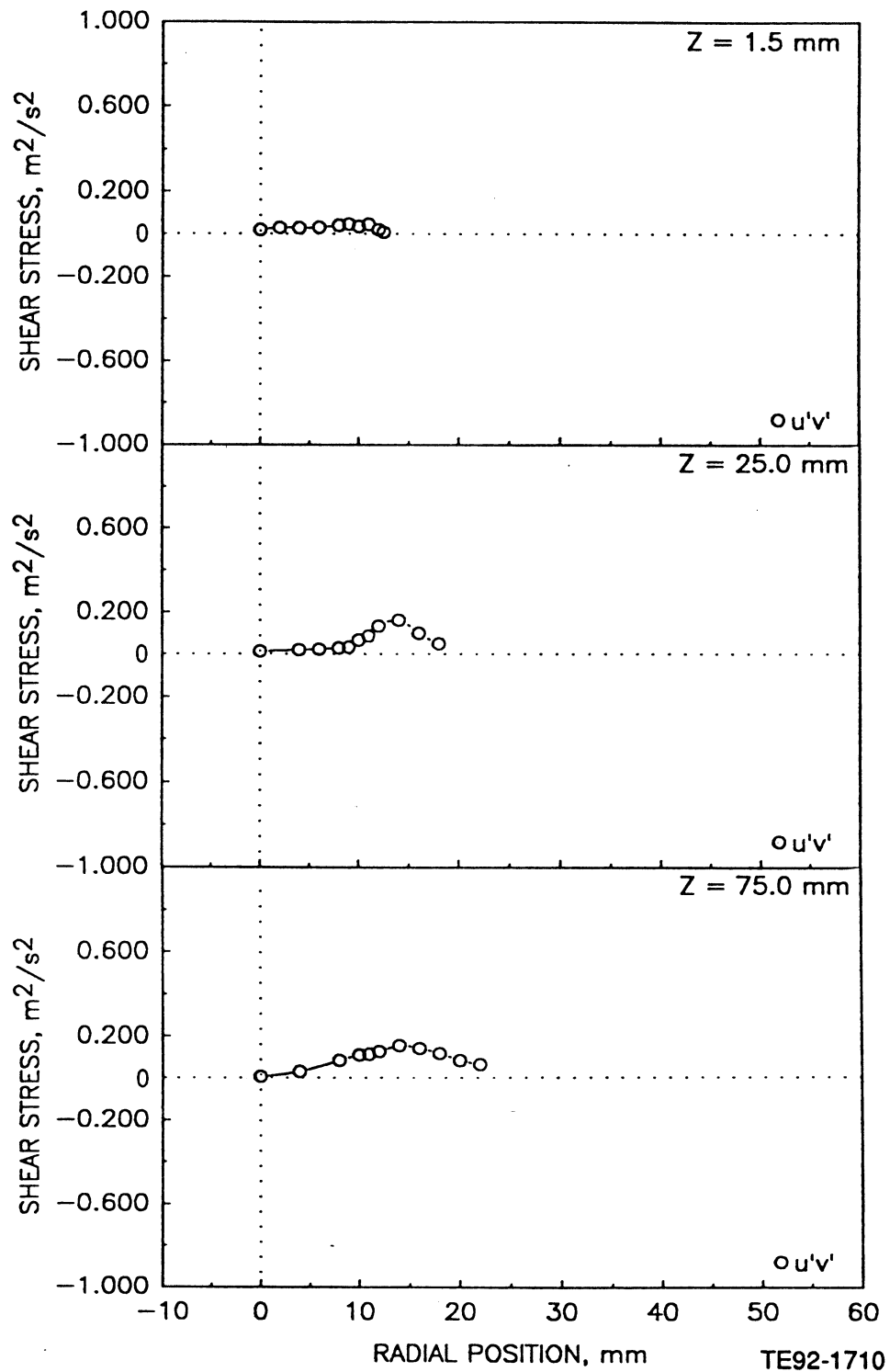


Figure 4.2.2-1. Radial profiles of gas phase velocity measurements in unconfined round jet laden with 100-110 micron glass beads with a bead-to-gas mass loading ratio of 0.2 (4 of 5).

e) Shear Stress Based on Axial and Azimuthal Velocities

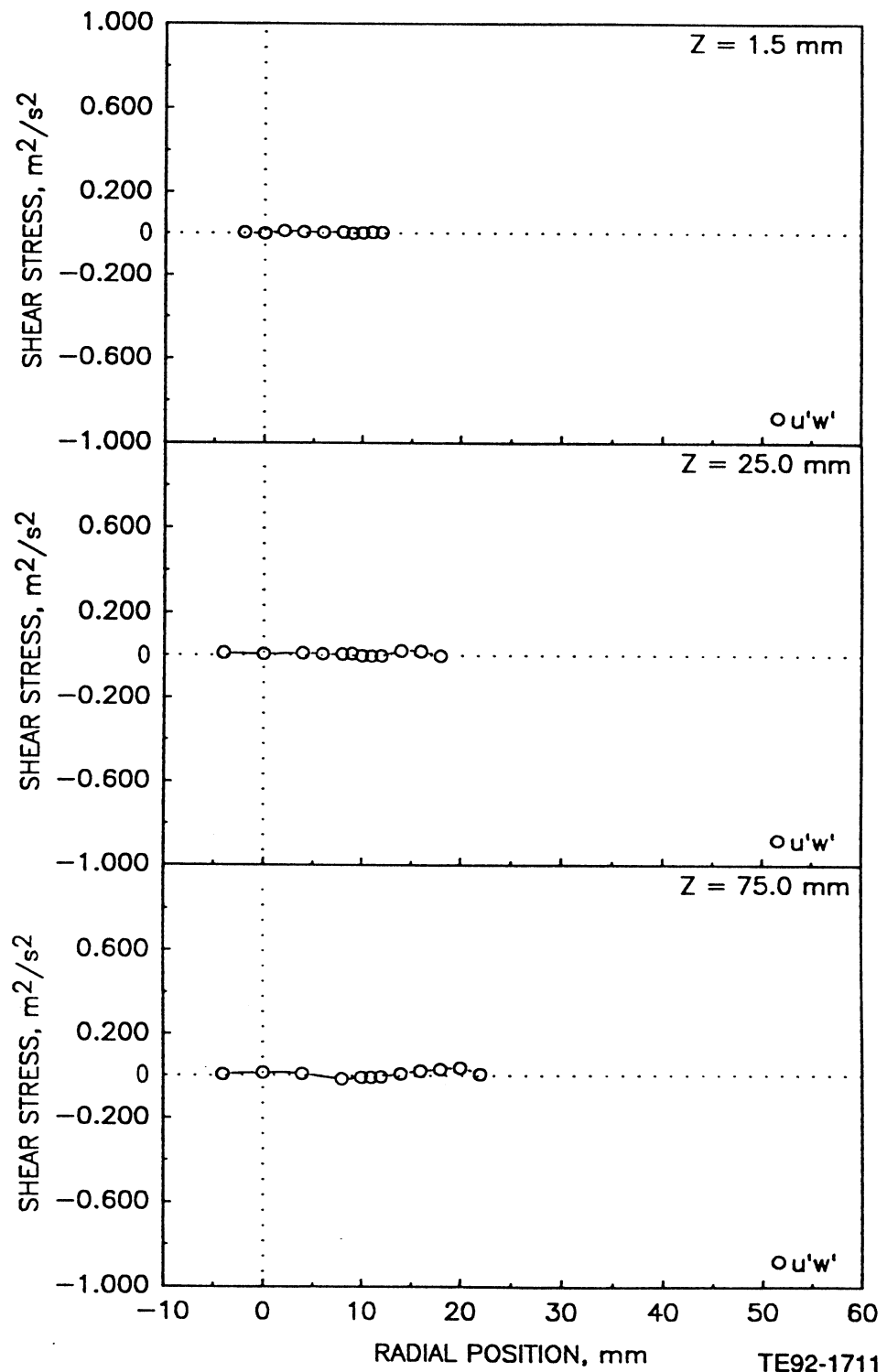


Figure 4.2.2-1. Radial profiles of gas phase velocity measurements in unconfined round jet laden with 100-110 micron glass beads with a bead-to-gas mass loading ratio of 0.2 (5 of 5).

a) Mean and Fluctuating Axial Velocities

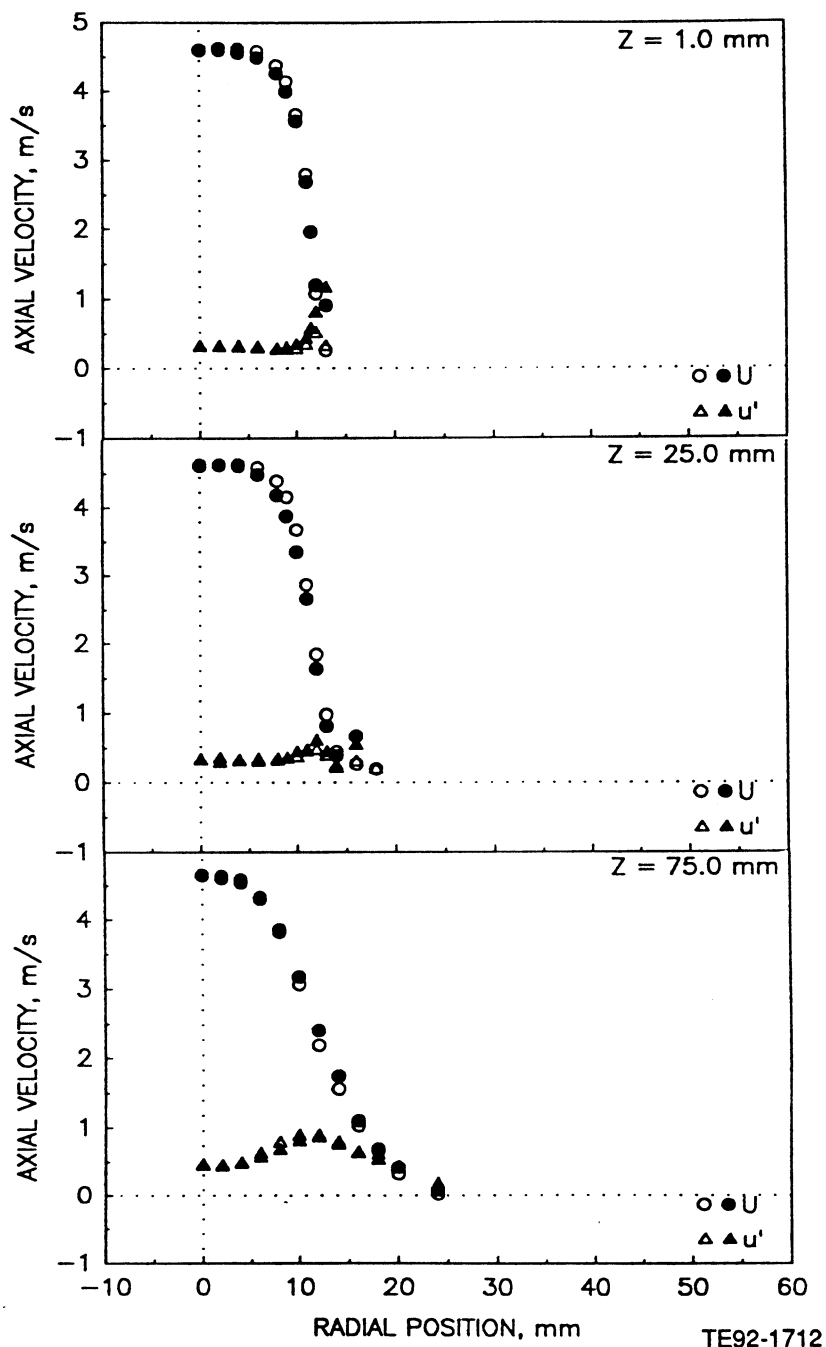


Figure 4.2.2-2. Radial profiles of gas phase velocity measurements in unconfined round jet laden with 100-110 micron glass beads with a bead-to-gas mass loading ratio of 1.0 (1 of 5).

b) Mean and Fluctuating Radial Velocities

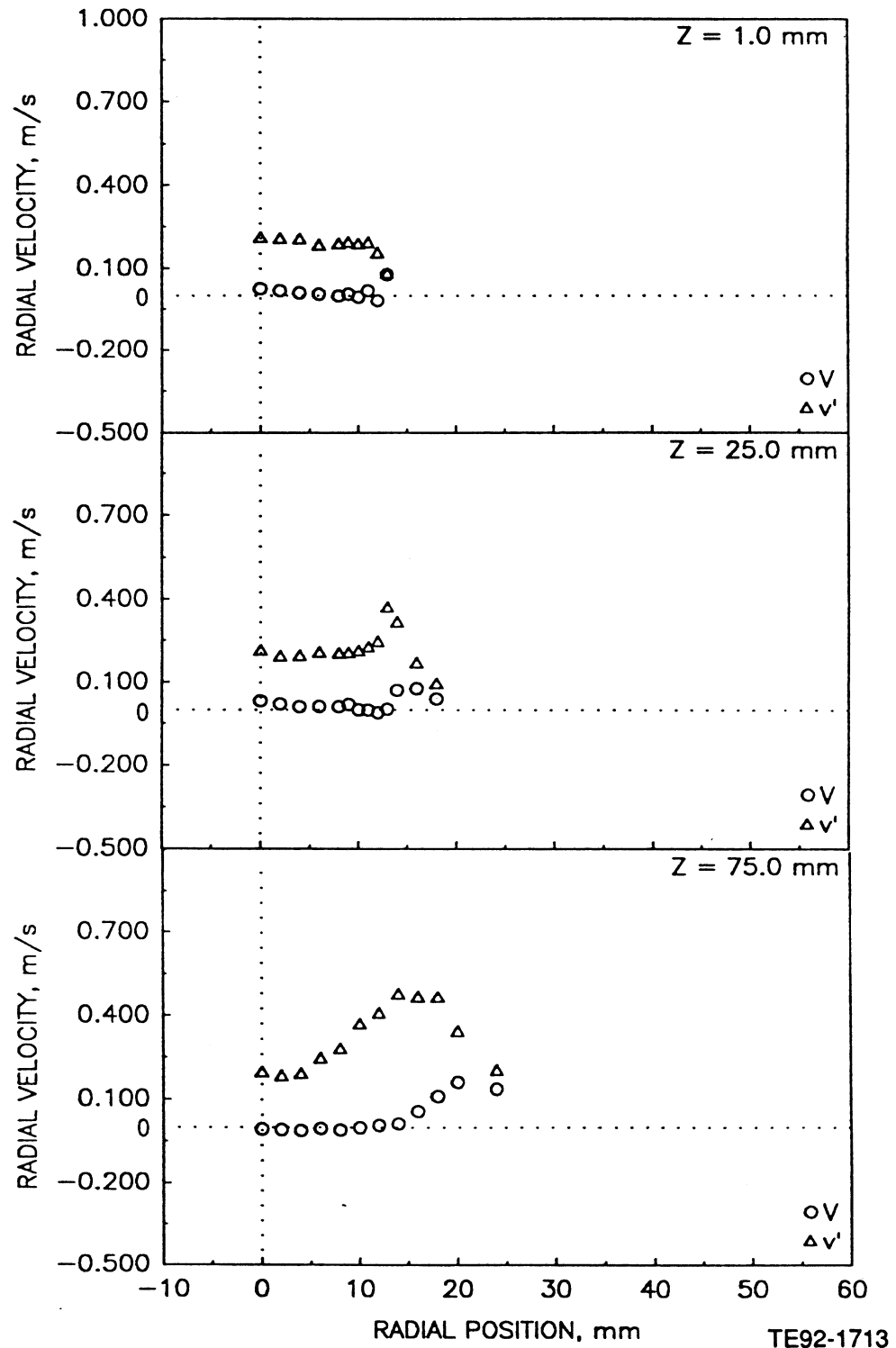
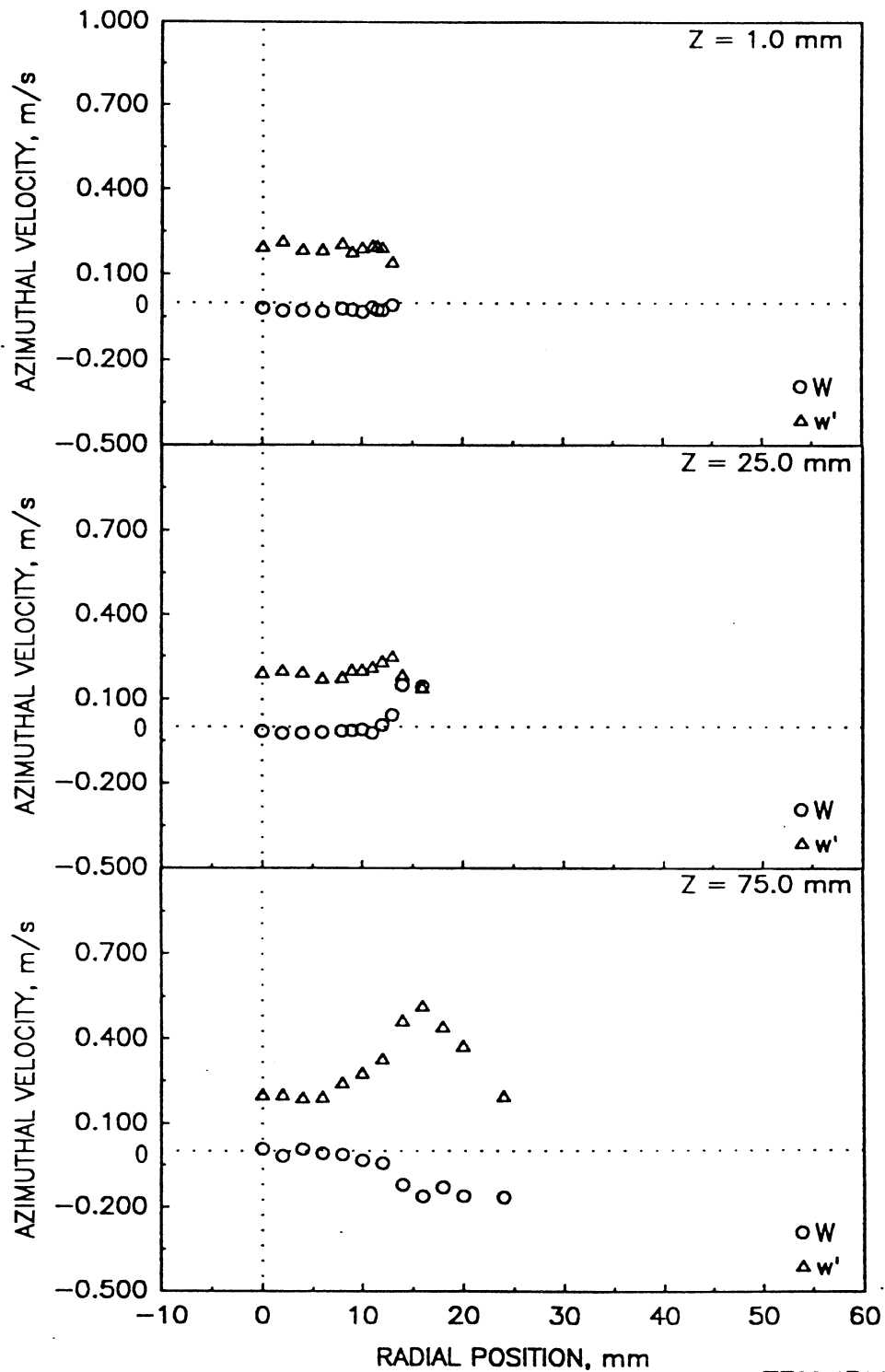


Figure 4.2.2-2. Radial profiles of gas phase velocity measurements in unconfined round jet laden with 100-110 micron glass beads with a bead-to-gas mass loading ratio of 1.0 (2 of 5).

c) Mean and Fluctuating Azimuthal Velocities



TE92-1714

Figure 4.2.2-2. Radial profiles of gas phase velocity measurements in unconfined round jet laden with 100-110 micron glass beads with a bead-to-gas mass loading ratio of 1.0 (3 of 5).

d) Shear Stress Based on Axial and Radial Velocities

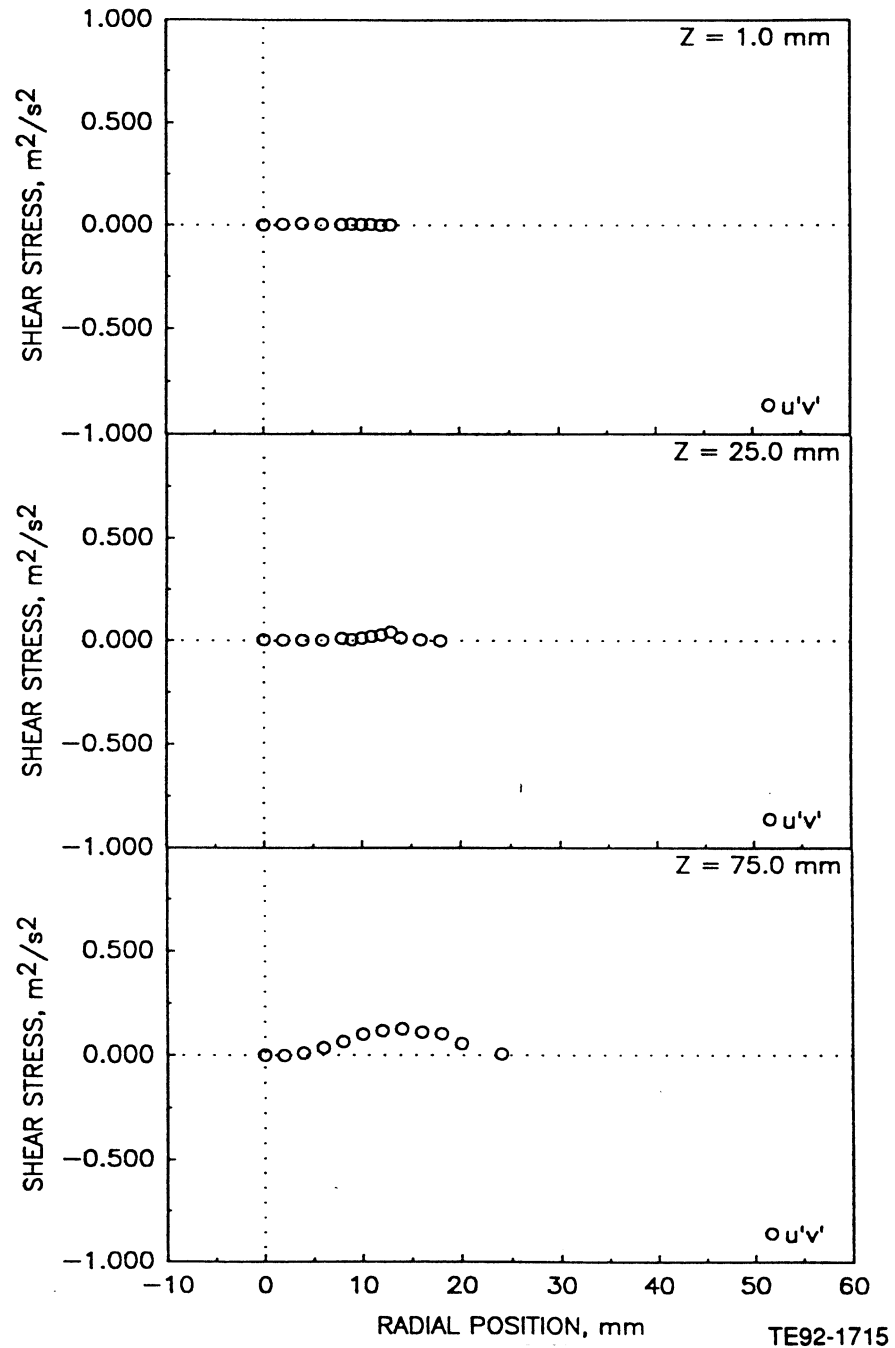


Figure 4.2.2-2. Radial profiles of gas phase velocity measurements in unconfined round jet laden with 100-110 micron glass beads with a bead-to-gas mass loading ratio of 1.0 (4 of 5).

e) Shear Stress Based on Axial and Azimuthal Velocities

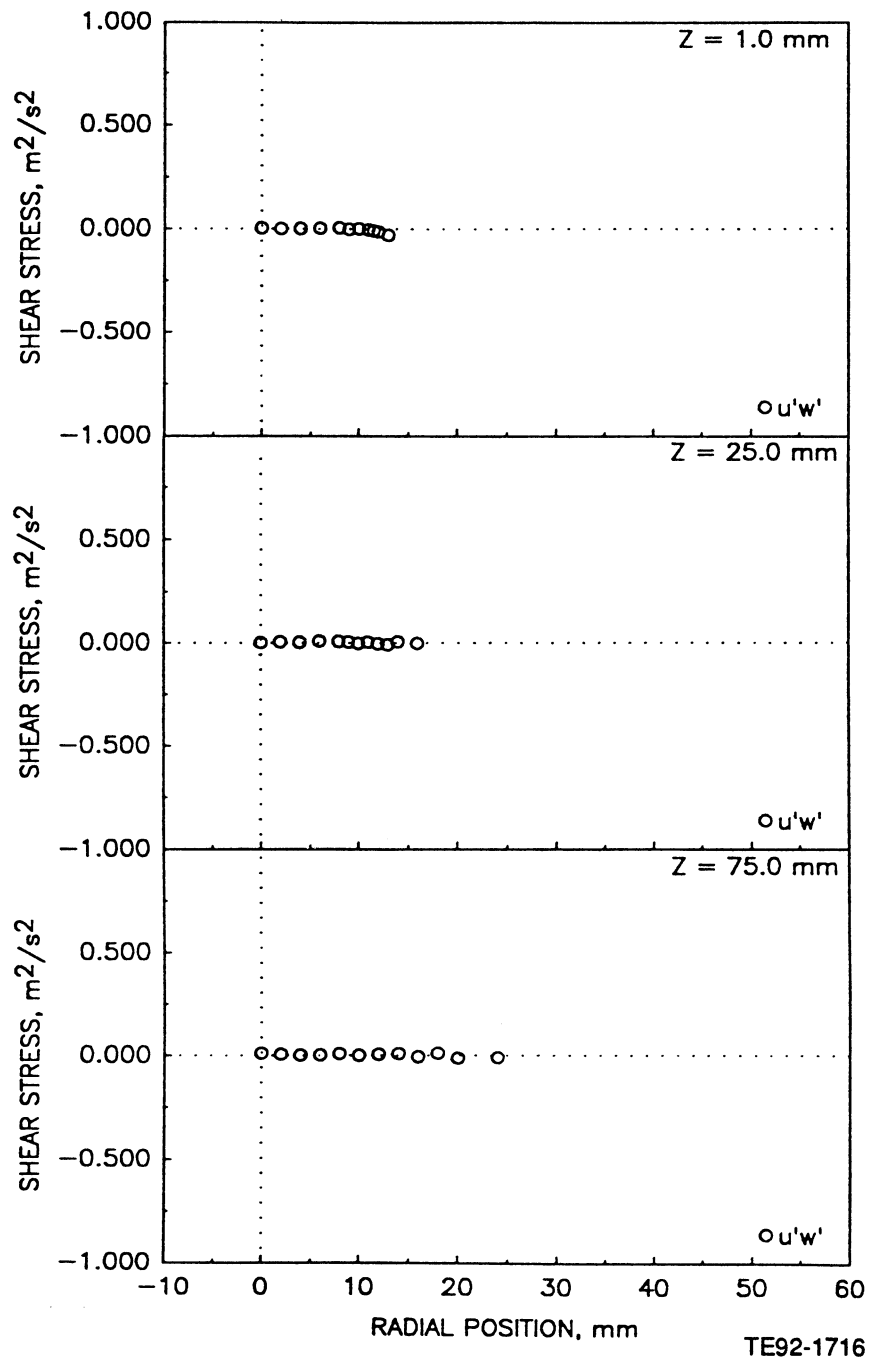


Figure 4.2.2-2. Radial profiles of gas phase velocity measurements in unconfined round jet laden with 100-110 micron glass beads with a bead-to-gas mass loading ratio of 1.0 (5 of 5).

a) Mean and Fluctuating Axial Velocities

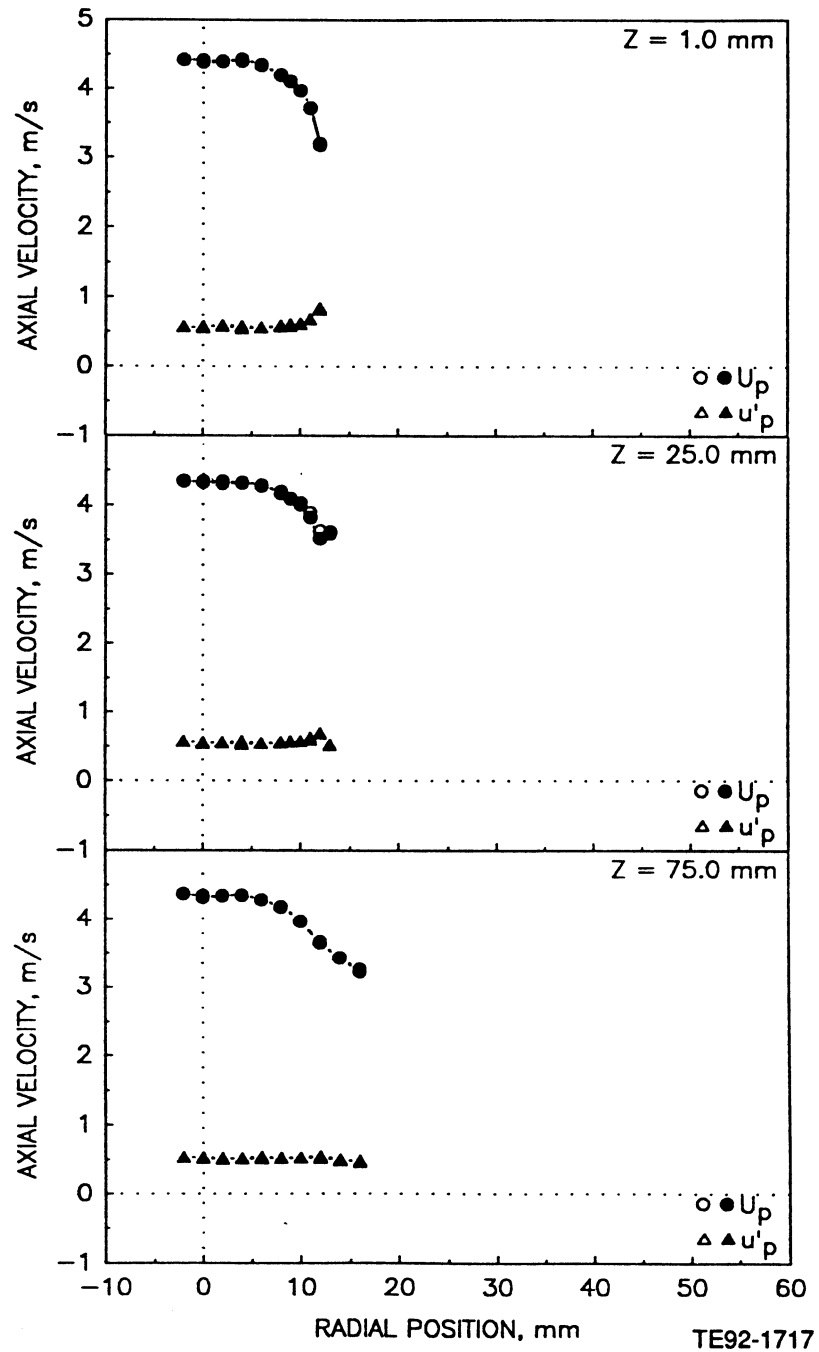


Figure 4.2.3-1. Radial profiles of particle measurements in unconfined round jet laden with 100-110 micron glass beads with a bead-to-gas mass loading ratio of 0.2 (1 of 5).

b) Mean and Fluctuating Radial Velocities

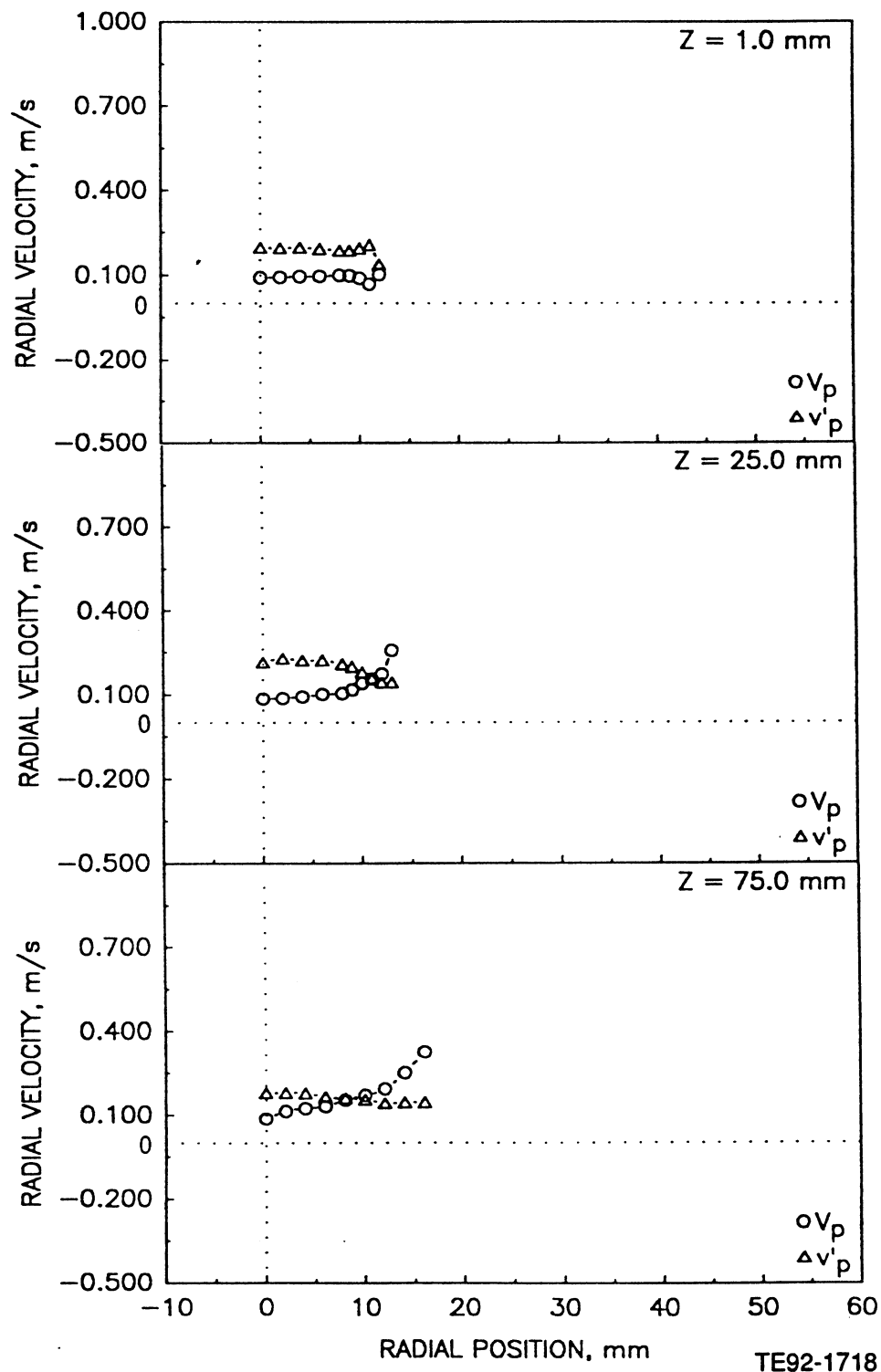


Figure 4.2.3-1. Radial profiles of particle measurements in unconfined round jet laden with 100-110 micron glass beads with a bead-to-gas mass loading ratio of 0.2 (2 of 5).

c) Mean and Fluctuating Azimuthal Velocities

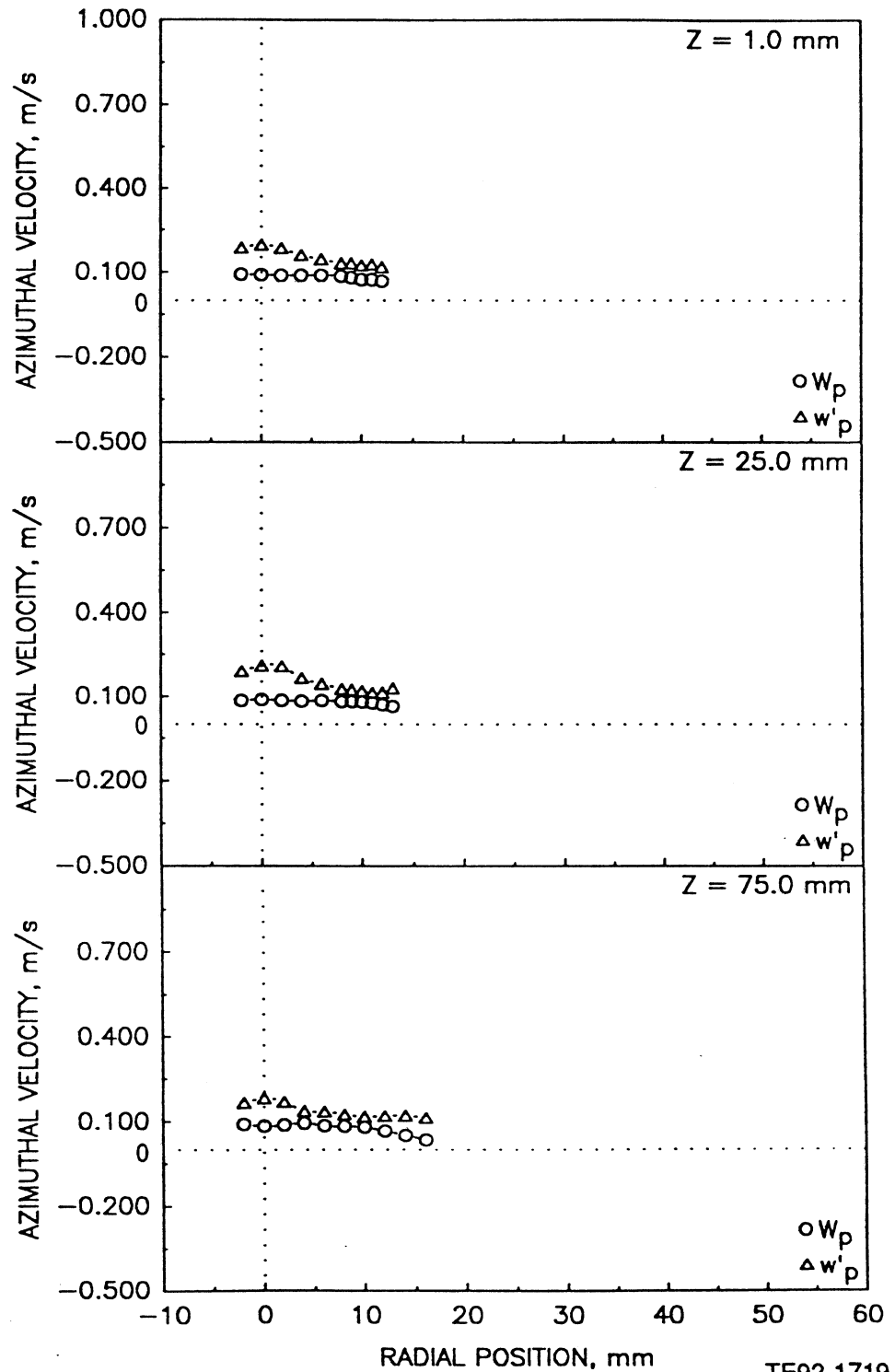


Figure 4.2.3-1. Radial profiles of particle measurements in unconfined round jet laden with 100-110 micron glass beads with a bead-to-gas mass loading ratio of 0.2 (3 of 5).

d) Particle Velocity Correlation Based on Axial and Radial Components

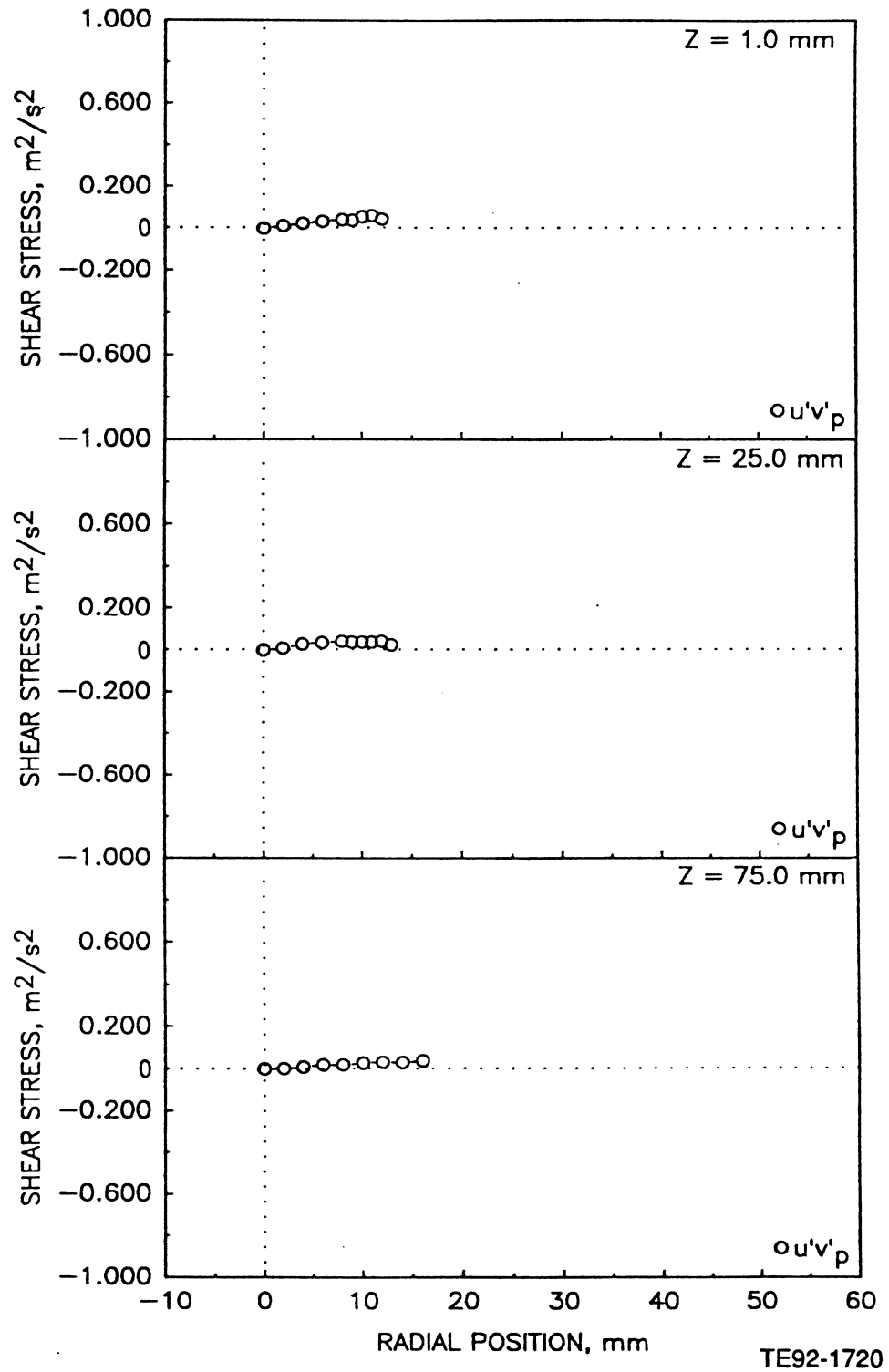


Figure 4.2.3-1. Radial profiles of particle measurements in unconfined round jet laden with 100-110 micron glass beads with a bead-to-gas mass loading ratio of 0.2 (4 of 5).

e) Particle Data Rate

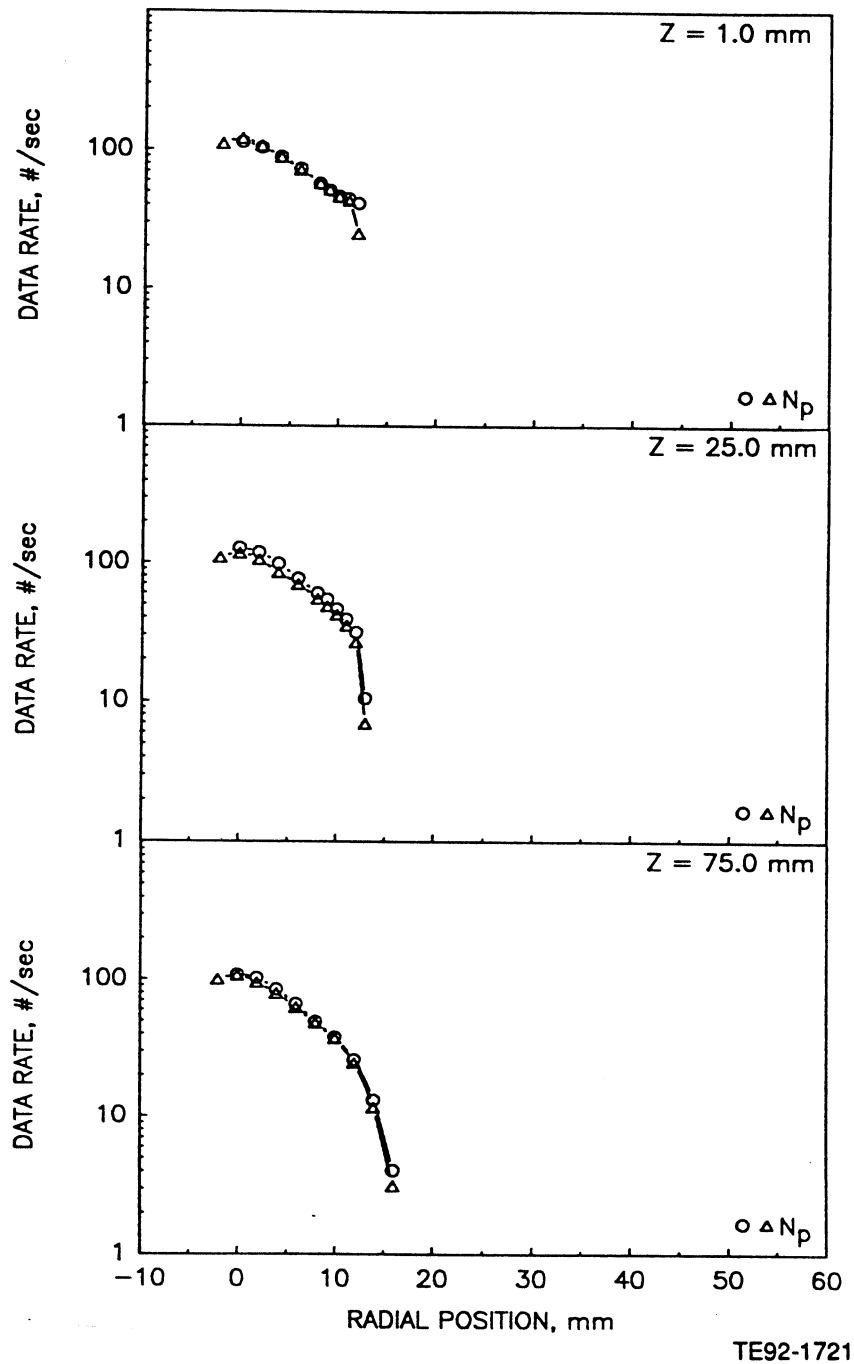


Figure 4.2.3-1. Radial profiles of particle measurements in unconfined round jet laden with 100-110 micron glass beads with a bead-to-gas mass loading ratio of 0.2 (5 of 5).

a) Mean and Fluctuating Axial Velocities

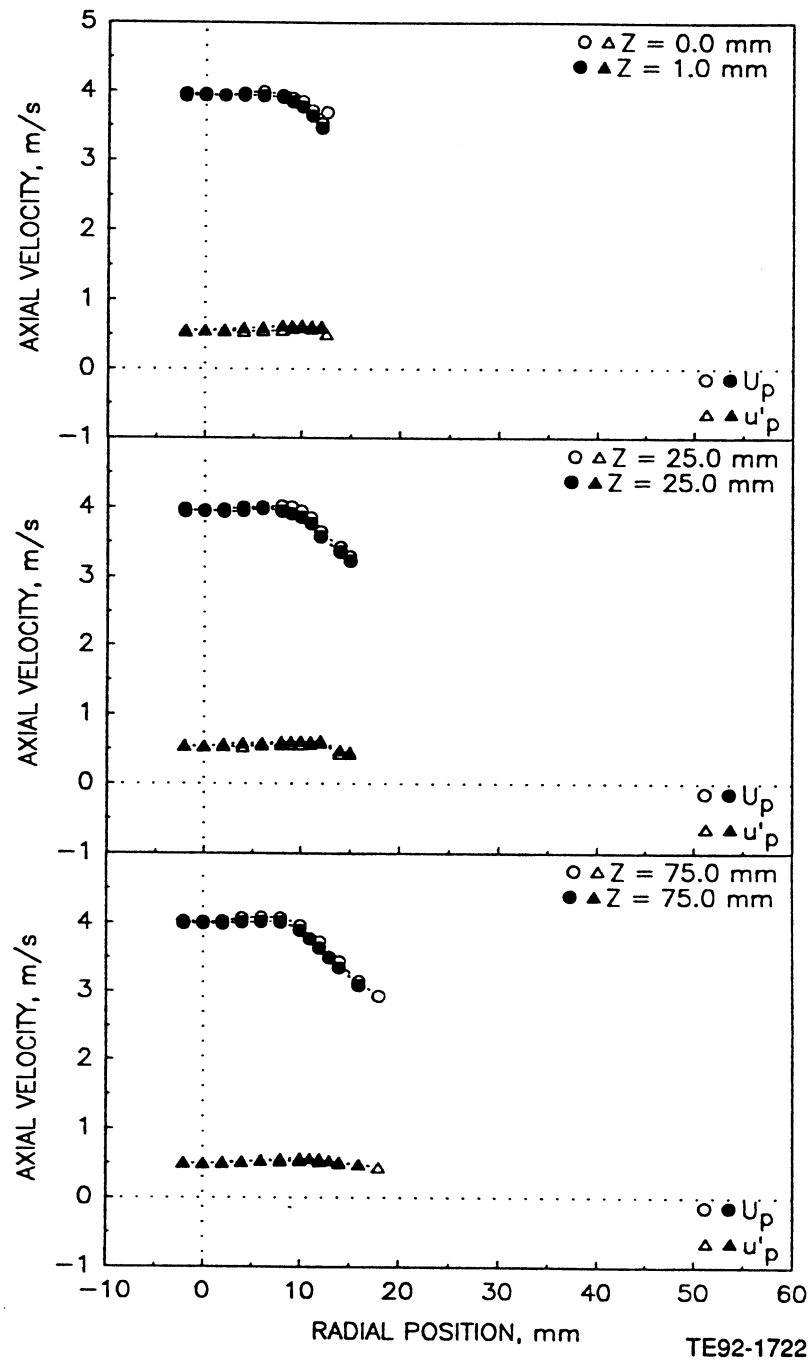


Figure 4.2.3-2. Radial profiles of particle measurements in unconfined round jet laden with 100-110 micron glass beads with a bead-to-gas mass loading ratio of 1.0 (1 of 5).

b) Mean and Fluctuating Radial Velocities

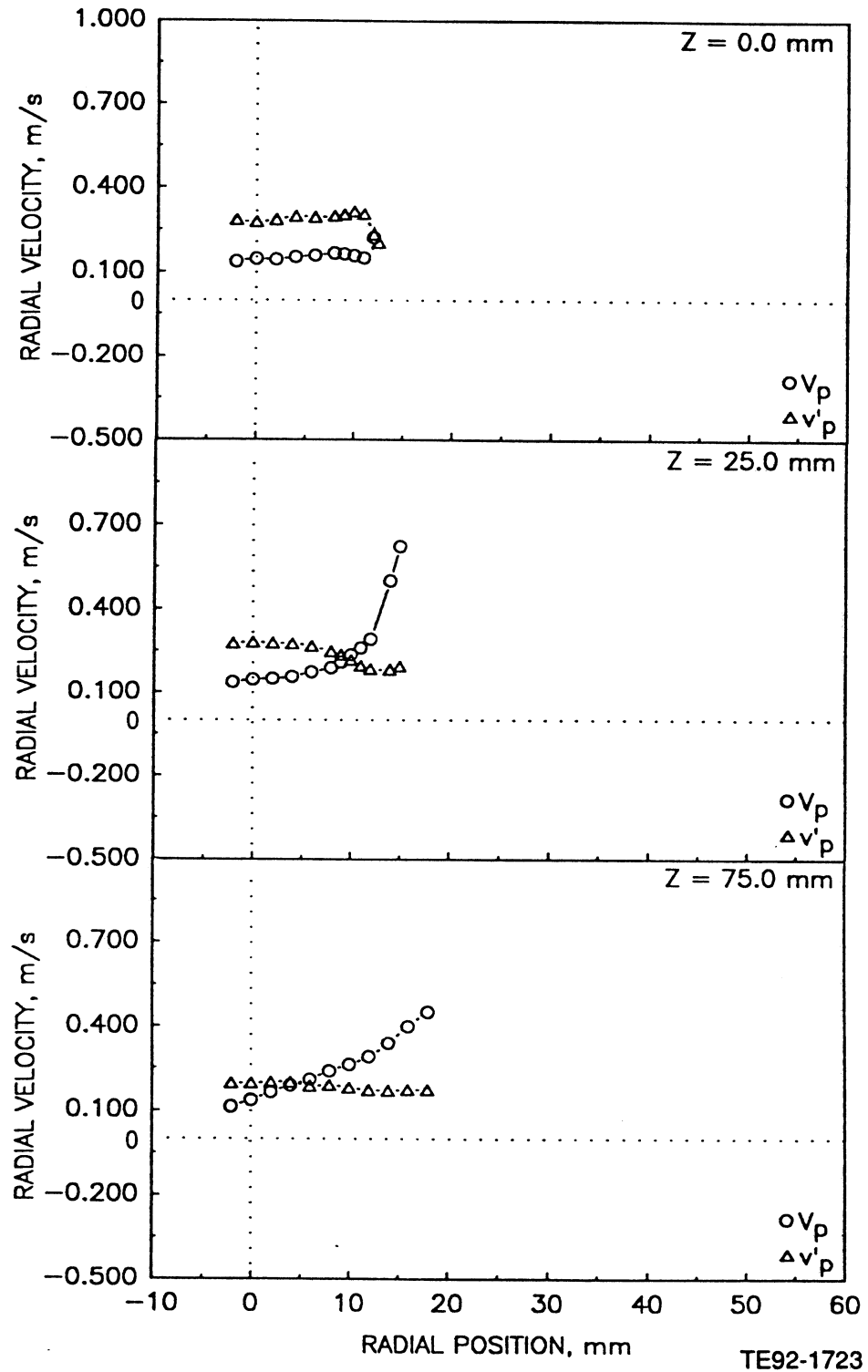


Figure 4.2.3-2. Radial profiles of particle measurements in unconfined round jet laden with 100-110 micron glass beads with a bead-to-gas mass loading ratio of 1.0 (2 of 5).

c) Mean and Fluctuating Azimuthal Velocities

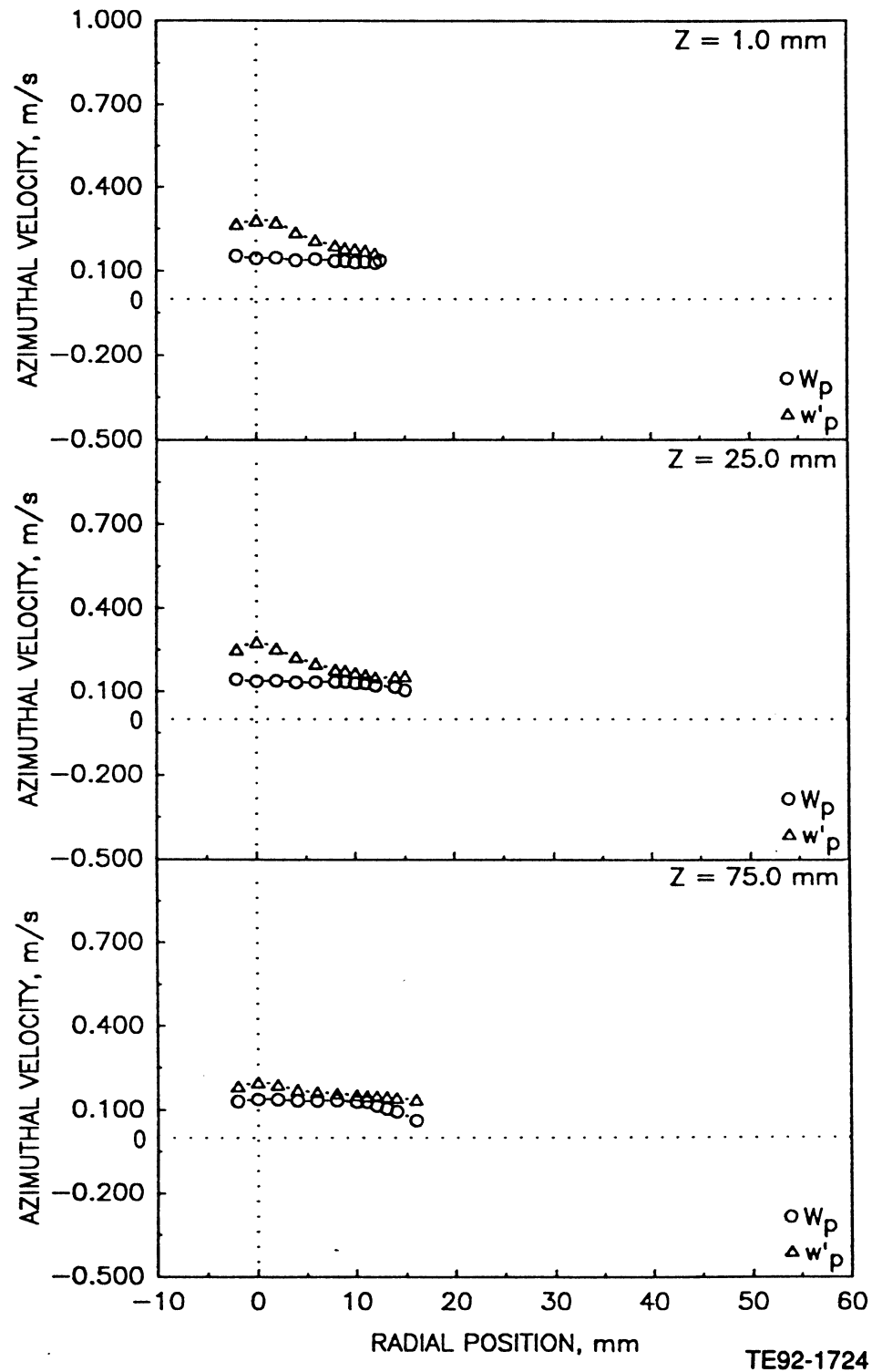


Figure 4.2.3-2. Radial profiles of particle measurements in unconfined round jet laden with 100-110 micron glass beads with a bead-to-gas mass loading ratio of 1.0 (3 of 5).

d) Particle Velocity Correlation Based on Axial and Radial Components

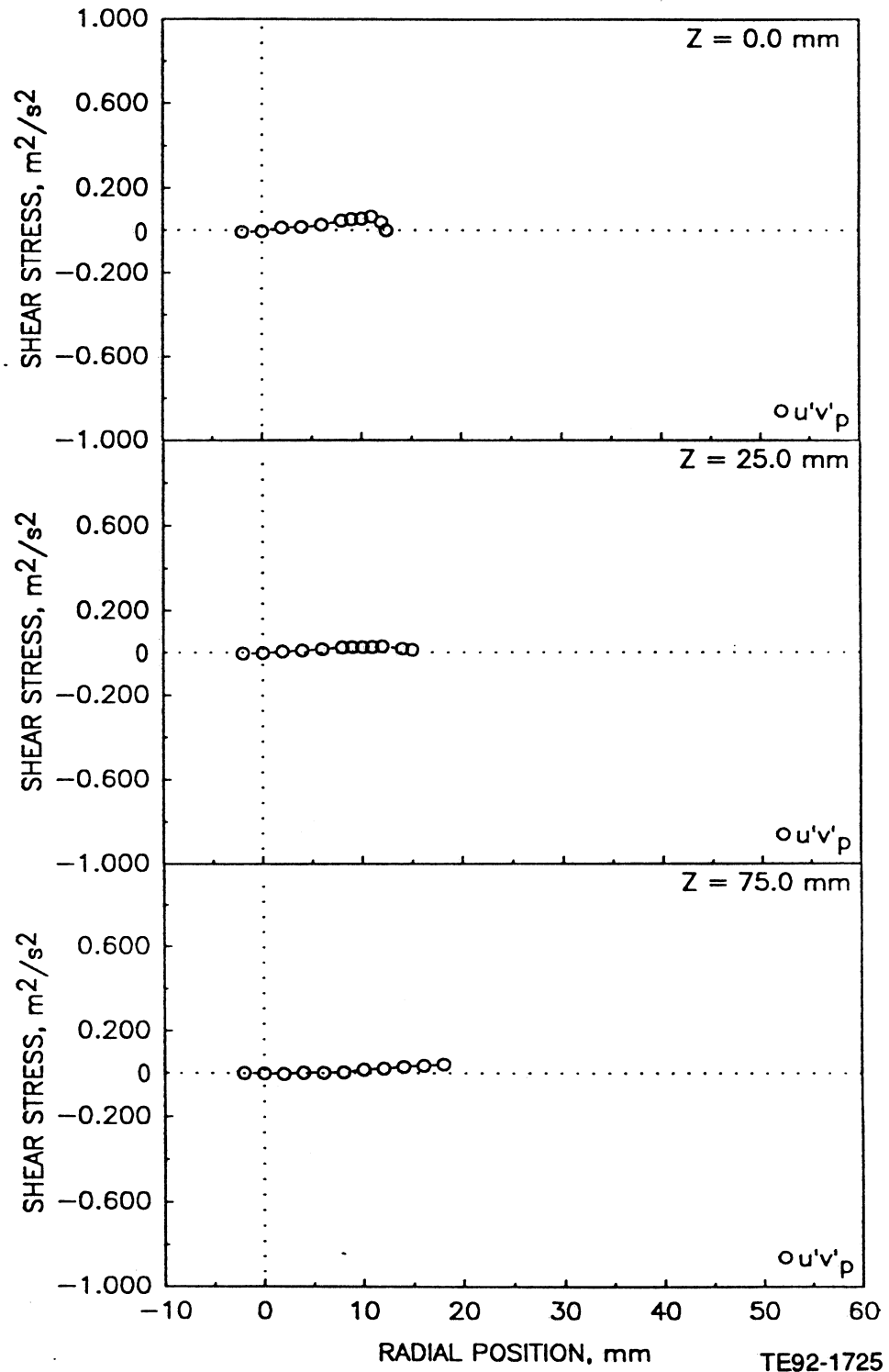


Figure 4.2.3-2. Radial profiles of particle measurements in unconfined round jet laden with 100-110 micron glass beads with a bead-to-gas mass loading ratio of 1.0 (4 of 5).

e) Particle Data Rate

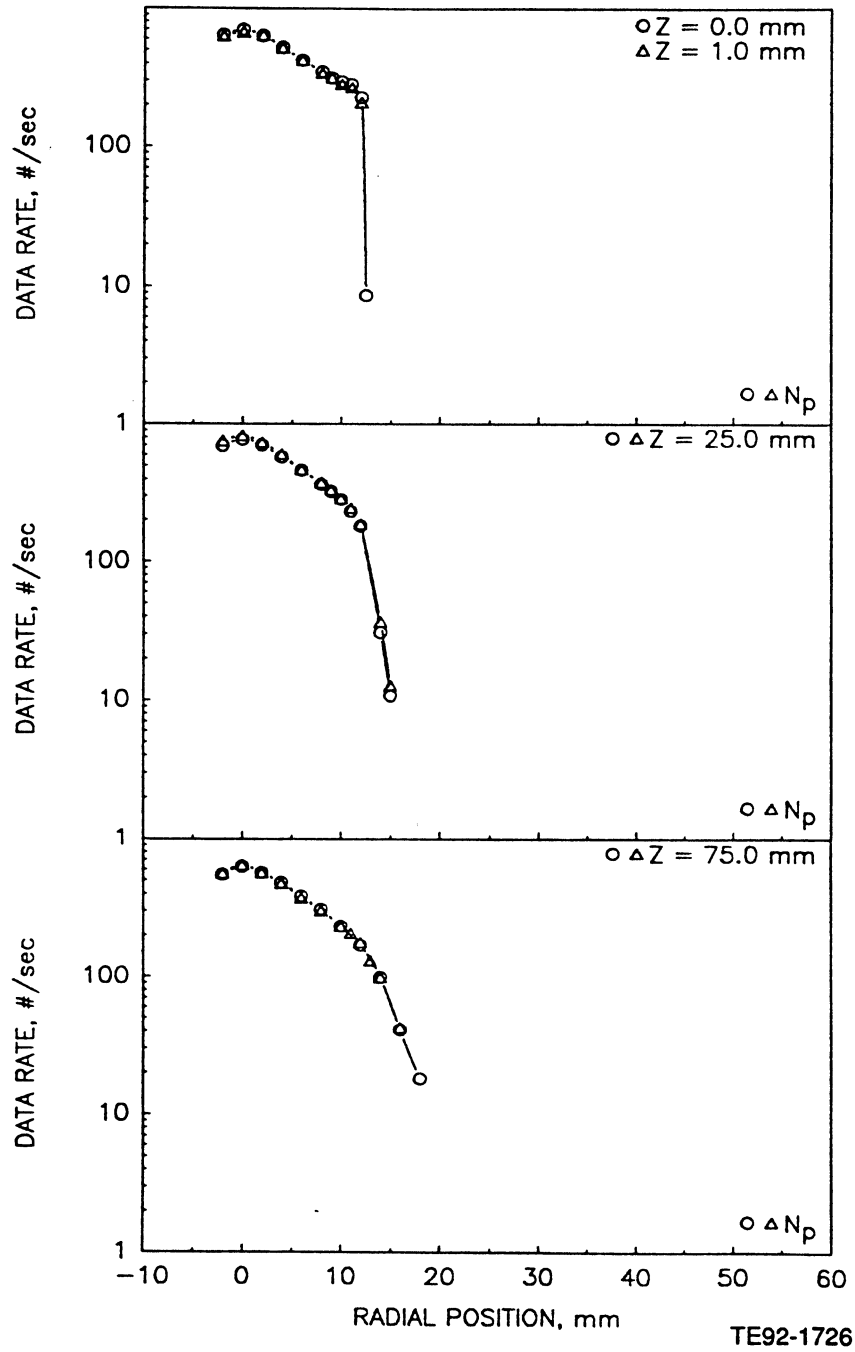


Figure 4.2.3-2. Radial profiles of particle measurements in unconfined round jet laden with 100-110 micron glass beads with a bead-to-gas mass loading ratio of 1.0 (5 of 5).

a) Mean and Fluctuating Axial Velocities

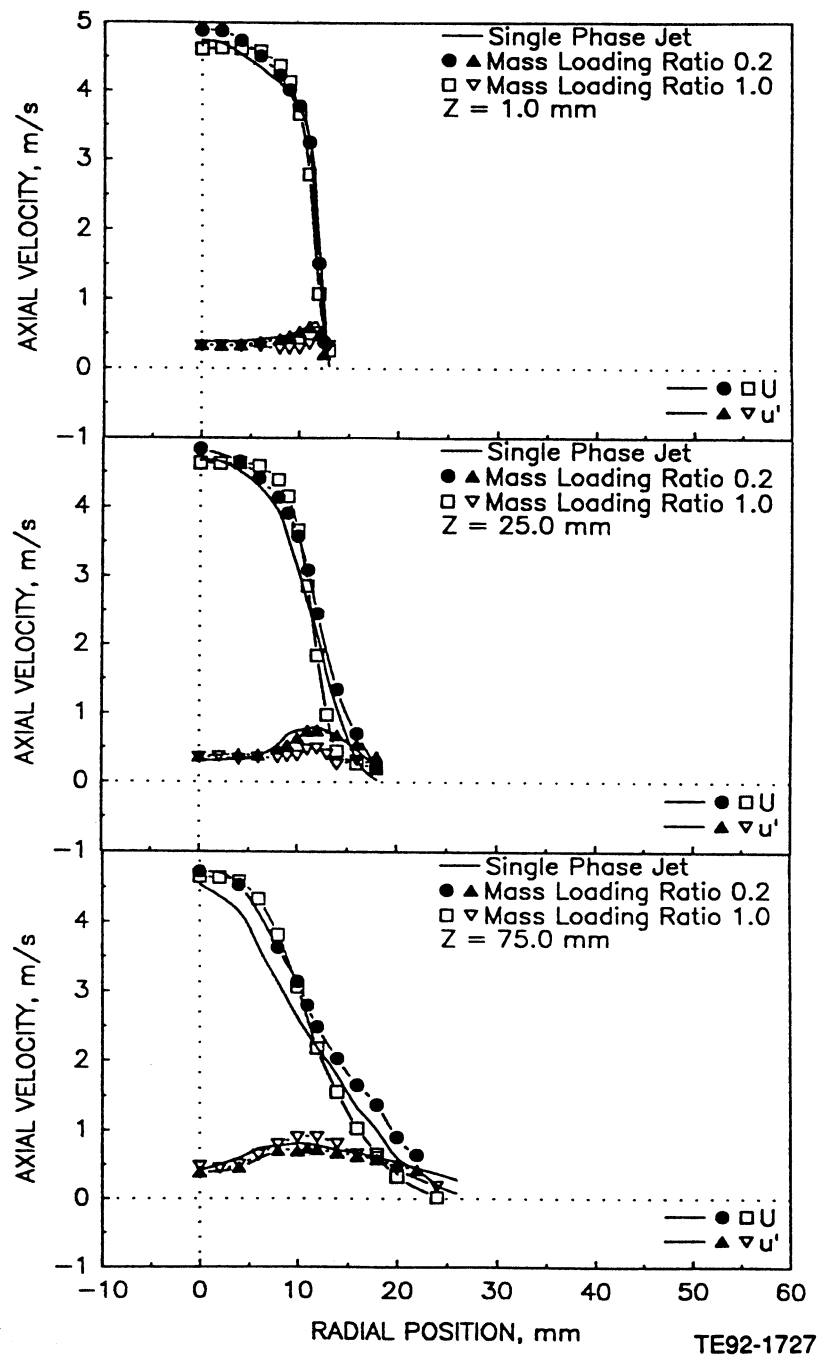


Figure 4.2.4-1. Comparison of gas phase velocities and shear stress in (1) unconfined single-phase round jet, (2) unconfined round jet laden with 100-110 micron particles at mass loading of 0.2, and (3) unconfined round jet laden with 100-110 micron particles at mass loading ratio of 1.0 (1 of 2).

b) Shear Stress Based on Axial and Radial Components

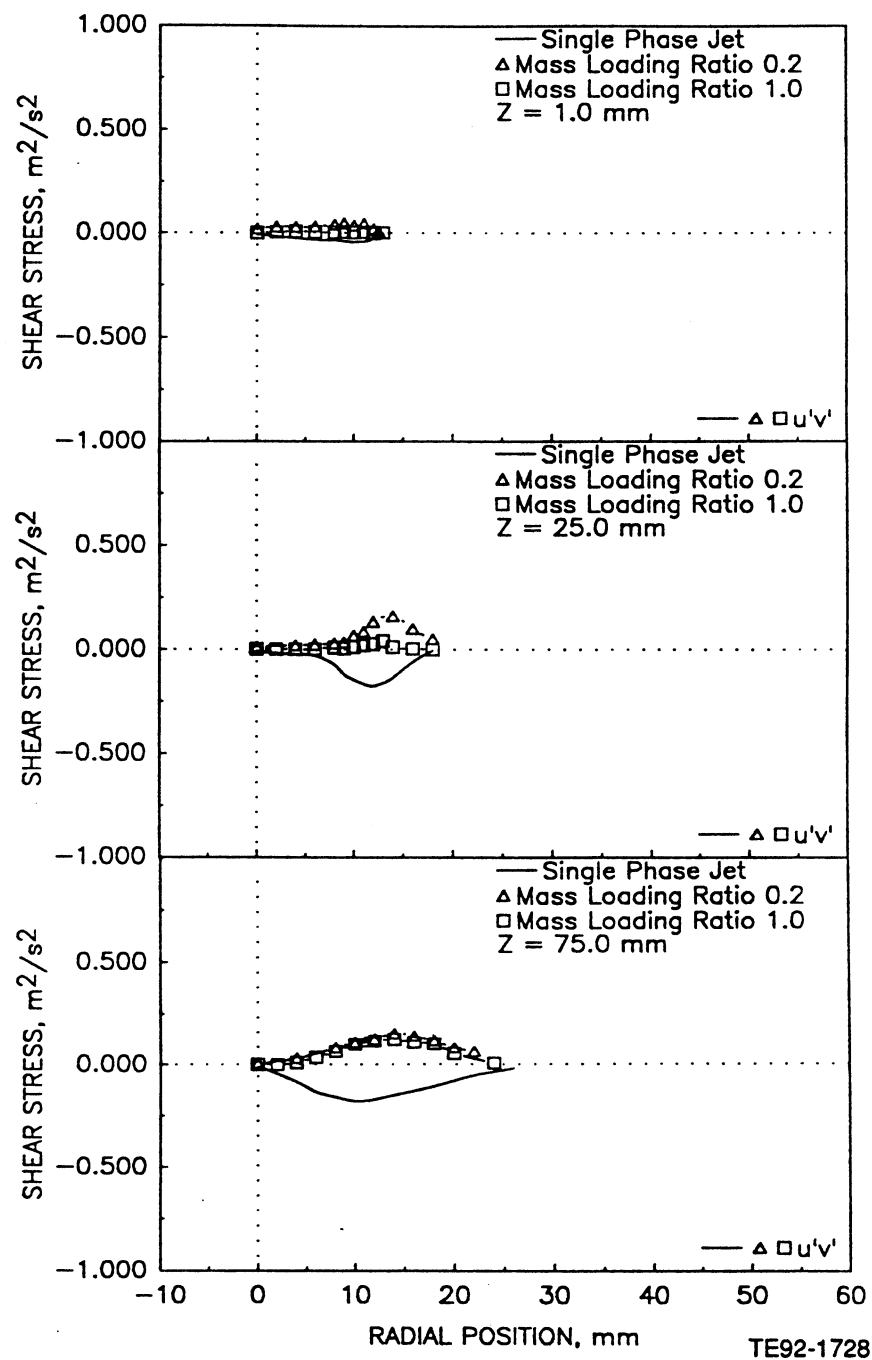


Figure 4.2.4-1. Comparison of gas phase velocities and shear stress in (1) unconfined single-phase round jet, (2) unconfined round jet laden with 100-110 micron particles at mass loading of 0.2, and (3) unconfined round jet laden with 100-110 micron particles at mass loading ratio of 1.0 (2 of 2).

a) Mean and Fluctuating Velocities

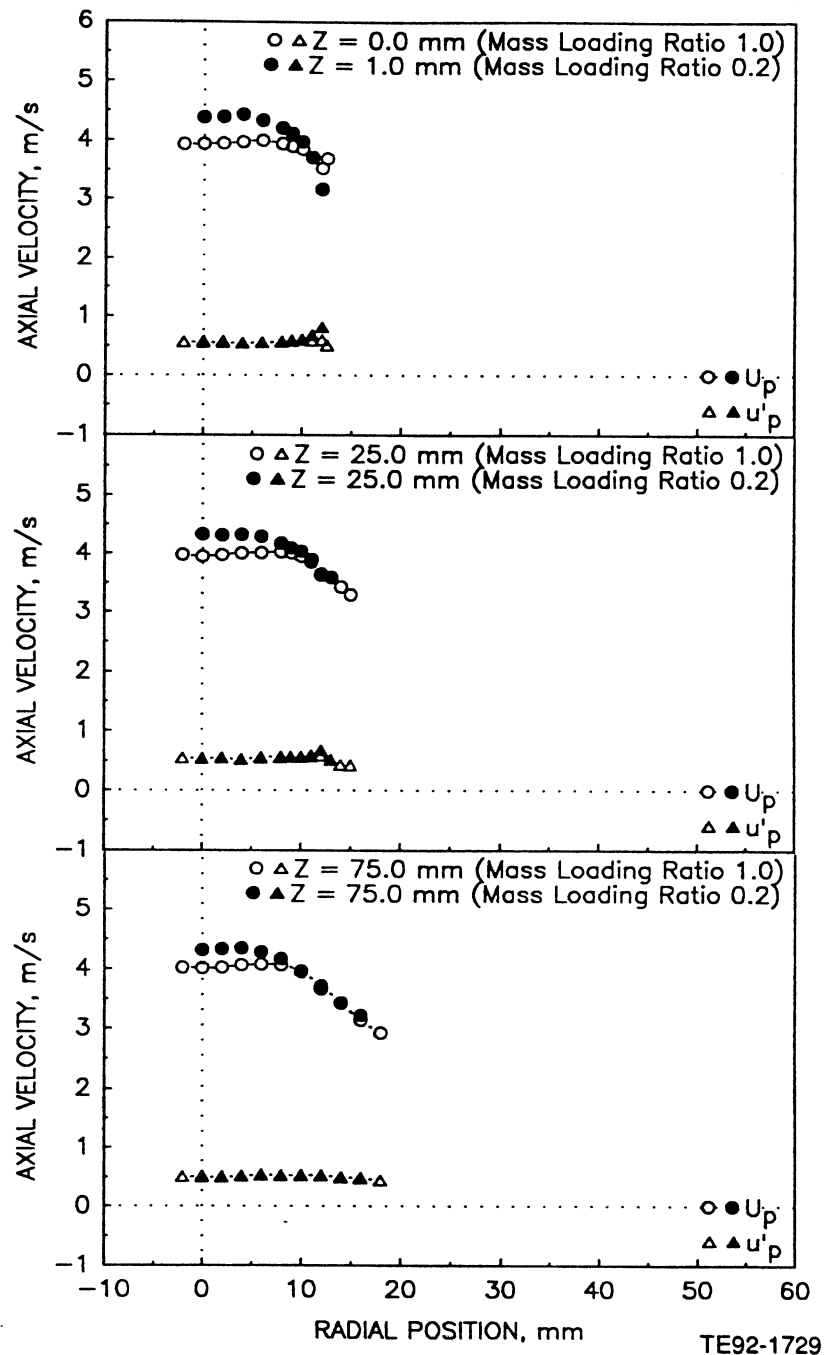


Figure 4.2.4-2. Comparison of particle velocities and data rate in unconfined round jet laden with particles at a mass loading ratio of 0.2 and 1.0 (1 of 2).

b) Data Rate

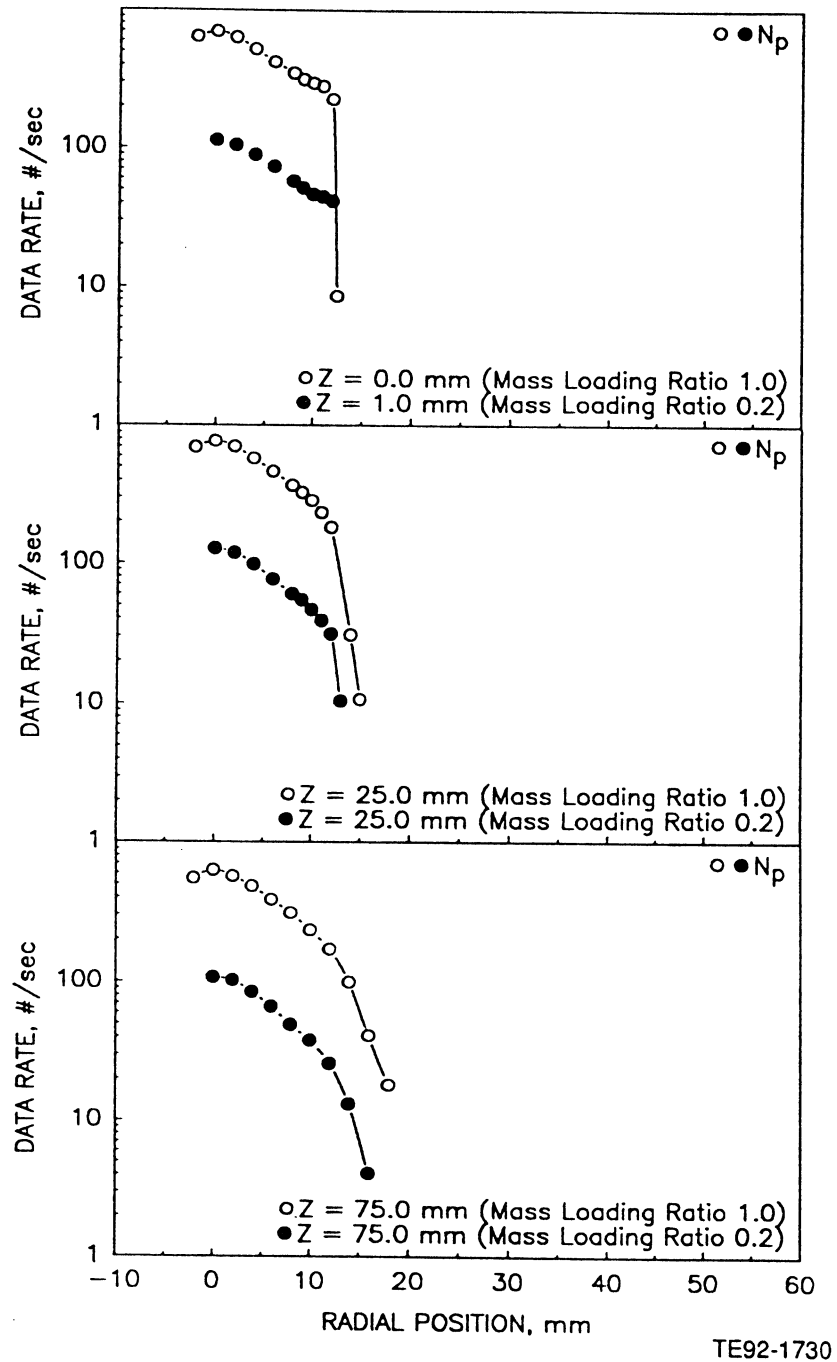


Figure 4.2.4-2. Comparison of particle velocities and data rate in unconfined round jet laden with particles at a mass loading ratio of 0.2 and 1.0 (2 of 2).

a) Mean and Fluctuating Axial Velocities

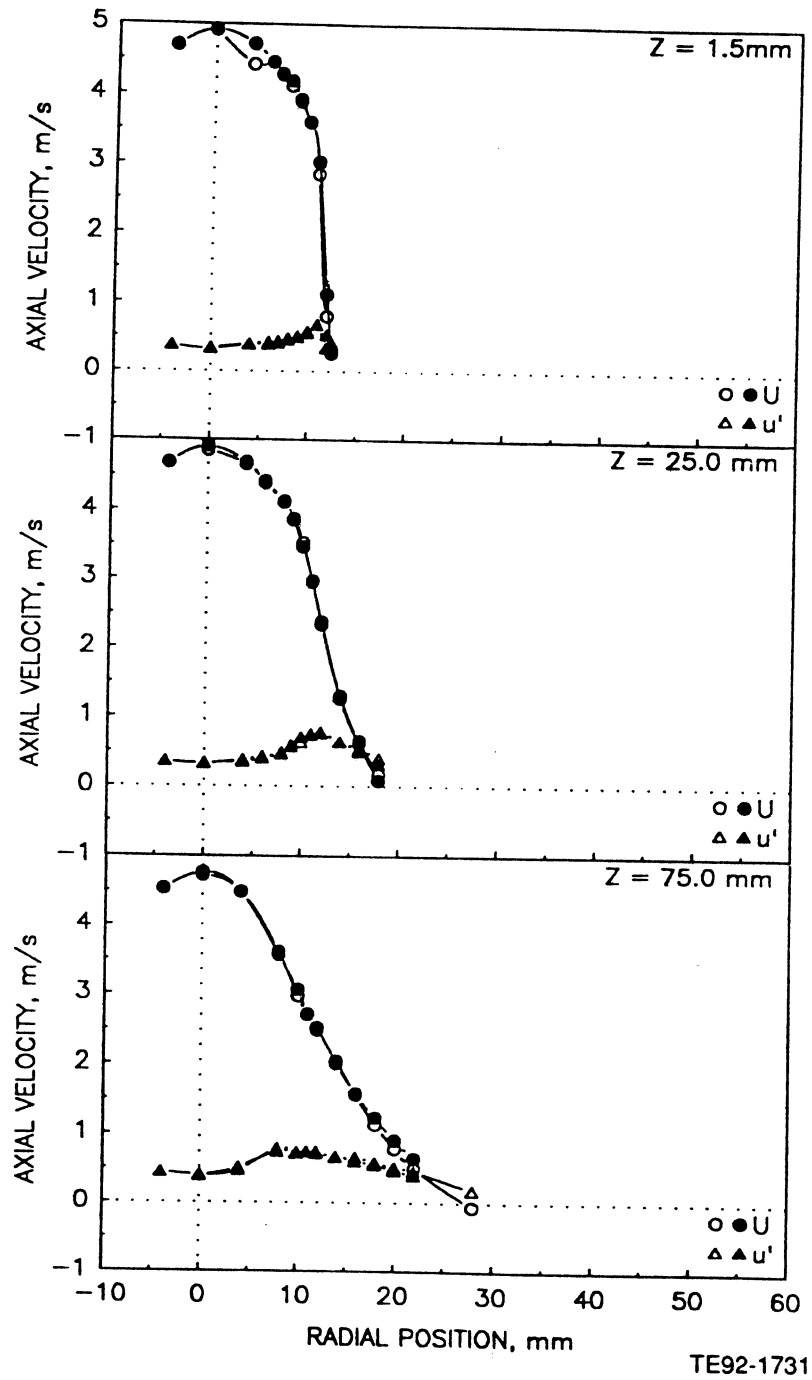


Figure 4.2.5-1. Radial profiles of gas phase velocity measurements in unconfined round jet laden with equal number of 20-30 micron and 100-110 micron glass beads with a bead-to-gas mass loading ratio of 0.2 (1 of 5).

b) Mean and Fluctuating Radial Velocities

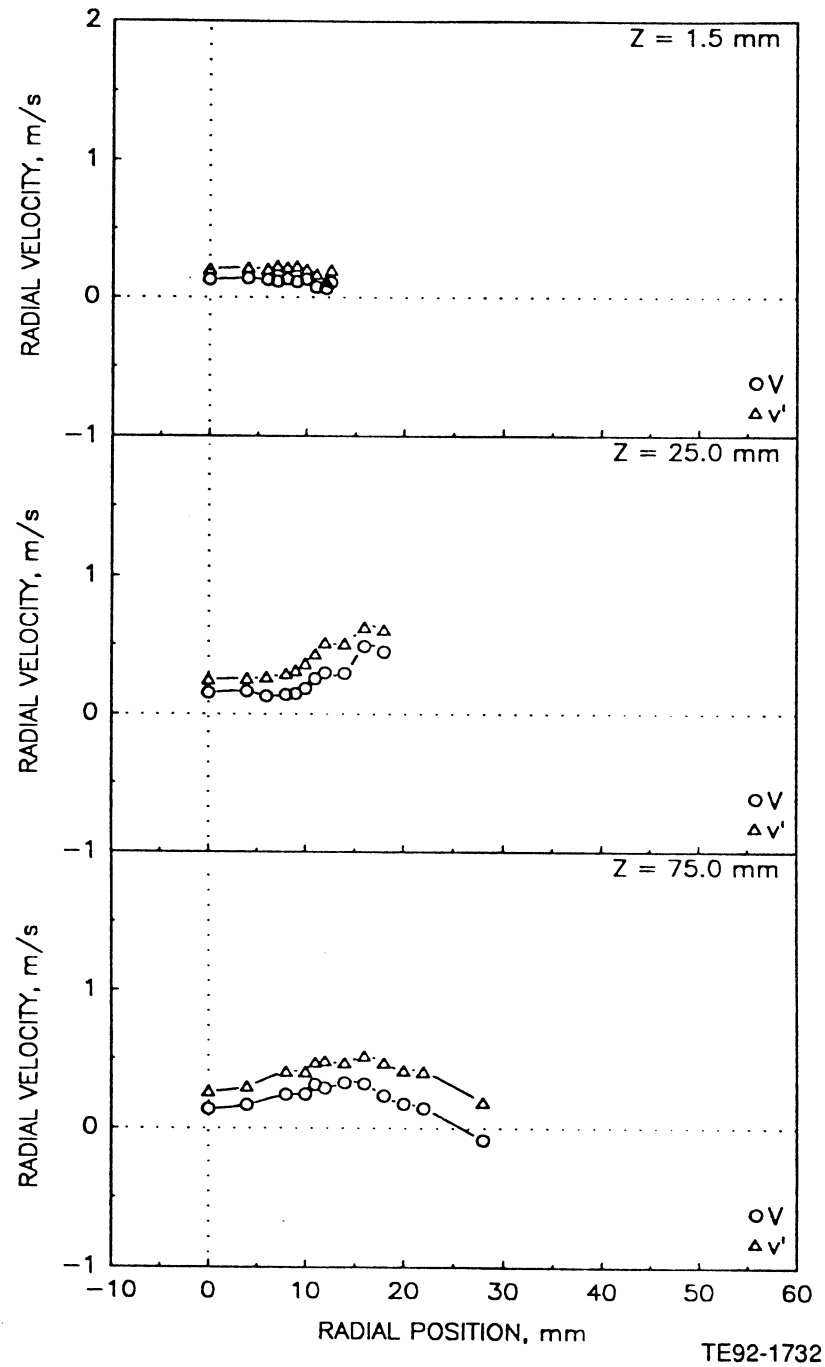


Figure 4.2.5-1. Radial profiles of gas phase velocity measurements in unconfined round jet laden with equal number of 20-30 micron and 100-110 micron glass beads with a bead-to-gas mass loading ratio of 0.2 (2 of 5).

c) Mean and Fluctuating Azimuthal Velocities

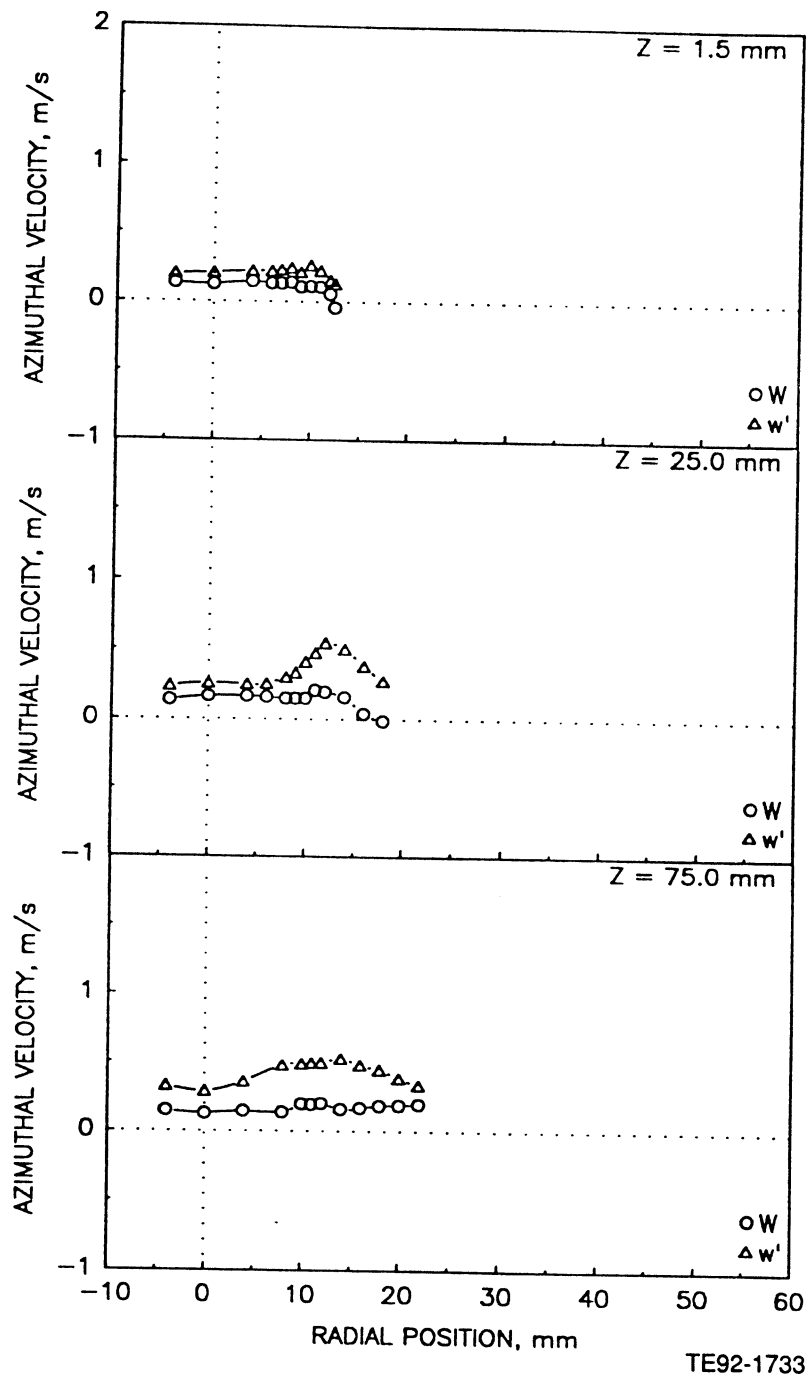


Figure 4.2.5-1. Radial profiles of gas phase velocity measurements in unconfined round jet laden with equal number of 20-30 micron and 100-110 micron glass beads with a bead-to-gas mass loading ratio of 0.2 (3 of 5).

d) Shear Stress Based on Axial and Radial Velocities

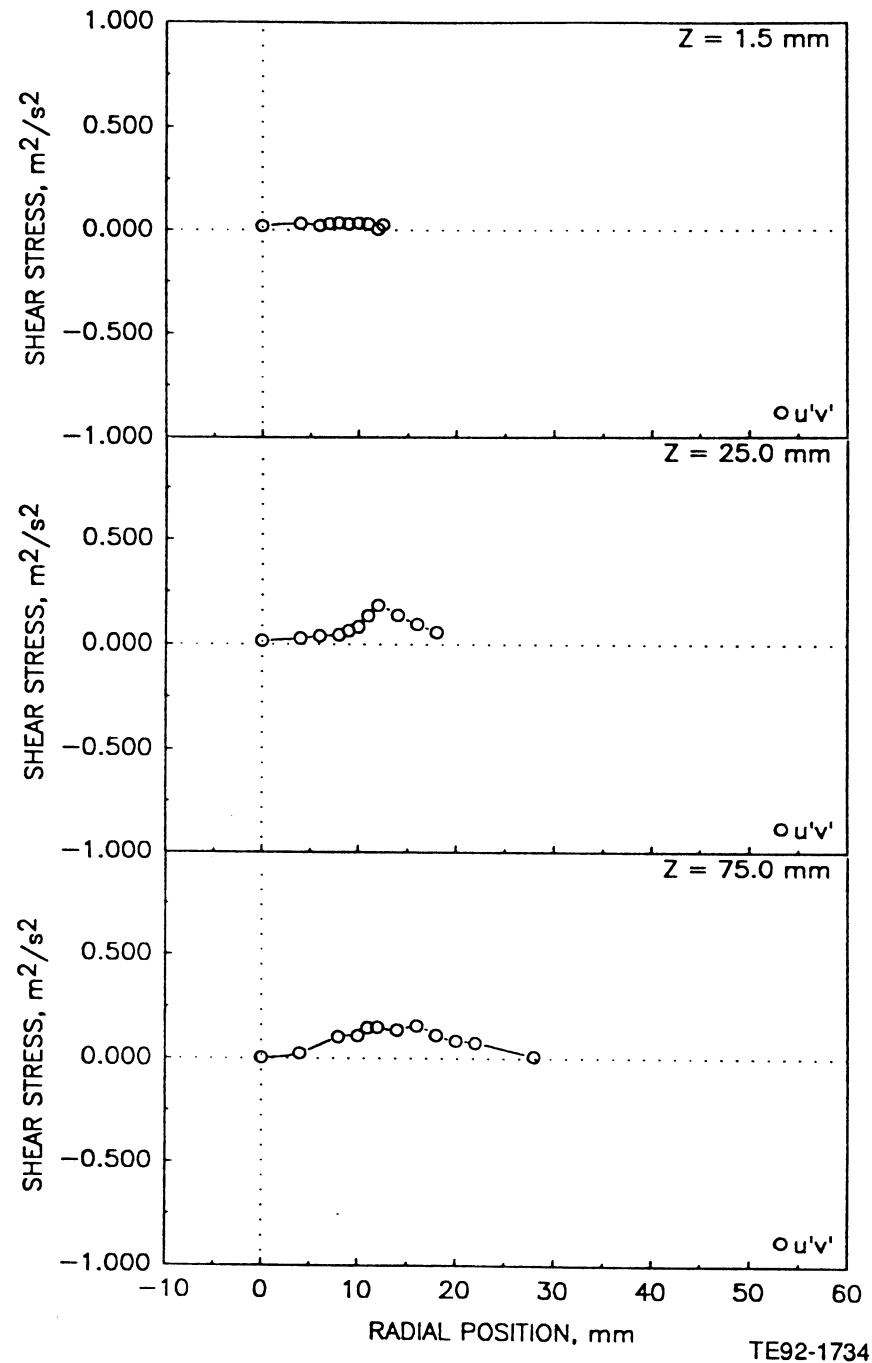


Figure 4.2.5-1. Radial profiles of gas phase velocity measurements in unconfined round jet laden with equal number of 20-30 micron and 100-110 micron glass beads with a bead-to-gas mass loading ratio of 0.2 (4 of 5).

e) Shear Stress Based on Axial and Azimuthal Velocities

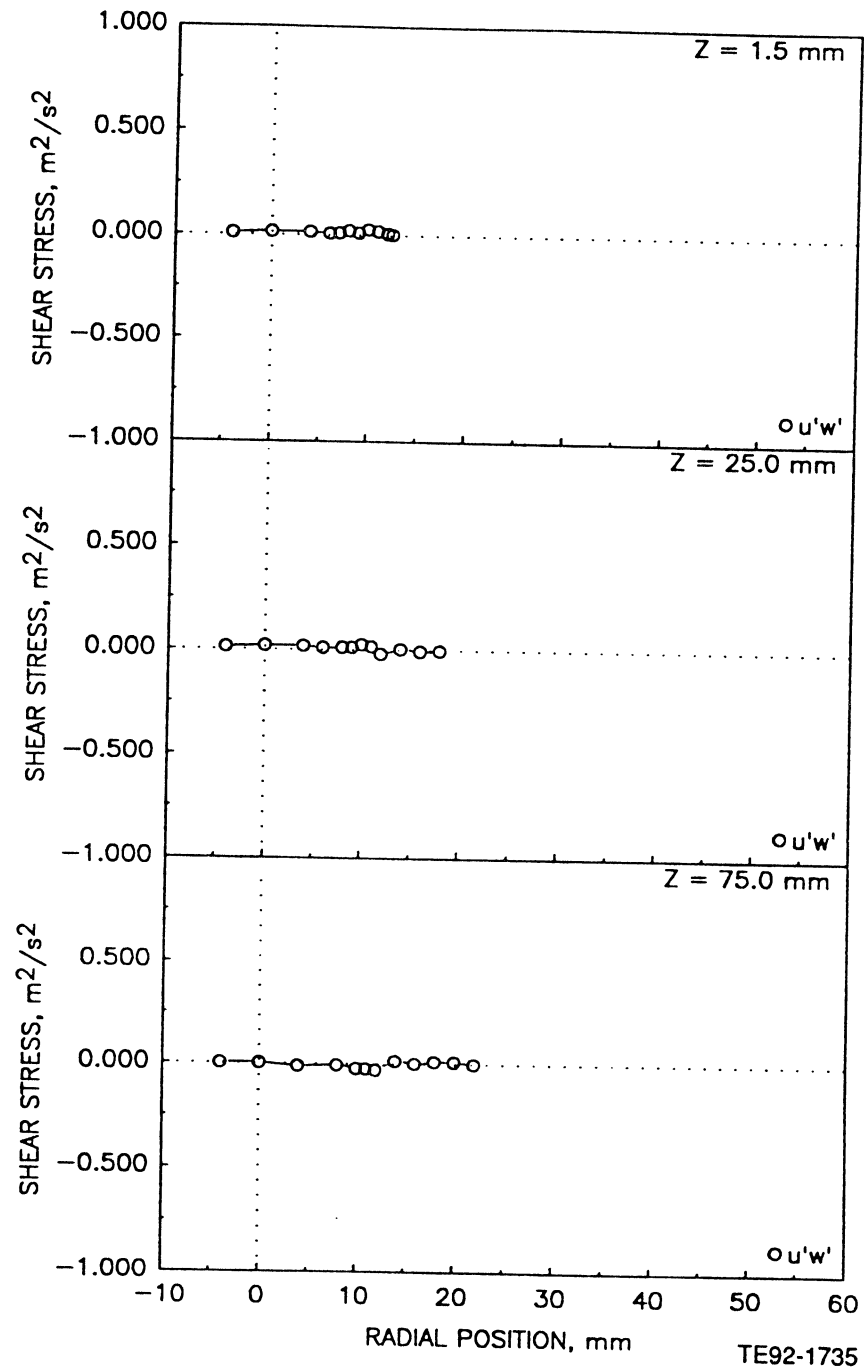


Figure 4.2.5-1. Radial profiles of gas phase velocity measurements in unconfined round jet laden with equal numbers of 20-30 micron and 100-110 micron glass beads with a bead-to-gas mass loading ratio of 0.2 (5 of 5).

a) Mean and Fluctuating Axial Velocities

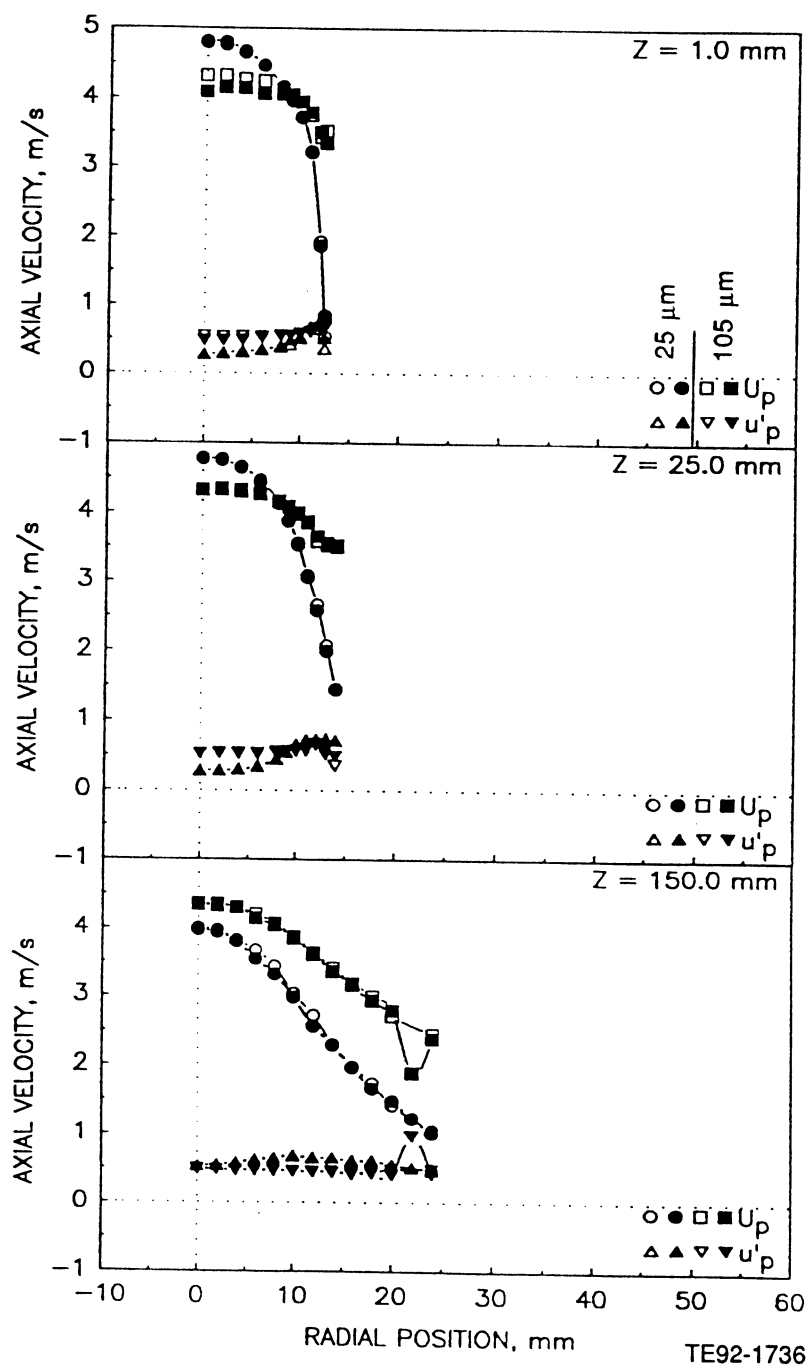


Figure 4.2.6-1. Radial profiles of particle measurements in unconfined round jet laden with equal numbers of 20-30 micron and 100-110 micron glass beads with a bead-to-gas mass loading ratio of 0.2 (1 of 5).

b) Mean and Fluctuating Radial Velocities

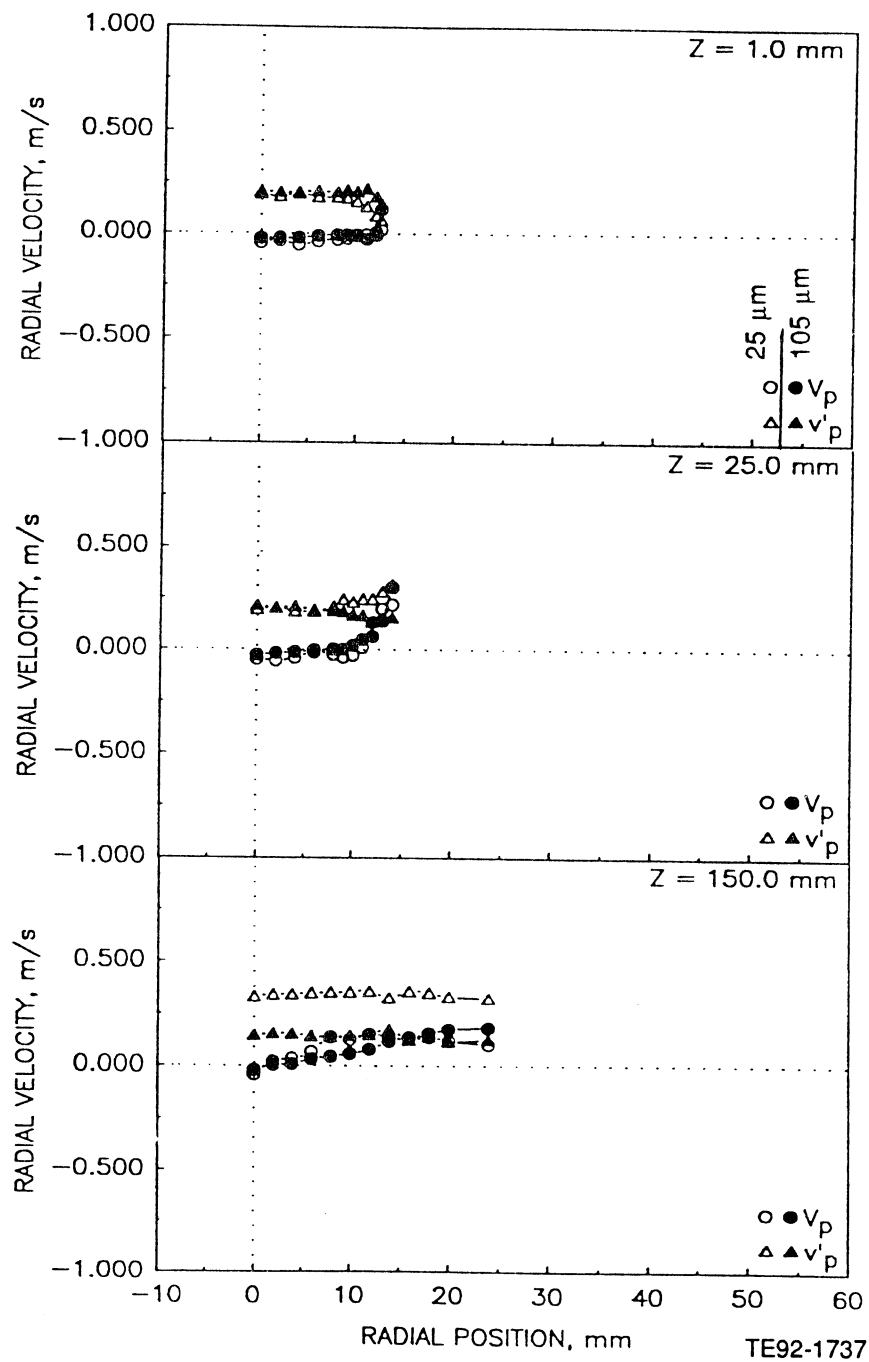


Figure 4.2.6-1. Radial profiles of particle measurements in unconfined round jet laden with equal numbers of 20-30 micron and 100-110 micron glass beads with a bead-to-gas mass loading ratio of 0.2 (2 of 5).

c) Mean and Fluctuating Azimuthal Velocities

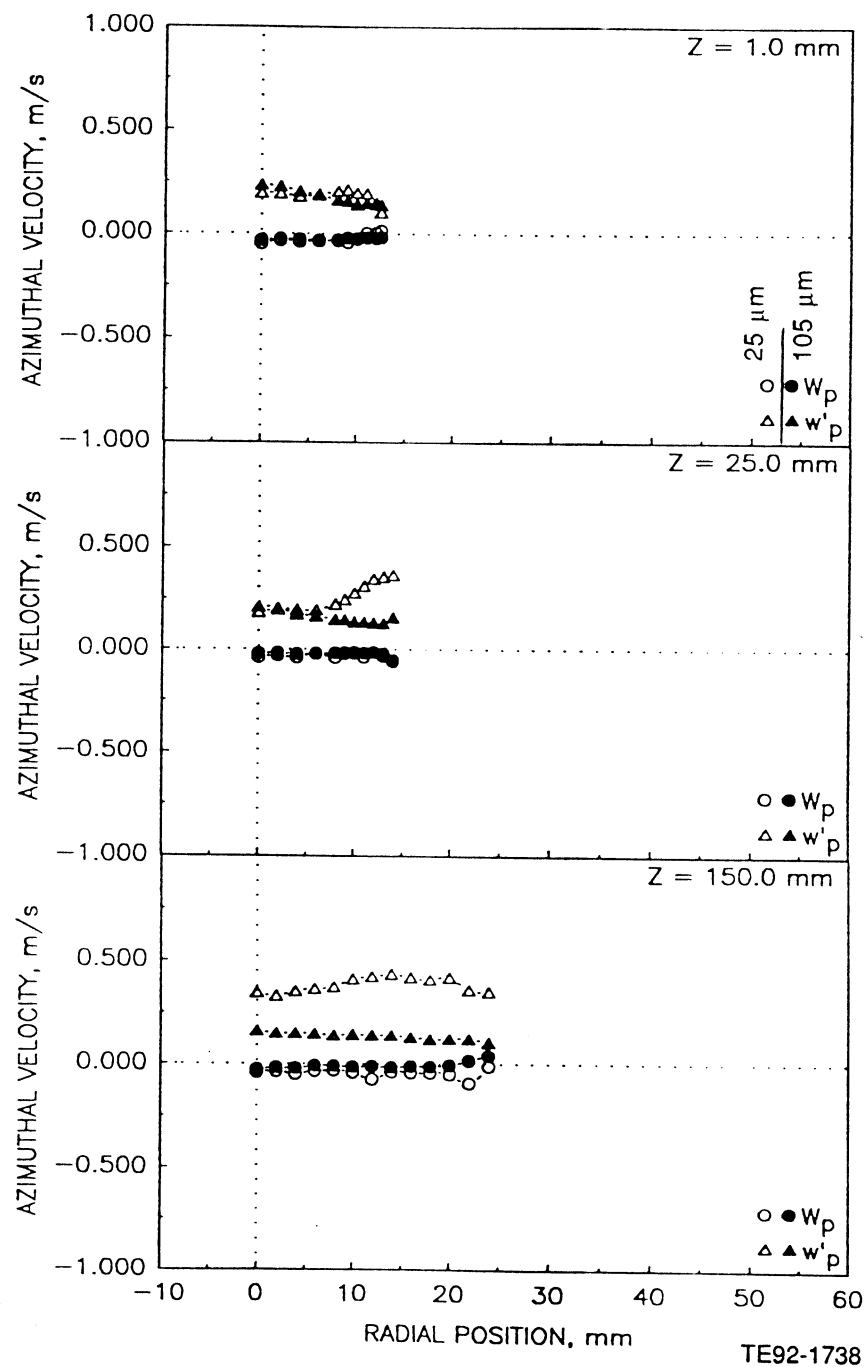


Figure 4.2.6-1. Radial profiles of particle measurements in unconfined round jet laden with equal numbers of 20-30 micron and 100-110 micron glass beads with a bead-to-gas mass loading ratio of 0.2 (3 of 5).

d) Particle Velocity Correlation Based on Axial and Radial Components

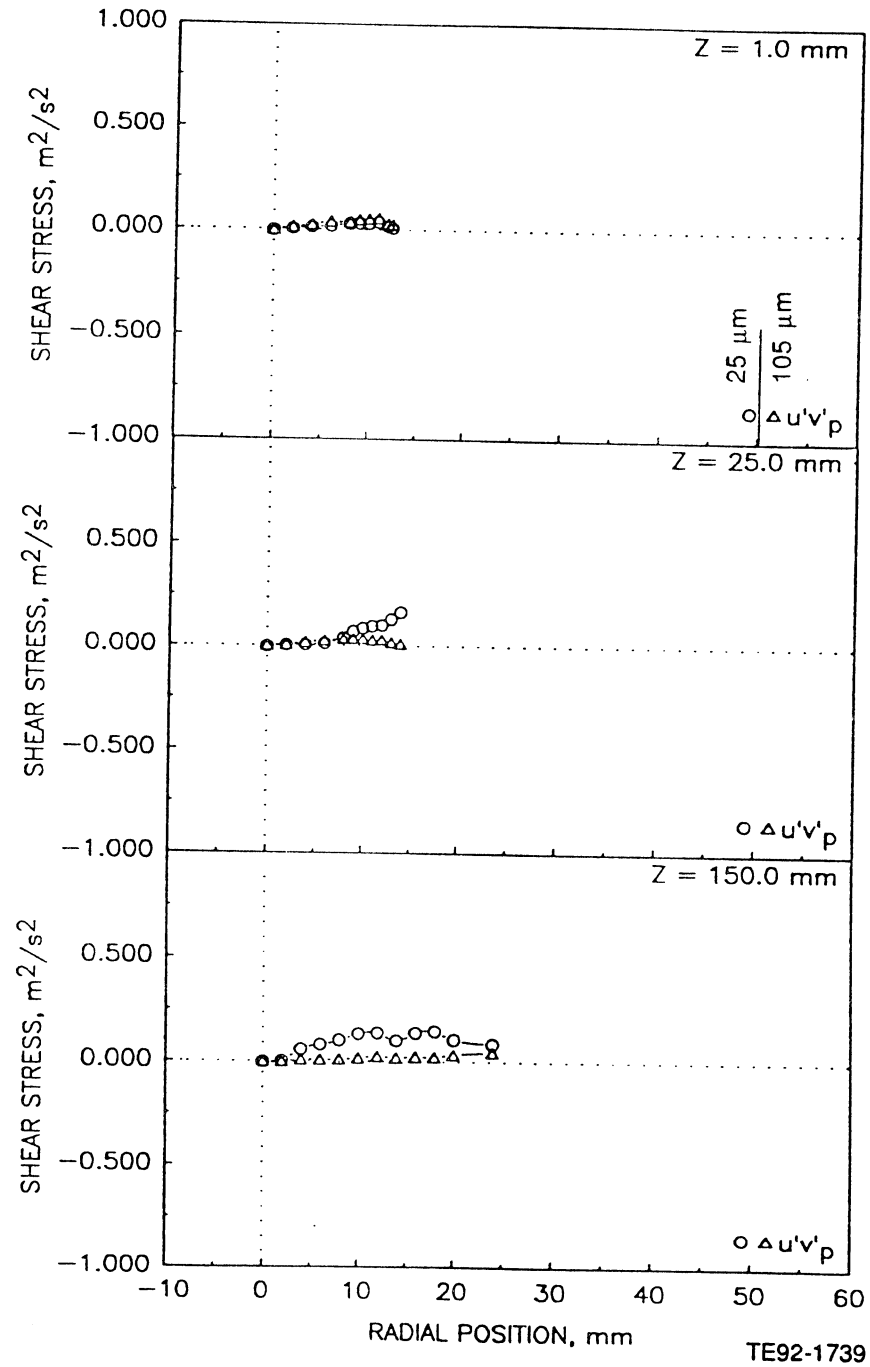


Figure 4.2.6-1. Radial profiles of particle measurements in unconfined round jet laden with equal numbers of 20-30 micron and 100-110 micron glass beads with a bead-to-gas mass loading ratio of 0.2 (4 of 5).

e) Particle Data Rate

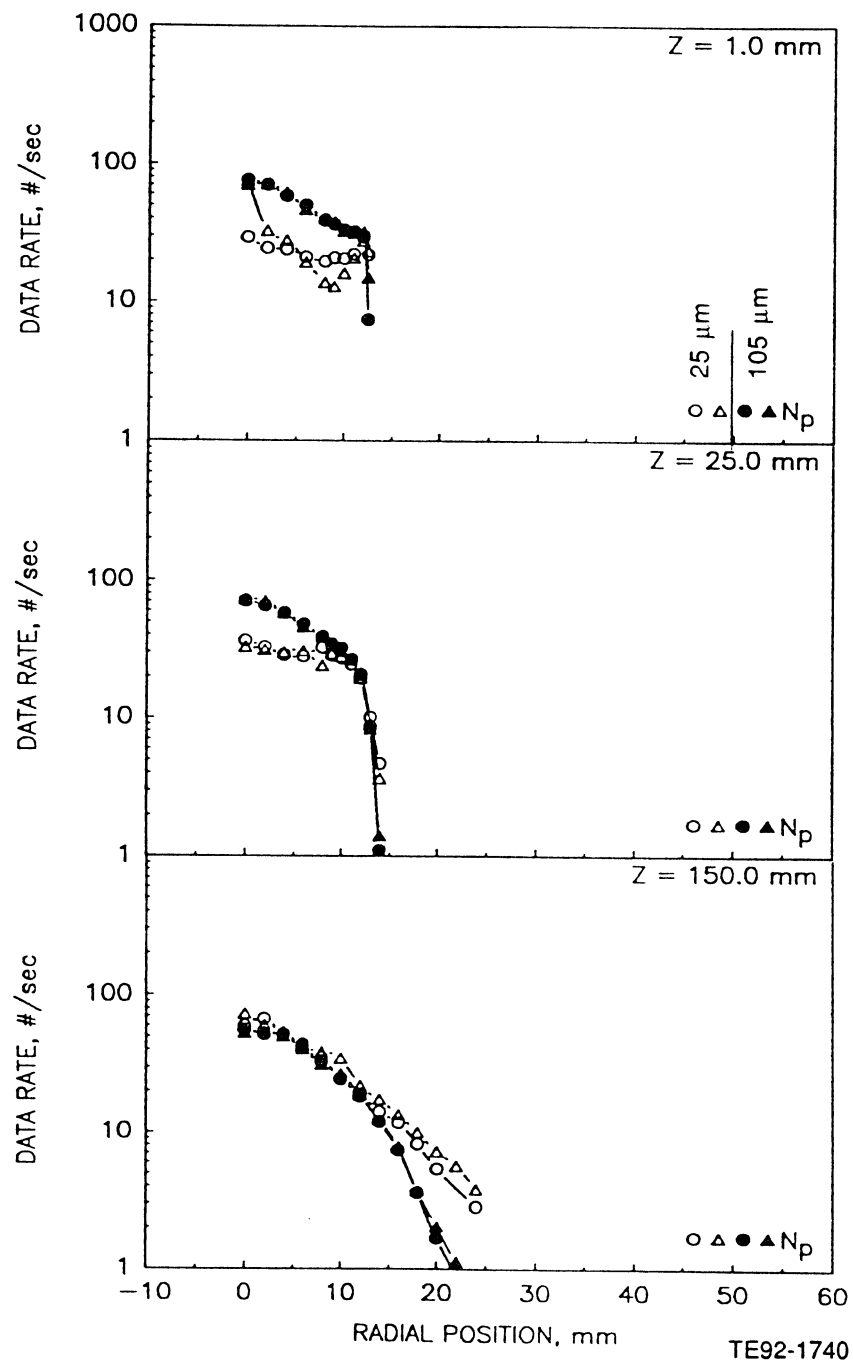
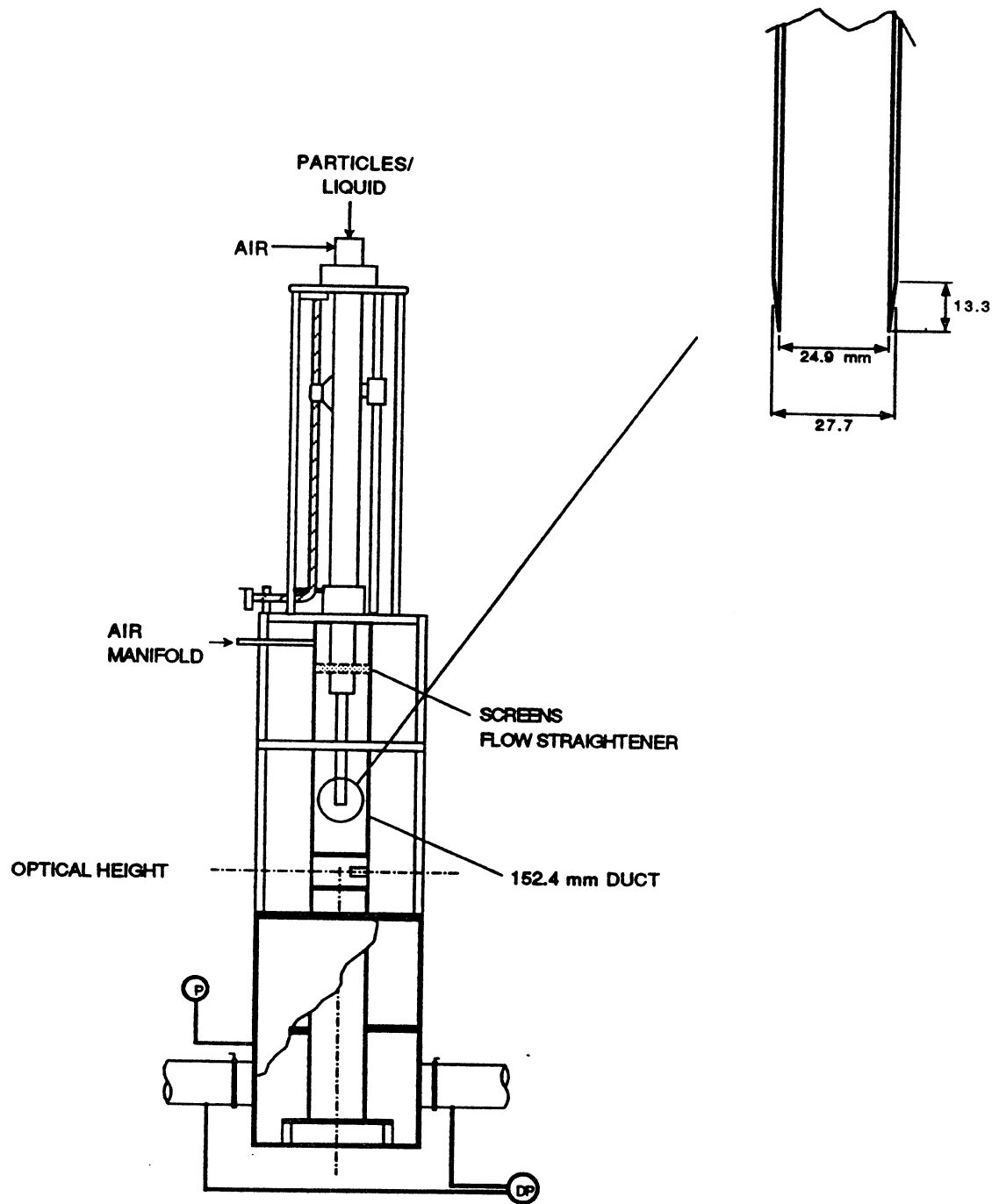


Figure 4.2.6-1. Radial profiles of particle measurements in unconfined round jet laden with equal numbers of 20-30 micron and 100-110 micron glass beads with a bead-to-gas mass loading ratio of 0.2 (5 of 5).



TE92-1741

Figure 4.2.7-1. Geometry utilized for confined single round jet.

a) Mean and Fluctuating Axial Velocities

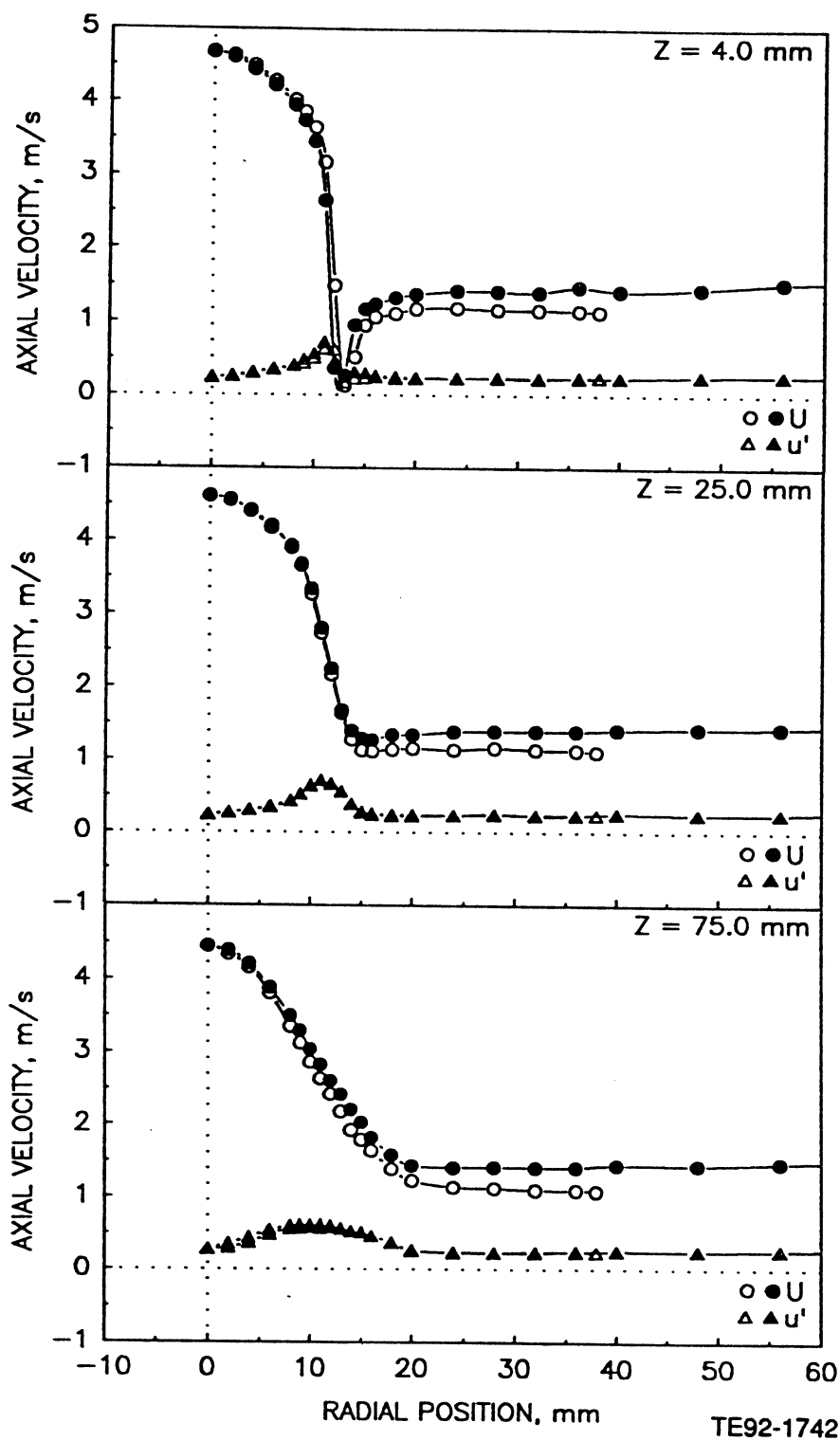
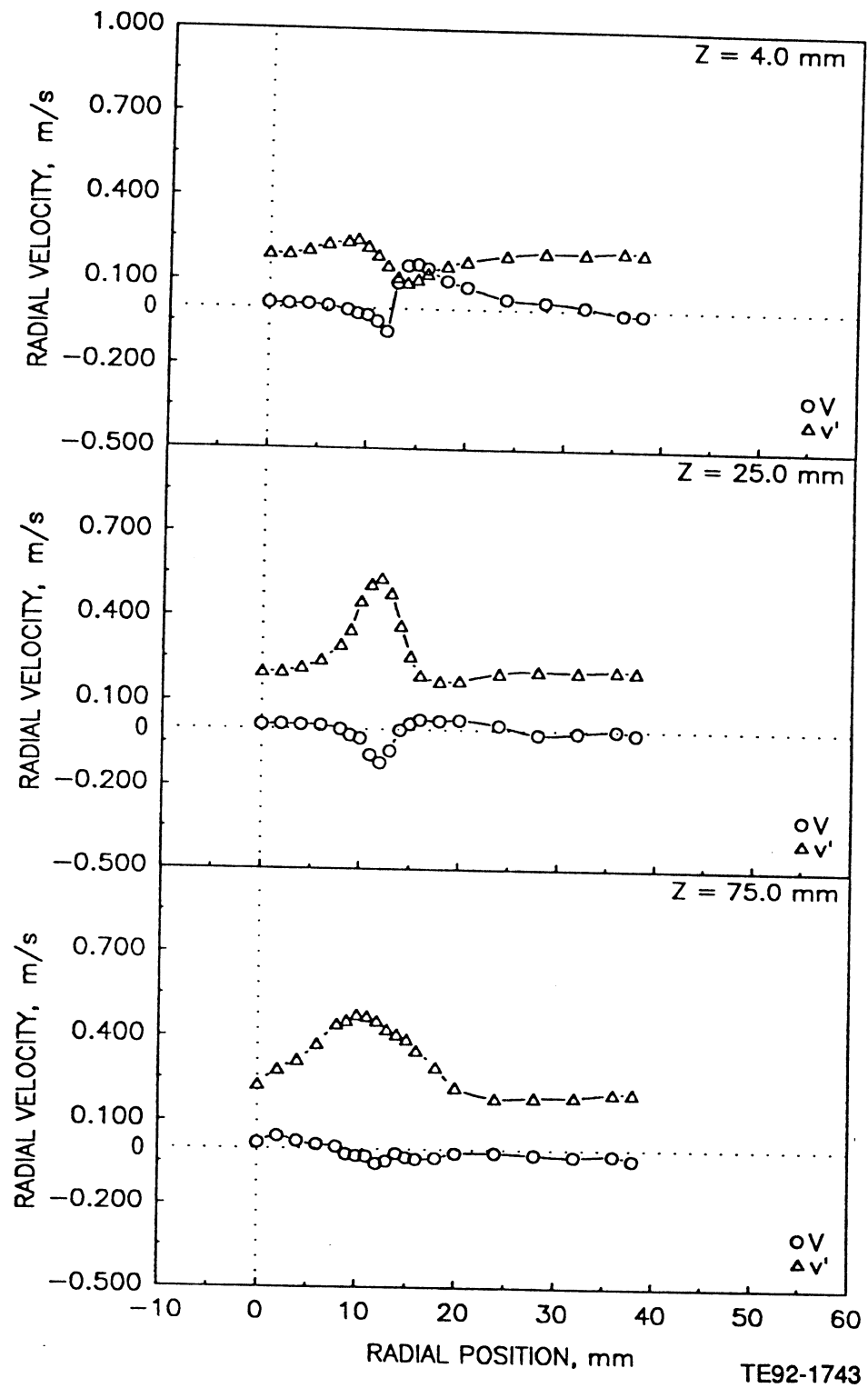


Figure 4.2.7-2. Radial profiles of gas phase statistics in confined single-phase round jet (1 of 5).

b) Mean and Fluctuating Radial Velocities



TE92-1743

Figure 4.2.7-2. Radial profiles of gas phase statistics in confined single-phase round jet (2 of 5).

c) Mean and Fluctuating Azimuthal Velocities

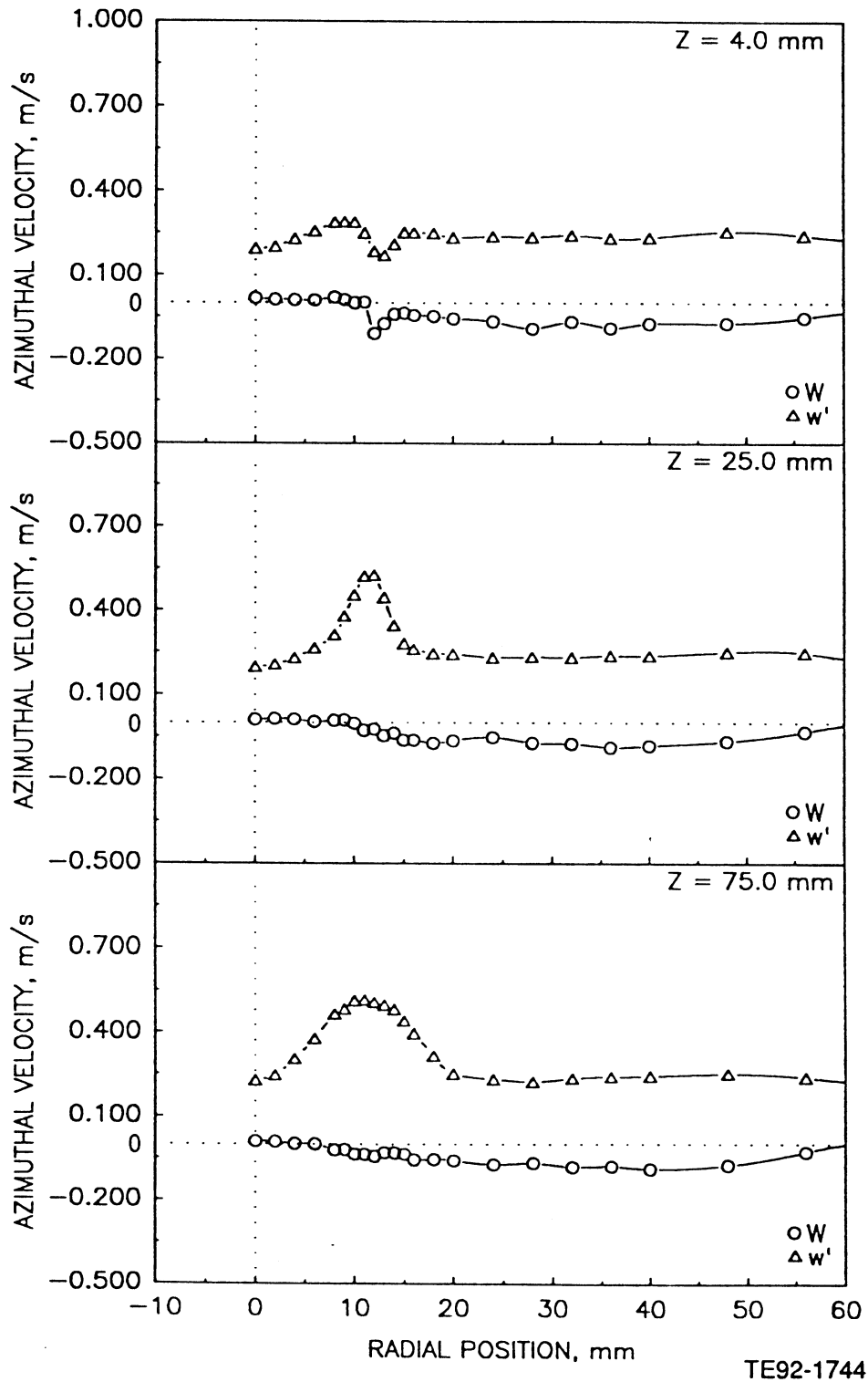
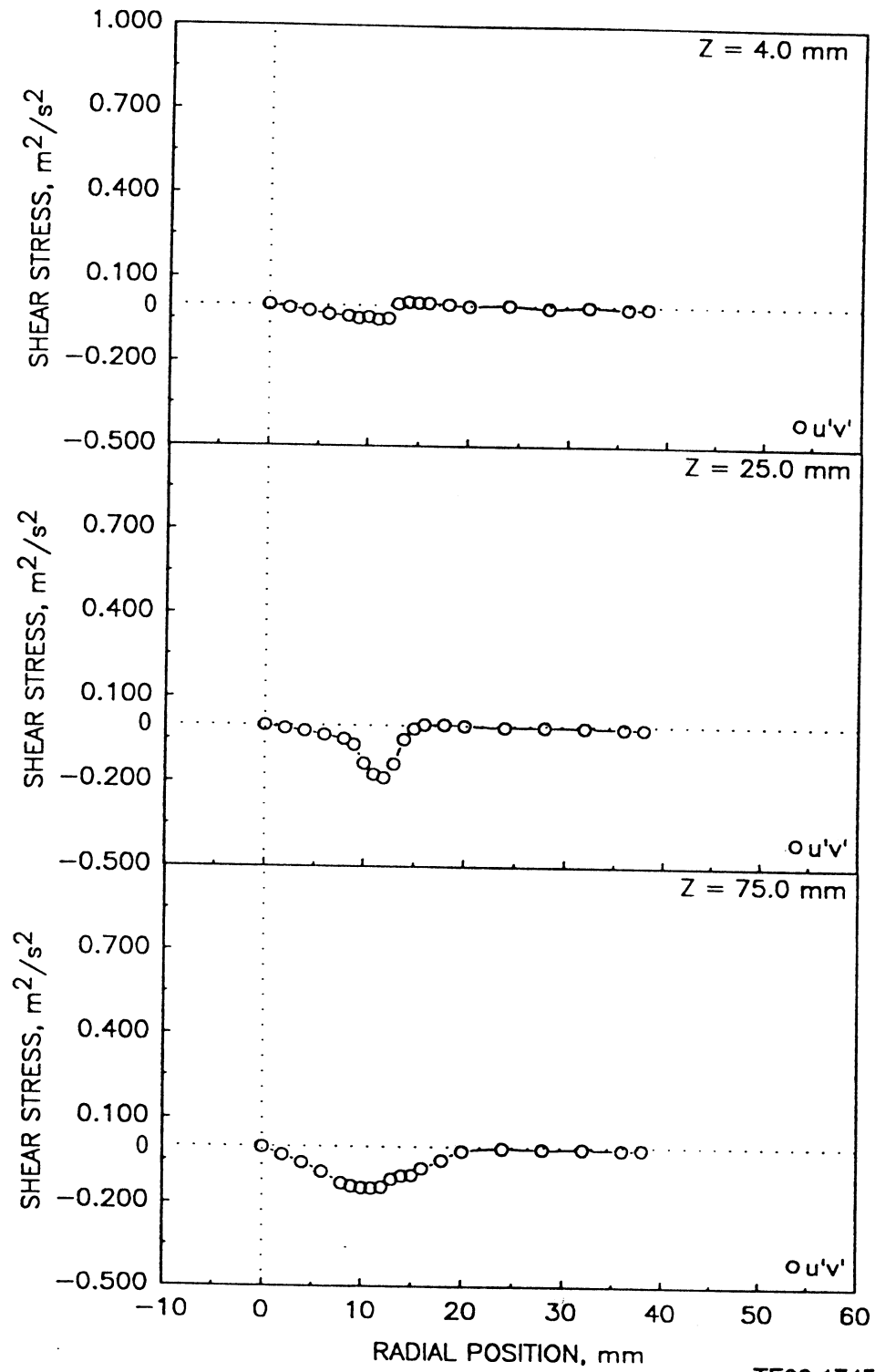


Figure 4.2.7-2. Radial profiles of gas phase statistics in confined single-phase round jet (3 of 5).

d) Shear Stress Based on Axial and Radial Velocities



TE92-1745

Figure 4.2.7-2. Radial profiles of gas phase statistics in confined single-phase round jet (4 of 5).

e) Shear Stress Based on Axial and Azimuthal Velocities

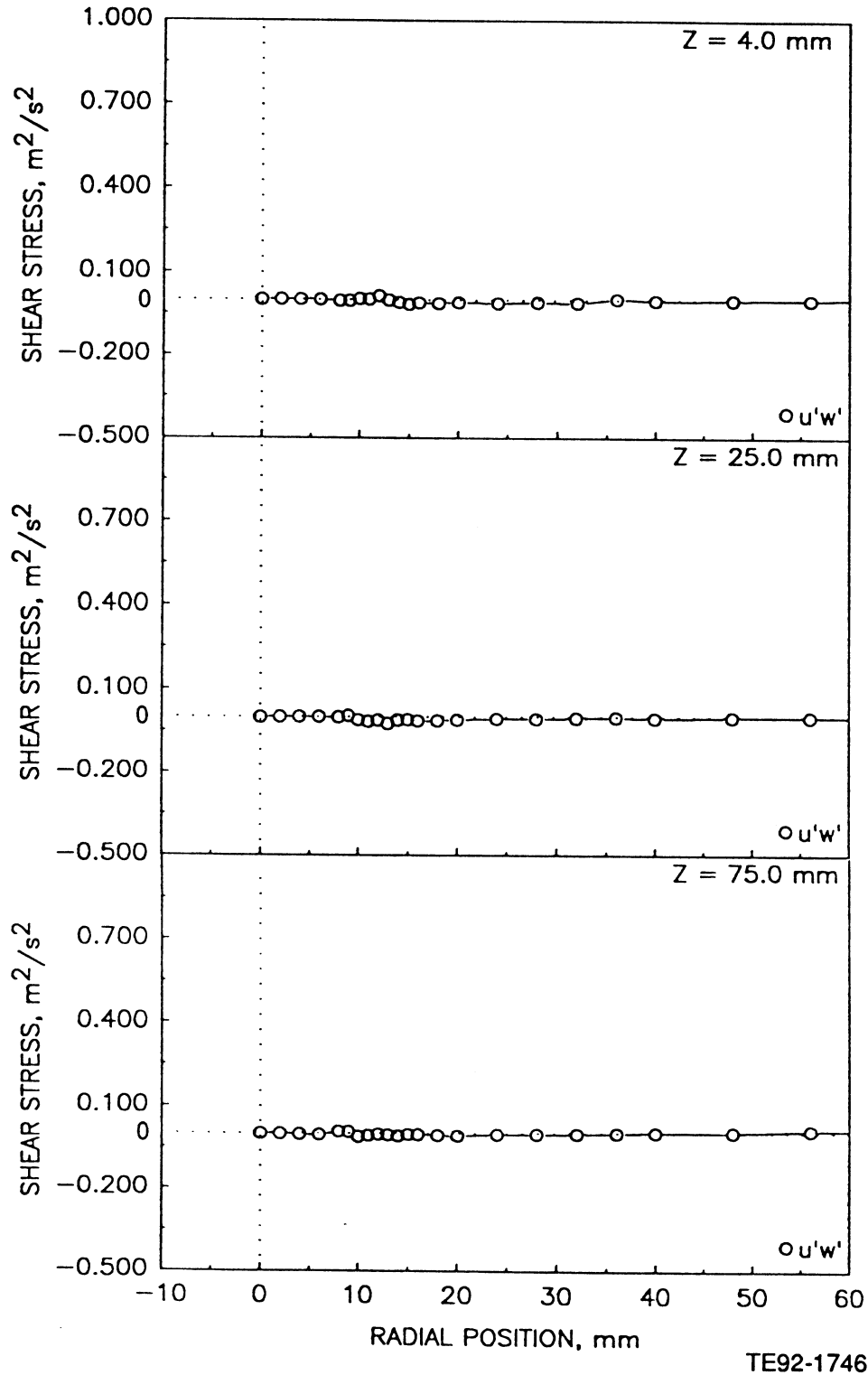


Figure 4.2.7-2. Radial profiles of gas phase statistics in confined single-phase round jet (5 of 5).

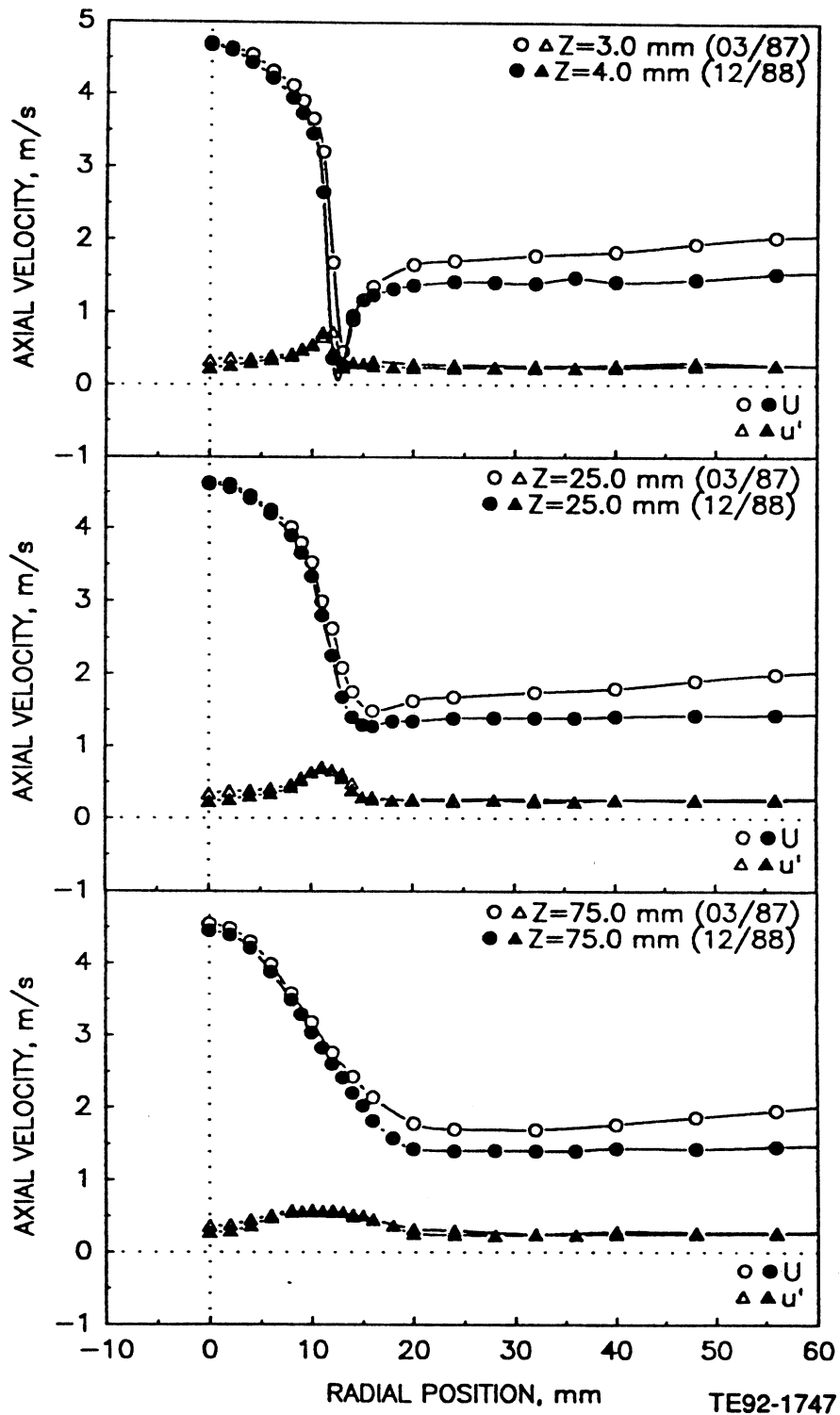


Figure 4.2.7-3. Repeatability of measurements of mean and fluctuating axial velocity in the confined single-phase round jet.

a) Mean and Fluctuating Axial Velocities

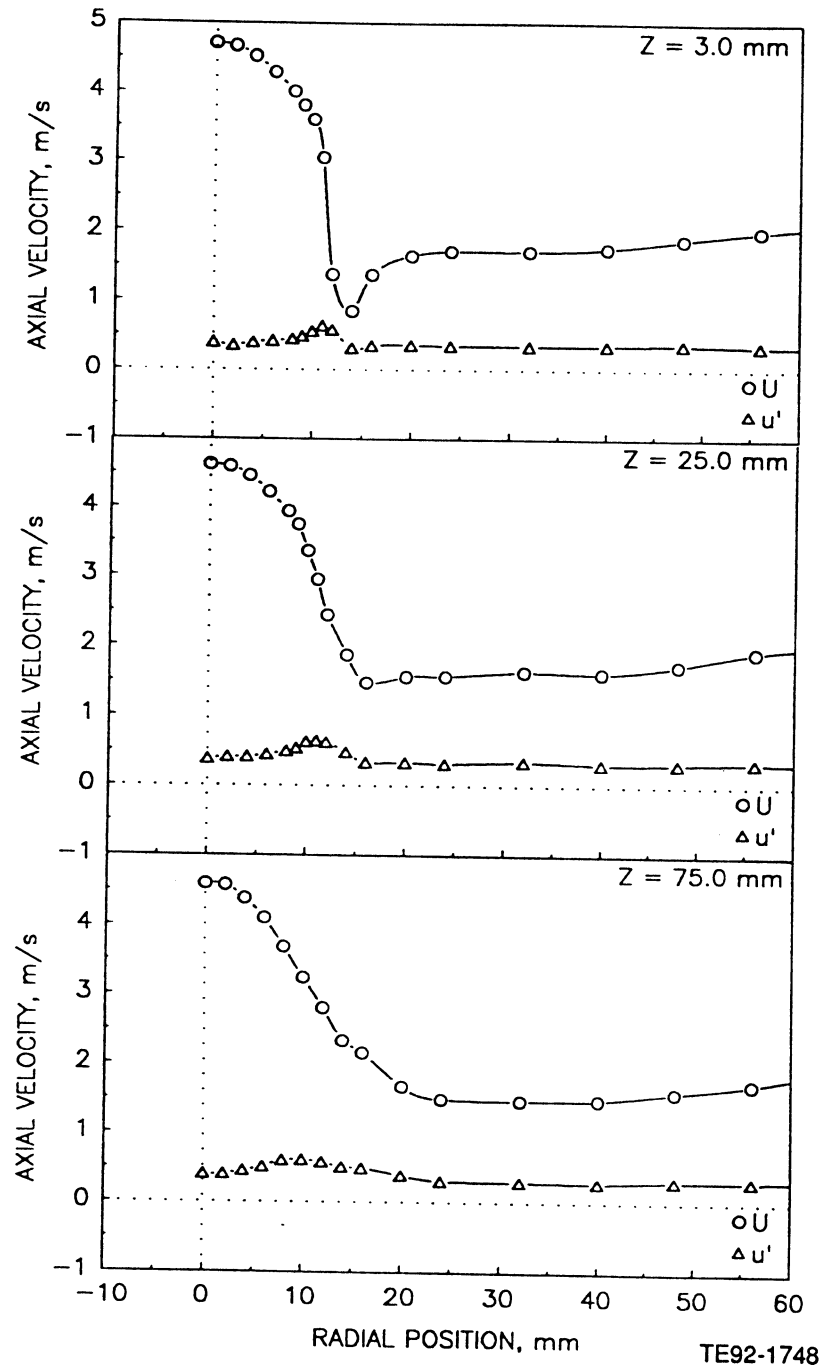


Figure 4.2.8-1. Radial profiles of gas phase velocity measurements in confined round jet laden with 100-110 micron glass beads with a bead-to-gas mass loading ratio of 0.2 (1 of 3).

b) Mean and Fluctuating Azimuthal Velocities

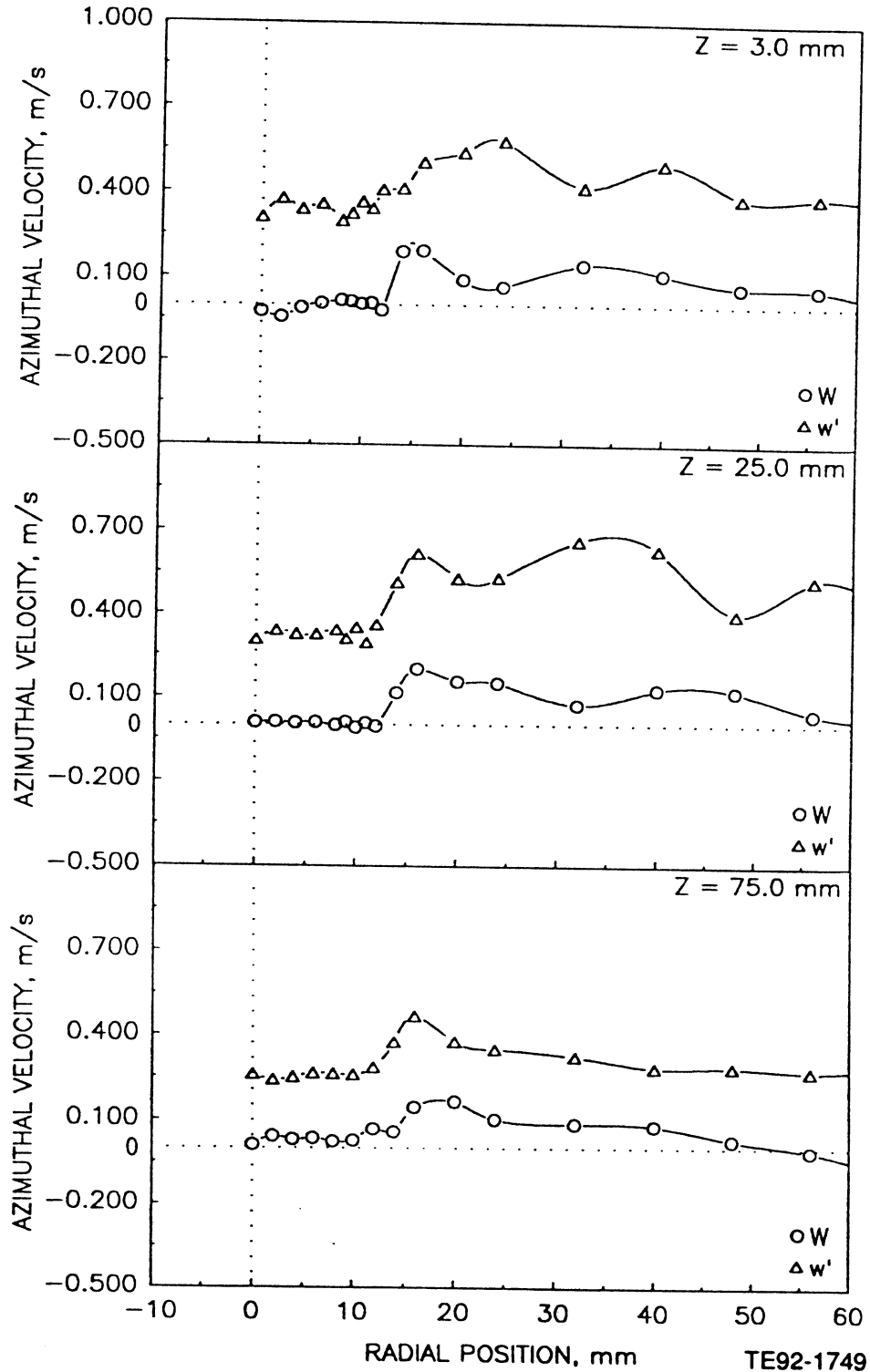


Figure 4.2.8-1. Radial profiles of gas phase velocity measurements in confined round jet laden with 100-110 micron glass beads with a bead-to-gas mass loading ratio of 0.2 (2 of 3).

c) Shear Stress Based on Axial and Azimuthal Velocities

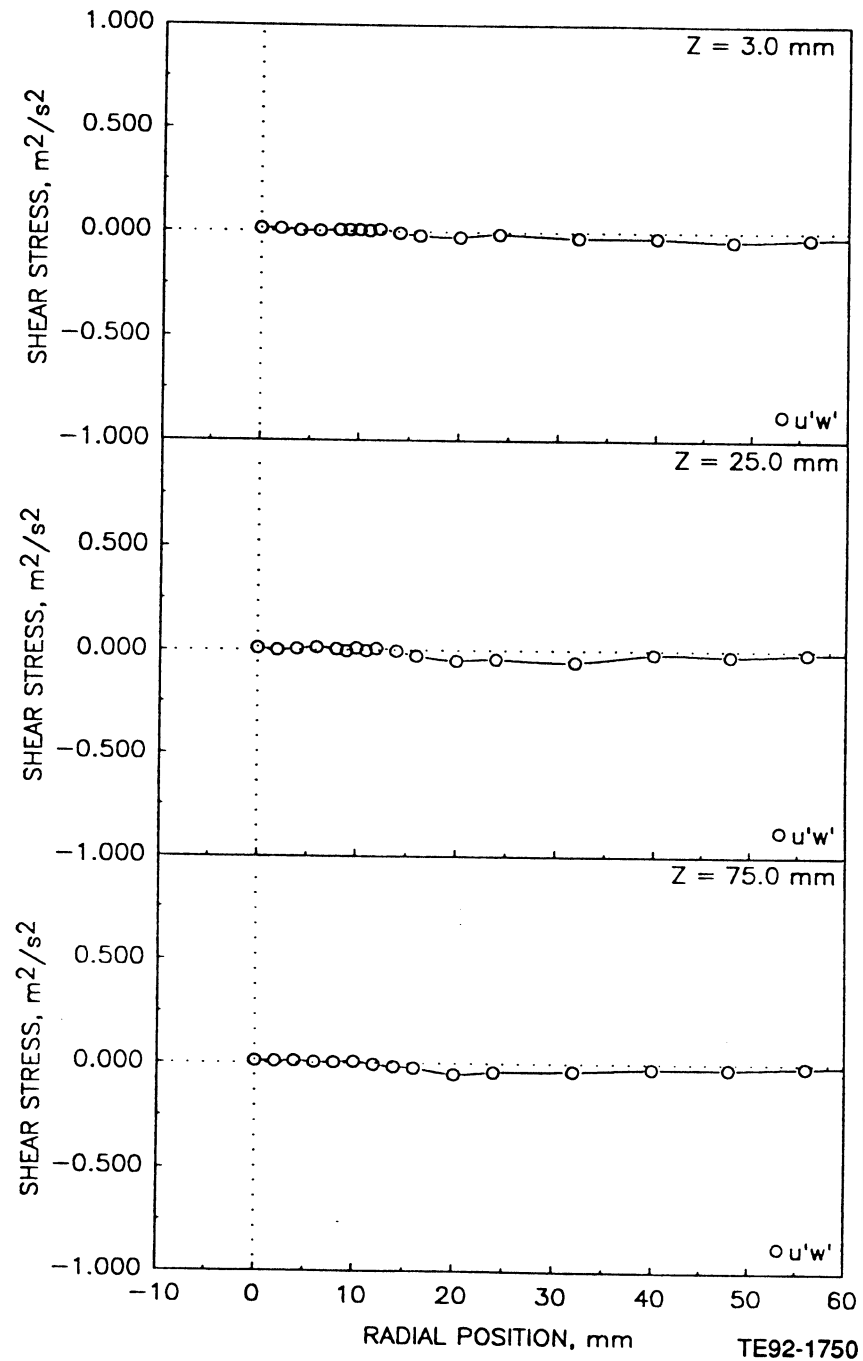


Figure 4.2.8-1. Radial profiles of gas phase velocity measurements in confined round jet laden with 100-110 micron glass beads with a bead-to-gas mass loading ratio of 0.2 (3 of 3).

a) Mean and Fluctuating Axial Velocities

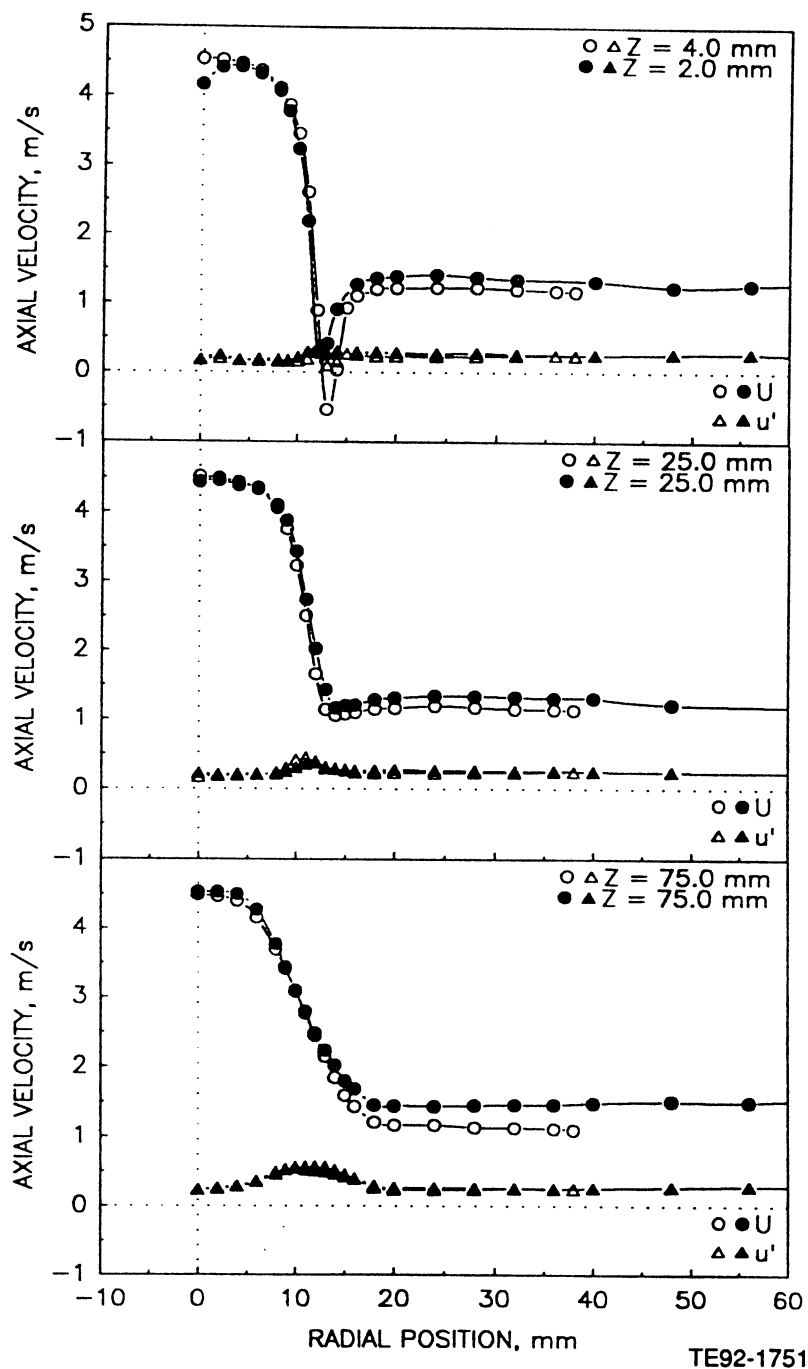


Figure 4.2.8-2. Radial profiles of gas phase velocity measurements in confined round jet laden with 100-110 micron glass beads with a bead-to-gas mass loading ratio of 1.0 (1 of 5).

b) Mean and Fluctuating Radial Velocities

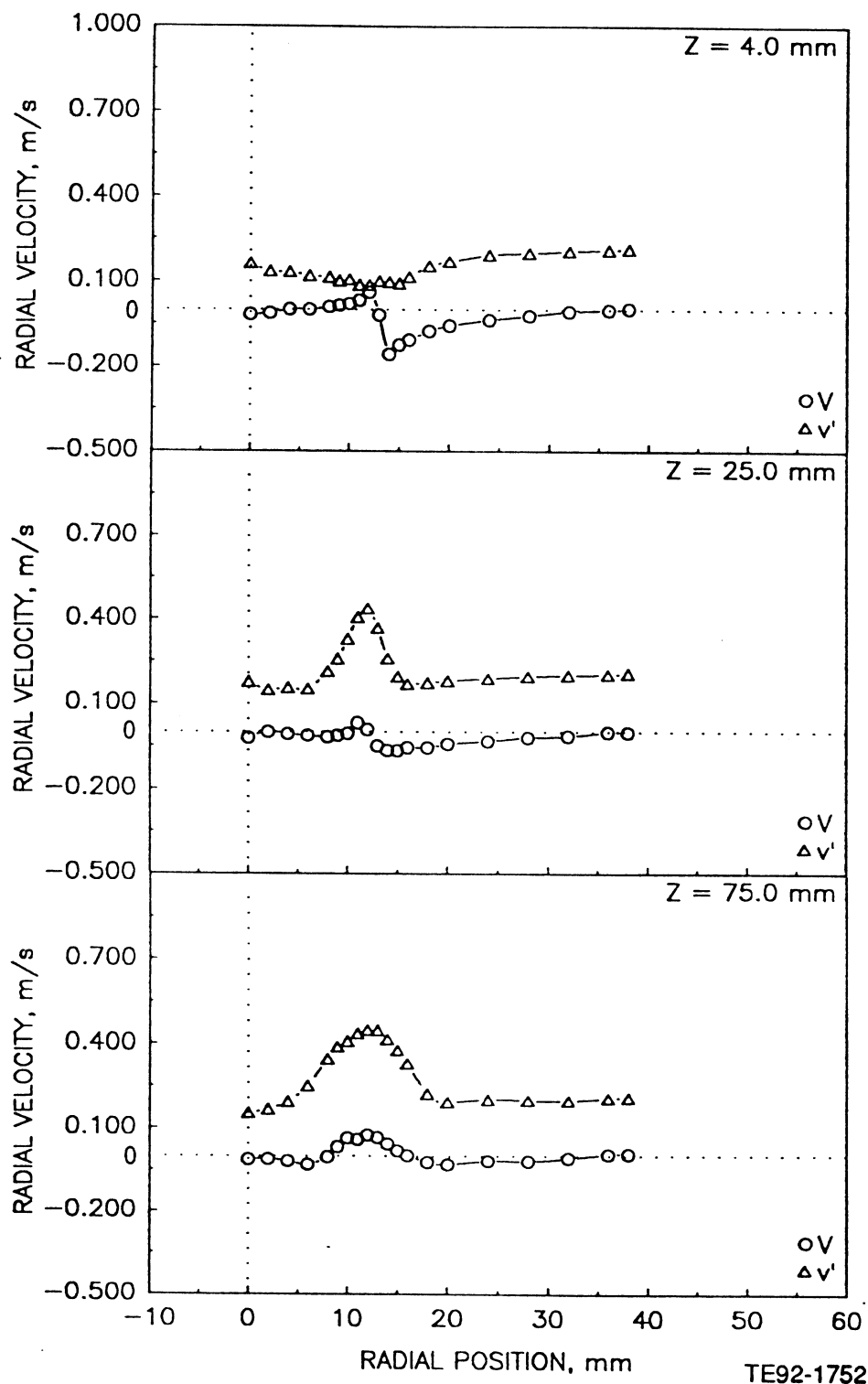


Figure 4.2.8-2. Radial profiles of gas phase velocity measurements in confined round jet laden with 100-110 micron glass beads with a bead-to-gas mass loading ratio of 1.0 (2 of 5).

c) Mean and Fluctuating Azimuthal Velocities

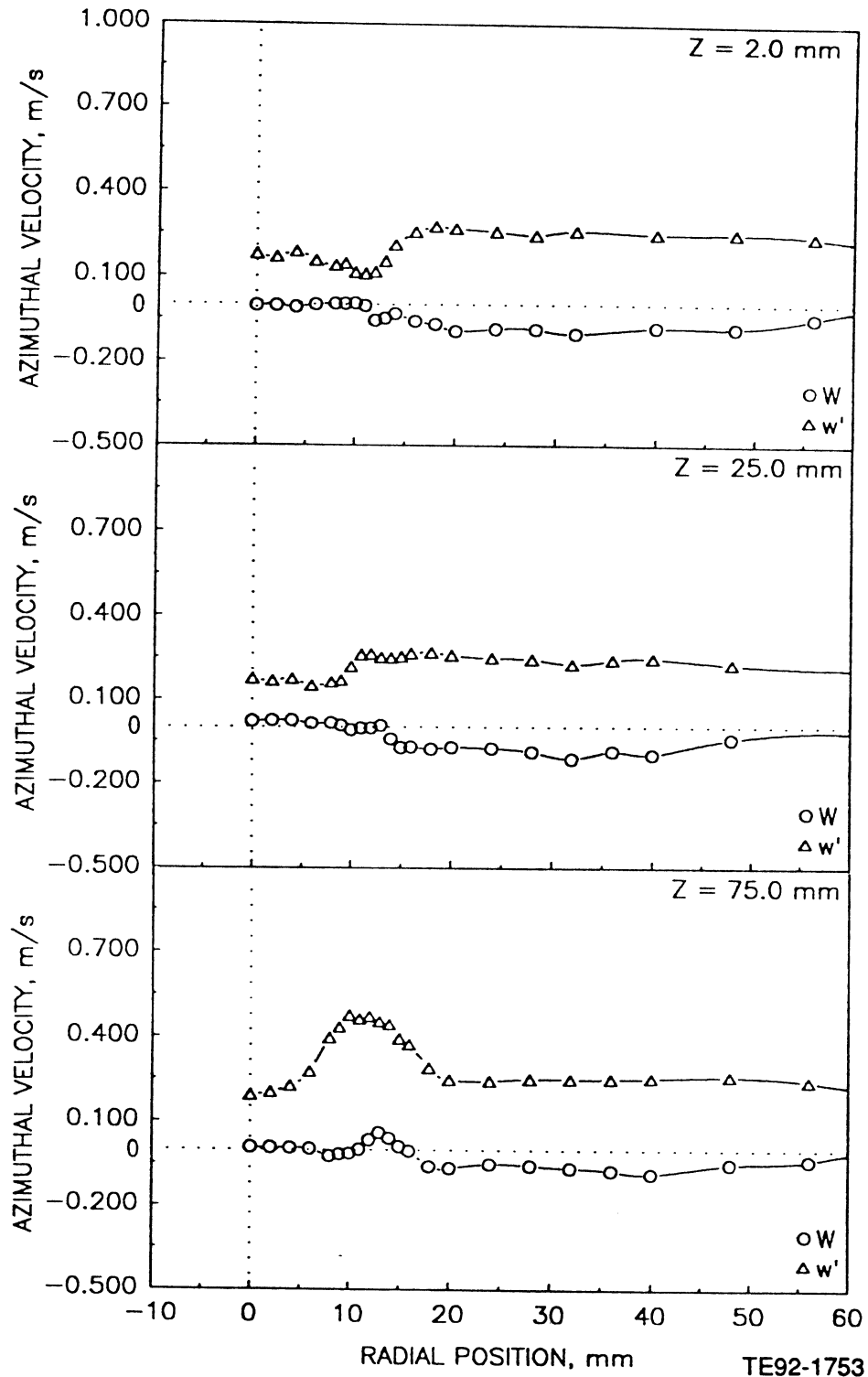


Figure 4.2.8-2. Radial profiles of gas phase velocity measurements in confined round jet laden with 100-110 micron glass beads with a bead-to-gas mass loading ratio of 1.0 (3 of 5).

d) Shear Stress Based on Axial and Radial Velocities

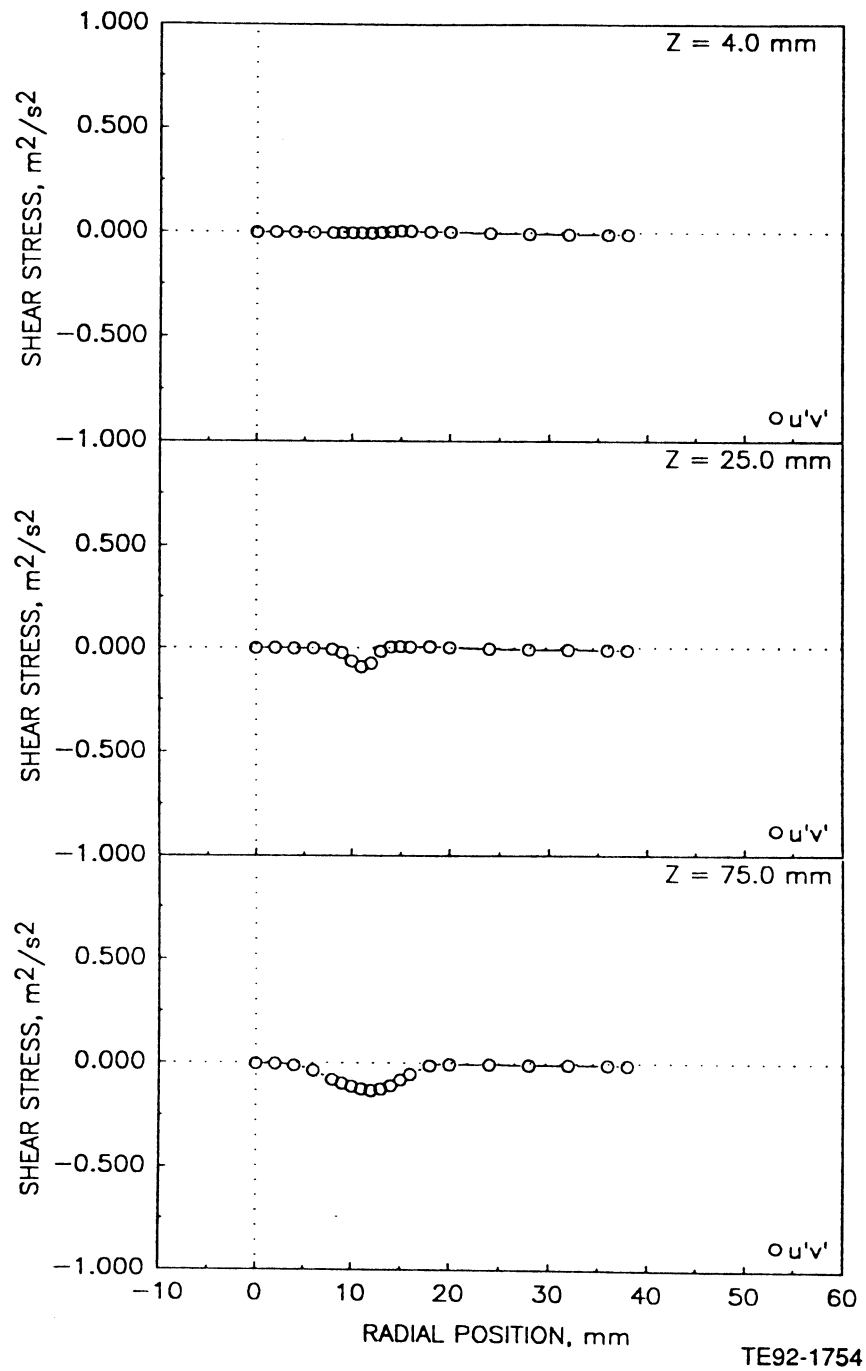


Figure 4.2.8-2. Radial profiles of gas phase velocity measurements in confined round jet laden with 100-110 micron glass beads with a bead-to-gas mass loading ratio of 1.0 (4 of 5).

e) Shear Stress Based on Axial and Azimuthal Velocities

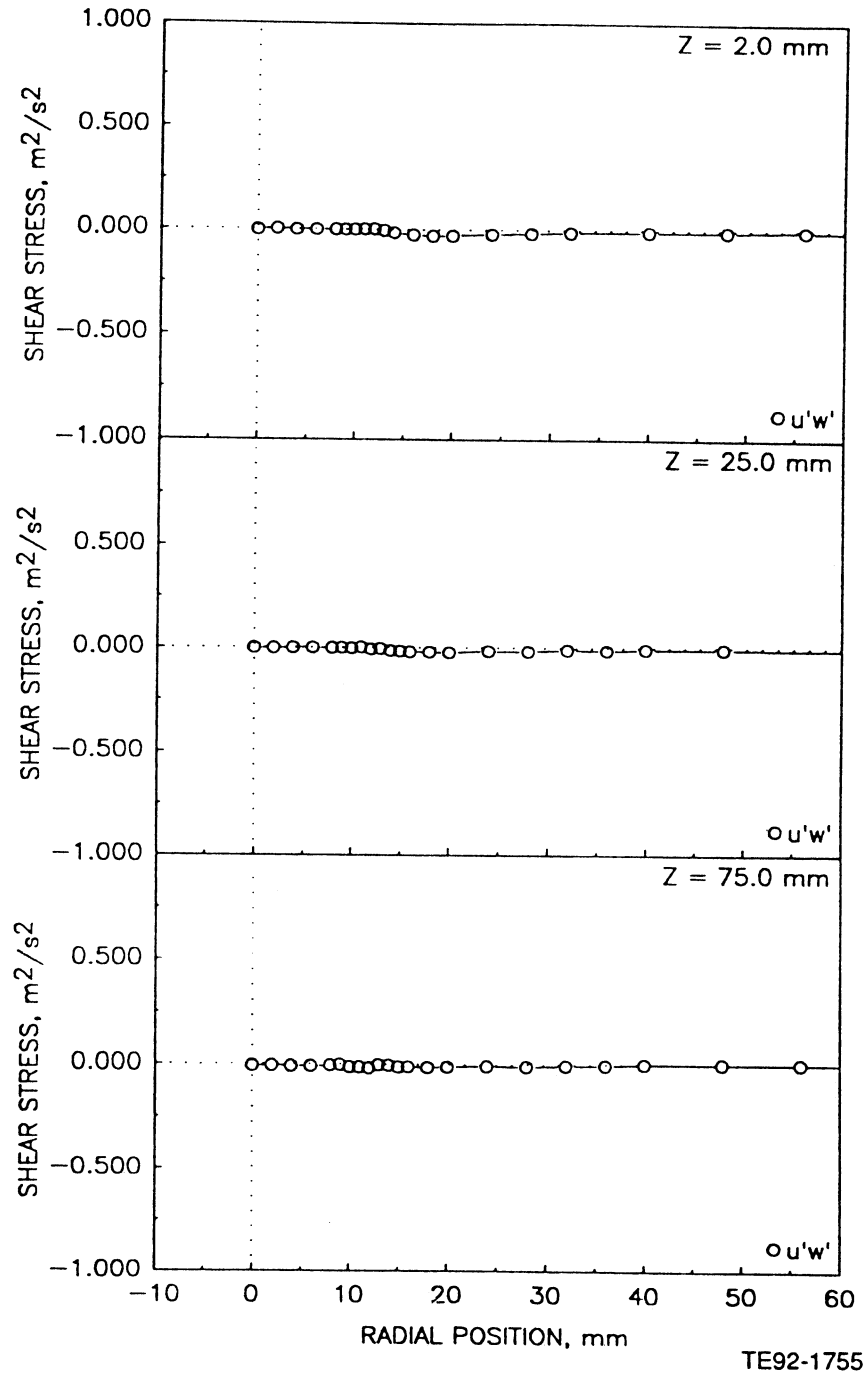
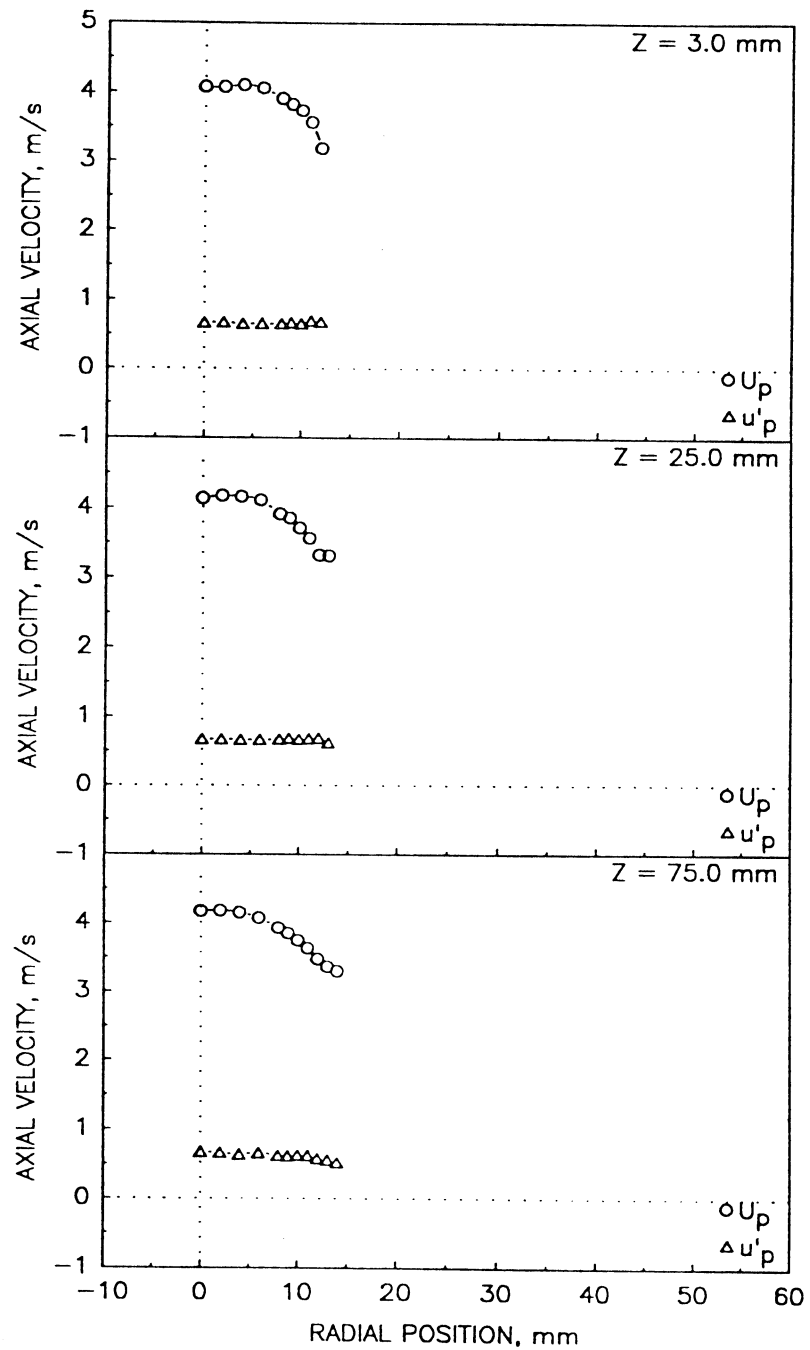


Figure 4.2.8-2. Radial profiles of gas phase velocity measurements in confined round jet laden with 100-110 micron glass beads with a bead-to-gas mass loading ratio of 1.0 (5 of 5).

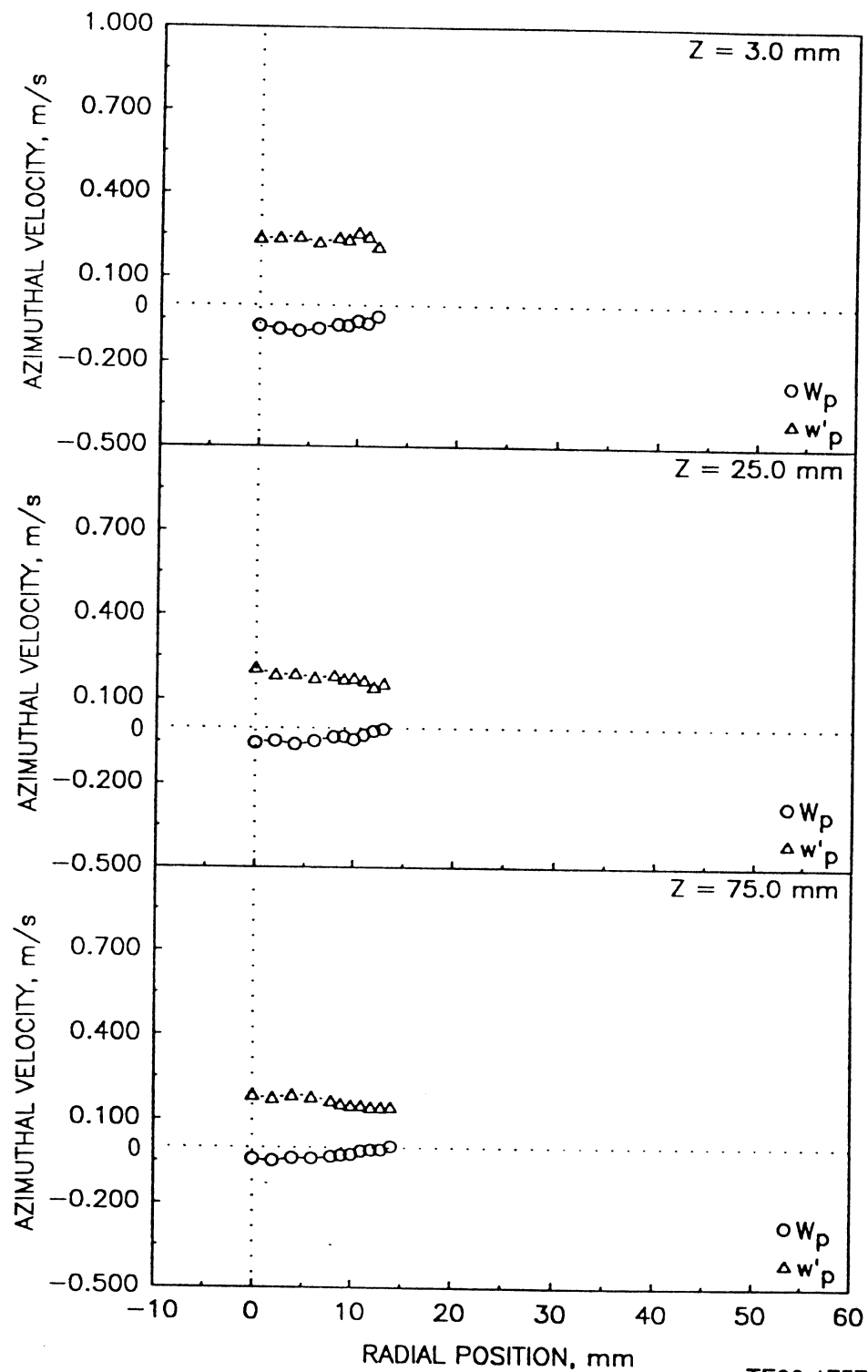
a) Mean and Fluctuating Axial Velocities



TE92-1756

Figure 4.2.9-1. Radial profiles of particle measurements in confined round jet laden with 100-110 micron glass beads with a bead-to-gas mass loading ratio of 0.2 (1 of 3).

b) Mean and Fluctuating Azimuthal Velocities



TE92-1757

Figure 4.2.9-1. Radial profiles of particle measurements in confined round jet laden with 100-110 micron glass beads with a bead-to-gas mass loading ratio of 0.2 (2 of 3).

c) Particle Data Rate

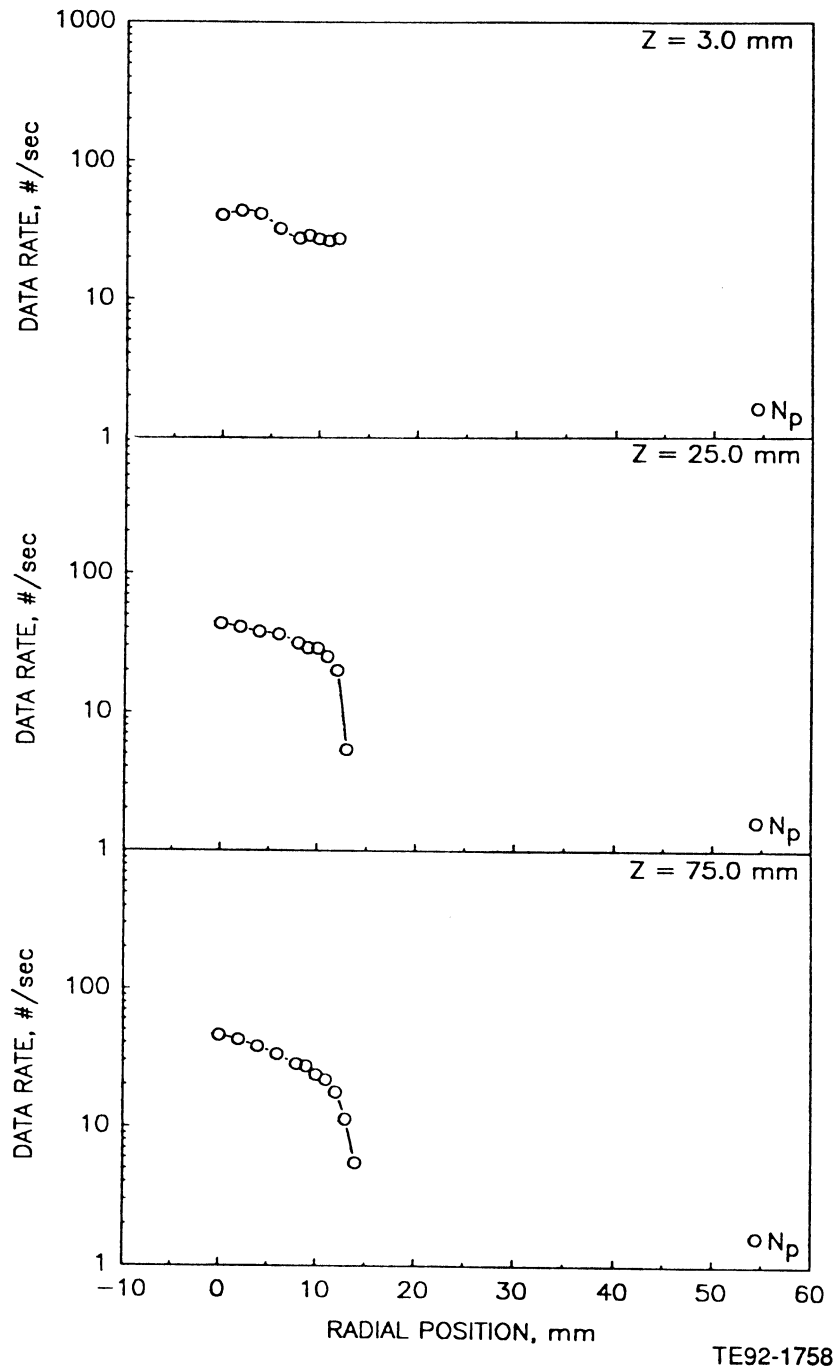


Figure 4.2.9-1. Radial profiles of particle measurements in confined round jet laden with 100-110 micron glass beads with a bead-to-gas mass loading ratio of 0.2 (3 of 3).

a) Mean and Fluctuating Axial Velocities

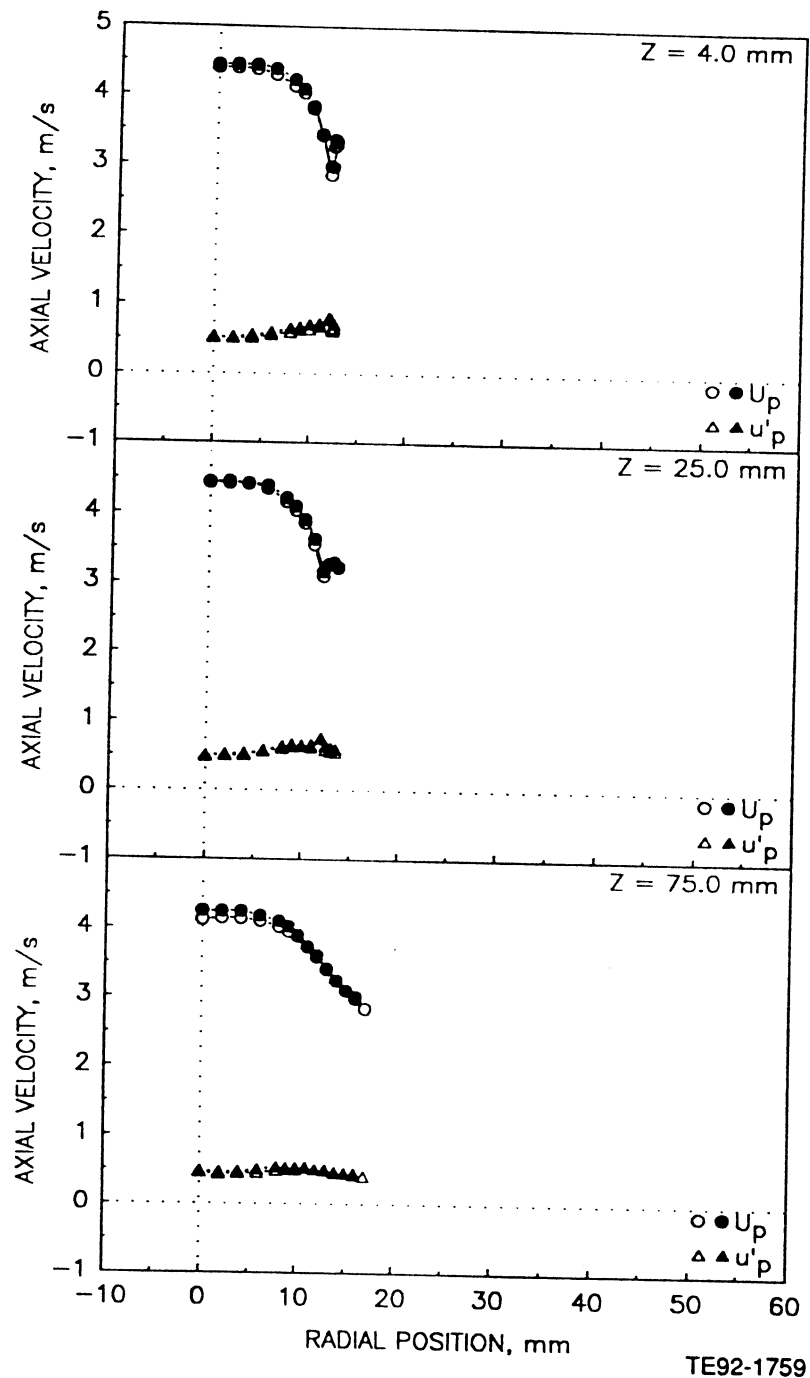


Figure 4.2.9-2. Radial profiles of particle measurements in unconfined round jet laden with 100-110 micron glass beads with a bead-to-gas mass loading ratio of 1.0 (1 of 5).

b) Mean and Fluctuating Radial Velocities

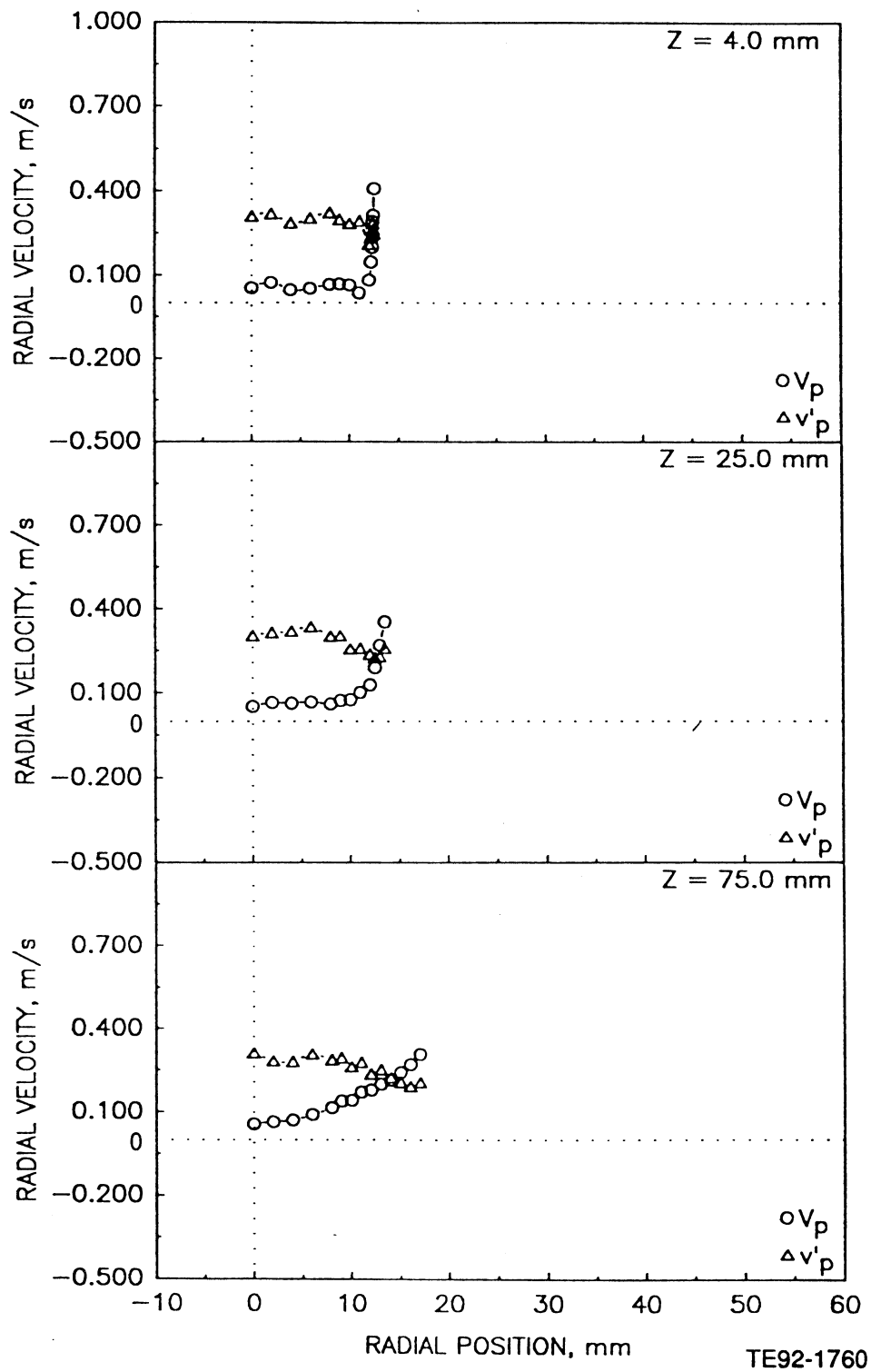


Figure 4.2.9-2. Radial profiles of particle measurements in unconfined round jet laden with 100-110 micron glass beads with a bead-to-gas mass loading ratio of 1.0 (2 of 5).

c) Mean and Fluctuating Azimuthal Velocities

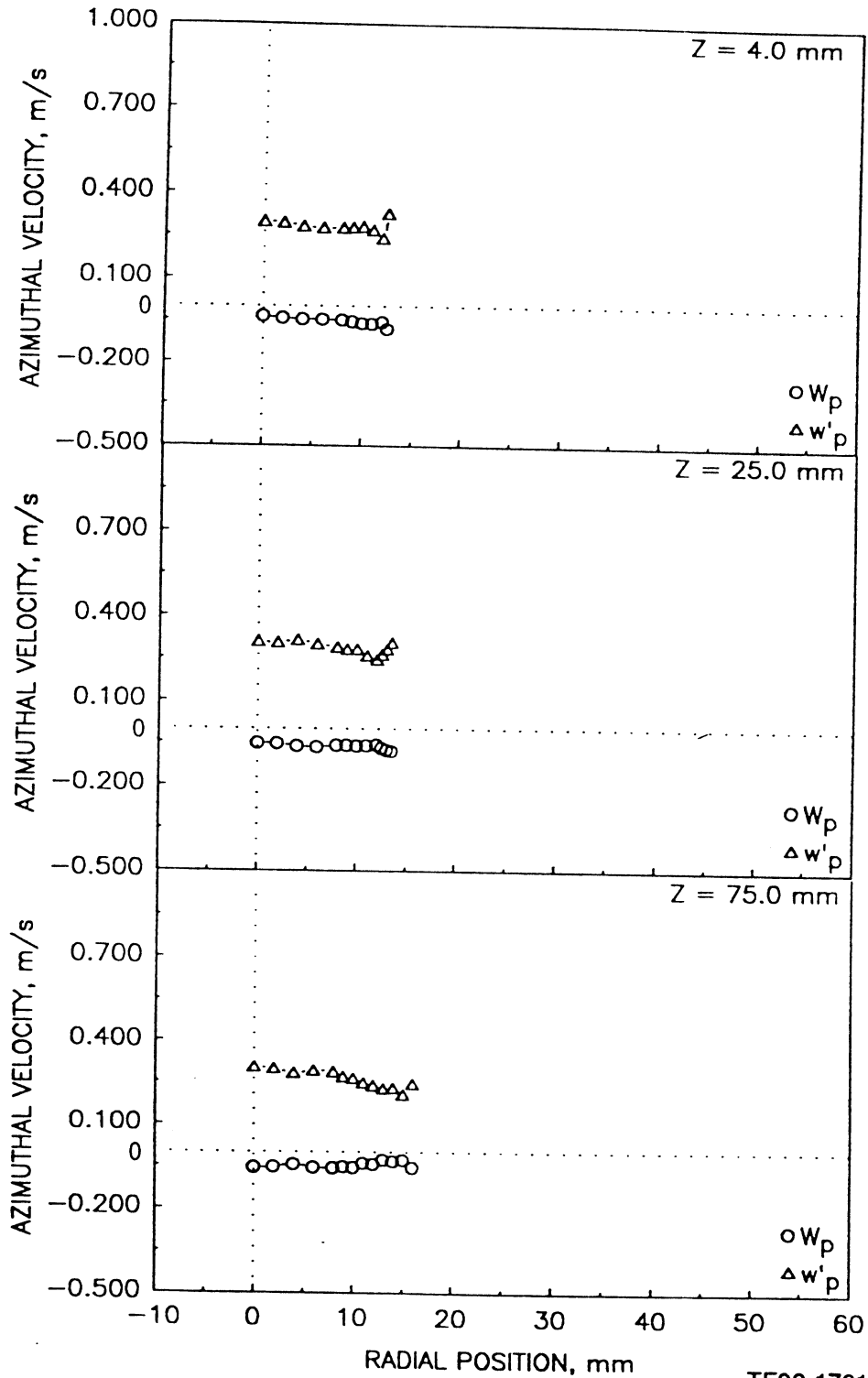


Figure 4.2.9-2. Radial profiles of particle measurements in unconfined round jet laden with 100-110 micron glass beads with a bead-to-gas mass loading ratio of 1.0 (3 of 5).

d) Particle Velocity Correlation Based on Axial and Radial Components

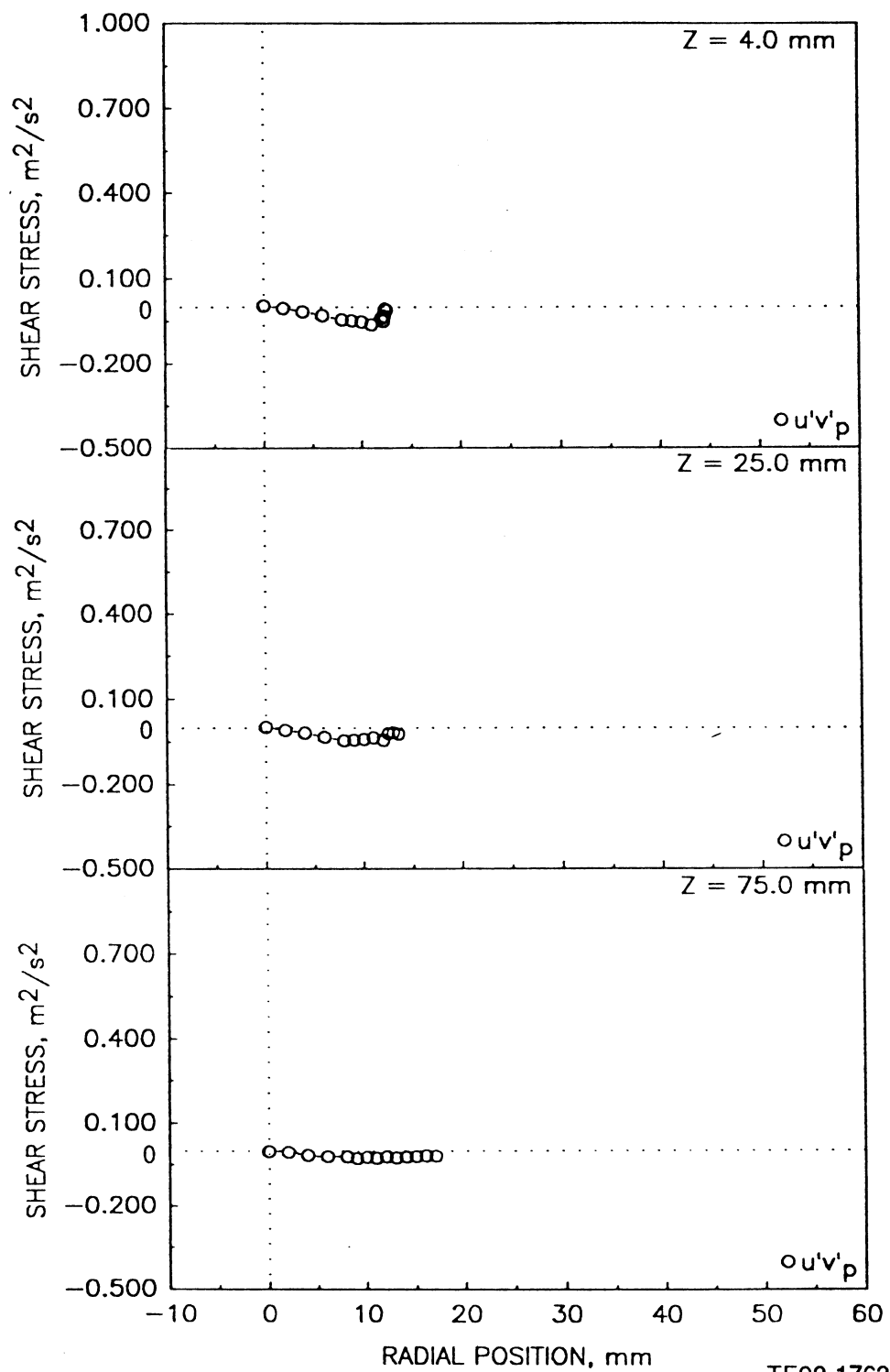
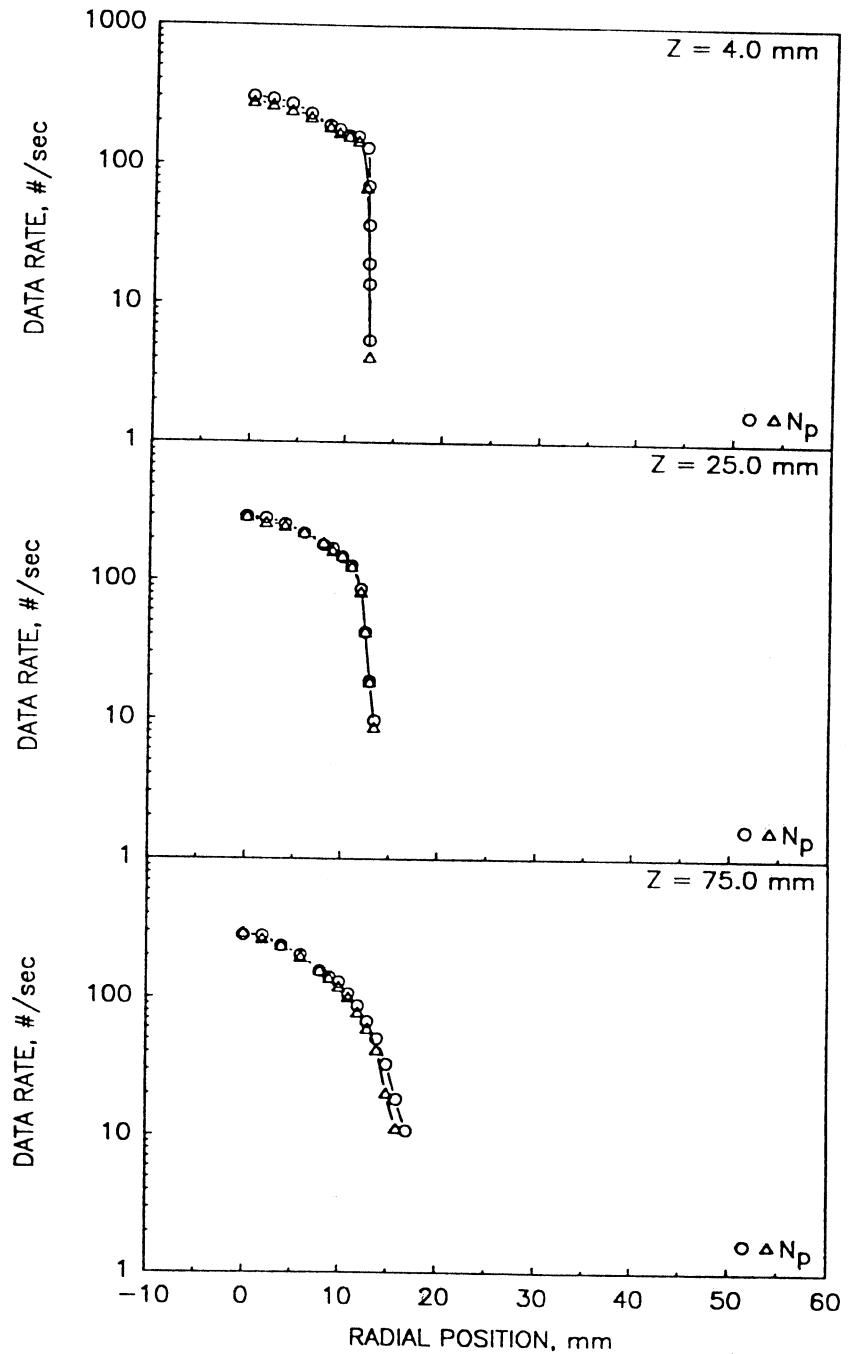


Figure 4.2.9-2. Radial profiles of particle measurements in unconfined round jet laden with 100-110 micron glass beads with a bead-to-gas mass loading ratio of 1.0 (4 of 5).

e) Particle Data Rate



TE92-1763

Figure 4.2.9-2. Radial profiles of particle measurements in unconfined round jet laden with 100-110 micron glass beads with a bead-to-gas mass loading ratio of 1.0 (5 of 5).

a) Mean and Fluctuating Axial Velocities

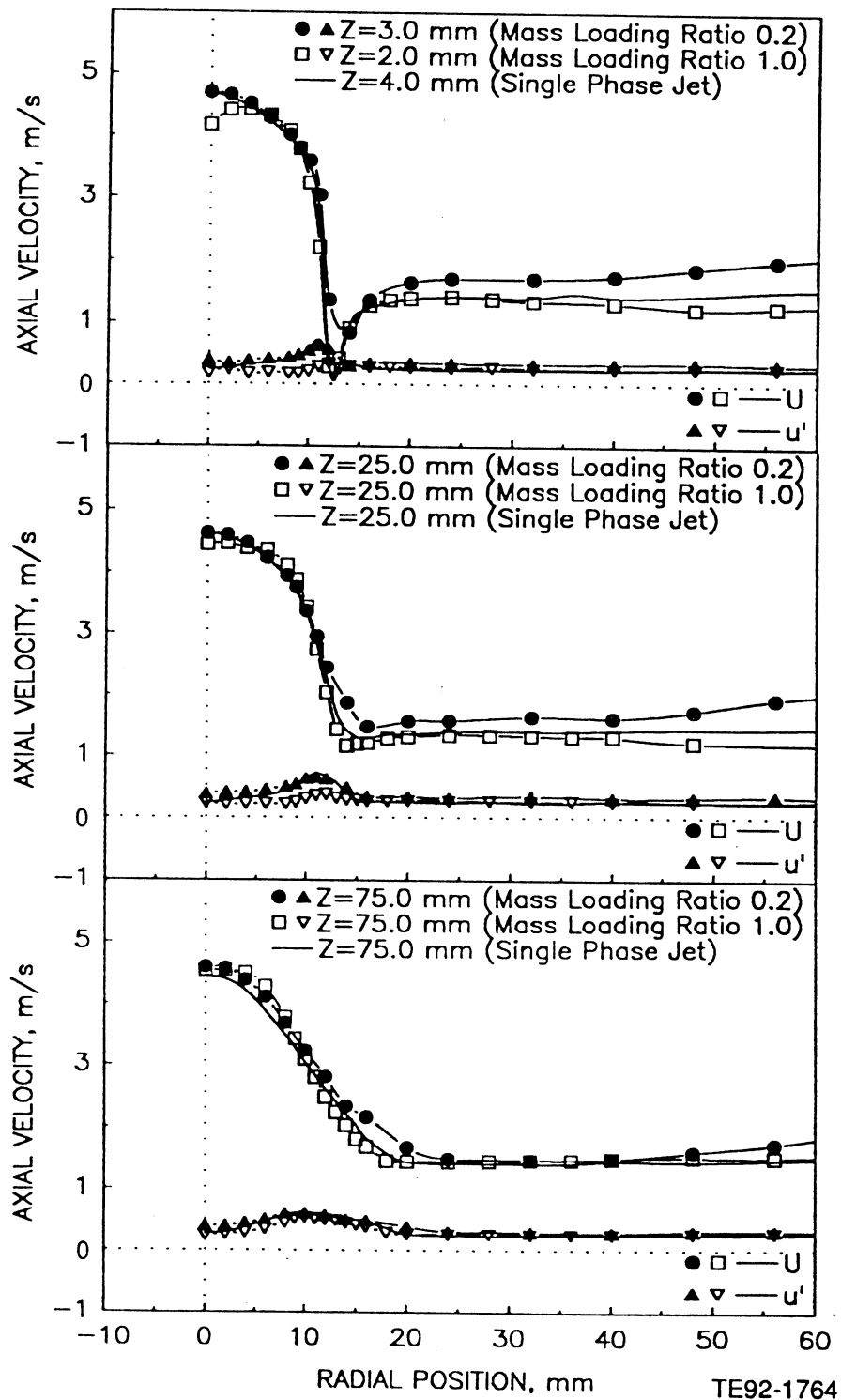


Figure 4.2.10-1. Comparison of gas phase velocities and shear stress in (1) confined single-phase round jet, (2) confined round jet laden with 100-110 micron particles at mass loading of 0.2, and (3) confined round jet laden with 100-110 micron particles at mass loading ratio of 1.0 (1 of 2).

b) Shear Stress Based on Axial and Radial Components

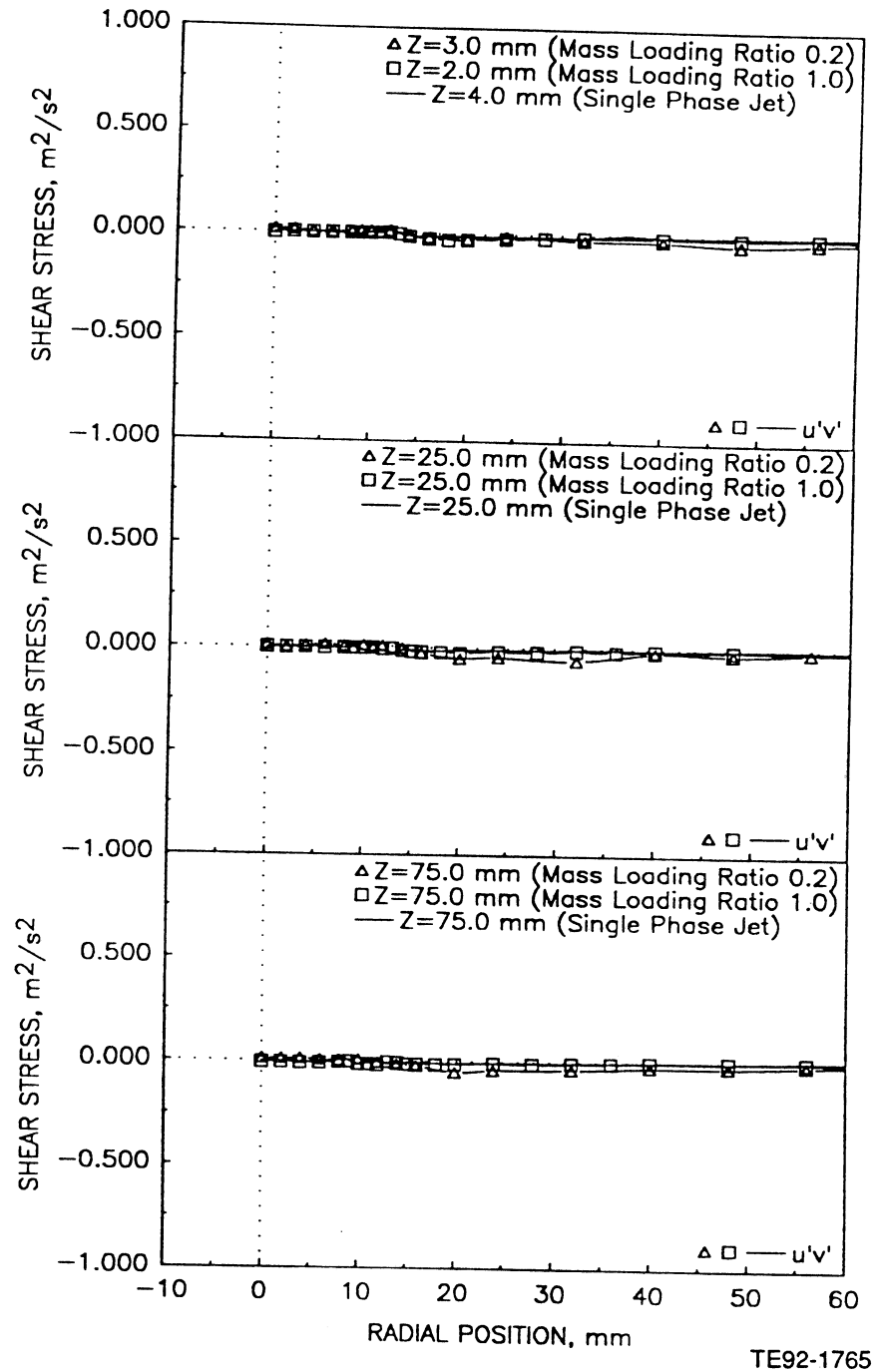
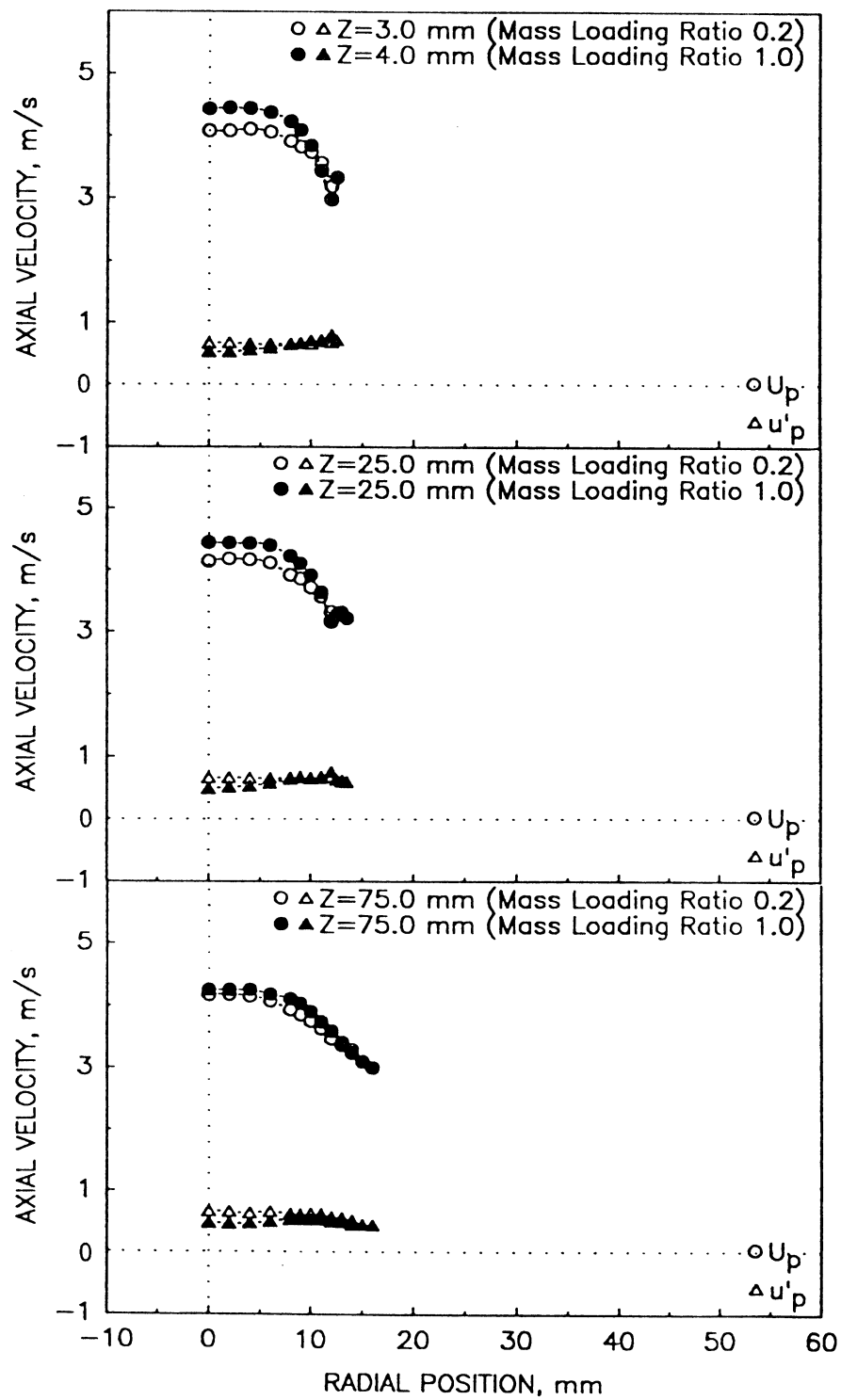


Figure 4.2.10-1. Comparison of gas phase velocities and shear stress in (1) confined single-phase round jet, (2) confined round jet laden with 100-110 micron particles at mass loading of 0.2, and (3) confined round jet laden with 100-110 micron particles at mass loading ratio of 1.0 (2 of 2).

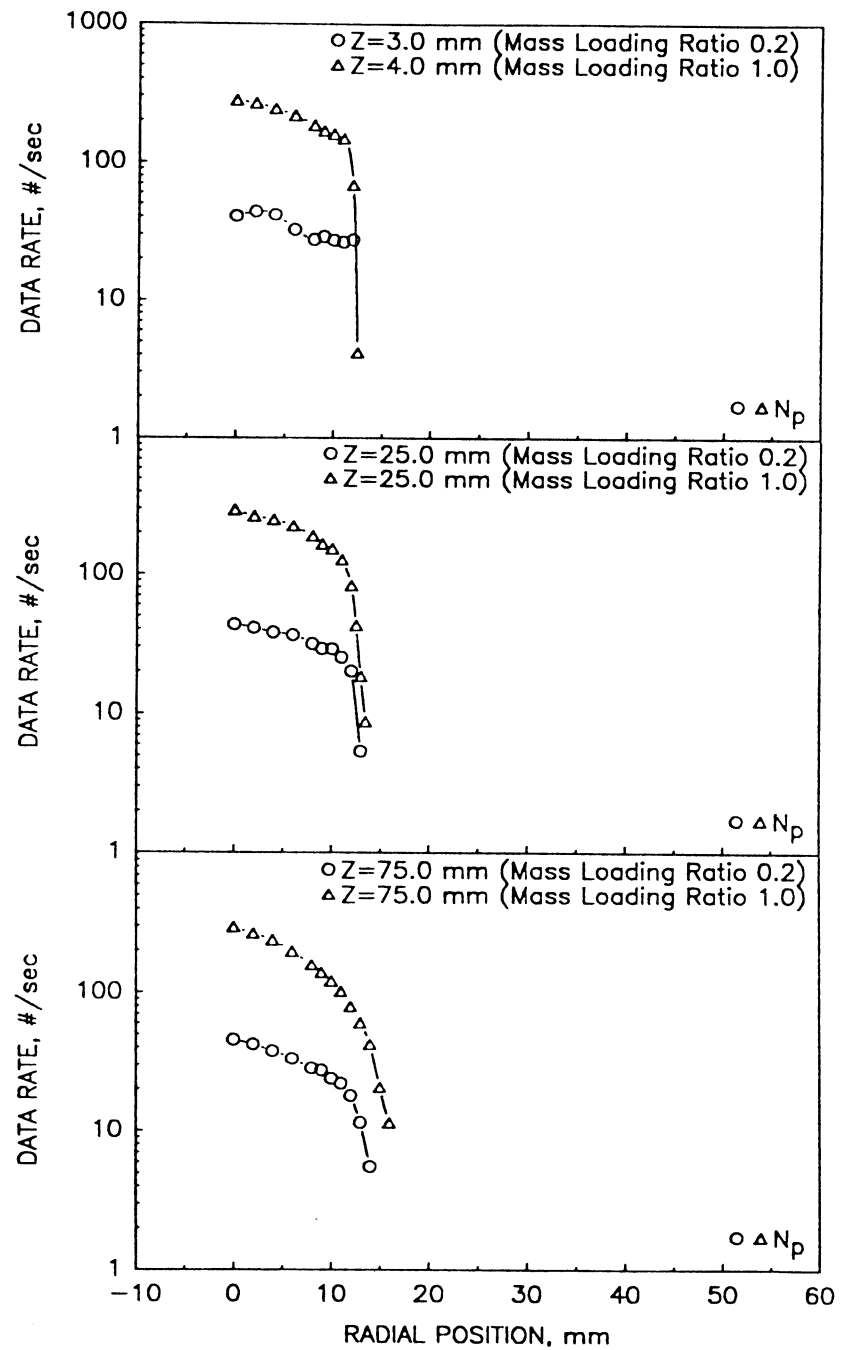
a) Mean and Fluctuating Velocities



TE92-1766

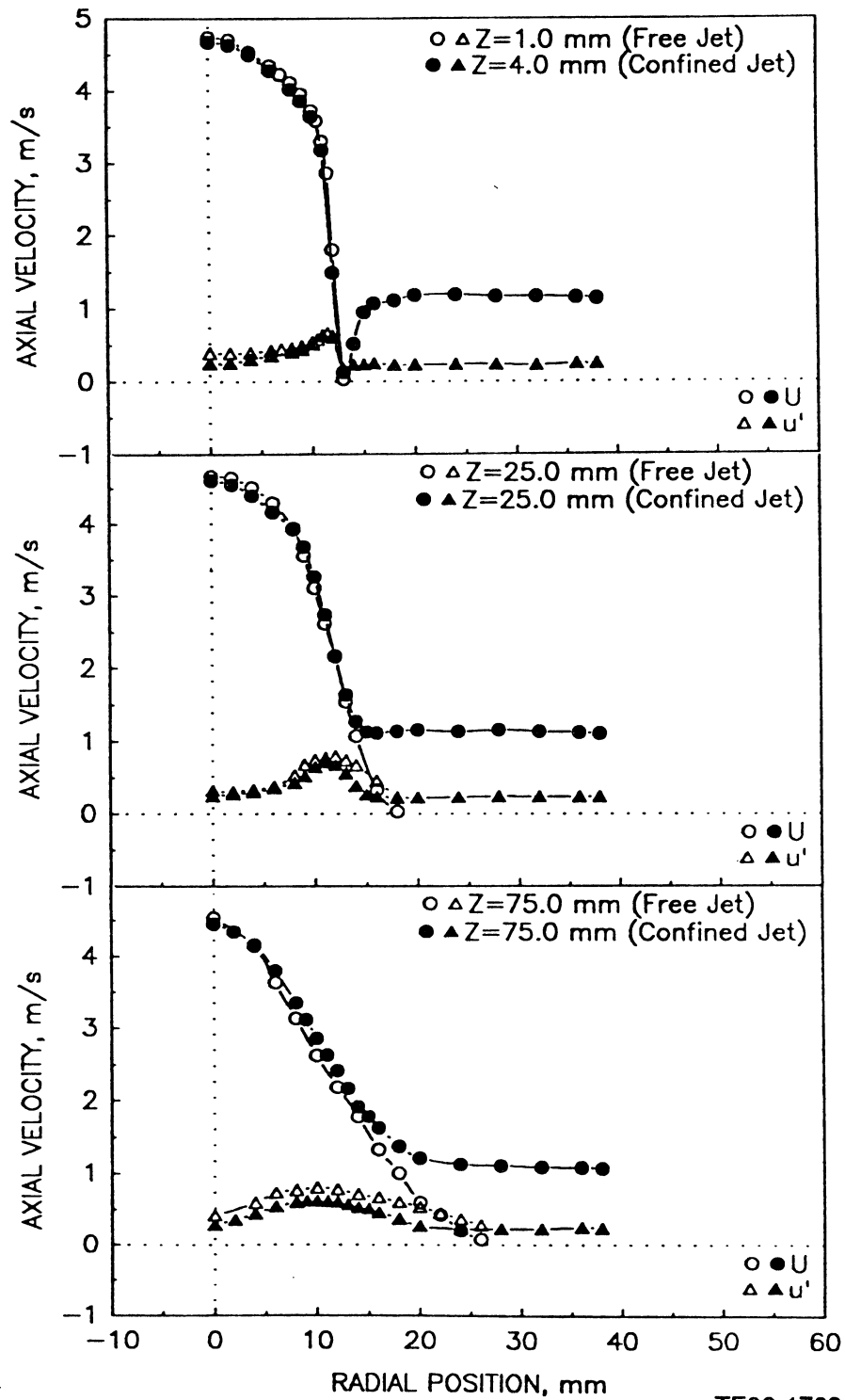
Figure 4.2.10-2. Comparison of particle velocities and data rate in confined round jet laden with particles at a mass loading ratio of 0.2 and 1.0 (1 of 2).

b) Data Rate



TE92-1767

Figure 4.2.10-2. Comparison of particle velocities and data rate in confined round jet laden with particles at a mass loading ratio of 0.2 and 1.0 (2 of 2).



TE92-1768

Figure 4.2.11-1. Comparison of mean and fluctuating axial velocities in the confined and unconfined single-phase round jet.

a) Mean and Fluctuating Velocities

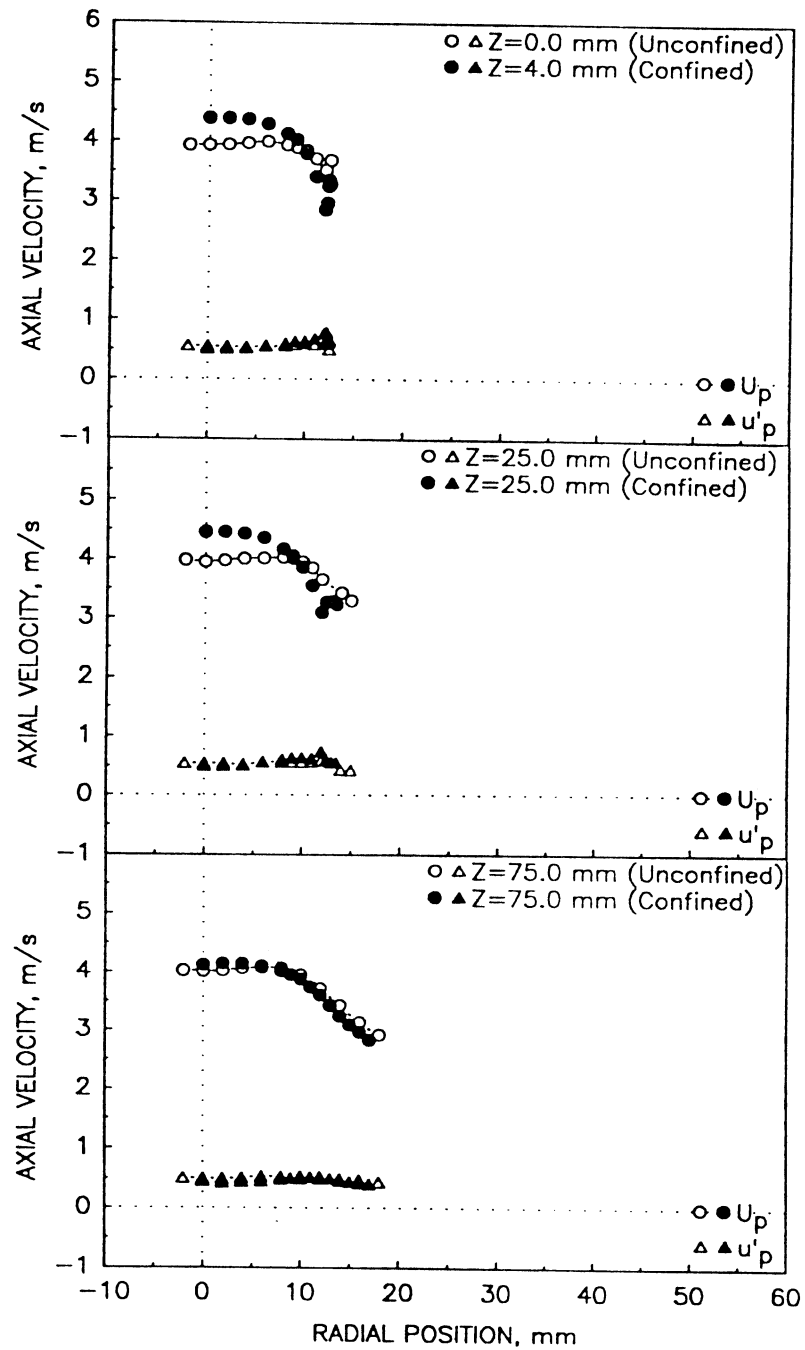


Figure 4.2.12-1. Comparison of mean and fluctuating axial velocities and data rates for 100-110 micron beads in the round jet with and without confinement for a bead-to-gas mass flow rate ratio of 1.0 (1 of 2).

b) Data Rate

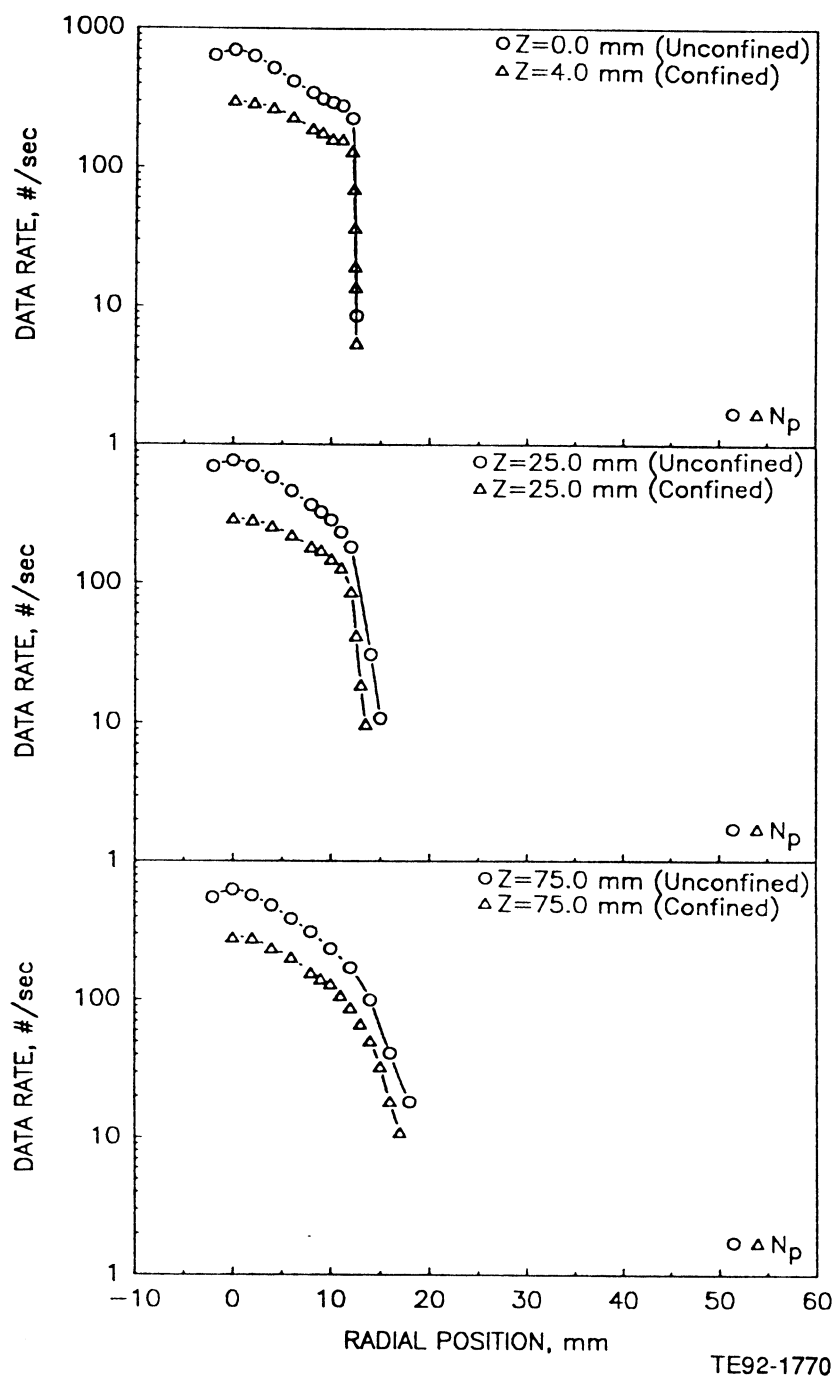


Figure 4.2.12-1. Comparison of mean and fluctuating axial velocities and data rates for 100-110 micron beads in the round jet with and without confinement for a bead-to-gas mass flow rate ratio of 1.0 (2 of 2).

4.3 SINGLE ANNULAR JET – CONF31#2

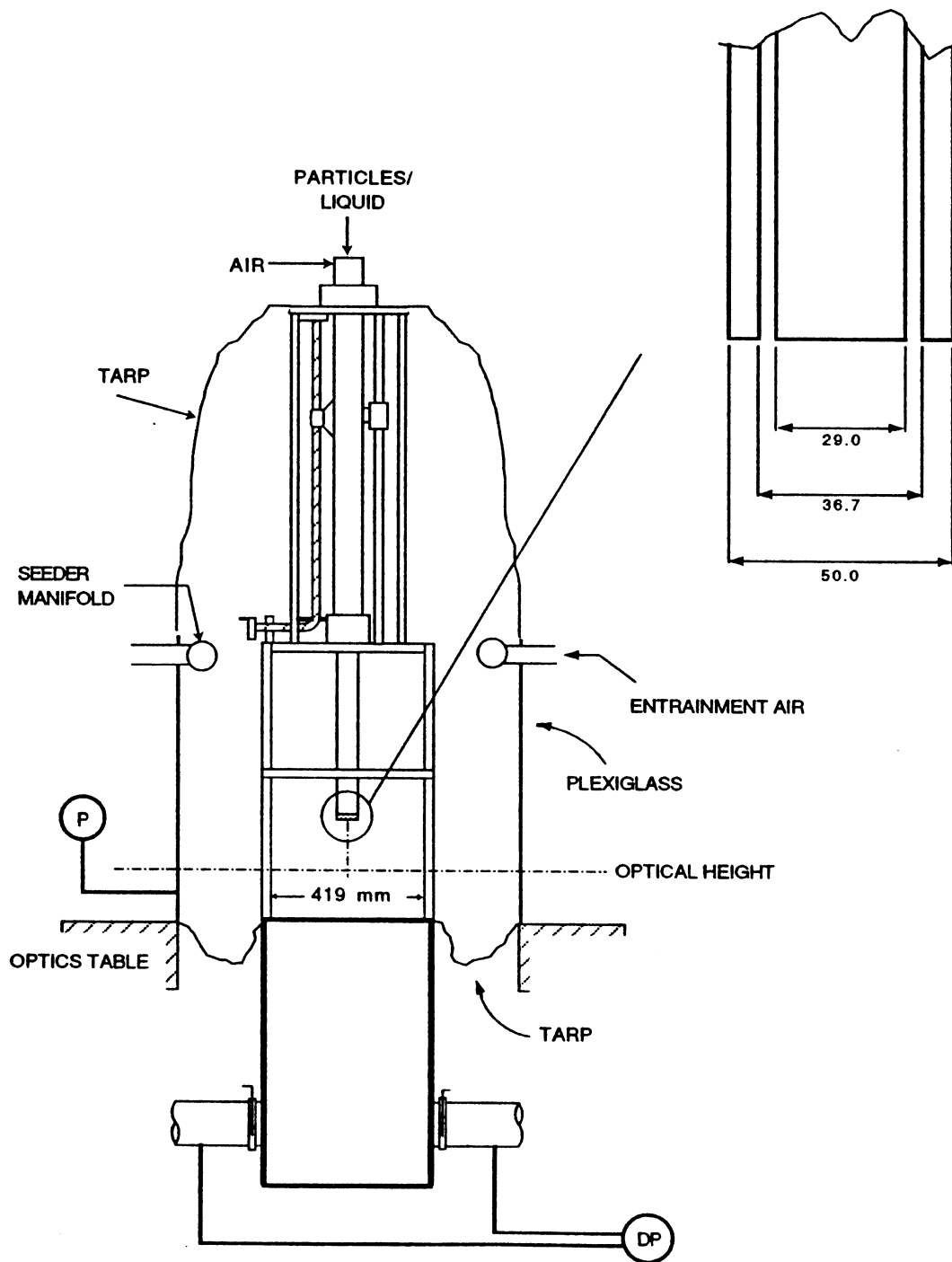
Figure 4.3-1 presents the geometry for the single annular jet. In this case, an annular jet is introduced into an unconfined environment. A cap is placed over the end of the pipe used for the jet studies so that the end of the pipe is a flat surface.

Figure 4.3-2 provides examples of the results obtained in this case. The mean and fluctuating axial velocities are presented in Figure 4.3-2 (a). The two profiles are obtained from the two orthogonal traverses required to measure the azimuthal and radial velocity components. Again, the symmetry is reasonable based on the axial velocity. Note that an on-axis recirculation zone persists to somewhere between 3 and 25 mm axially. By 75 mm axially, the profiles become nearly fully developed.

The radial velocities are presented in Figure 4.3-2 (b). There are strong velocities towards the centerline at 3.0 mm, which give rise to high velocities away from centerline at 25 mm. High fluctuating radial velocities at the centerline are observed at 25 mm, reflecting some unsteadiness in the flow.

The azimuthal velocities are shown in Figure 4.3-2 (c). The mean velocities reveal mostly zero values as expected.

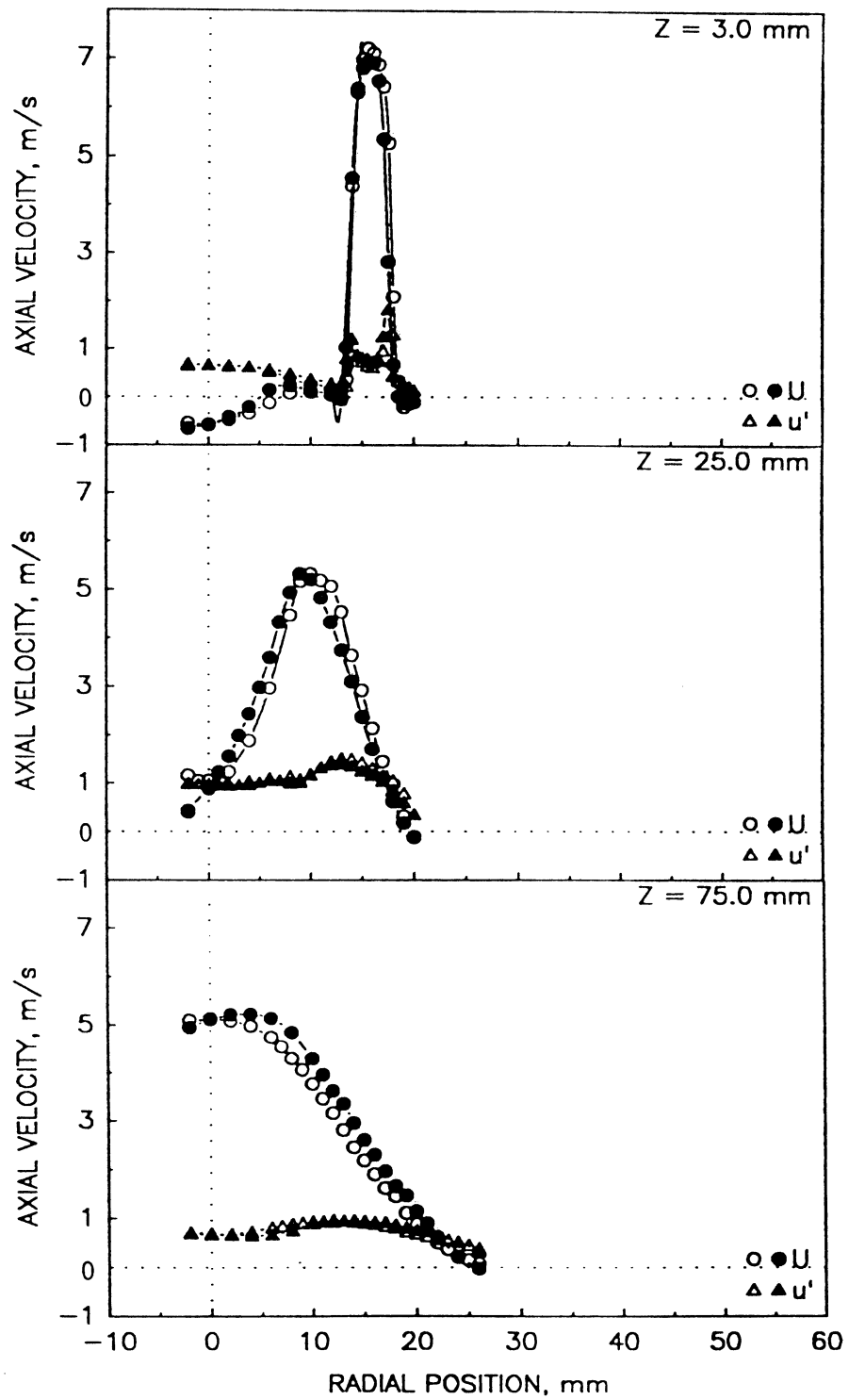
The shear stress components (Figure 4.3-2 [d and e]) show expected behavior.



TE92-1771

Figure 4.3-1. Geometry utilized for unconfined single-phase annular jet.

a) Mean and Fluctuating Axial Velocities



TE92-1772

Figure 4.3-2. Radial profiles of gas phase statistics in unconfined single-phase annular jet (1 of 5).

b) Mean and Fluctuating Radial Velocities

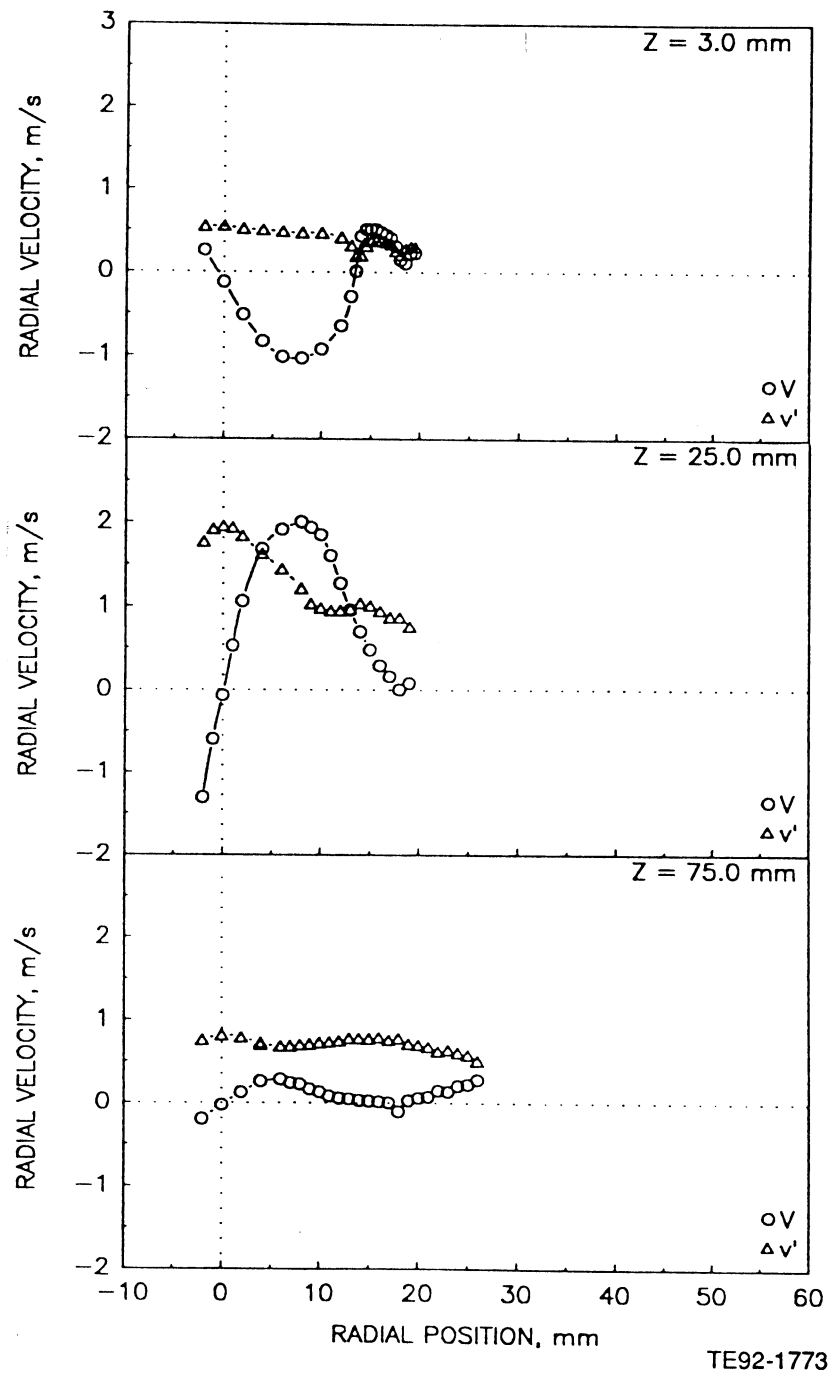
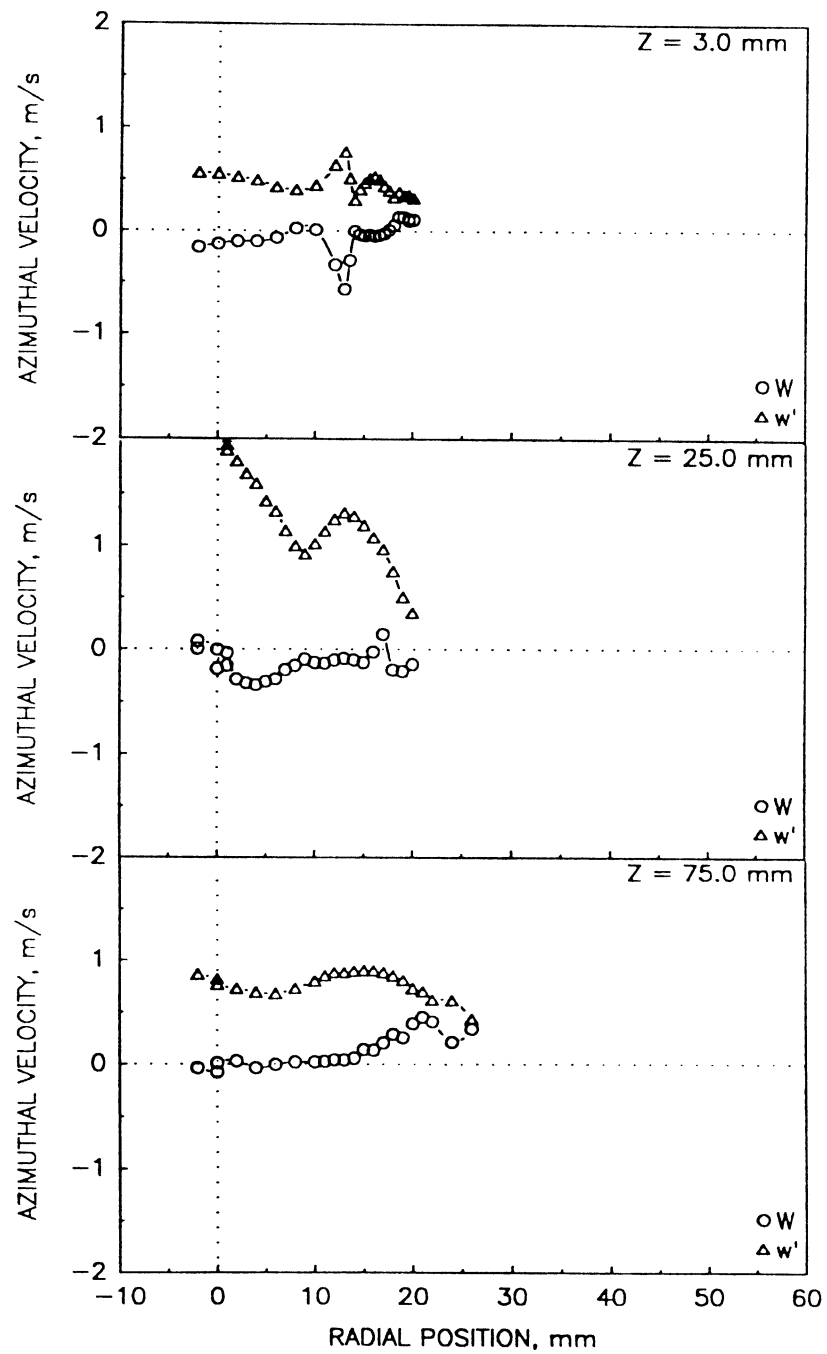


Figure 4.3-2. Radial profiles of gas phase statistics in unconfined single-phase annular jet (2 of 5).

c) Mean and Fluctuating Azimuthal Velocities



TE92-1774

Figure 4.3-2. Radial profiles of gas phase statistics in unconfined single-phase annular jet (3 of 5).

d) Shear Stress Based on Axial and Radial Velocities

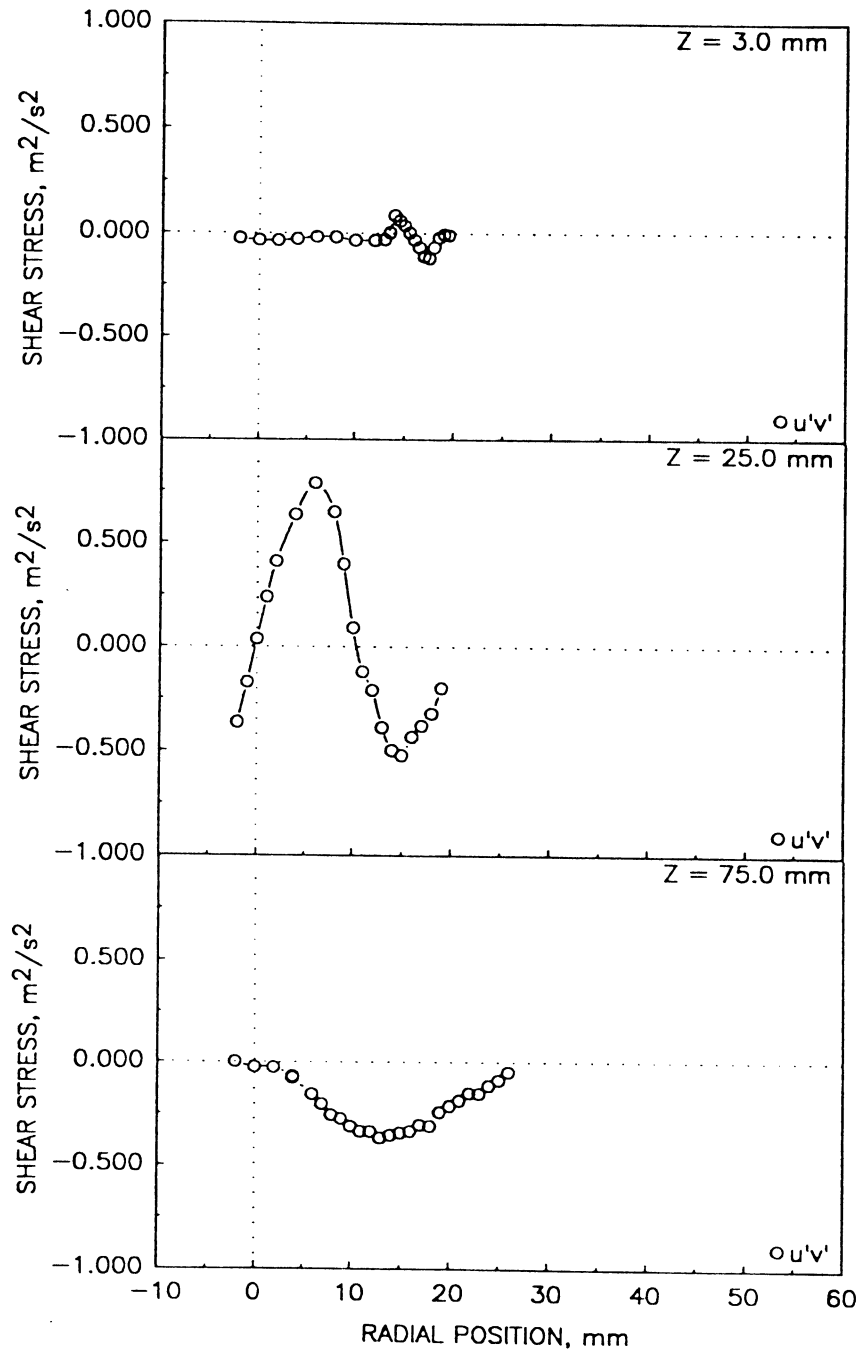


Figure 4.3-2. Radial profiles of gas phase statistics in unconfined single-phase annular jet (4 of 5).

e) Shear Stress Based on Axial and Azimuthal Velocities

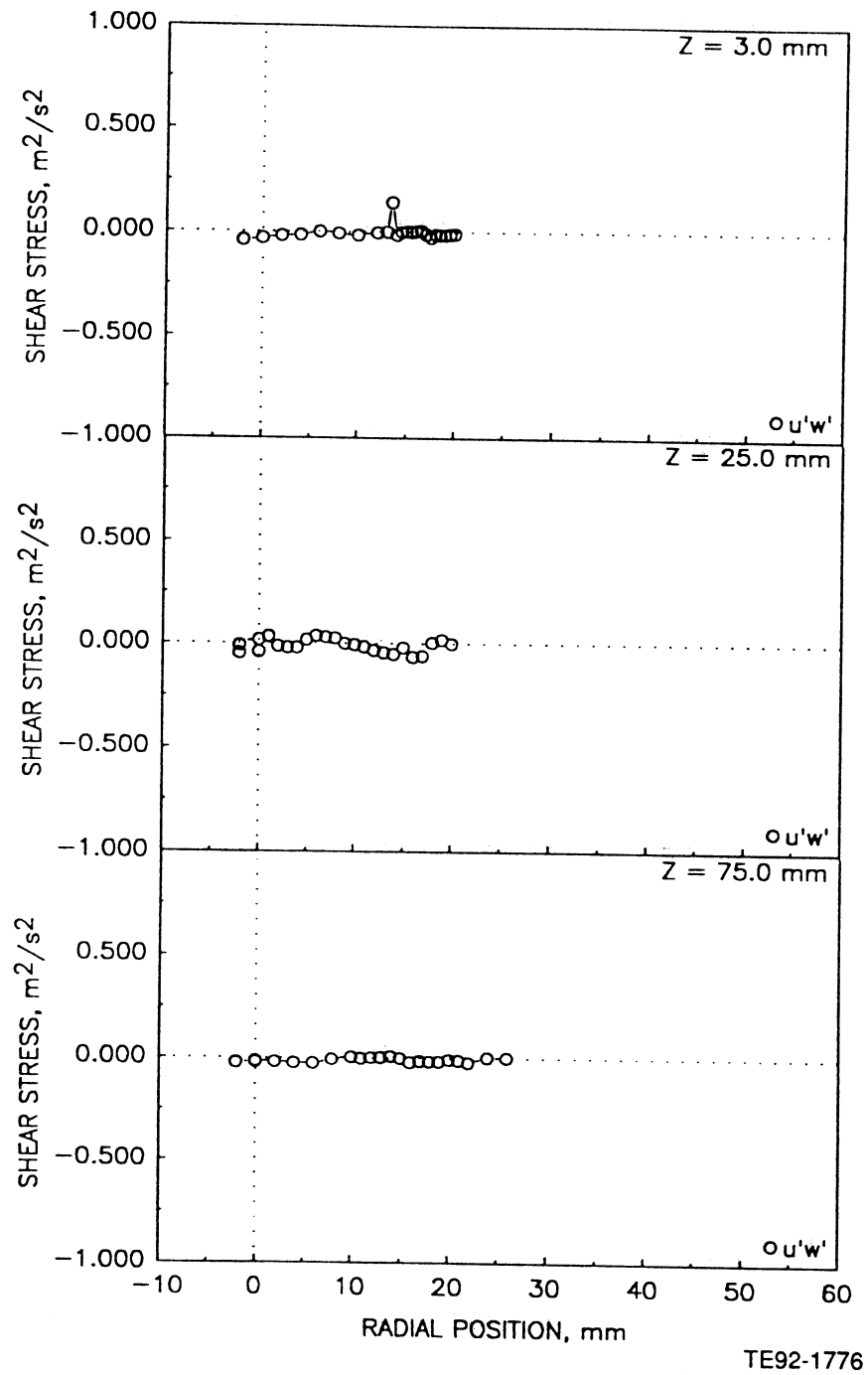


Figure 4.3-2. Radial profiles of gas phase statistics in unconfined single-phase annular jet (5 of 5).

4.4 SINGLE SWIRLING ANNULAR JET

In this case, both unconfined and confined studies were conducted.

4.4.1 Unconfined Case – CONF32#1

Figure 4.4.1-1 shows the geometry employed for the swirling annular jet. It is the same as for the non-swirling case (Figure 4.3-1), but the 60 deg swirl vanes are in place.

Figure 4.4.1-2 shows examples of the results obtained. The results for the axial velocity (Figure 4.4.1-2 [a]) reveal good symmetry at $Z = 3.0$ and 25.0 mm. The 75 mm station, however, shows some asymmetry in the mean velocity.

The effects of the bluff body at the center of the flow exiting the annular jet and entrainment is apparent from the radial velocities (Figure 4.4.1-2 [b]), where strong flow towards the centerline is revealed by the measurements.

The swirling velocities (Figure 4.4.1-2 [c]) show that the strong swirl decays rapidly. The mean velocity shows values of zero at the centerline, as expected.

The cross correlations of the fluctuating velocity components reveal behavior which is as expected (Figure 4.4.1-2 [d and e]).

4.4.2 Confined Case – CONF34#1

Figure 4.4.2-1 presents the geometry employed for the confined annular swirling jet. It is identical to that used for the unconfined case, only it is placed concentrically within the 152.4 mm duct.

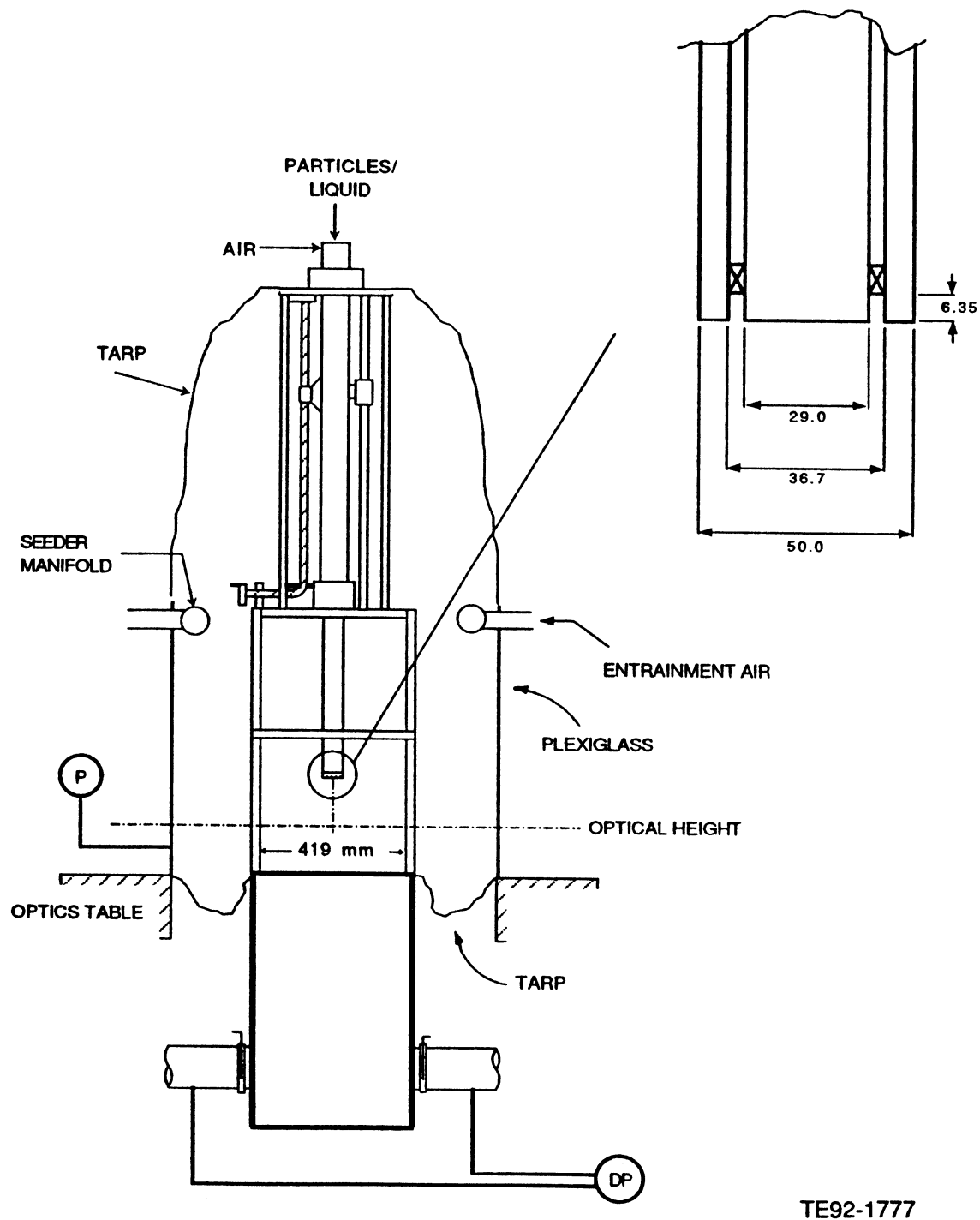
Figure 4.4.2-2 provides examples of the results. The results for the mean axial velocity (Figure 4.4.2-2 [a]) reveal reasonable symmetry and exhibit a strong on-axis recirculation zone. The radial and azimuthal velocities appear similar as they did for the unconfined case (section 4.4.1).

4.4.3 Effect of Swirl

To better examine the effect of swirl on the flow from the unconfined annular jet, Figure 4.4.3-1 provides a comparison of the axial velocities for the cases presented in sections 4.3 and 4.4.1. The inlet plane shows similarities, but the swirl shifts the momentum radial outwards. With increased distance, the strong recirculation zone which forms with swirl does not appear in the absence of swirl. The swirl also moves the radial location of the highest axial velocity fluctuations away from the centerline.

4.4.4 Effect of Confinement

To better show the impact of confinement on the swirling annular jet, Figure 4.4.4-1 presents a comparison of the cases with (section 4.4.2) and without (section 4.4.1) confinement. For this case, confinement appears to have little impact on the behavior of the axial velocity.



TE92-1777

Figure 4.4.1-1. Geometry utilized for unconfined single-phase swirling annular jet.

a) Mean and Fluctuating Axial Velocities

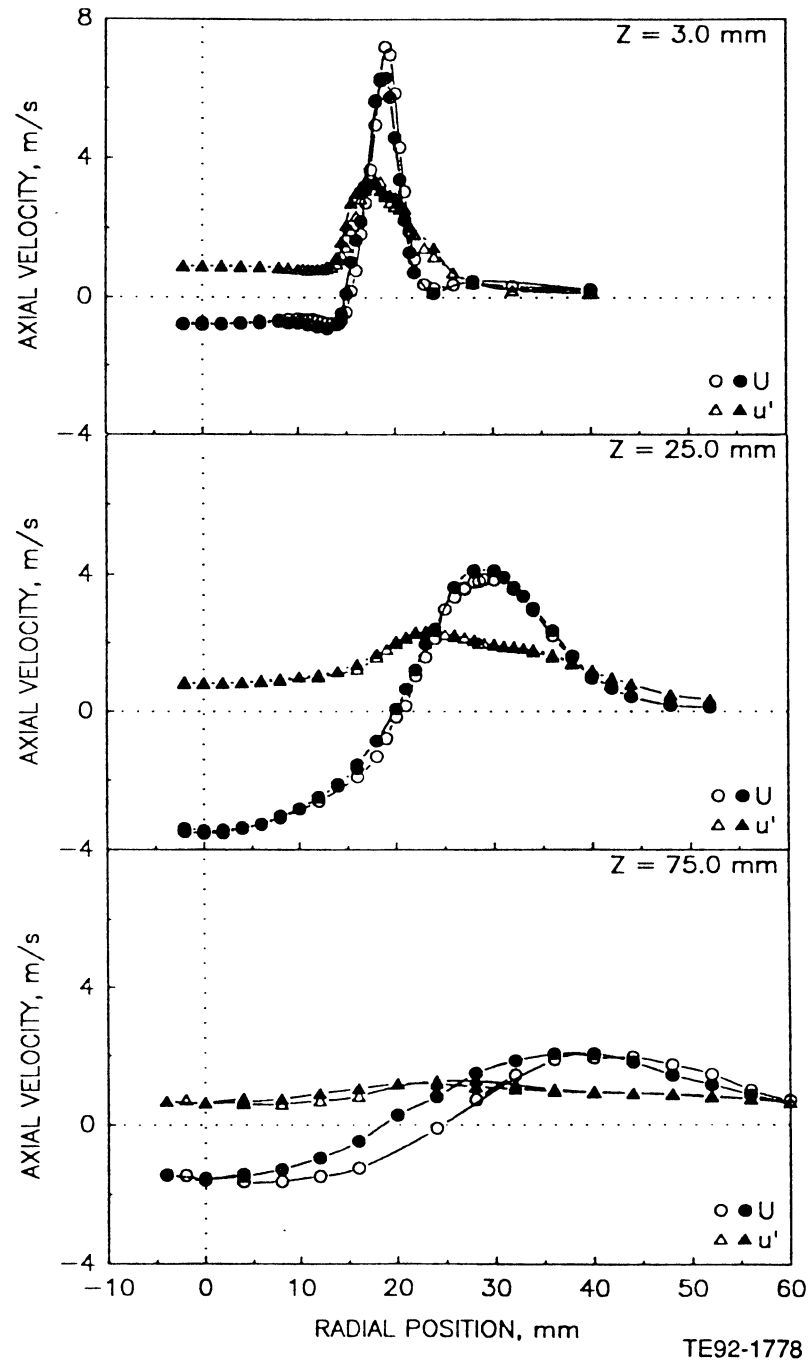


Figure 4.4.1-2. Radial profiles of gas phase statistics in unconfined single-phase swirling annular jet (1 of 5).

b) Mean and Fluctuating Radial Velocities

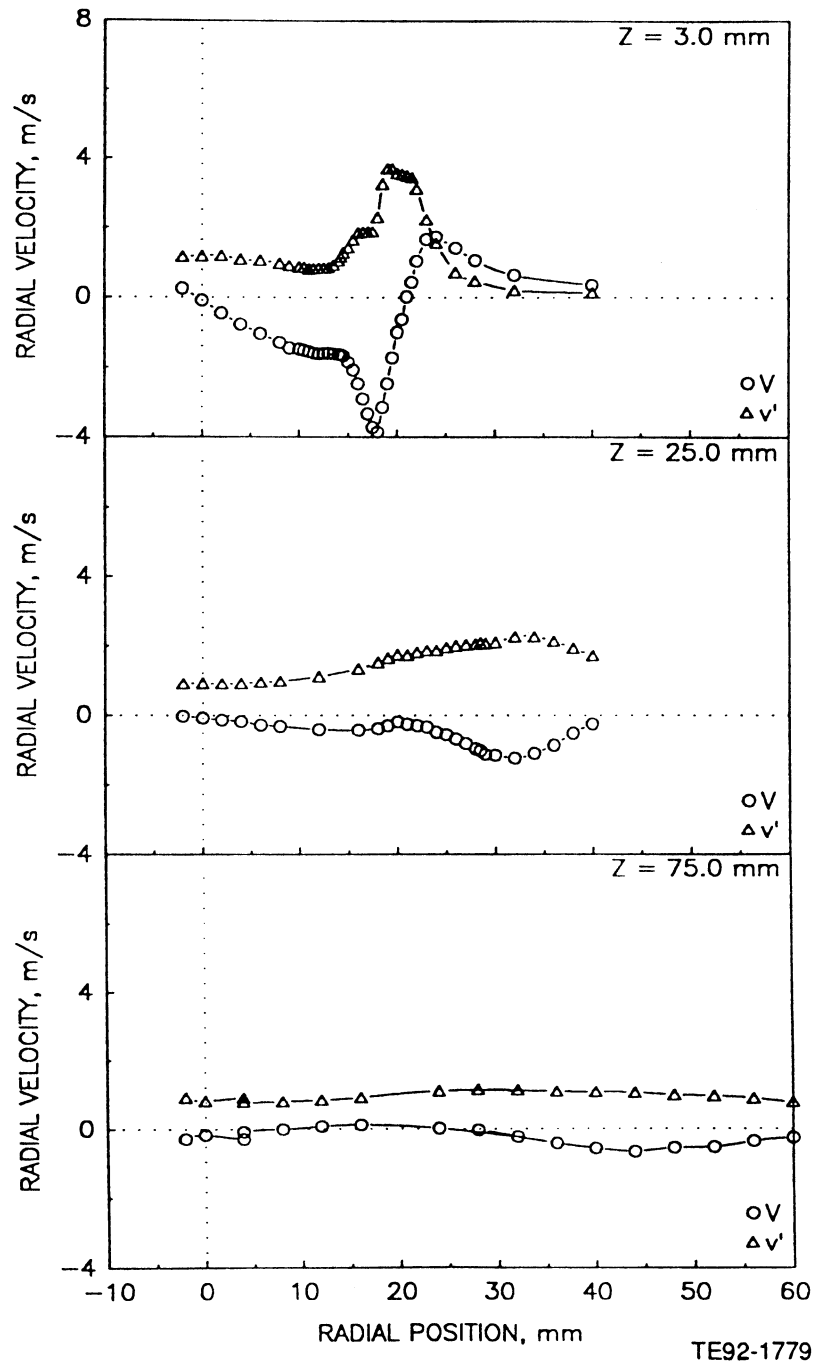


Figure 4.4.1-2. Radial profiles of gas phase statistics in unconfined single-phase swirling annular jet (2 of 5).

c) Mean and Fluctuating Azimuthal Velocities

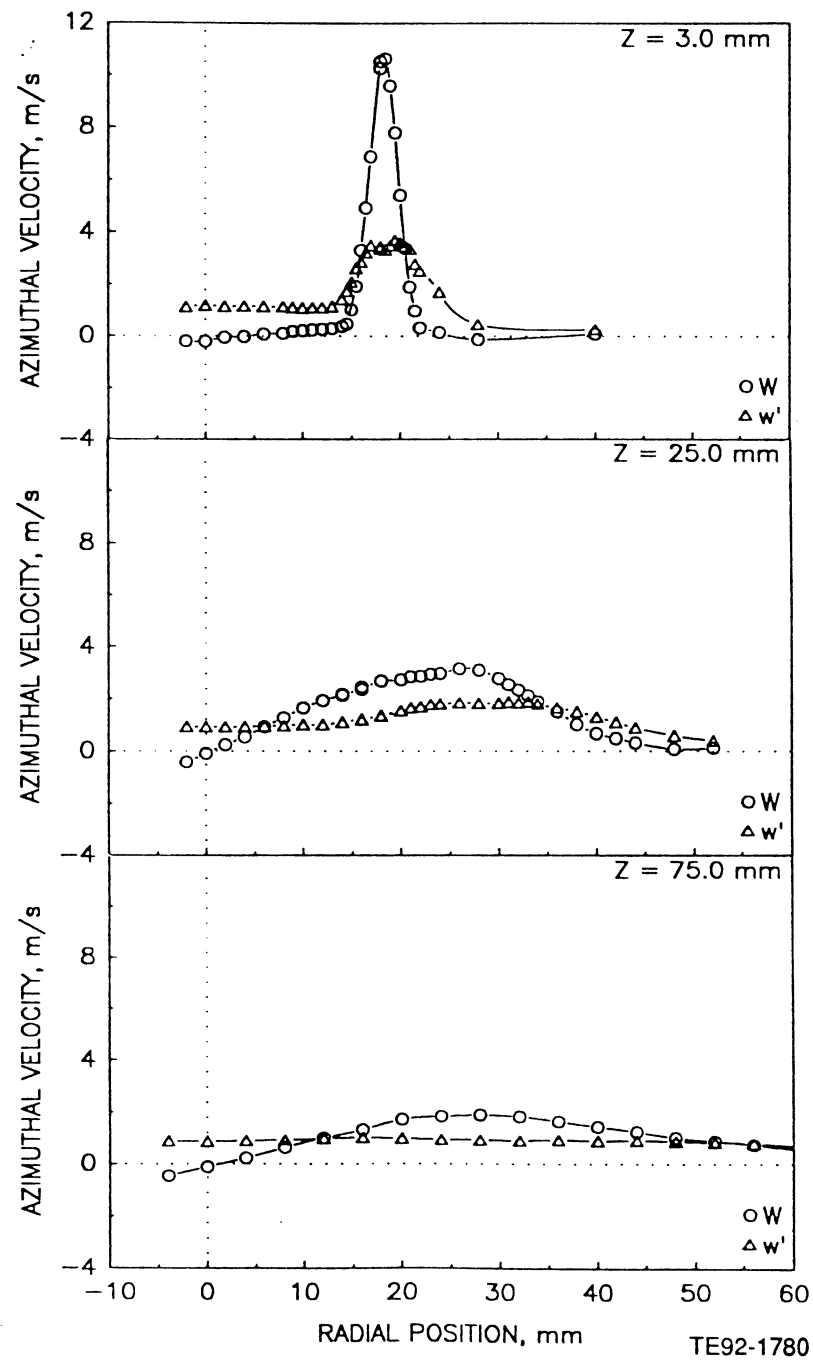


Figure 4.4.1-2. Radial profiles of gas phase statistics in unconfined single-phase swirling annular jet (3 of 5).

d) Shear Stress Based on Axial and Radial Velocities

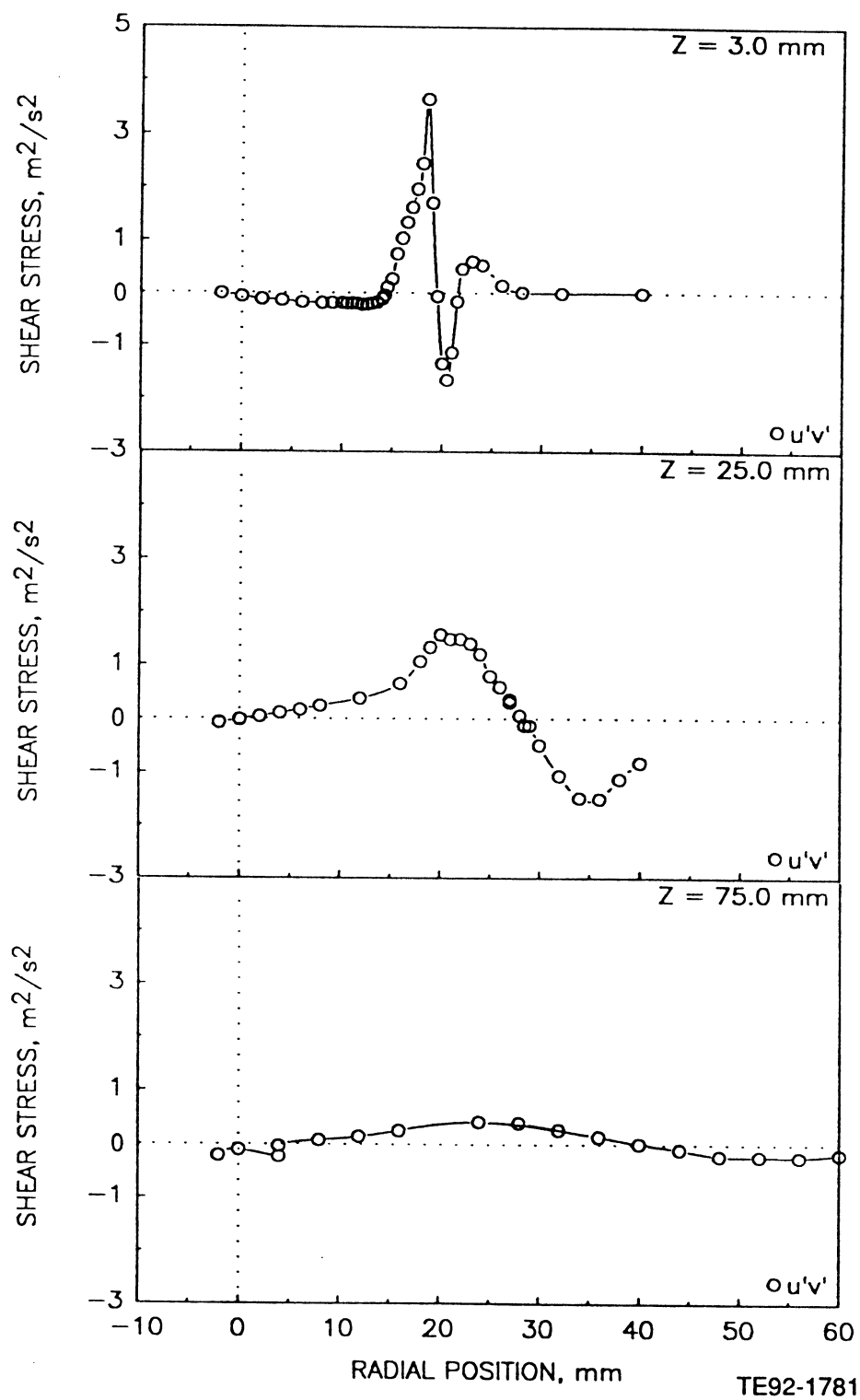


Figure 4.4.1-2. Radial profiles of gas phase statistics in unconfined single-phase swirling annular jet (4 of 5).

e) Shear Stress Based on Axial and Azimuthal Velocities

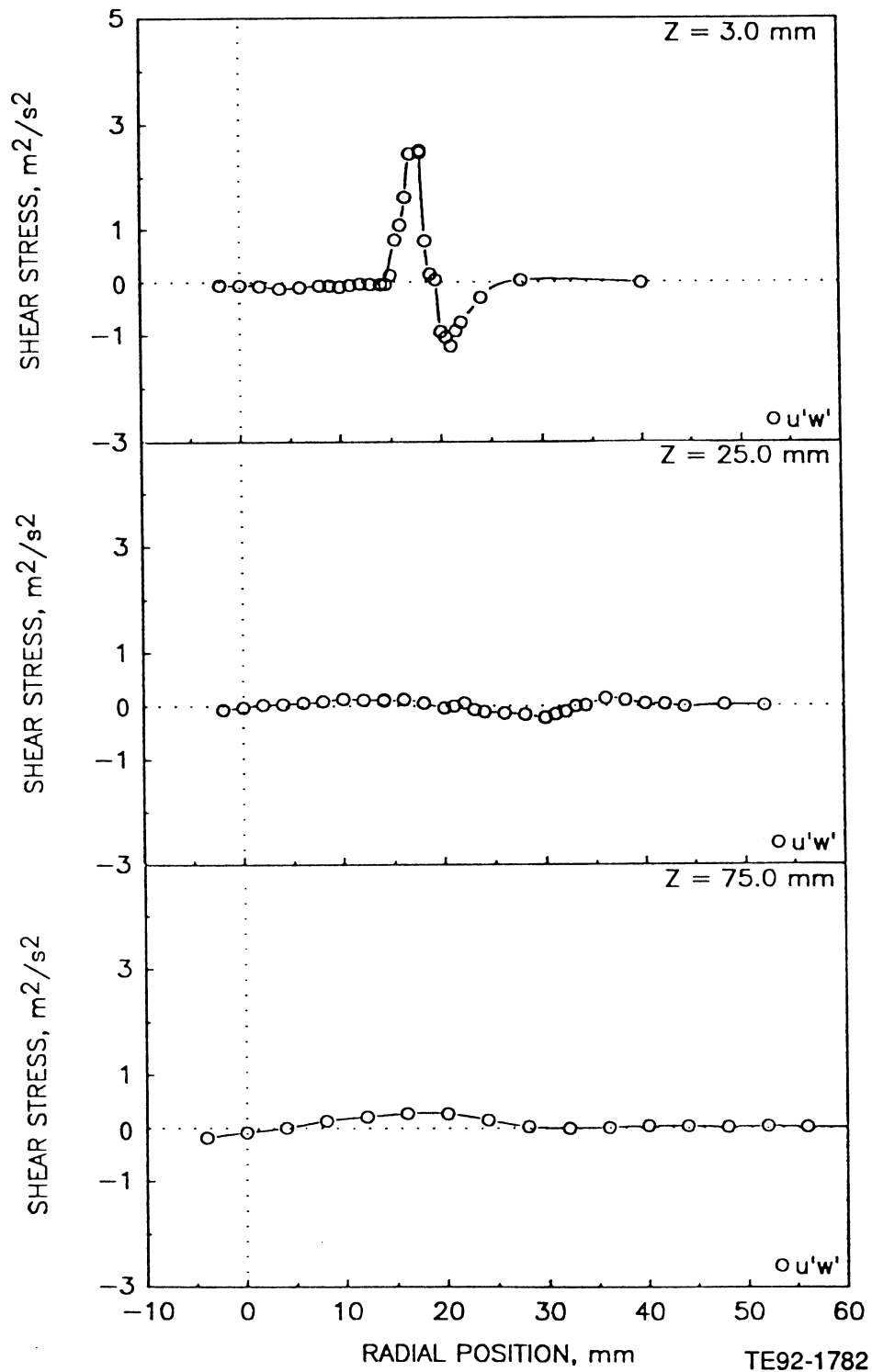
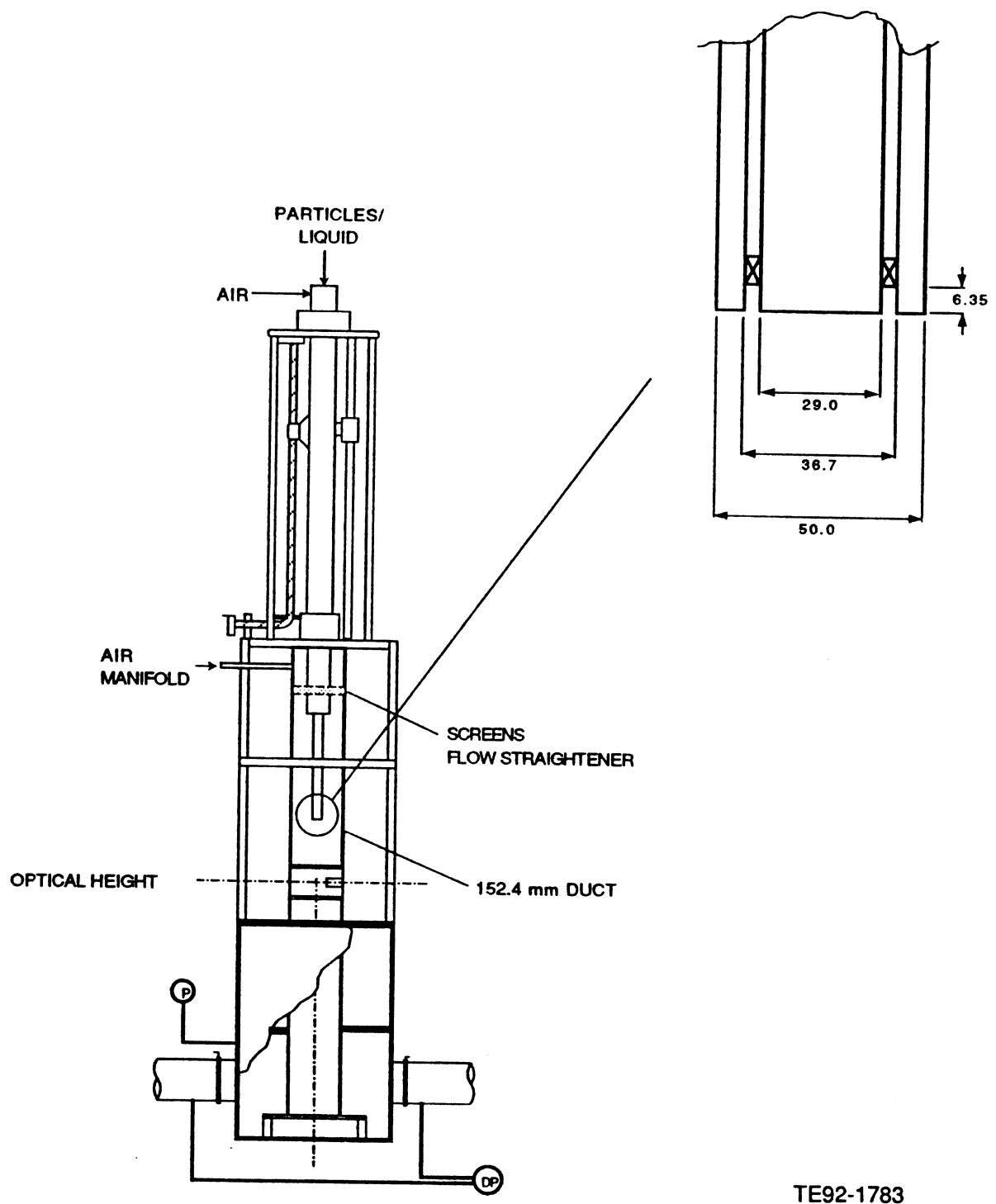


Figure 4.4.1-2. Radial profiles of gas phase statistics in unconfined single-phase swirling annular jet (5 of 5).



TE92-1783

Figure 4.4.2-1. Geometry utilized for confined single-phase swirling annular jet.

a) Mean and Fluctuating Axial Velocities

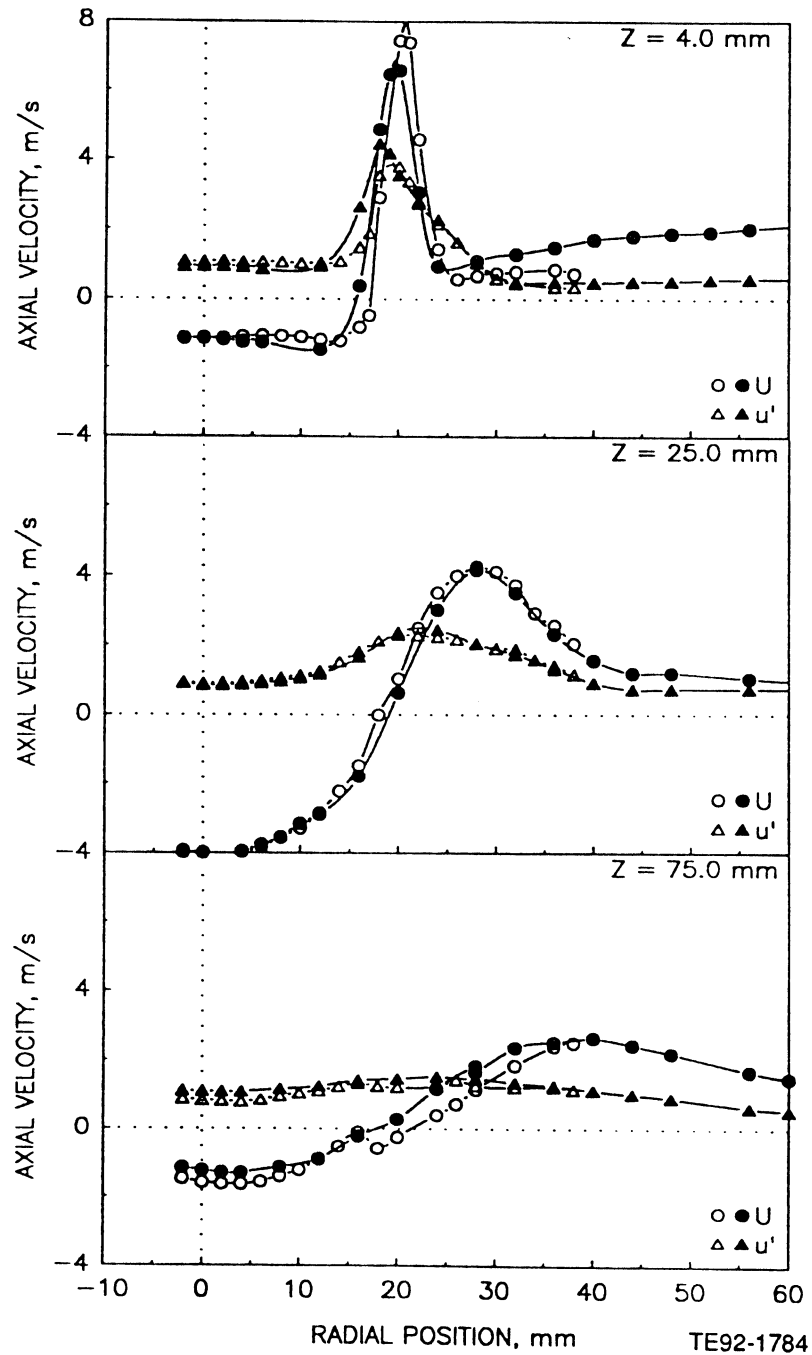


Figure 4.4.2-2. Radial profiles of gas phase statistics in confined single-phase swirling annular jet (1 of 5).

b) Mean and Fluctuating Radial Velocities

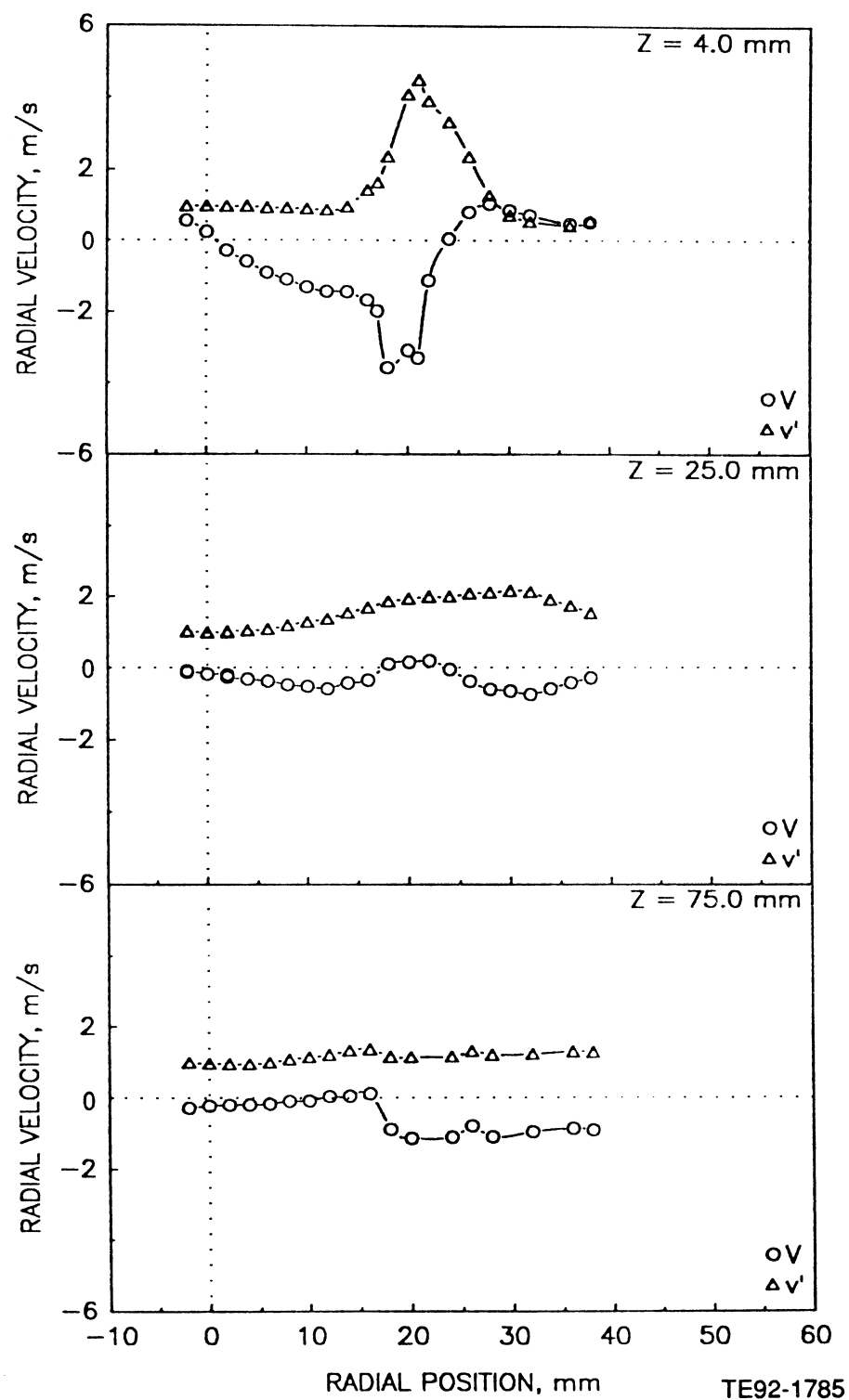


Figure 4.4.2-2. Radial profiles of gas phase statistics in confined single-phase swirling annular jet (2 of 5).

c) Mean and Fluctuating Azimuthal Velocities

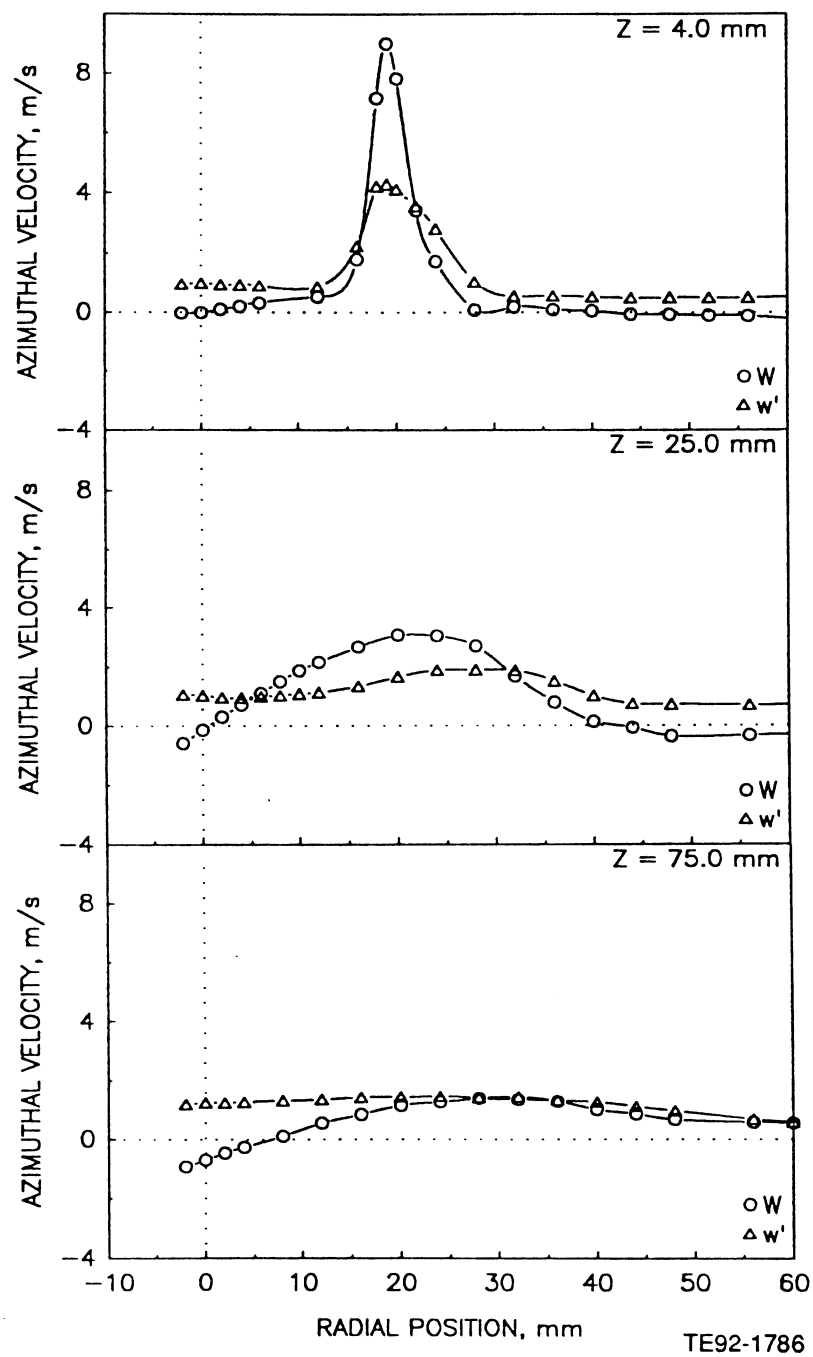


Figure 4.4.2-2. Radial profiles of gas phase statistics in confined single-phase swirling annular jet (3 of 5).

d) Shear Stress Based on Axial and Radial Velocities

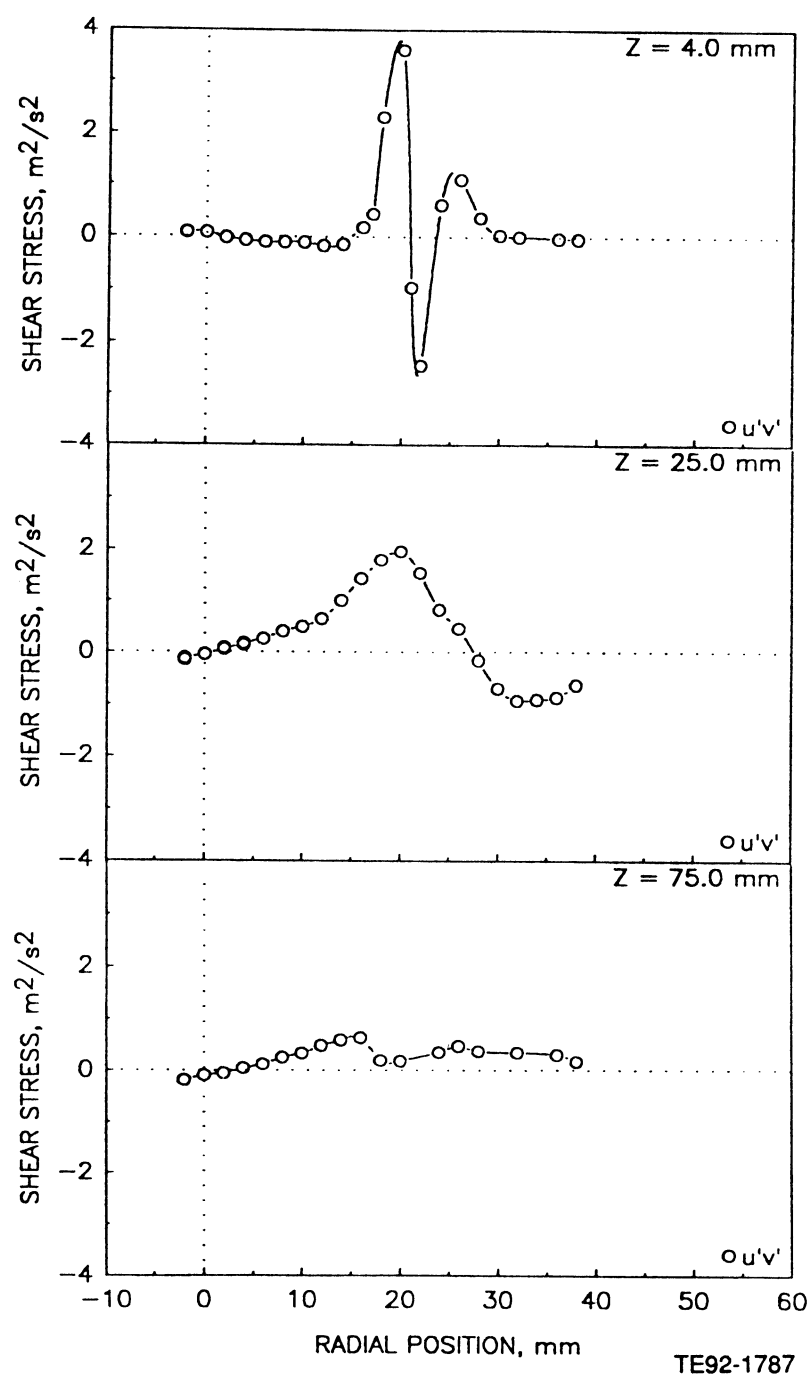


Figure 4.4.2-2. Radial profiles of gas phase statistics in confined single-phase swirling annular jet (4 of 5).

e) Shear Stress Based on Axial and Azimuthal Velocities

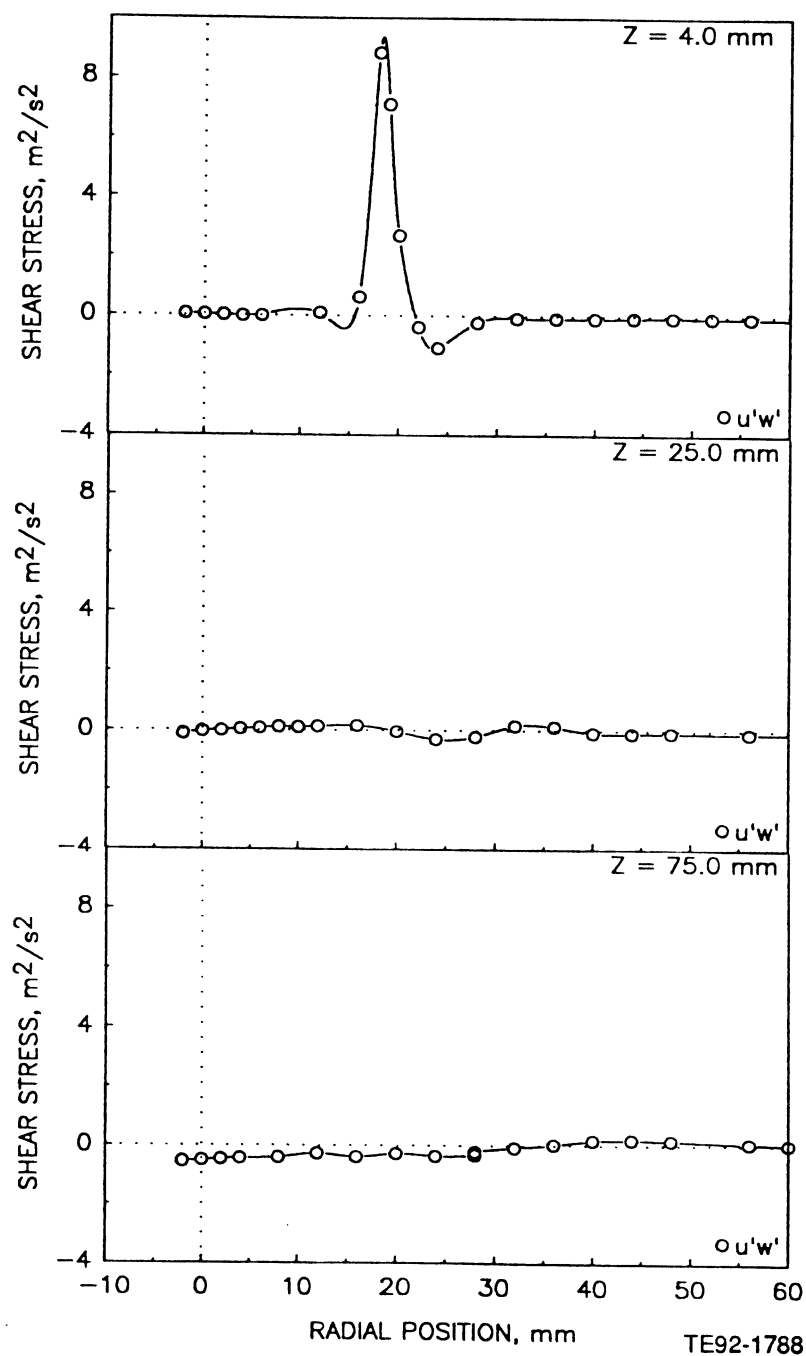


Figure 4.4.2-2. Radial profiles of gas phase statistics in confined single-phase swirling annular jet (5 of 5).

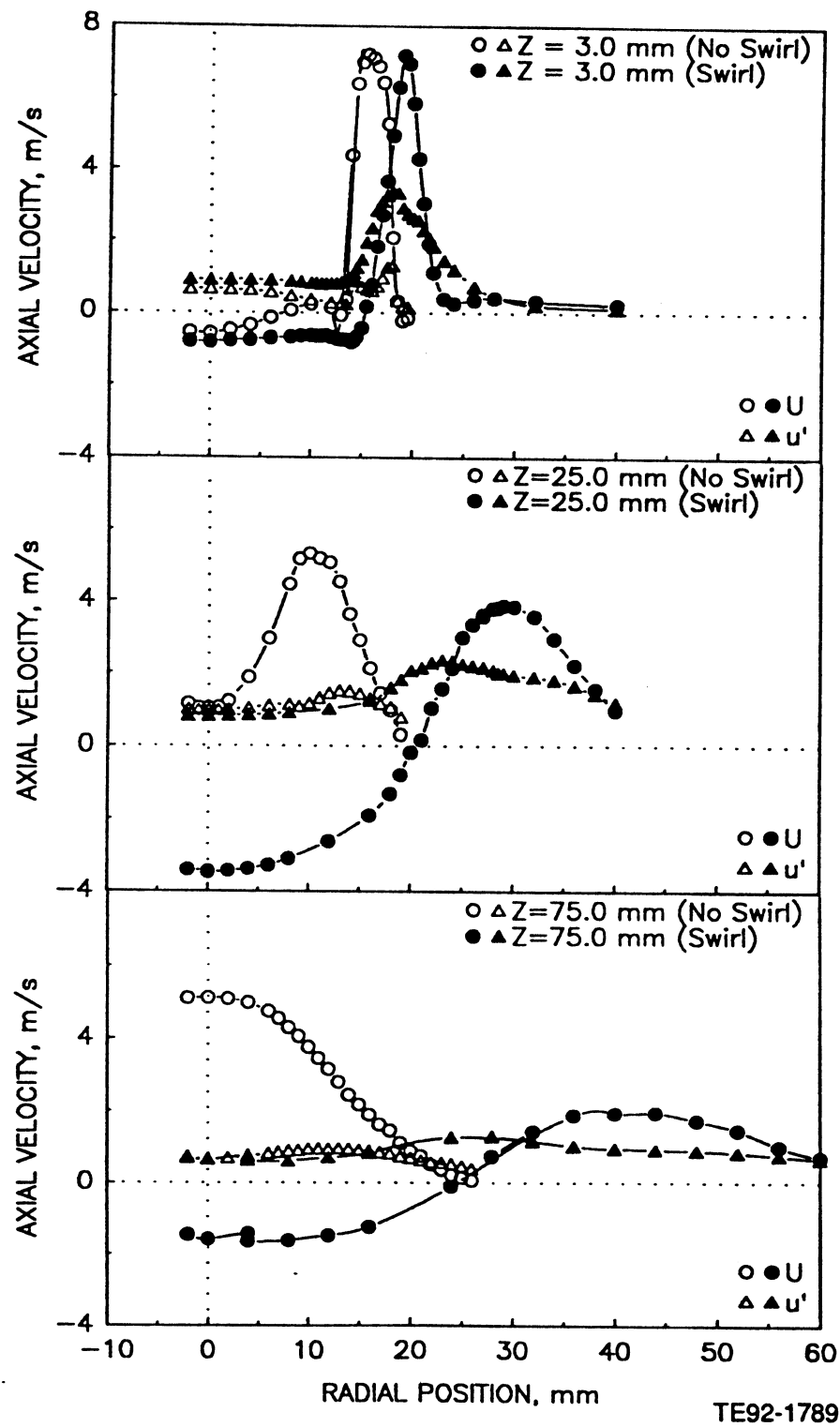


Figure 4.4.3-1. Comparison of mean and fluctuating axial velocities in the single-phase unconfined annular jets with and without swirl.

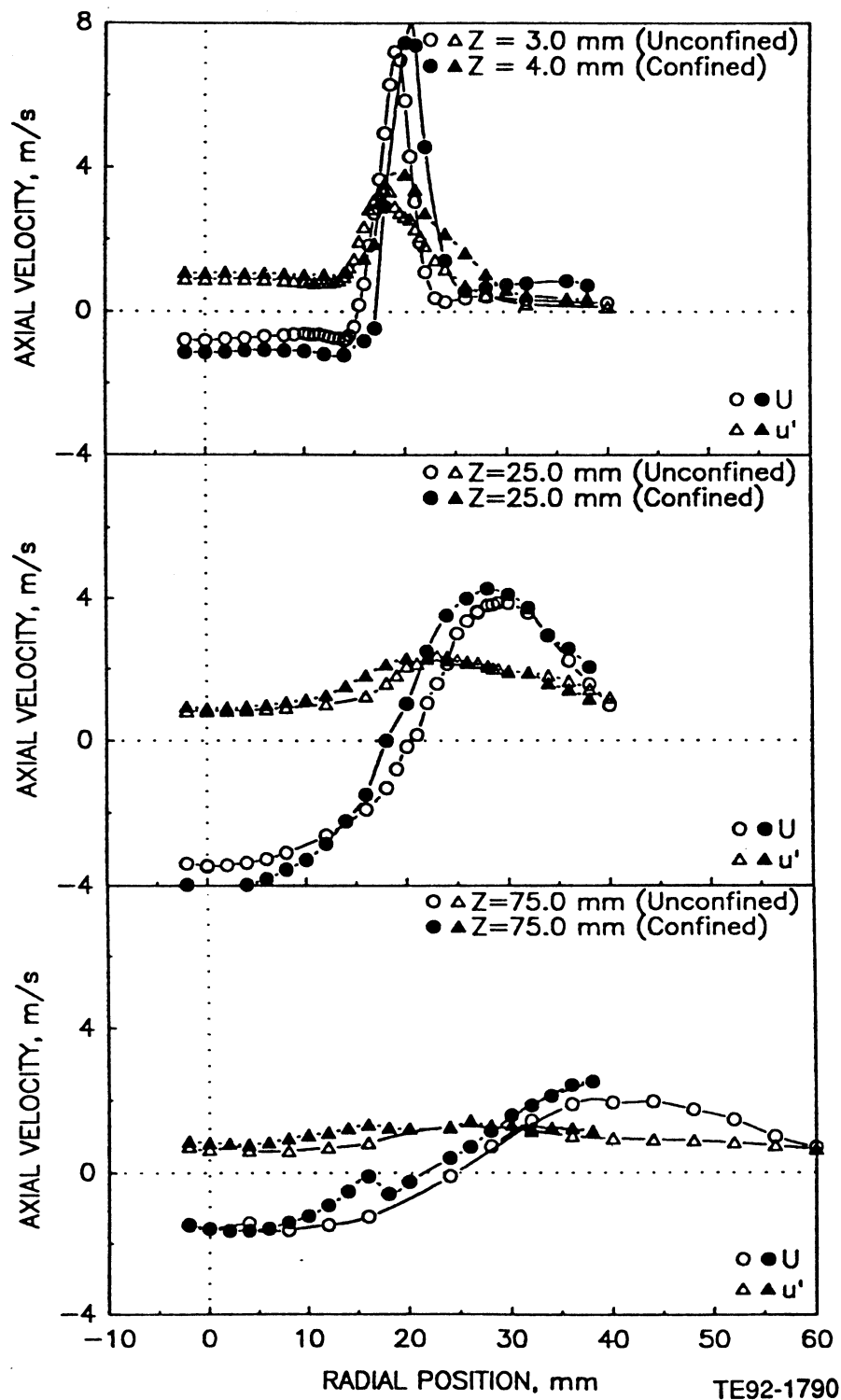


Figure 4.4.4-1. Comparison of mean and fluctuating axial velocities in the single-phase swirling annular jet with and without confinement.

4.5 COAXIAL JETS

Several coflowing geometries were considered for the present study, including confined and unconfined cases. Two particle loading ratios were again considered, although the higher loading ratio cases were conducted only in the confined geometry.

4.5.1 Unconfined Coaxial Jets – CONF02#3

Figure 4.5.1-1 presents the geometry used for the unconfined coaxial jets. In this case, the geometry is similar to that described in section 4.3, but the end cap is now removed and the central jet is operated with a mass flow of 0.0021 kg/s of air. The annular airflow rate being 0.0033 kg/s.

Figure 4.5.1-2 presents examples of the results. The axial velocity results are presented in Figure 4.5.1-2 (a) and reveal excellent symmetry. The two jet flows are quite distinct at $Z = 5.0$ mm. The two jets then form a shear layer which moves towards the centerline with increasing axial distance downstream.

The radial velocity (Figure 4.5.1-2 [b]) reveals the mixing of the two air streams more clearly. The central jet moves away from the centerline, while the outer annular jet moves towards the centerline. By 75 mm, the core of jet is expanding slightly and outside air is being strongly entrained.

The mean azimuthal velocity should be everywhere equal to zero. This is essentially true as shown in Figure 4.5.1-2 (c).

The cross correlation between the fluctuating velocities behaves as expected (Figure 4.5.1-2 [d and e]).

To illustrate the repeatability of the measurements, Figure 4.5.1-3 provides comparisons of measurements made one year apart in the same flow. The axial velocity (Figure 4.5.1-3 [a]) shows very repeatable results. The radial velocities (Figure 4.5.1-3 [b]) do not repeat as well as the axial velocities. In this case, the later data set reflects improvements made in the transmitter and improvements in the alignment. Finally, the cross correlation between the fluctuating axial and radial velocities' components are shown in Figure 4.5.1-3 (c). In this case, the sign of one case has been inverted due to the optical alignment. However, the trends are quite similar between the two cases, although the later case shows more clearly defined structure.

4.5.2 Effect of Coflow on Single Jet

To better reveal the impact of the coflowing jet on the behavior of the central jet, Figure 4.5.2-1 provides a comparison between the cases presented in sections 4.5.1 and 4.2.1. The coflowing jet causes the centerline velocity of the central jet to decay more rapidly due to the expansion associated with the shear layer between the streams.

4.5.3 Unconfined Jets in the Presence of 100-110 Micron Beads at Loading Ratio 0.2 – CONF08#1

Figure 4.5.3-1 presents the results for the gas phase in the presence of monodispersed glass beads. Figure 4.5.3-1 (a) provides the axial velocity. The symmetry of the flow remains quite good. In general, the structure of the flow appears similar to that of the single-phase case (section 4.5.1).

The nonzero radial velocities at the centerline (Figure 4.5.3-1 [b and c]) are attributed to a slight misalignment of the optics and to a small difference in the actual and input fringe spacing.

4.5.4 Glass Beads in the Unconfined Jets at Loading Ratios of 0.2 – CONF08#2

Figure 4.5.4-1 provides results for the 100-110 micron glass beads in the unconfined coflowing jets. Figure 4.5.4-1 (a and e) shows that the symmetry of the flow is quite good. The bead radial and azimuthal mean

velocities reveal a slight nonzero value at the centerline, which is again attributed to mismatch of the actual and input fringe spacing and to nonoptimized optical alignment.

4.5.5 Effect of Coflow on Glass Beads

To better assess the effect of the coflowing air stream on the behavior of the beads, Figure 4.5.5-1 compares results from the coflowing case to a case with only the central jet (section 4.2.3). Near the centerline, the effect of the coflow is small and any differences observed are likely within experimental error. However, with increased distance downstream, the coflowing annular entrains some of the particles and accelerates them, resulting in a more uniform velocity profile for that case. This difference is also revealed in the data rate profiles (Figure 4.5.5-1 [b]) although it is not as clear.

4.5.6 Confined Single-Phase Coaxial Jets – CONF05#2

Figure 4.5.6-1 provides the geometry used for the studies of confined particle-laden coflowing jets.

Figure 4.5.6-2 presents the results for the single-phase coflowing jets. Based on the two orthogonal profiles for the axial velocity (Figure 4.5.6-2 [a]), the symmetry of the flow is good. Many of the attributes of the unconfined case are revealed (section 4.5.1) with two distinct jet flows merging together to form a single flow. The primary exception is the flow in the outer part of the duct ($R > 25$ mm), which does not decay to 0.0 m/s as it does in the unconfined case.

Figure 4.5.6-2 (c) reveals the presence of a modest azimuthal component which occurs in the region where the axial velocity is negative. This is evidence of a maldistribution in air in one of the three passages, most likely the annular section. Despite this, the dependency between the axial and azimuthal fluctuating components is small (Figure 4.5.6-2 [e]).

To evaluate the degree to which the flows and measurements are repeatable, Figure 4.5.6-3 provides a comparison of the axial velocities measured nearly two years apart. In this case, the early measurement featured higher coflow in the outer passage. However, in the region of the flow where the jets dominate the structure, the repeatability is excellent for both mean and fluctuating velocities.

4.5.7 Confined Jets in the Presence of 100-110 Micron Beads at Loading Ratios of 0.2 and 1.0 – CONF11#1,#3

Two particle-laden cases were run for the confined coflowing jets. The first case was done at a bead-to-air mass loading ratio (in the central jet) of 0.2. In this case, only U and W were measured. The optical access necessary to measure V as well had not been established by the time these data were acquired. Figure 4.5.7-1 provides the results for the gas phase in the presence of the beads.

The results shown reveal a structure which is similar to that observed in the single-phase case (section 4.5.3).

The results from the higher loading ratio are presented in Figure 4.5.7-2. The results look quite similar to the single-phase case (section 4.5.3) with the exception of a flatter axial velocity profile near the centerline. The results will be compared more completely in section 4.5.9.

4.5.8 Glass Beads in the Confined Jets at Loading Ratios of 0.2 and 1.0 – CONF11#2,#4

Figure 4.5.8-1 provides results for the glass beads in the confined coflowing jets with a loading ratio of 0.2. In this case, the behavior is similar to that in the unconfined coflowing jets. The peak mean axial velocities occur along the centerline, while the fluctuating components peak at the edge of the flow. The bead concentration has a maximum at the centerline and reveals a reduction with increased radial distance.

The results for the higher loading ratio are presented in Figure 4.5.8-2. Aside from the similarity to the lower loading ratio, the results from the two orthogonal profiles attest (U , u' , Np) to the degree of symmetry associated with the flow.

4.5.9 Effect of Particle Mass Loading Ratio in the Confined Jet

To compare the effect of the mass loading ratio on the gas phase behavior, Figure 4.5.9-1 presents a comparison of the measurements in the two cases. At the centerline, the higher loading ratio results in a slightly flatter axial velocity profile. Differences away from the center of the jet are due to flow rate variations.

Figure 4.5.9-2 provides a comparison of the bead characteristics. The main differences are a slightly higher fluctuating component for the low loading ratio, and a sharper velocity gradient at $Z = 75$ mm. Of course, the data rate is roughly five times higher for the higher loading ratio (Figure 4.5.9-2 [b]).

4.5.10 Effect of Confinement on Coaxial Jets

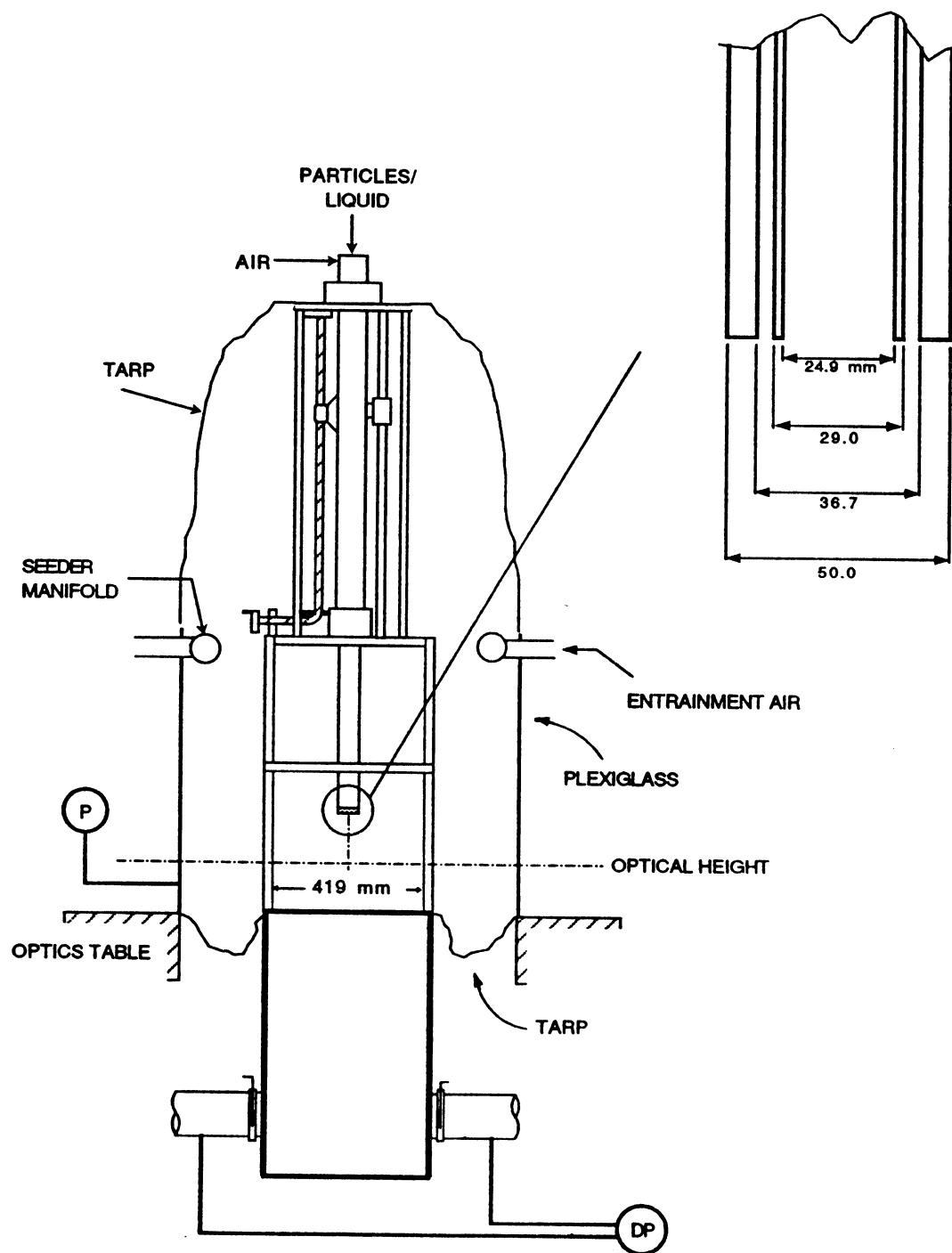
To illustrate the impact that confinement has on the behavior of the coflowing jets, Figure 4.5.10-1 provides a comparison of the axial velocities for the unconfined (section 4.5.1) and confined (section 4.5.6) coflowing jets. The main difference is that the shear layer on the outside of the flow is less severe, resulting in higher velocities along the outer edge of the jet. Also, the peak velocities associated with the annular jet are higher for the confined case (note the different Z value used for the inlet plane).

4.5.11 Effect of Coflow on Confined Jet

To illustrate the effect of coflow on the confined jet, Figure 4.5.11-1 compares the measurements in the confined single jet (section 4.2.7) to those obtained in the confined coflowing jets (section 4.5.6). The differences observed are similar to those observed in the unconfined case (section 4.5.2).

4.5.12 Effect of Confinement on Glass Beads in Coaxial Jets

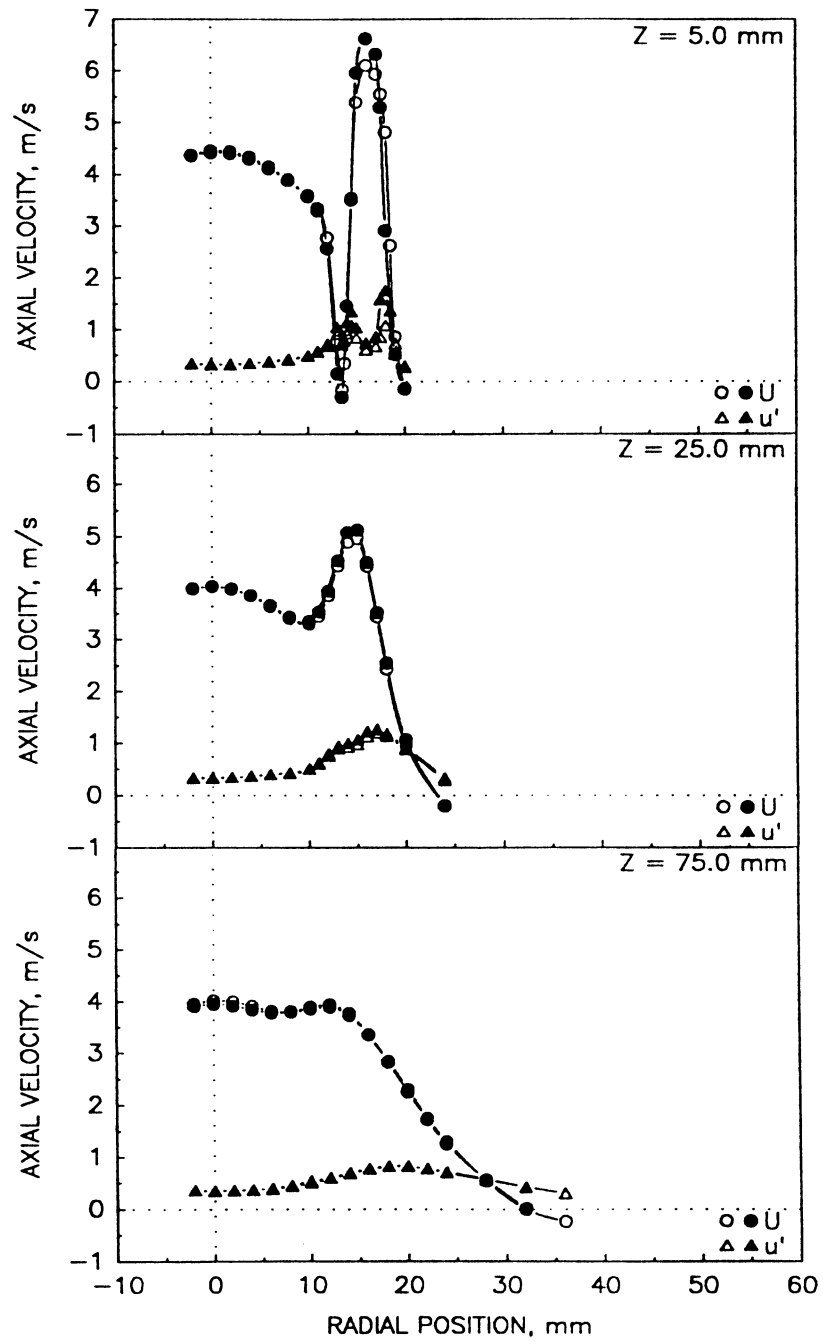
To illustrate the effect of confinement on the behavior of the glass beads, Figure 4.5.12-1 (a and b) presents a comparison of the bead velocities and data rates for the unconfined and confined cases. In the confined case, the gradients farther downstream are larger. Also, the data rate gradients are steeper for the unconfined case.



TE92-1791

Figure 4.5.1-1. Geometry utilized for unconfined coaxial jets.

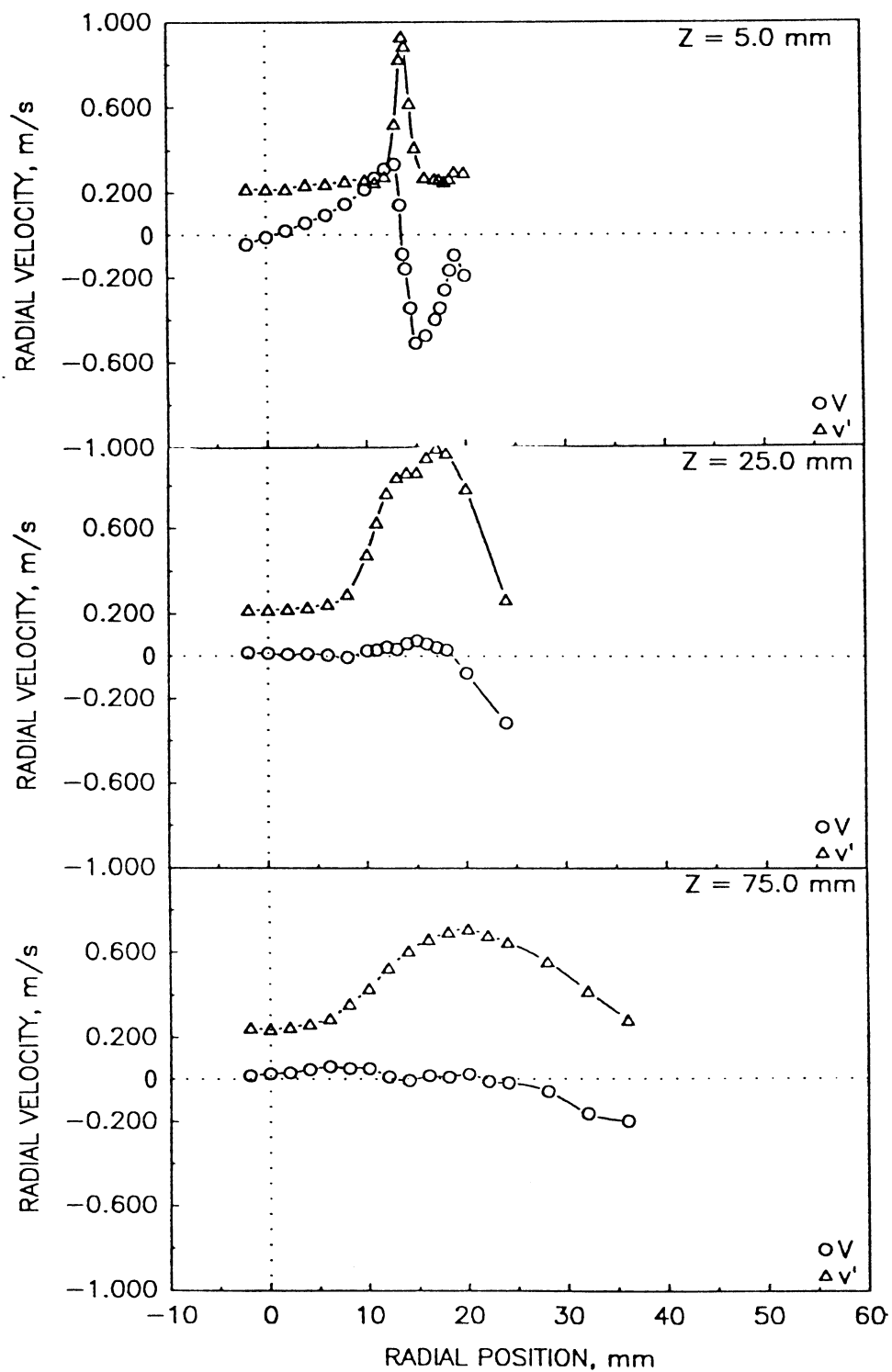
a) Mean and Fluctuating Axial Velocities



TE92-1792

Figure 4.5.1-2. Radial profiles of gas phase statistics in the unconfined single-phase coaxial jets (1 of 5).

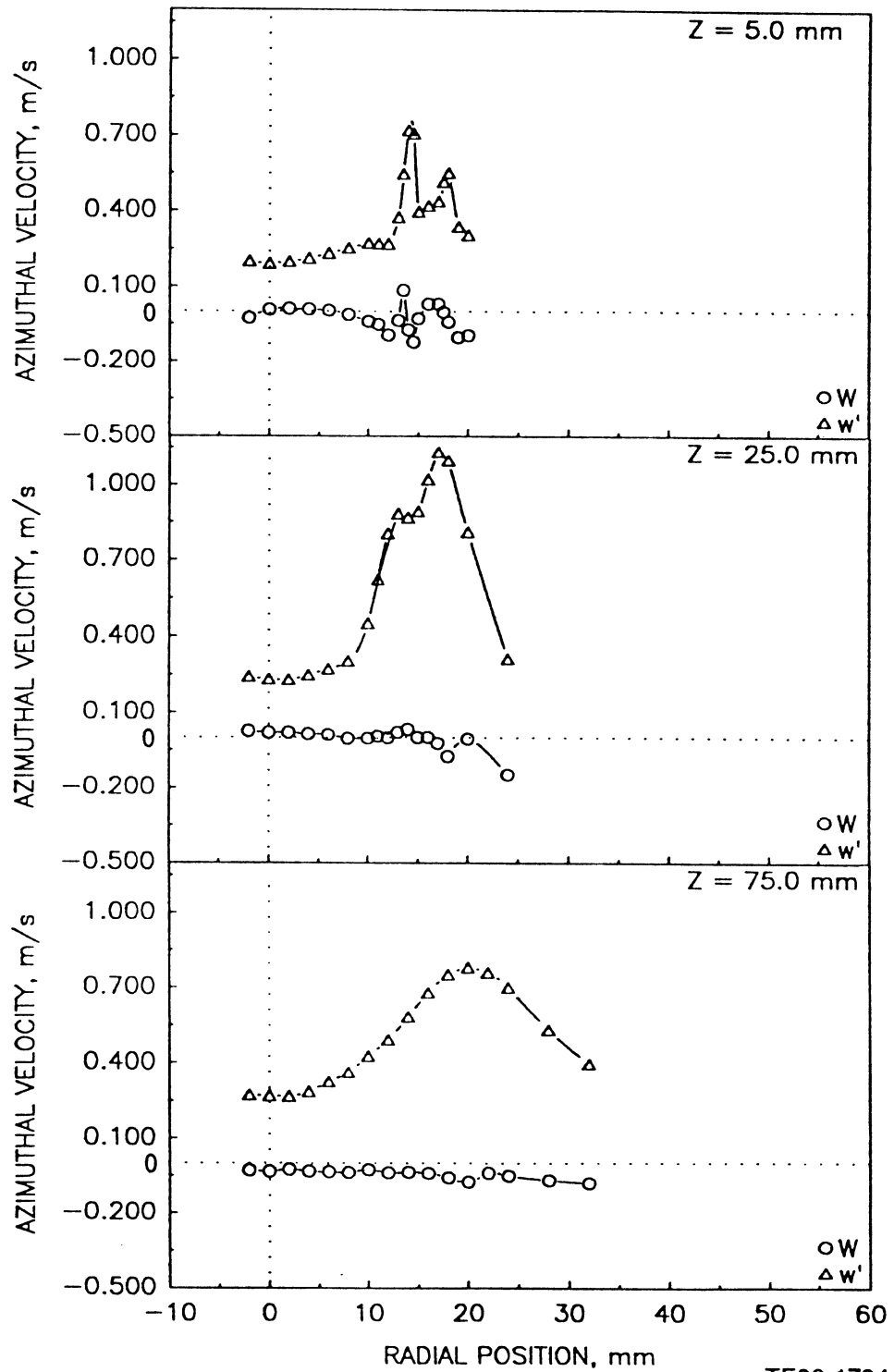
b) Mean and Fluctuating Radial Velocities



TE92-1793

Figure 4.5.1-2. Radial profiles of gas phase statistics in the unconfined single-phase coaxial jets (2 of 5).

c) Mean and Fluctuating Azimuthal Velocities



TE92-1794

Figure 4.5.1-2. Radial profiles of gas phase statistics in the unconfined single-phase coaxial jets (3 of 5).

d) Shear Stress Based on Axial and Radial Velocities

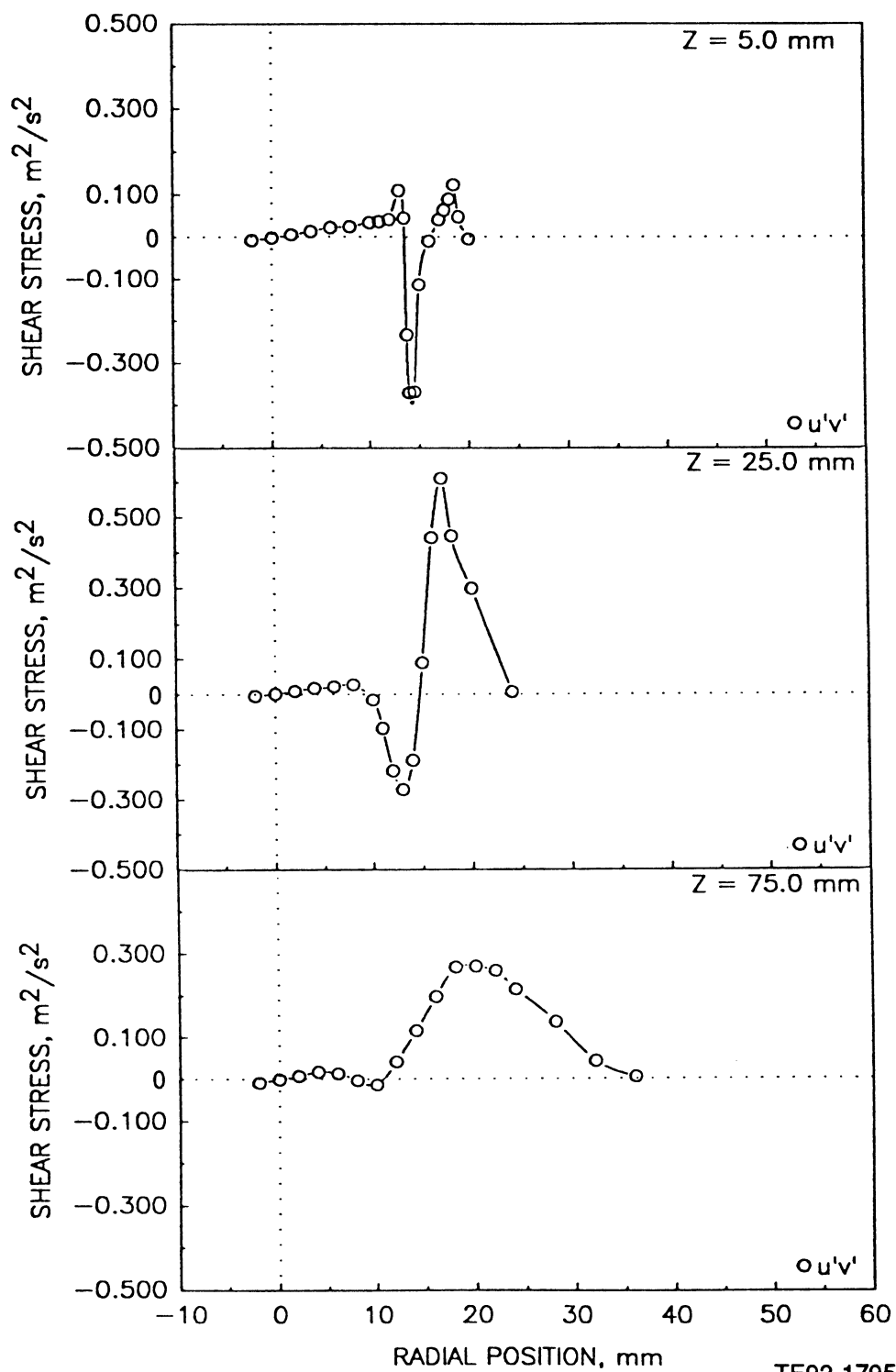
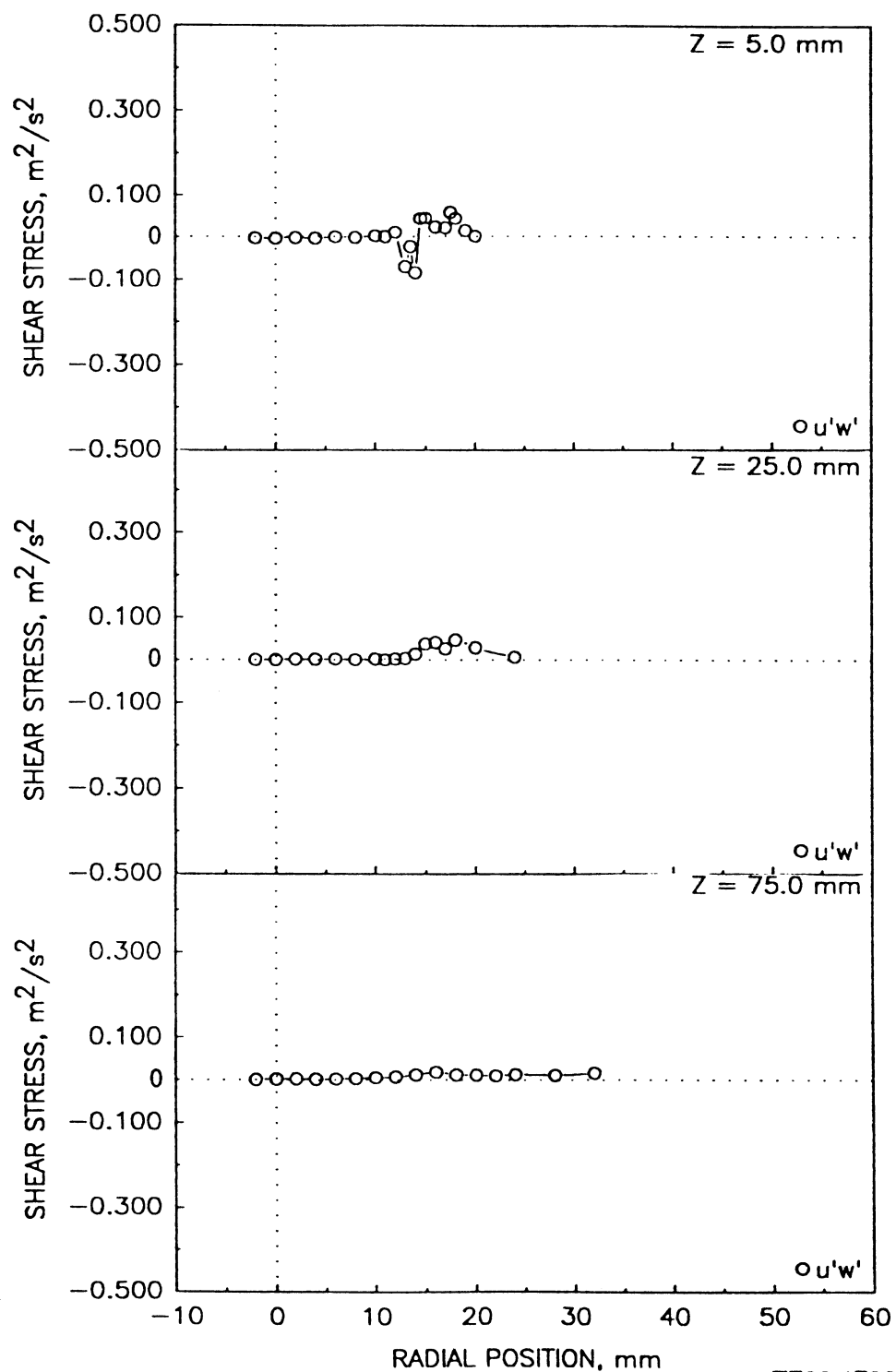


Figure 4.5.1-2. Radial profiles of gas phase statistics in the unconfined single-phase coaxial jets (4 of 5).

e) Shear Stress Based on Axial and Azimuthal Velocities



TE92-1796

Figure 4.5.1-2. Radial profiles of gas phase statistics in the unconfined single-phase coaxial jets (5 of 5).

a) Mean and Fluctuating Axial Velocity

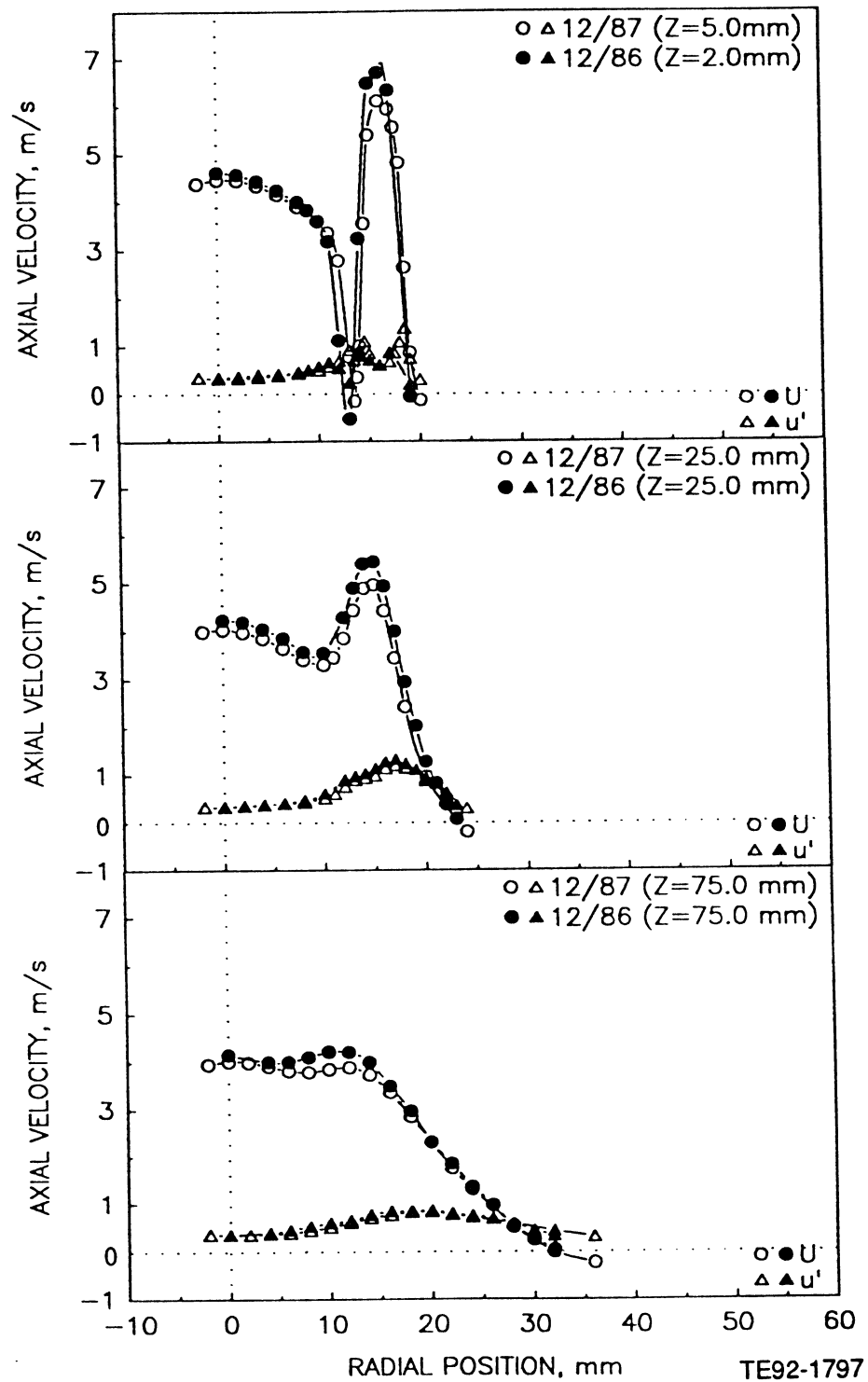


Figure 4.5.1-3. Assessment of repeatability in the unconfined single-phase coaxial jets (1 of 3).

b) Mean and Fluctuating Radial Velocity

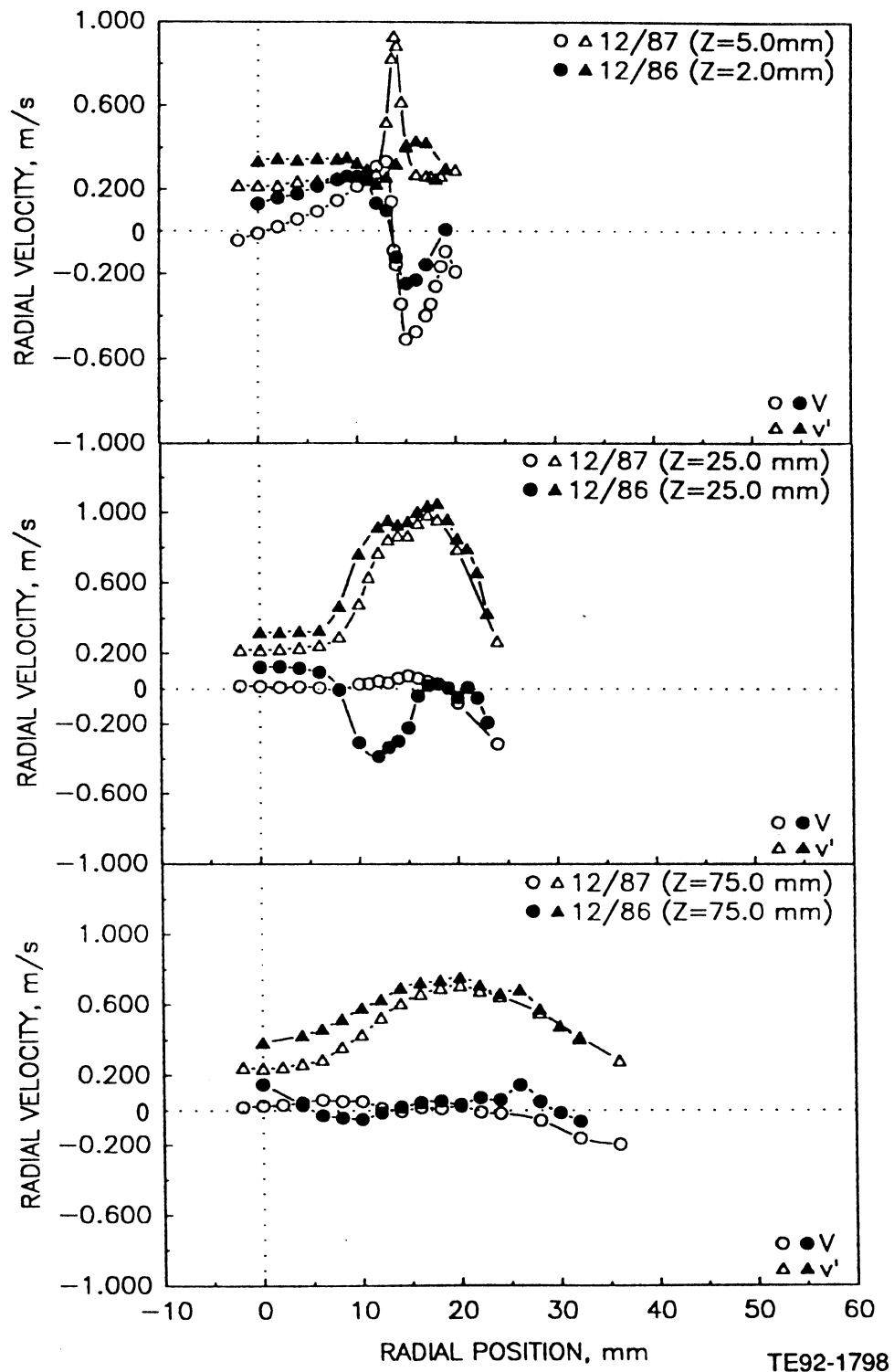


Figure 4.5.1-3. Assessment of repeatability in the unconfined single-phase coaxial jets (2 of 3).

c) Shear Stress Based on Axial and Radial Velocities

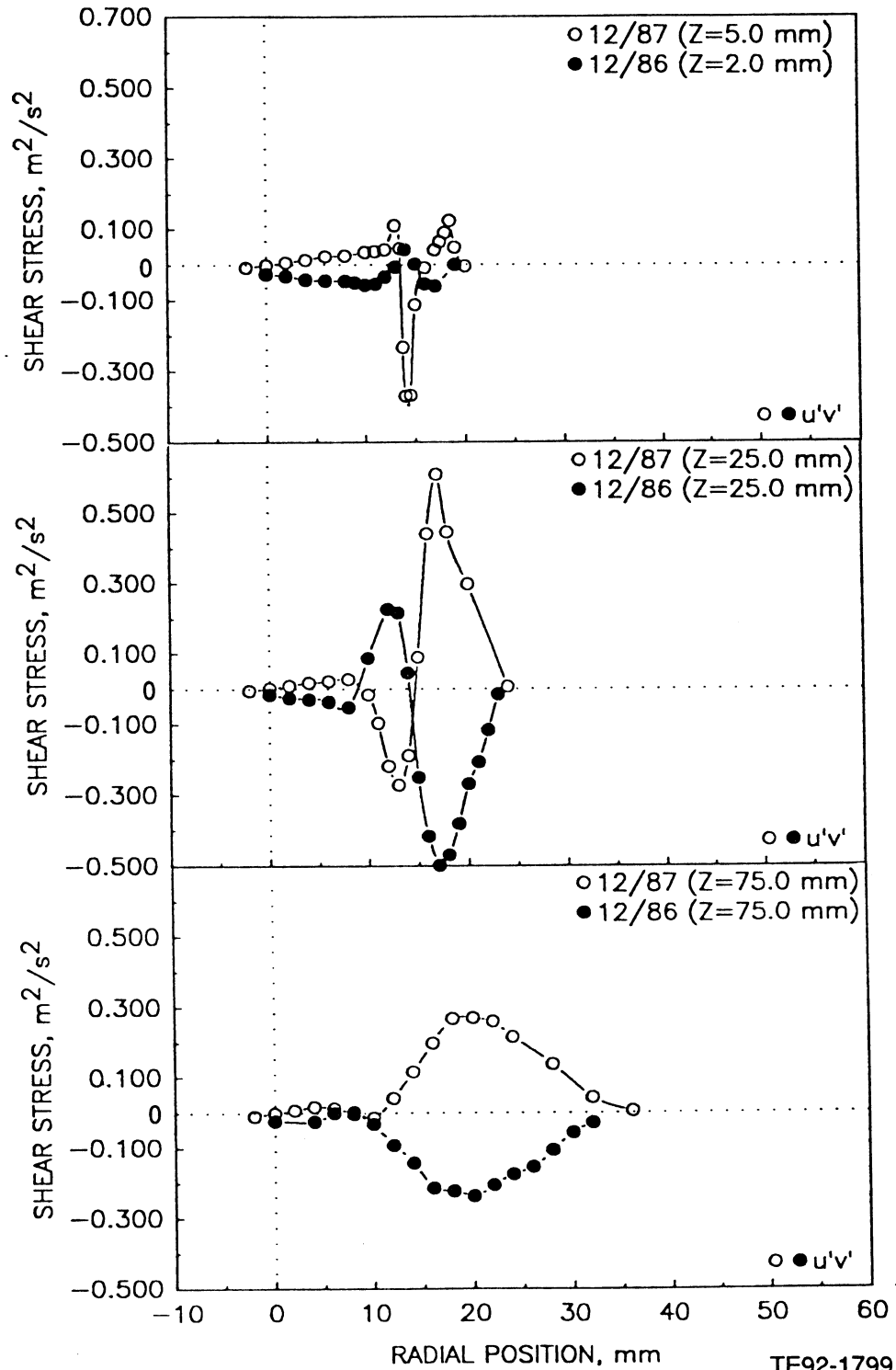


Figure 4.5.1-3. Assessment of repeatability in the unconfined single-phase coaxial jets (3 of 3).

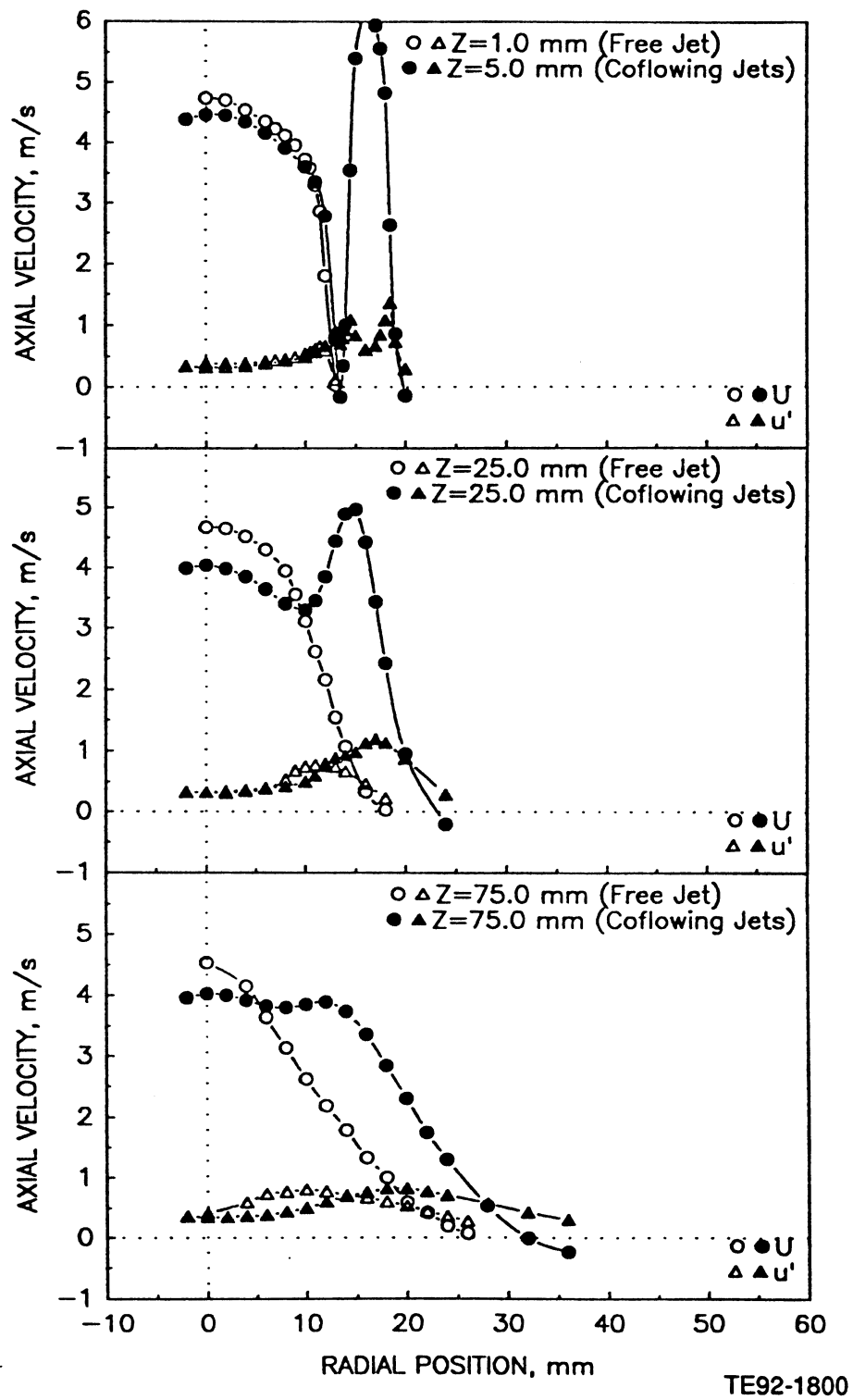


Figure 4.5.2-1. Comparison of mean and fluctuating axial velocities in unconfined single-phase round and coaxial jets.

a) Mean and Fluctuating Axial Velocities

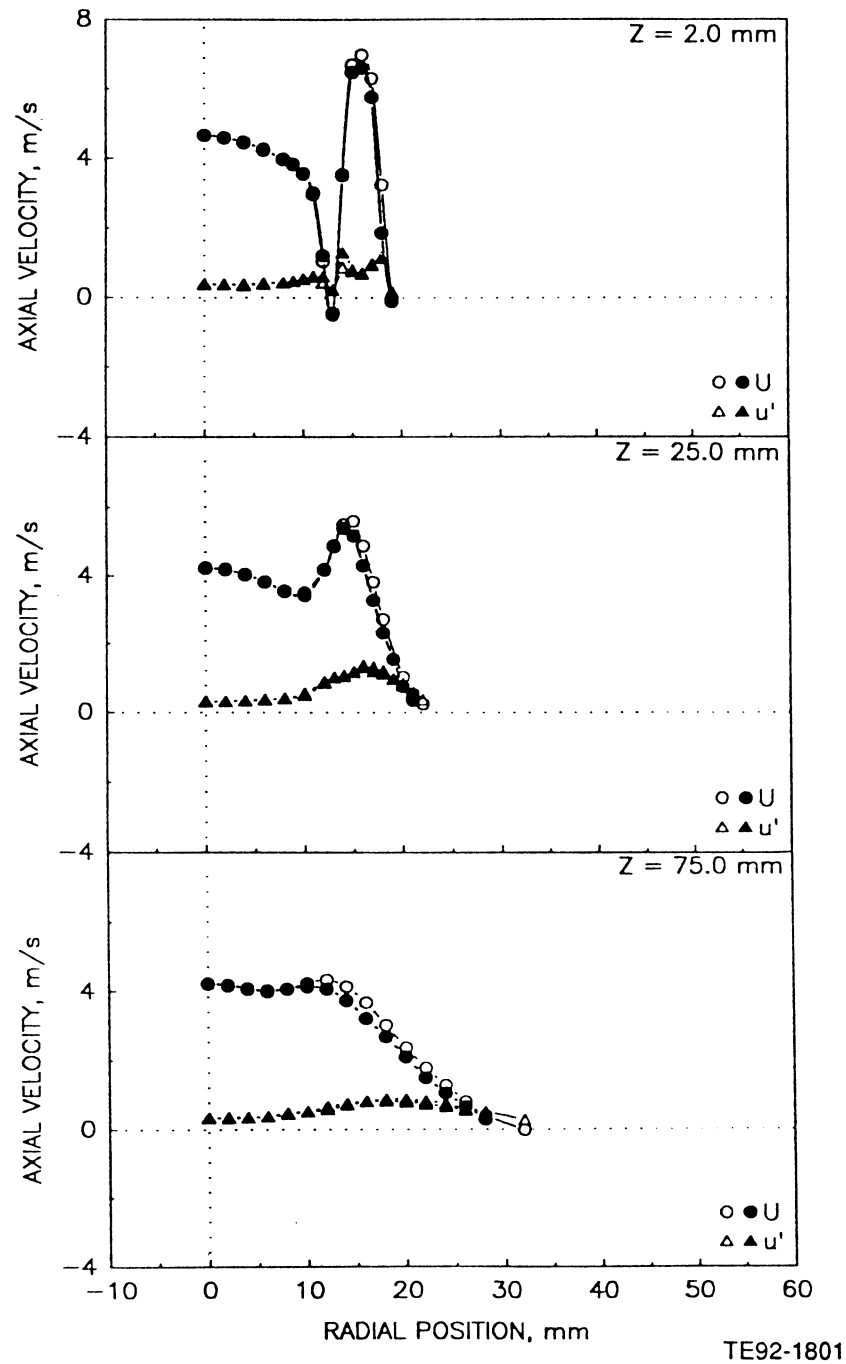


Figure 4.5.3-1. Radial profiles of gas phase velocity measurements in unconfined coaxial jets with central jet laden with 100-110 micron glass beads at a bead-to-gas mass loading ratio of 0.2 (1 of 5).

b) Mean and Fluctuating Radial Velocities

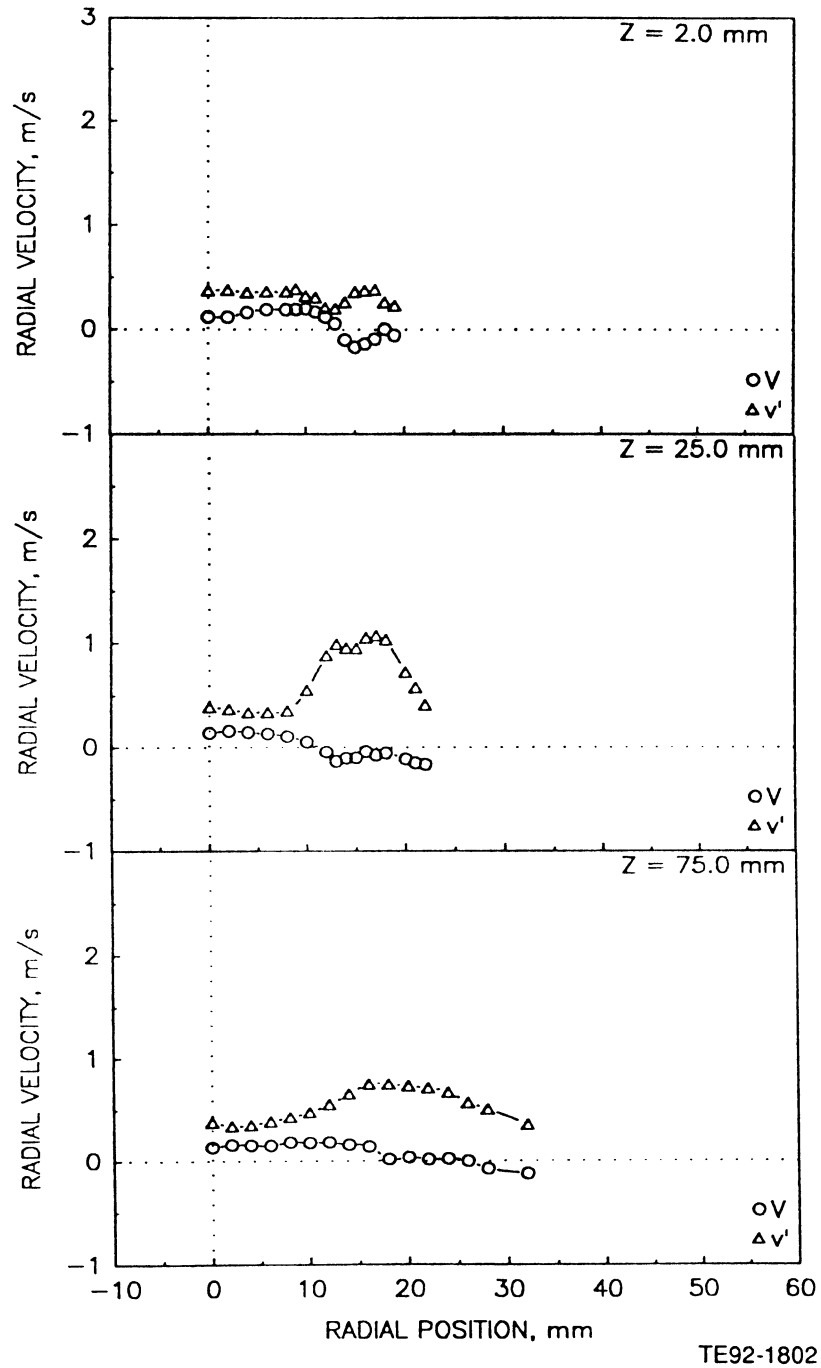
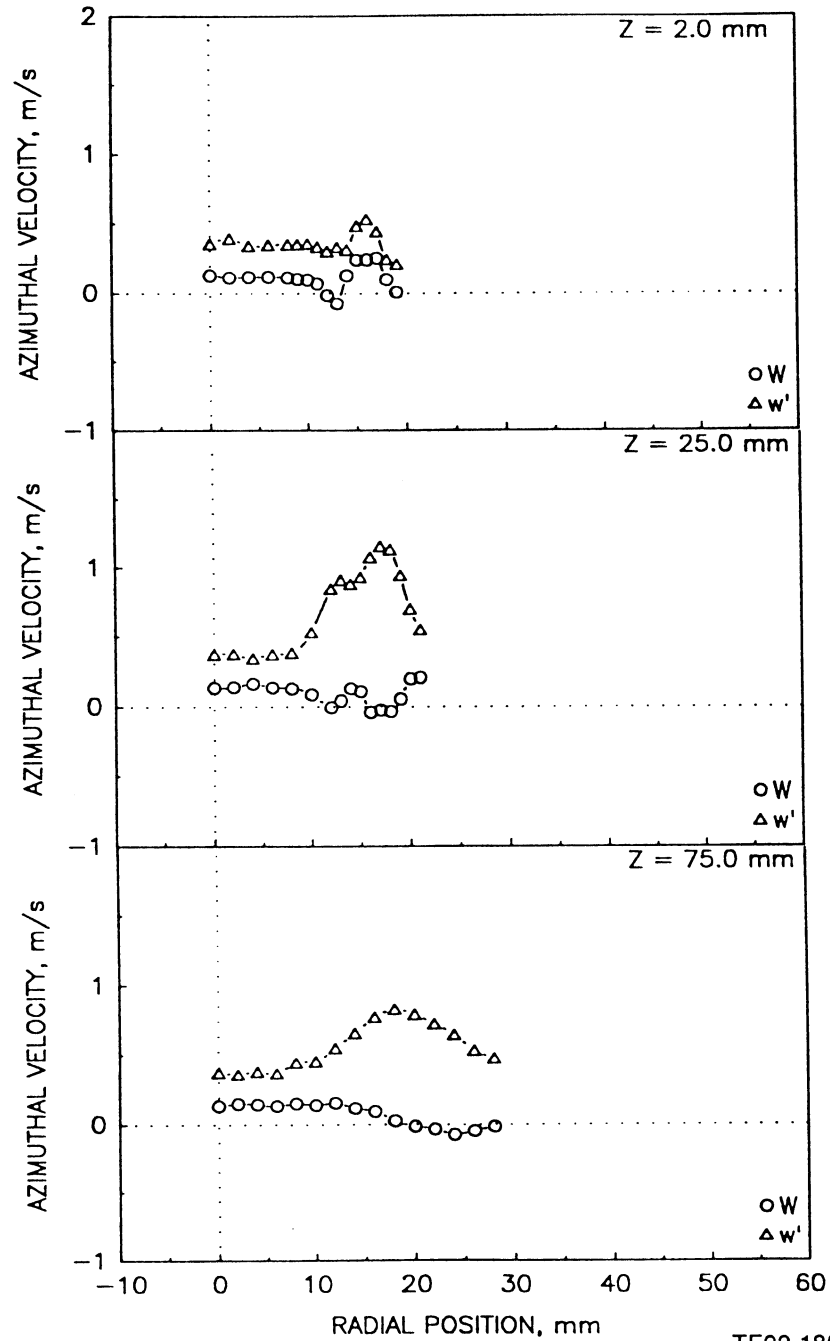


Figure 4.5.3-1. Radial profiles of gas phase velocity measurements in unconfined coaxial jets with central jet laden with 100-110 micron glass beads at a bead-to-gas mass loading ratio of 0.2 (2 of 5).

c) Mean and Fluctuating Azimuthal Velocities



TE92-1803

Figure 4.5.3-1. Radial profiles of gas phase velocity measurements in unconfined coaxial jets with central jet laden with 100-110 micron glass beads at a bead-to-gas mass loading ratio of 0.2 (3 of 5).

d) Shear Stress Based on Axial and Radial Velocities

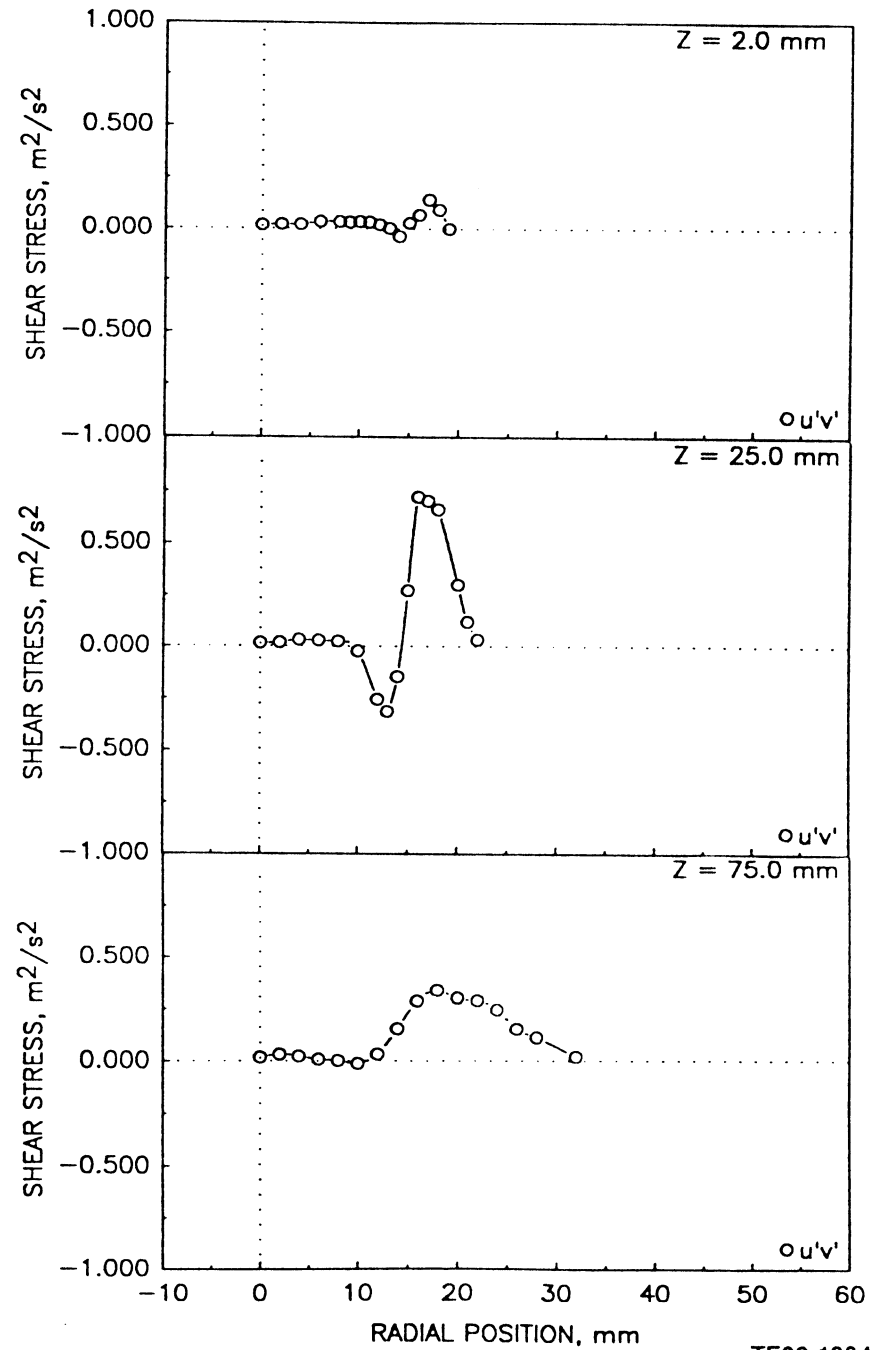


Figure 4.5.3-1. Radial profiles of gas phase velocity measurements in unconfined coaxial jets with central jet laden with 100-110 micron glass beads at a bead-to-gas mass loading ratio of 0.2 (4 of 5).

e) Shear Stress Based on Axial and Azimuthal Velocities

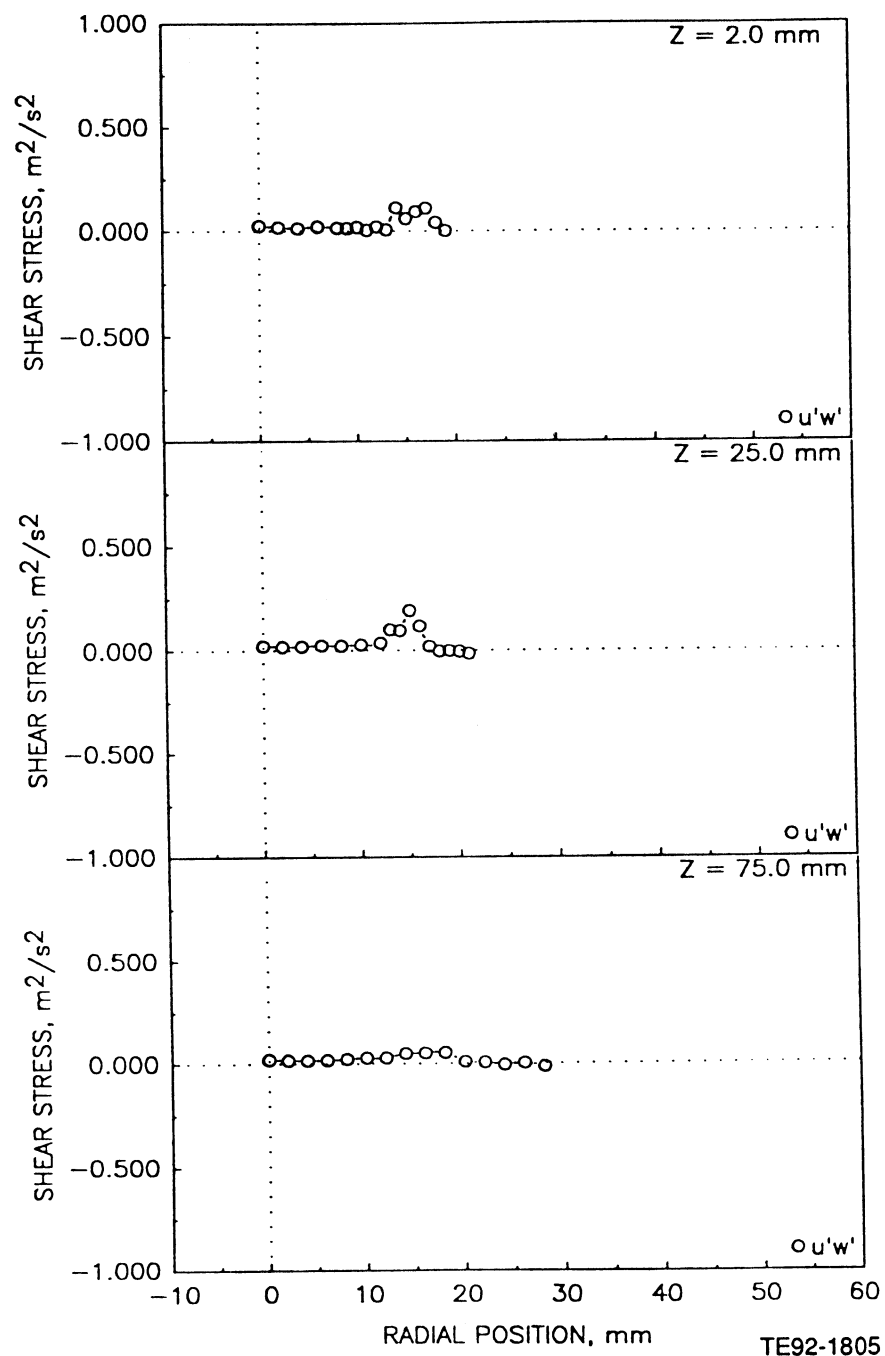


Figure 4.5.3-1. Radial profiles of gas phase velocity measurements in unconfined coaxial jets with central jet laden with 100-110 micron glass beads at a bead-to-gas mass loading ratio of 0.2 (5 of 5).

a) Mean and Fluctuating Axial Velocities

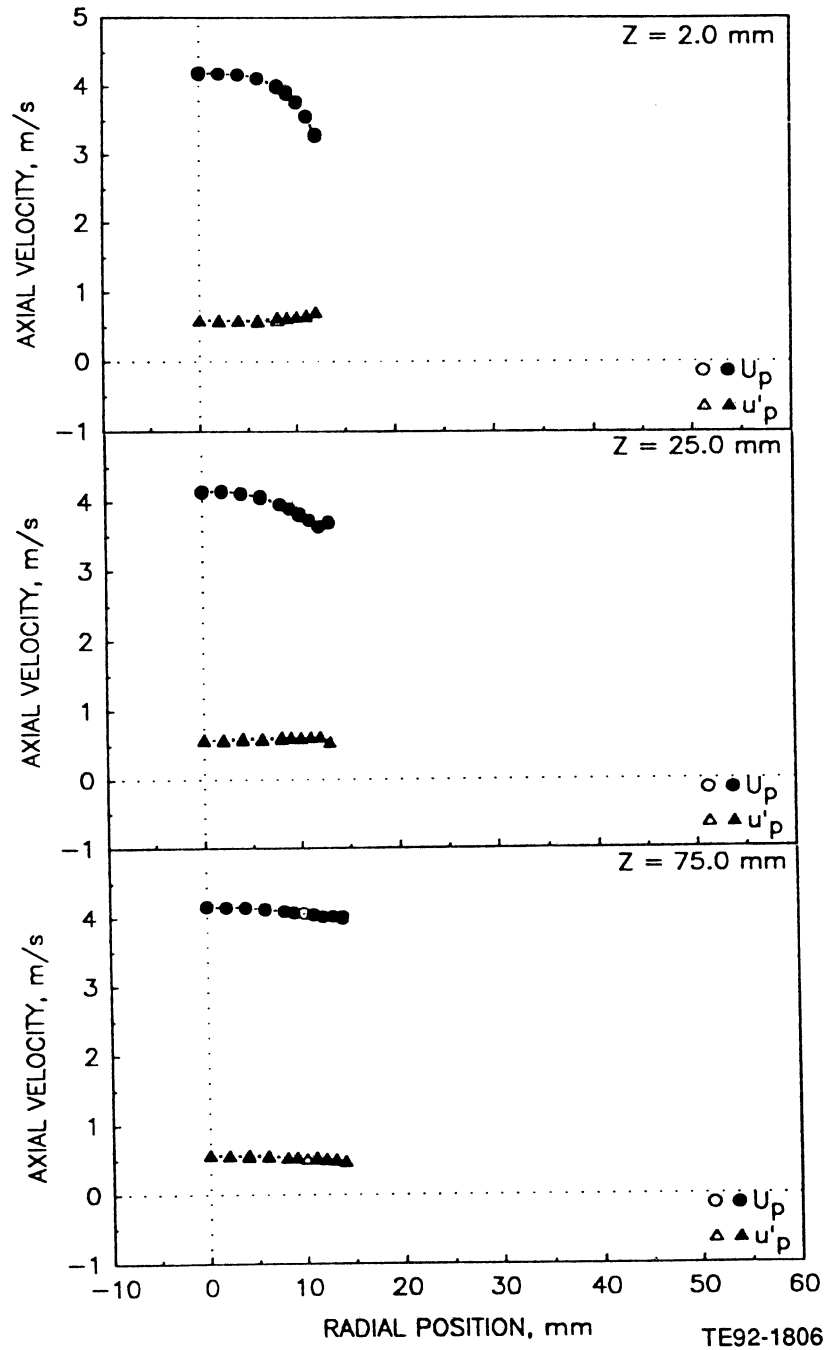


Figure 4.5.4-1. Radial profiles of particle measurements in unconfined coaxial jets with central jet laden with 100-110 micron glass beads at a bead-to-gas mass loading ratio of 0.2 (1 of 5).

b) Mean and Fluctuating Radial Velocities

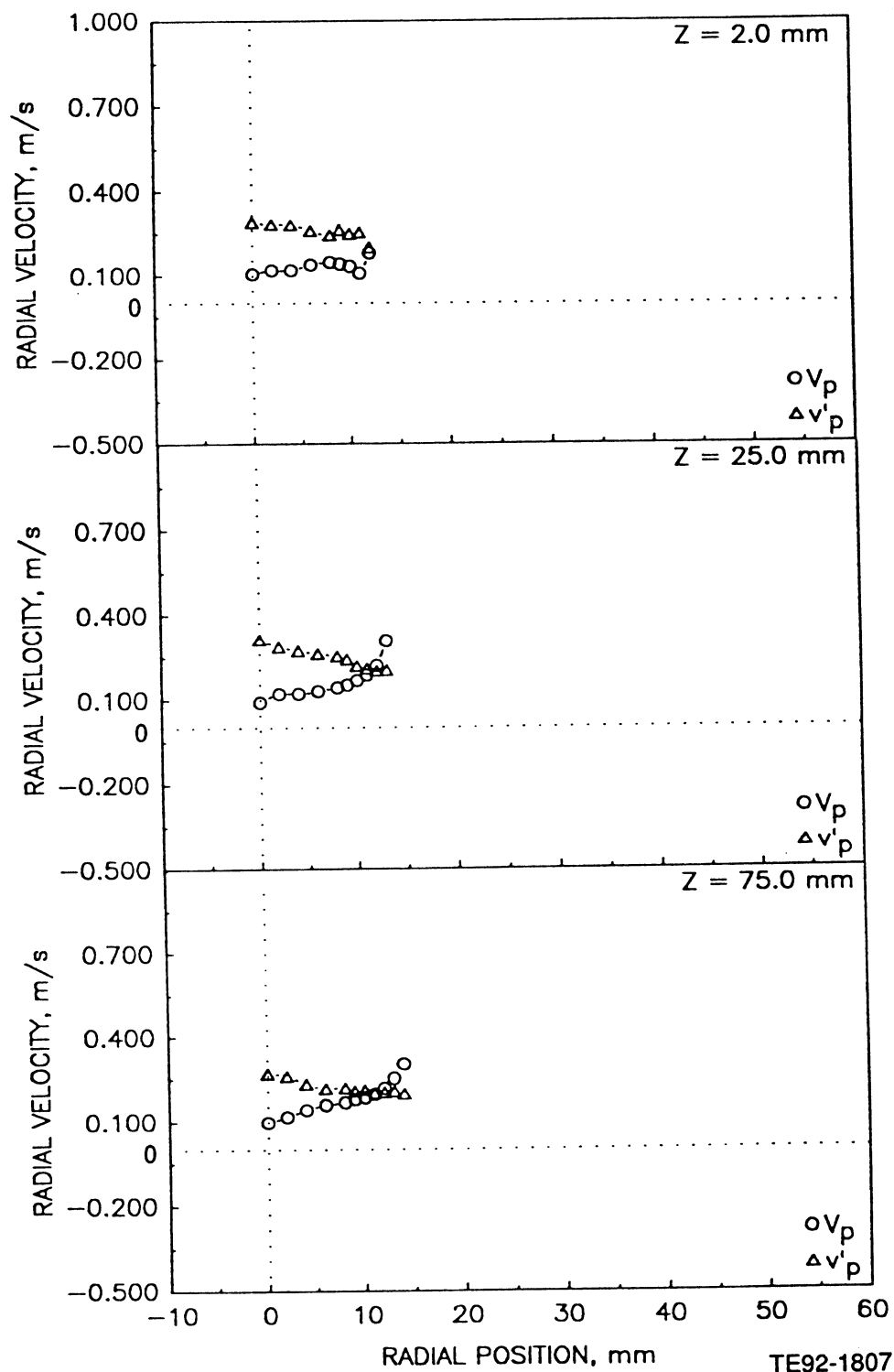


Figure 4.5.4-1. Radial profiles of particle measurements in unconfined coaxial jets with central jet laden with 100-110 micron glass beads at a bead-to-gas mass loading ratio of 0.2 (2 of 5).

c) Mean and Fluctuating Azimuthal Velocities

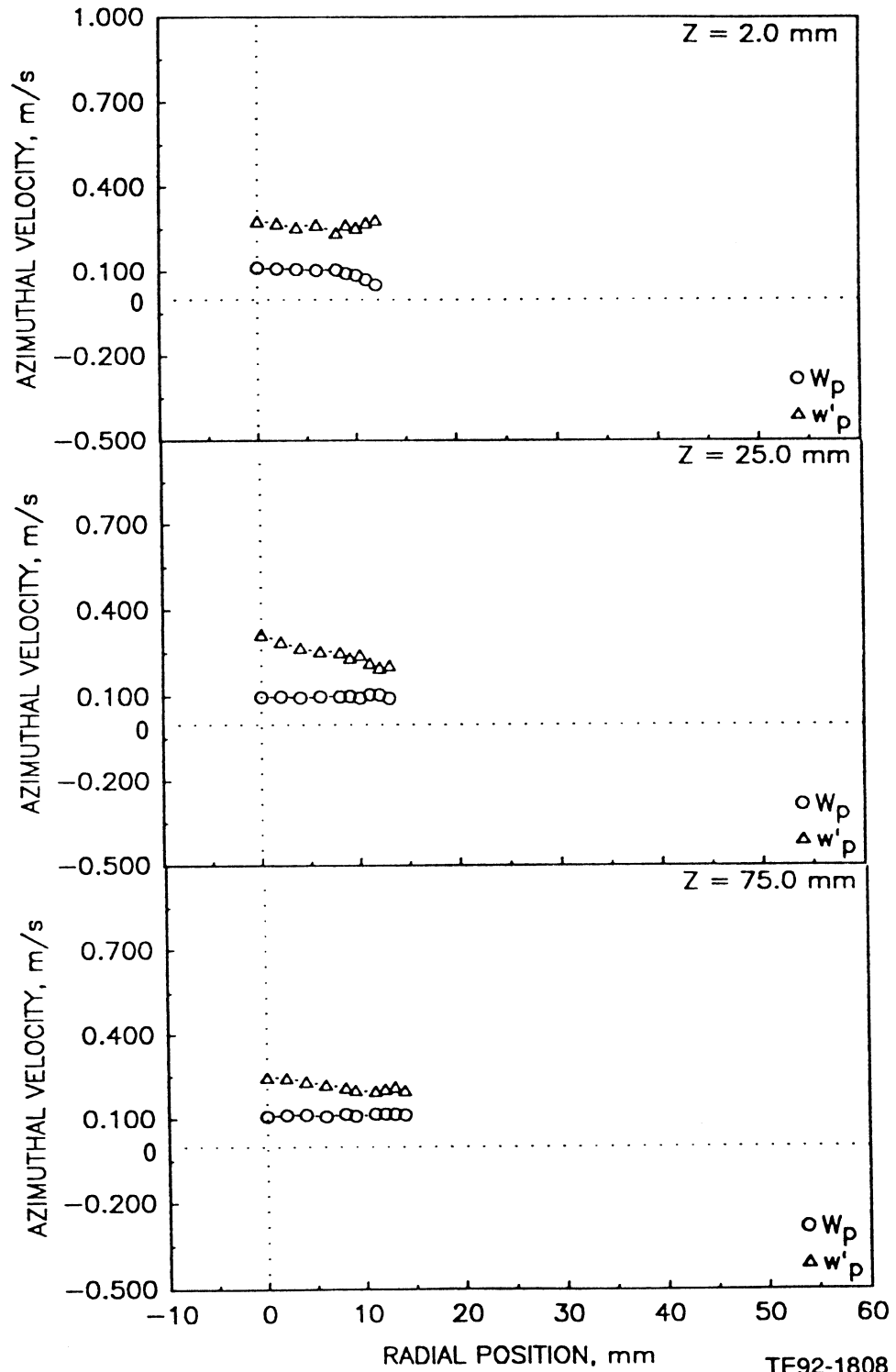


Figure 4.5.4-1. Radial profiles of particle measurements in unconfined coaxial jets with central jet laden with 100-110 micron glass beads at a bead-to-gas mass loading ratio of 0.2 (3 of 5).

d) Particle Velocity Correlation Based on Axial and Radial Components

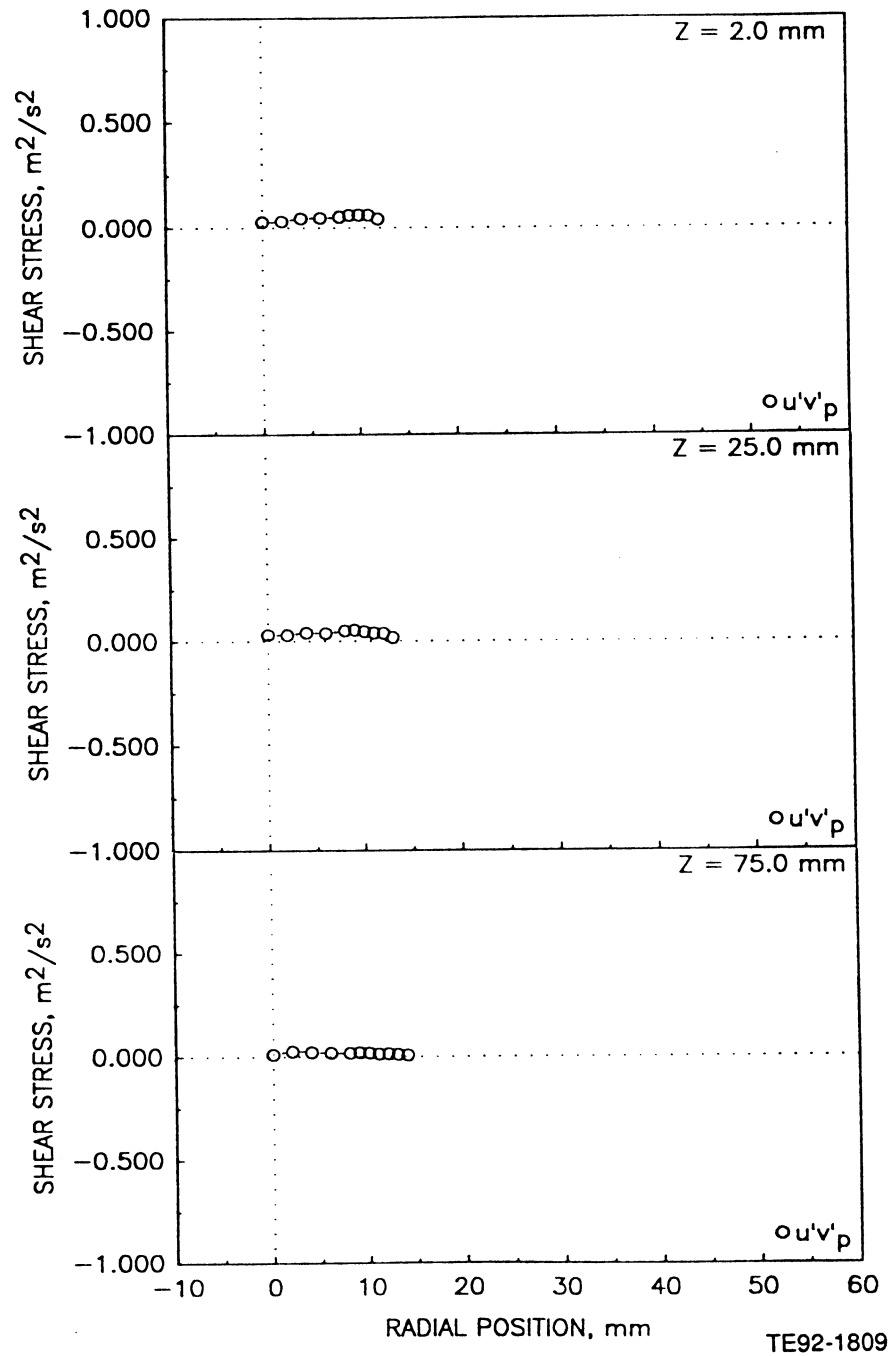


Figure 4.5.4-1. Radial profiles of particle measurements in unconfined coaxial jets with central jet laden with 100-110 micron glass beads at a bead-to-gas mass loading ratio of 0.2 (4 of 5).

e) Particle Data Rate

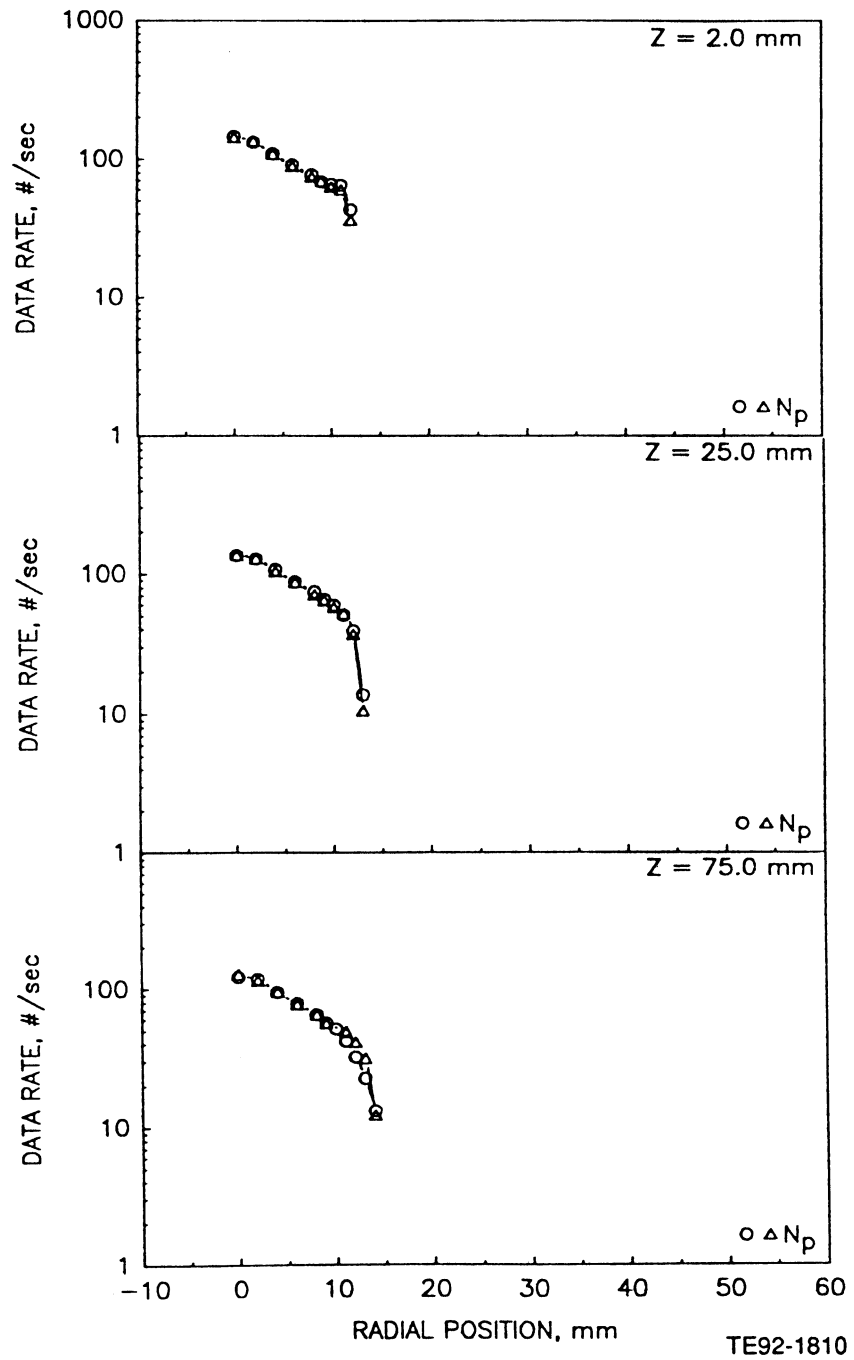


Figure 4.5.4-1. Radial profiles of particle measurements in unconfined coaxial jets with central jet laden with 100-110 micron glass beads at a bead-to-gas mass loading ratio of 0.2 (5 of 5).

a) Mean and Fluctuating Velocities

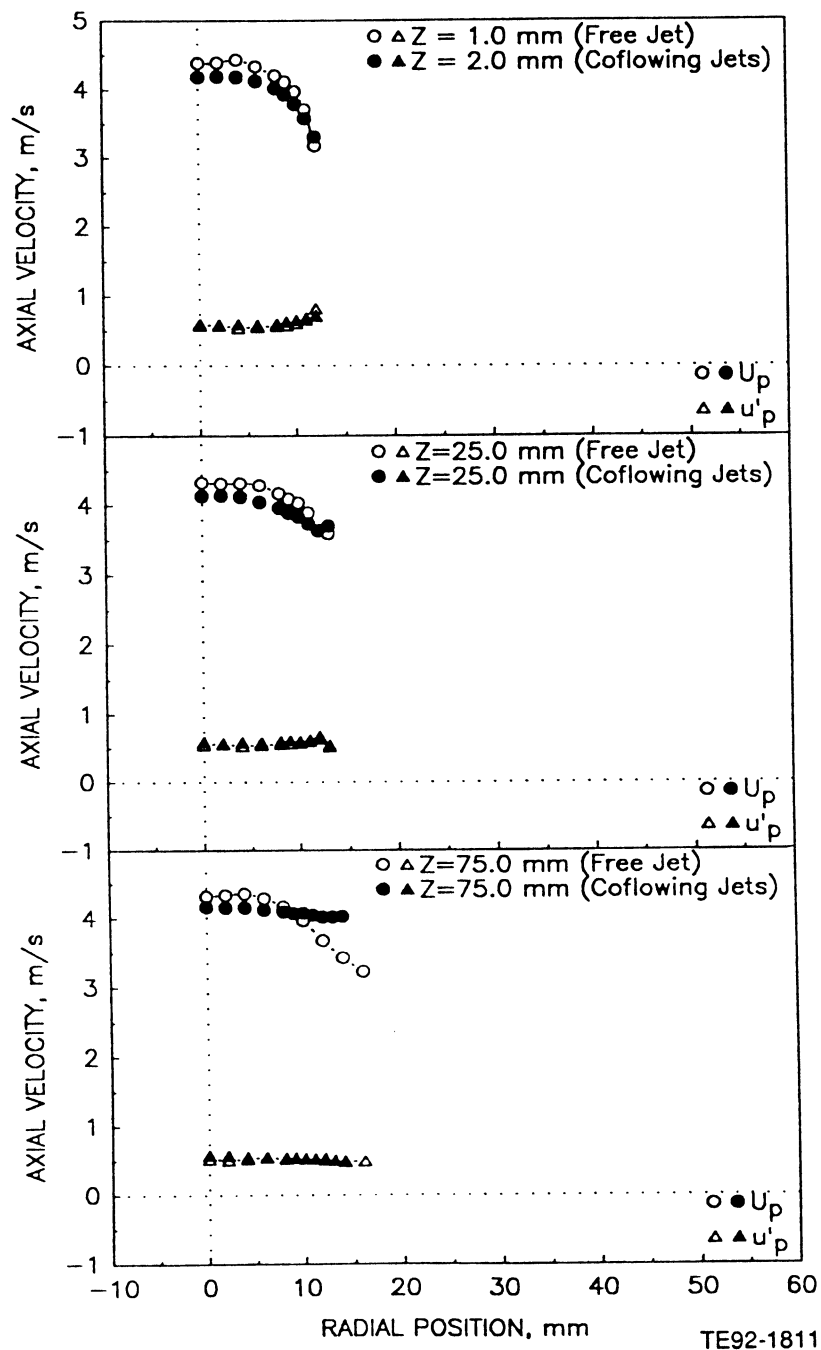


Figure 4.5.5-1. Comparison of mean and fluctuating axial velocities and data rates for 100-110 micron beads in the round jet with and without coflow for a bead-to-gas mass flow rate ratio of 0.2 (1 of 2).

b) Data Rate

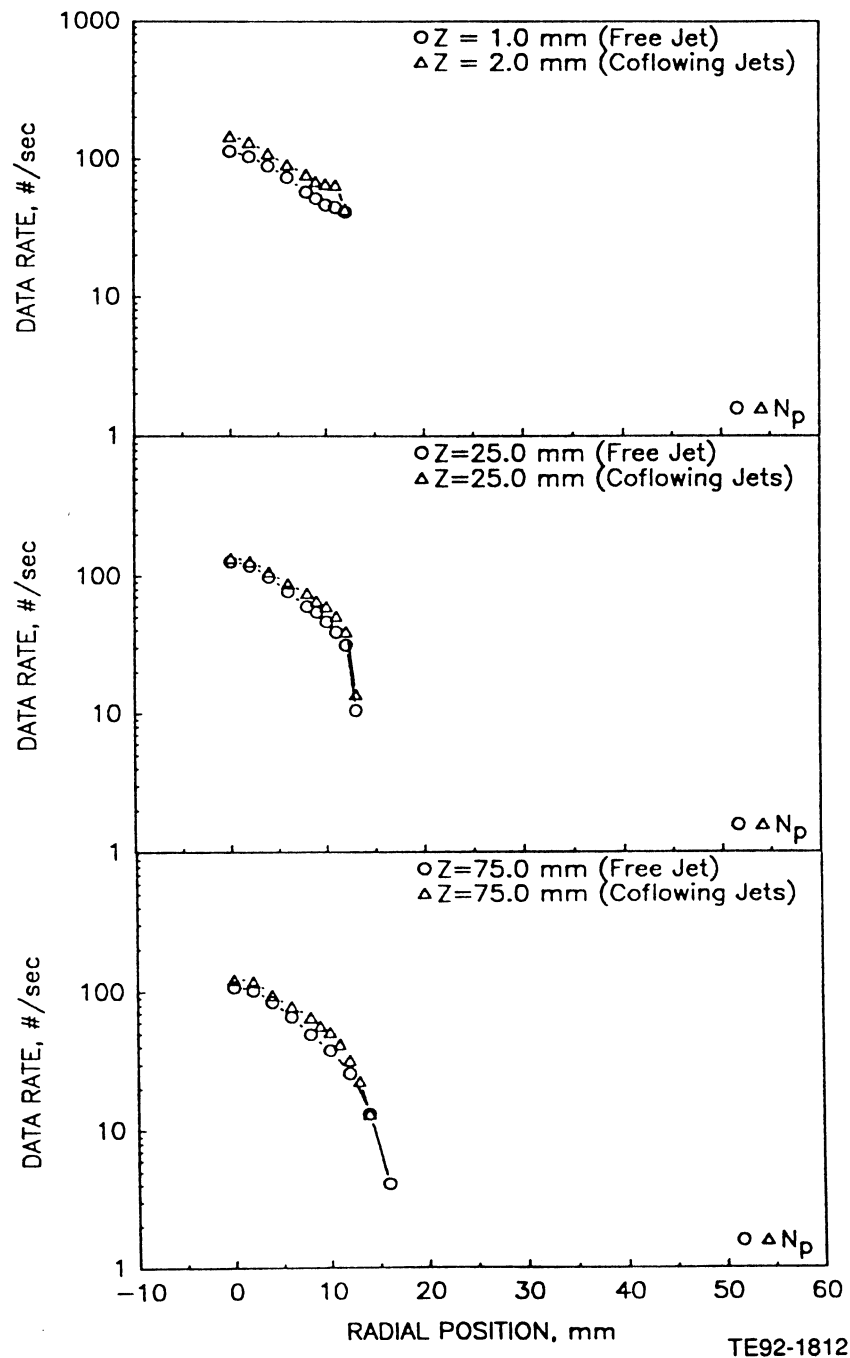
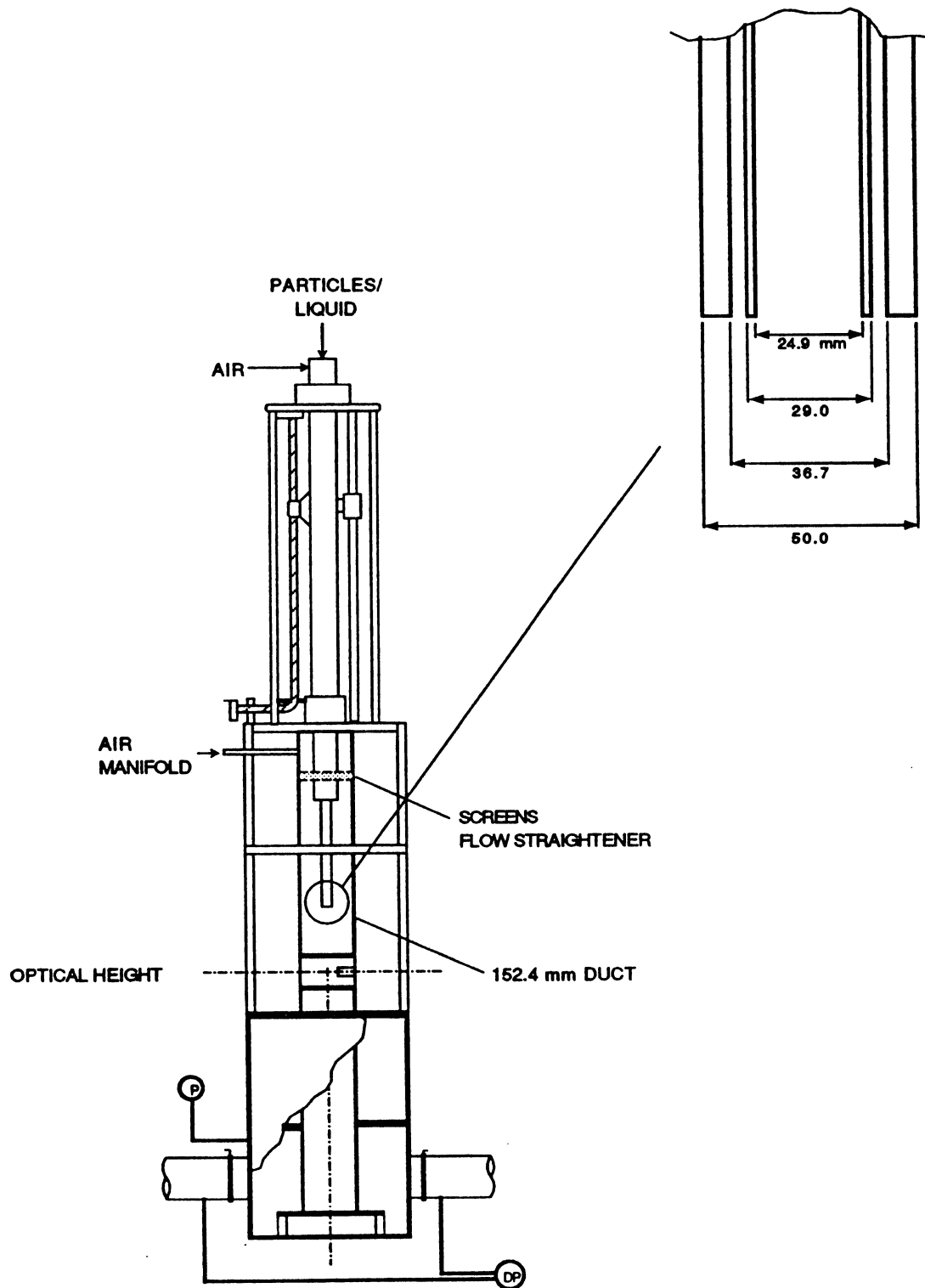


Figure 4.5.5-1. Comparison of mean and fluctuating axial velocities and data rates for 100-110 micron beads in the round jet with and without coflow for a bead-to-gas mass flow rate ratio of 0.2 (2 of 2).



TE92-1813

Figure 4.5.6-1. Geometry utilized for confined coaxial jets.

a) Mean and Fluctuating Axial Velocities

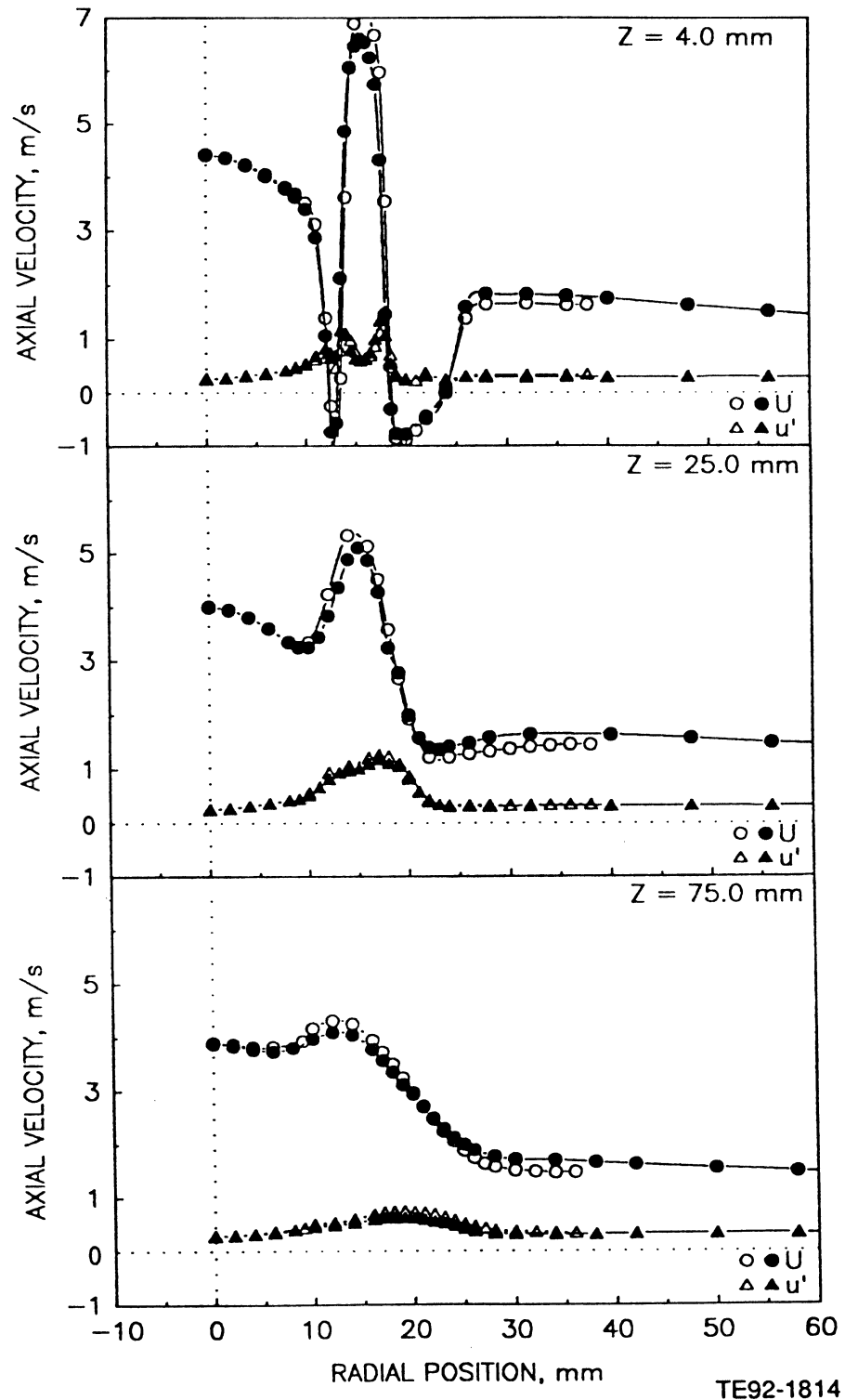


Figure 4.5.6-2. Radial profiles of gas phase statistics in the confined single-phase coaxial jets (1 of 5).

b) Mean and Fluctuating Radial Velocities

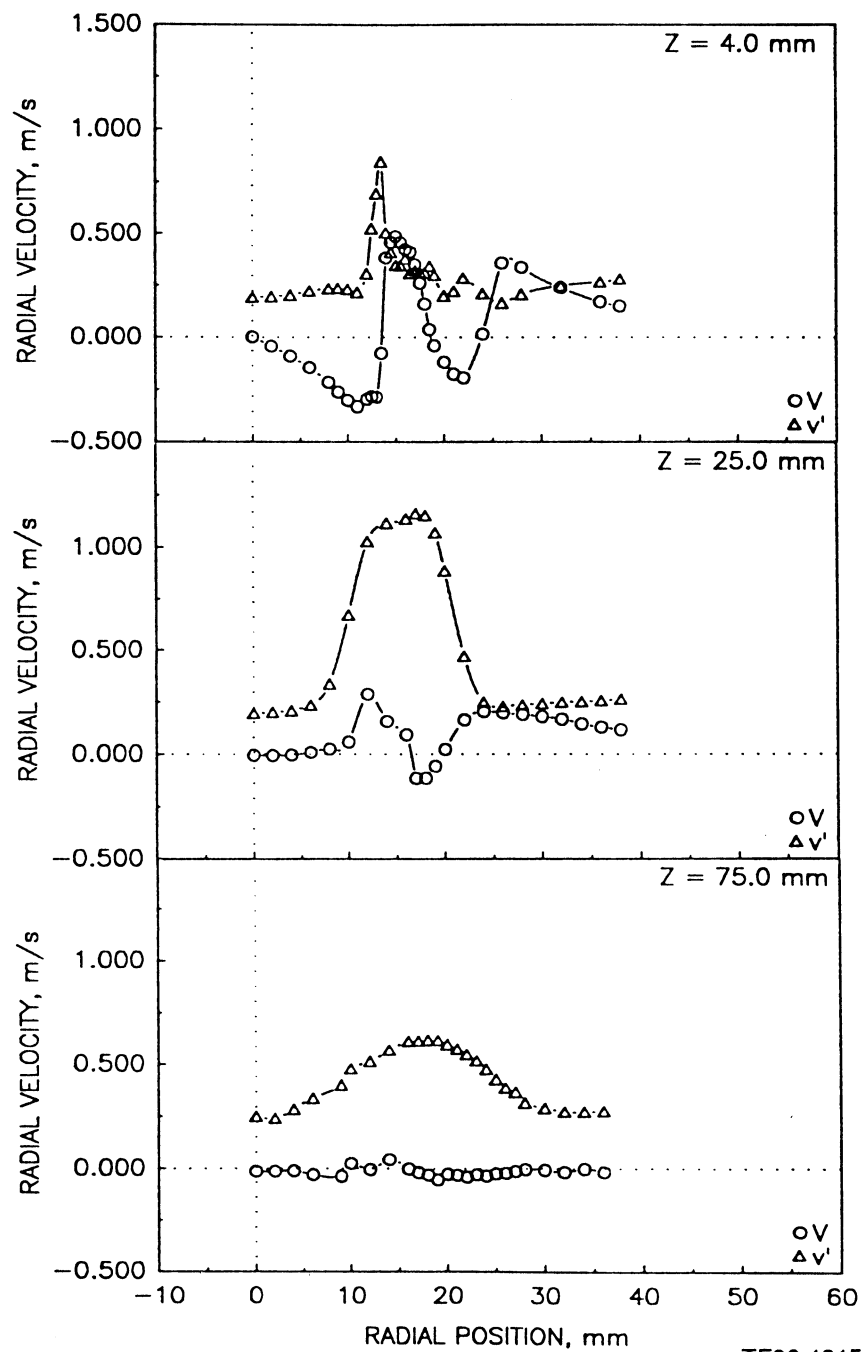


Figure 4.5.6-2. Radial profiles of gas phase statistics in the confined single-phase coaxial jets (2 of 5).

c) Mean and Fluctuating Azimuthal Velocities

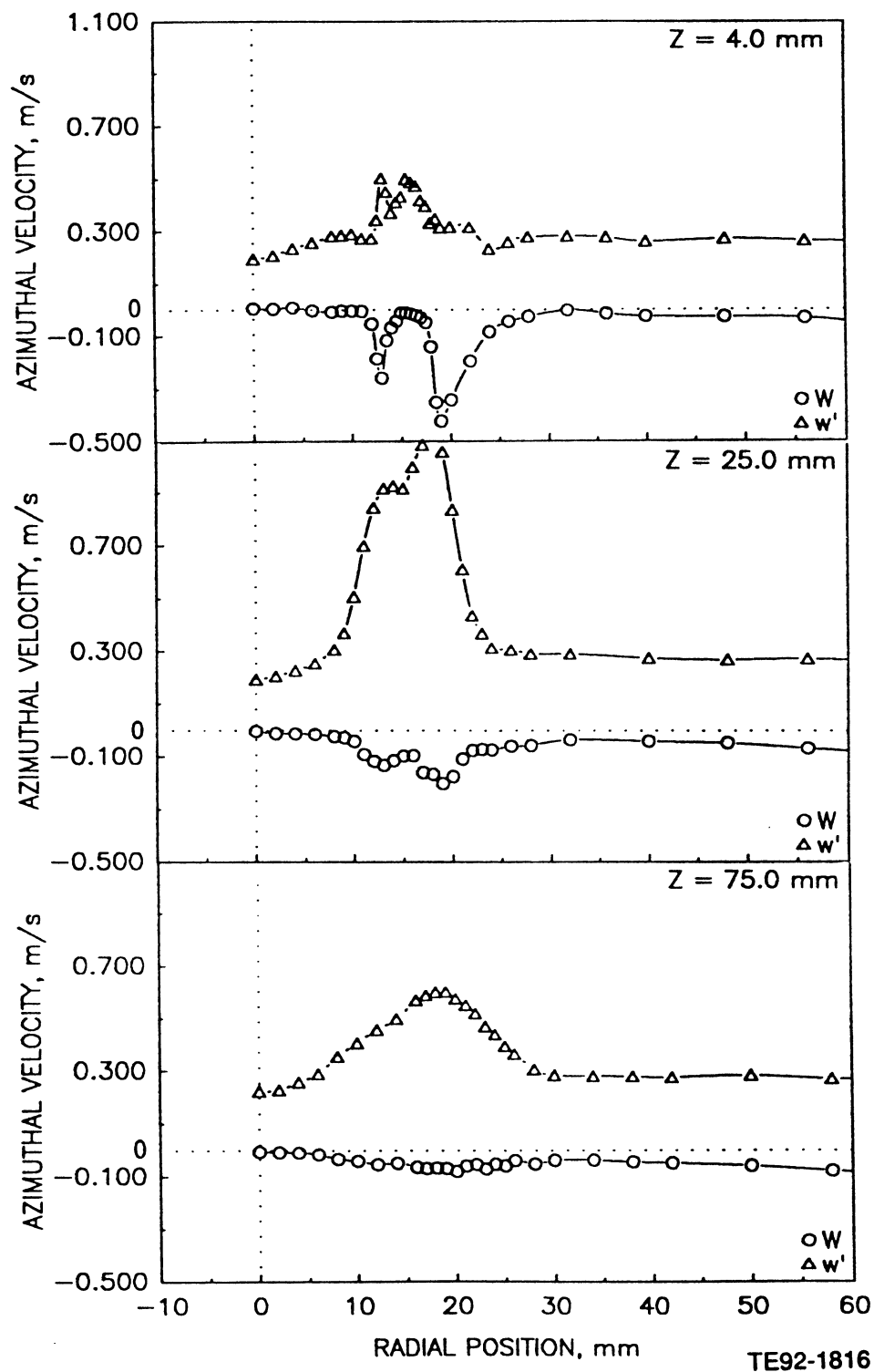


Figure 4.5.6-2. Radial profiles of gas phase statistics in the confined single-phase coaxial jets (3 of 5).

d) Shear Stress Based on Axial and Radial Velocities

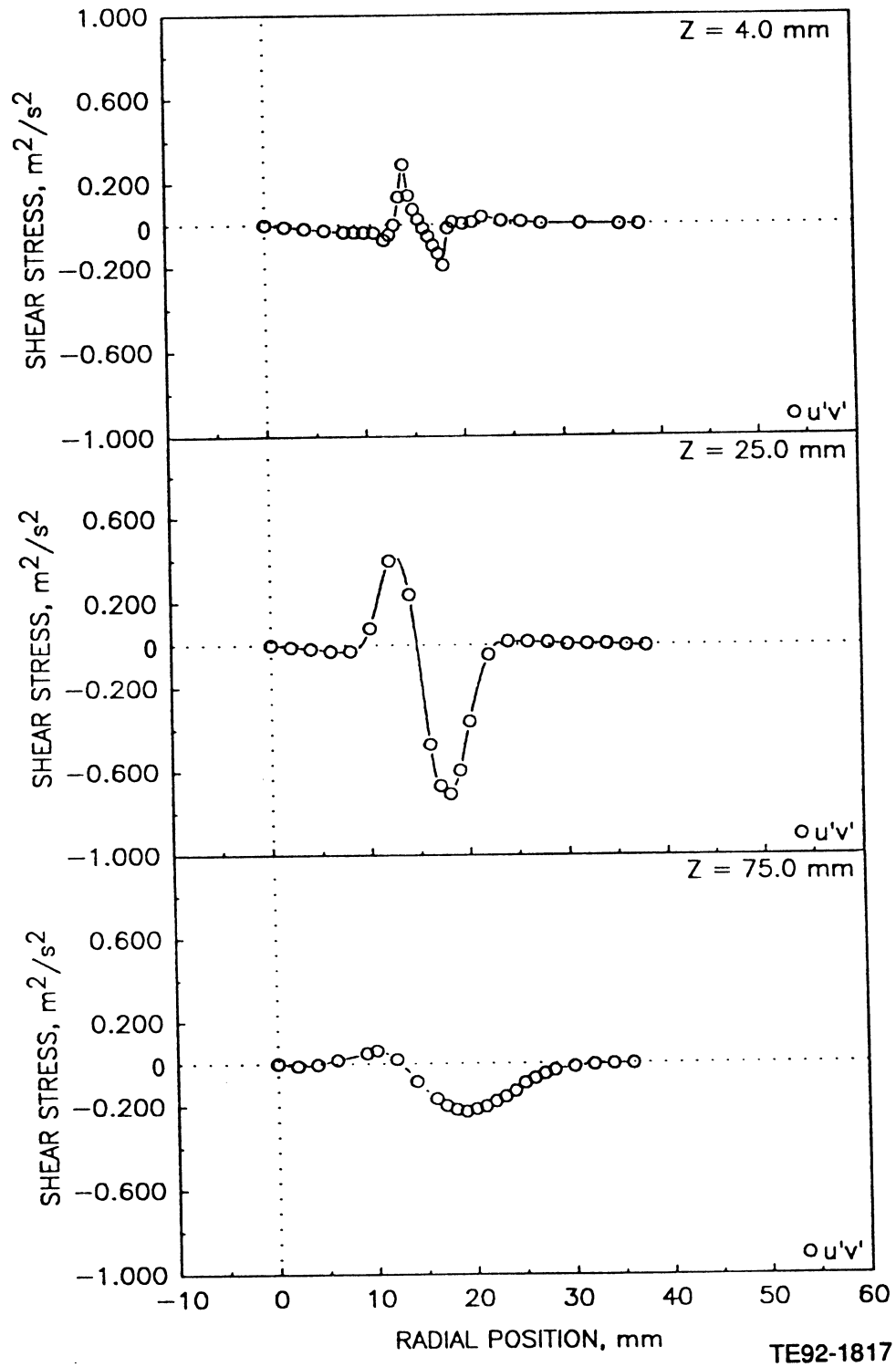


Figure 4.5.6-2. Radial profiles of gas phase statistics in the confined single-phase coaxial jets (4 of 5).

e) Shear Stress Based on Axial and Azimuthal Velocities

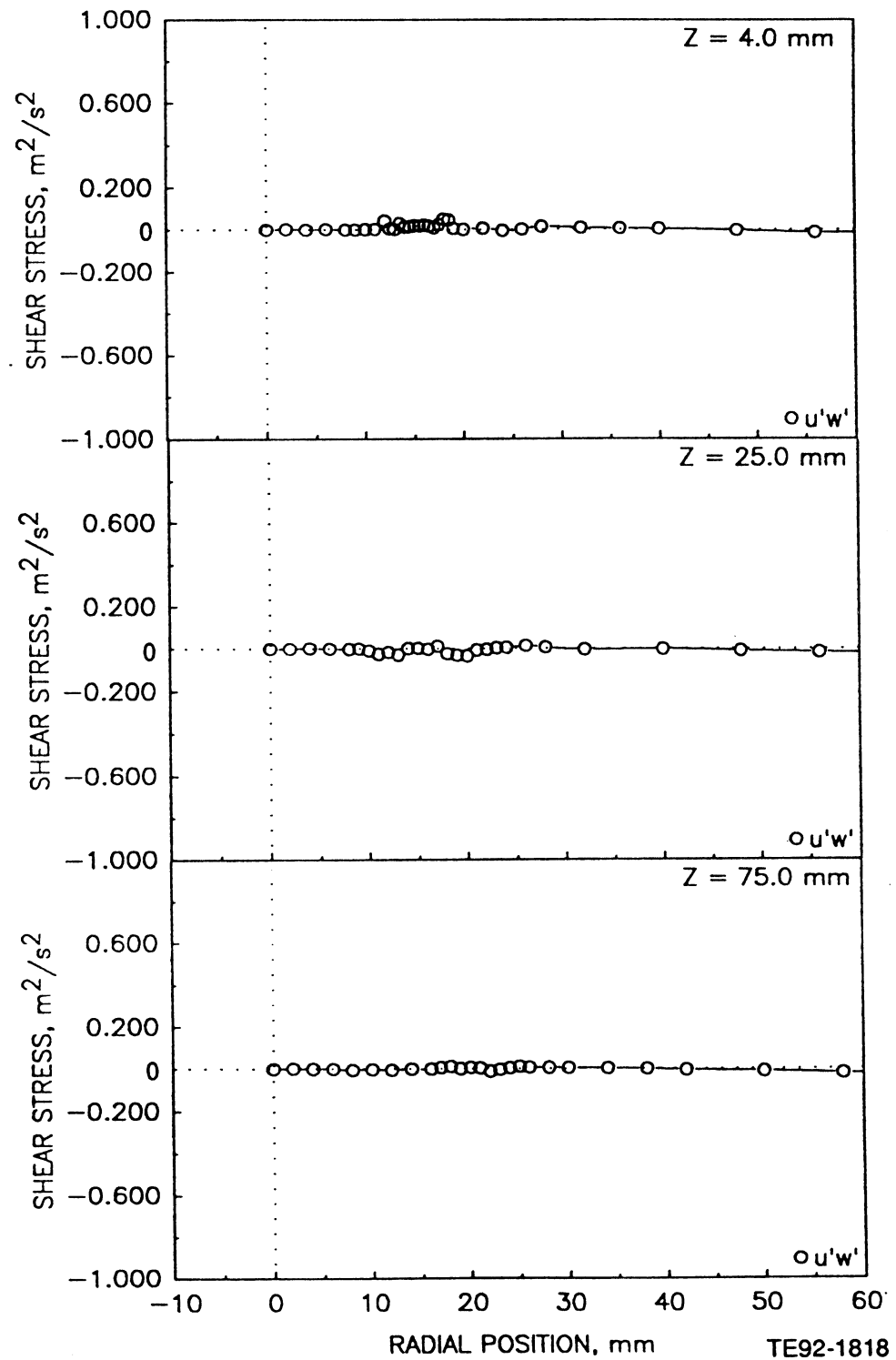


Figure 4.5.6-2. Radial profiles of gas phase statistics in the confined single-phase coaxial jets (5 of 5).

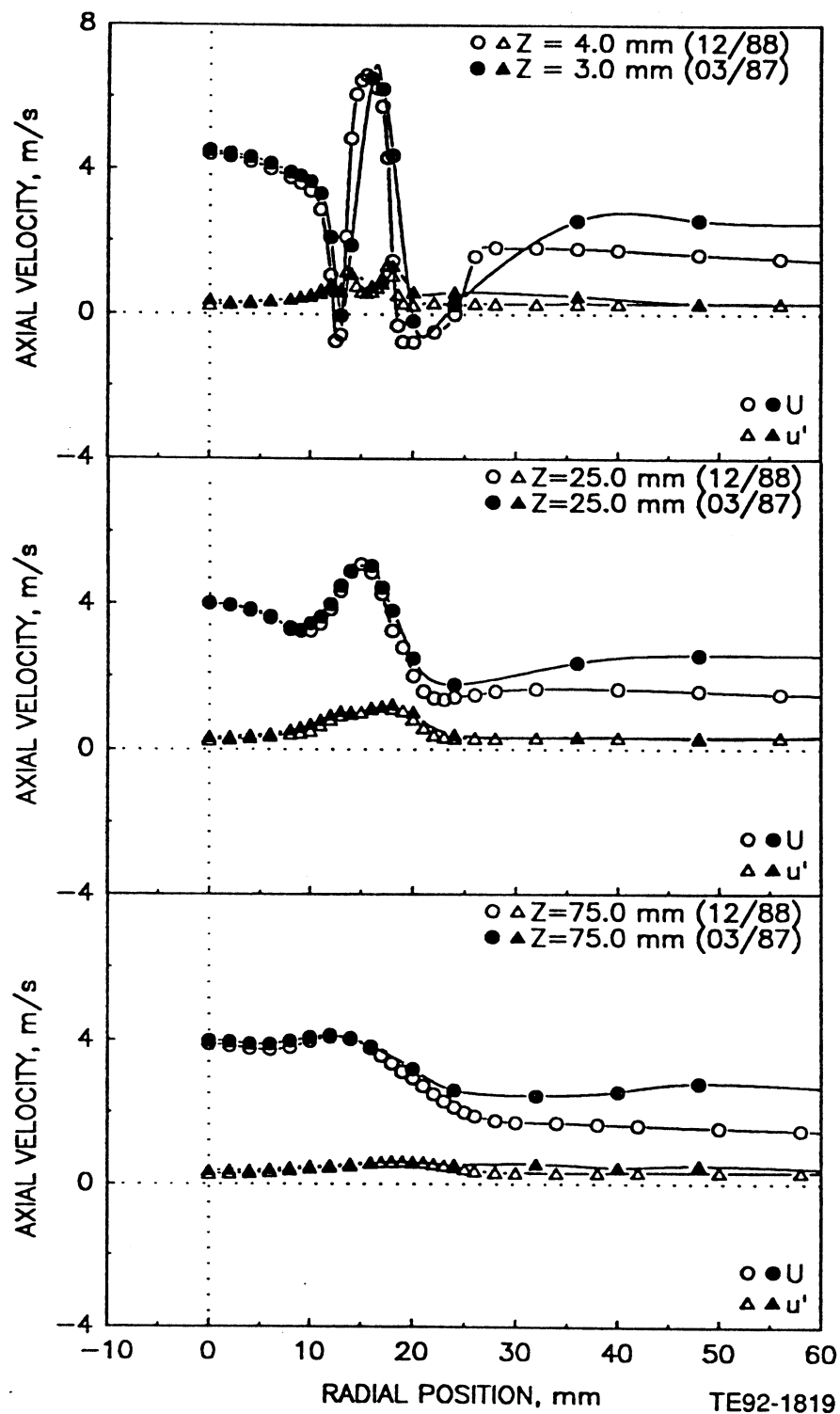


Figure 4.5.6-3. Assessment of repeatability of mean and fluctuating axial velocities in confined single-phase coaxial jets.

a) Mean and Fluctuating Axial Velocities

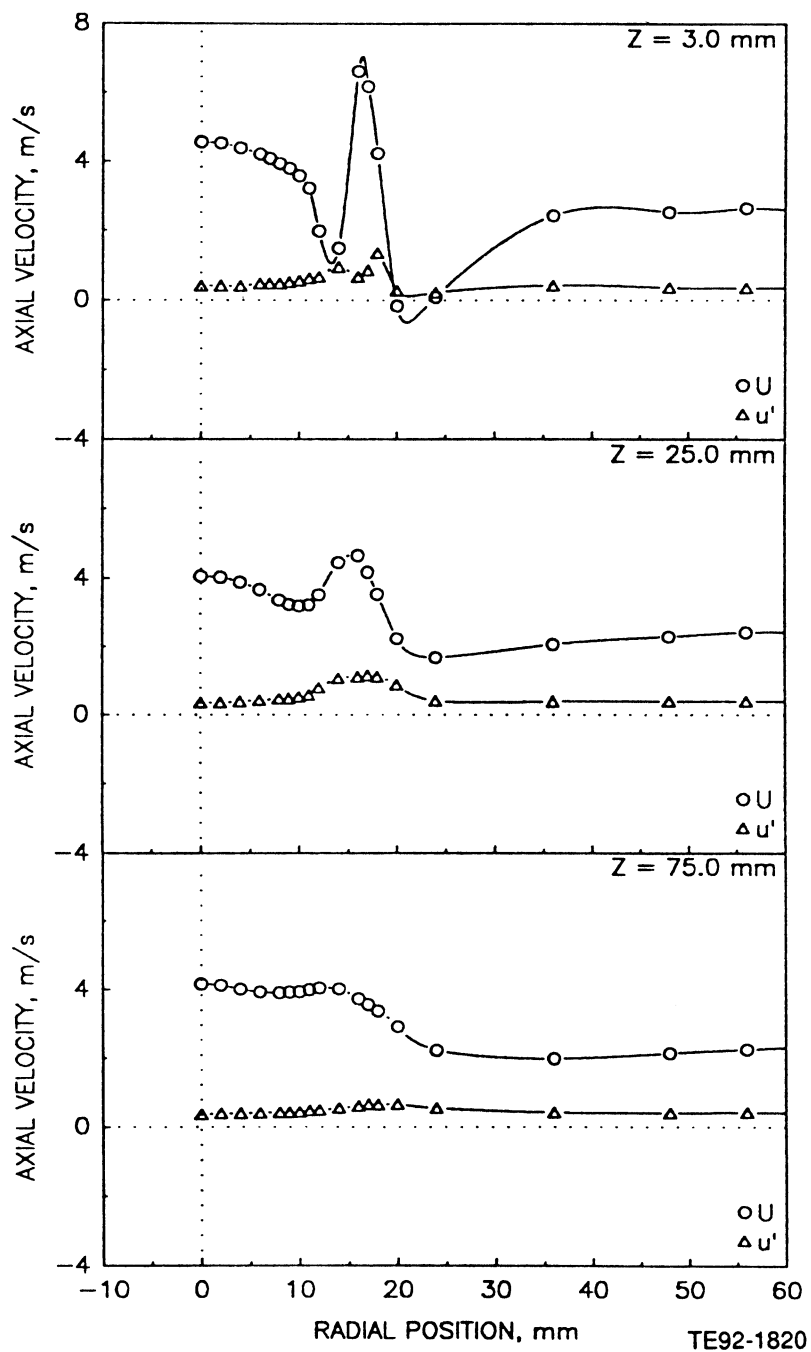


Figure 4.5.7-1. Radial profiles of gas phase velocity measurements in confined coaxial jets with central jet laden with 100-110 micron glass beads at a bead-to-gas mass loading ratio of 0.2 (1 of 3).

b) Mean and Fluctuating Azimuthal Velocities

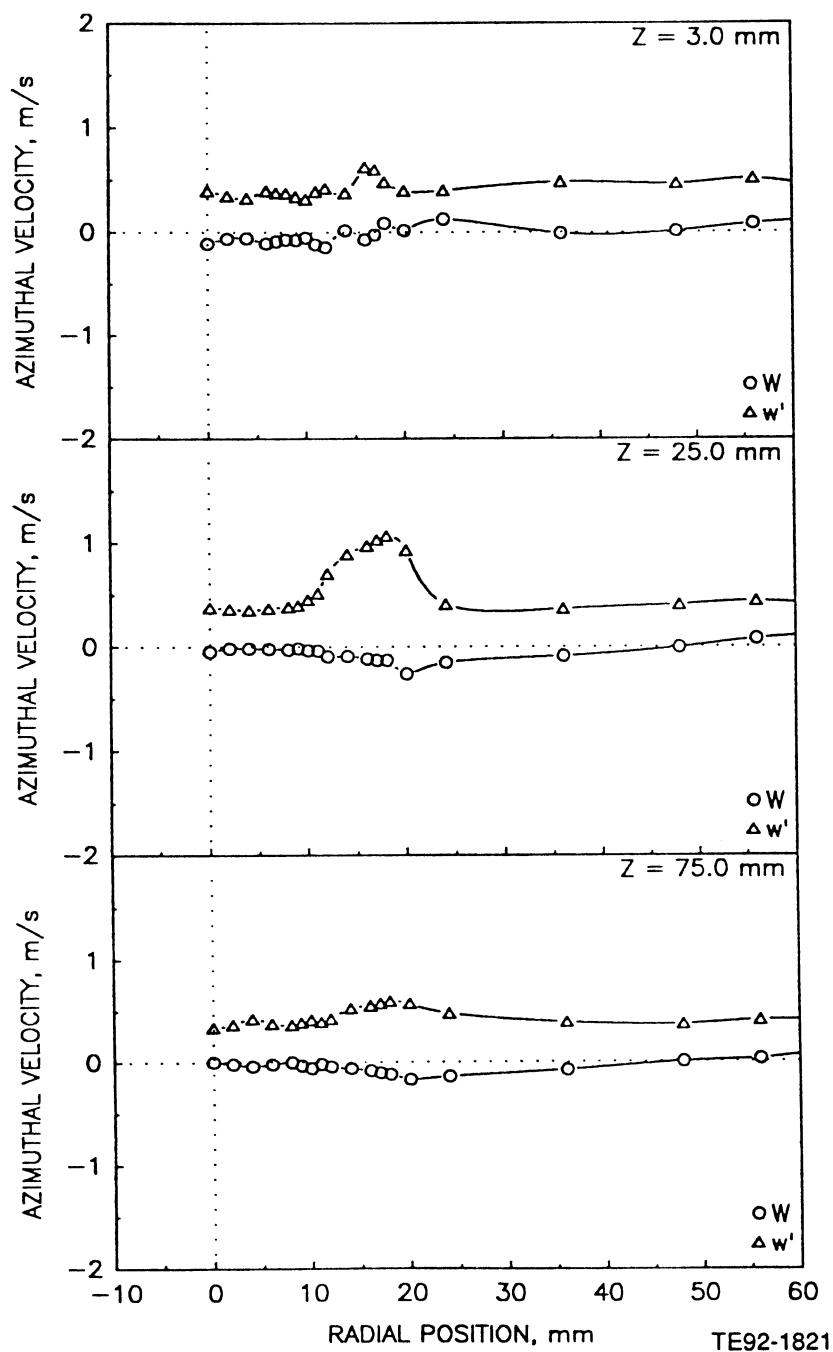


Figure 4.5.7-1. Radial profiles of gas phase velocity measurements in confined coaxial jets with central jet laden with 100-110 micron glass beads at a bead-to-gas mass loading ratio of 0.2 (2 of 3).

c) Shear Stress Based on Axial and Azimuthal Velocities

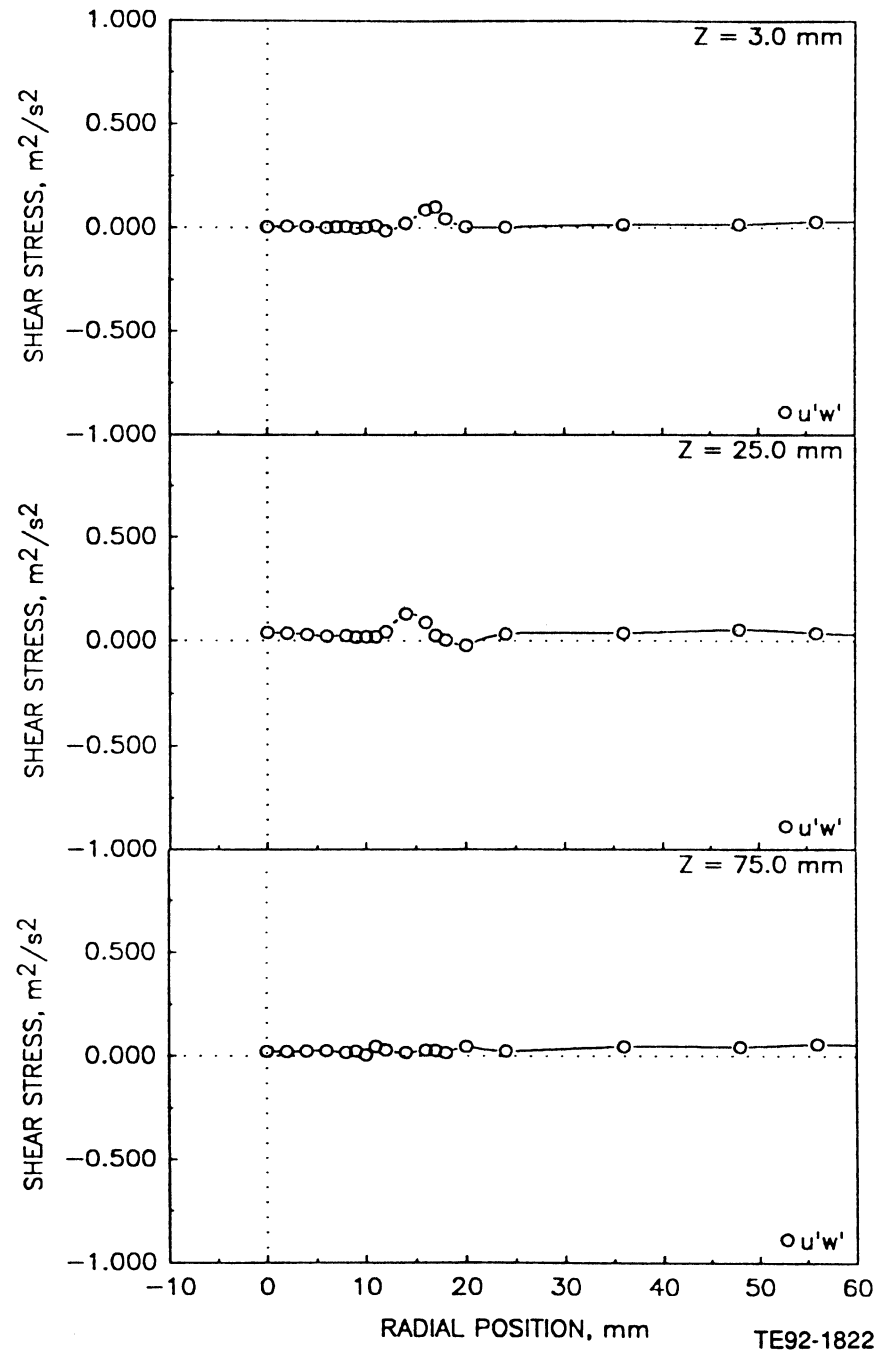


Figure 4.5.7-1. Radial profiles of gas phase velocity measurements in confined coaxial jets with central jet laden with 100-110 micron glass beads at a bead-to-gas mass loading ratio of 0.2 (3 of 3).

a) Mean and Fluctuating Axial Velocities

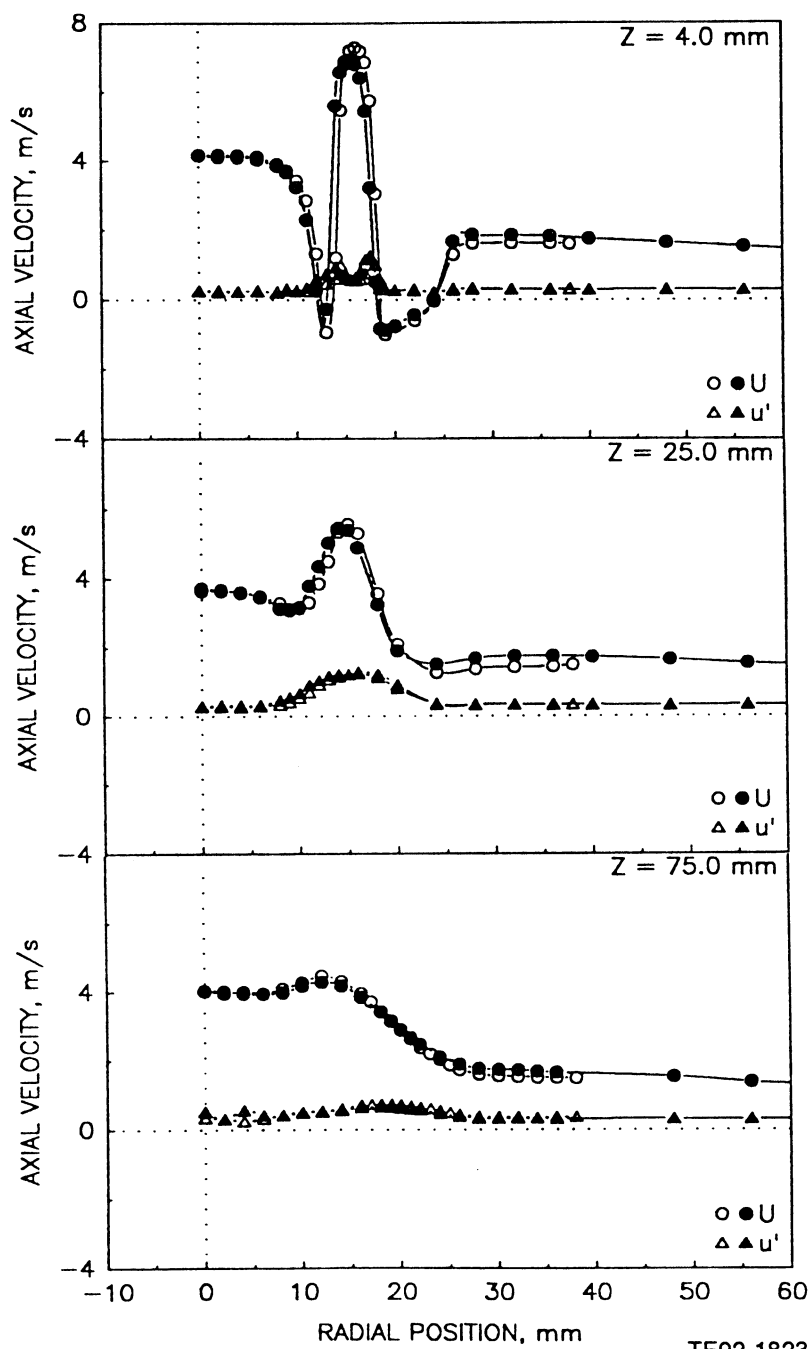


Figure 4.5.7-2. Radial profiles of gas phase velocity measurements in confined coaxial jets with central jet laden with 100-110 micron glass beads at a bead-to-gas mass loading ratio of 0.2 (1 of 5).

b) Mean and Fluctuating Radial Velocities

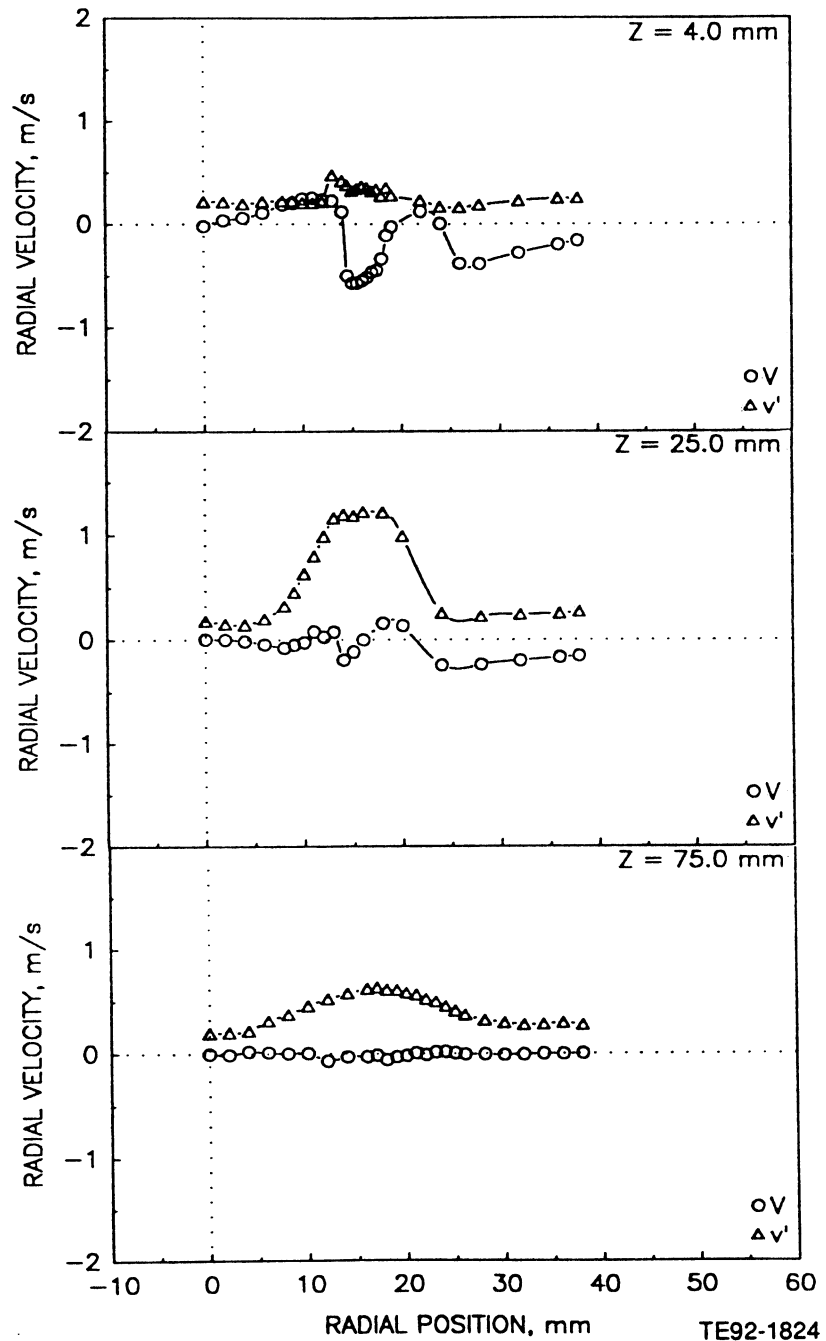


Figure 4.5.7-2. Radial profiles of gas phase velocity measurements in confined coaxial jets with central jet laden with 100-110 micron glass beads at a bead-to-gas mass loading ratio of 0.2 (2 of 5).

c) Mean and Fluctuating Azimuthal Velocities

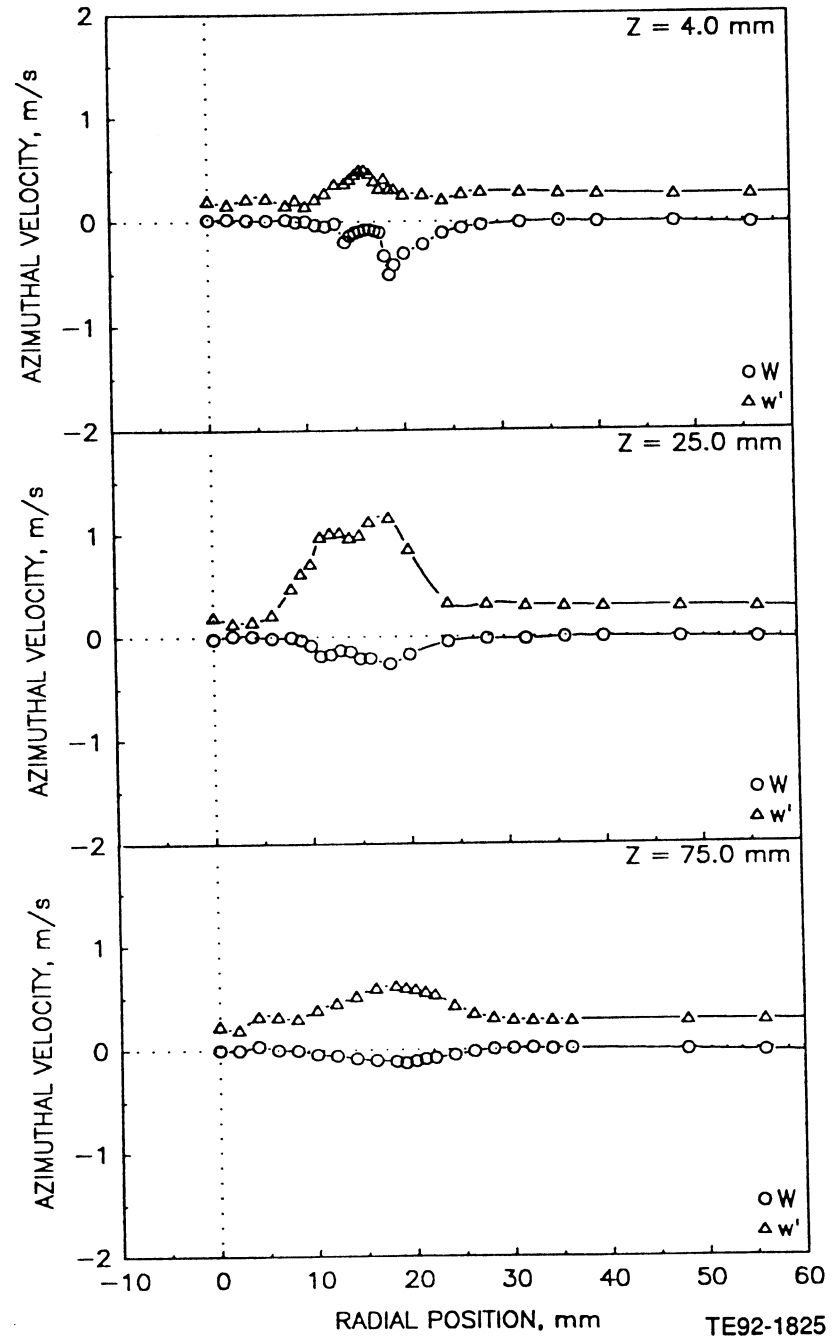


Figure 4.5.7-2. Radial profiles of gas phase velocity measurements in confined coaxial jets with central jet laden with 100-110 micron glass beads at a bead-to-gas mass loading ratio of 0.2 (3 of 5).

d) Shear Stress Based on Axial and Radial Velocities

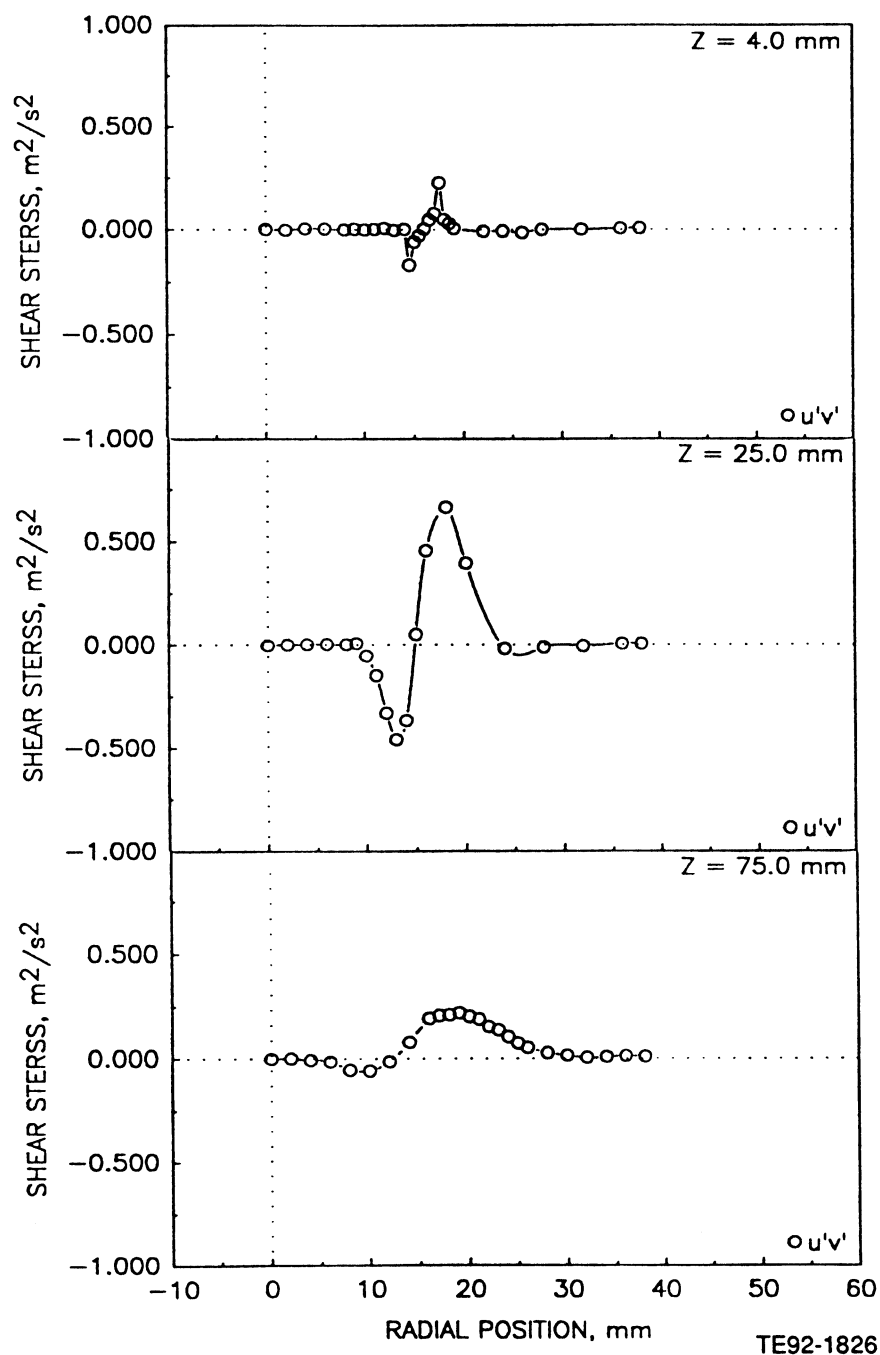


Figure 4.5.7-2. Radial profiles of gas phase velocity measurements in confined coaxial jets with central jet laden with 100-110 micron glass beads at a bead-to-gas mass loading ratio of 0.2 (4 of 5).

e) Shear Stress Based on Axial and Azimuthal Velocities

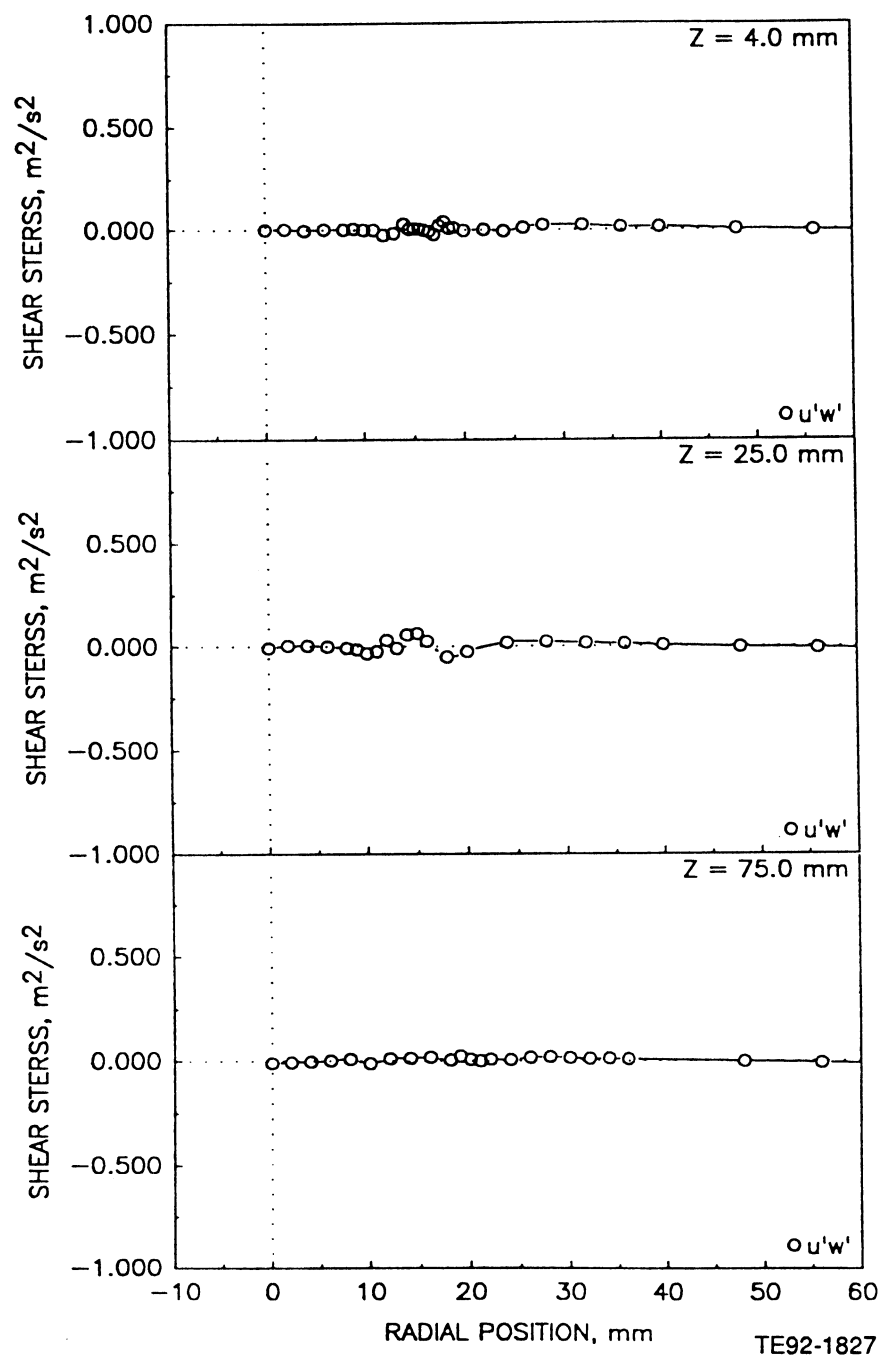


Figure 4.5.7-2. Radial profiles of gas phase velocity measurements in confined coaxial jets with central jet laden with 100-110 micron glass beads at a bead-to-gas mass loading ratio of 0.2 (5 of 5).

a) Mean and Fluctuating Axial Velocities

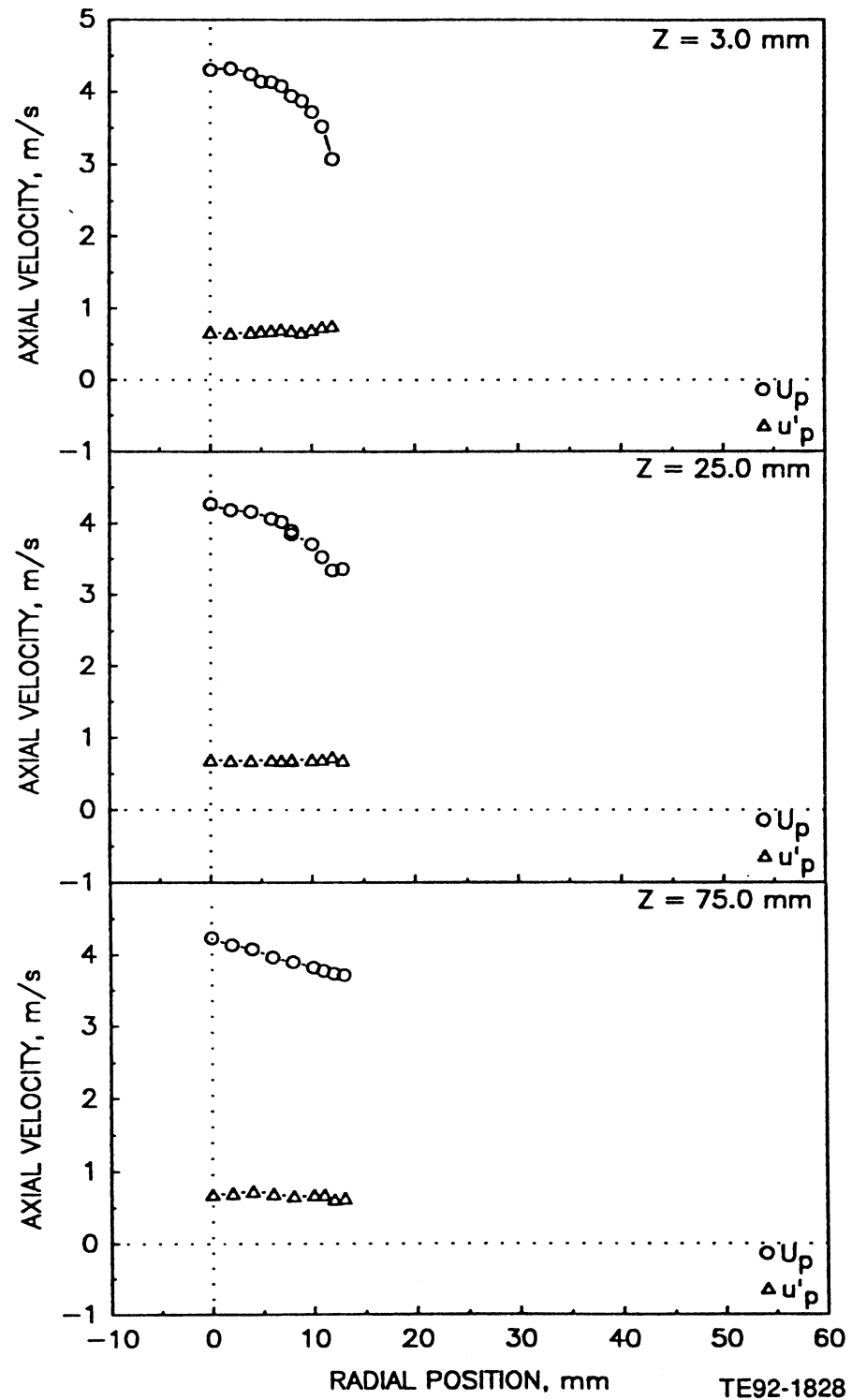


Figure 4.5.8-1. Radial profiles of particle measurements in confined coaxial jets with central jet laden with 100-110 micron glass beads with a bead-to-gas mass loading ratio of 0.2 (1 of 3).

b) Mean and Fluctuating Azimuthal Velocities

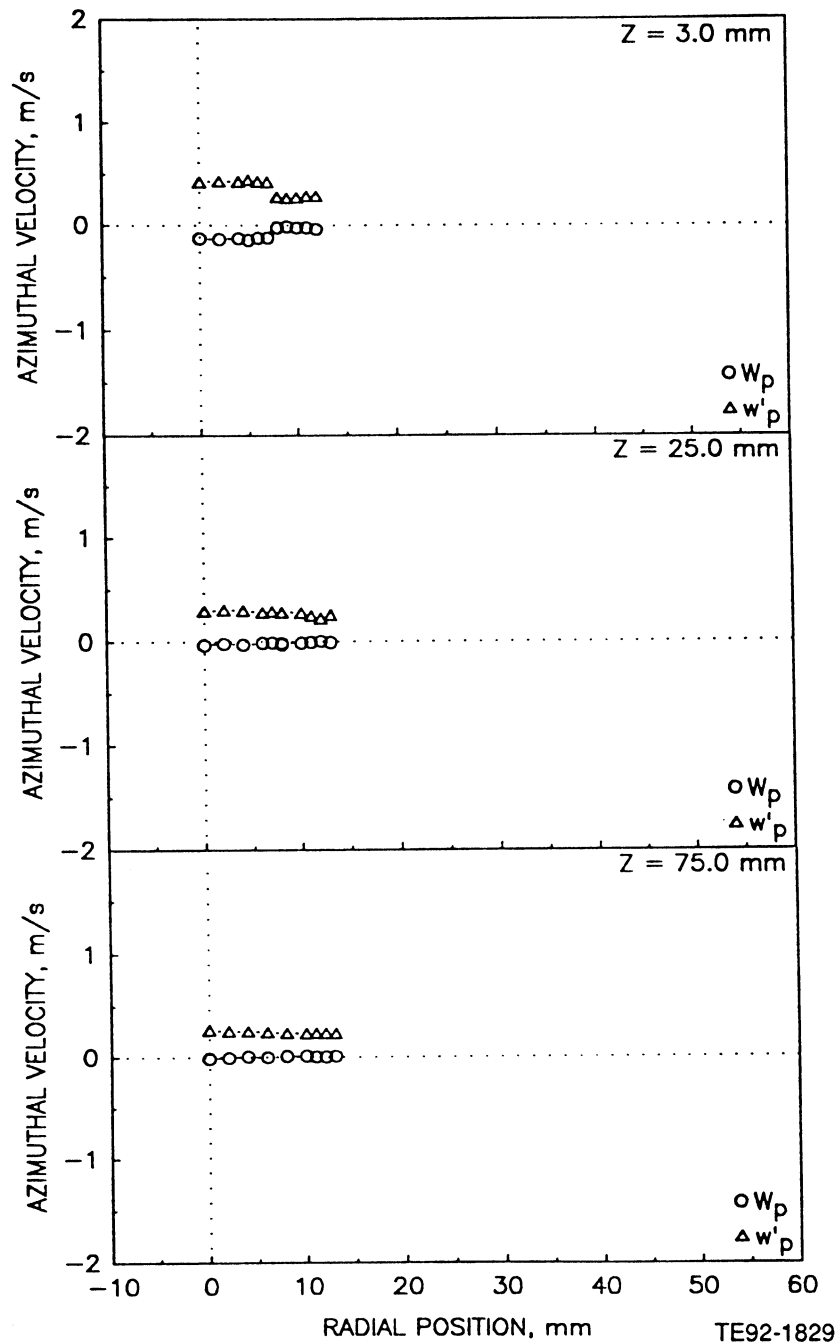


Figure 4.5.8-1. Radial profiles of particle measurements in confined coaxial jets with central jet laden with 100-110 micron glass beads with a bead-to-gas mass loading ratio of 0.2 (2 of 3).

c) Particle Data Rate

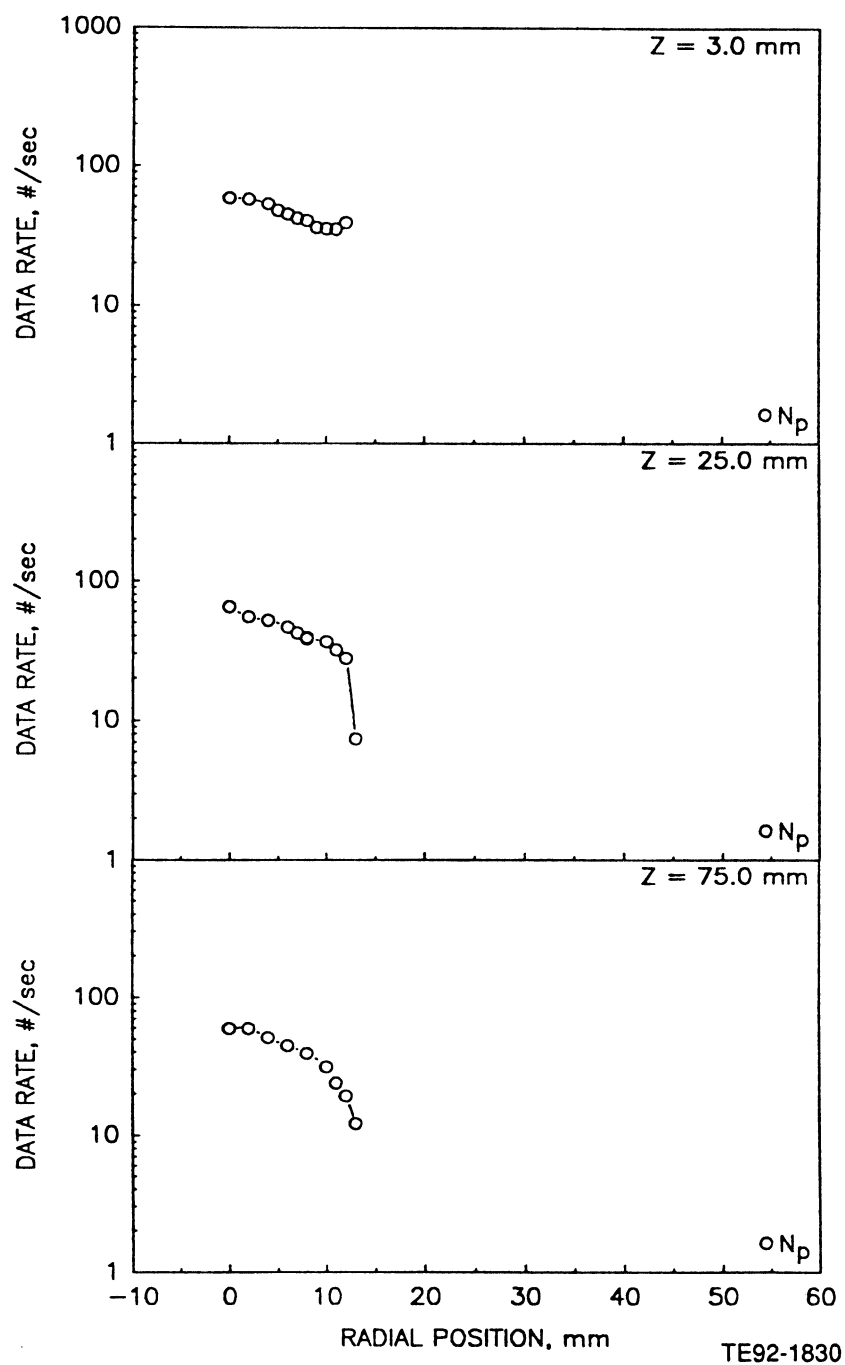


Figure 4.5.8-1. Radial profiles of particle measurements in confined coaxial jets with central jet laden with 100-110 micron glass beads with a bead-to-gas mass loading ratio of 0.2 (3 of 3).

a) Mean and Fluctuating Axial Velocities

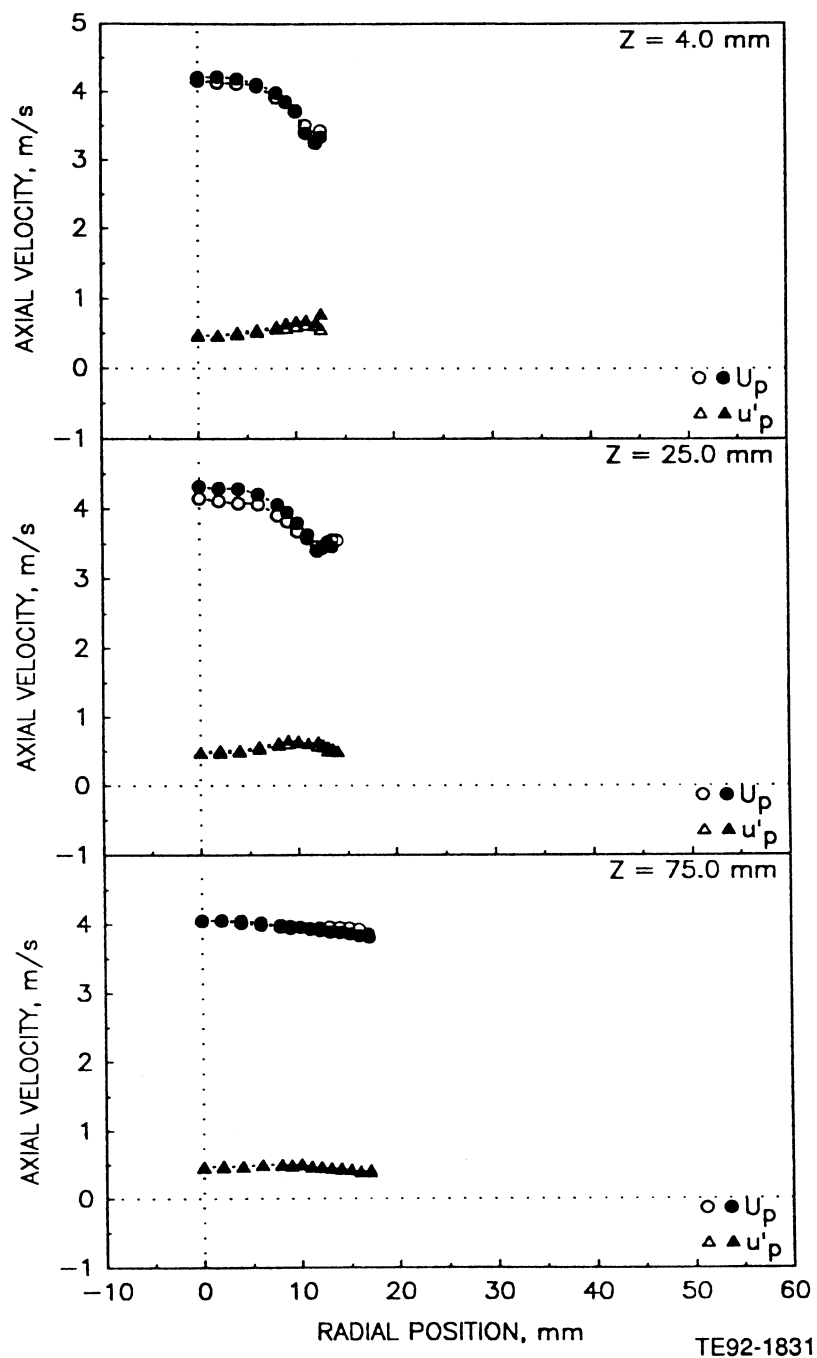


Figure 4.5.8-2. Radial profiles of particle measurements in confined coaxial jets with central jet laden with 100-110 micron glass beads with a bead-to-gas mass loading ratio of 1.0 (1 of 5).

b) Mean and Fluctuating Radial Velocities

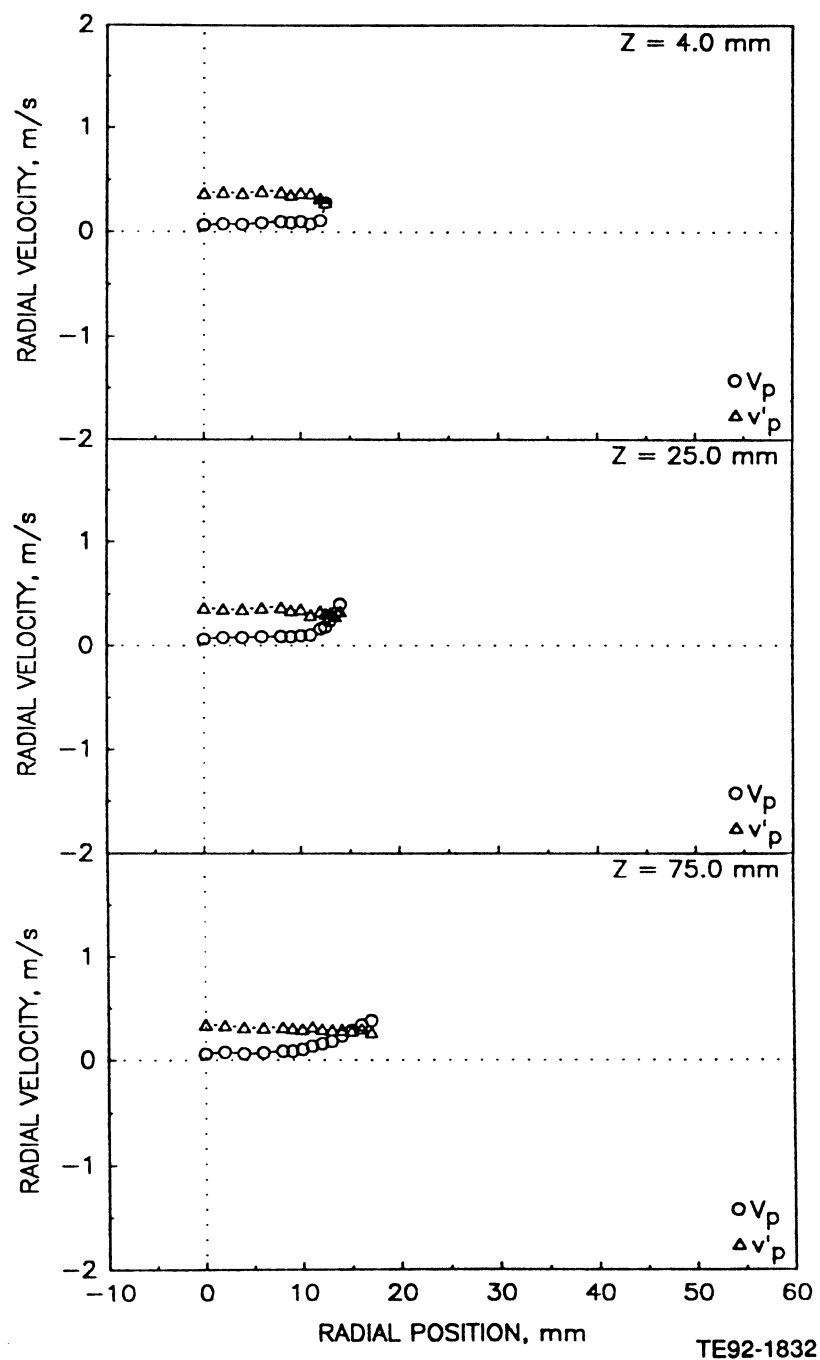


Figure 4.5.8-2. Radial profiles of particle measurements in confined coaxial jets with central jet laden with 100-110 micron glass beads with a bead-to-gas mass loading ratio of 1.0 (2 of 5).

c) Mean and Fluctuating Azimuthal Velocities

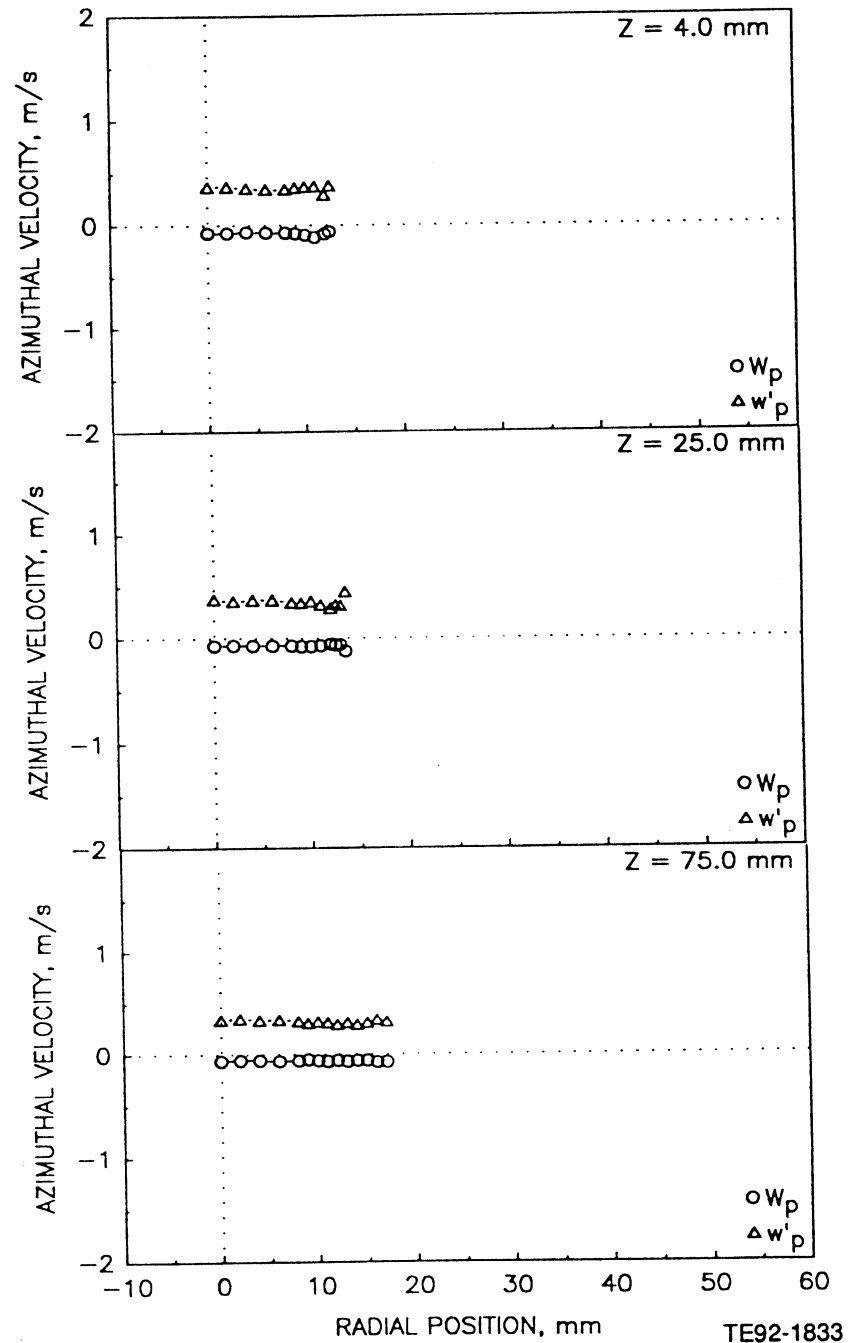


Figure 4.5.8-2. Radial profiles of particle measurements in confined coaxial jets with central jet laden with 100-110 micron glass beads with a bead-to-gas mass loading ratio of 1.0 (3 of 5).

d) Particle Velocity Correlation Based on Axial and Radial Components

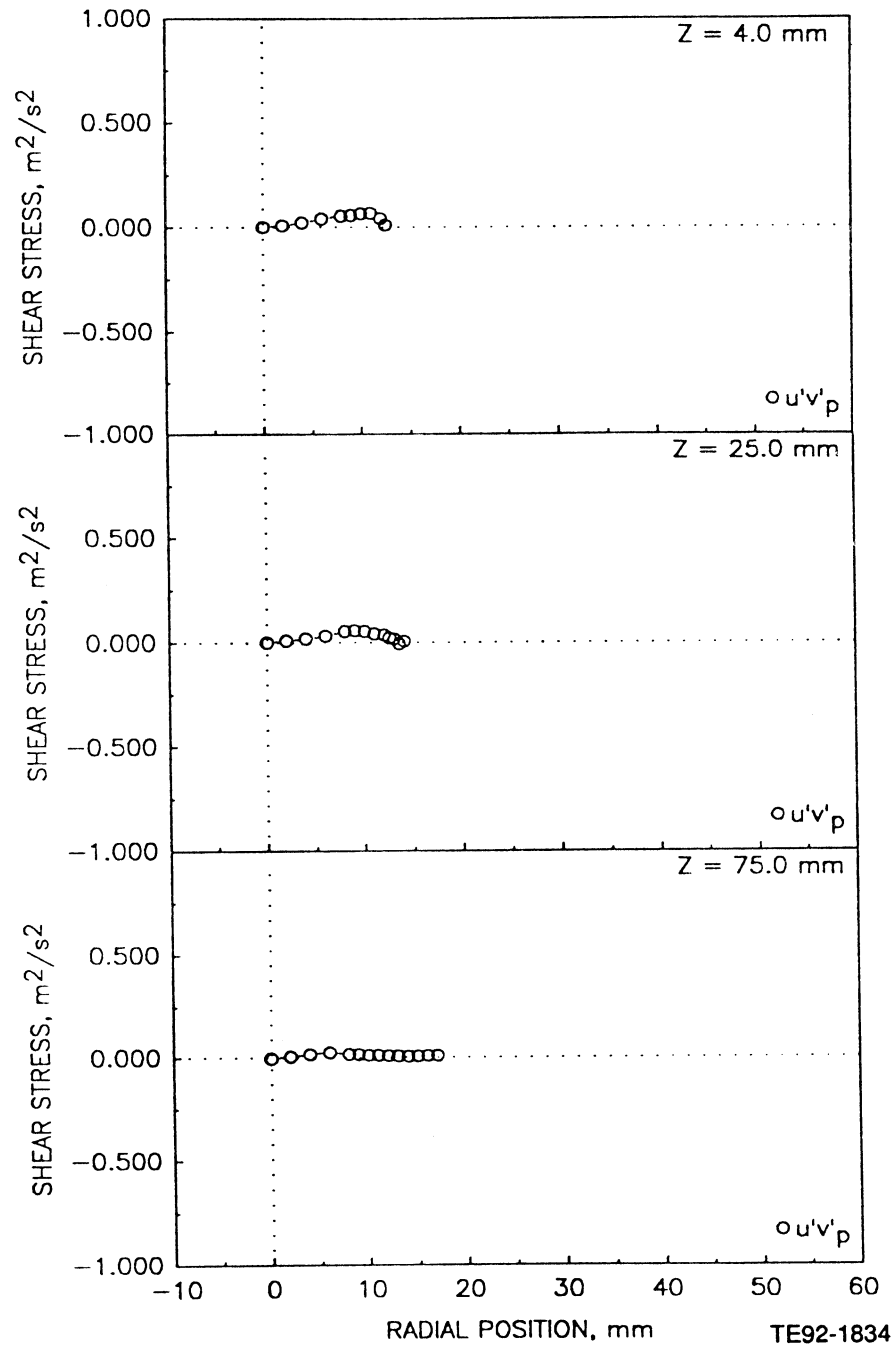


Figure 4.5.8-2. Radial profiles of particle measurements in confined coaxial jets with central jet laden with 100-110 micron glass beads with a bead-to-gas mass loading ratio of 1.0 (4 of 5).

e) Particle Data Rate

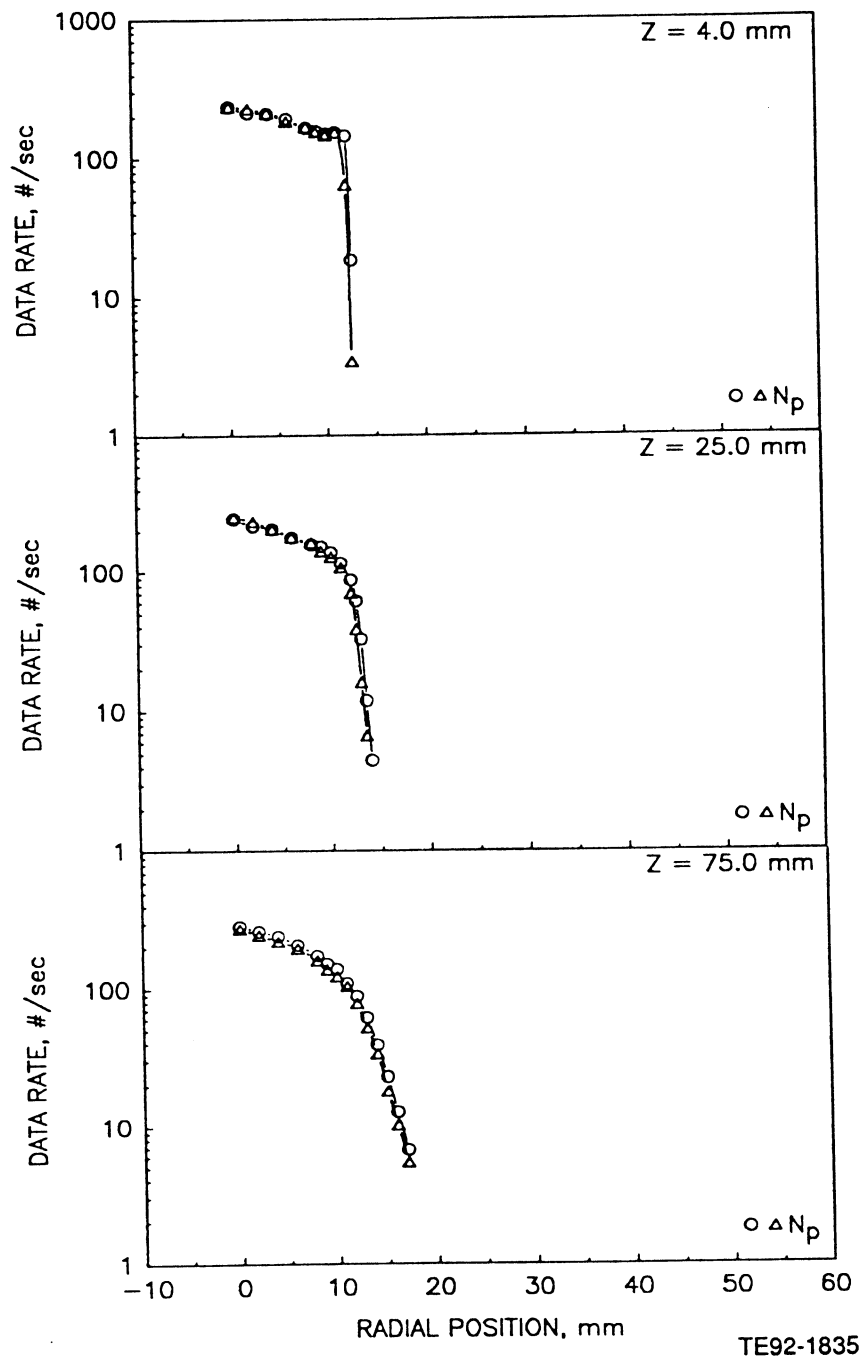


Figure 4.5.8-2. Radial profiles of particle measurements in confined coaxial jets with central jet laden with 100-110 micron glass beads with a bead-to-gas mass loading ratio of 1.0 (5 of 5).

a) Mean and Fluctuating Axial Velocities

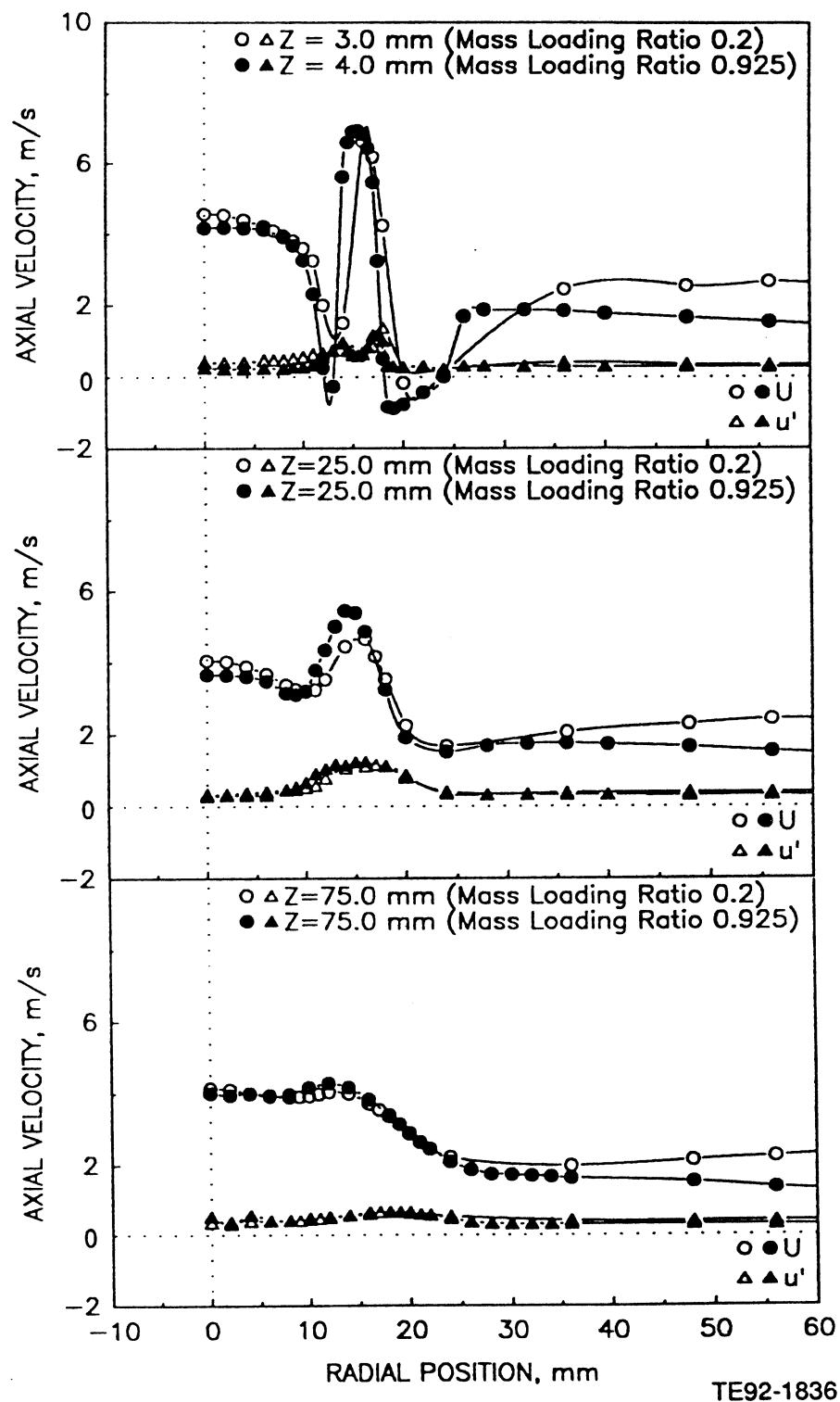
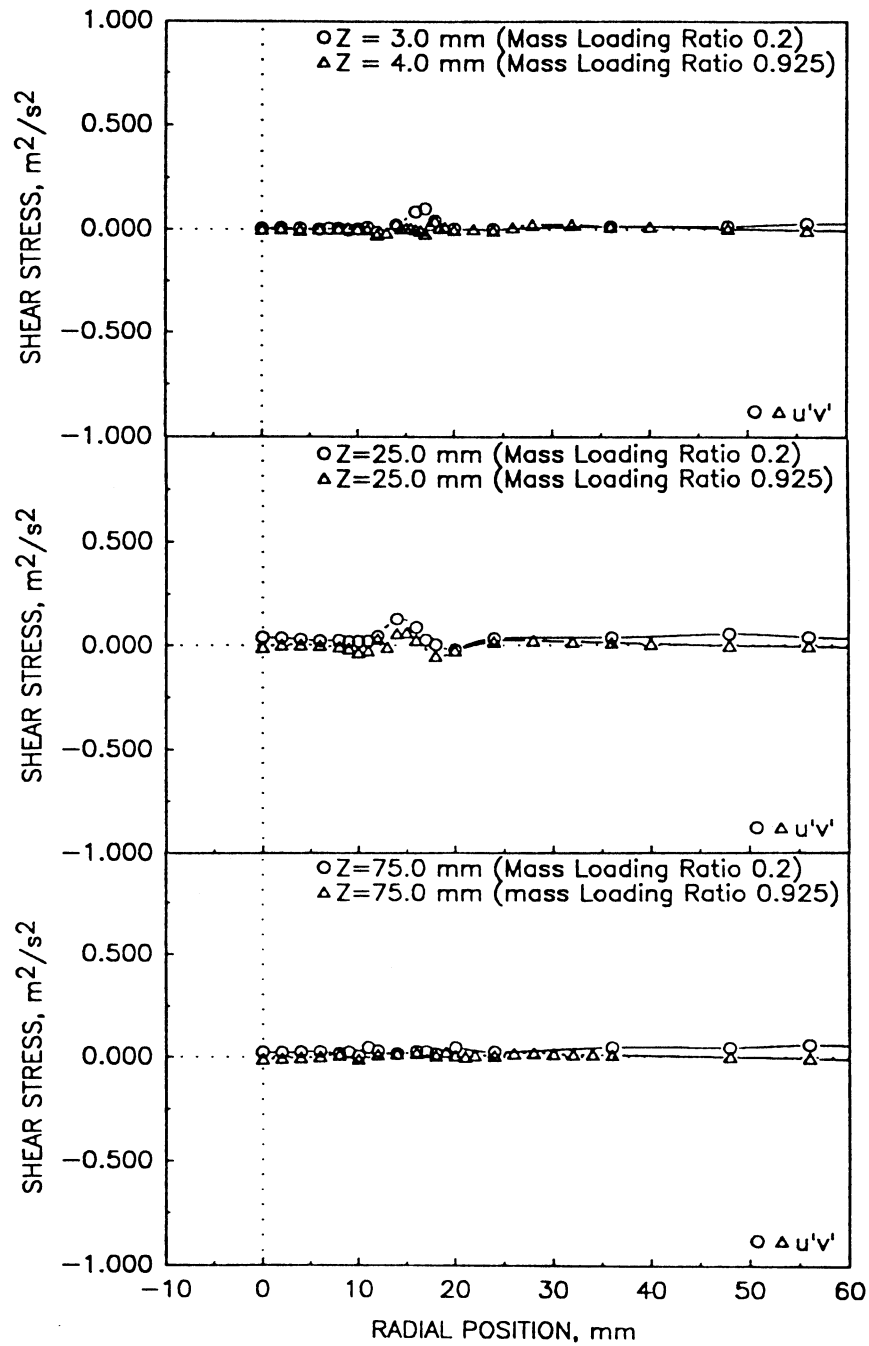


Figure 4.5.9-1. Comparison of gas phase velocity and shear stress in confined coaxial jets with central jet laden with 100-110 micron particles at two particle-to-gas mass loading ratios (1 of 2).

b) Shear Stress Based on Axial and Radial Velocities



TE92-1837

Figure 4.5.9-1. Comparison of gas phase velocity and shear stress in confined coaxial jets with central jet laden with 100-110 micron particles at two particle-to-gas mass loading ratios (2 of 2).

a) Mean and Fluctuating Axial Velocities

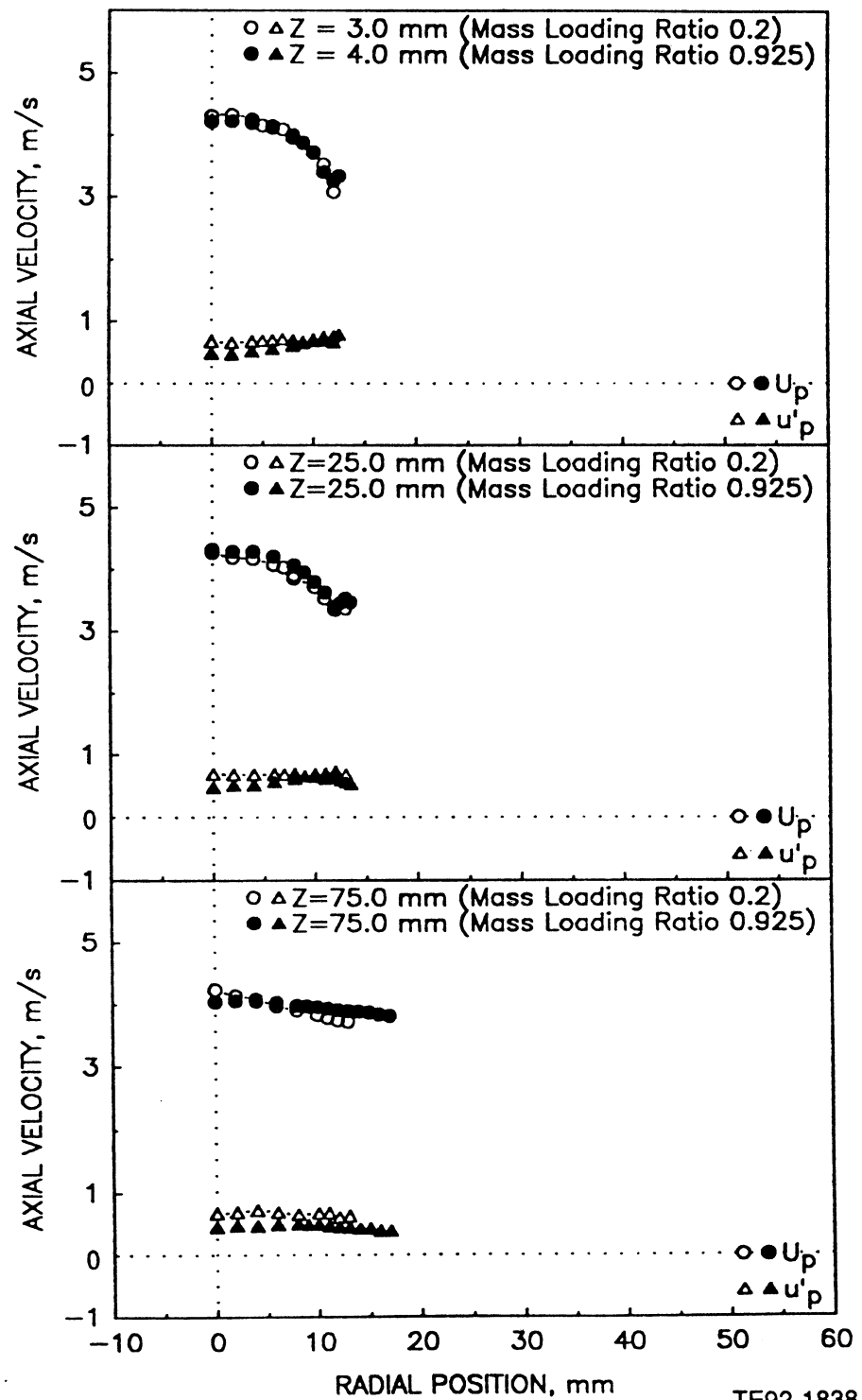


Figure 4.5.9-2. Comparison of particle velocity and data rate in confined coaxial jets with central jet laden with 100-110 micron particles at two particle-to-gas mass loading ratios (1 of 2).

b) Data Rate

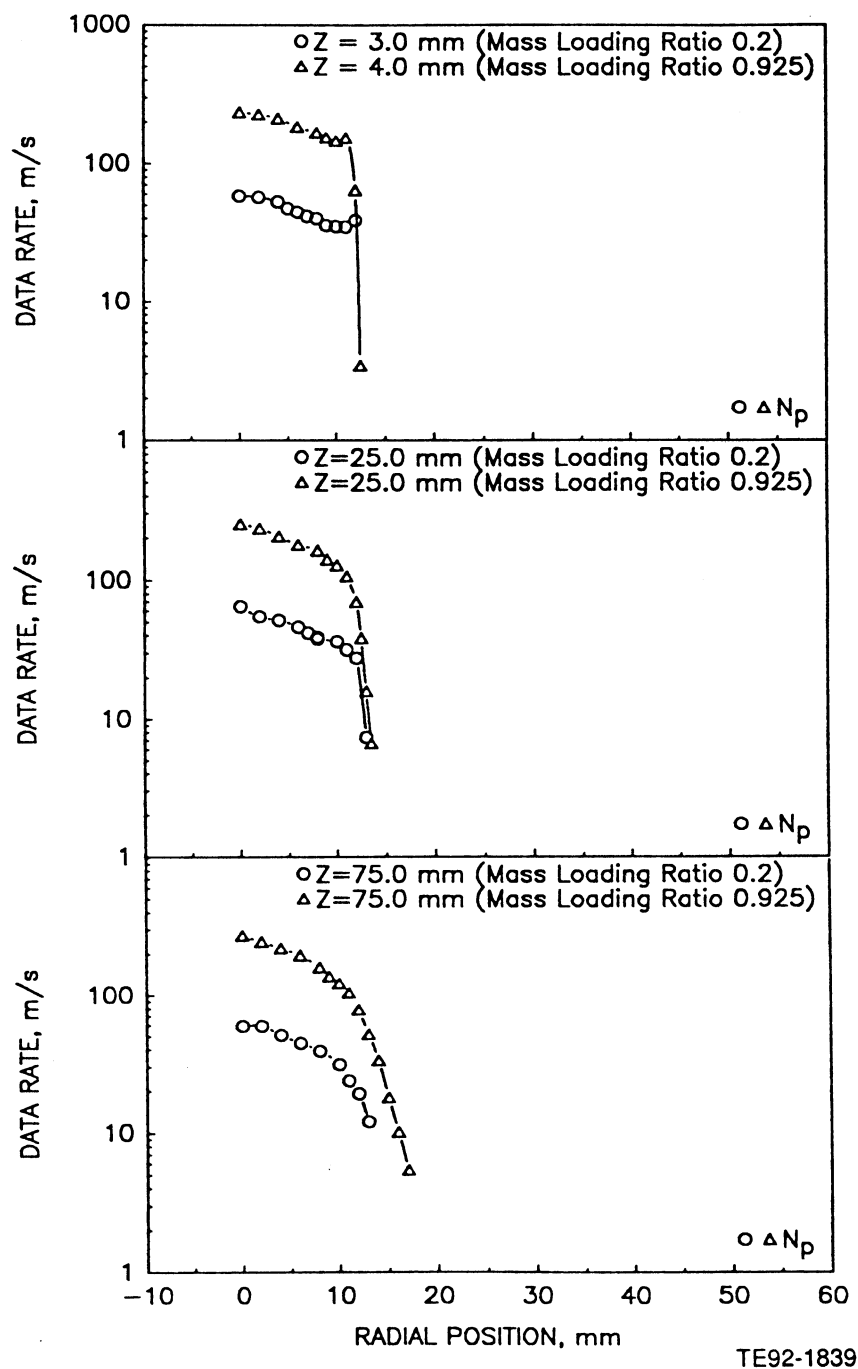


Figure 4.5.9-2. Comparison of particle velocity and data rate in confined coaxial jets with central jet laden with 100-110 micron particles at two particle-to-gas mass loading ratios (2 of 2).

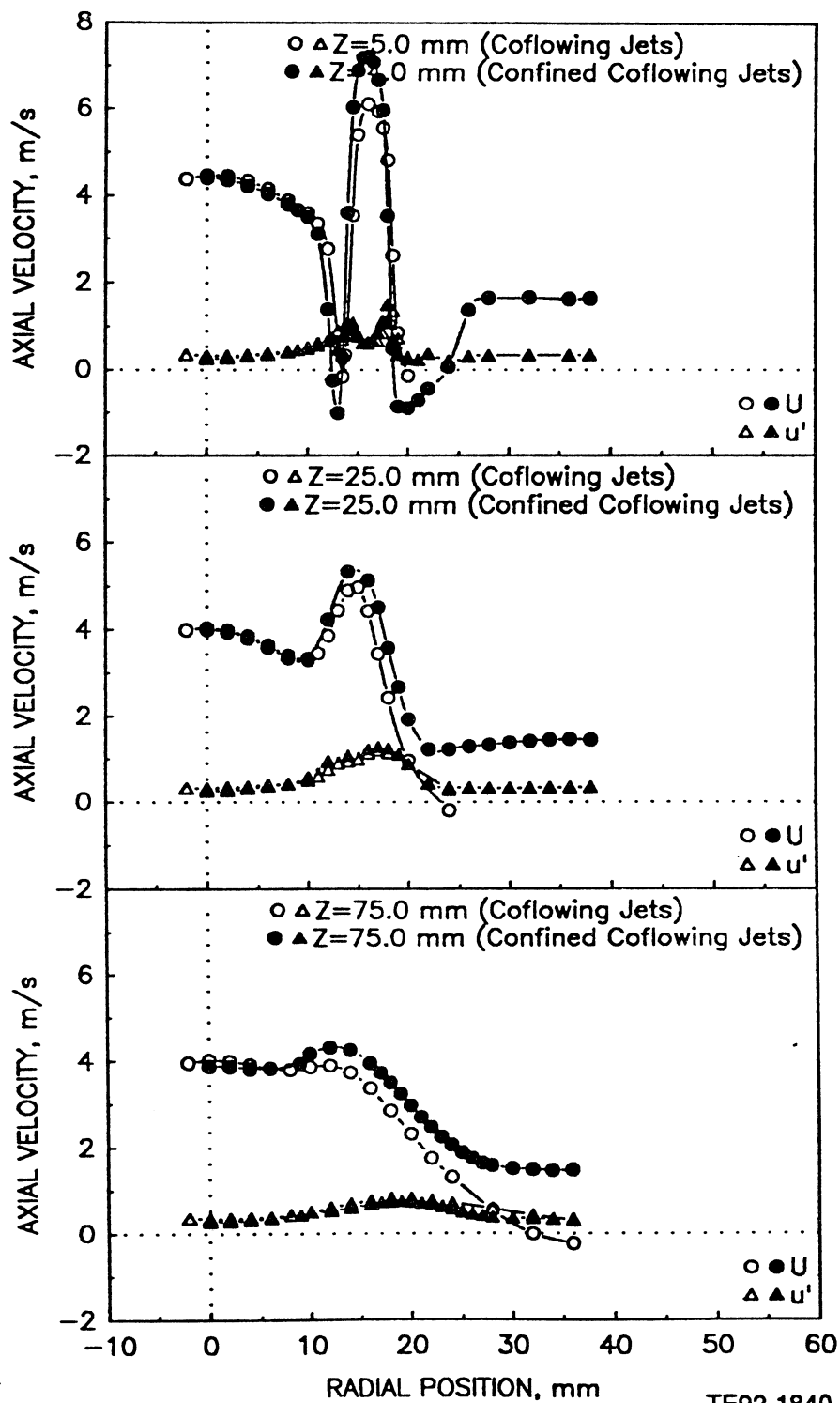


Figure 4.5.10-1. Comparison of gas phase mean and fluctuating axial velocities in confined and unconfined single-phase coaxial jets.

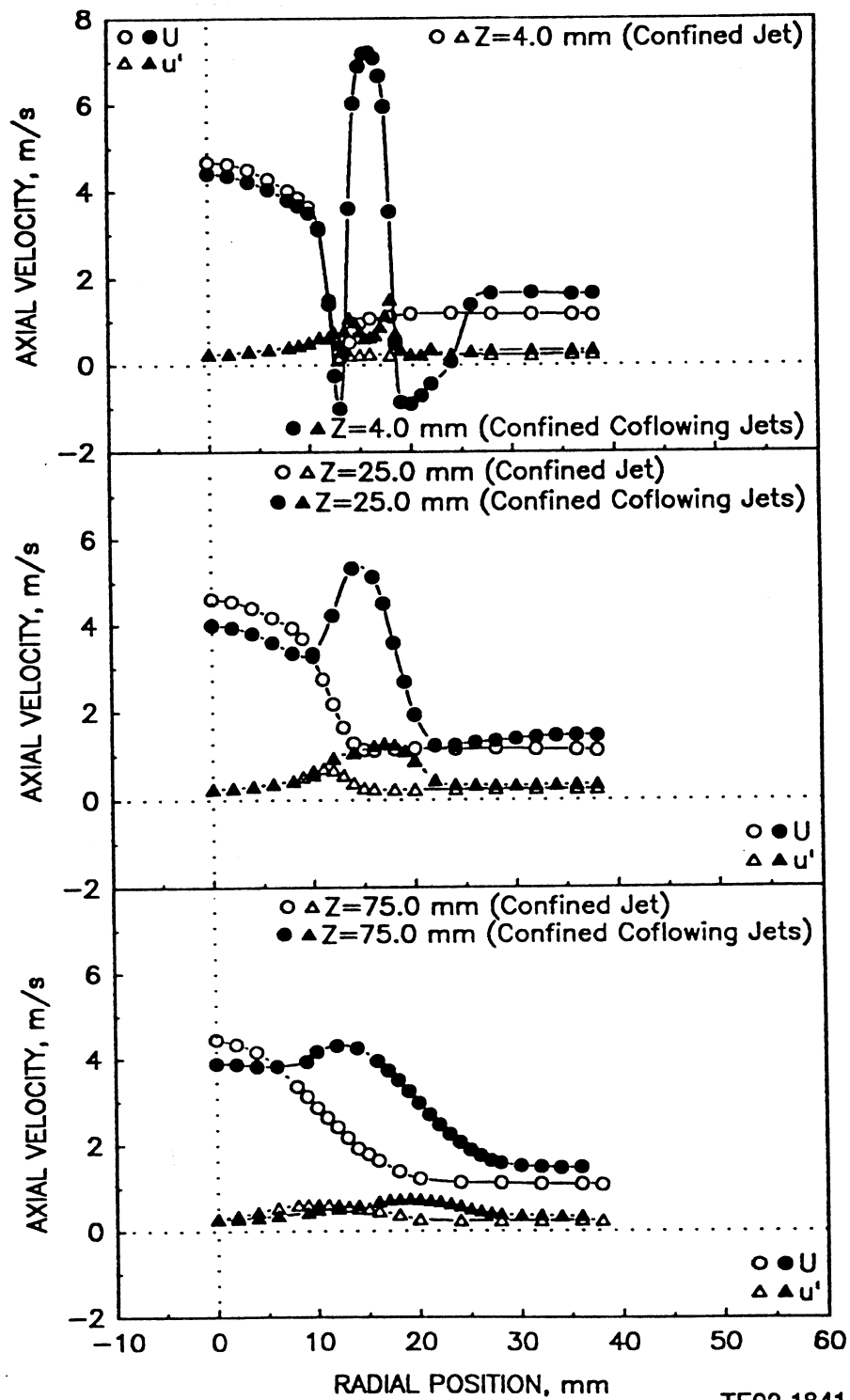


Figure 4.5.11-1. Comparison of gas phase mean and fluctuating axial velocities in confined single-phase jets with and without coaxial flow.

a) Mean and Fluctuating Axial Velocities

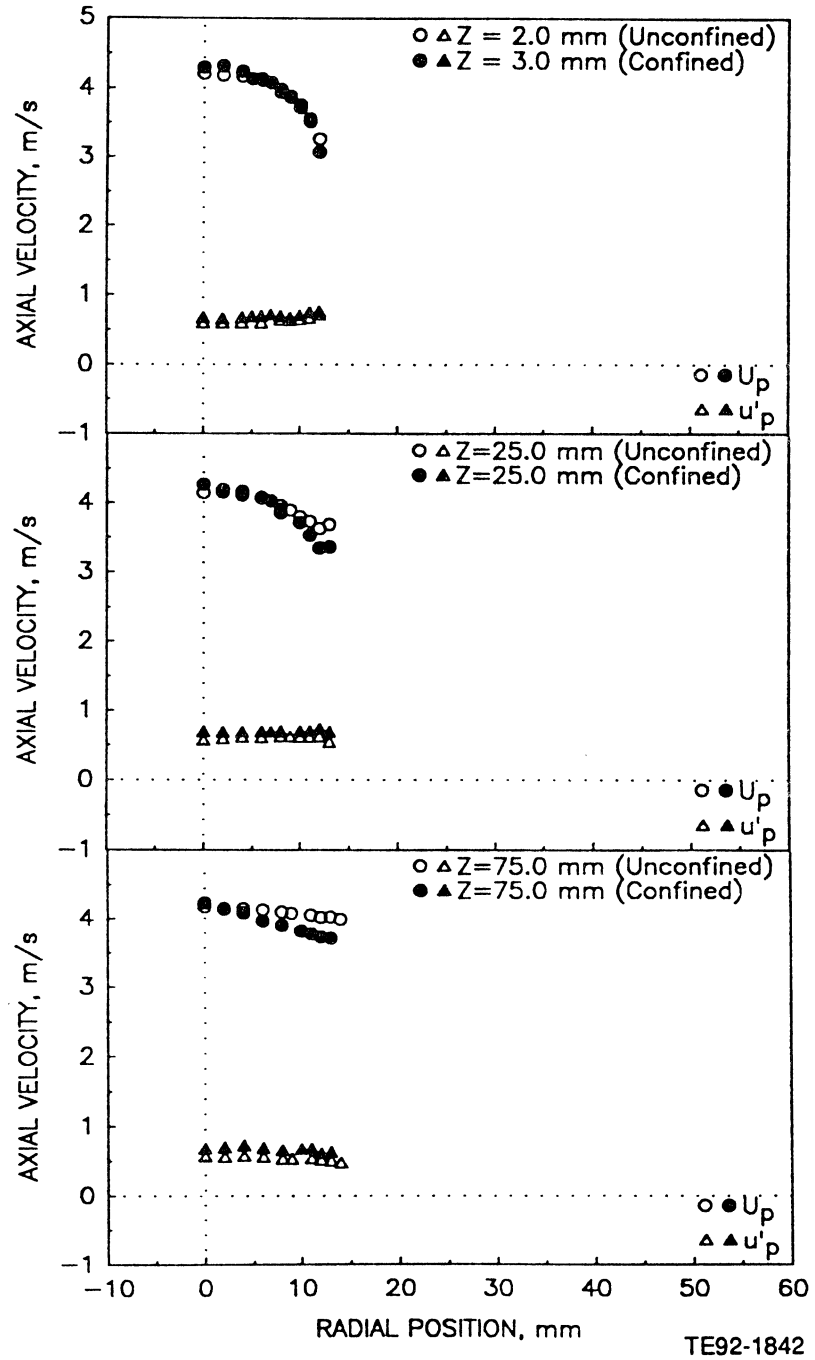


Figure 4.5.12-1. Comparison of particle axial velocities and data rate in confined and unconfined coaxial jets with the central jet laden with 100-110 micron particles at a particle-to-gas mass loading ratio of 0.2 (1 of 2).

b) Data Rate

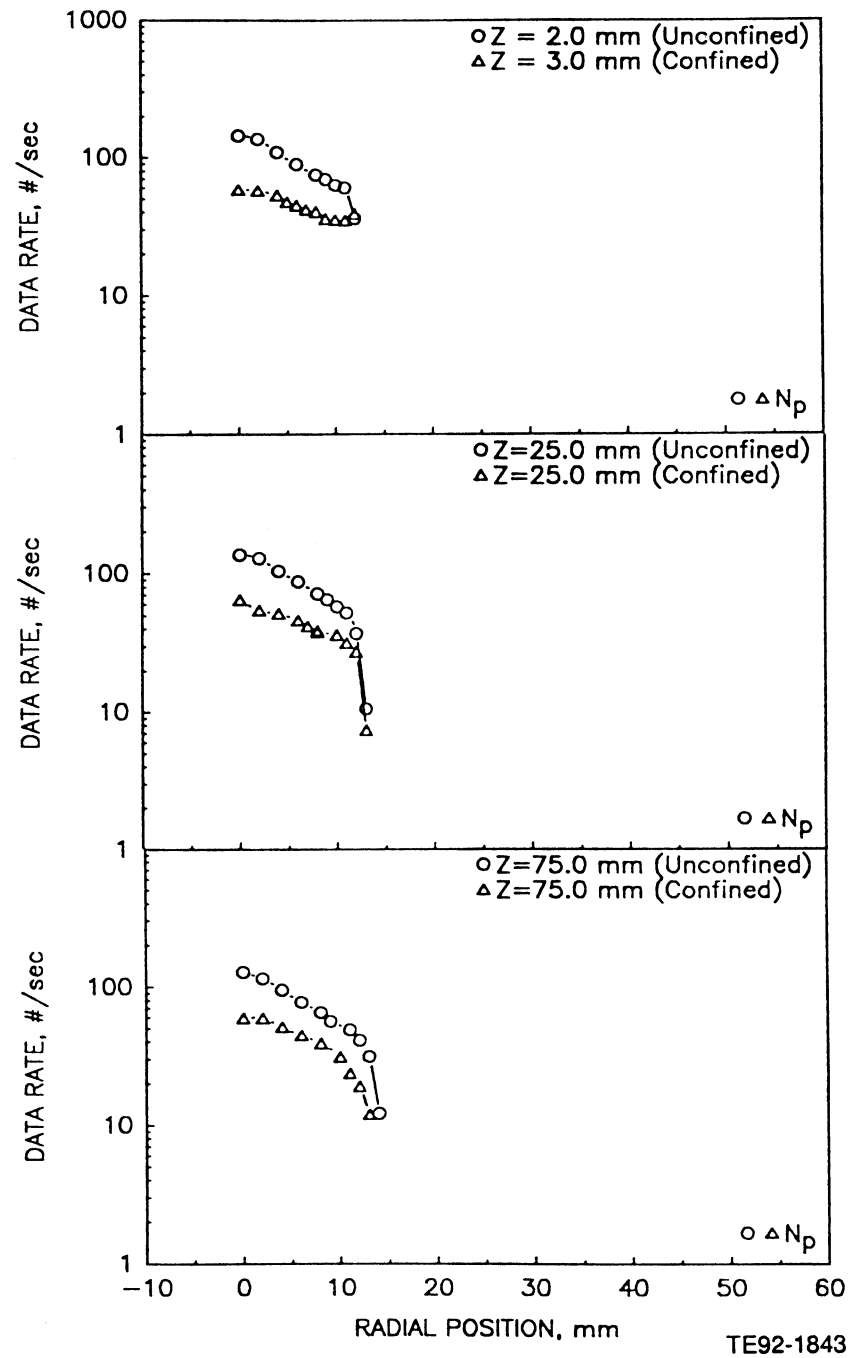


Figure 4.5.12-1. Comparison of particle axial velocities and data rate in confined and unconfined coaxial jets with the central jet laden with 100-110 micron particles at a particle-to-gas mass loading ratio of 0.2 (2 of 2).

4.6 COAXIAL JETS WITH SWIRLING ANNULAR FLOW

Figure 4.6-1 presents the geometry utilized for the studies of coaxial jets with swirling annular flow.

4.6.1 Unconfined Single-Phase Jets – CONF03#3

Figure 4.6.1-1 provides the results for the single-phase study. At the inlet plane, the two jet flows remain distinct. With increasing distance downstream, the axial velocities near the centerline decelerate and begin to reveal recirculation. In addition, the jet flow spreads rapidly. The symmetry of the flows is reasonable.

Evidence for the rapid spreading is provided in Figure 4.6.1-1 (b), where strong velocities away from centerline persist over the flow domain.

Although quite strong initially, the swirl decays rapidly (Figure 4.6.1-1 [c]).

The cross correlations (Figure 4.6.1-1 [d and e]) between the velocity component fluctuations reveal reasonable behavior, although they do show some noise which is attributed to the complexity of the flow.

4.6.2 Effect of Swirl on Coflowing Jets

To illustrate the impact that swirling the annular air flow has on the structure of the coflowing jets, Figure 4.6.2-1 presents a comparison of the axial velocity profiles from the nonswirling (section 4.6.1) and swirling (section 4.6.1) cases. The swirl has a strong effect even at an axial distance of 5.0 mm. The flow spreads radially much quicker in the case of swirl, as expected.

4.6.3 Unconfined Swirling Jets in the Presence of 100-110 Micron Beads – CONF09#4

Figure 4.6.3-1 provides results for the gas phase in the presence of 100-110 micron glass beads in a bead-to-gas loading ratio of 0.925. The results appear similar to those obtained for the single-phase case (section 4.6.1).

4.6.4 100-110 Micron Glass Beads in the Unconfined Swirling Jets – CONF09#3

Figure 4.6.4-1 provides the characteristics of the glass beads in the swirling jets. Unlike the gas phase characteristics, the bead results (Figure 4.6.4-1 [a and e]) exhibit excellent symmetry, suggesting that the swirl vane is the primary cause of the asymmetry.

Figure 4.6.4-1 (b and c) reveals that the swirl imparts significant radial and azimuthal momentum to the beads.

4.6.5 Effect of Swirl on 100-110 Micron Glass Beads in Unconfined Flow

To better illustrate the effect of swirl on the behavior of the beads, Figure 4.6.5-1 presents a comparison of the bead characteristics in the free jet (section 4.2.3) and in the free jet with swirling annular air.

The axial velocity results reveal strong similarities at the inlet plane. However, as the flow progresses downstream, the beads are decelerated by the gas phase in the swirling case. In addition, the beads spread radially (Figure 4.6.5-1 [b]).

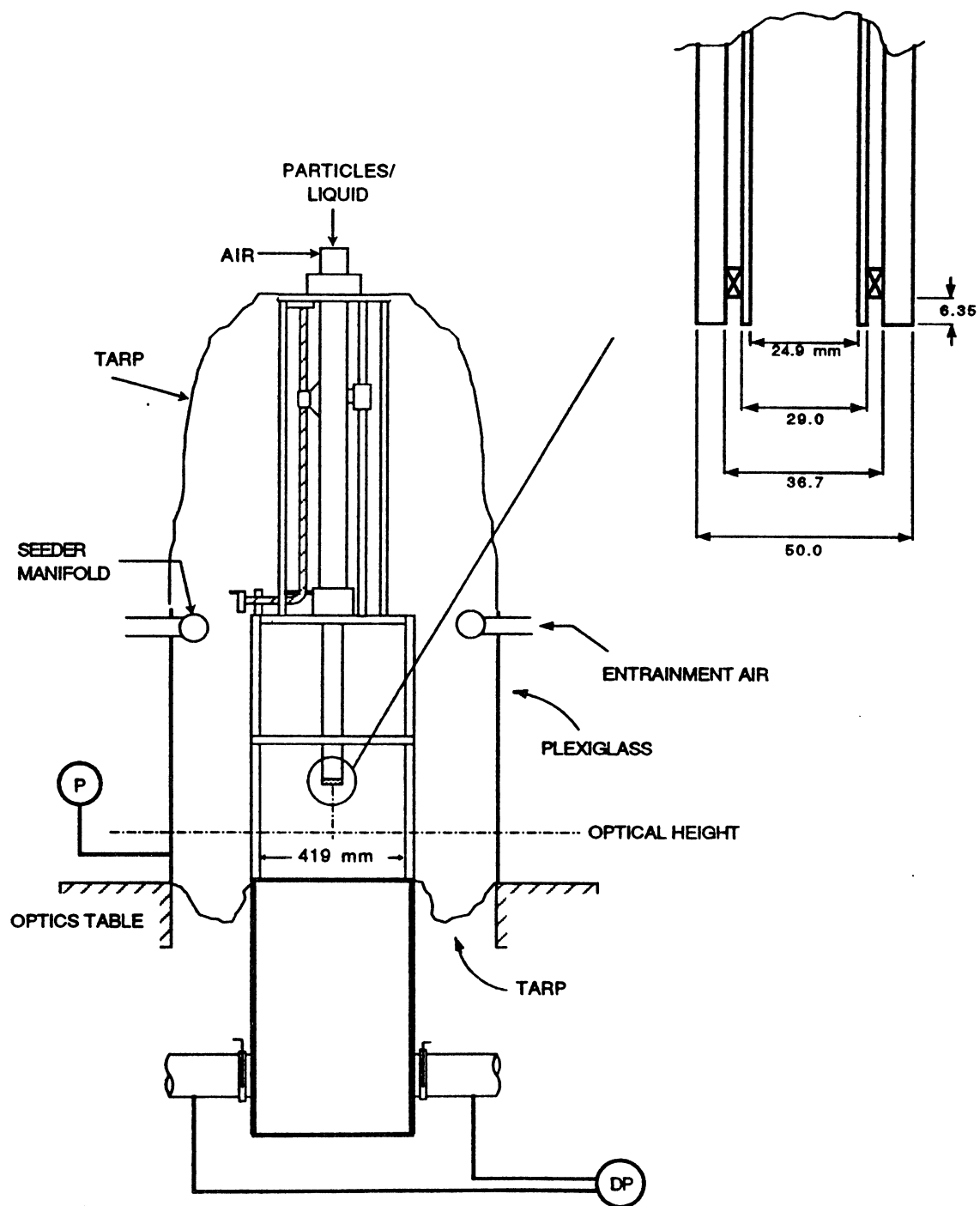
4.6.6 100-110 Micron Glass Beads in the Confined Swirling Jet – CONF12#4

The geometry utilized for the confined jet with swirling annular air flow is shown in Figure 4.6.6-1. Figure 4.6.6-2 provides the results for the glass beads.

The redundant measurements (Figure 4.6.6-2 [a and e]) reveal reasonable symmetry. Overall, the behavior is similar to that observed in the unconfined case (section 4.6.4). However, the radial and azimuthal velocities at the centerline are not zero and the results suggest that less swirl is imparted to the beads in the confined case.

4.6.7 Effect of Swirl on Glass Beads in the Confined Flow

To illustrate the effect of swirl on the beads in the confined flow, Figure 4.6.7-1 provides results which compare the measurements made with and without swirl. The comparison is nearly identical to that made for the unconfined flow (section 4.6.5).



TE92-1844

Figure 4.6-1. Geometry utilized for unconfined round jet with swirling annular flow.

a) Mean and Fluctuating Axial Velocities

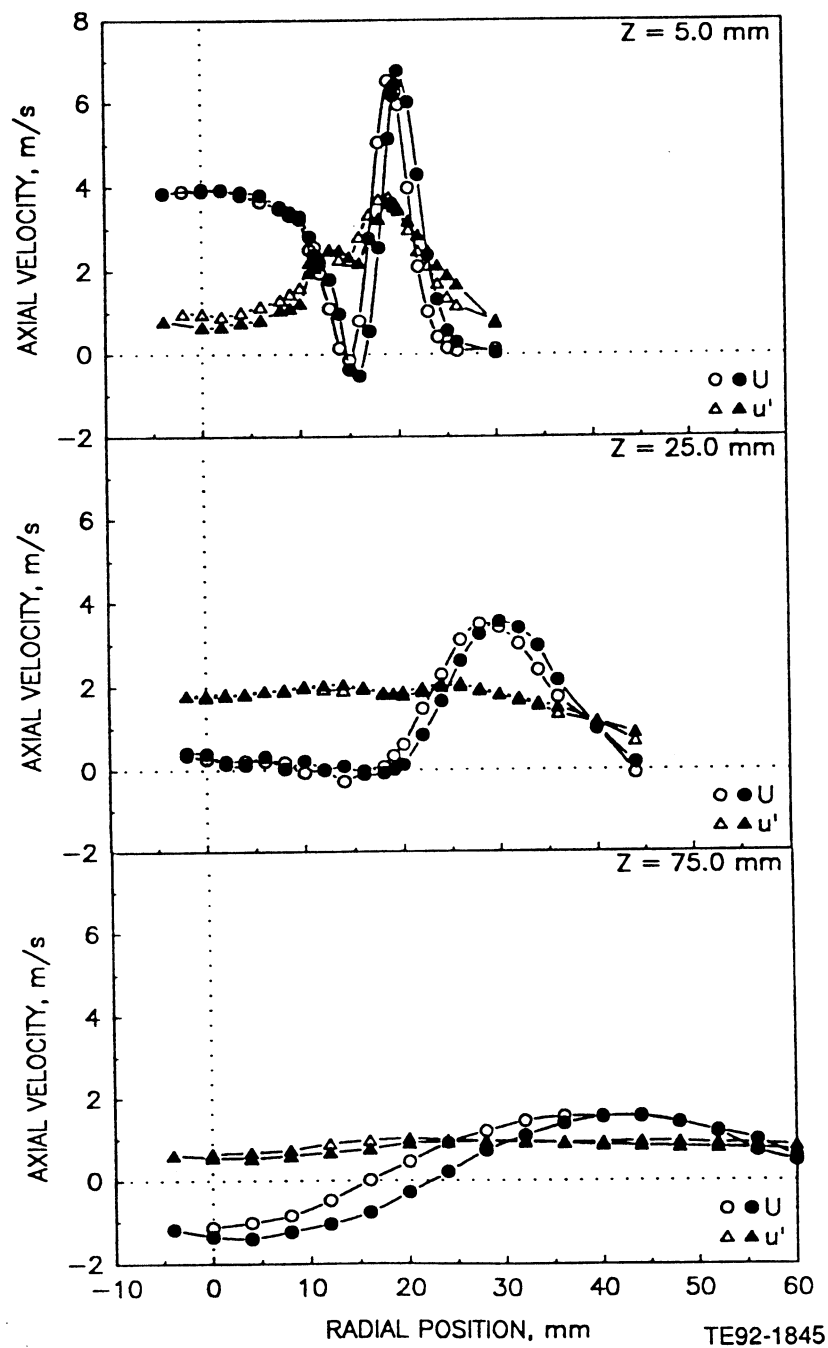


Figure 4.6.1-1. Radial profiles of gas phase statistics in the unconfined single-phase coaxial jets with swirling annular air (1 of 5).

b) Mean and Fluctuating Radial Velocities

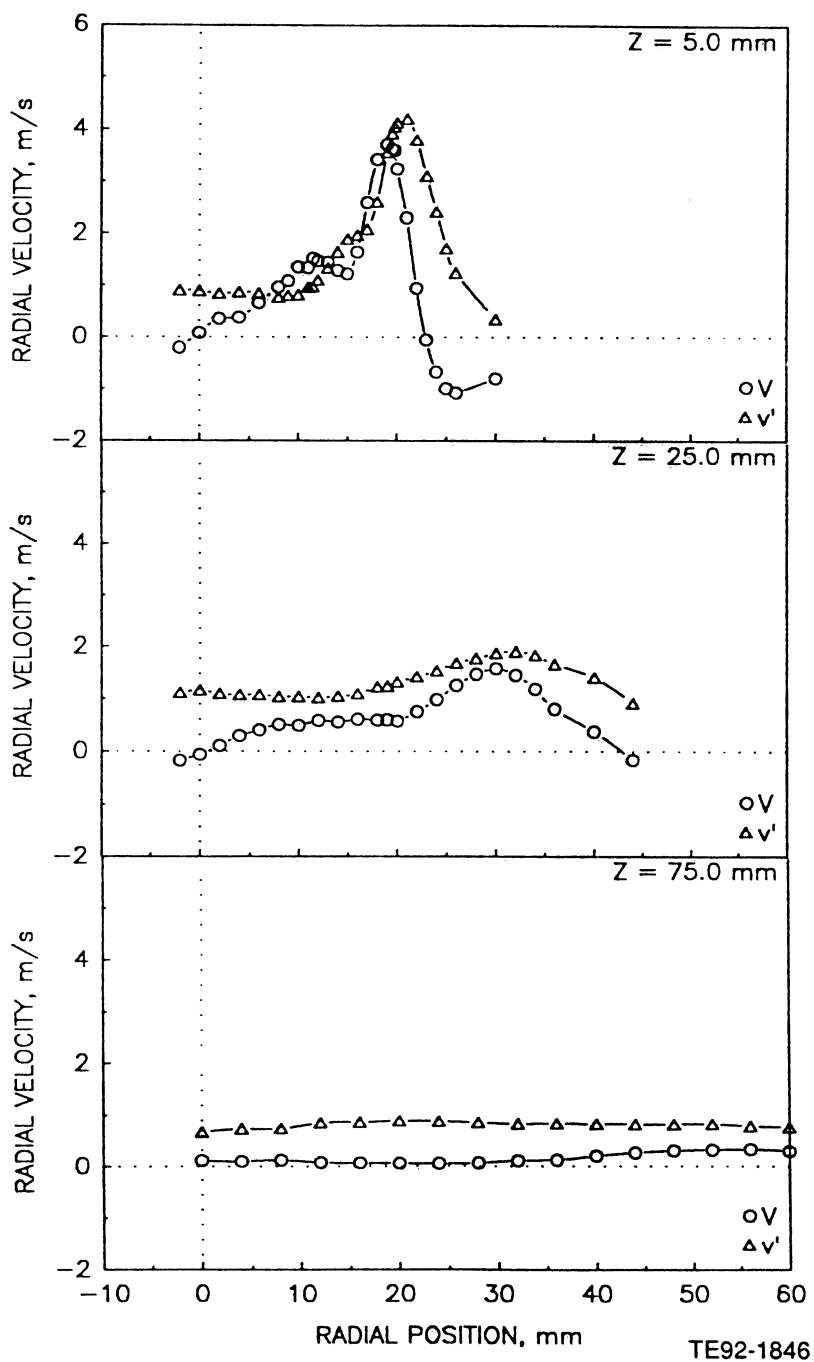
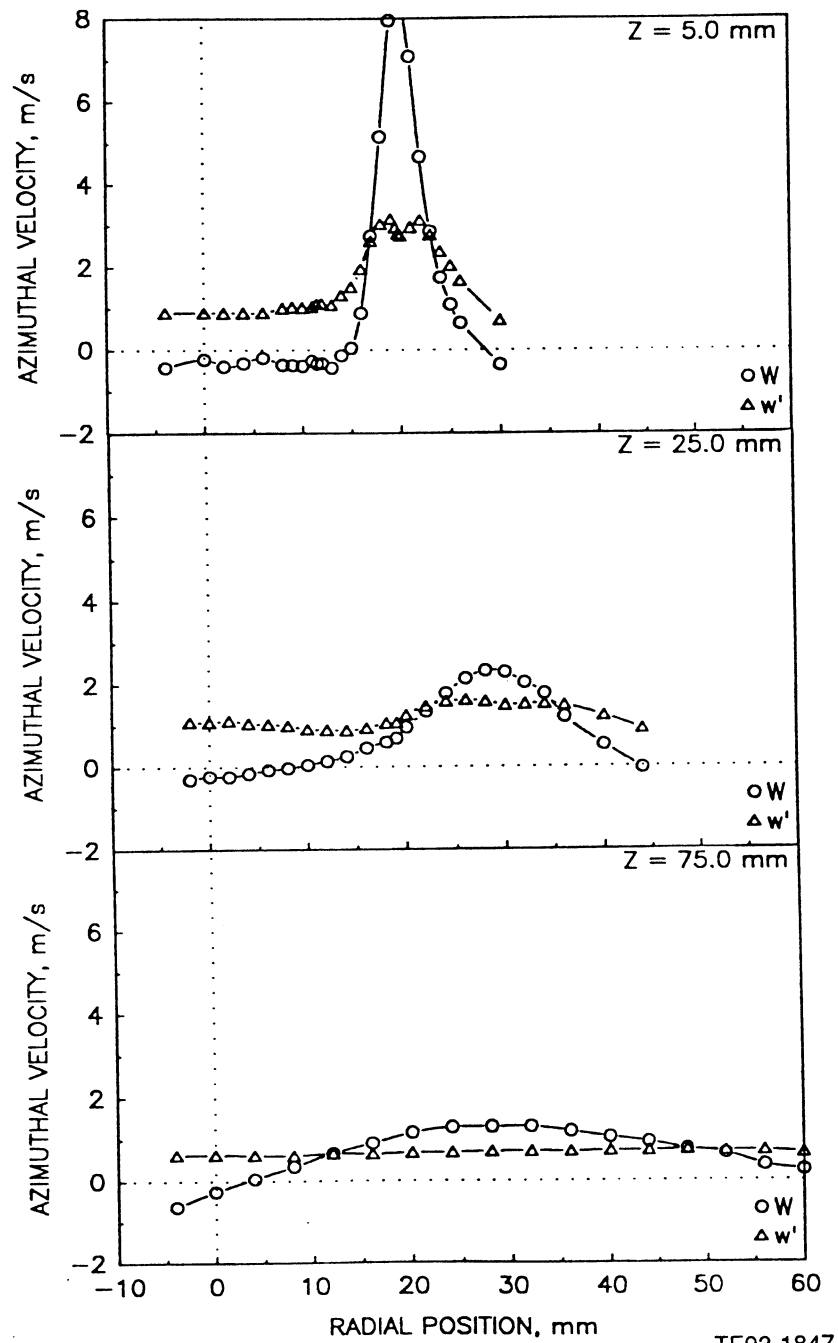


Figure 4.6.1-1. Radial profiles of gas phase statistics in the unconfined single-phase coaxial jets with swirling annular air (2 of 5).

c) Mean and Fluctuating Azimuthal Velocities



TE92-1847

Figure 4.6.1-1. Radial profiles of gas phase statistics in the unconfined single-phase coaxial jets with swirling annular air (3 of 5).

d) Shear Stress Based on Axial and Radial Velocities

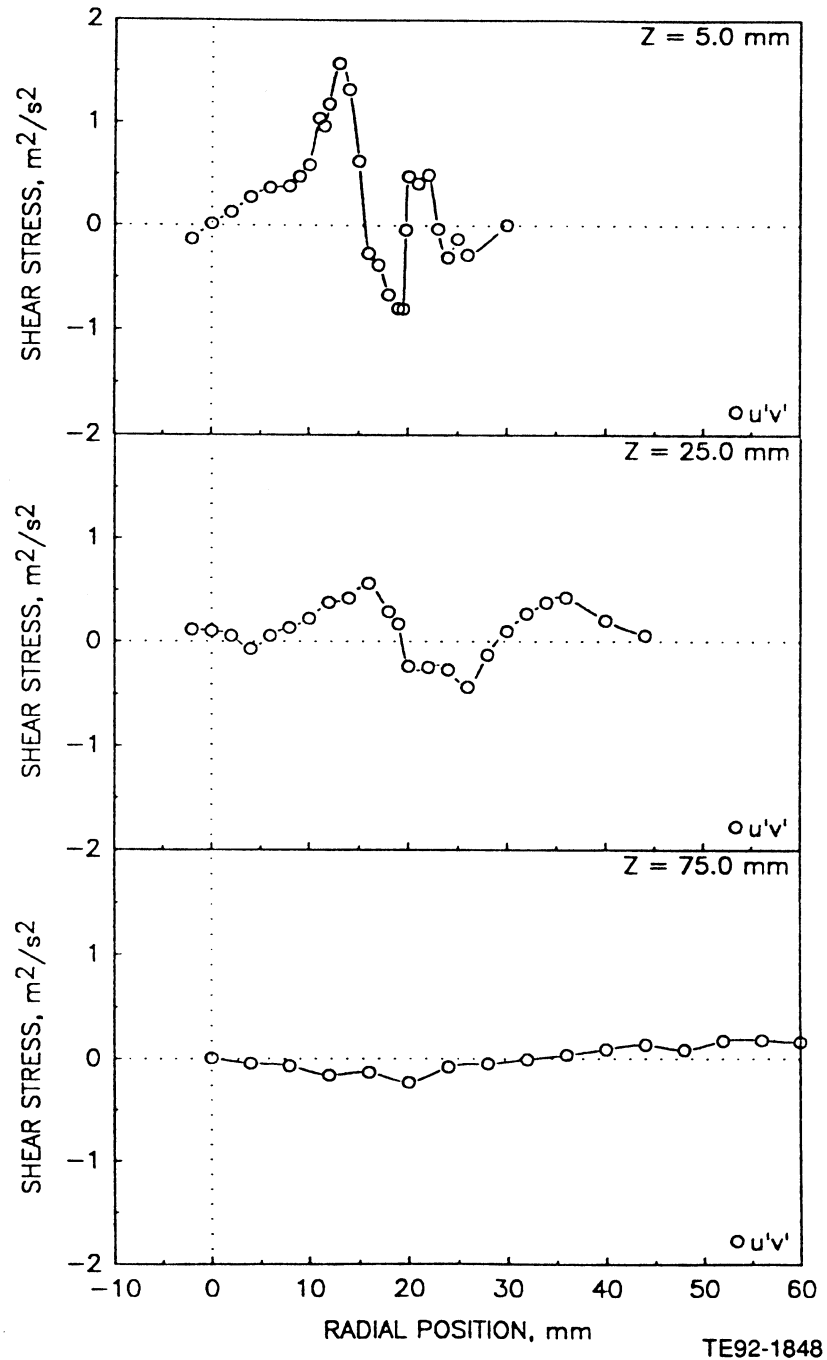


Figure 4.6.1-1. Radial profiles of gas phase statistics in the unconfined single-phase coaxial jets with swirling annular air (4 of 5).

e) Shear Stress Based on Axial and Azimuthal Velocities

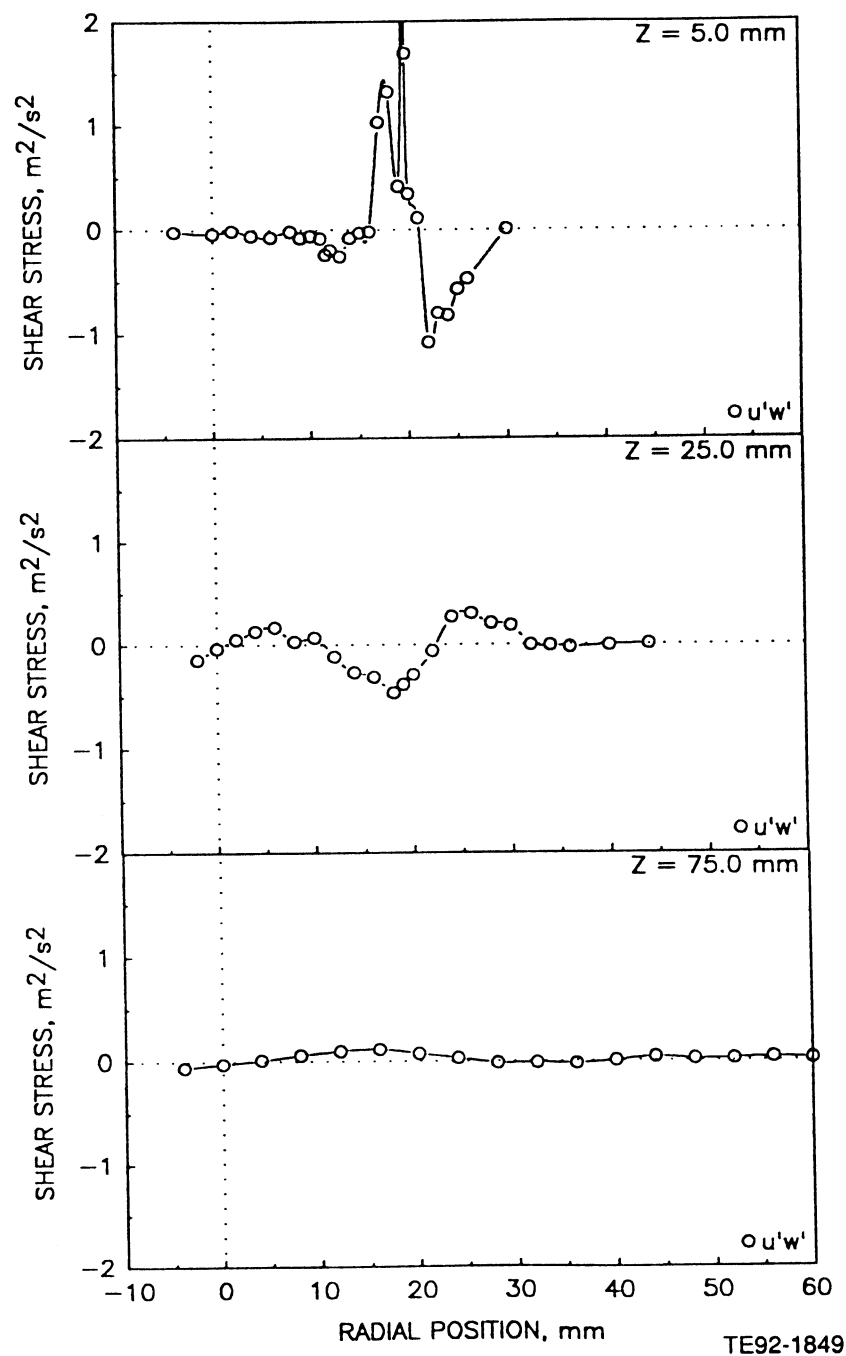
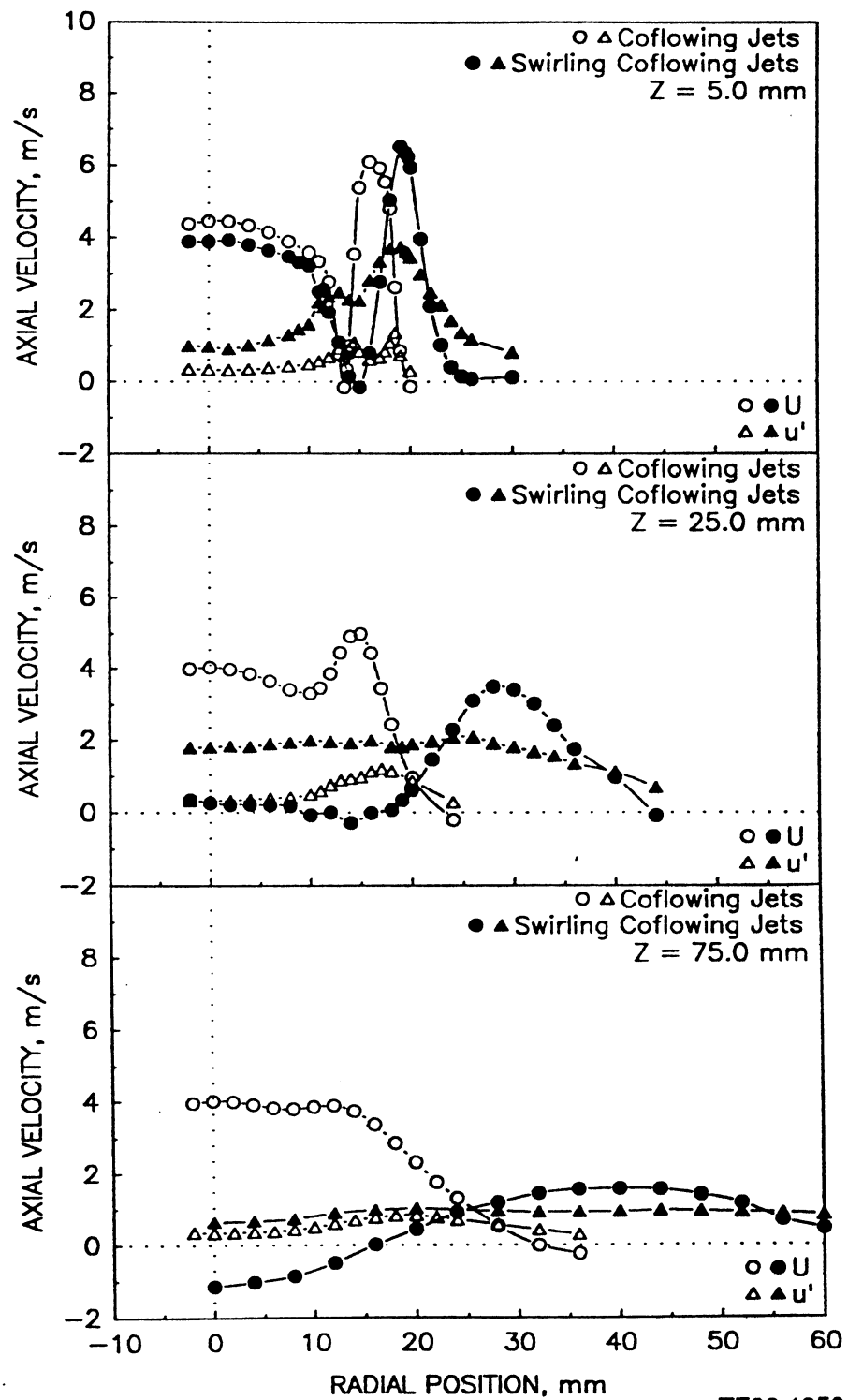


Figure 4.6.1-1. Radial profiles of gas phase statistics in the unconfined single-phase coaxial jets with swirling annular air (5 of 5).



TE92-1850

Figure 4.6.2-1. Comparison of mean and fluctuating axial velocities in unconfined coflowing jets with and without swirling annular air.

a) Mean and Fluctuating Axial Velocities

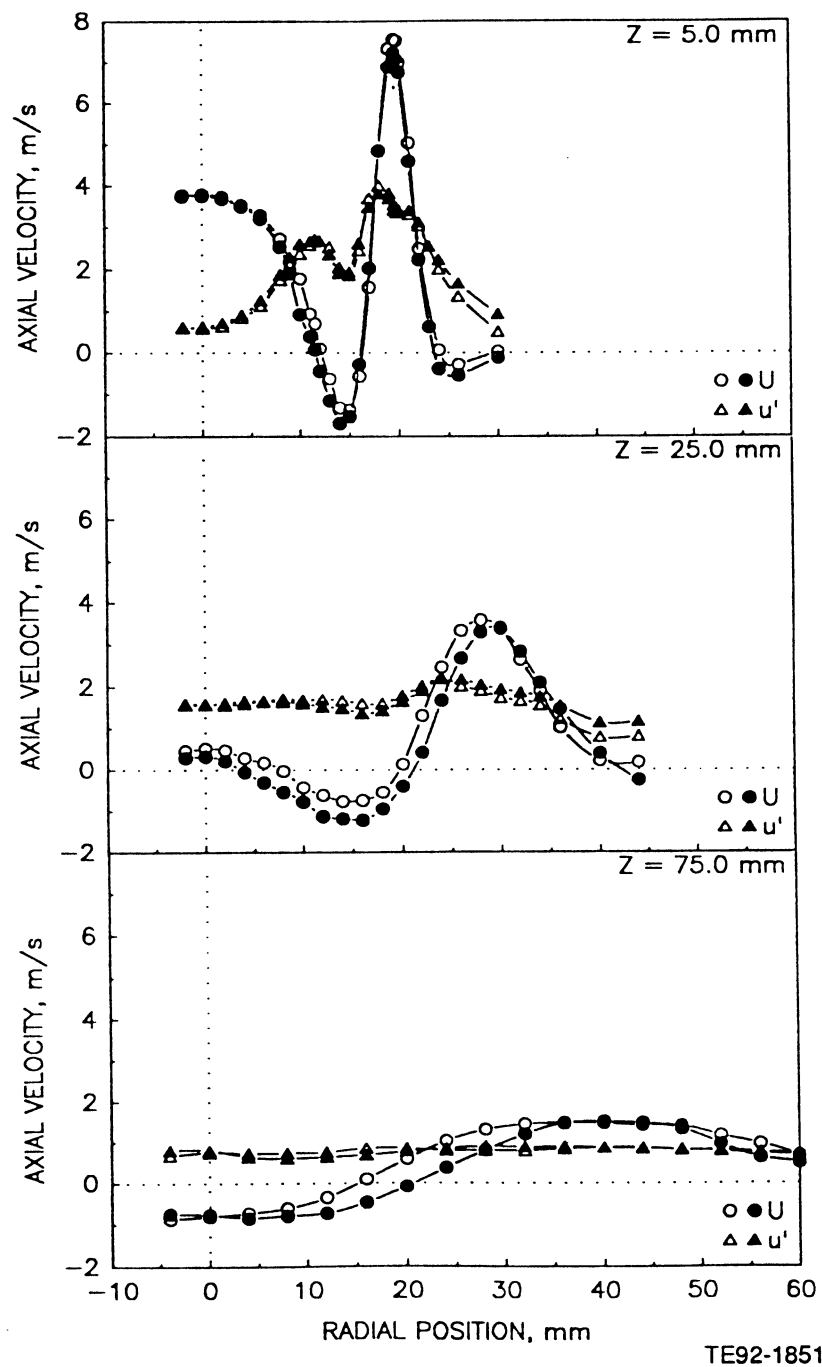


Figure 4.6.3-1. Radial profiles of gas phase velocities in the unconfined jet with swirling annular air flow with the central jet laden with 100-110 micron particles in a particle-to-gas mass loading ratio of 0.2 (1 of 5).

b) Mean and Fluctuating Radial Velocities

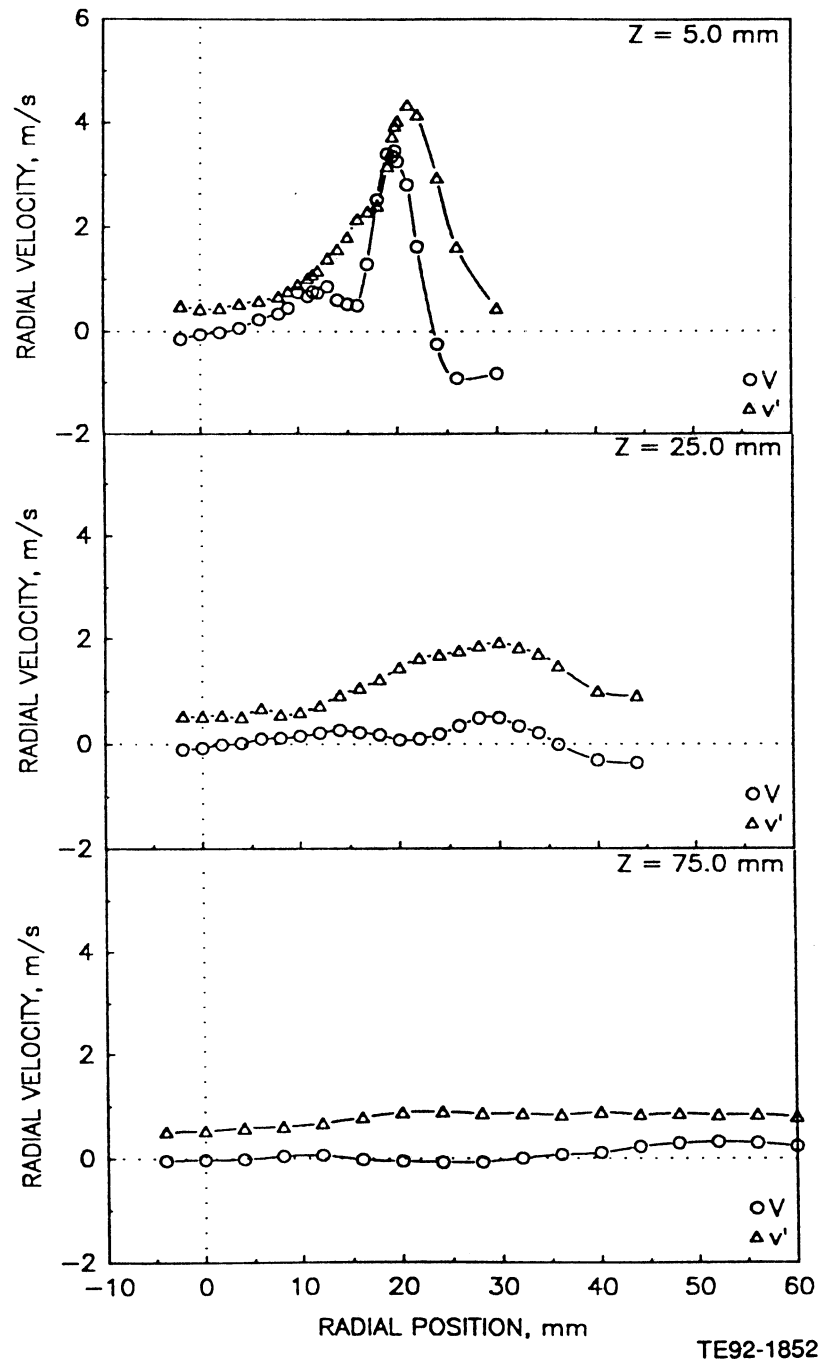


Figure 4.6.3-1. Radial profiles of gas phase velocities in the unconfined jet with swirling annular air flow with the central jet laden with 100-110 micron particles in a particle-to-gas mass loading ratio of 0.2 (2 of 5).

c) Mean and Fluctuating Azimuthal Velocities

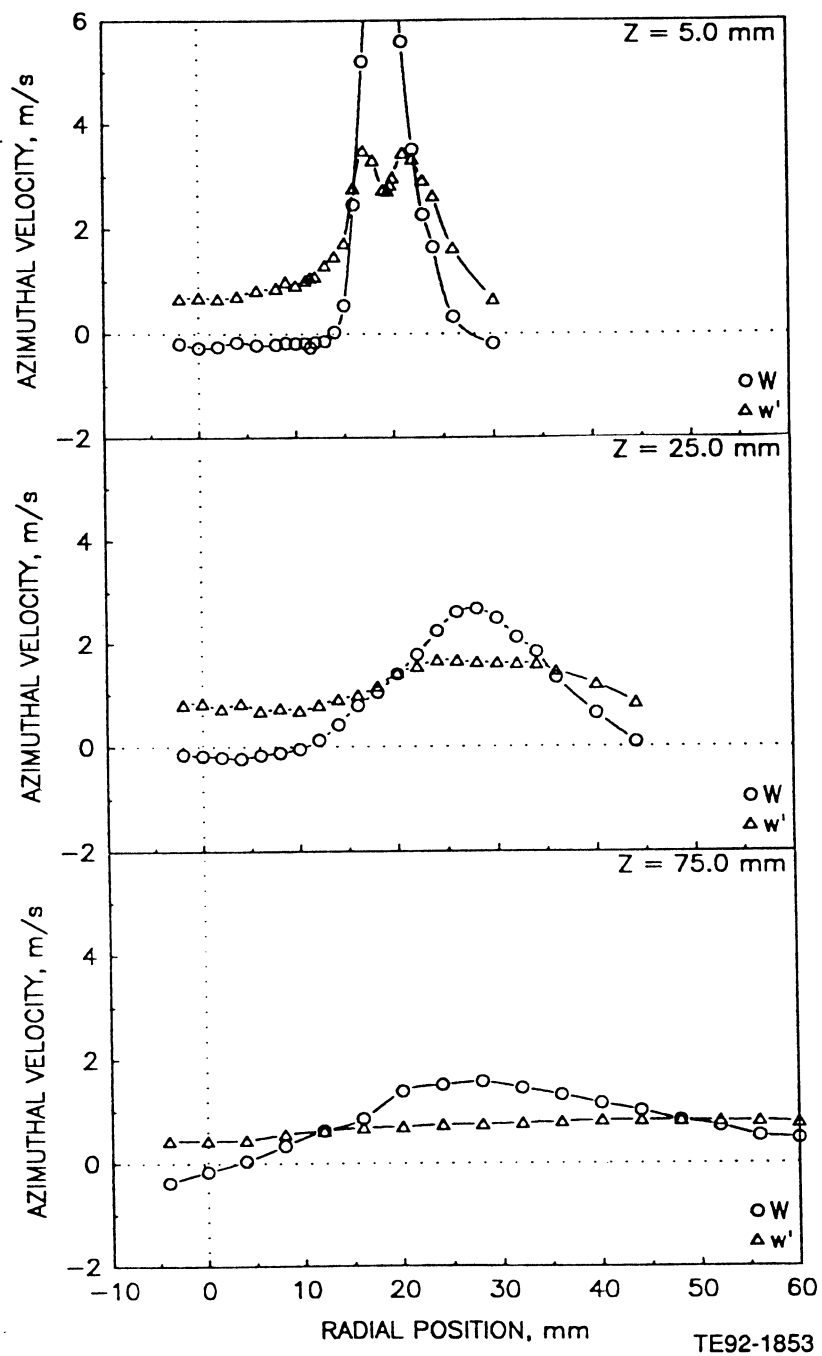


Figure 4.6.3-1. Radial profiles of gas phase velocities in the unconfined jet with swirling annular air flow with the central jet laden with 100-110 micron particles in a particle-to-gas mass loading ratio of 0.2 (3 of 5).

d) Shear Stress Based on Axial and Radial Velocities

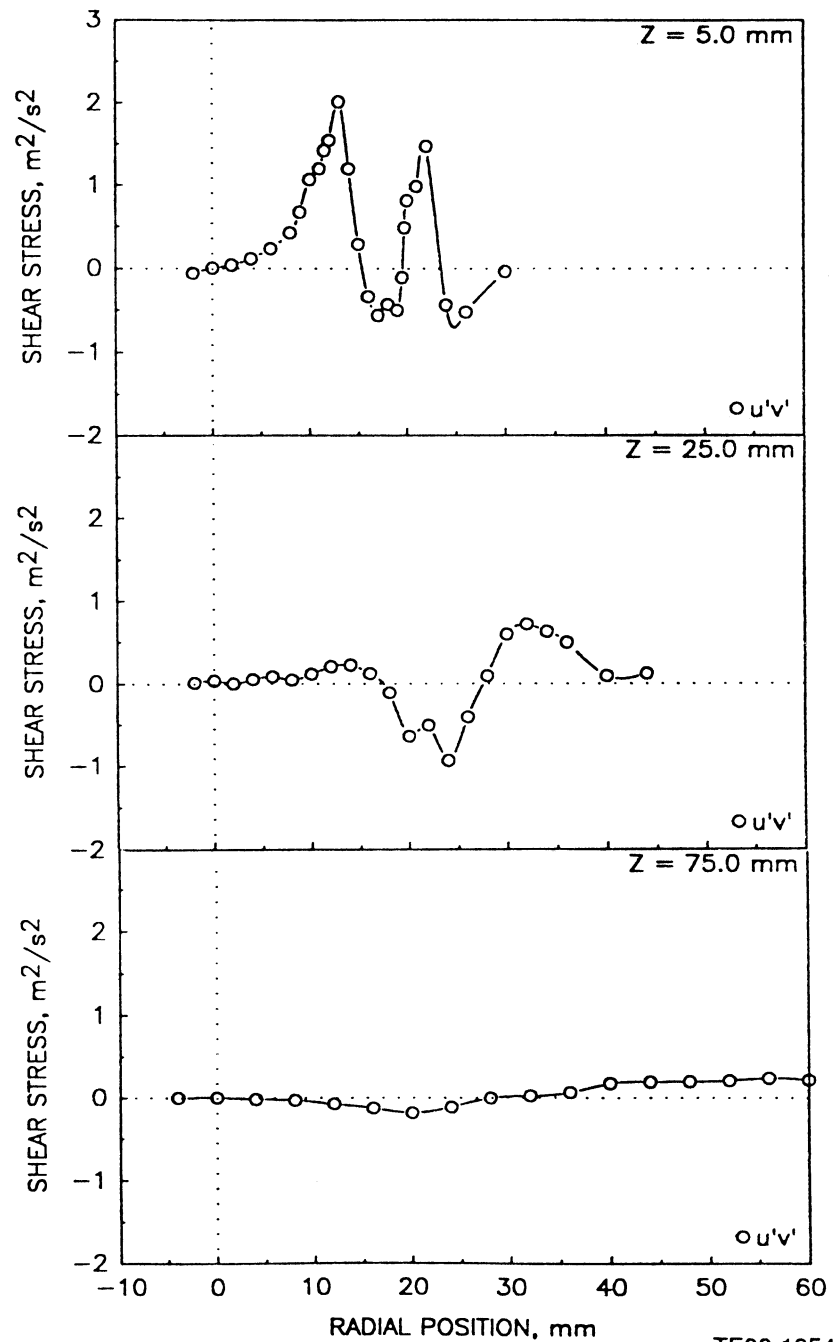


Figure 4.6.3-1. Radial profiles of gas phase velocities in the unconfined jet with swirling annular air flow with the central jet laden with 100-110 micron particles in a particle-to-gas mass loading ratio of 0.2 (4 of 5).

e) Shear Stress Based on Axial and Azimuthal Velocities

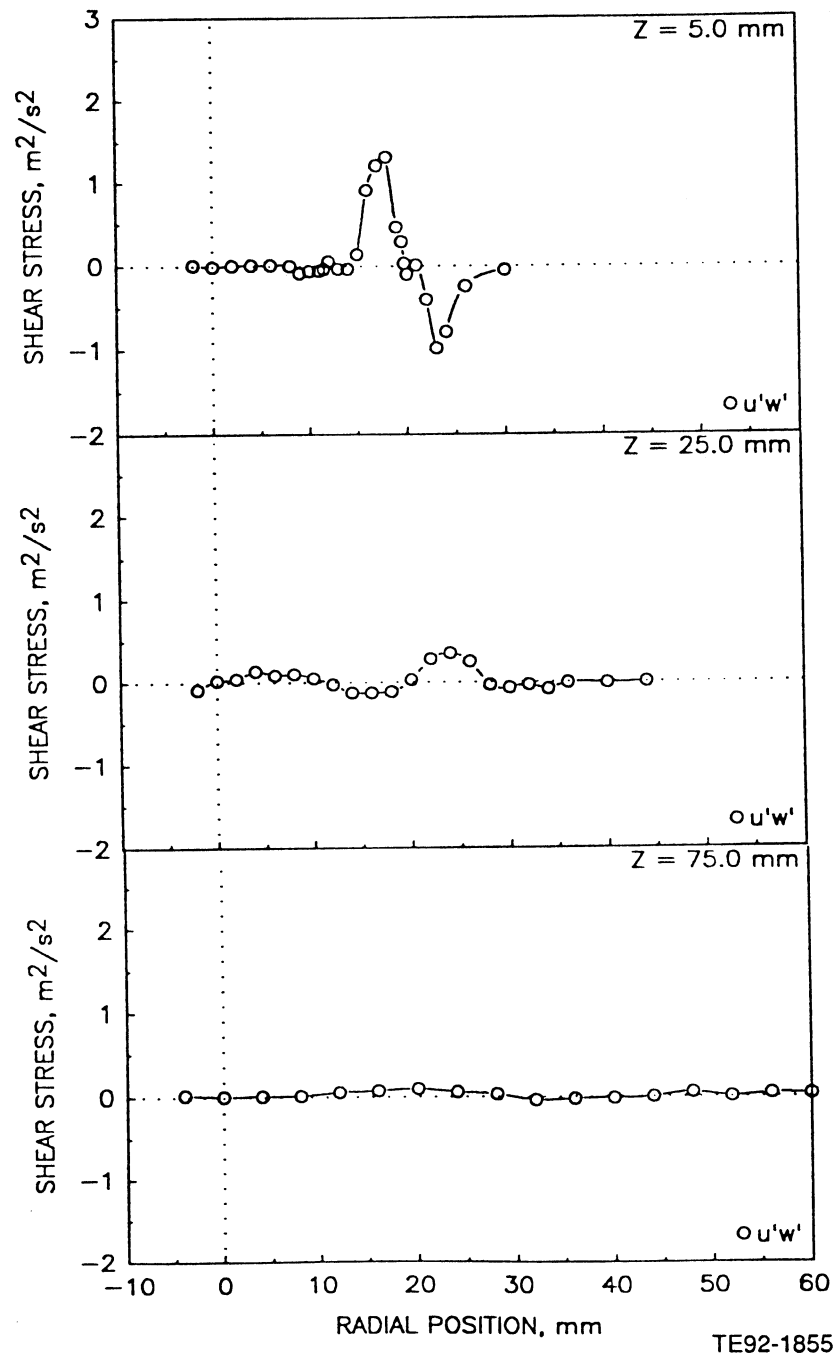
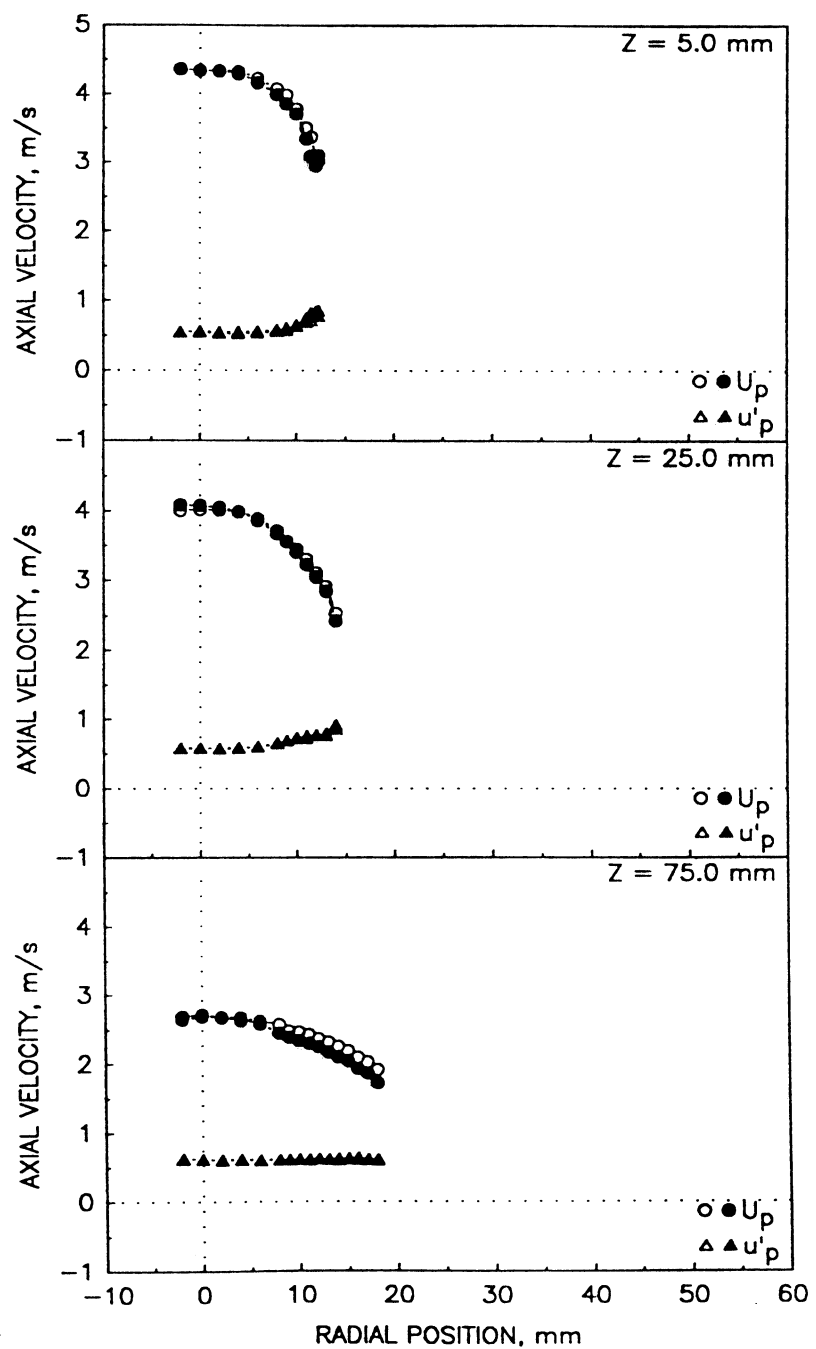


Figure 4.6.3-1. Radial profiles of gas phase velocities in the unconfined jet with swirling annular air flow with the central jet laden with 100-110 micron particles in a particle-to-gas mass loading ratio of 0.2 (5 of 5).

a) Mean and Fluctuating Axial Velocities



TE92-1856

Figure 4.6.4-1. Radial profiles of particle velocities in the unconfined jet with swirling annular air flow with the central jet laden with 100-110 micron particles in a particle-to-gas mass loading ratio of 0.2 (1 of 5).

b) Mean and Fluctuating Radial Velocities

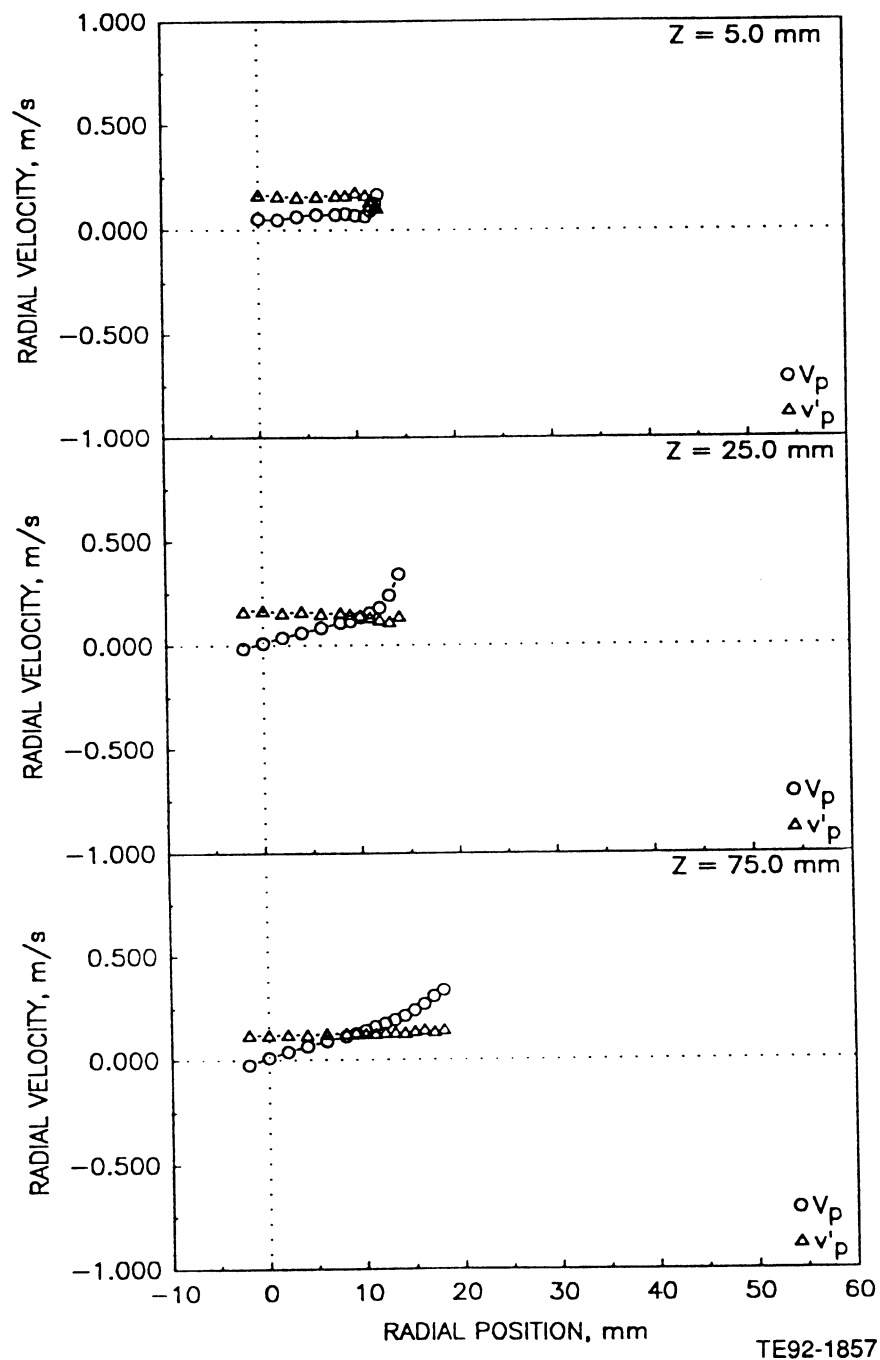


Figure 4.6.4-1. Radial profiles of particle velocities in the unconfined jet with swirling annular air flow with the central jet laden with 100-110 micron particles in a particle-to-gas mass loading ratio of 0.2 (2 of 5).

c) Mean and Fluctuating Azimuthal Velocities

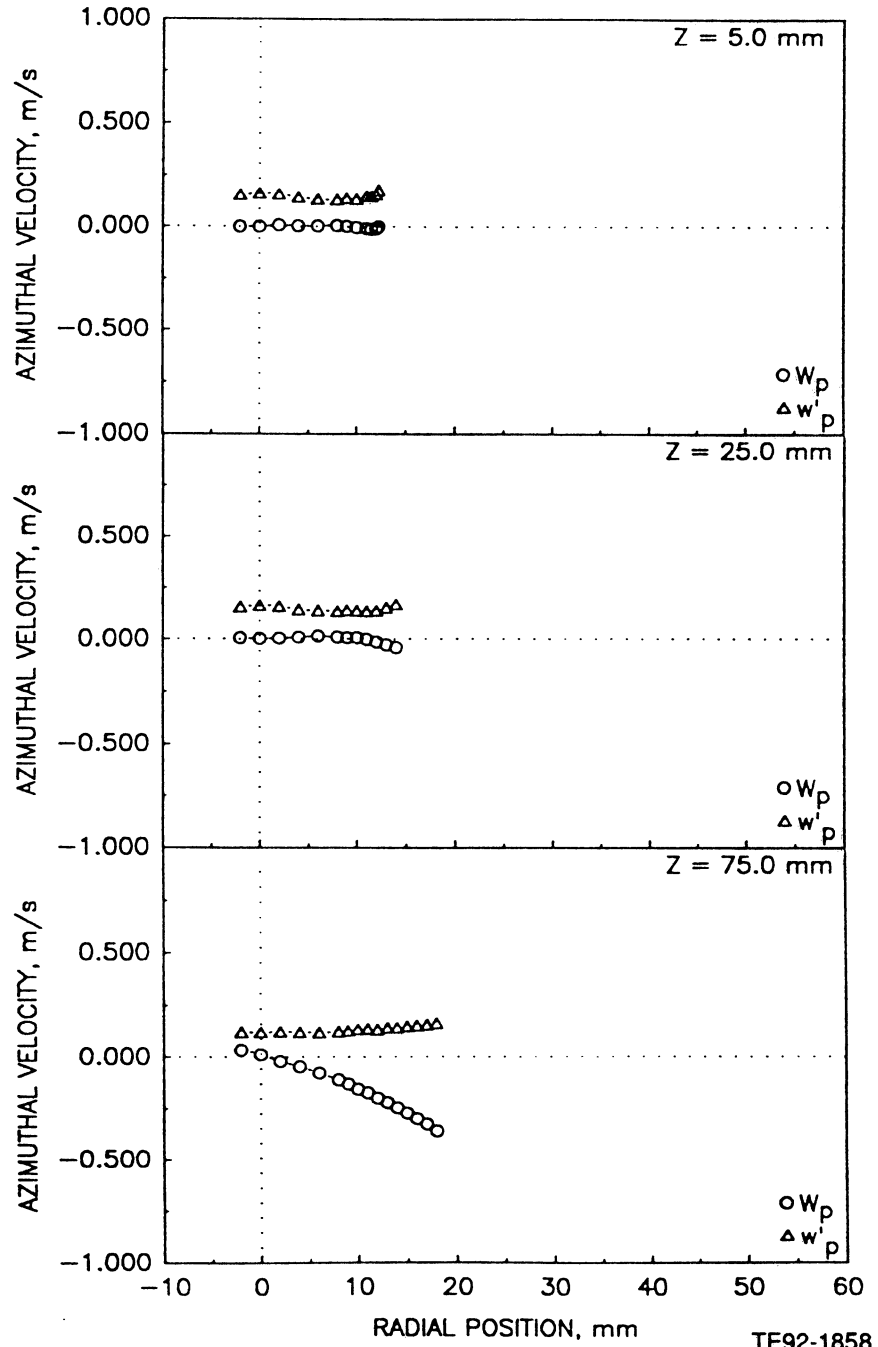


Figure 4.6.4-1. Radial profiles of particle velocities in the unconfined jet with swirling annular air flow with the central jet laden with 100-110 micron particles in a particle-to-gas mass loading ratio of 0.2 (3 of 5).

d) Shear Stress Based on Axial and Radial Velocities

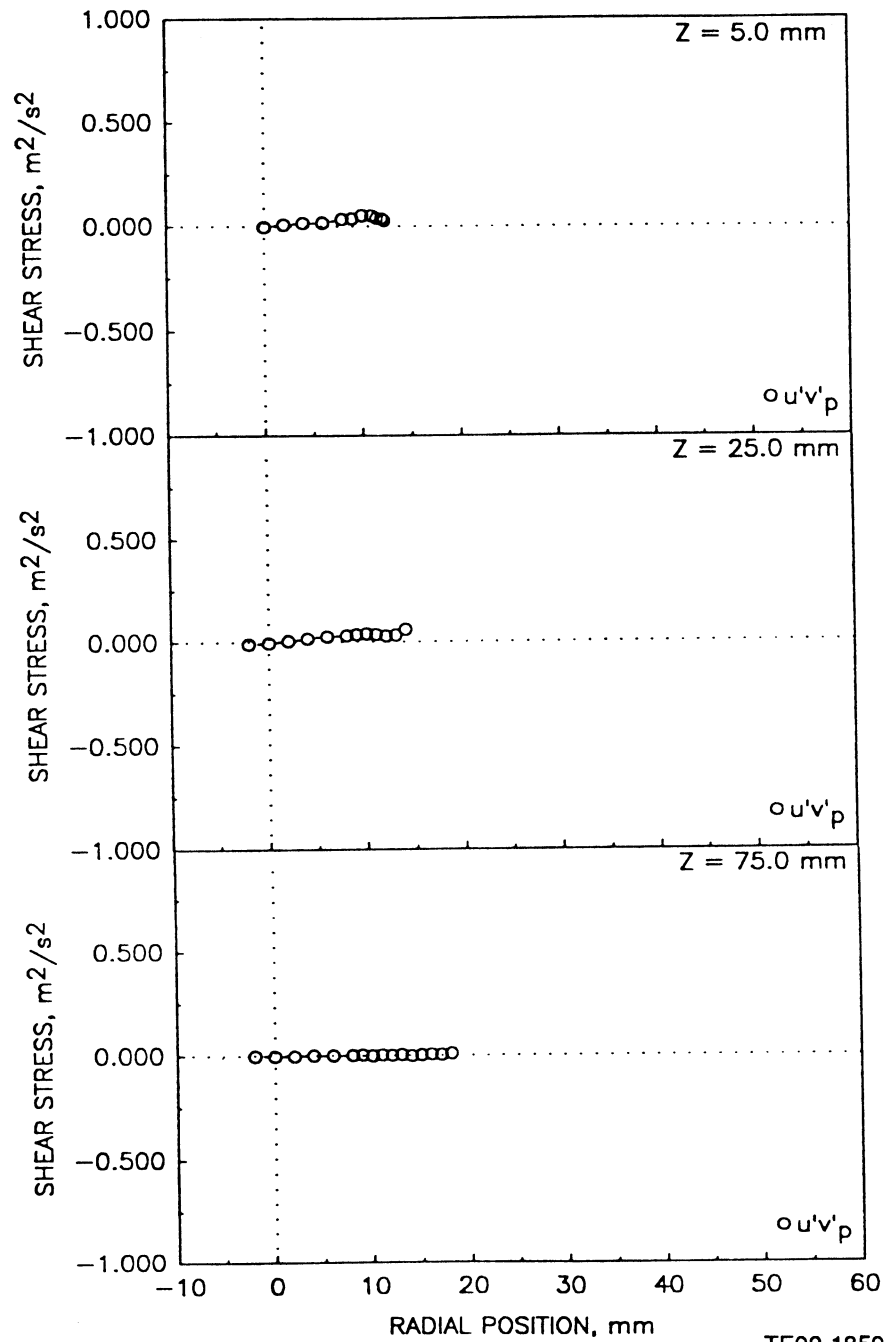


Figure 4.6.4-1. Radial profiles of particle velocities in the unconfined jet with swirling annular air flow with the central jet laden with 100-110 micron particles in a particle-to-gas mass loading ratio of 0.2 (4 of 5).

e) Particle Data Rate

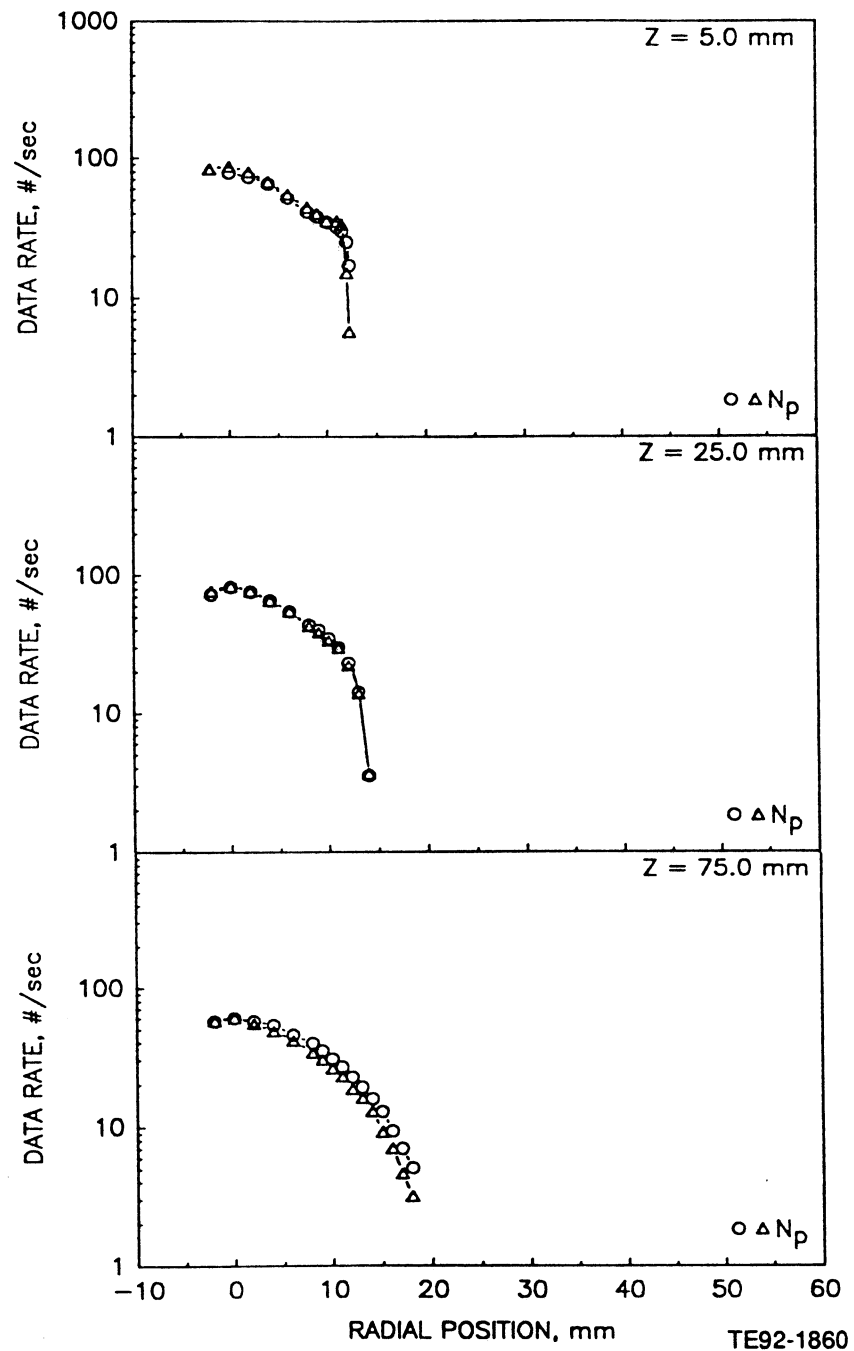


Figure 4.6.4-1. Radial profiles of particle velocities in the unconfined jet with swirling annular air flow with the central jet laden with 100-110 micron particles in a particle-to-gas mass loading ratio of 0.2 (5 of 5).

a) Mean and Fluctuating Axial Velocity

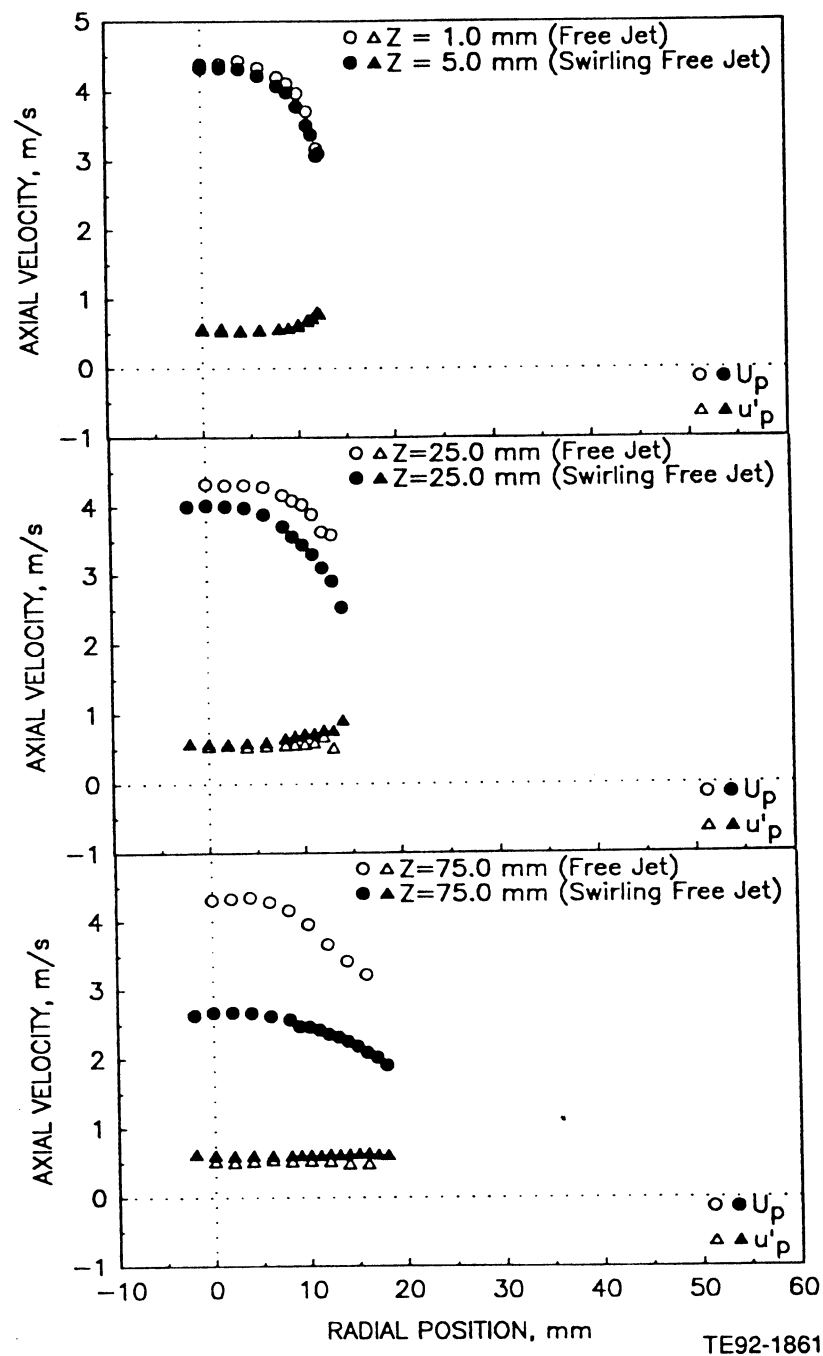


Figure 4.6.5-1. Comparison of particle velocities and data rate in unconfined flows with the central jet laden with 100-110 micron particles at a particle-to-gas mass loading ratio of 0.2: free jet versus swirling annular coflow (1 of 2).

b) Particle Data Rate

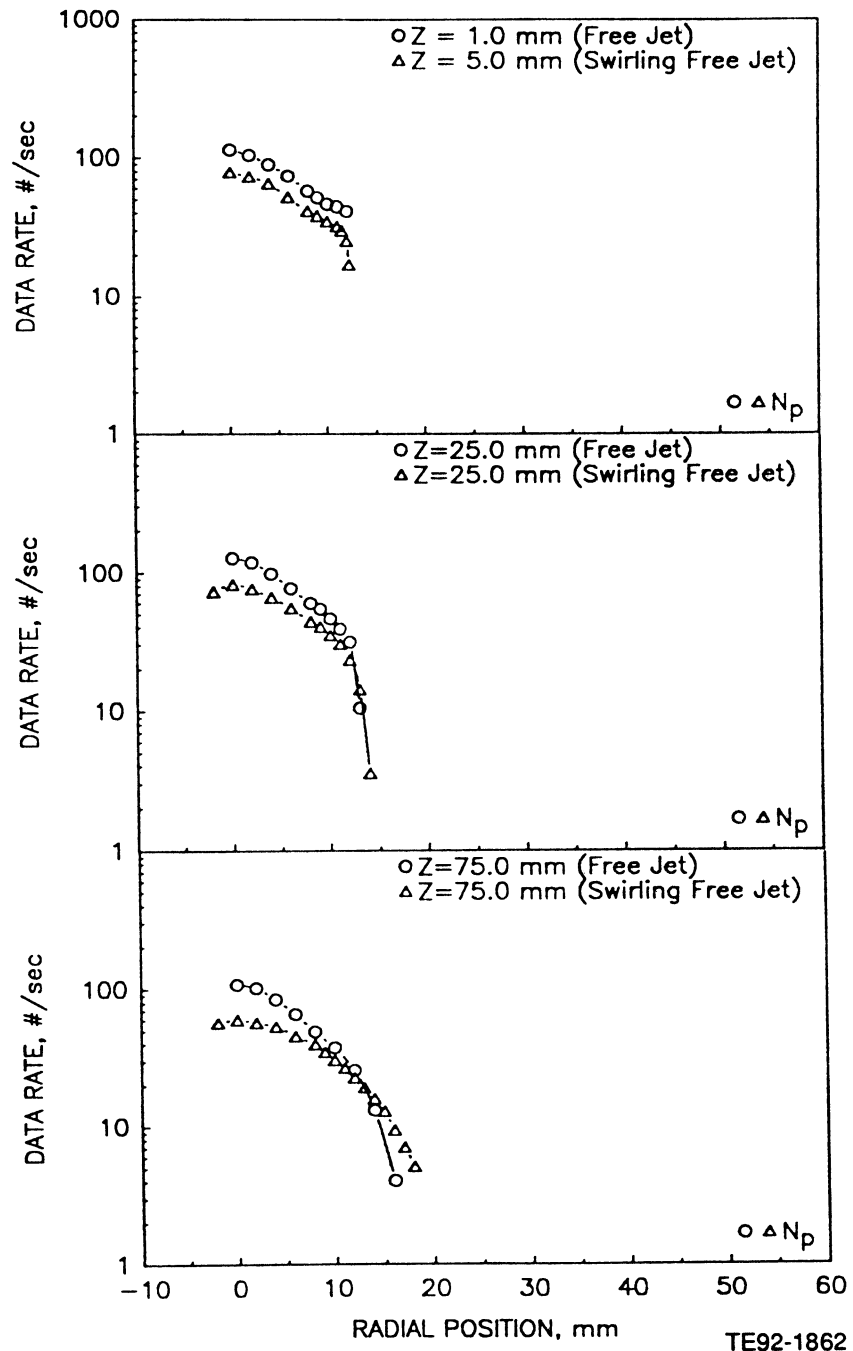
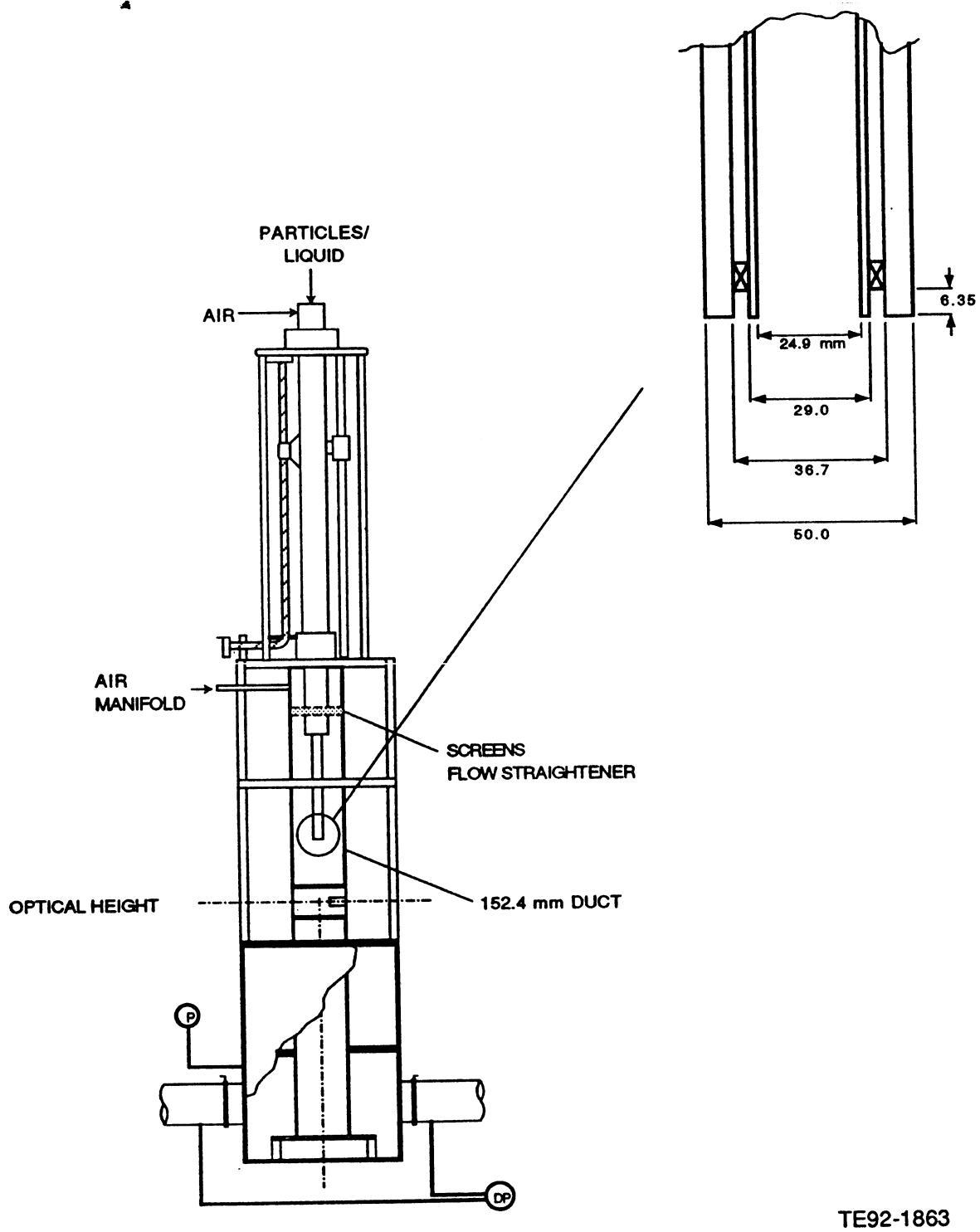


Figure 4.6.5-1. Comparison of particle velocities and data rate in unconfined flows with the central jet laden with 100-110 micron particles at a particle-to-gas mass loading ratio of 0.2: free jet versus swirling annular coflow (2 of 2).



TE92-1863

Figure 4.6.6-1. Geometry utilized for confined round jet with swirling annular air.

a) Mean and Fluctuating Axial Velocities

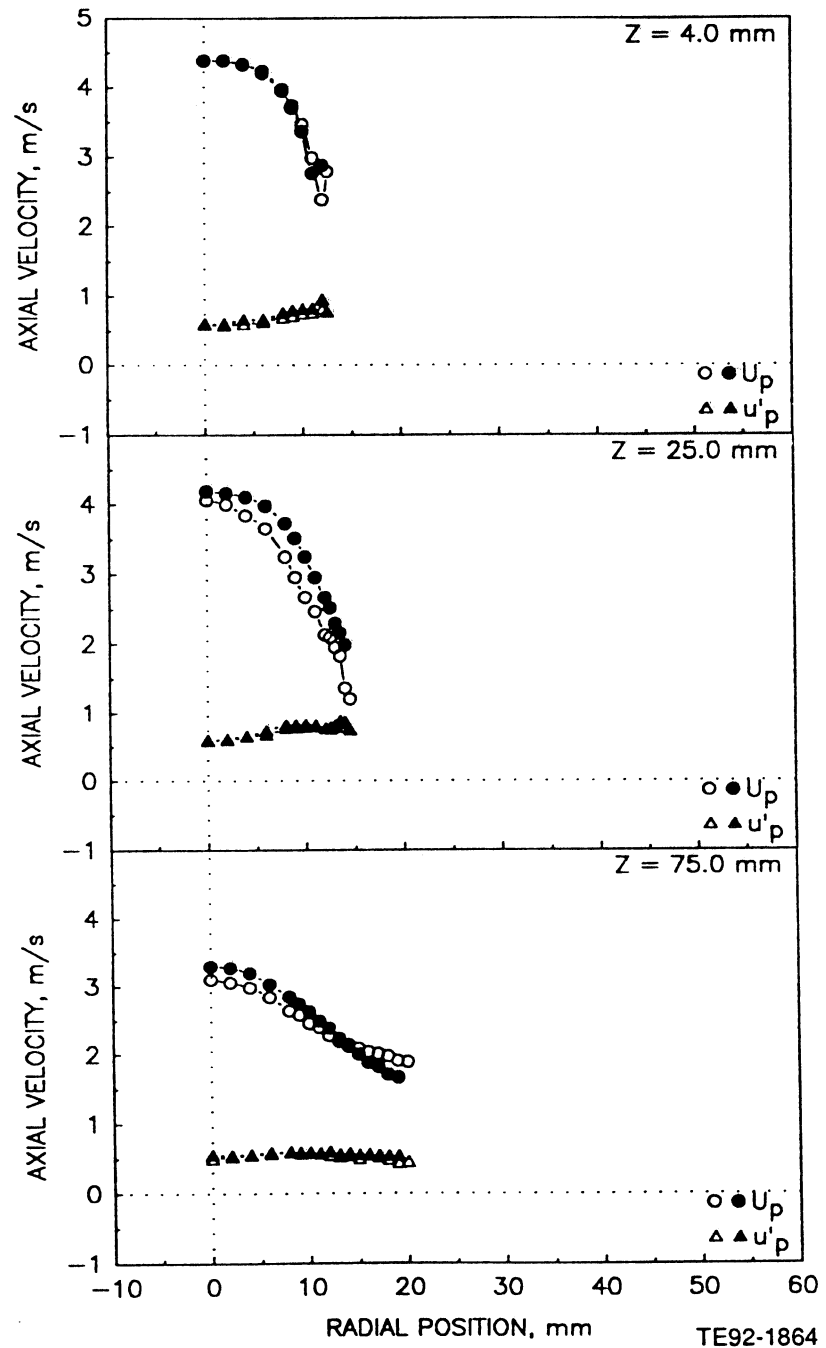
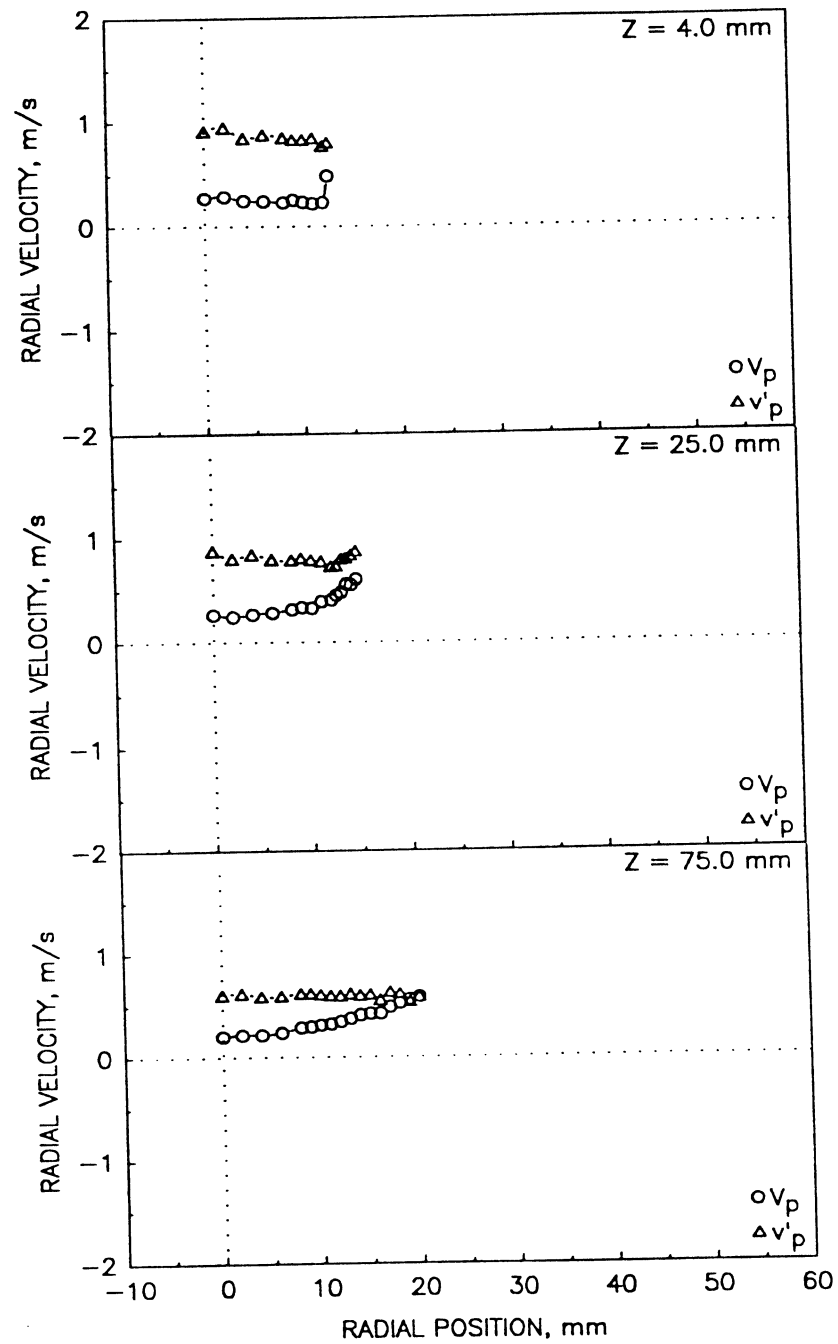


Figure 4.6.6-2. Radial profiles of particle measurements in confined coaxial jets with swirling annular air with central jet laden with 100-110 micron particles at a particle-to-gas mass loading ratio of 1.0 (1 of 5).

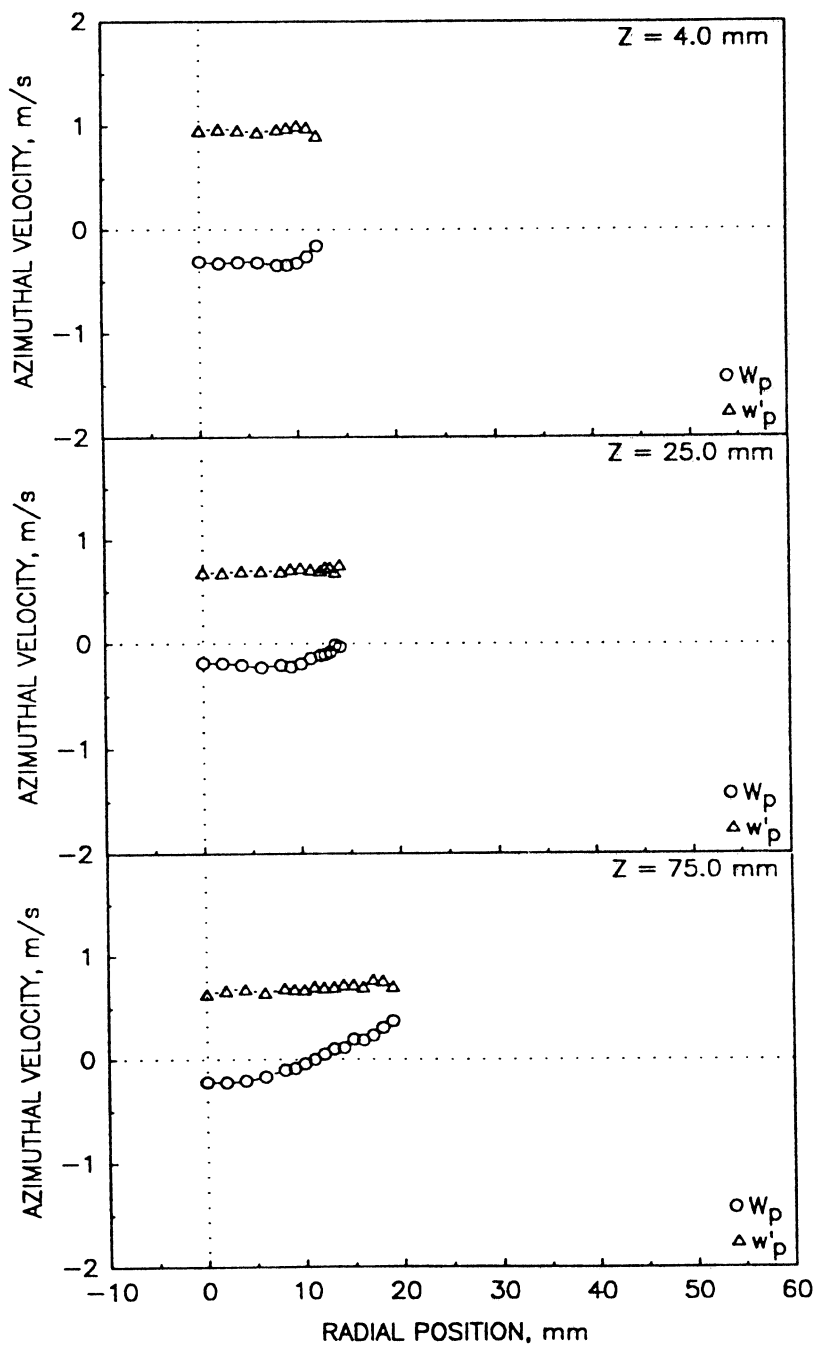
b) Mean and Fluctuating Radial Velocities



TE92-1865

Figure 4.6.6-2. Radial profiles of particle measurements in confined coaxial jets with swirling annular air with central jet laden with 100-110 micron particles at a particle-to-gas mass loading ratio of 1.0 (2 of 5).

c) Mean and Fluctuating Azimuthal Velocities



TE92-1866

Figure 4.6.6-2. Radial profiles of particle measurements in confined coaxial jets with swirling annular air with central jet laden with 100-110 micron particles at a particle-to-gas mass loading ratio of 1.0 (3 of 5).

d) Shear Stress Based on Axial and Radial Velocities

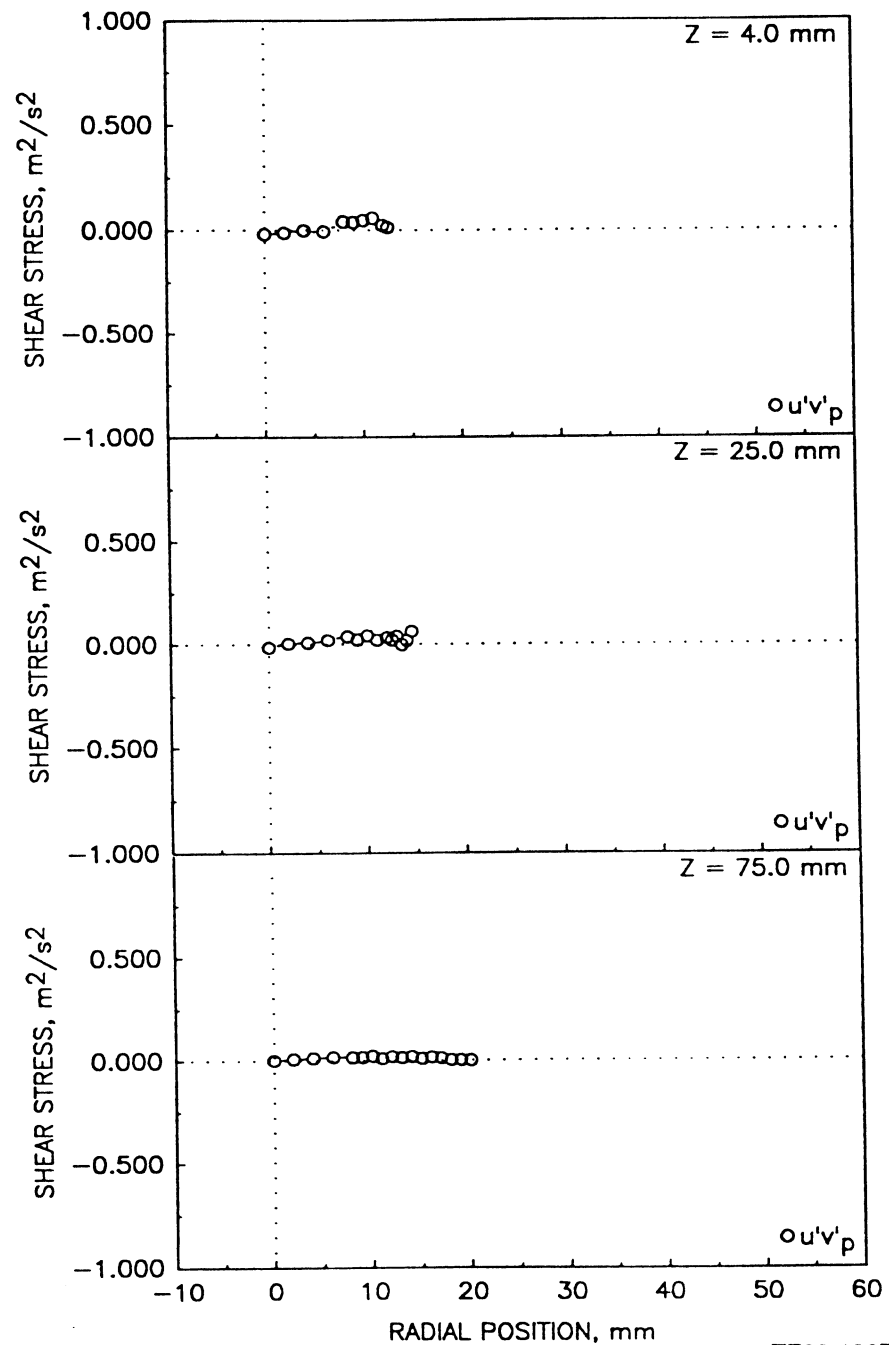


Figure 4.6.6-2. Radial profiles of particle measurements in confined coaxial jets with swirling annular air with central jet laden with 100-110 micron particles at a particle-to-gas mass loading ratio of 1.0 (4 of 5).

e) Particle Data Rate

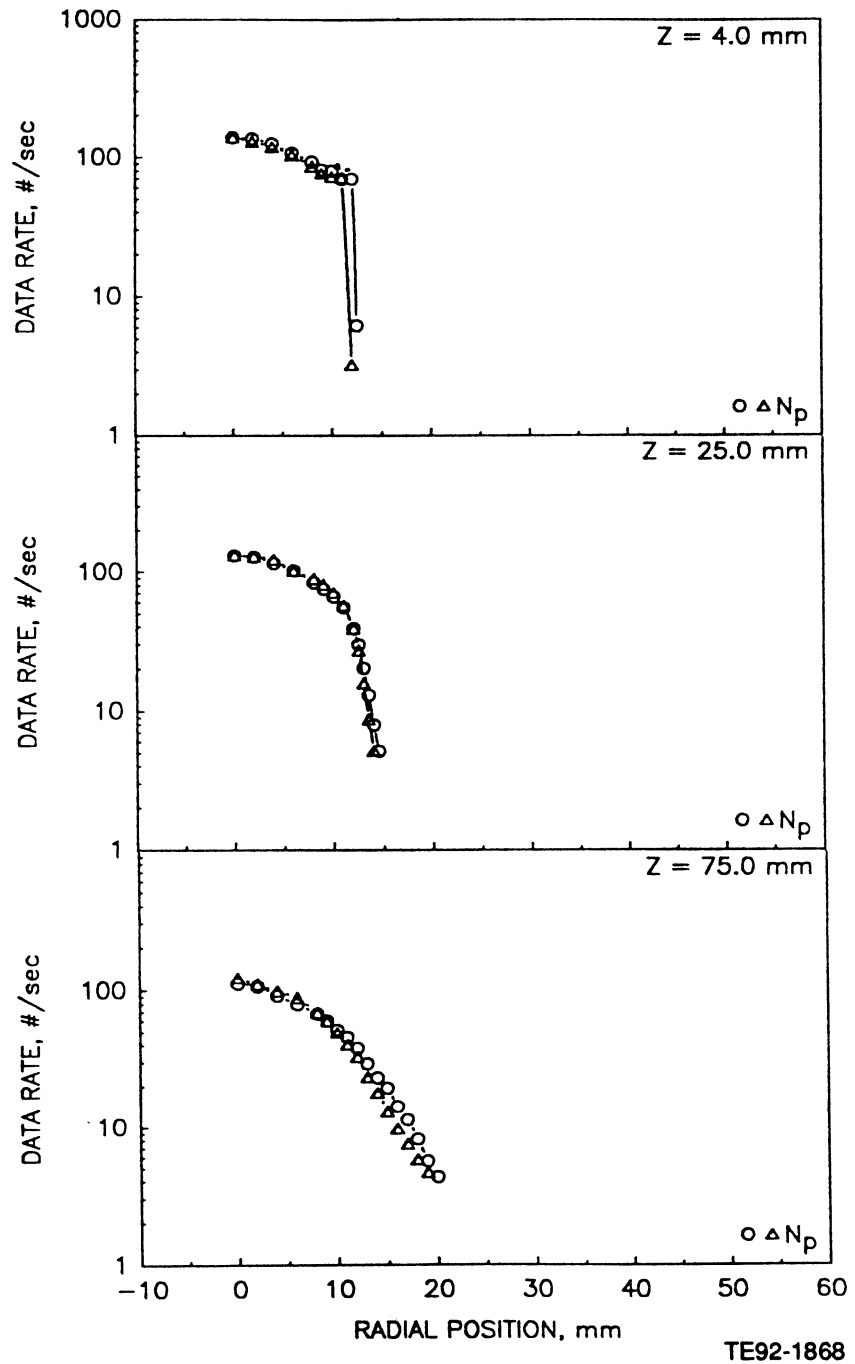
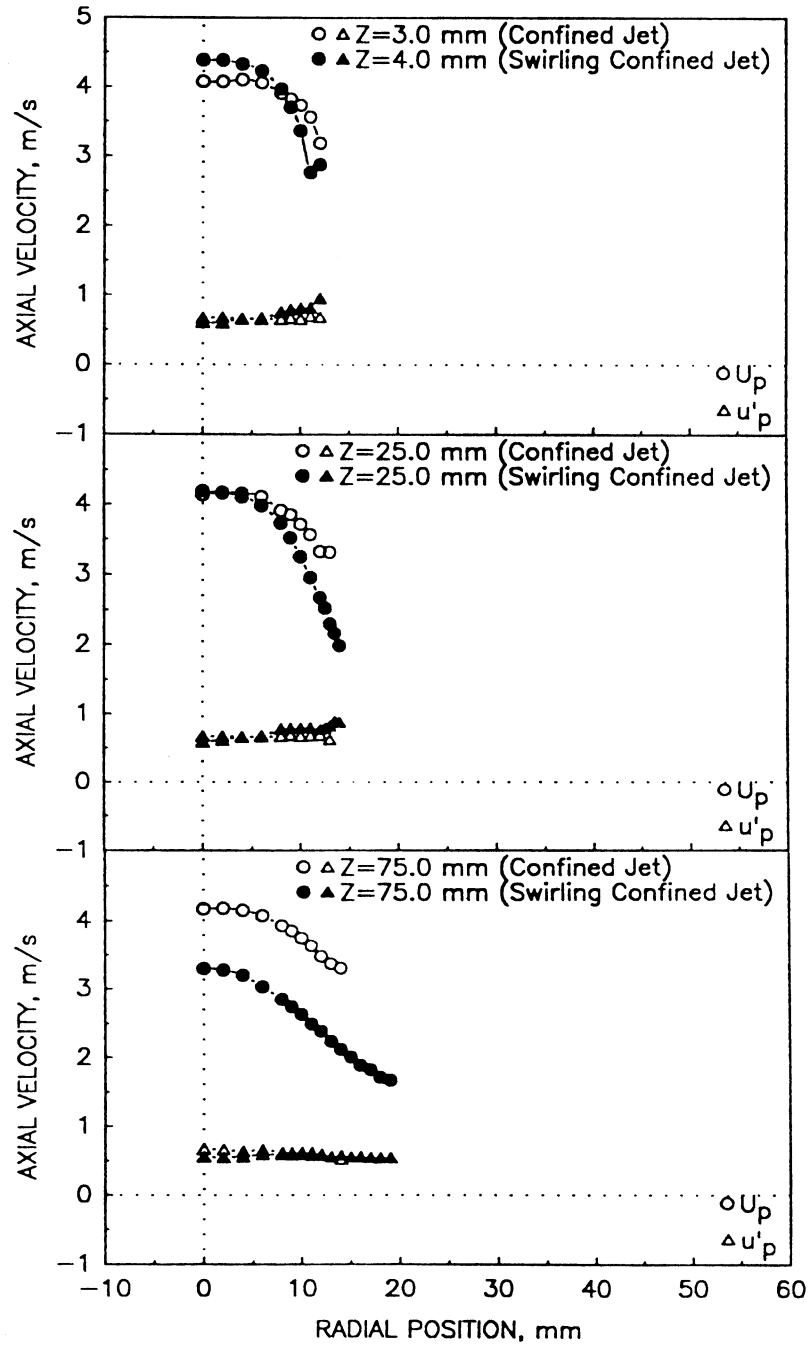


Figure 4.6.6-2. Radial profiles of particle measurements in confined coaxial jets with swirling annular air with central jet laden with 100-110 micron particles at a particle to gas mass loading ratio of 1.0 (5 of 5).

a) Mean and Fluctuating Axial Velocities



TE92-1869

Figure 4.6.7-1. Comparison of particle axial velocity and data rate in confined round jet laden with 100-110 micron particles in a particle-to-gas mass loading of 1.0 with and without swirling annular air (1 of 2).

b) Particle Data Rate

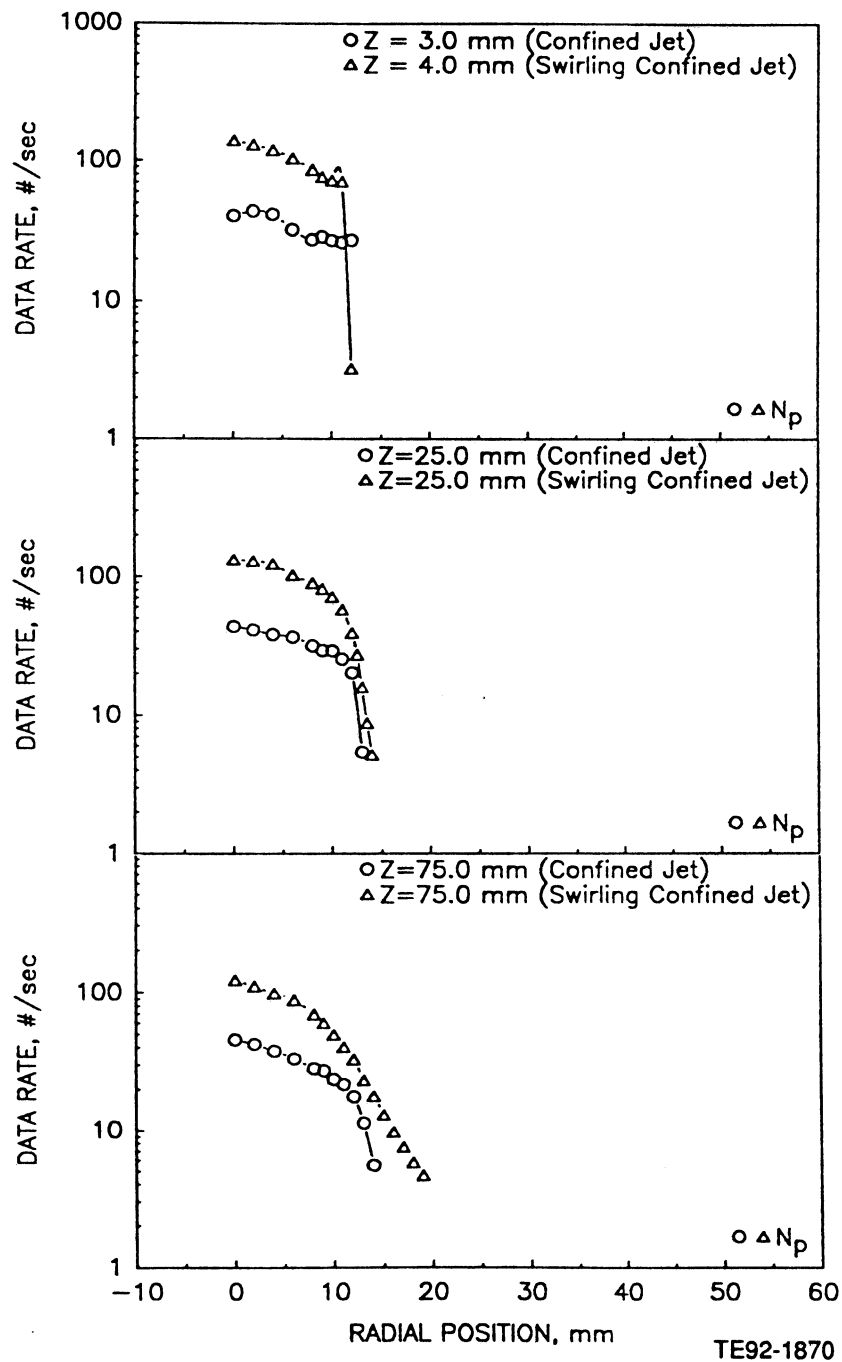


Figure 4.6.7-1. Comparison of particle axial velocity and data rate in confined round jet laden with 100-110 micron particles in a particle-to-gas mass loading of 1.0 with and without swirling annular air (2 of 2).

4.7 AIRBLAST INJECTOR

Results reported in this section were obtained in the flow field produced by the airblast injector in the absence of either swirling or nonswirling coflow. In the case of confinement, air flow is retained in the outer portion of the duct to mitigate recirculation of the spray and to reduce impingement on the windows.

4.7.1 Confined Single-Phase – CONF22#1

The geometry utilized for this study is shown in Figure 4.7.1-1. Examples of the results obtained are shown in Figure 4.7.1-2. The mean axial velocity reveals very high gradients near the centerline. In fact, the high axial velocities precluded the acquisition of high quality data for the other two components in this region. The axial velocity decays with increasing axial distance. The low velocity coflow in the outer portion of the duct is also apparent.

The radial velocity (Figure 4.7.1-2 [b]) reveals strong inward velocities near the centerline. By 25 mm downstream, the flow begins to expand.

The azimuthal velocities (Figure 4.7.1-2 [c]) are high near the exit plane but decay quickly with increasing downstream distance. Note that the maximum fluctuating velocities occur along the centerline.

4.7.2 Gas in the Presence of Confined Methanol Spray – CONF28#2

Figure 4.7.2-1 presents the gas phase velocities in the presence of the methanol spray. Based on the two orthogonal profiles, the flowfield is symmetric. Many of the attributes of the single-phase case are retained. The next section focuses on the differences between the two cases.

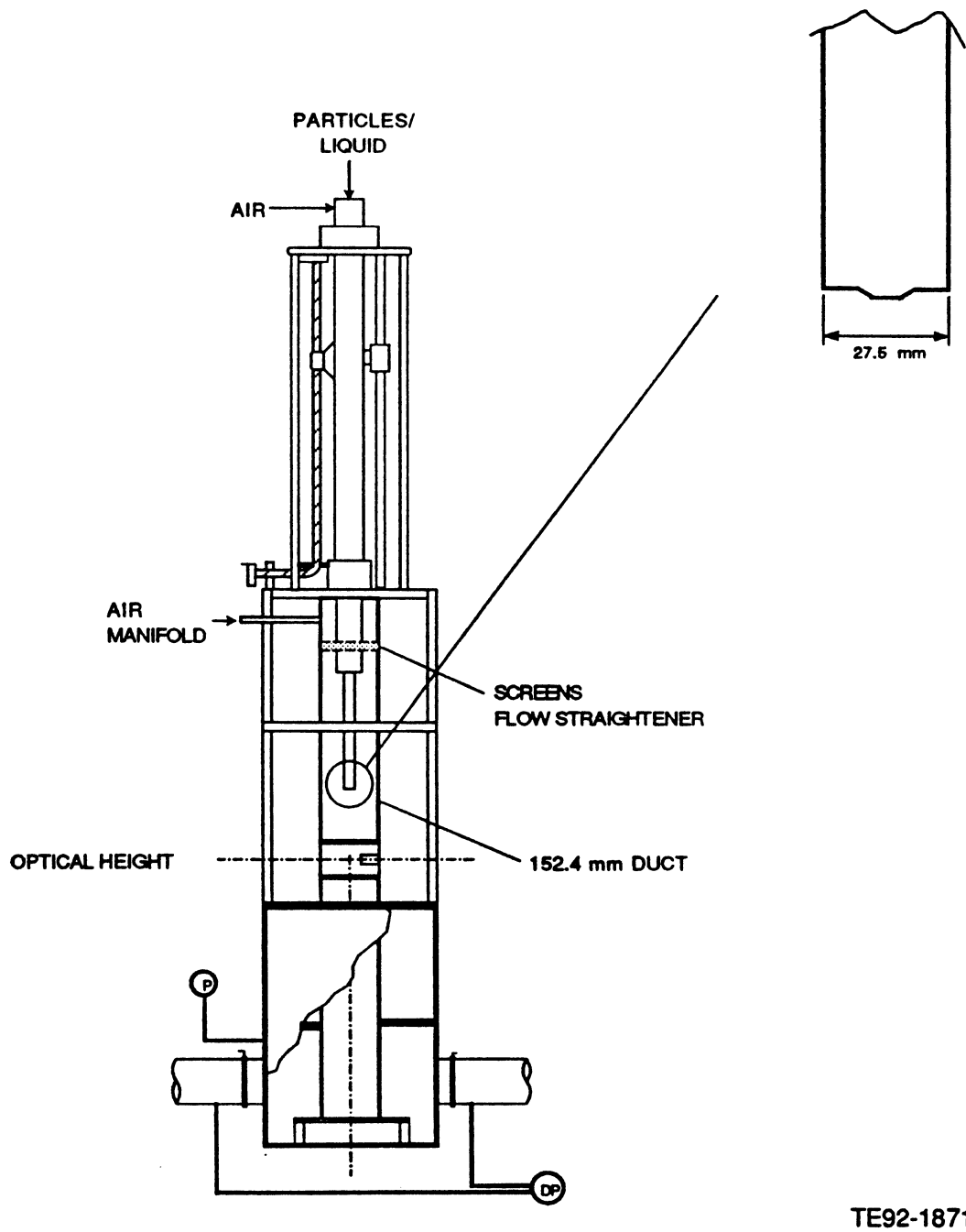
4.7.3 Effect of Spray on Gas Phase Behavior in Confined Spray

Figure 4.7.3-1 provides results which compare the measurements made with and without the spray. The results reveal some interesting differences. First, the presence of the spray reduces the width of the profiles and increases the maximum velocities. Second, the spray reduces the fluctuating velocities in both the axial and radial directions. The presence of the spray also increases the magnitude of the radial velocities away from the centerline at the edge of the spray.

The reason for these differences is not clear, as discussed in Section III. The presence of the spray leads to interaction between phases, resulting in potential for momentum transfer which could, in principle, lead to changes in the gas phase velocities. However, the presence of the spray also changes the effective area of the atomizer, resulting in higher velocities for the same mass flow rate of air. Hence, some contributions of each phenomena give rise to the differences observed.

4.7.4 Confined Methanol Spray – CONF28#1

The characteristics of the droplets in the confined methanol spray are presented in Figure 4.7.4-1. The mean axial velocity shows good symmetry based on the two orthogonal profiles (Figure 4.7.4-1 [a and d]). The velocity profiles exhibit trends similar to those for the gas phase. Again, the highest fluctuating velocities are observed at the centerline. The profiles of D_{32} are shown in Figure 4.7.4-1 (d). These results show that the atomizer produces many fine droplets near the centerline and larger ones at the edge of the spray.



TE92-1871

Figure 4.7.1-1. Geometry utilized for the confined methanol spray.

a) Mean and Fluctuating Axial Velocity

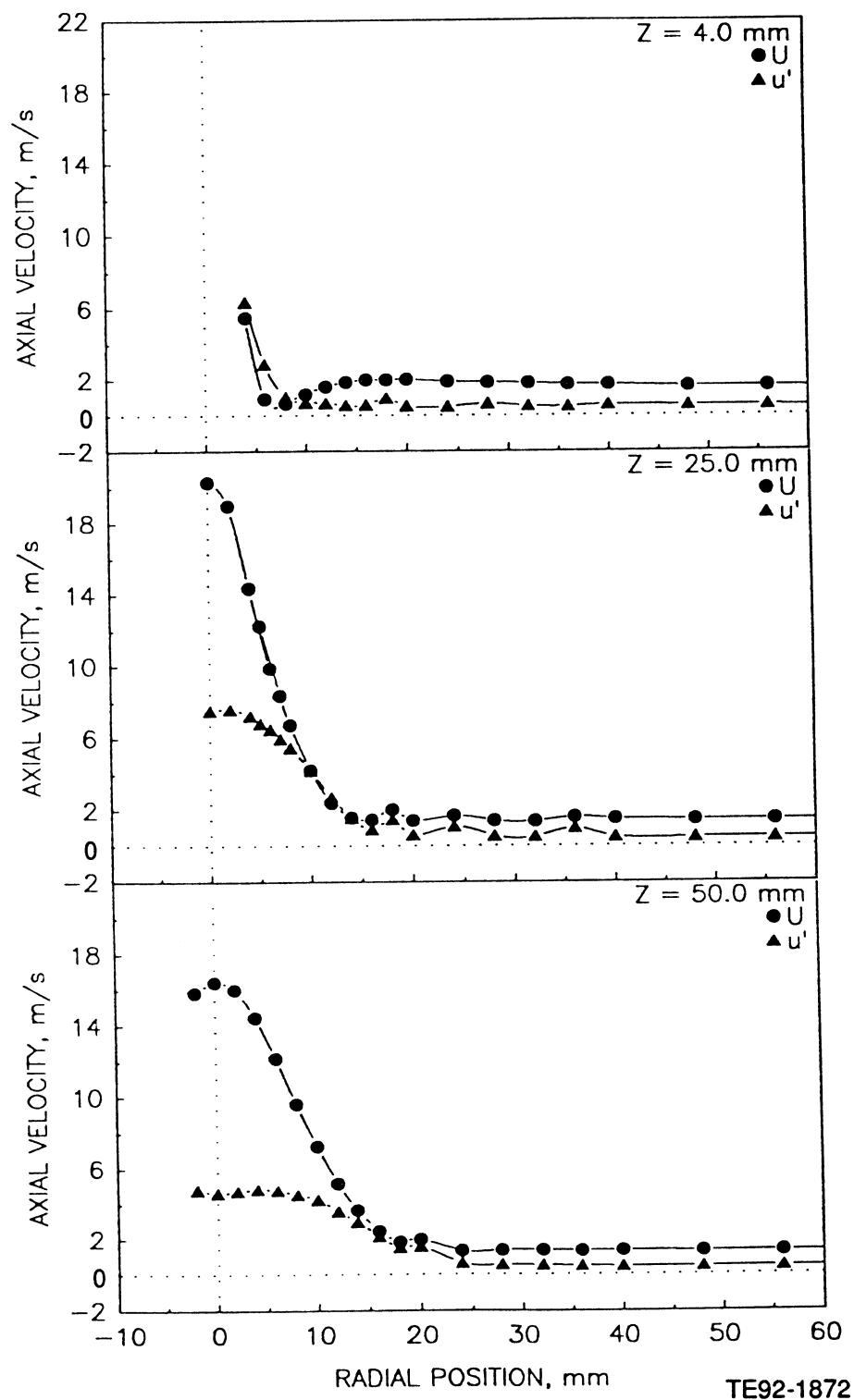


Figure 4.7.1-2. Radial profiles of gas phase statistics in confined single-phase flow from air-blast injector (1 of 3).

b) Mean and Fluctuating Azimuthal Velocity

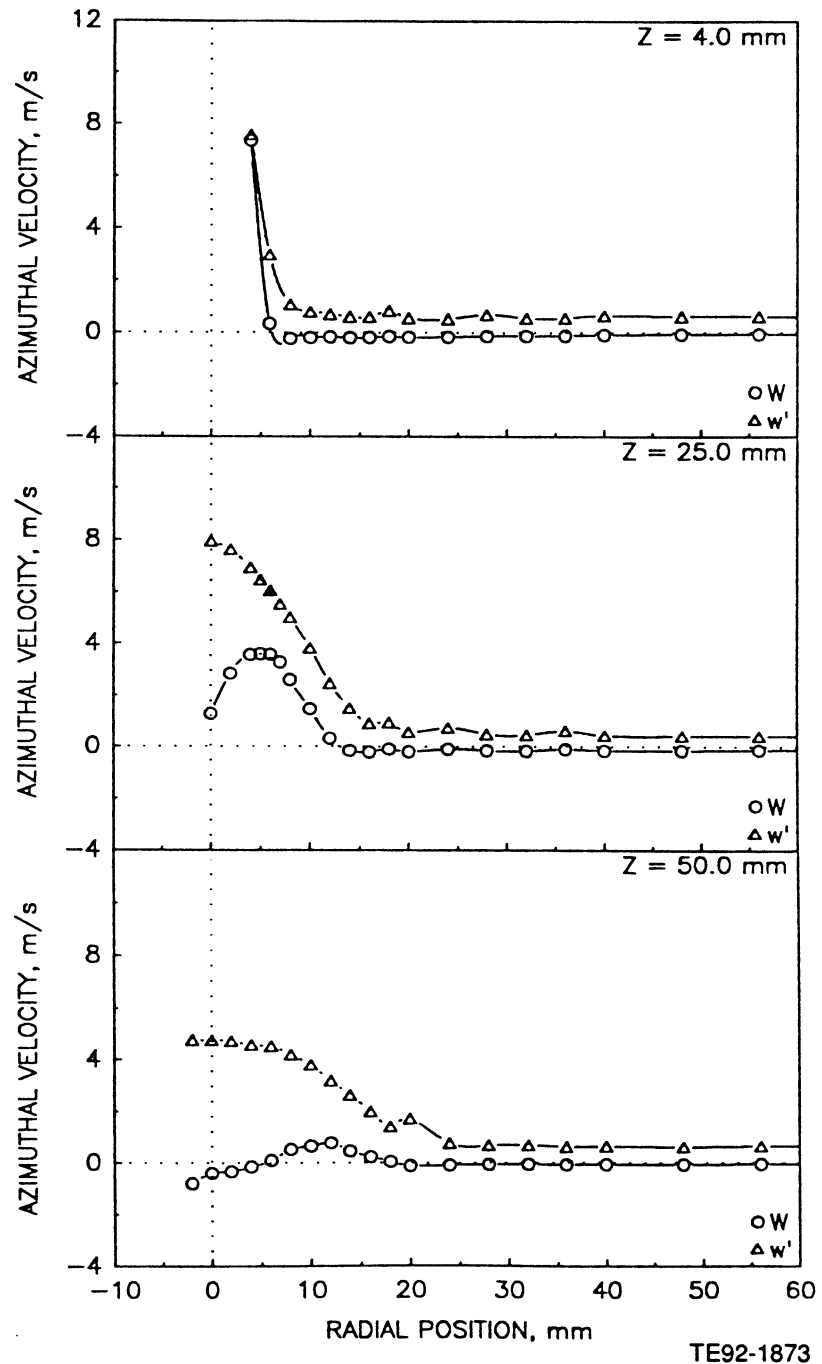
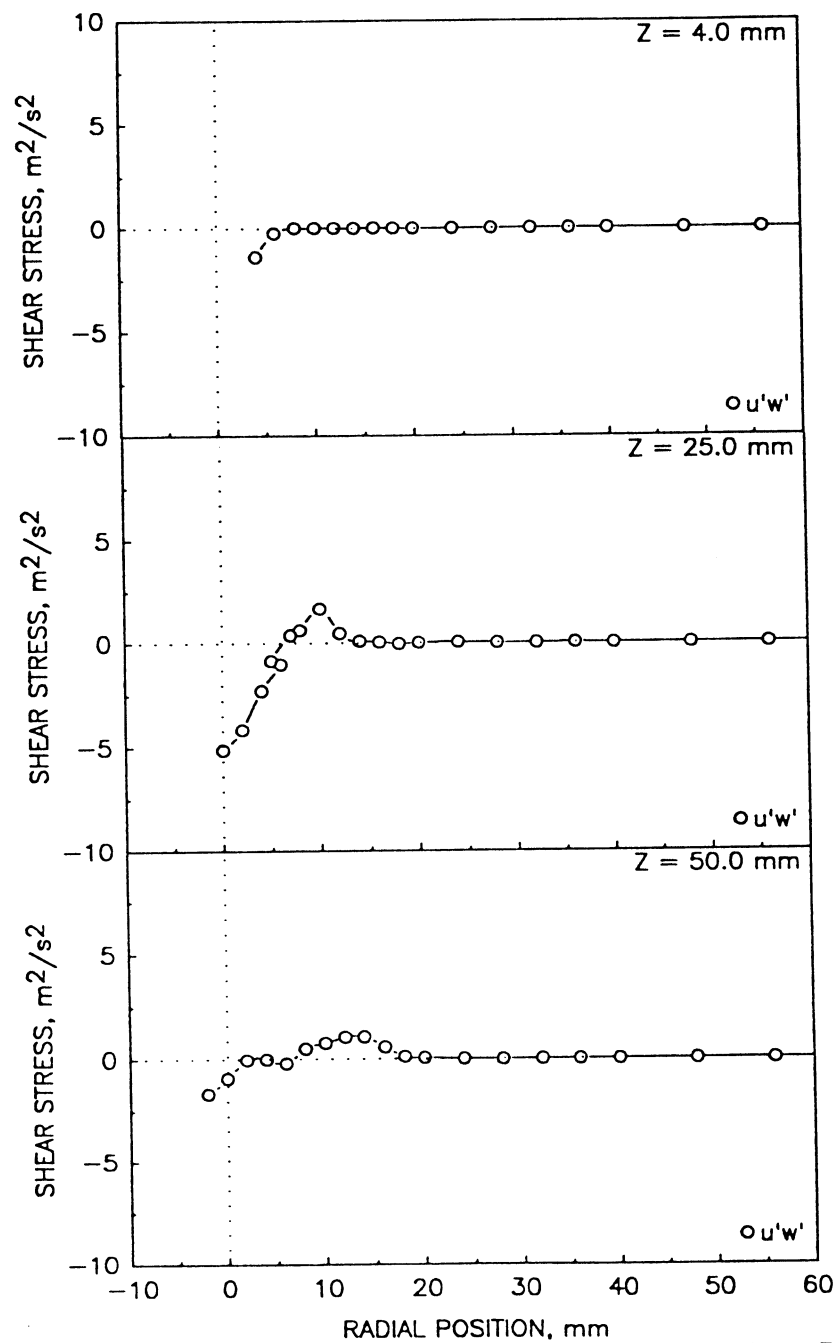


Figure 4.7.1-2. Radial profiles of gas phase statistics in confined single-phase flow from air-blast injector (2 of 3).

c) Shear Stress Based on Axial and Azimuthal Velocities



TE92-1874

Figure 4.7.1-2. Radial profiles of gas phase statistics in confined single-phase flow from air-blast injector (3 of 3).

a) Mean and Fluctuating Axial Velocities

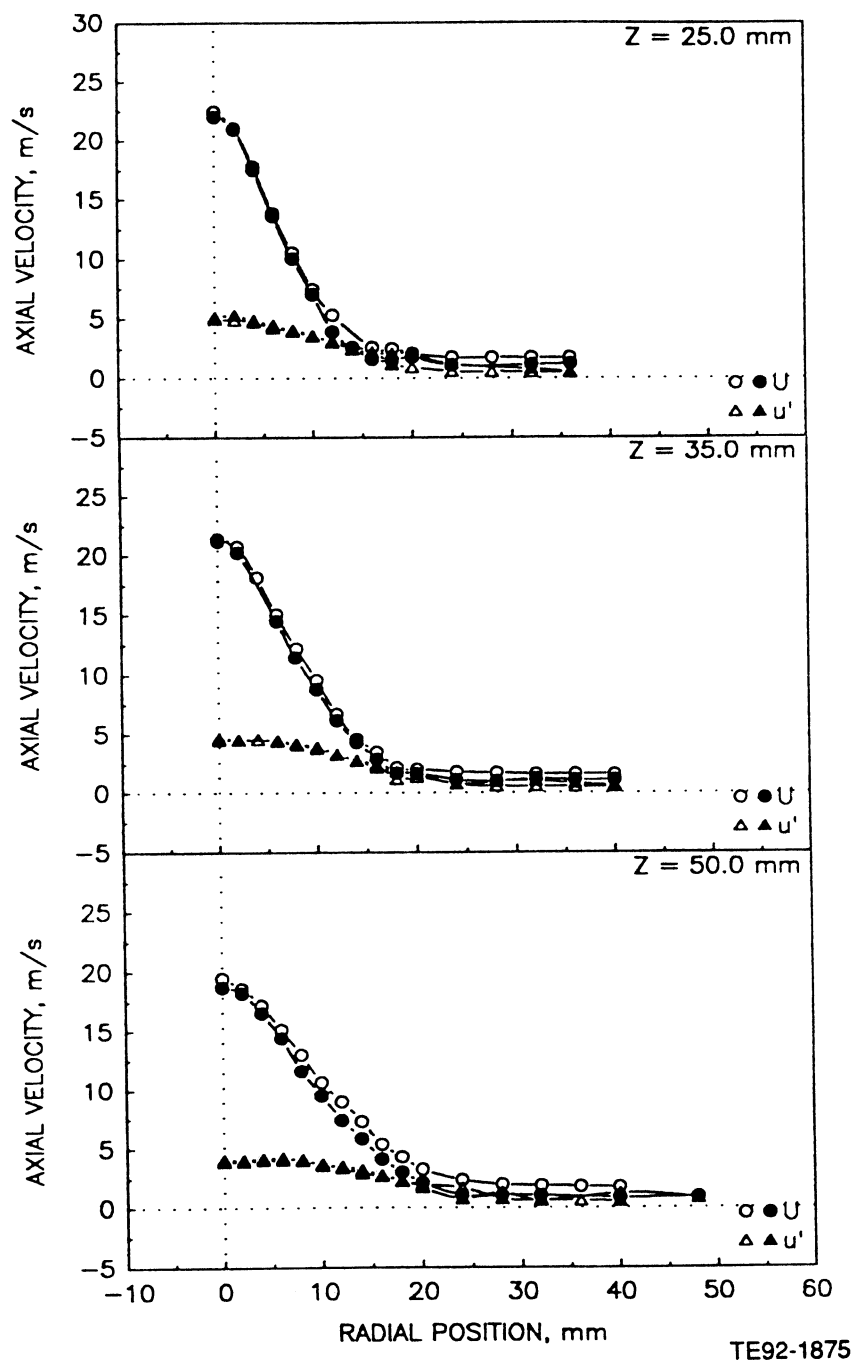


Figure 4.7.2-1. Radial profiles of the gas phase measurements in the confined methanol spray (1 of 5).

b) Mean and Fluctuating Radial Velocities

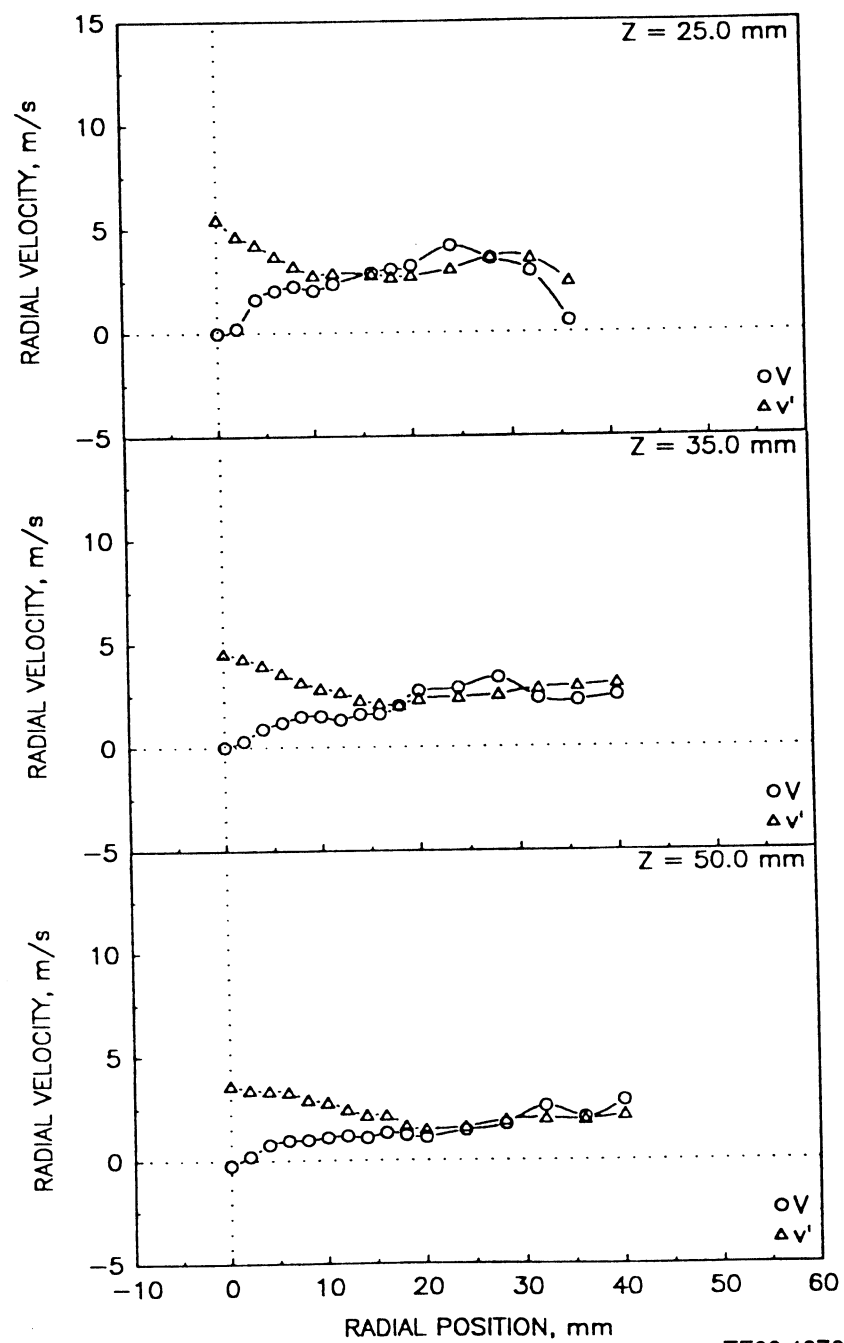


Figure 4.7.2-1. Radial profiles of the gas phase measurements in the confined methanol spray (2 of 5).

c) Mean and Fluctuating Azimuthal Velocities

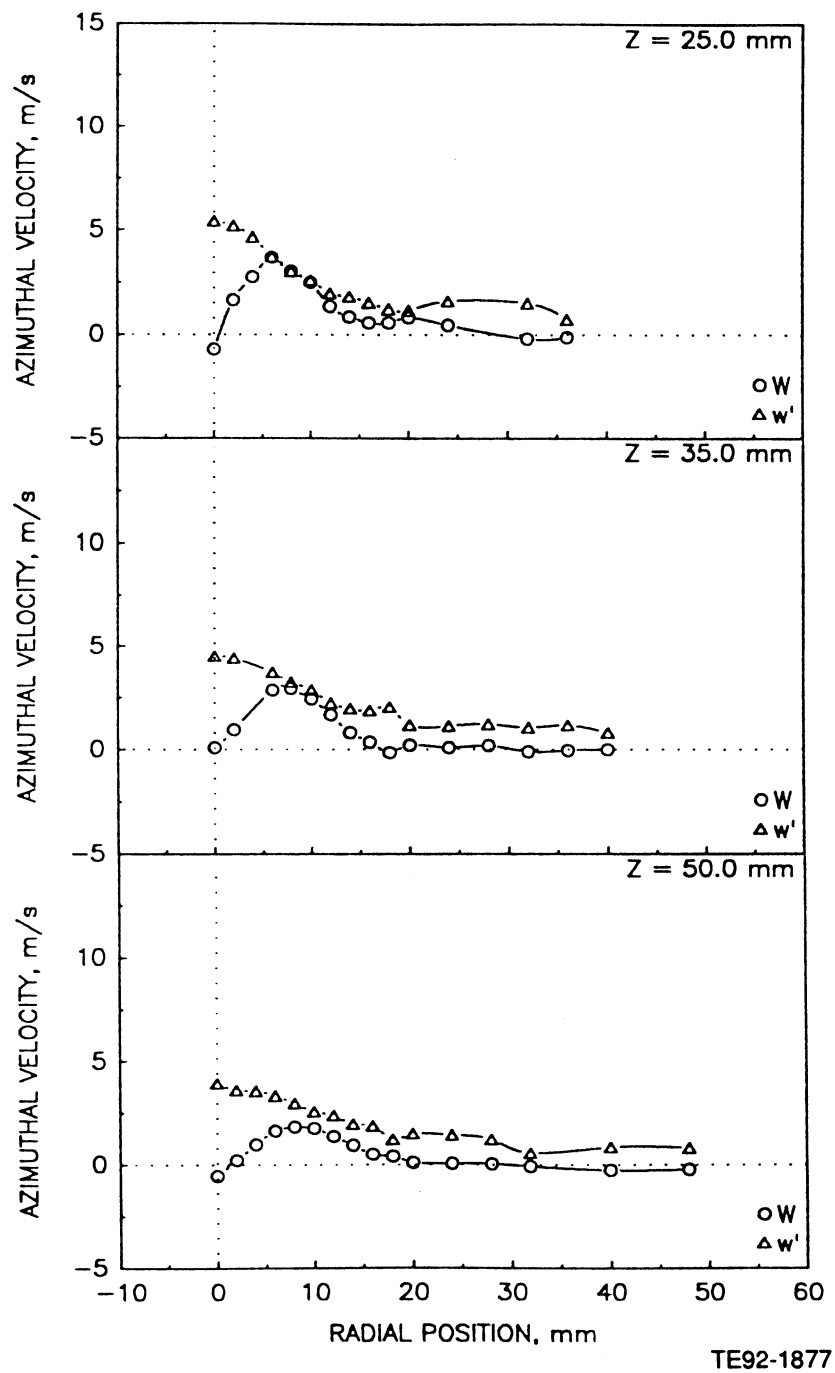


Figure 4.7.2-1. Radial profiles of the gas phase measurements in the confined methanol spray (3 of 5).

d) Shear Stress Based on Axial and Radial Velocities

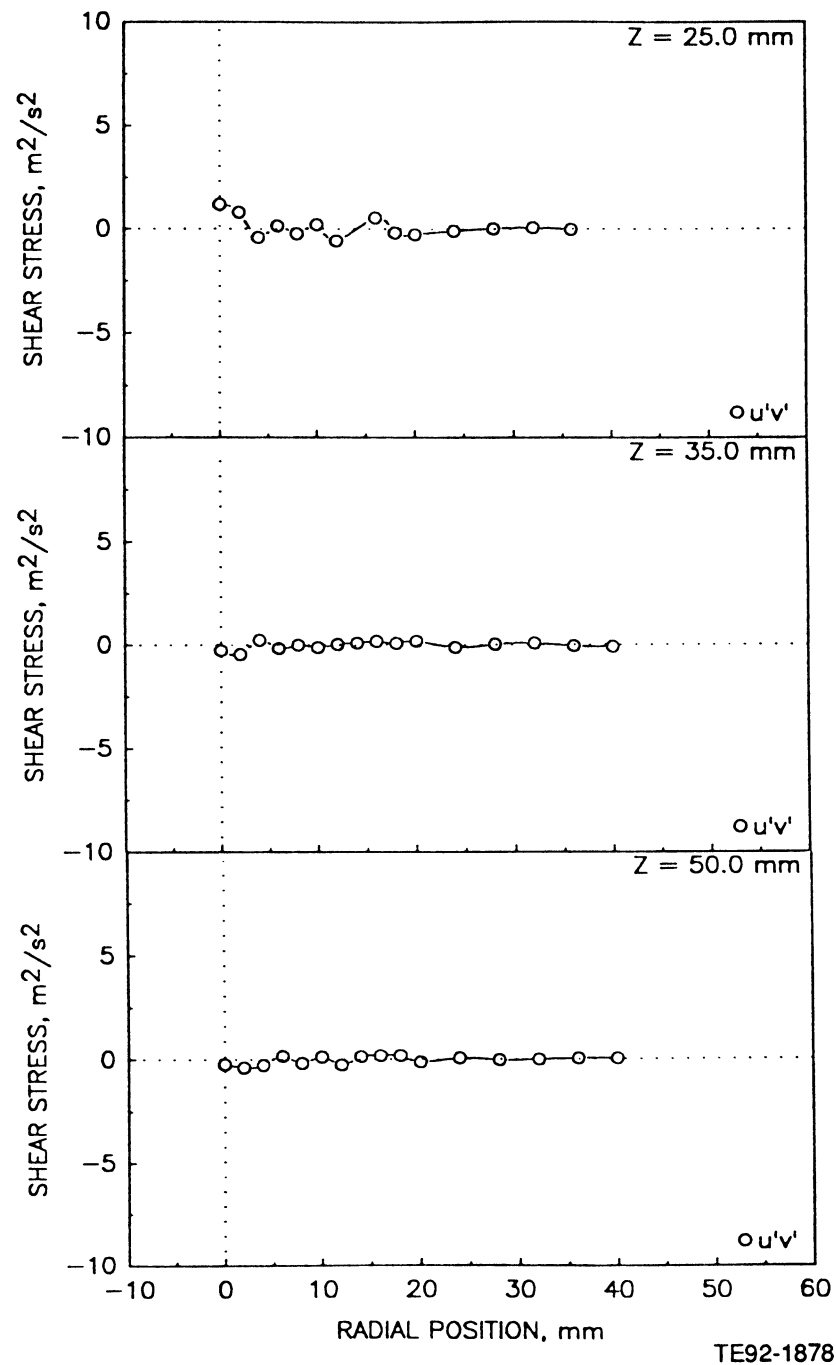


Figure 4.7.2-1. Radial profiles of the gas phase measurements in the confined methanol spray (4 of 5).

e) Shear Stress Based on Axial and Azimuthal Velocities

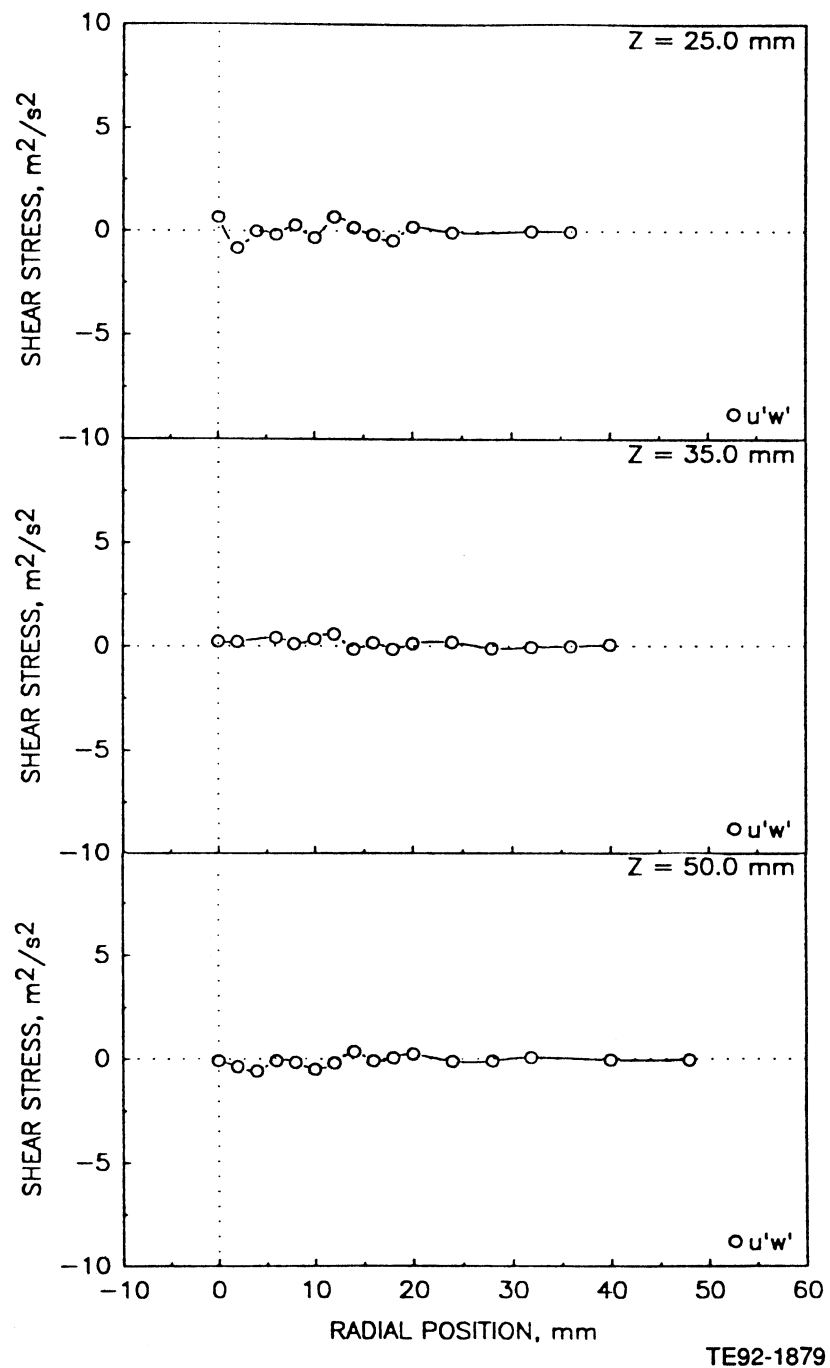


Figure 4.7.2-1. Radial profiles of the gas phase measurements in the confined methanol spray (5 of 5).

a) Mean and Fluctuating Axial Velocity

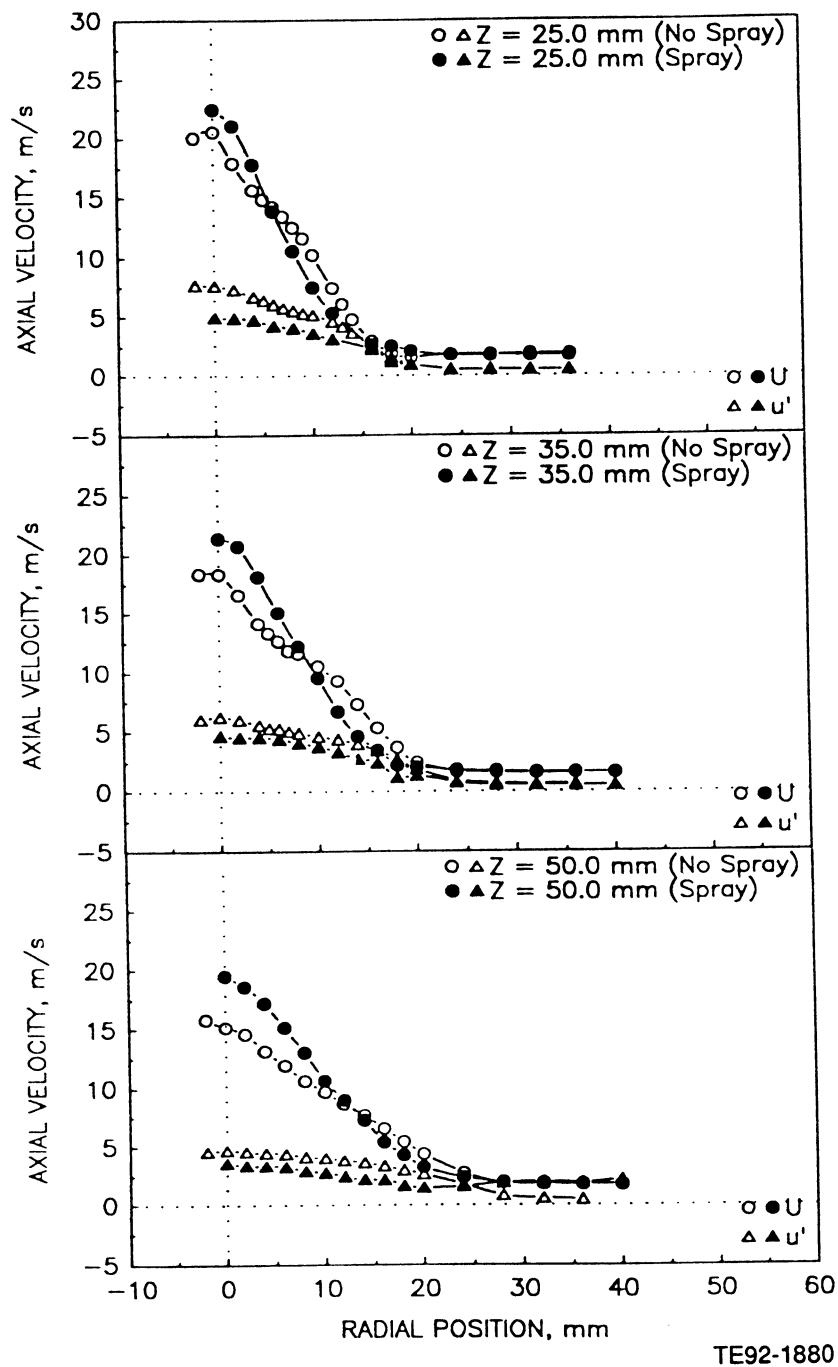
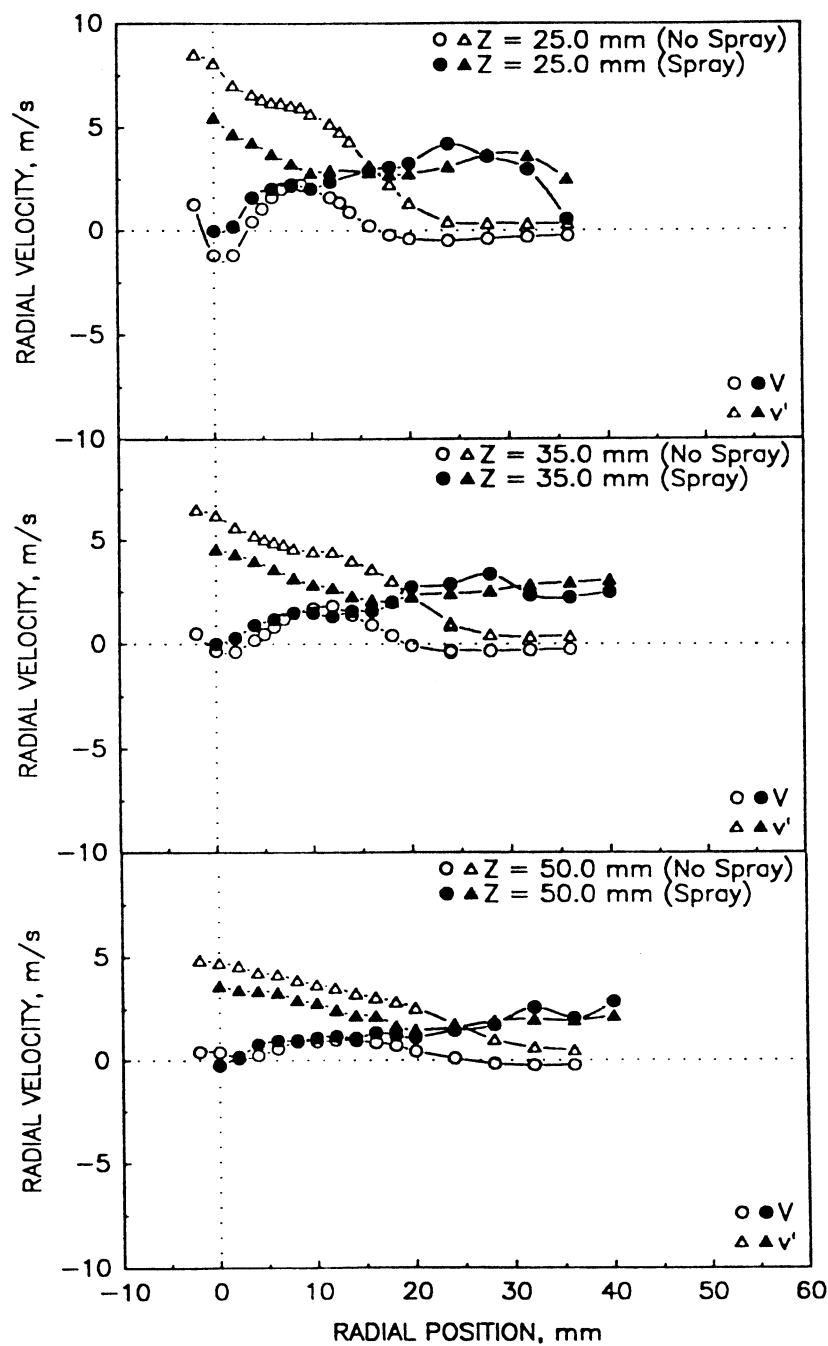


Figure 4.7.3-1. Comparison of gas phase measurements in the confined air-blast atomizer flow with and without methanol (1 of 3).

b) Mean and Fluctuating Radial Velocity



TE92-1881

Figure 4.7.3-1. Comparison of gas phase measurements in the confined air-blast atomizer flow with and without methanol (2 of 3).

c) Shear Stress Based on Axial and Radial Velocities

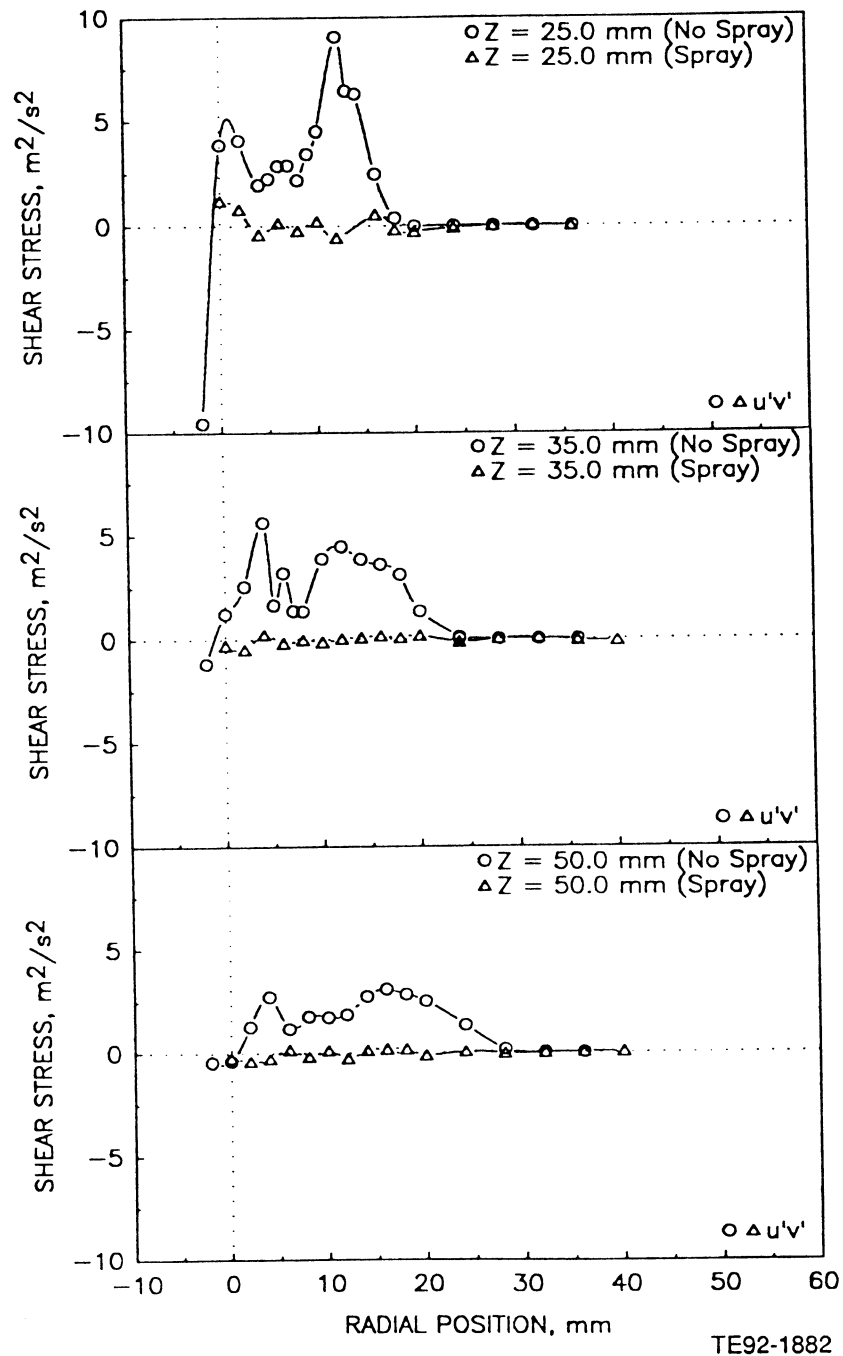


Figure 4.7.3-1. Comparison of gas phase measurements in the confined air-blast atomizer flow with and without methanol (3 of 3).

a) Mean and Fluctuating Axial Velocities

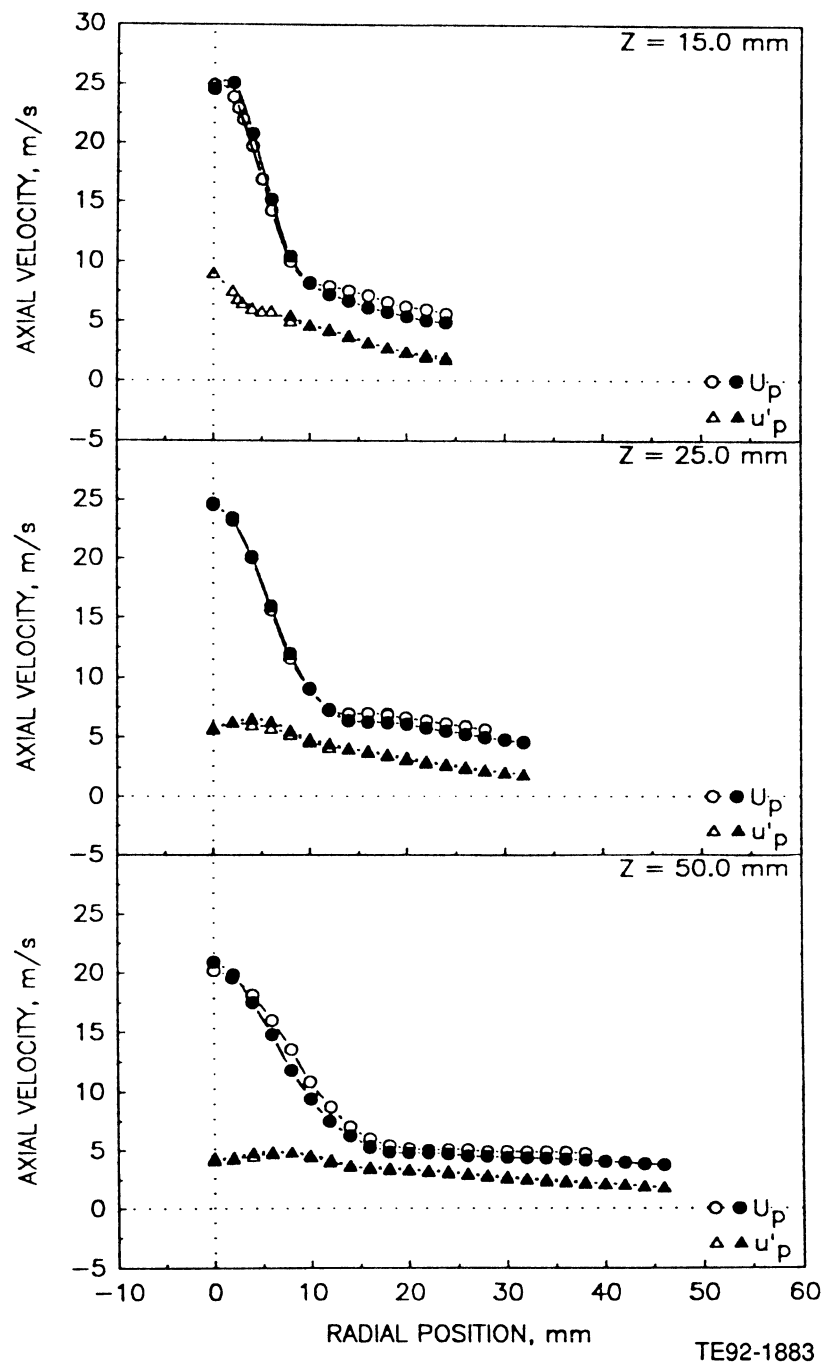


Figure 4.7.4-1. Radial profiles of the droplet measurements in the confined methanol spray (1 of 4).

b) Mean and Fluctuating Radial Velocities

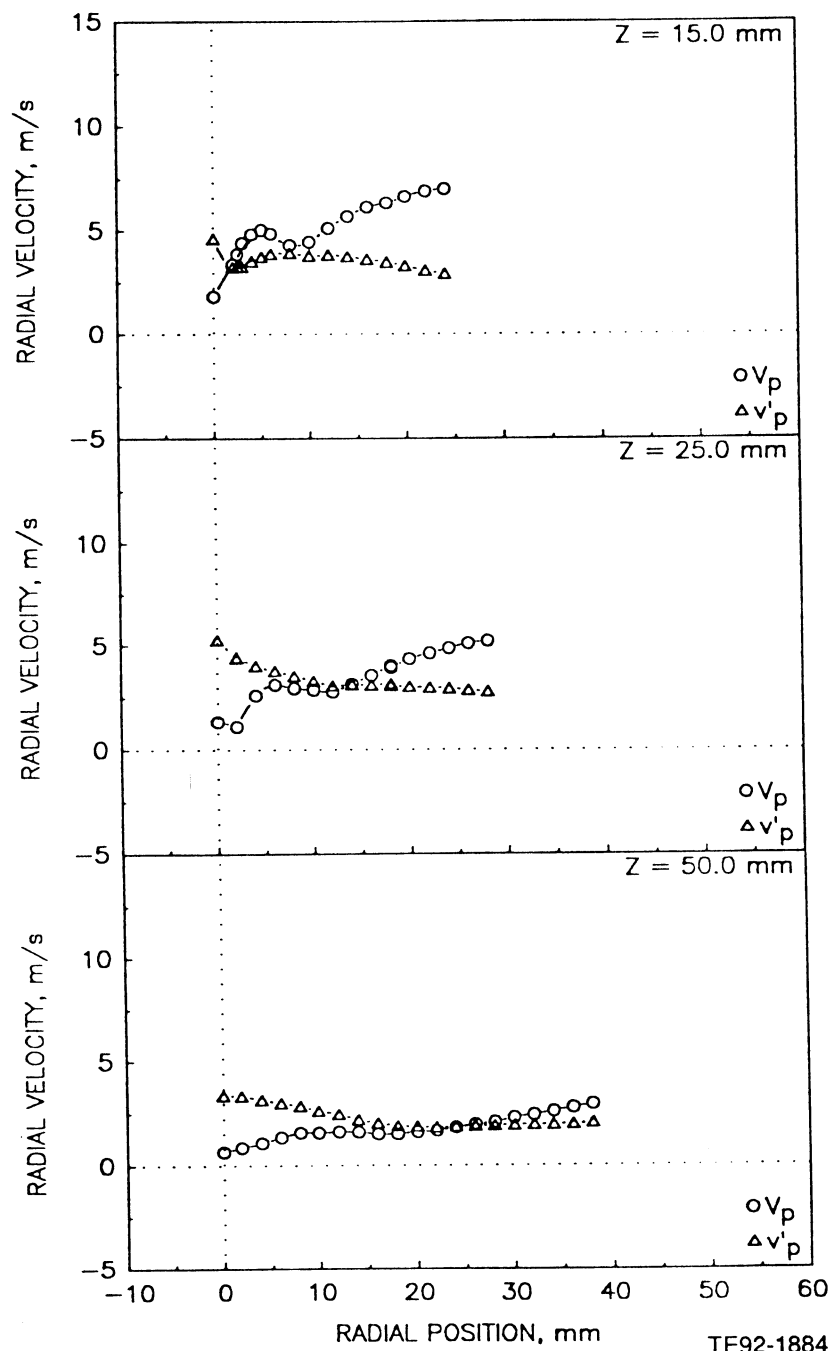


Figure 4.7.4-1. Radial profiles of the droplet measurements in the confined methanol spray (2 of 4).

c) Mean and Fluctuating Azimuthal Velocities

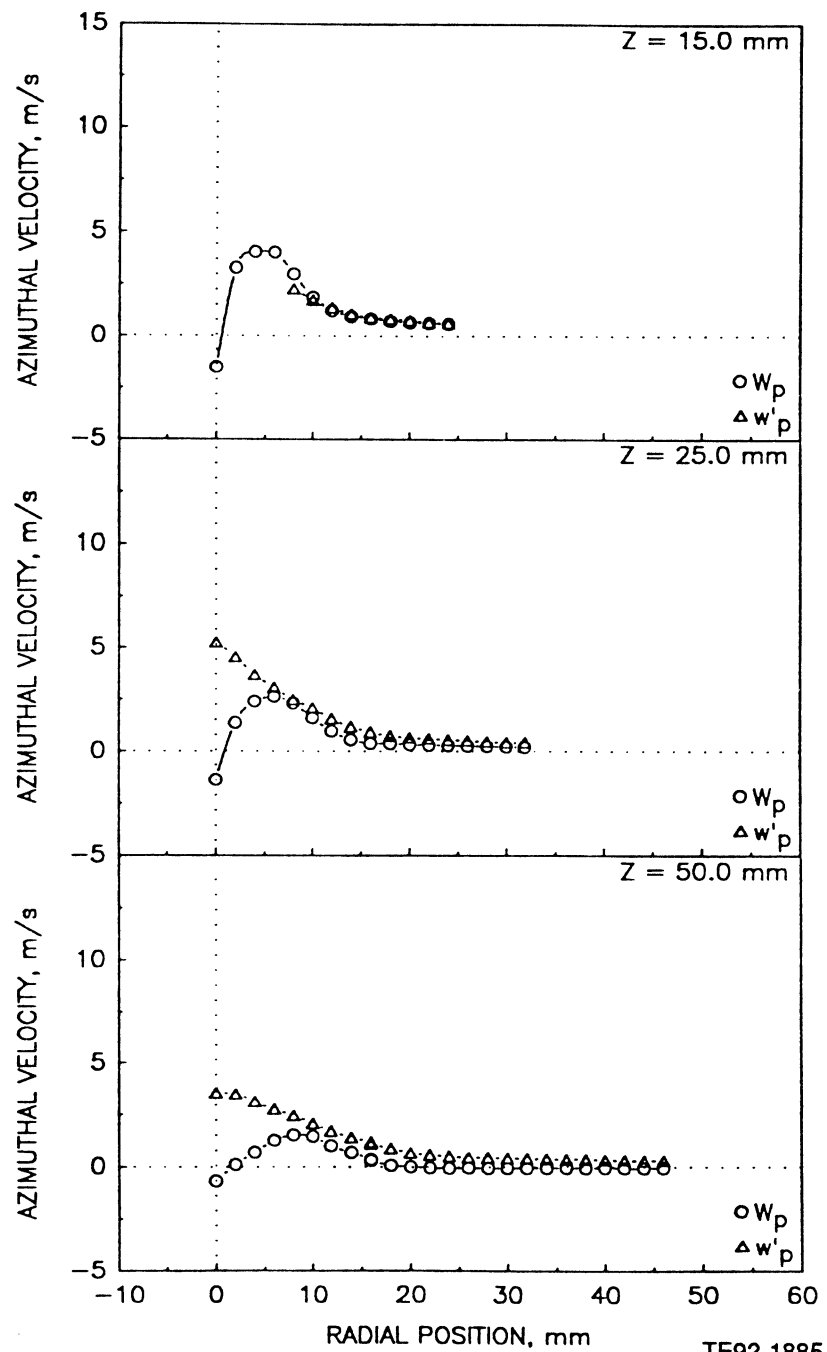


Figure 4.7.4-1. Radial profiles of the droplet measurements in the confined methanol spray (3 of 4).

d) Sauter Mean Diameter

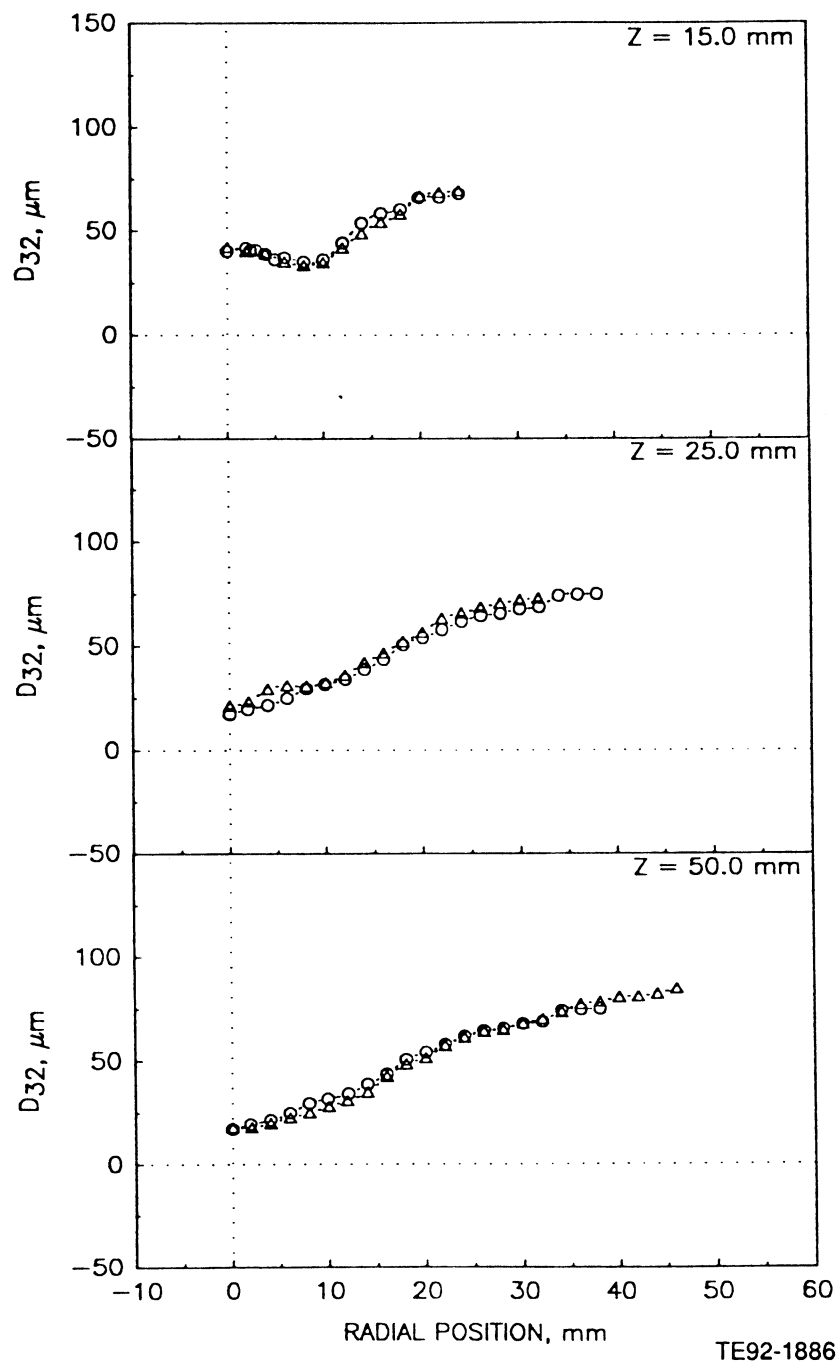


Figure 4.7.4-1. Radial profiles of the droplet measurements in the confined methanol spray (4 of 4).

4.8 AIRBLAST INJECTOR WITH ANNULAR JET

Two cases were considered for the nozzle with annular jet, confined and unconfined. The unconfined spray was used as a baseline.

4.8.1 Gas in the Presence of Unconfined Methanol Spray – CONF26#2

Figure 4.8.1-1 presents the geometry utilized for the unconfined spray in the presence of the annular jet. Figure 4.8.1-2 provides examples of the results obtained. Based on the orthogonal profiles of the axial velocity (Figure 4.8.1-2 [a]), the flow field is reasonably symmetric. In this case, unlike that of the jet (section 4.5.1), the axial velocities from the two jets are not distinct. This is attributed to the much higher velocities of the atomizer.

The radial velocities (Figure 4.8.1-2 [b]) exhibit some evidence of the two distinct flow passages with a local minimum between 10 and 20 mm from the centerline.

4.8.2 Unconfined Methanol Spray – CONF26#1

Figure 4.8.2-1 presents results from the methanol spray. Again, based on orthogonal profiles (Figure 4.8.2-1 [a and d]), the flow is symmetric. The droplet velocities resemble those of the gas phase discussed above. The droplet sizes appear similar to those for the case in the absence of the coflow (section 4.7.4).

To add some insight into the interaction between phases, Figure 4.8.2-2 (a and b) presents a comparison of the measurements of the gas phase and droplets for the unconfined methanol spray with annular coflow. The results for the axial velocity (Figure 4.8.2-2 [a]) indicate that the droplet velocity is lower than that of the gas phase up to about 50 mm downstream of the injector. Since the liquid is injected with nearly no velocity, the gas phase accelerates the liquid. By 50 mm, the greater momentum of the droplets causes them to reach axial velocities which are greater than that of the gas phase, which is continually decaying.

The radial velocities reveal little difference between the two cases near the centerline. However, away from the centerline, the droplet radial velocity is significantly higher than that of the gas phase.

4.8.3 Confined Single-Phase – CONF23#1

Figure 4.8.3-1 provides the geometry employed for the confined spray with annular coflow.

Figure 4.8.3-2 presents examples of the results obtained for the single-phase flow. Based on the two orthogonal profiles (Figure 4.8.3-2 [a]), the flow is symmetric. At 4.0 mm, evidence of the two air streams is evident. Data were not obtained near the centerline due to insufficient frequency shift on the second component. The radial (Figure 4.8.3-2 [b]) and azimuthal (Figure 4.8.3-2 [c]) profiles show that a slight mismatch between the geometric and aerodynamic centerlines was present. The radial velocities also reveal high entrainment rates near the injector.

4.8.4 Effect of Coflow on Gas Phase

Figure 4.8.4-1 provides a comparison of the measurements made with and without coflow in the confined duct.

4.8.5 Confined Methanol Spray – CONF29#1

Figure 4.8.5-1 presents examples of the results obtained from the confined spray with coflow. Based on the two orthogonal profiles (Figure 4.8.5-1 [a and d]), the spray is symmetric. The trends observed are similar to those observed for the case without coflow (section 4.7.4).

4.8.6 Effect of Coflow on Spray

Figure 4.8.6-1 presents a comparison of the confined methanol spray with and without coflow. The coflow has little impact on either the droplet velocities or the droplet size.

4.8.7 Effect of Confinement on Spray

Figure 4.8.7-1 provides a comparison of the measurements made in the confined and unconfined methanol sprays with coflow. Small differences are observed, primarily in the mean axial velocity at the edge of the spray and in the size. Overall, the effect is small.

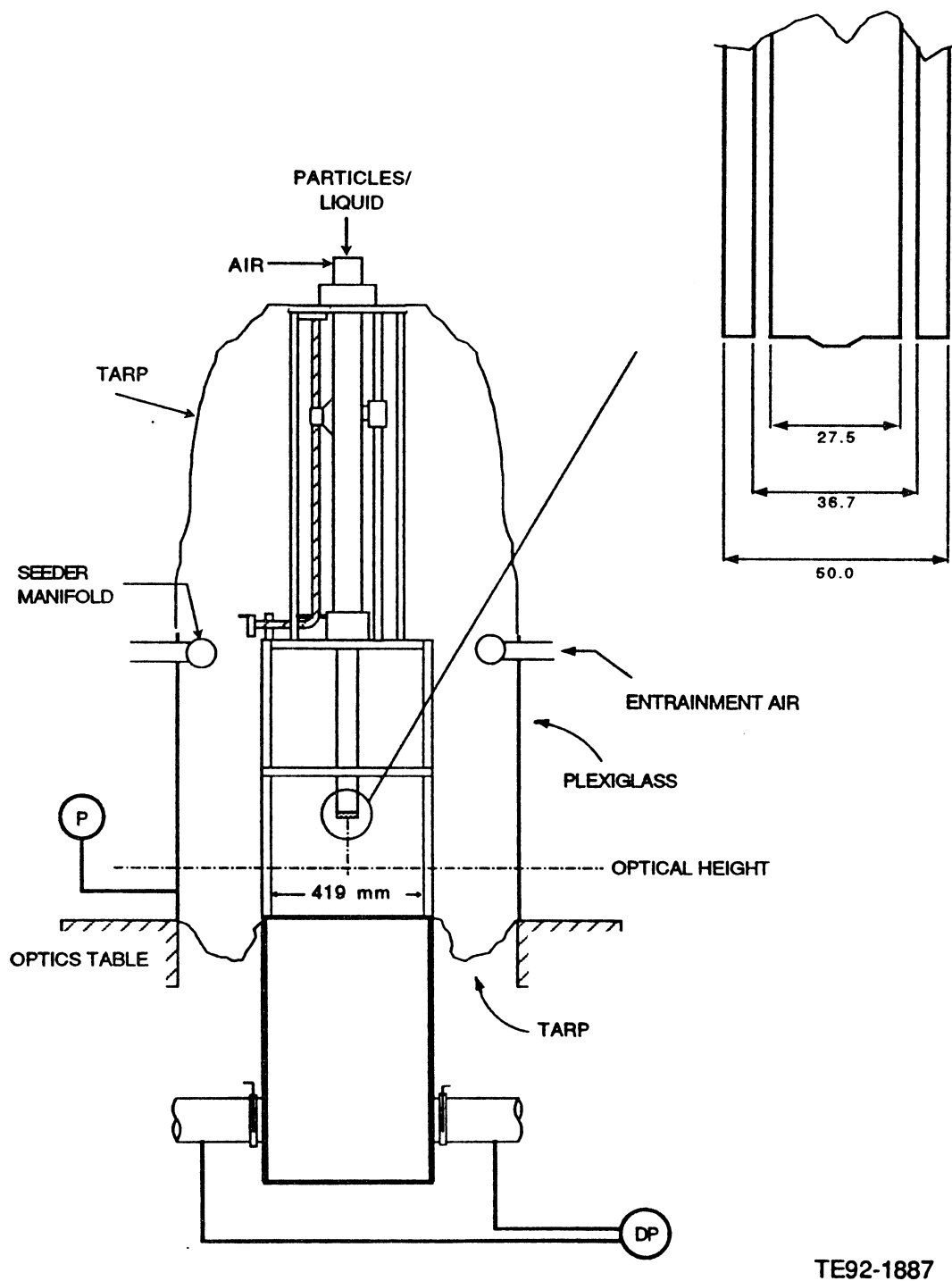


Figure 4.8.1-1. Geometry utilized for unconfined methanol spray with annular coflow.

a) Mean and Fluctuating Axial Velocities

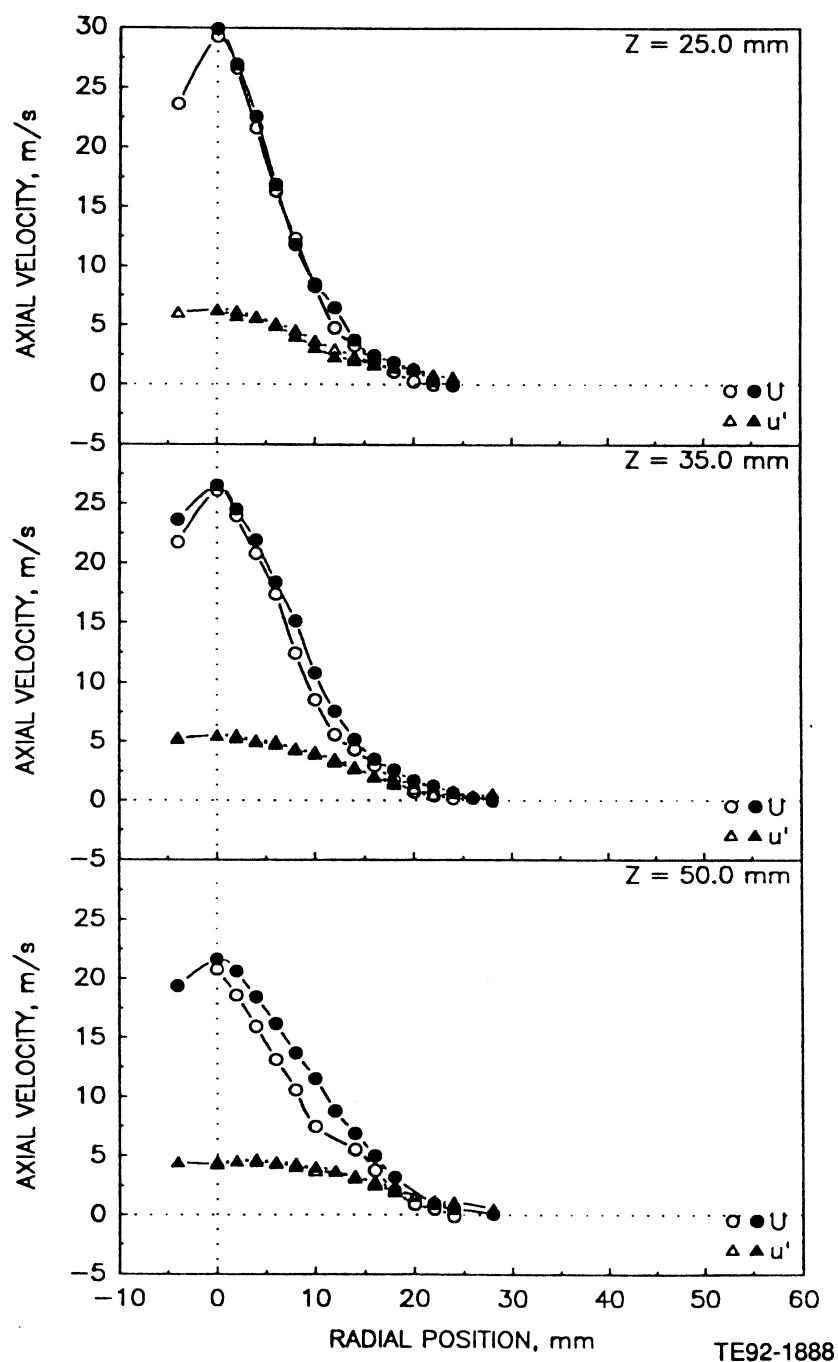


Figure 4.8.1-2. Radial profiles of the gas phase measurements in the unconfined methanol spray with annular coflow (1 of 5).

b) Mean and Fluctuating Radial Velocities

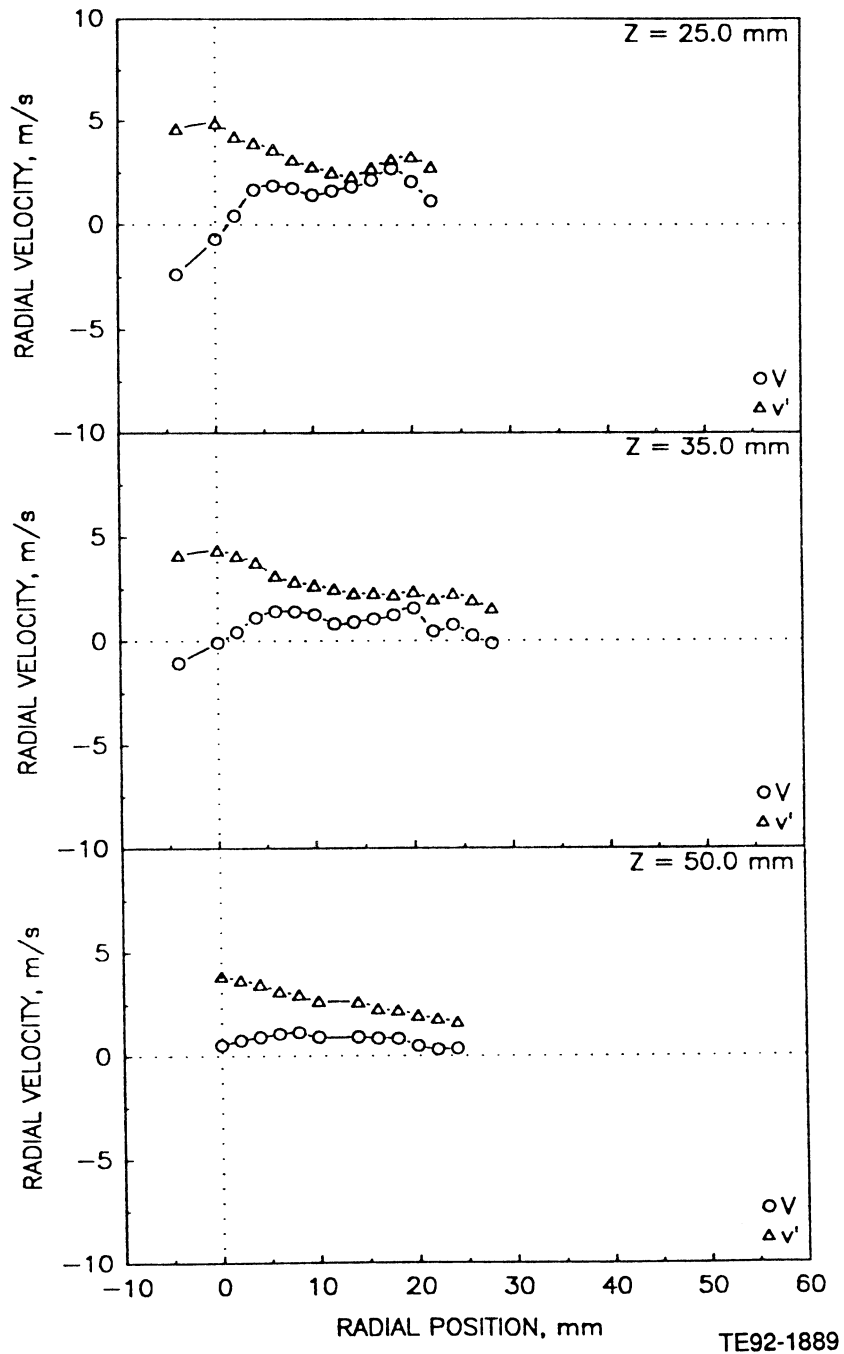
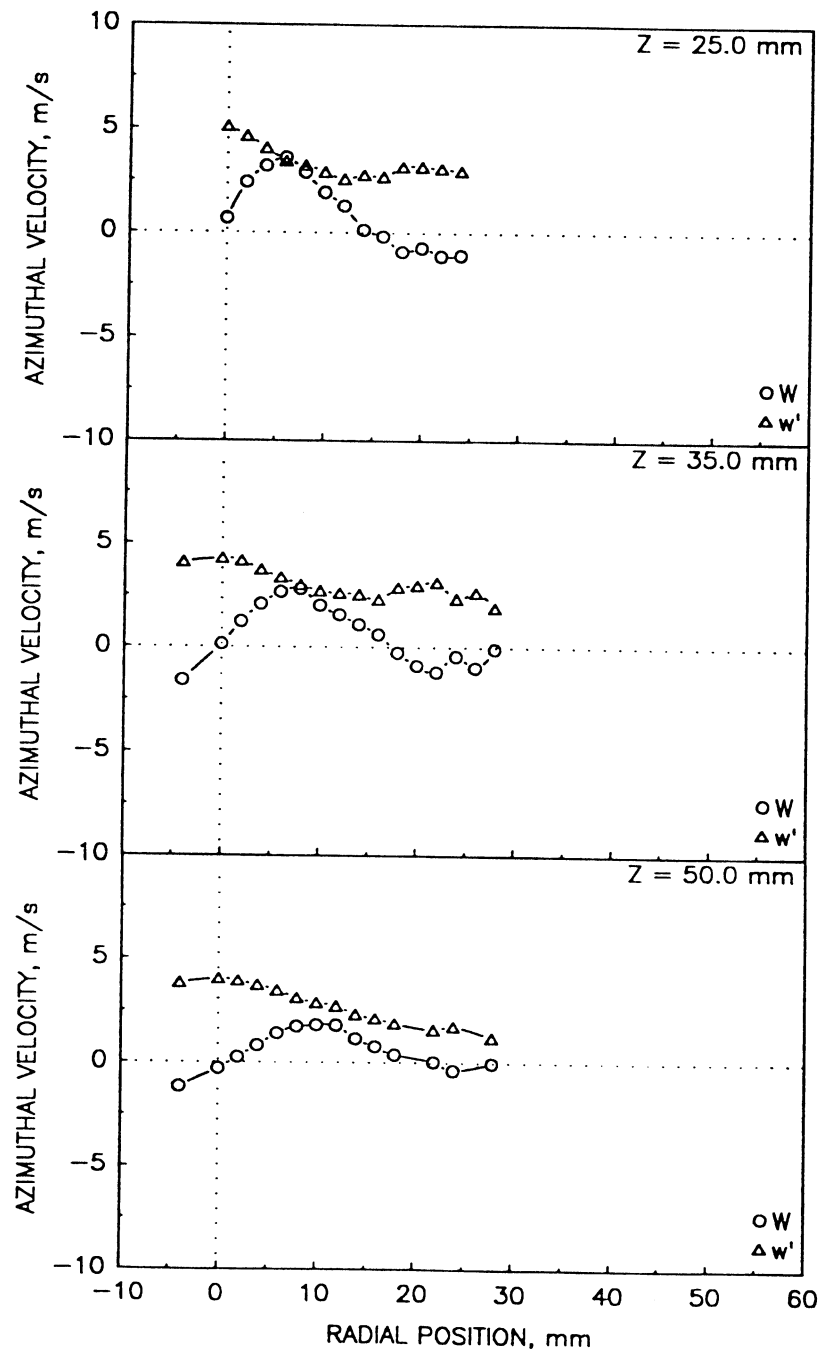


Figure 4.8.1-2. Radial profiles of the gas phase measurements in the unconfined methanol spray with annular coflow (2 of 5).

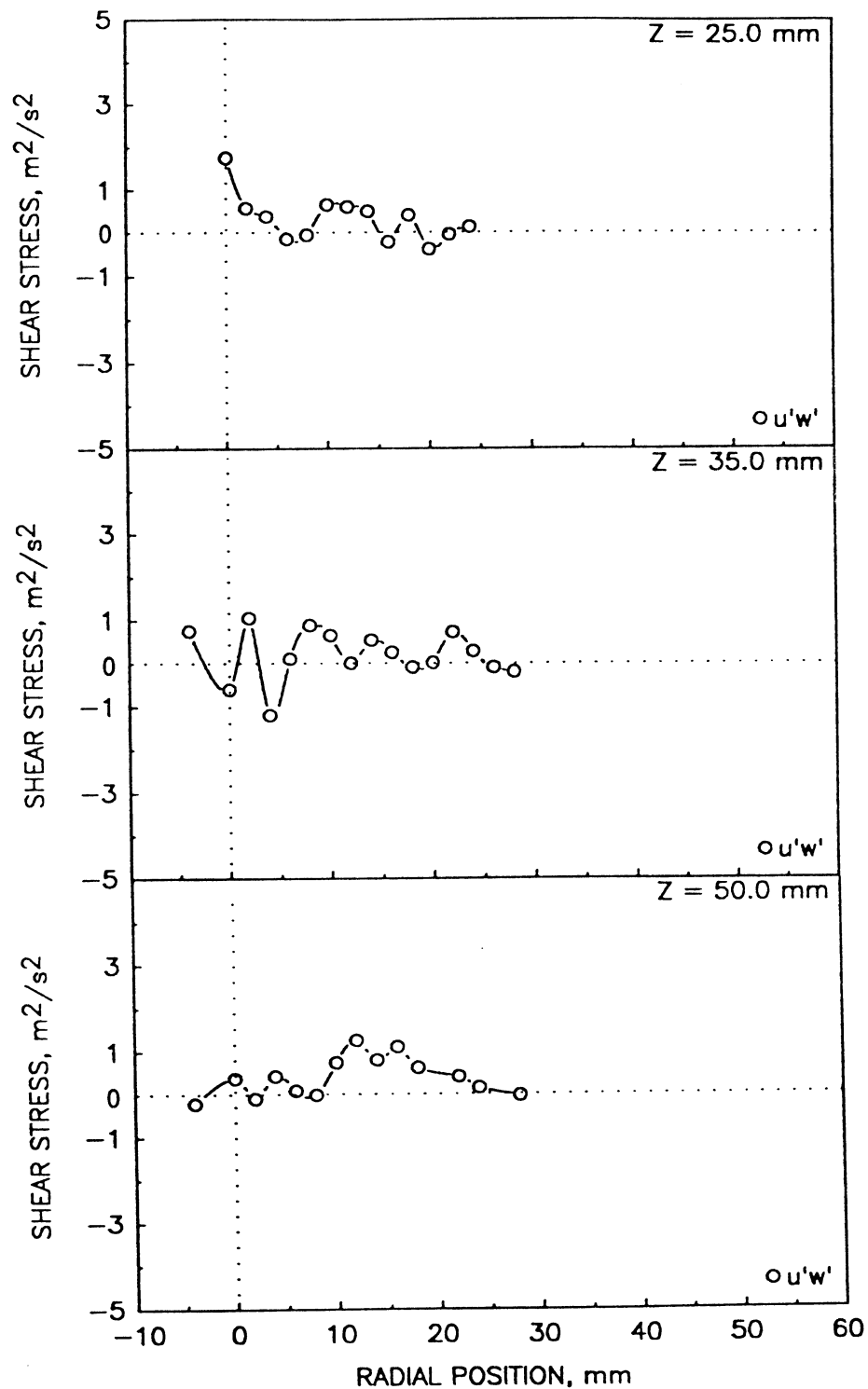
c) Mean and Fluctuating Azimuthal Velocities



TE92-1890

Figure 4.8.1-2. Radial profiles of the gas phase measurements in the unconfined methanol spray with annular coflow (3 of 5).

e) Shear Stress Based on Axial and Azimuthal Velocities



TE92-1892

Figure 4.8.1-2. Radial profiles of the gas phase measurements in the unconfined methanol spray with annular coflow (4 of 5).

d) Shear Stress Based on Axial and Radial Velocities

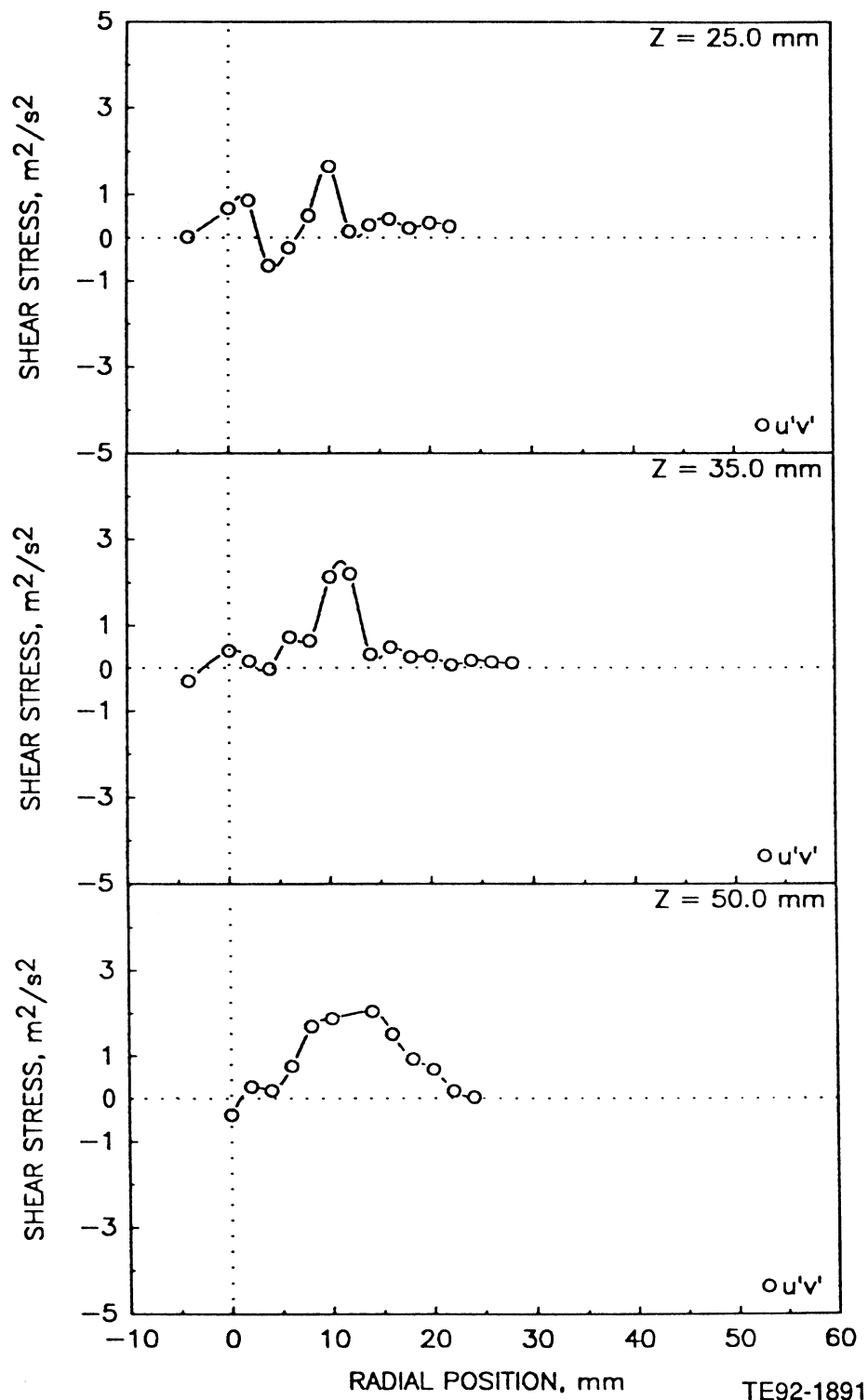
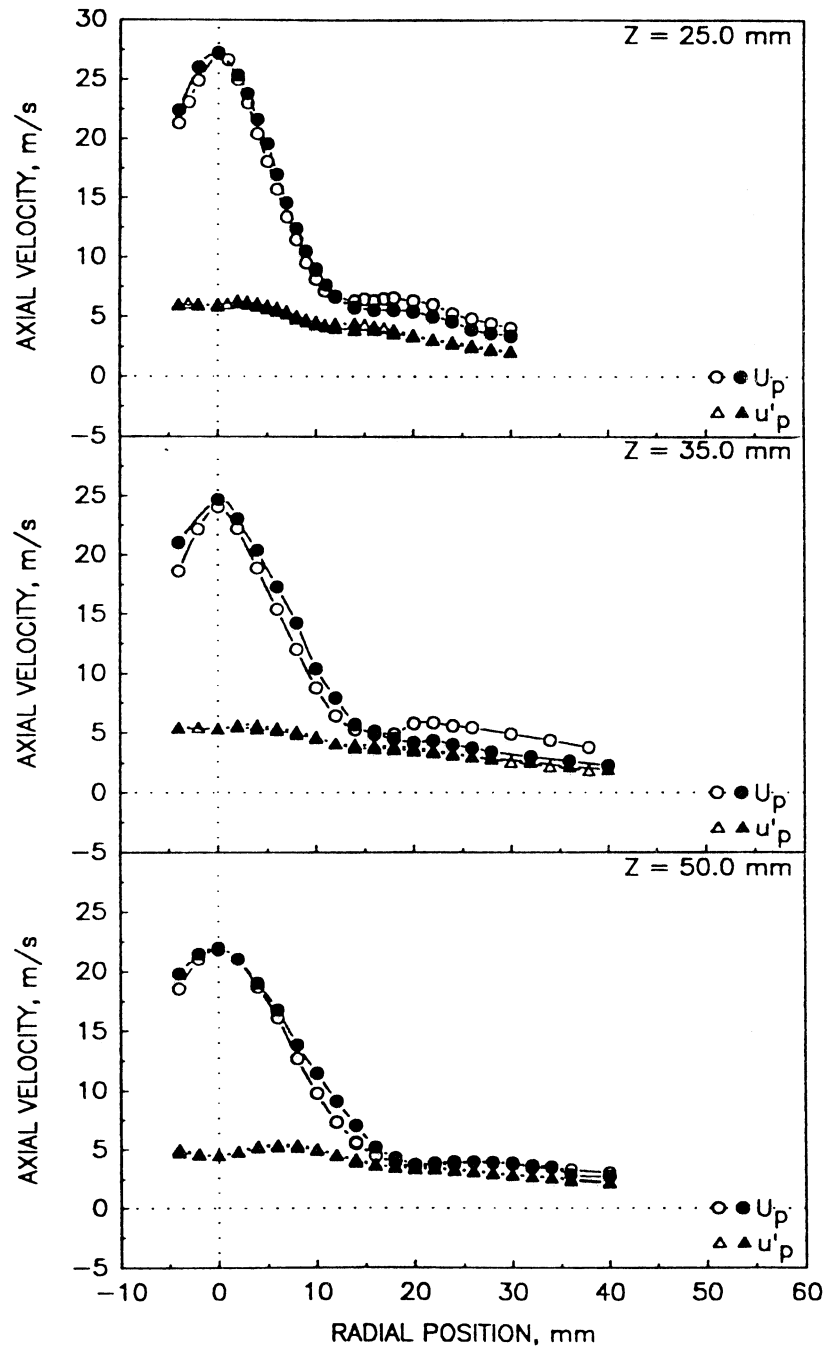


Figure 4.8.1-2. Radial profiles of the gas phase measurements in the unconfined methanol spray with annular coflow (5 of 5).

a) Mean and Fluctuating Axial Velocities



TE92-1893

Figure 4.8.2-1. Radial profiles of the droplet measurements in the unconfined methanol spray with annular air (1 of 4).

b) Mean and Fluctuating Radial Velocities

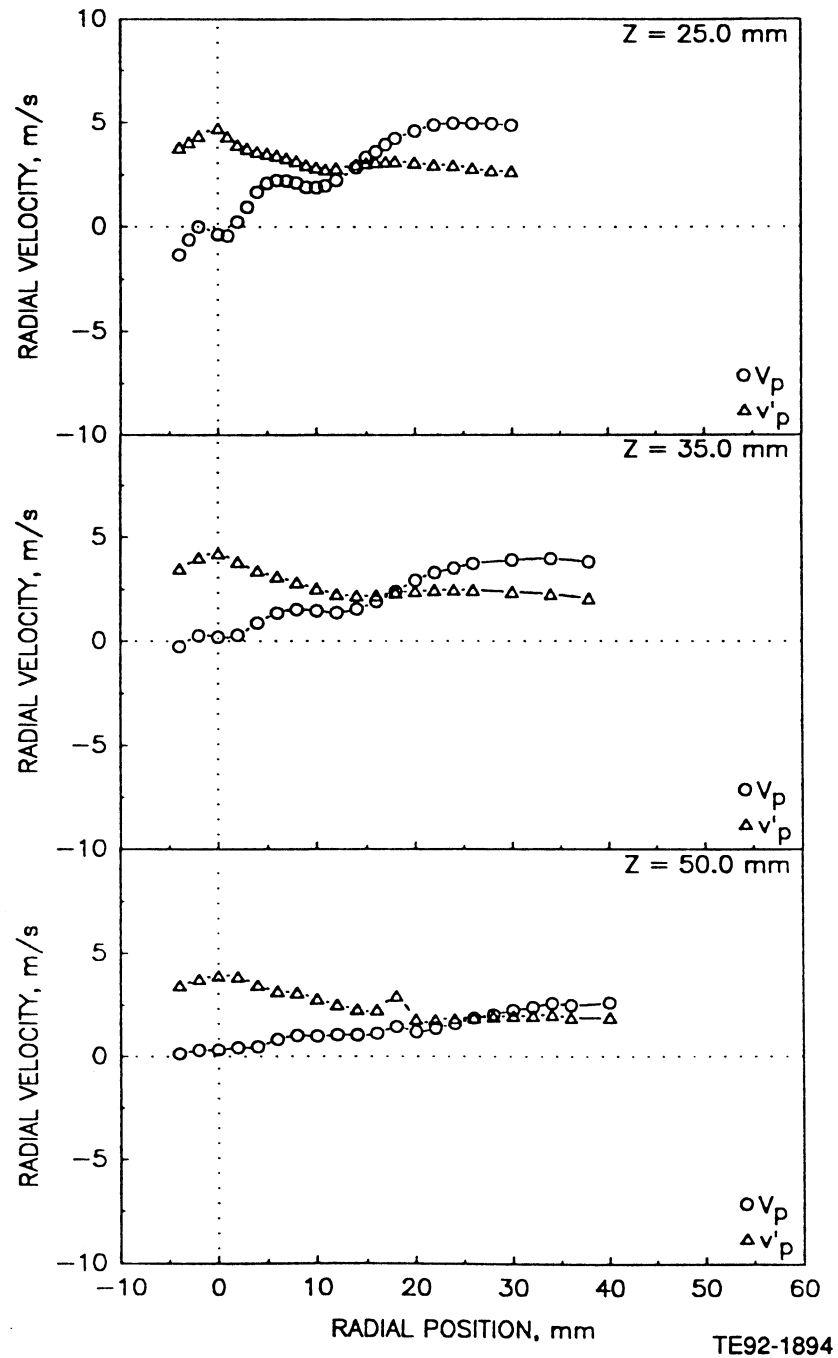


Figure 4.8.2-1. Radial profiles of the droplet measurements in the unconfined methanol spray with annular air (2 of 4).

c) Mean and Fluctuating Azimuthal Velocities

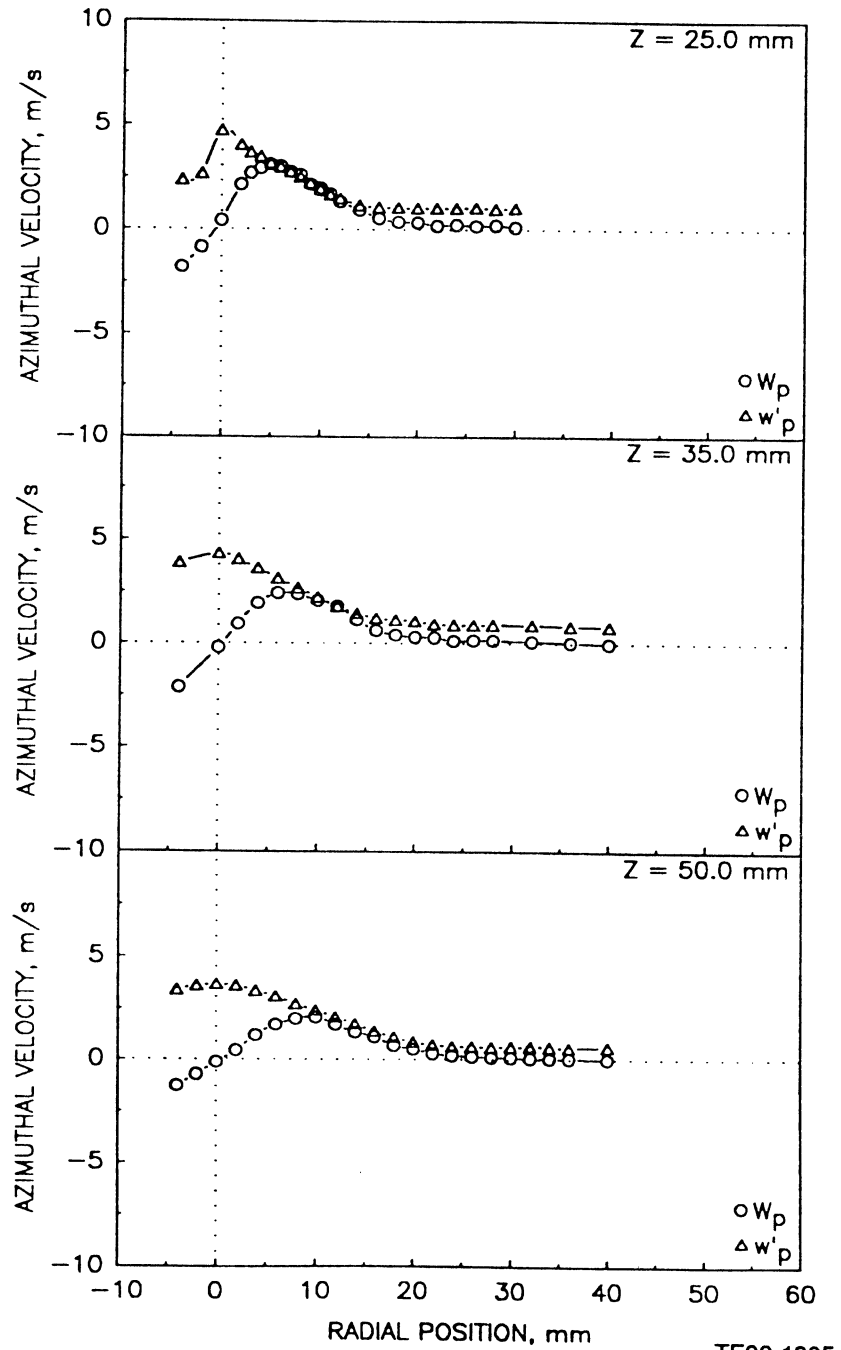


Figure 4.8.2-1. Radial profiles of the droplet measurements in the unconfined methanol spray with annular air (3 of 4).

d) Sauter Mean Diameter

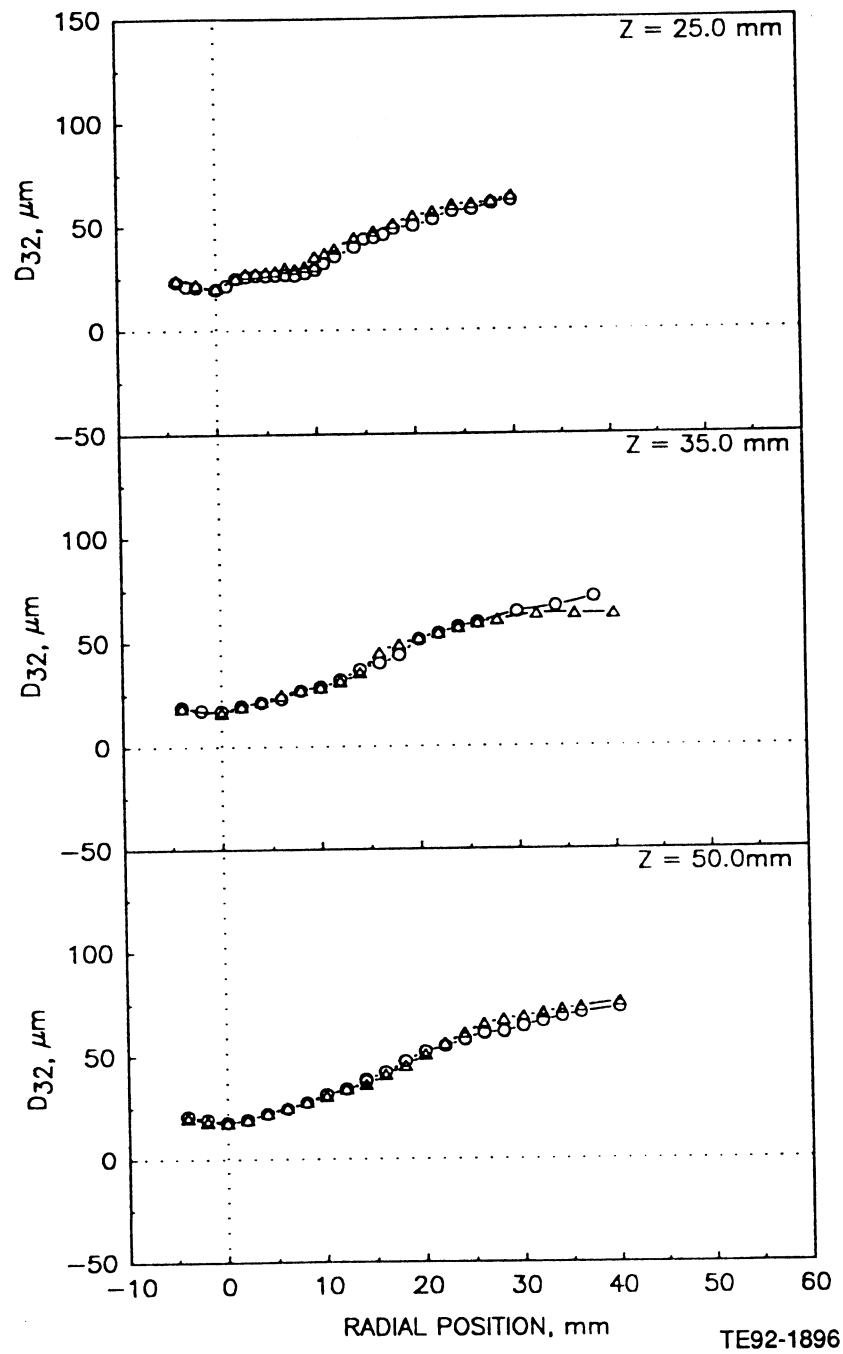
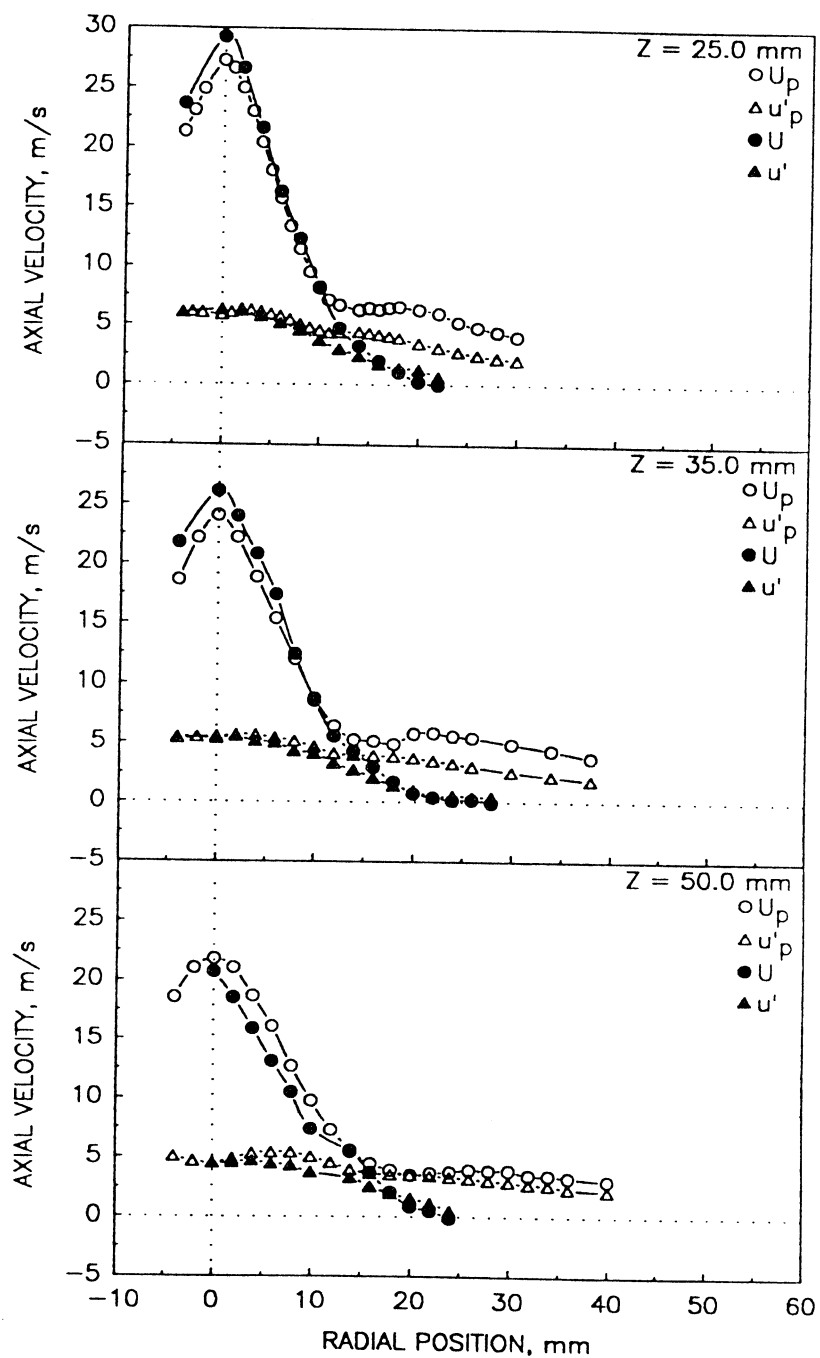


Figure 4.8.2-1. Radial profiles of the droplet measurements in the unconfined methanol spray with annular air (4 of 4).

a) Mean and Fluctuating Axial Velocities



TE92-1897

Figure 4.8.2-2. Comparison of the gas phase and droplet velocities in the unconfined methanol spray with annular coflow (1 of 2).

b) Mean and Fluctuating Radial Velocities

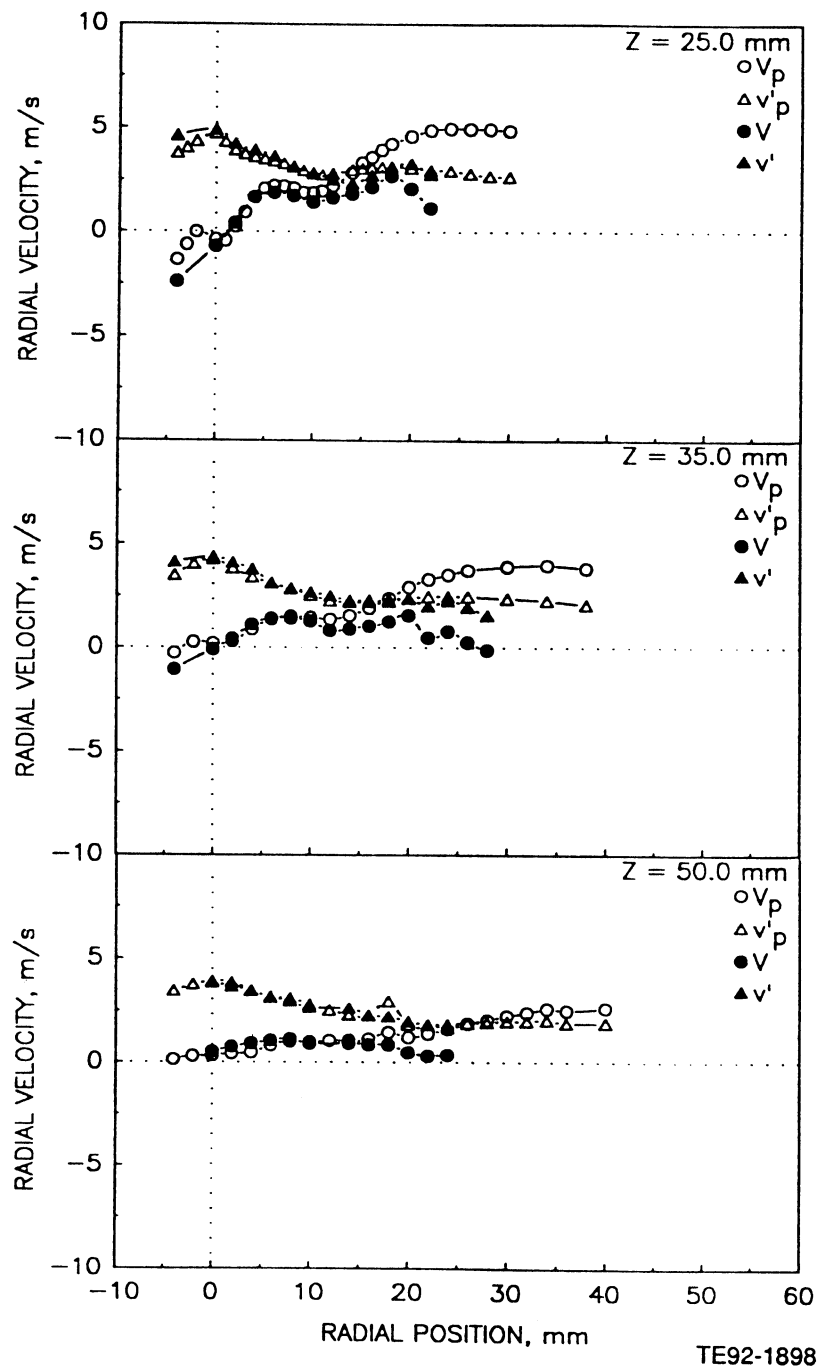


Figure 4.8.2-2. Comparison of the gas phase and droplet velocities in the unconfined methanol spray with annular coflow (2 of 2)

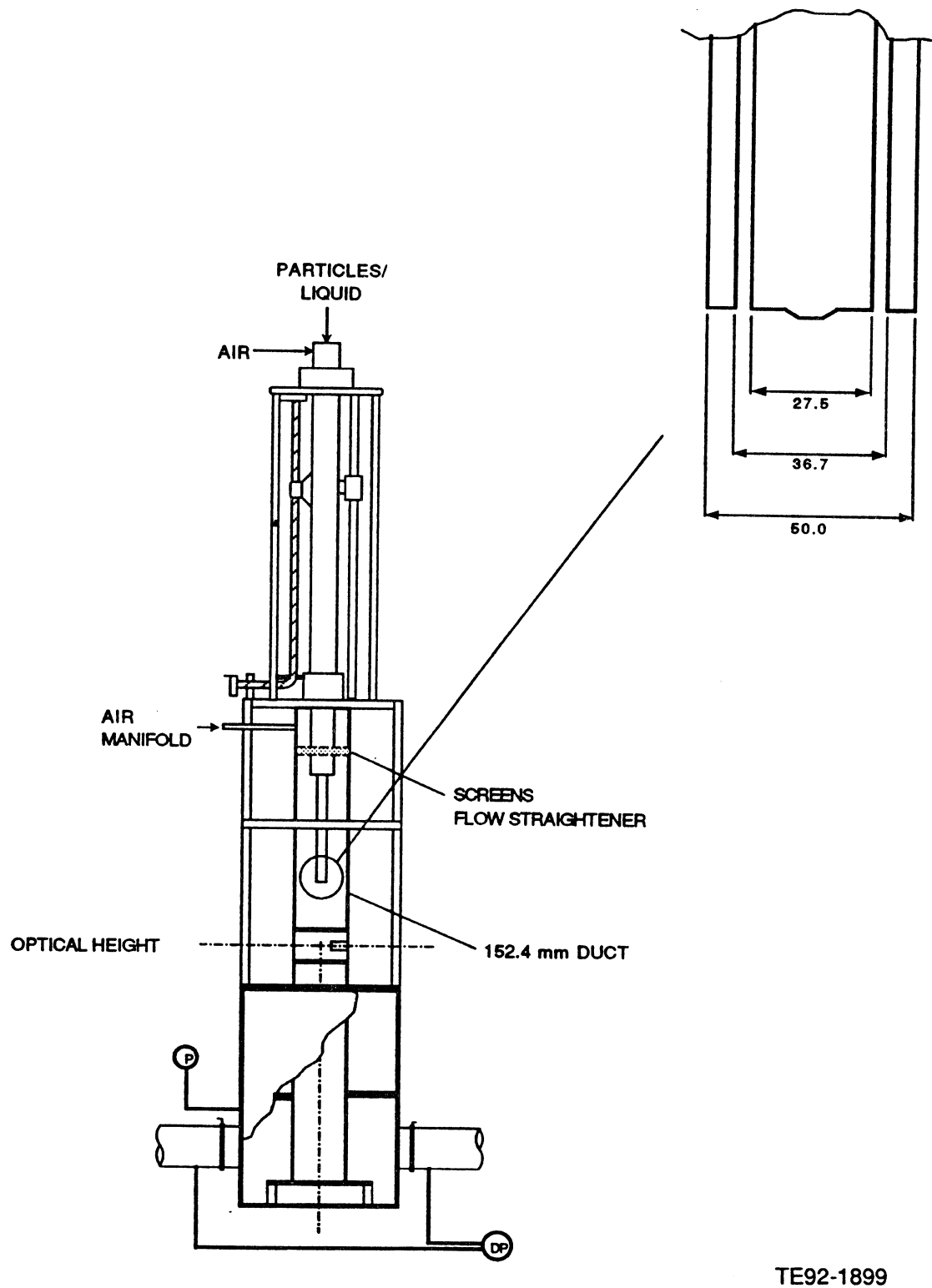
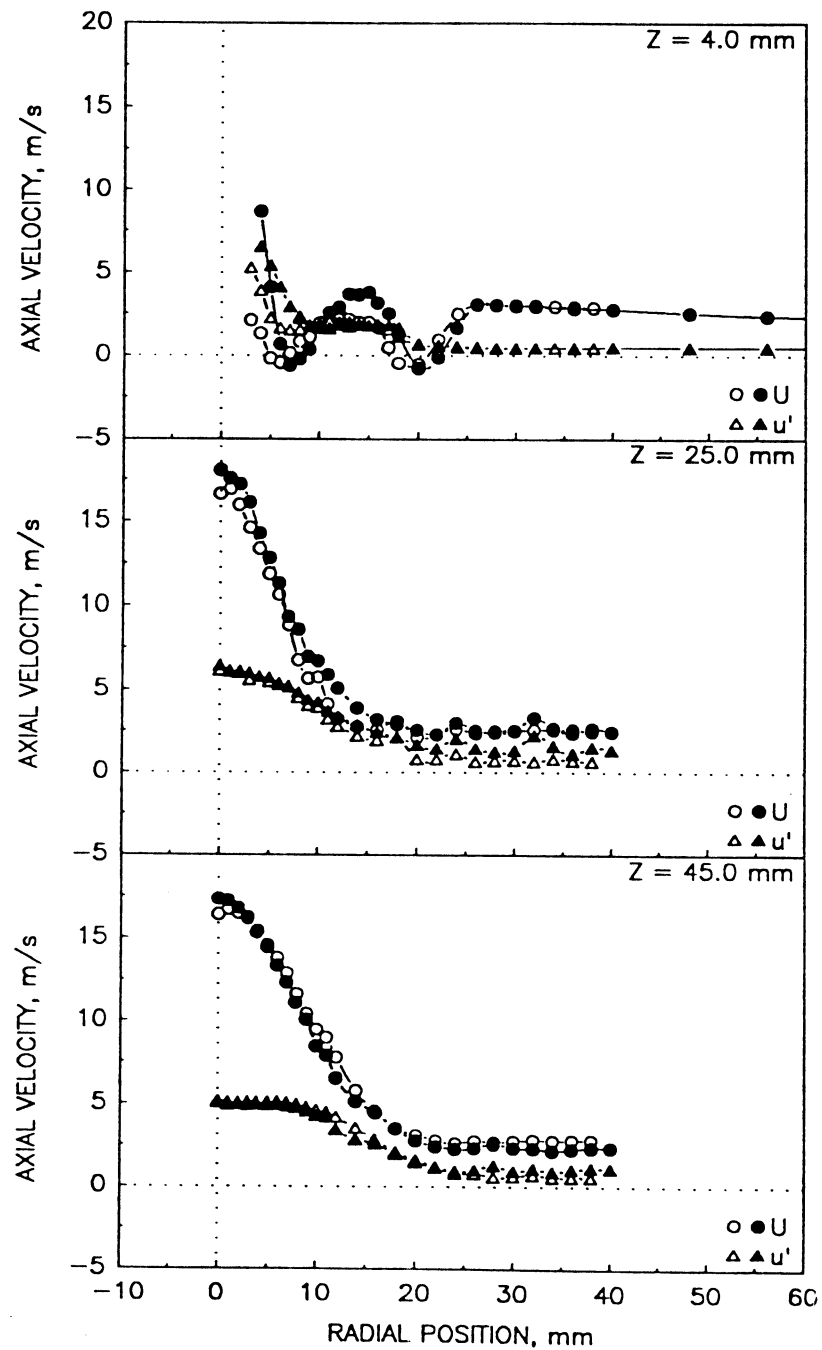


Figure 4.8.3-1. Geometry utilized for the confined methanol spray with annular coflow.

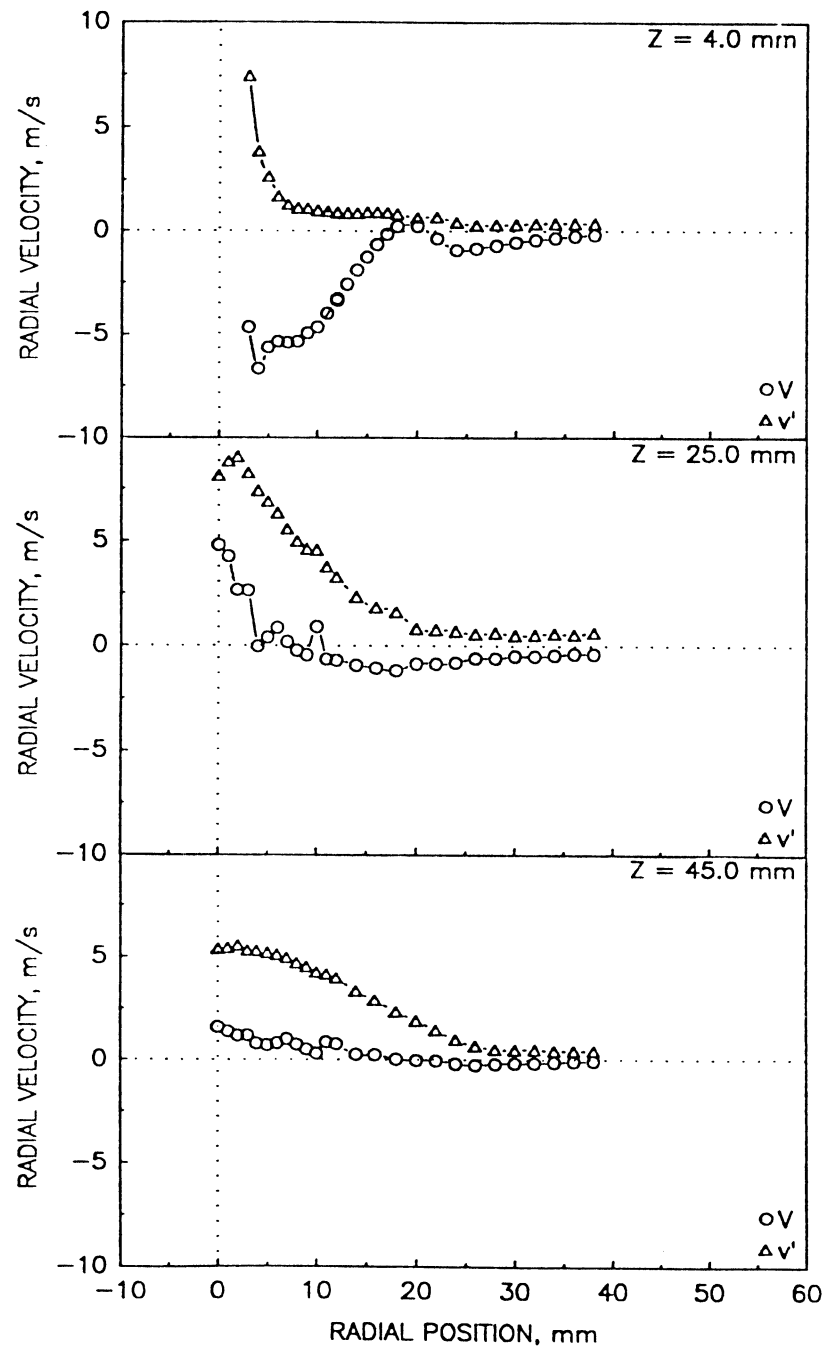
a) Mean and Fluctuating Axial Velocities



TE92-1900

Figure 4.8.3-2. Radial profiles of the gas phase measurements in the confined methanol spray with annular coflow (1 of 5).

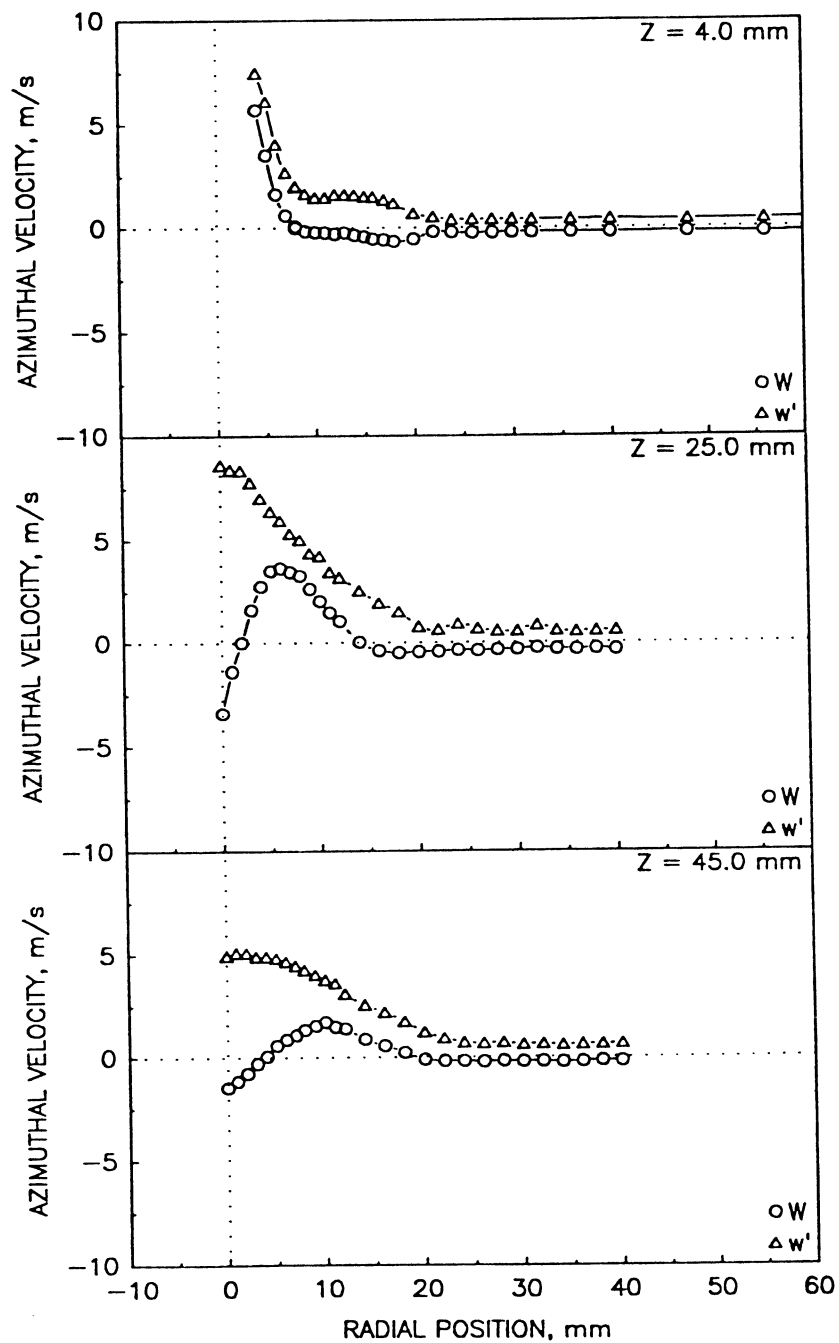
b) Mean and Fluctuating Radial Velocities



TE92-1901

Figure 4.8.3-2. Radial profiles of the gas phase measurements in the confined methanol spray with annular coflow (2 of 5).

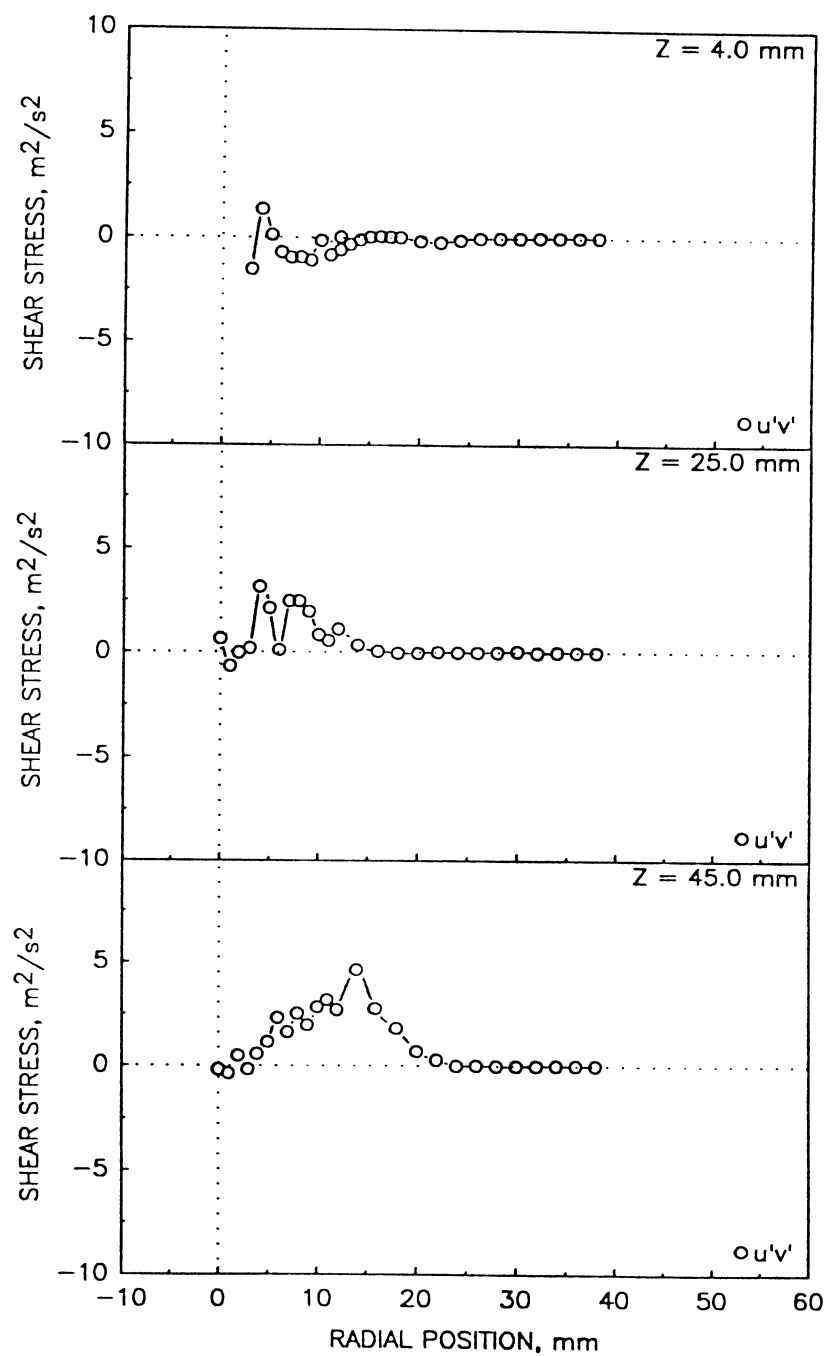
c) Mean and Fluctuating Azimuthal Velocities



TE92-1902

Figure 4.8.3-2. Radial profiles of the gas phase measurements in the confined methanol spray with annular coflow (3 of 5).

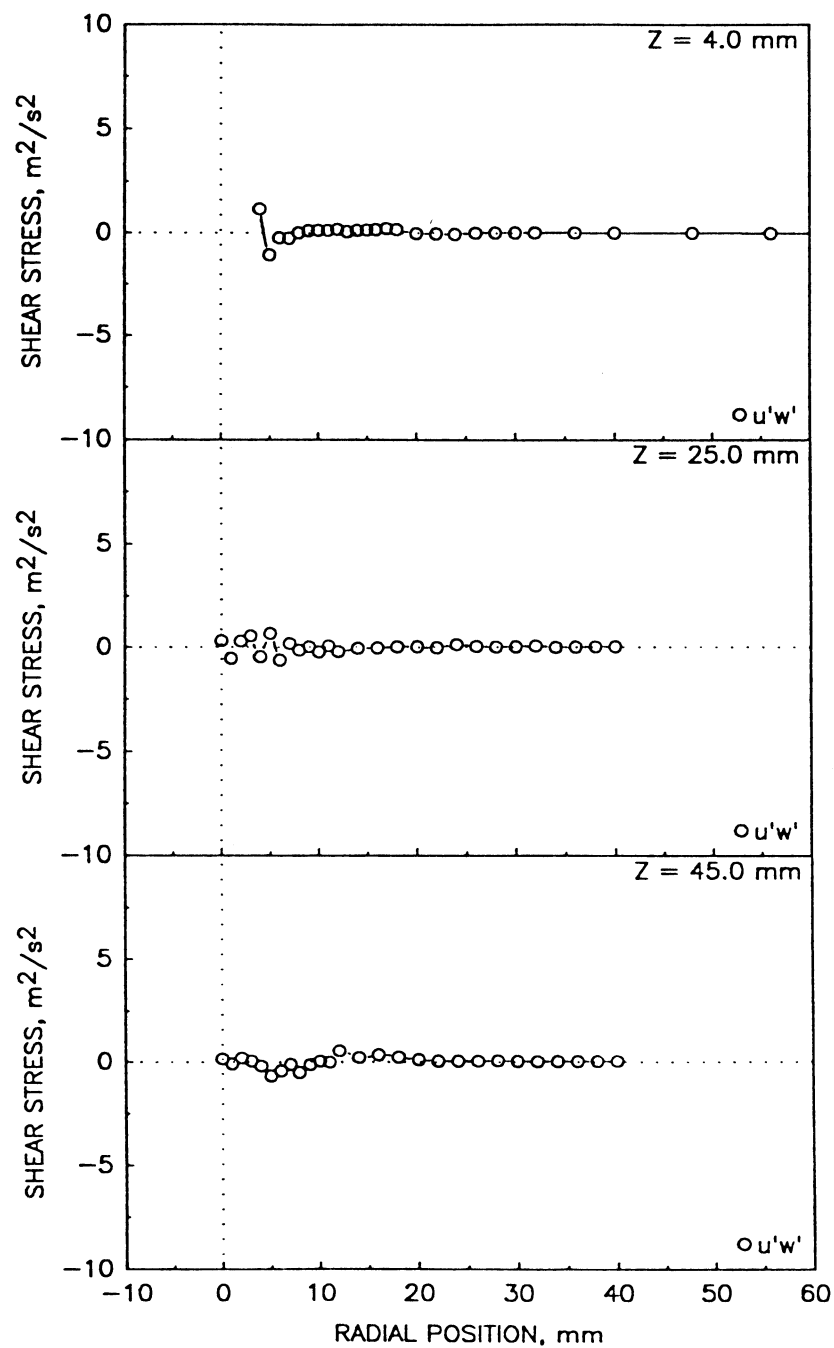
d) Shear Stress Based on Axial and Radial Velocities



TE92-1903

Figure 4.8.3-2. Radial profiles of the gas phase measurements in the confined methanol spray with annular coflow (4 of 5).

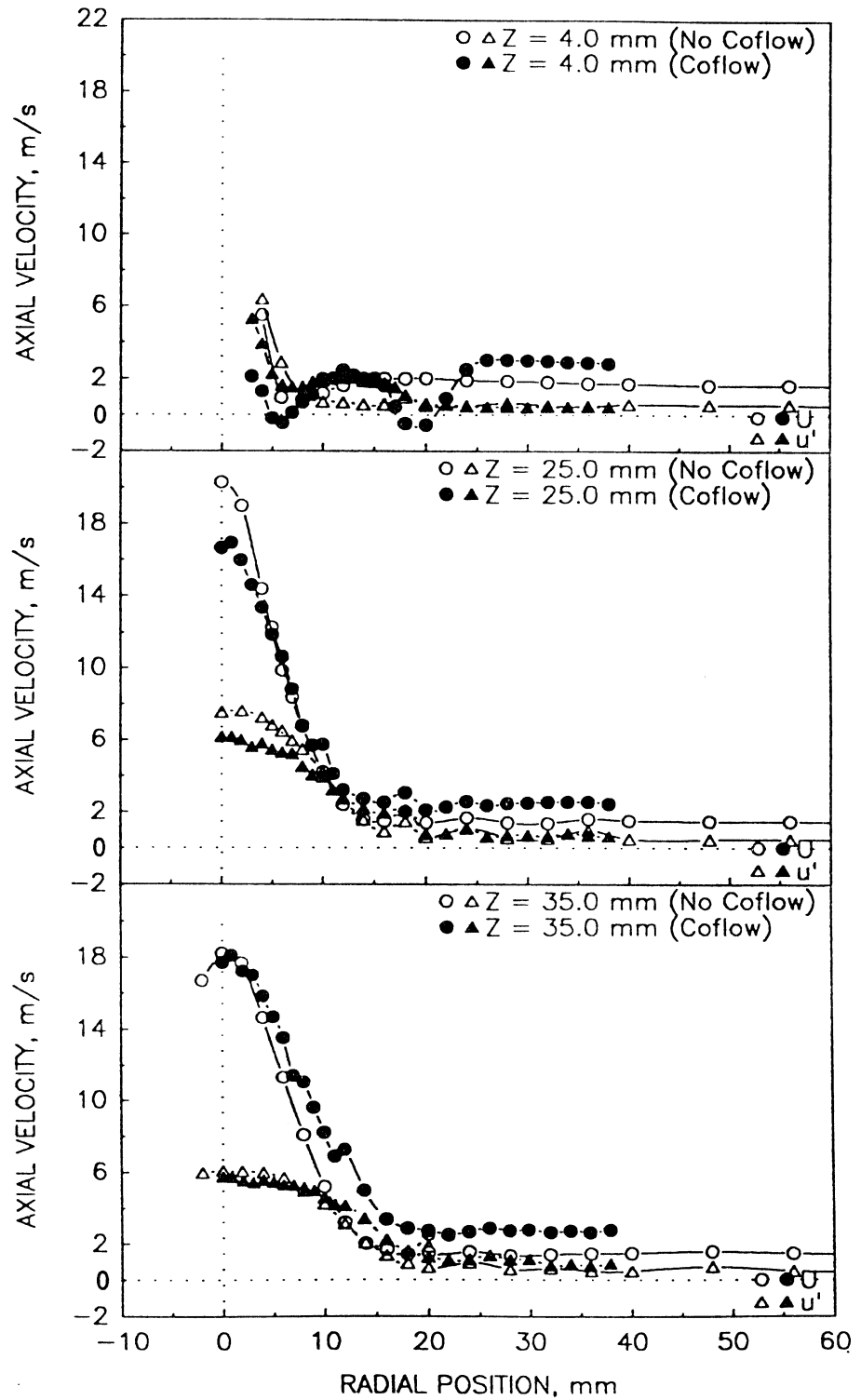
e) Shear Stress Based on Axial and Azimuthal Velocities



TE92-1904

Figure 4.8.3-2. Radial profiles of the gas phase measurements in the confined methanol spray with annular coflow (5 of 5).

a) Mean and Fluctuating Axial Velocities



TE92-1905

Figure 4.8.4-1. Comparison of gas phase velocities in the confined single-phase flow from the air-blast atomizer with and without coflow (1 of 3).

b) Mean and Fluctuating Radial Velocities

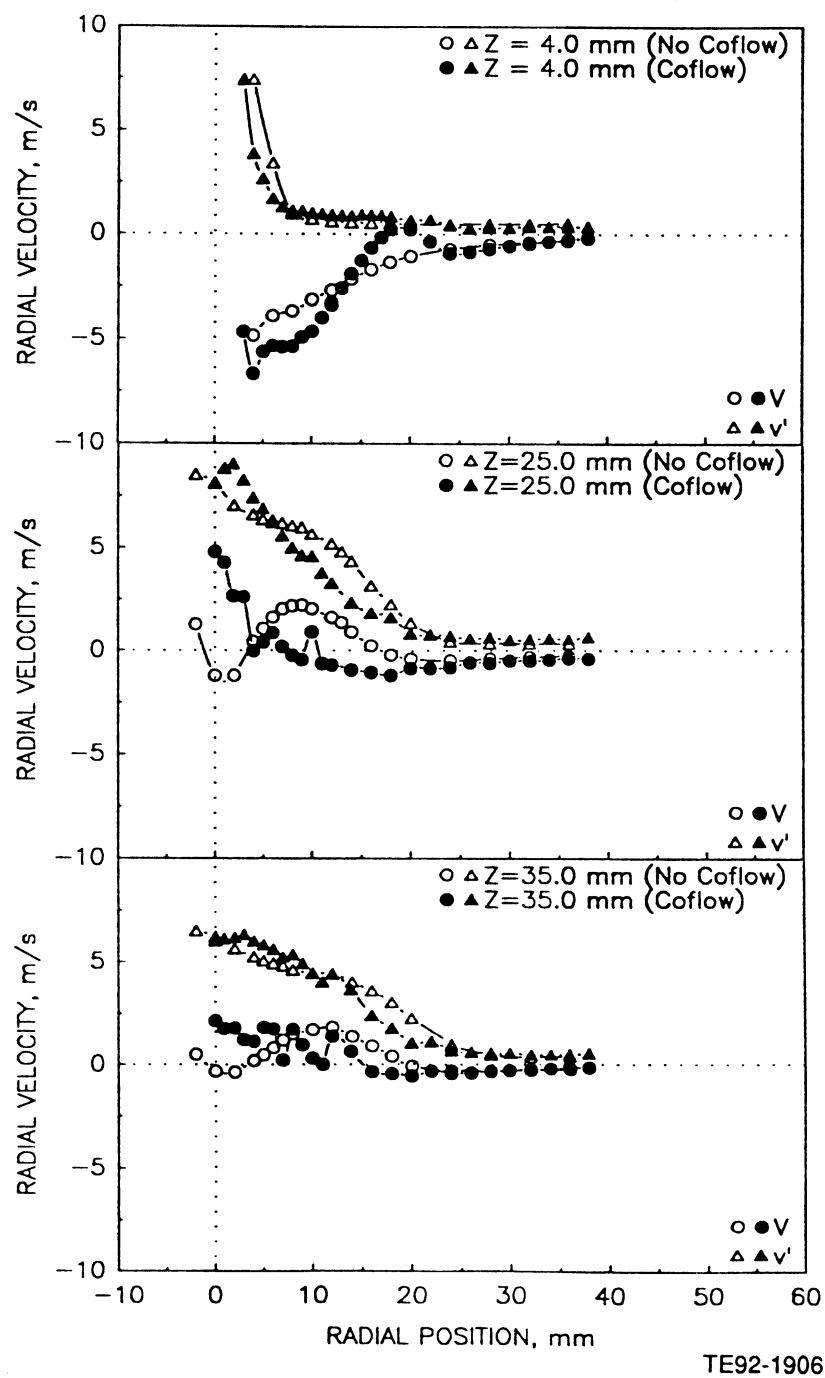


Figure 4.8.4-1. Comparison of gas phase velocities in the confined single-phase flow from the air-blast atomizer with and without coflow (2 of 3).

c) Shear Stress Based on Axial and Radial Velocities

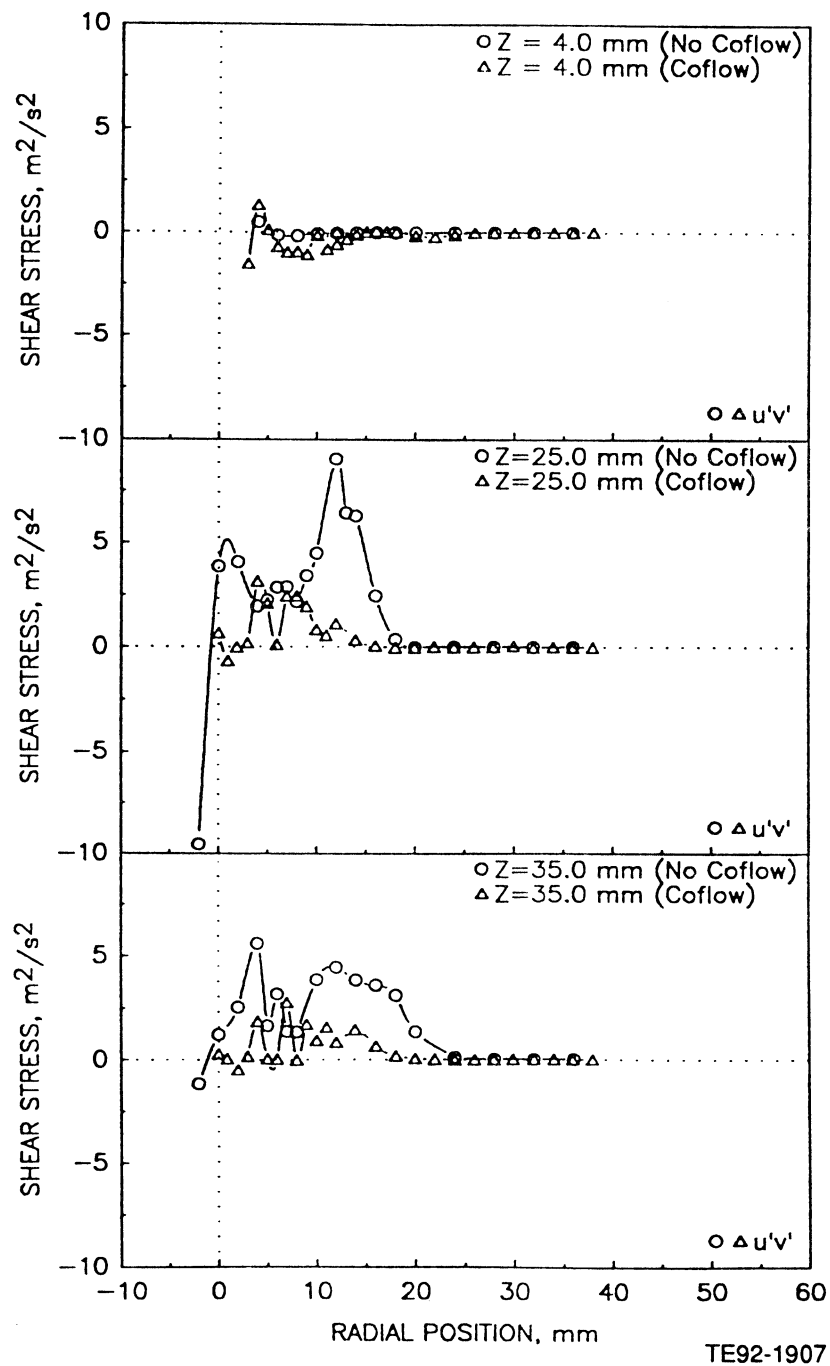


Figure 4.8.4-1. Comparison of gas phase velocities in the confined single-phase flow from the air-blast atomizer with and without coflow (3 of 3).

a) Mean and Fluctuating Axial Velocities

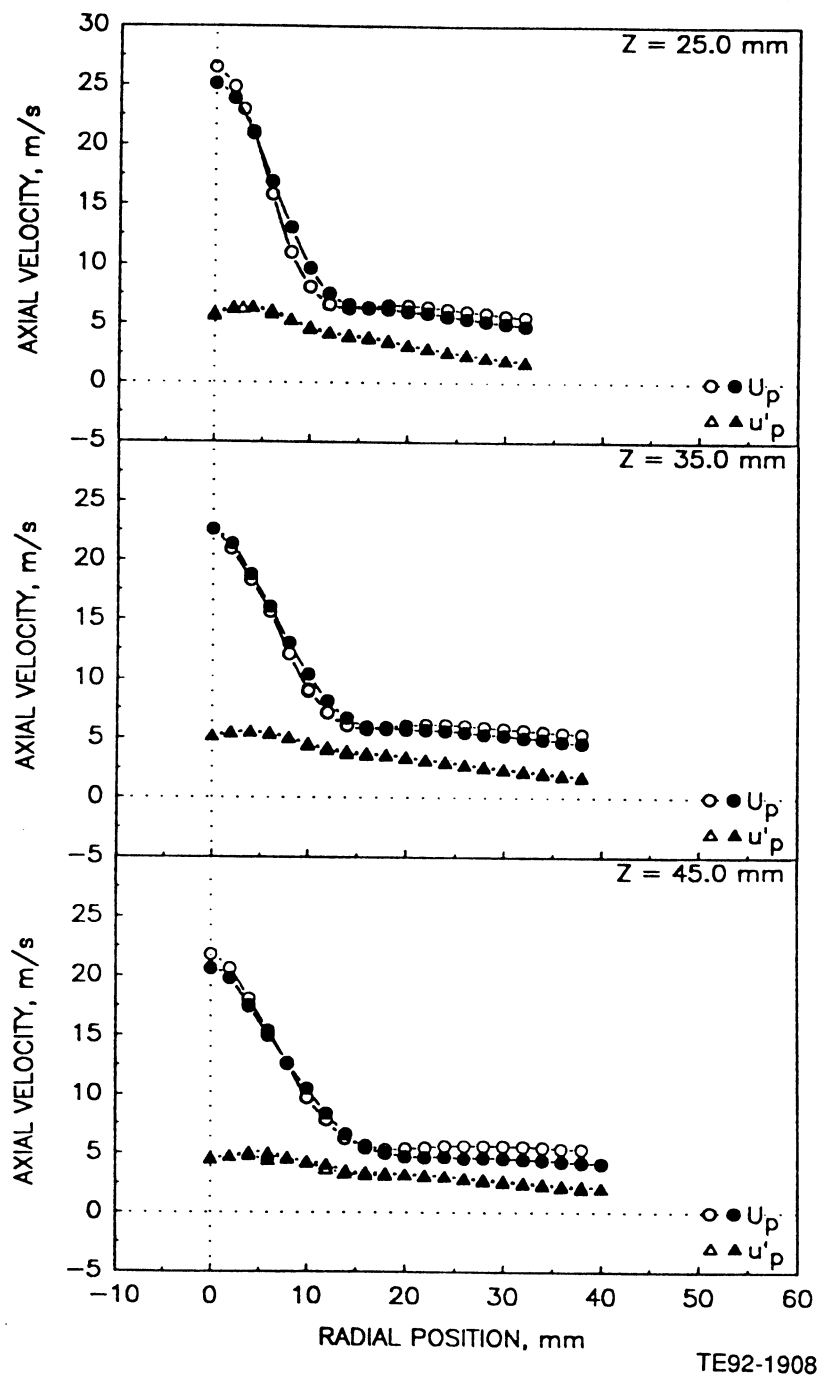


Figure 4.8.5-1. Radial profiles of the droplet measurements in the confined methanol spray with annular coflow (1 of 4).

b) Mean and Fluctuating Radial Velocities

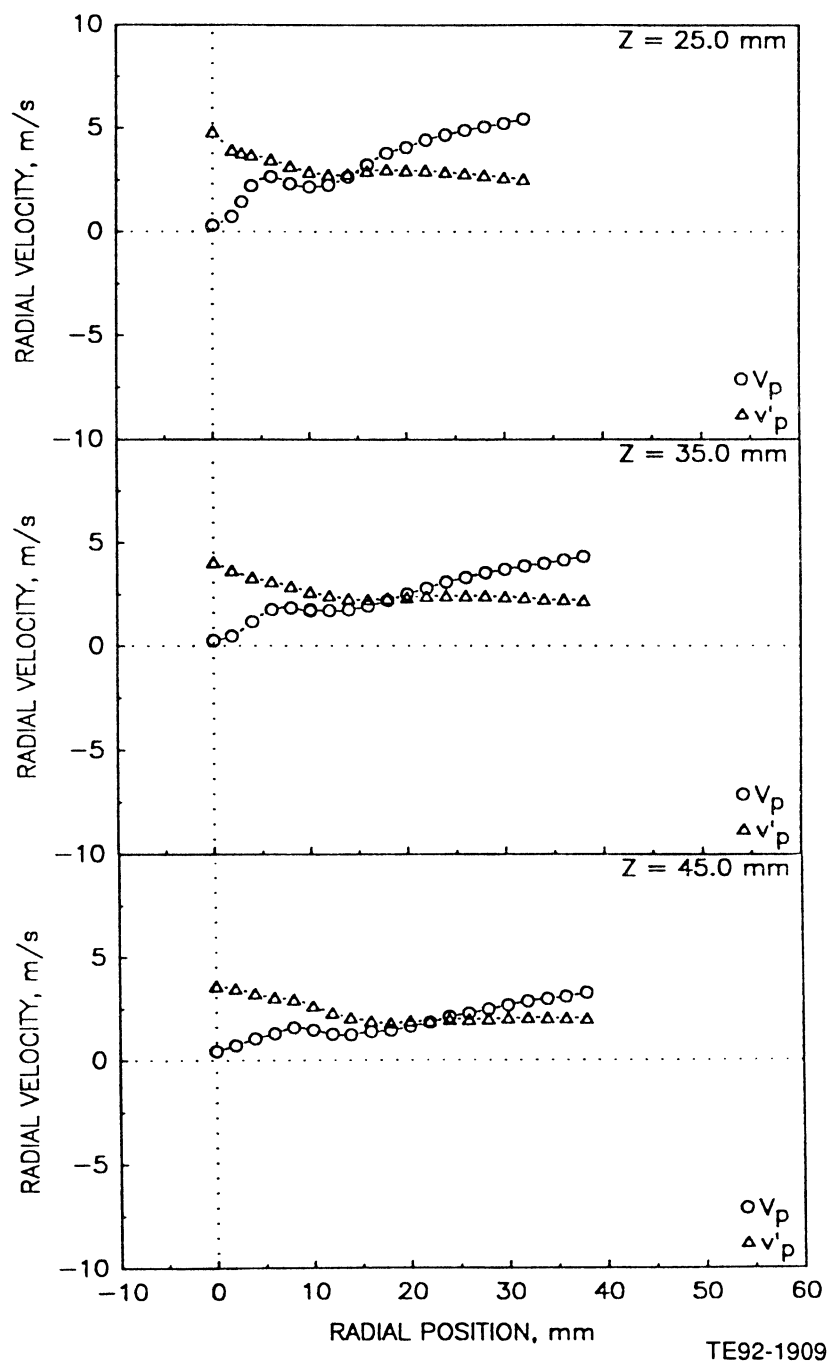


Figure 4.8.5-1. Radial profiles of the droplet measurements in the confined methanol spray with annular coflow (2 of 4).

c) Mean and Fluctuating Azimuthal Velocities

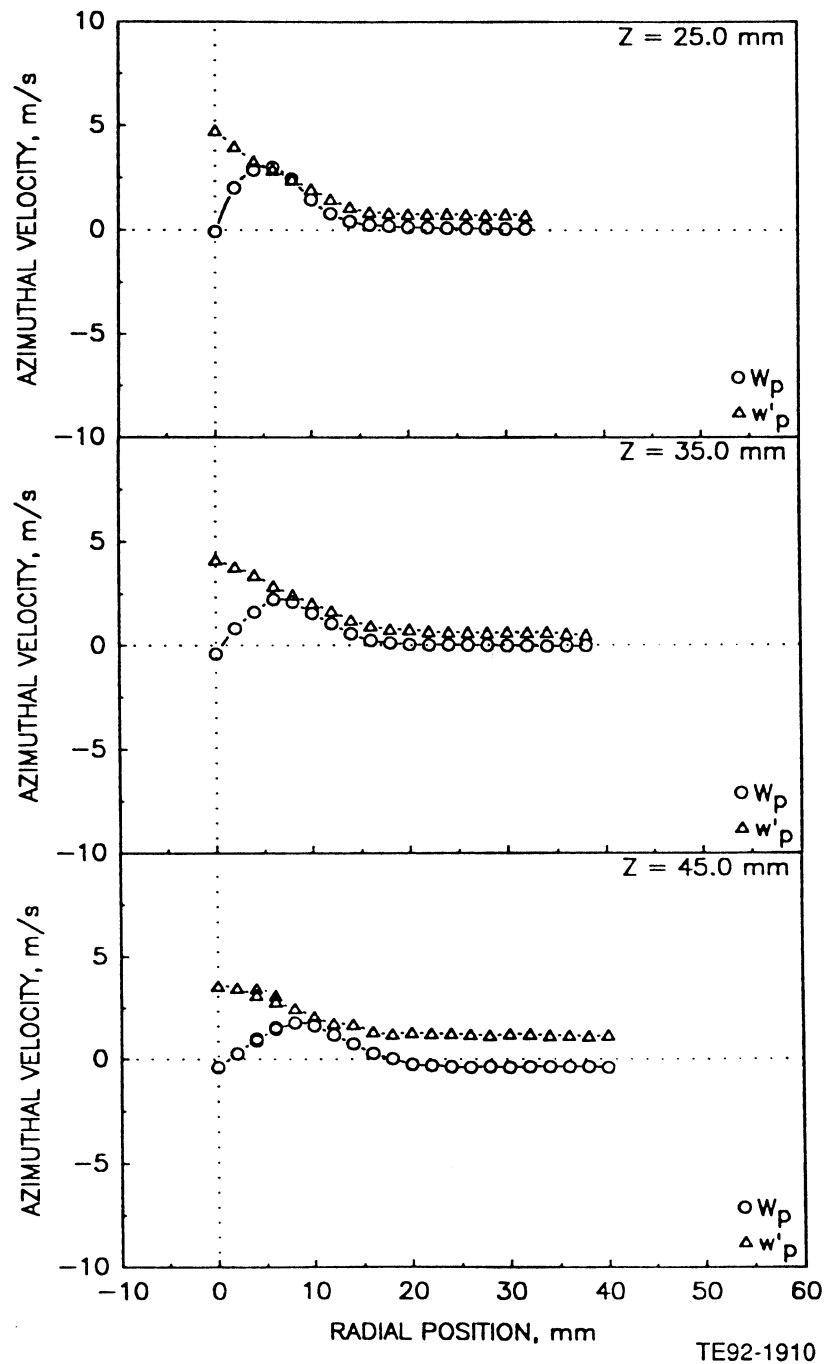
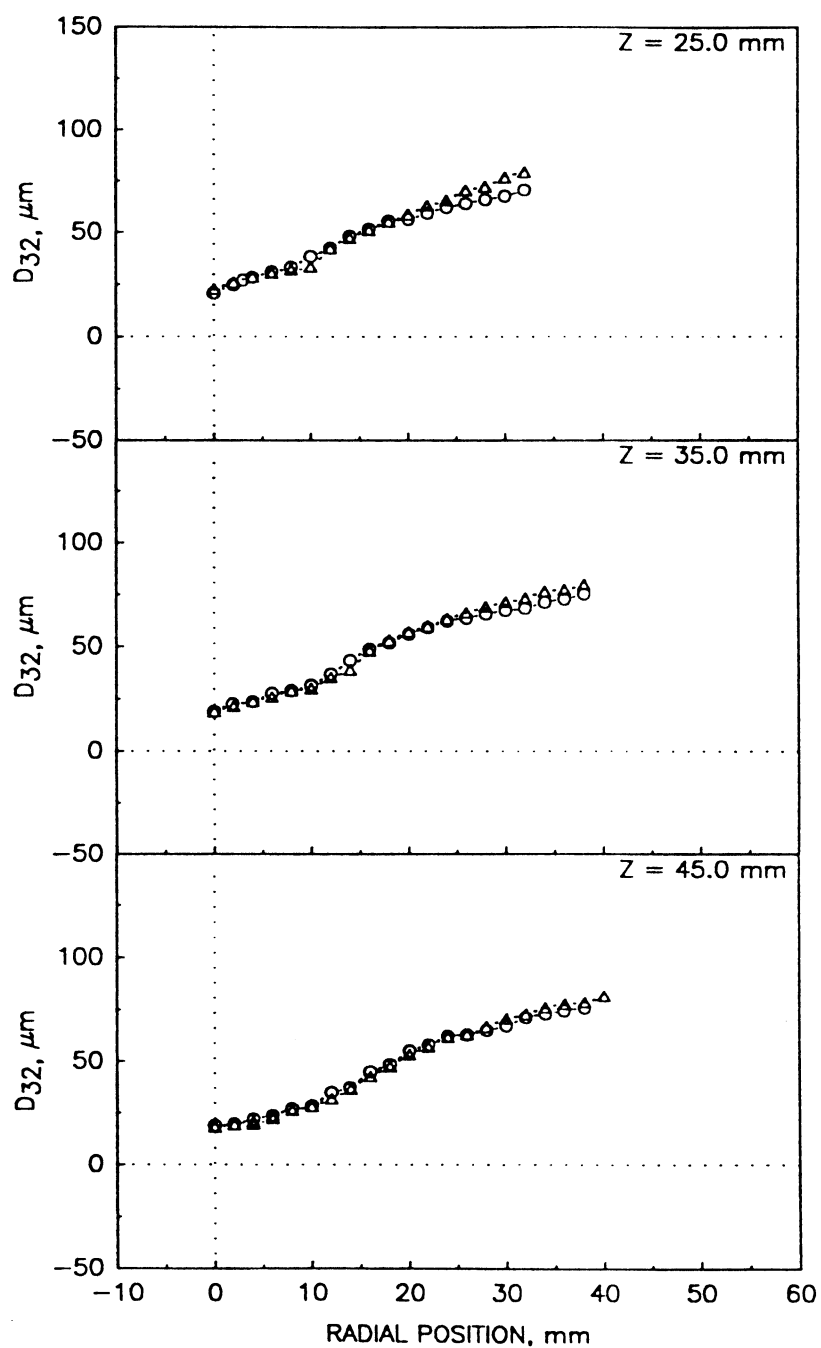


Figure 4.8.5-1. Radial profiles of the droplet measurements in the confined methanol spray with annular coflow (3 of 4).

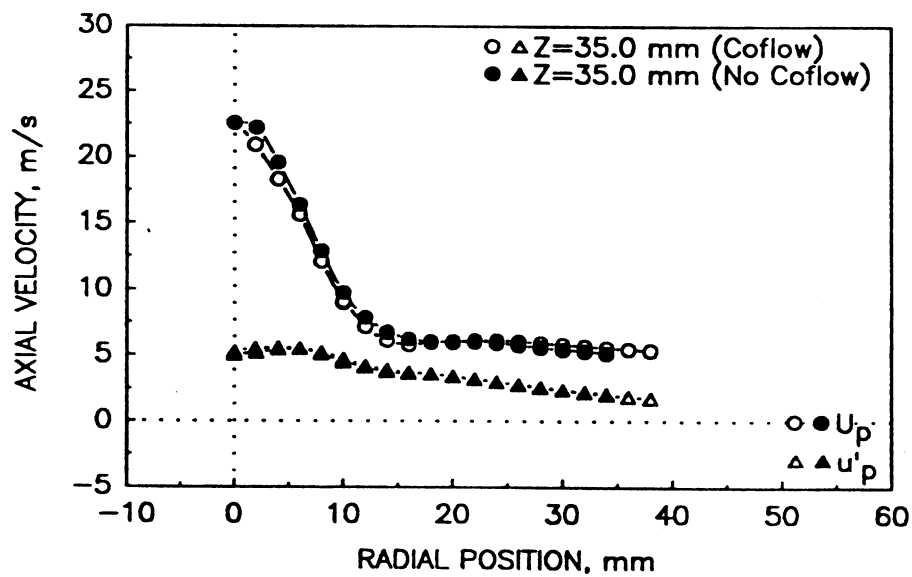
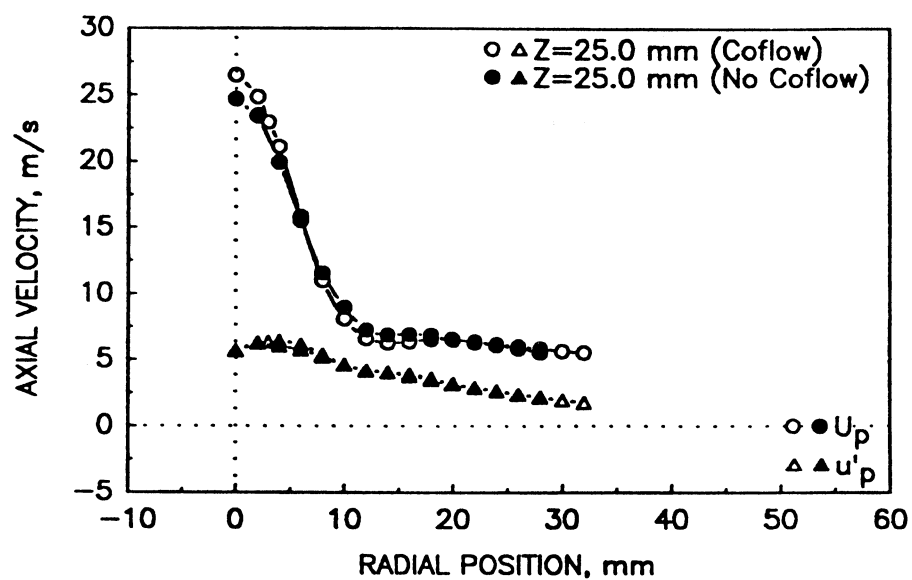
d) Sauter Mean Diameter



TE92-1911

Figure 4.8.5-1. Radial profiles of the droplet measurements in the confined methanol spray with annular coflow (4 of 4).

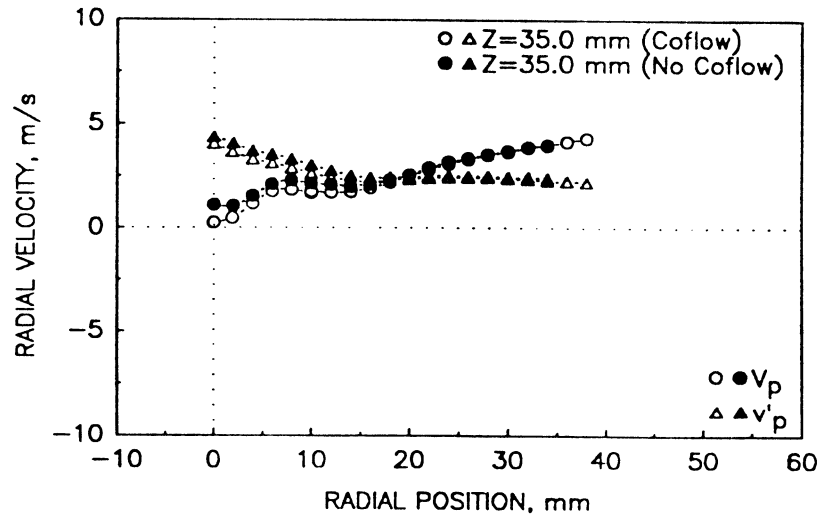
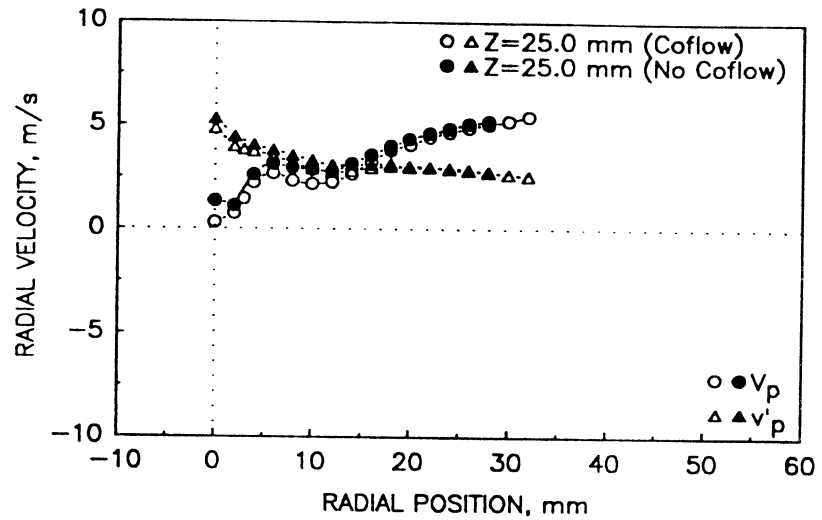
a) Mean and Fluctuating Axial Velocities



TE92-1912

Figure 4.8.6-1. Comparison of droplet measurements in the confined methanol spray with and without coflow (1 of 3).

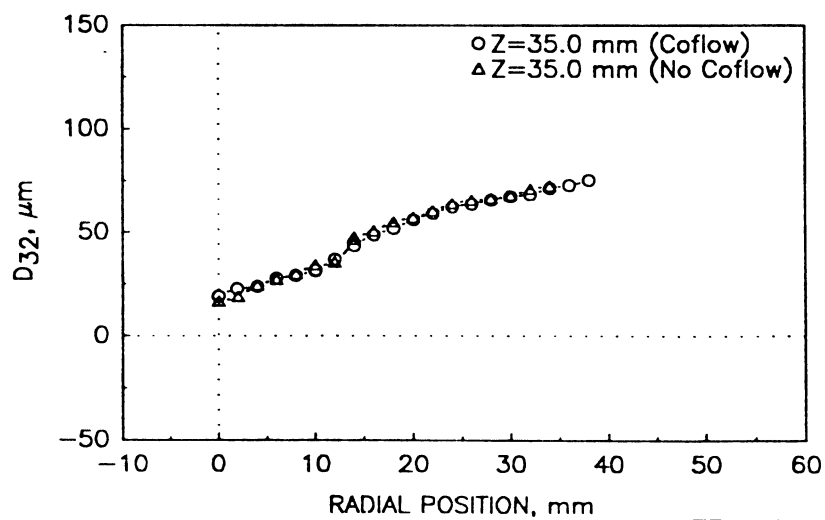
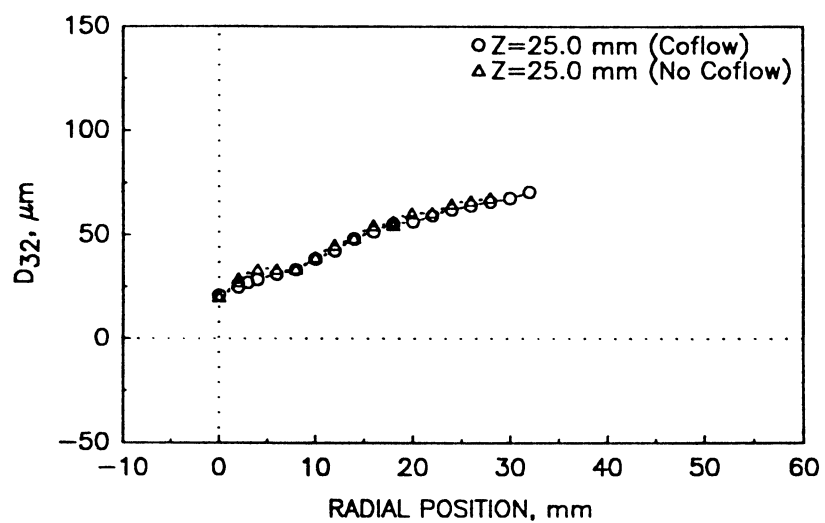
b) Mean and Fluctuating Radial Velocities



TE92-1913

Figure 4.8.6-1. Comparison of droplet measurements in the confined methanol spray with and without coflow (2 of 3).

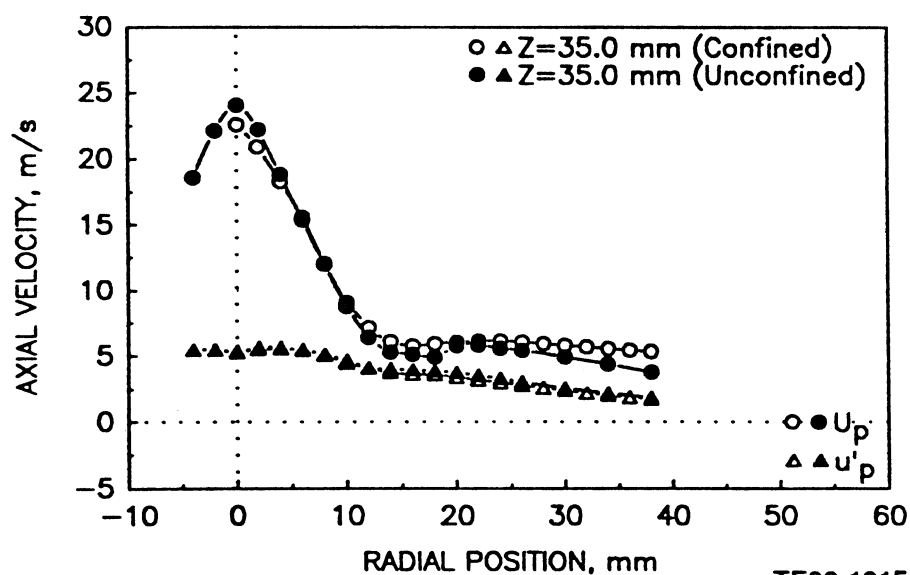
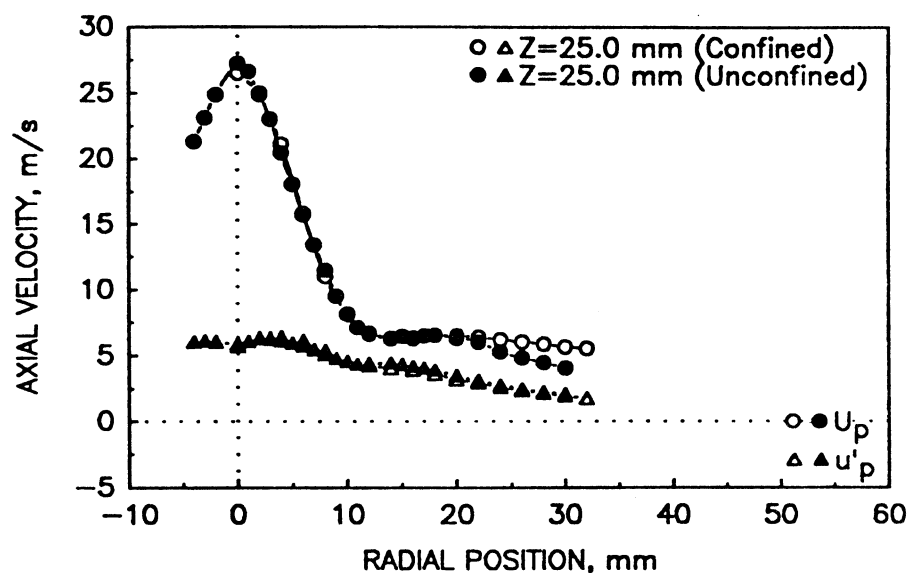
c) Sauter Mean Diameter



TE92-1914

Figure 4.8.6-1. Comparison of droplet measurements in the confined methanol spray with and without coflow (3 of 3).

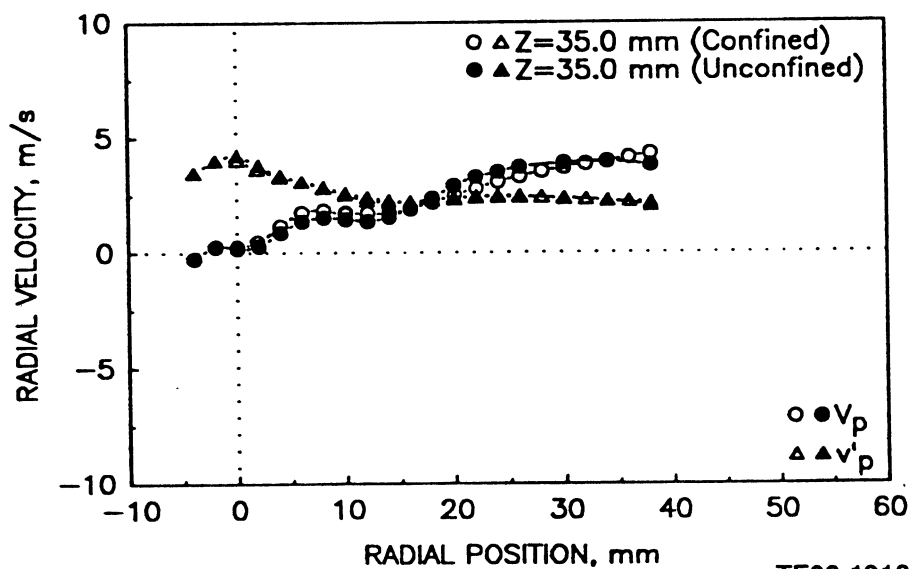
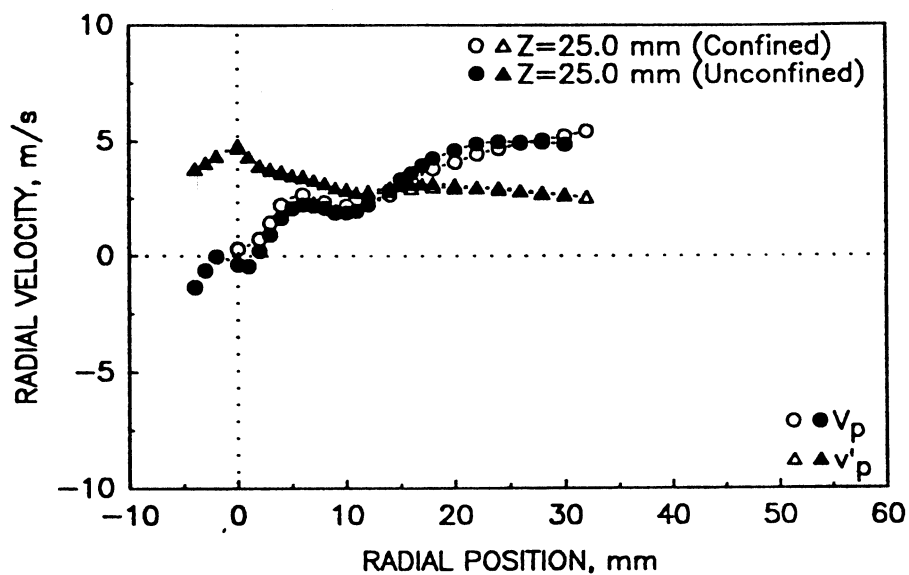
a) Mean and Fluctuating Axial Velocity



TE92-1915

Figure 4.8.7-1. Comparison of the droplet measurements in the methanol spray with and without confinement (1 of 3).

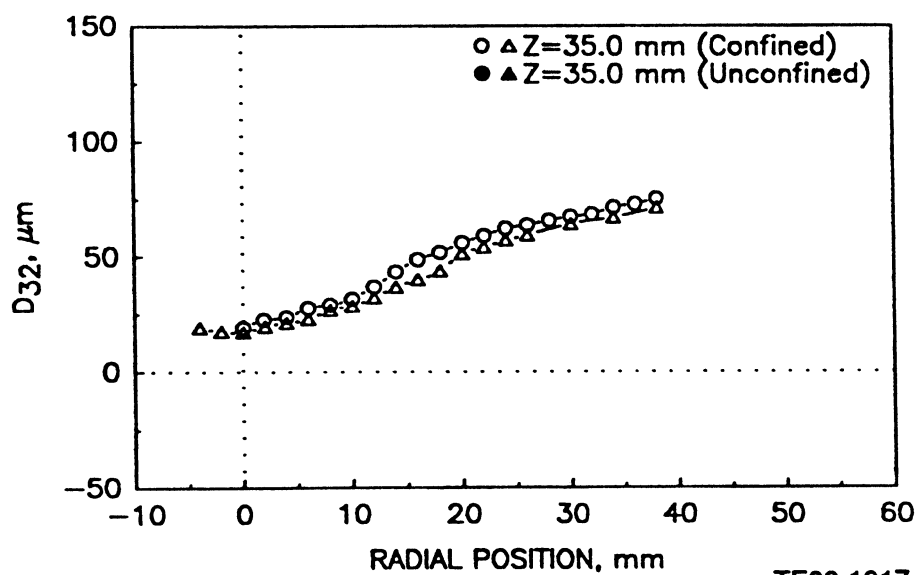
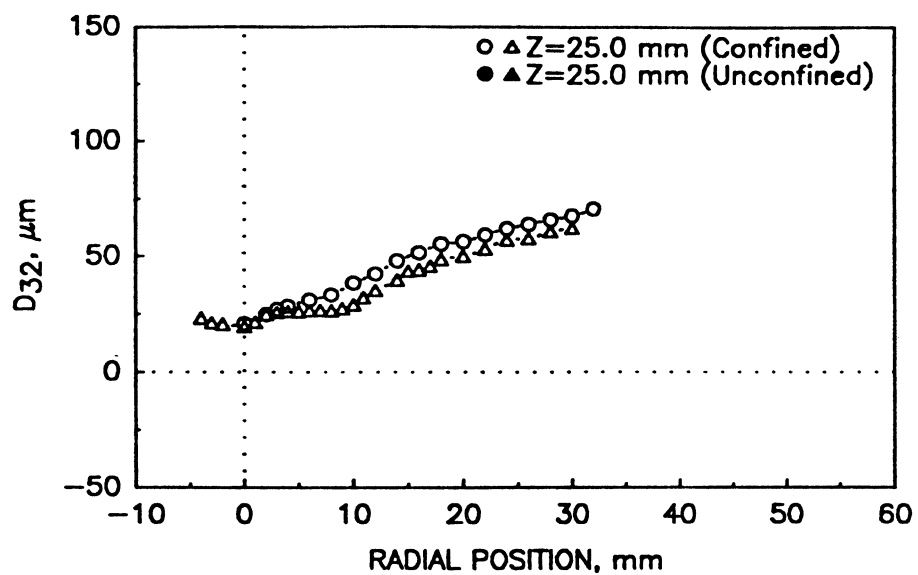
b) Mean and Fluctuating Radial Velocities



TE92-1916

Figure 4.8.7-1. Comparison of the droplet measurements in the methanol spray with and without confinement (2 of 3).

c) Sauter Mean Diameter



TE92-1917

Figure 4.8.7-1. Comparison of the droplet measurements in the methanol spray with and without confinement (3 of 3).

REFERENCES

- Faeth, G. M. and Samuelsen, G. S., 1986, "Fast-Reaction Nonpremixed Combustion," *Progress in Energy and Combustion Science*, 12, 305.
- McDonell, V. G., 1987a, "Detailed Data Set: Two-Component Gas and Particle Velocity Statistics in a Particle-Laden Axisymmetric Jet," UCI Combustion Laboratory, University of California, Irvine, ARTR-87-15.
- McDonell, V. G., 1987b, "Detailed Data Set: Two-Component Gas and Particle Velocity Statistics in Axisymmetric Methanol Sprays," UCI Combustion Laboratory, University of California, Irvine, ARTR-87-16.
- McDonell, V. G. and Samuelsen, G. S., 1991, "Data Quality Control Evaluation of the Aerometrics Two-Component Phase Doppler Interferometer," UCI Combustion Laboratory Report UCI-ARTR-91-1.

REPORT DOCUMENTATION PAGE			Form Approved OMB No. 0704-0188	
Public reporting burden for this collection of information is estimated to average 1 hour per response, including the time for reviewing instructions, searching existing data sources, gathering and maintaining the data needed, and completing and reviewing the collection of information. Send comments regarding this burden estimate or any other aspect of this collection of information, including suggestions for reducing this burden, to Washington Headquarters Services, Directorate for information Operations and Reports, 1215 Jefferson Davis Highway, Suite 1204, Arlington, VA 22202-4302, and to the Office of Management and Budget, Paperwork Reduction Project (0704-0188), Washington, DC 20503.				
1. AGENCY USE ONLY (Leave blank)		2. REPORT DATE March 1993		3. REPORT TYPE AND DATES COVERED Final Contractor Report
4. TITLE AND SUBTITLE Fuel Injector— Air Swirl Characterization Aerothermal Modeling Phase II Final Report – Volume I			5. FUNDING NUMBERS WU-505-62-52 NAS3-24350	
6. AUTHOR(S) M. Nikjooy, H.C. Mongia, V.G. McDonell, and G.S. Samuelson				
7. PERFORMING ORGANIZATION NAME(S) AND ADDRESS(ES) Allison Gas Turbine Division General Motors Corporation P.O. Box 420 Indianapolis, Indiana 40206-0420			8. PERFORMING ORGANIZATION REPORT NUMBER E-7593	
9. SPONSORING/MONITORING AGENCY NAMES(S) AND ADDRESS(ES) National Aeronautics and Space Administration Lewis Research Center Cleveland, Ohio 44135-3191			10. SPONSORING/MONITORING AGENCY REPORT NUMBER NASA CR-189193	
11. SUPPLEMENTARY NOTES Project Manager, James D. Holdeman, (216) 433-5846.				
12a. DISTRIBUTION/AVAILABILITY STATEMENT Unclassified - Unlimited Subject Category 07			12b. DISTRIBUTION CODE	
13. ABSTRACT (Maximum 200 words) A well integrated experimental/analytical investigation was conducted to provide benchmark quality data relevant to prefilming type airblast fuel nozzle and its interaction with combustor dome air swirler. The experimental investigation included a systematic study of both single-phase flows that involved single and twin co-axial jets with and without swirl. A two-component Phase Doppler Particle Analyzer (PDPA) equipment was used to document the interaction of single and co-axial air jets with glass beads that simulate nonevaporating spray and simultaneously avoid the complexities associated with fuel atomization processes and attendant issues about the specification of relevant boundary conditions. The interaction of jets with methanol spray produced by practical airblast nozzle was also documented in the spatial domain of practical interest. Model assessment activities included the use of three turbulence models (k-ε, algebraic second moment [ASM] and differential second moment [DSM]) for the carrier phase, deterministic or stochastic Lagrangian treatment of the dispersed phase, and advanced numerical schemes. Although qualitatively good comparison with data was obtained for most of the cases investigated, the model deficiencies in regard to modeled dissipation rate transport equation, single length scale, pressure-strain correlation and other critical closure issues need to be resolved before one can achieve the degree of accuracy required to analytically design combustion systems.				
14. SUBJECT TERMS Fuel nozzles; Swirling flows; Gas turbine combustion; Experimental data; Turbulent flow model validation; Two-phase flows; Turbulence modeling			15. NUMBER OF PAGES 414	
			16. PRICE CODE A18	
17. SECURITY CLASSIFICATION OF REPORT Unclassified	18. SECURITY CLASSIFICATION OF THIS PAGE Unclassified	19. SECURITY CLASSIFICATION OF ABSTRACT Unclassified	20. LIMITATION OF ABSTRACT	

National Aeronautics and
Space Administration

Lewis Research Center
Cleveland, Ohio 44135

Official Business
Penalty for Private Use \$300

FOURTH CLASS MAIL

ADDRESS CORRECTION REQUESTED



Postage and Fees Paid
National Aeronautics and
Space Administration
NASA 451

NASA
